

nature

LIVING THE HIGH LIFE

A molecular mechanism that helps flowering plants flourish at extreme altitudes

Catalytic conundrum
Why chemists struggle to cut palladium from the equation

Resource planning
Simple ways to slash energy demand and beat the fuel crisis

Carbon chains
Buckyballs get connected to form 2D sheets

Nature.2022.06.19

[Sun, 19 Jun 2022]

- [This Week](#)
- [News in Focus](#)
- [Books & Arts](#)
- [Opinion](#)
- [Work](#)
- [Research](#)
- [Amendments & Corrections](#)

This Week

- **Diversity in science prizes: why is progress so slow?** [15 Jun 2022]
 - Many prize-givers still don't publish details of nominations — a key step towards ensuring that awards are fair and unbiased.
- **Research must do no harm: new guidance addresses all studies relating to people** [14 Jun 2022]
 - Springer Nature editors urge consideration of the potential harms of all research relating to human populations, not just that directly involving human participants.
- **The human microbiome: there is much left to do** [15 Jun 2022]
 - It's time to make the survey of humanity's 'second genome' more complete.

- EDITORIAL
- 15 June 2022

Diversity in science prizes: why is progress so slow?

Many prize-givers still don't publish details of nominations — a key step towards ensuring that awards are fair and unbiased.



The organizers of the Nobel prizes should consider publishing aggregate data on the diversity of nominators and nominees for prizes. Credit: Mary Altaffer/AFP/Getty

Prizes boost careers and create role models. But some of the most prestigious awards are also among those with the most secretive selection processes — and that fuels the under-representation of women and people from minority groups among winners.

At its annual general assembly in Vienna last month, the European Geosciences Union (EGU) did something unusual. The chair of its awards committee, Thomas Blunier, presented a breakdown, by gender, of prize nominees and nominators since 2014. The data were revealing. Although women make up 37% of the society's members, they made just 20% of nominations — suggesting that women are less likely to nominate than men. The data also showed that people tend to favour their own gender when making nominations — with men most likely to nominate other men.

This is clearly a problem, but awareness of the situation opens the door to fixing it. Although women are still under-represented in EGU nominations, their share of awards is now approaching their representation among EGU members, thanks to corrective measures taken by the organization's awards committee. Sadly, however, the EGU is among the outliers — most scientific societies do not make nomination data public. They should consider doing so, because understanding patterns in nominations and nominees is integral to determining why members of groups that are marginalized in science remain under-represented among prizewinners.

Systemic barriers mean that women and people of colour, and especially women of colour, are under-represented in science in high-income nations. But this alone doesn't suffice as an explanation for award-givers, because even when the imbalance is taken into account, women remain under-represented in prizes. According to an analysis of 141 top prizes awarded over the period from 2001 to 2020, the proportion given to women fell short of the proportion of female professors in several fields¹.

The situation could well be even worse for minority genders and people of colour, but the data needed to assess this are rarely collected. The authors of an [unpublished analysis of almost 9,000 winners of science prizes](#) dating back to the eighteenth century (presented at this year's EGU meeting) managed to identify just one woman of colour.

That said, some efforts are under way to make prizes fairer. In mathematics, for example, the International Mathematical Union, which awards the Fields Medal, has introduced guidelines to make nominators and award-committee members aware of unconscious bias. Many prize nomination forms now include statements encouraging nominators to consider diversity, and the

committees that award Nobel prizes have told *Nature* that they are attempting to increase diversity in nominees and that the proportion of women nominated is rising. No Black person has won a natural-science prize in the awards' 121-year history, and just 22 women have done so.

However, neither the organizers of the Fields Medal nor the organizers of the Nobel prizes publish up-to-date aggregate data on nominators or nominees. Similarly, these data are not published for awards and prizes given by *Nature*. We are taking measures to improve diversity, and, in future, will publish aggregate data on how applications break down by region and by gender.

The necessity of data

Nobel committee members revealed to *Science* last year that women made up just 7–8% of 2021 chemistry nominees², although this, they said, was double the figure in 2018. The EGU's example shows the necessity of such data to understanding where imbalances lie and correcting them. Prize-givers, including *Nature*, should find ways to collect and publish nomination data, in particular information on race, ethnicity and country of origin; Blunier noted that the EGU does not yet record these data.

Prize-givers also need to widen their nomination pools. In 2019, *Nature* suggested that award organizers might cast their nets wider when seeking nominations³ by approaching networks that include academies of science in low- and middle-income countries, such as the International Science Council and the World Academy of Sciences. This is still not happening on the scale that it needs to. Of the three major prize-awarding organizations approached by *Nature*, only the Norwegian Academy of Science and Letters, which is responsible for the Kavli prizes and the Abel Prize, does so; it has done this since at least 2018. Members of the committees awarding Nobel prizes in physics, chemistry and economics say that invitations are global, going each year to faculty members at around 200 of 1,600 universities, chosen on a rotating basis. However, no information is released on their geographical distribution.

Universities can also play a part, particularly in boosting diversity in awards for which nominations are open, rather than invitation-only. Institutions can encourage a wider range of staff to submit nominations by training them in how to do it successfully, helping them with the administrative burden and encouraging them to put forward colleagues from under-represented groups.

Sadly, these measures will not make science prizes match global diversity, at least not straight away. Many prizes are based on work carried out decades ago, when the barriers to entering science were even higher than they are today for people from under-represented groups and countries. Excellent science and scientists exist everywhere. At the very least, professional societies must ensure that their nomination pools are representative of their communities. Greater transparency and a wider, more-diverse pool of nominees increases the chance of awards rewarding excellence, rather than amplifying existing networks of prestige.

Nature **606**, 433–434 (2022)

doi: <https://doi.org/10.1038/d41586-022-01608-z>

References

1. Meho, L. I. *Quant. Sci. Stud.* **2**, 976–989 (2021).
2. Langin, K. *Science* <https://doi.org/10.1126/science.acx9351> (2021).
3. *Nature* **574**, 295 (2019).

This article was downloaded by **calibre** from <https://www.nature.com/articles/d41586-022-01608-z>

- EDITORIAL
- 14 June 2022

Research must do no harm: new guidance addresses all studies relating to people

Springer Nature editors urge consideration of the potential harms of all research relating to human populations, not just that directly involving human participants.



The new guidance is founded on the first article of the 1948 Universal Declaration of Human Rights — all humans are “equal in dignity and rights”. Credit: Universal History Archive/Universal Images Group/Getty

In 1971, psychologist Philip Zimbardo set out to examine how the situations we find ourselves in affect our behaviour. He put human volunteers in a mock prison on the Stanford University campus in California. Participants were assigned the roles of ‘prisoner’ or ‘guard’ and asked to behave in ways befitting their roles. The experiment was extraordinary in its realism — ‘prisoners’ were even ‘arrested’ by local police. Although intended to run for two weeks, it ended on the sixth day. ‘Guards’ had subjected ‘prisoners’ to increasingly abusive, dehumanizing and brutal behaviours, causing extraordinary distress ([P. G. Zimbardo *Cognition* 2, 243–256; 1973](#)).

The Stanford prison experiment prompted much discussion about the ethics of psychological research, and rules were tightened. It could not be reproduced today — ethics committees and institutional review boards would not approve research posing such a high risk of psychological harm to participants, no matter the potential benefit to knowledge.

There are now several well-established ethics frameworks that govern studies involving human participants, including the 1964 Declaration of Helsinki (amended most recently in 2013; see [World Medical Association *JAMA* 310, 2191–2194; 2013](#)) and the 1979 Belmont Report (see [go.nature.com/3mj33xy](#)). But these are generally silent about the benefits and harms of academic research whose conclusions could affect groups of people that haven’t directly participated. Examples include research that could lead to people being stigmatized, discriminated against or subjected to racism, sexism or homophobia, among other things. Such work might be used to justify undermining the rights of specific groups, simply because of their social characteristics.

Guidance developed by Springer Nature editors aims to fill this gap in the frameworks (see [go.nature.com/3mcuoqj](#)). In essence, it encourages authors, reviewers and editors to respect the dignity and rights of groups of people. Specifically, it means at least three things: first, that the research community should consider potentially harmful implications of research as applied to groups; second, that the community should strive to minimize the potential

for misuse and the risks of harm to these groups; and third, that authors should use respectful, non-stigmatizing language in their manuscripts.

The guidance applies principles that are already cornerstones of research ethics (see go.nature.com/3anccnr): beneficence (a moral obligation to act for the benefit of others) and non-maleficence (a duty to avoid harm). It takes as a foundation the first article of the Universal Declaration of Human Rights — all humans are “equal in dignity and rights”. The declaration was adopted by the United Nations in 1948, following the atrocities of the Second World War, which the international community pledged would never happen again.

Editors, authors and reviewers should together consider and discuss benefits and harms that might emerge from manuscripts dealing with human population groups, and discuss when potential harms warrant revisions. Ethical concerns need to be flagged about research that could fuel hate speech; about potentially denigrating images; about content that could be used to undermine the dignity or rights of a human group; and about content that could cause harm in other ways. Although cases are not always clear cut, if publication risks people being harmed, authors and editors need to consider those risks against any benefits that could arise from publication.

The past few years have seen several examples of not just correction or retraction, but also removal of the kind of content that this guidance seeks to discourage. The removal of retracted content distorts the historical record, impedes accountability and prevents current and future generations from critically examining both the work and our actions. Unless there is a legal or public-health imperative, content published by Nature Portfolio journals that is retracted because it was deemed harmful to human population groups will be labelled with a retraction notice but will not be removed from the record (see go.nature.com/3qihqbd).

This guidance is ultimately about protecting people from harm. It is not about stifling ethically conducted research on differences between individuals or human groups, or discouraging work that is socially or academically controversial. Science has for too long been used to [prop up structural inequalities and discrimination in society](#), perpetuating injustice. Our guidance takes a step towards countering this. Academic freedom is a

fundamental and non-negotiable premise of scholarship. However, it is not without limits. All academic research requires ethical consideration to maximize benefits and reduce or eliminate harms.

Nature **606**, 434 (2022)

doi: <https://doi.org/10.1038/d41586-022-01607-0>

This article was downloaded by **calibre** from <https://www.nature.com/articles/d41586-022-01607-0>

| [Section menu](#) | [Main menu](#) |

- WORLD VIEW
- 15 June 2022

The human microbiome: there is much left to do



It's time to make the survey of humanity's 'second genome' more complete.

- [Ruth Ley](#)

This week marks the tenth anniversary of the first big survey of microbial diversity in the human body, published in *Nature* by the Human Microbiome Project (HMP) Consortium, of which I was a member.

Before then, microbiologists knew that the body played host to a large mass of microorganisms — a heady mix of bacteria, along with archaea, fungi and viruses, spread over the skin, in the mouth and in the gut — together dubbed the microbiome. But until 2012, we lacked an inventory of them.

In fact, this inventory — an index of 10 trillion cells belonging to thousands of species, weighing a combined 200 grams in each person — is still incomplete. It's time to build on this early work ([Human Microbiome Project Consortium](#) *Nature* **486**, 207–214; 2012), and revamp the project to represent humanity in all its complexity.

It took a long time to begin that early work, and the pace of change over the past ten years has been stunning. Only once high-throughput gene-sequencing technologies — first developed to investigate the human genome — became cheap and easy enough to use could the HMP begin.

After launching in 2007, the consortium sequenced the DNA of microbes found in and on 242 people from 2 US cities — Boston, Massachusetts, and Houston, Texas, chosen for their proximity to the two pre-eminent sequencing centres of the time, the Broad Institute of MIT and Harvard near Boston, and Baylor College of Medicine in Houston. Our activities were funded by the US National Institutes of Health's Common Fund, and the project pulled in academic microbiome bioinformaticians to work on the data after we'd generated them.

The result was the first comprehensive catalogue of a healthy US human microbiome: a full list of the genes in the microbes in the gut. The HMP showed that the gut's cellular organisms consist of thousands of species, with a genetic footprint 150 times the size of the human genome. Eventually, this abundance led biologists to view the microbiome as an environmentally acquired 'second genome', hidden in the human host.

Ten years on, we know a whole lot more. The microbiome is essential for the proper functioning of our bodies, key to digesting food and staving off pathogens. Experiments in mice have shown that microbiome compositions affect levels of social engagement and anxiety. Common illnesses such as cardiovascular disease and obesity are linked to distinct microbiomes. How babies acquire their microbiomes — and what influences the microbiomes' development — is also becoming clearer.

(Given how fundamental microbes are to our health, I still find it astonishing that we outsource so many functions to myriad organisms that we pick up from our environment, starting at birth.)

We have plenty of unanswered academic questions, too. Where did the microbiome first come from in human evolution? How are humanity's microbiomes different from those of other primates, mammals or animals more generally? How do microbiomes move from person to person? And what do changing diets and sanitized lifestyles mean for the long-term health of the microbiome?

That first analysis ten years ago, recruiting people from just two US cities, miserably failed to capture the true diversity of the human microbiome. We now know that people living in Europe and in North America have less diverse microbiomes than people living in less industrialized regions — but too little is known about differences across groups of humans.

And even less is known about the multitude of other animals that themselves contain multitudes. We know that the microbiomes of captive animals are different from those of animals living in the wild, in much the same ways that industrialized human microbiomes differ from non-industrialized ones. But most of what we know about animal microbes comes from captive-animal studies. As we lose animal diversity to rapid global change, we're also losing microbiome diversity.

Learning more will require a new consortium, sampling thousands of people and animals. We need wildlife biologists and microbiome scientists working side by side, with crews around the world. Ten years ago, analysis was so new and difficult that we spared little thought for sample acquisition. Now, sample acquisition from sources globally should lead the process.

Some might ask why we need a new, grand, expensive consortium when data are already trickling in — one study at a time, conducted by laboratories working alone. But industrialization moves fast, and modern economic forces have the power to annihilate microbial diversity faster than it can be observed.

A new consortium would empower scientists to finally fill in the microbiome map. It's like a human census: you don't wait for individual towns to report their population numbers; you make a single concerted effort to do it consistently and quickly, before it changes.

A vast new diversity analysis of humanity's microbiome, and of the broader vertebrate microbiome, will finally place our own species' data in the context of the tree of life. Only then can we truly extend the label 'human' to the microbiome.

Nature **606**, 435 (2022)

doi: <https://doi.org/10.1038/d41586-022-01610-5>

This article was downloaded by **calibre** from <https://www.nature.com/articles/d41586-022-01610-5>

| [Section menu](#) | [Main menu](#) |

News in Focus

- [**Opioid-crisis peak, science prizes and tree-species puzzle**](#) [15 Jun 2022]
 - The latest science news, in brief.
- [**NASA's Perseverance rover begins key search for life on Mars**](#) [02 Jun 2022]
 - Rolling up an ancient river delta in Jezero Crater, the rover starts crucial rock sampling.
- [**Gene therapy's comeback: how scientists are trying to make it safer**](#) [31 May 2022]
 - Unwanted immune responses threaten to derail some gene therapies. But researchers are seeking ways to combat harmful inflammation.
- [**Monkeypox vaccination begins — can the global outbreaks be contained?**](#) [08 Jun 2022]
 - Some countries have begun to use smallpox vaccines to protect people exposed to the monkeypox virus. But researchers see challenges ahead.
- [**Why call it BA.2.12.1? A guide to the tangled Omicron family**](#) [27 May 2022]
 - Nature explores how subvariants are named, and why none of Omicron's family members has been upgraded to a 'variant of concern'.
- [**Indigenous knowledge reveals history of fire-prone California forest**](#) [07 Jun 2022]
 - A collaboration between scientists and Native American tribes finds tree density in parts of the Klamath Mountains is at a record high, and at risk of serious wildfires.
- [**Why chemists can't quit palladium**](#) [14 Jun 2022]
 - A retracted paper highlights chemistry's history of trying to avoid the expensive, toxic — but necessary — catalyst.
- [**How months-long COVID infections could seed dangerous new variants**](#) [15 Jun 2022]
 - Tracking SARS-CoV-2 evolution during persistent cases provides insight into the origins of Omicron and other global variants. What can scientists do with this knowledge?

| [Next section](#) | [Main menu](#) | [Previous section](#) |

- NEWS ROUND-UP
- 15 June 2022

Opioid-crisis peak, science prizes and tree-species puzzle

The latest science news, in brief.



The *pingan* tree's fruit (left) is distinct from the *lumok* tree's (right), but Western scientists misclassified the two trees as one species for almost two centuries. Credit: left, Elias Ednie; right, Elliot Gardner

The Iban people knew all along that one tree is actually two

Western science has long considered an Asian tree with the scientific name *Artocarpus odoratissimus* to be a single species. But a genetic study ([E. M. Gardner et al. Curr. Biol. 32, R511–R512; 2022](#)) now confirms that the trees

that researchers have been lumping together as *A. odoratissimus* [actually belong to two species](#) — as reflected in the names used by the local Iban people, each of which refers to a distinct variety of the tree.

Artocarpus odoratissimus was first incorporated into Western taxonomy in 1837. In 2016, scientists working in the Malaysian state of Sarawak noticed that local botanists used two names to refer to the tree. Those botanists, who were members of Sarawak's Indigenous Iban people, called the trees with large fruit and leaves *lumok*, and those with smaller, less-sweet fruit *pingan* (pictured, *pingan* fruit).

To test whether the trees' DNA reflected this distinction, the researchers compared the genetics of *lumok* and *pingan*. The team found that the two tree types were related but distinct enough genetically to be considered separate species. *Lumok* retains the name *A. odoratissimus* and *pingan* has been given the scientific name *Artocarpus mutabilis*.

Awards named after men less likely to go to women

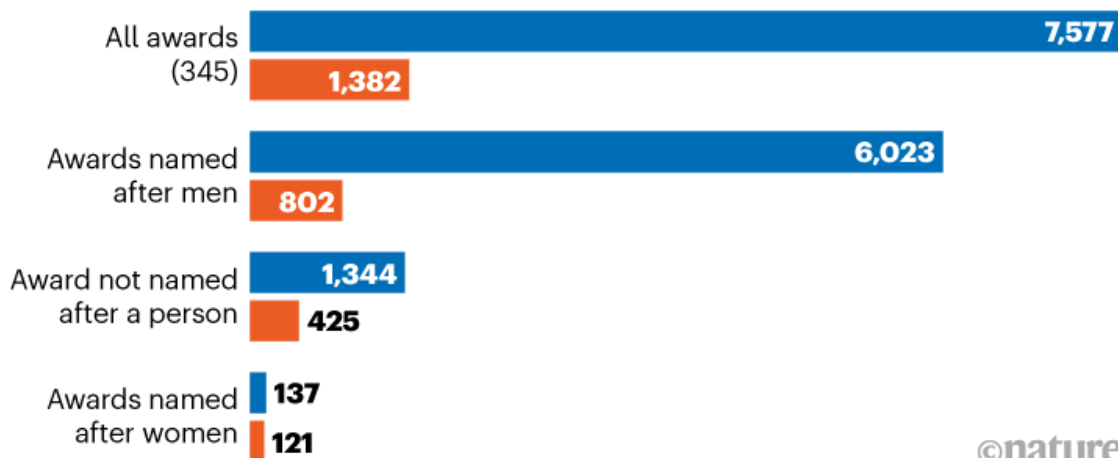
Women are more likely to [win awards that aren't named after a person](#) than to win prizes named after a man, research has found.

The study, presented on 25 May at the European Geosciences Union (EGU) general assembly in Vienna, reviewed almost 9,000 prize recipients across almost 350 awards in the fields of Earth and environmental sciences and cardiology, as well as prizes given out by national scientific bodies in the United Kingdom and United States. The study has yet to be published ([S. Krause and K. Gehmlich EGU General Assembly EGU22-2562](#) <https://doi.org/hzn2; 2022>).

AWARD WINNERS BY GENDER

An analysis of 345 scientific awards revealed that only 15.4% of winners were women. Female scientists had a better chance of winning prizes named after a woman or not named after a person than of winning those named after a man.

■ Male winners ■ Female winners



©nature

Source: Krause, S. & Gehmlich, K. EGU General Assembly EGU22-2562
<https://doi.org/hzn2> (2022)

It found that women have received only around 15% of these awards, going back to the eighteenth century. For the 214 awards that are named after men, female winners fall to just 12% (see ‘Award winners by gender’). But women were the winners 24% of the time for the 93 awards not named after anyone — a trend that was consistent over time, says Stefan Krause, an Earth and environmental scientist at the University of Birmingham, UK, who presented the research at the EGU meeting.

The results suggest that there might be a link between the name of an award and who receives it, he says. “If the awards are not named after a person, the gender balance in prizes is more balanced,” he adds.



A man holds a piece of foil that he used to smoke the potent opioid fentanyl. Credit: John Moore/Getty

US opioid overdose deaths to crest

An [opioid crisis in the United States might soon peak](#) and then start to abate, a model suggests ([T. Y. Lim et al. Proc. Natl Acad. Sci. USA 119, e2115714119; 2022](#)).

Since 1999, some 760,000 people in the country have died after overdosing on prescription and illicit opioids, including the deadly synthetic opioid fentanyl (pictured, foil used to smoke fentanyl). Treatments such as injections of the drug naloxone, which reverses overdoses, are useful. But the number of deaths continues to rise every year.

Mohammad Jalali, a systems scientist at Harvard University in Cambridge, Massachusetts, and his colleagues collected data on US opioid use and deaths between 1999 and 2020. They built a model that incorporated factors that have changed over the past 20 years, such as the prevalence of fentanyl

and the distribution of naloxone. The model relied heavily on feedback loops: an increase in fatal overdoses owing to the presence of fentanyl, for instance, might raise concern in a community and decrease overall use.

The researchers then projected future scenarios. In all of these, they found, overdose deaths are likely to peak before 2025 and then decline. In an ‘optimistic’ scenario, 543,000 people would die between 2020 and 2032, whereas a ‘pessimistic’ one would see 842,000 deaths over this period.

Nature **606**, 439 (2022)

doi: <https://doi.org/10.1038/d41586-022-01611-4>

This article was downloaded by **calibre** from <https://www.nature.com/articles/d41586-022-01611-4>

| [Section menu](#) | [Main menu](#) |

- NEWS
- 02 June 2022

NASA's Perseverance rover begins key search for life on Mars

Rolling up an ancient river delta in Jezero Crater, the rover starts crucial rock sampling.

- [Alexandra Witze](#)



Perseverance arrived at the base of an ancient river delta on Mars in April. Credit: NASA/JPL-Caltech

More than 15 months after [landing in Jezero Crater on Mars](#), NASA's Perseverance rover has finally begun its hunt for ancient life in earnest.

On 28 May, Perseverance ground a 5-centimetre-wide circular patch into a rock at the base of what was once a river delta in the crater. This delta formed billions of years ago, when a long-vanished river deposited layers of sediment into Jezero, and it is [the main reason that NASA sent the rover there](#). On Earth, river sediment is usually teeming with life.

Images of the freshly ground spot show small sediment grains, which scientists are hoping will contain chemical or other traces of life. Poet William Blake's “‘To see a world in a grain of sand’ comes to mind,” wrote Sanjeev Gupta, a planetary geologist at Imperial College London, [on Twitter](#).



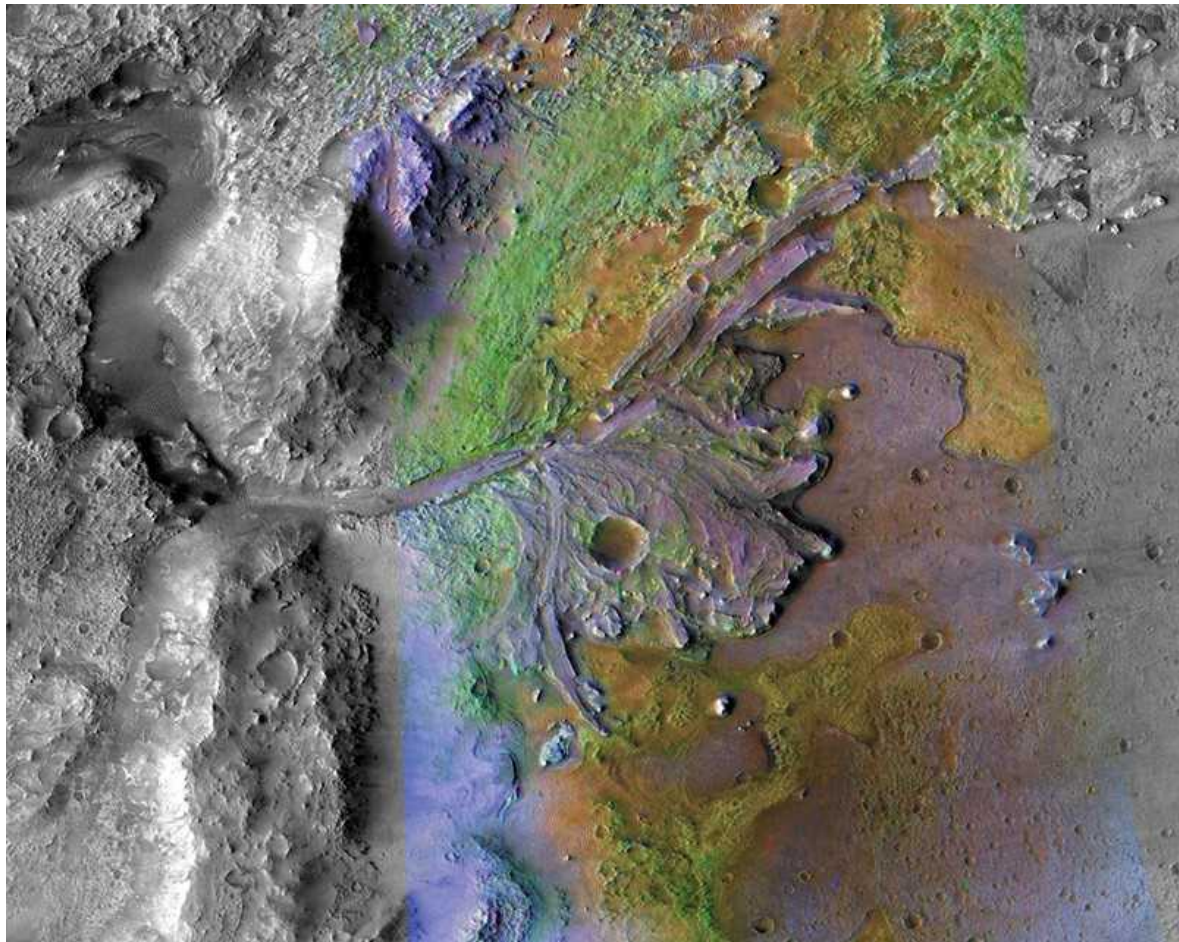
The rover ground into its first rock at the river delta in late May, clearing a circular patch for inspection.Credit: NASA/JPL-Caltech/ASU

The rover will spend the next few months exploring the Jezero delta, while mission scientists decide where they want to drill and extract rock samples. NASA and the European Space Agency (ESA) plan to retrieve those samples and fly them back to Earth for study, no earlier than 2033, in the first-ever sample return from Mars.

‘Going to the buffet’

Perseverance [landed](#) in February 2021, several kilometres from the delta’s edge. It spent many of its early months exploring the crater floor — which [unexpectedly is made of igneous rocks](#), a type that forms as molten materials cool. That was a scientific jackpot because scientists can date igneous rocks on the basis of the radioactive decay of their chemical elements. But many researchers have been keen for Perseverance to get to the delta, whose fine-grained sediments have the best chance of harbouring evidence of Martian life.

The rover finally arrived at the delta’s base in April. It soon spotted grey, thinly layered rocks called mudstones, which could have formed from sediments deposited by a slow river or lake. It also found sandstones with coarse grains, which might have formed in a fast-flowing river. These kinds of rock are excellent targets for studying a variety of Martian environments where life could have thrived, Katie Stack Morgan, Perseverance’s deputy project scientist at the Jet Propulsion Laboratory (JPL) in Pasadena, California, said on 17 May during the online portion of the 2022 Astrobiology Science Conference.



A delta formed in Jezero Crater billions of years ago, when an ancient river (whose bed is shown on the left) flowed into the formation and deposited sediment (centre of image). Sediment tends to contain organic matter, making it a good place to look for signs of ancient life. Credit: NASA/JPL/JHUAPL/MSSS/Brown University

Mission engineers then drove Perseverance away from this region, named Enchanted Lake, and towards another area known as Hawksbill Gap, where it is currently working. The freshly abraded patch was made in a sandstone in one of the lowest rock layers in the delta, which means it is one of the oldest rocks formed by Jezero's ancient river and thus an excellent place to hunt for signs of ancient life.

The delta rises about 40 metres above the crater floor. Rover drivers plan to send Perseverance up the front of the delta and then back down again, assessing where and how to take samples. "It's like going to the buffet

before you fill your plate,” says Jennifer Trosper, the mission’s project manager at JPL. On the way up, it will scout the rocks, including abrading more patches to see rock interiors. On the way down, it will drill and collect samples of the most intriguing ones.

Like a child assembling a set of gemstones for their prized collection, mission scientists are deliberating over which rocks the rover should sample to amass the most geologically diverse cache. Perseverance carries 43 tubes for samples, each a little thicker than a pencil. NASA and ESA are planning to bring around 30 filled tubes back to Earth.

Mission scientists are already considering where to set down the first set of samples for a future spacecraft to retrieve. Once the rover makes its way back down, it might put some tubes at the delta’s base, in a large flat region between Enchanted Lake and Hawksbill Gap. “There is a very strong possibility we may put down the first cache” when the rover gets there, says Kenneth Farley, the mission’s project scientist and a geochemist at the California Institute of Technology in Pasadena. “That’s when it gets real.”

Mission planners hadn’t expected to lay down samples so soon, but the location is excellent — flat and with few rocks that could get in the way of a future sample-return spacecraft. “It’s just a great place to land on Mars,” Trosper says.

NASA plans to organize a community meeting for planetary scientists in September, to assess whether the collection it has so far is ‘scientifically worthy’ enough to be picked up. That’s a key question because of all the time and money required to return the tubes. NASA wants the broader community to evaluate the mission team’s view that “we have assembled the highest value cache that we believe this site has available to us”, Farley says.

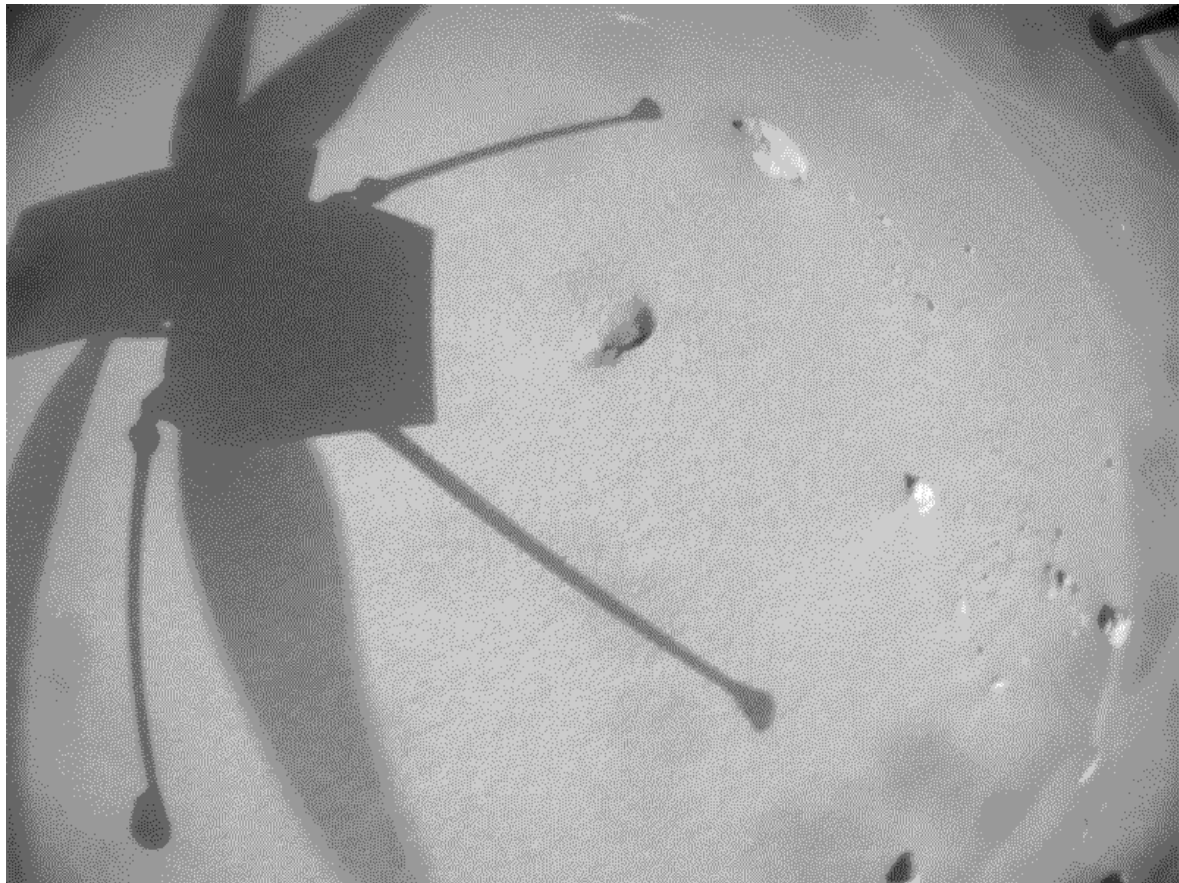
A productive mission

NASA and ESA are working on a US\$5-billion plan to send two landers to Mars — carrying a rover that would pick up the samples, and a rocket that would send them into Mars orbit — as well as a spacecraft that would grab them out of orbit and fly them back to Earth. The first launches were

supposed to happen in 2026, but that timeline was changed by Russia's invasion of Ukraine. ESA halted all cooperation with Russia's space agency over the war. The [tensions have derailed](#) a planned Russian–European Mars rover — and now NASA and ESA are redrawing their Mars-landing plans. They have some time: Perseverance's sampling tubes are designed to last for decades under Martian conditions.

Along with taking rock samples, Perseverance has made other discoveries in Jezero, including how dust devils [loft large amounts of dust](#) into the air¹ and how the speed of sound fluctuates in Mars's carbon dioxide-rich atmosphere². The rover has so far driven more than 11 kilometres, and it set an extraterrestrial distance record when it covered 5 kilometres in 30 Martian days, in March and April.

Perseverance's sidekick, [the tiny helicopter Ingenuity](#), has been instrumental in some of the rover's achievements — but its time on Mars might be coming to a close. Originally designed to make just 5 flights, it defied expectations by completing 28. From its vantage point in the skies, it has helped to scout the best routes for Perseverance, and it surveyed the flat area at the delta's base where future missions could land.



The rover's sidekick helicopter, Ingenuity, filmed this footage during its 25th flight on 8 April. It was its longest and fastest flight to date (although this GIF has been sped up by a factor of five, for viewability). Credit: NASA/JPL-Caltech

In early May, however, Ingenuity lost communication with the rover when dust in the atmosphere blocked sunlight, which the helicopter needs to charge its solar panels and battery. Ingenuity is now facing dusty skies and colder temperatures as the Martian winter descends, and might eventually have trouble flying.

“No matter what happens,” Farley says, “Ingenuity has been successful.”

Nature **606**, 441-442 (2022)

doi: [*https://doi.org/10.1038/d41586-022-01543-z*](https://doi.org/10.1038/d41586-022-01543-z)

References

1. Newman, C. E. *et al.* *Sci. Adv.* **8**, eabn3783 (2022).
2. Maurice, S. *et al.* *Nature* **605**, 653–658 (2022).

This article was downloaded by **calibre** from <https://www.nature.com/articles/d41586-022-01543-z>

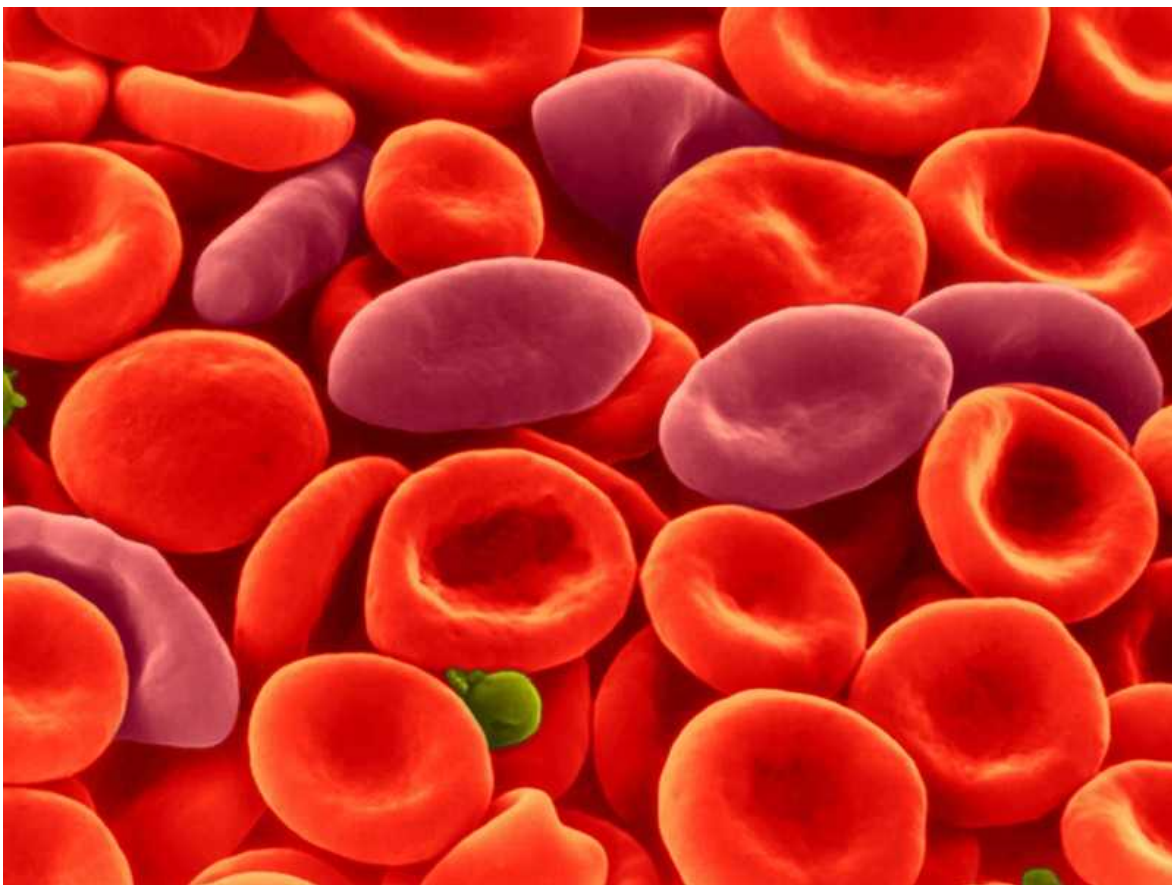
| [Section menu](#) | [Main menu](#) |

- NEWS
- 31 May 2022

Gene therapy's comeback: how scientists are trying to make it safer

Unwanted immune responses threaten to derail some gene therapies. But researchers are seeking ways to combat harmful inflammation.

- [Heidi Ledford](#)



Gene therapies for sickle-cell disease have shown promise in clinical trials. Credit: Dennis Kunkel Microscopy/SPL

After years of disappointment, gene-therapy research has undergone a renaissance, with several high-profile drug approvals and a string of promising clinical-trial results against devastating genetic diseases, including sickle-cell disease and some blood cancers.

But as researchers attempt to develop treatments for new conditions, they are also trying to work out how to cope with worrying signs that immune responses to the therapies could hinder their efforts — and generate dangerous side effects.

The concern was a popular topic at the American Society of Gene and Cell Therapy (ASGCT) annual meeting in Washington DC, held from 16 to 19 May, as presenters discussed the effects of inflammation on gene therapy and how to mitigate them. “Inflammation is par for the course, but often we don’t talk about it,” said Christine Kay, a surgeon at Vitreoretinal Associates in Gainesville, Florida, during a talk about gene therapies for eye disorders. “I’m glad that we’re beginning to.”

Safety has long been a primary concern in gene-therapy research, particularly after the death of a gene-therapy trial participant and the discovery of gene-therapy-linked cancers around the turn of the century closed clinical trials and caused investors to pull away from the burgeoning field.

But the field has resurged over the past decade, and several gene therapies have been approved by regulators around the world to treat conditions including cancer, blindness and a metabolic disorder. “We are on a roll with gene therapy,” Francis Collins, acting science adviser to US President Joe Biden, told the ASGCT meeting. “But we still have thousands of diseases that have not been approached.”

Immune interference

Researchers have long been wary of how immune responses could make gene therapies less effective. The treatments often rely on a virus to ferry a gene into cells, but if the recipient already has antibodies against that virus, an immune response could hinder the treatment. As a result, participation in

gene-therapy clinical trials is often limited to people who do not already have such antibodies.

In most gene-therapy studies, the gene is carried by one of several adeno-associated viruses (AAVs), a group of small viruses that have been studied for use in the field for nearly four decades. Thousands of people have received an AAV-based gene therapy, said Denise Sabatino, a haematology researcher at Children's Hospital of Philadelphia in Pennsylvania, at the meeting. Some gene therapies approved by the US Food and Drug Administration — including Zolgensma (onasemnogene abeparvovec), a treatment for spinal muscular atrophy, and Luxturna (voretigene neparvovec), which treats a form of retinal dystrophy that can cause blindness — rely on these viruses.

AAV vectors are also being used in clinical trials of gene-editing therapies, including those based on the popular CRISPR–Cas9 system. And the US National Institutes of Health (NIH) has launched a programme to study AAV vectors, in the hope of fostering a gene-therapy pipeline in which developers can simply swap a new therapeutic gene into the viral genome to treat a particular disease, without having to conduct large clinical trials to establish safety. Large clinical trials are particularly difficult when it comes to treatments for rare genetic disorders.

But as researchers push to treat more conditions and improve the effectiveness of their therapies, “this has become a real and present concern in AAV gene therapy”, said Fraser Wright, a gene-therapy researcher and co-founder of Spark Therapeutics in Philadelphia, which developed Luxturna, at the meeting. “As we've gone up in AAV dosing in human subjects, we have seen more and more severe adverse events.” Some of those events have included deaths, Fraser added.

Inflammatory response

The main concern used to be that antibodies against an AAV or its cargo would prevent the gene therapy from working or preclude the possibility of giving multiple doses, said Wright. But more recently, researchers have realized that antibodies could stimulate the production of inflammatory

molecules, activate cell-death pathways and trigger the development of killer T cells that could target AAV-containing cells for destruction.

Researchers at the ASGCT meeting reported efforts to tackle this inflammation from a variety of angles. Some are looking for alternatives to AAVs, and Collins noted that the NIH's Somatic Cell Genome Editing programme is studying both viral and non-viral vectors. "I think a lot of us are worried about depending on AAV forever, and would like to have things with maybe less in the way of plausible risk," he said.

At the Wyss Institute for Biologically Inspired Engineering at Harvard University in Boston, Massachusetts, viral immunologist Ying Kai Chan is trying to engineer safer AAV vectors. Risks increase when investigators use higher amounts of AAV, he said at the meeting: "I'm a huge fan of reducing the dose." But to do so, he added, might require the development of more potent treatments that use less virus.

Some are trying to 'humanize' the AAV genome, to make it less likely to activate immune pathways. For example, in humans, when the DNA base C is followed directly in the genome sequence by the base G, it often carries a chemical group called a methyl. AAV has a higher percentage of CG groups without a methyl — a potential red flag to the immune system. Wright presented data showing that increasing the methylation of CG-rich regions decreased the activation of inflammation-promoting molecules called cytokines. But, he added, there is a potential trade-off: the same methylation, if used too heavily, might also suppress gene expression, including that of the therapeutic gene carried by the AAV.

Suppressed immunity

Others are working on ways to suppress harmful immune responses. Gene therapies are often given with immunosuppressants such as steroids, but there are concerns that such treatments are sometimes ineffective, and can render recipients vulnerable to infection. Anastasia Conti, who studies stem cells at the San Raffaele Telethon Institute for Gene Therapy in Milan, Italy, reported at the ASGCT meeting that a drug called anakinra reduced inflammation triggered by gene editing. The drug might also enhance the

potency of gene-editing treatment by reducing the number of edited blood stem cells that become senescent — meaning that they are still alive but have stopped dividing.

At Selecta Biosciences in Watertown, Massachusetts, researchers are developing nanoparticles designed to be taken up by immune cells and coupled to a drug called rapamycin that is sometimes used to suppress the immune system after organ transplantation. In non-human primates, the team found that three monthly doses of the nanoparticles prevented antibody responses to the AAV's protein shell, chief scientific officer Kei Kishimoto said at the meeting. And researchers at Spark have tested a drug that inhibits an immune regulator called IL-6. They found that the treatment lowered the level of antibodies against AAV shells in non-human primates. In mice, it reduced immune responses enough to allow the animals to receive multiple rounds of gene therapy.

In the end, it will probably take a “toolbox of strategies” to tackle the inflammation problem, said Chan. And as the reach of gene therapies continues to expand, researchers need to develop tools to monitor potentially dangerous inflammation in difficult-to-access parts of the body, such as the brain, he added. Many studies on inflammation have been conducted in the eye, where researchers can relatively easily visualize changes that occur even months after therapy. “How will we really know what is happening in the central nervous system or the ear?” Chan asked. “We could fool ourselves for a long time.”

Nature **606**, 443-444 (2022)

doi: <https://doi.org/10.1038/d41586-022-01518-0>

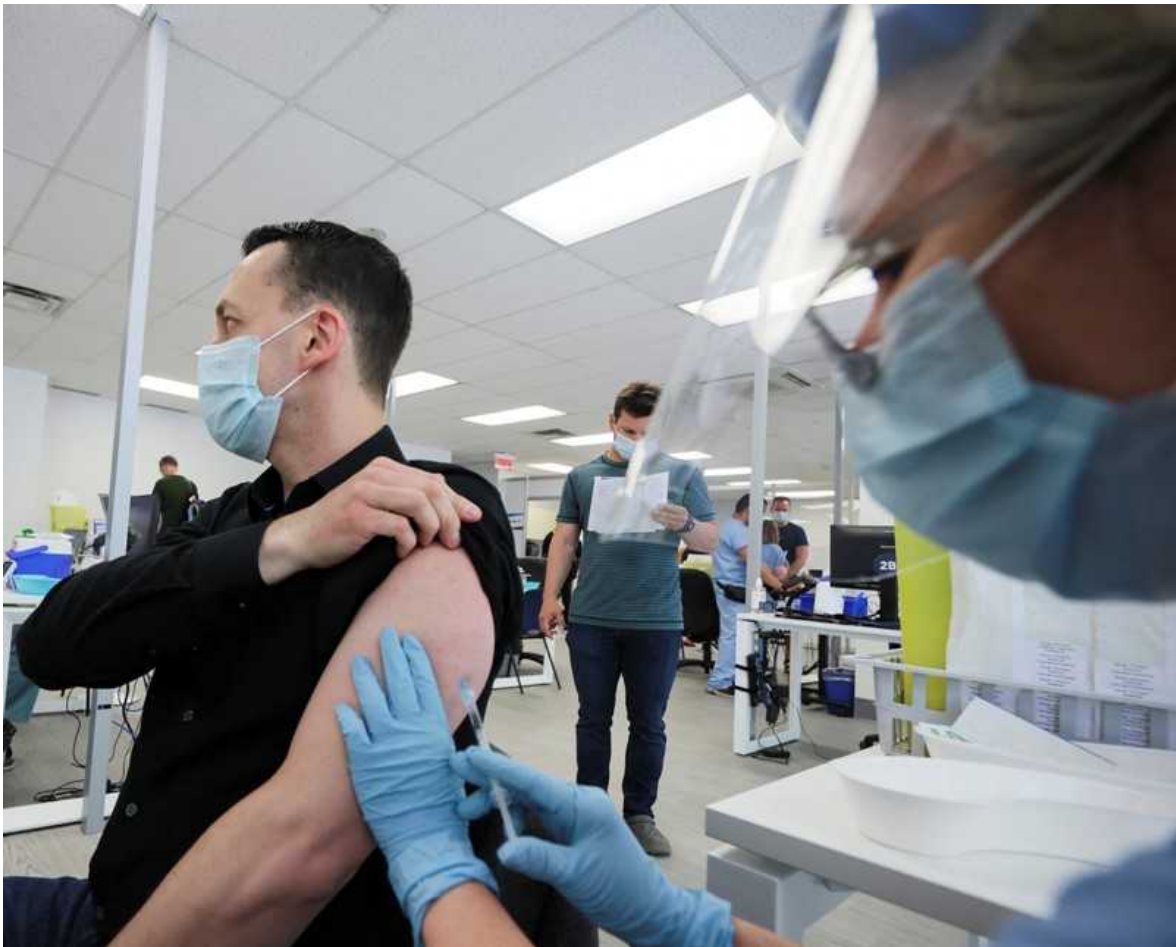
This article was downloaded by **calibre** from <https://www.nature.com/articles/d41586-022-01518-0>

- NEWS
- 08 June 2022

Monkeypox vaccination begins — can the global outbreaks be contained?

Some countries have begun to use smallpox vaccines to protect people exposed to the monkeypox virus. But researchers see challenges ahead.

- [Max Kozlov](#)



A man receives a vaccine at a monkeypox clinic in Montreal, Canada, on 6 June. Credit: Christinne Muschi/Reuters

As global monkeypox cases continue to rise, public-health officials and researchers are questioning whether the current outbreaks can be contained. The World Health Organization (WHO) has said that the situation is unlikely to escalate into a full-blown pandemic. But there are now more than 1,000 confirmed infections in nearly 30 countries where outbreaks do not usually occur (see ‘Unusual spread’).

Countries including Canada, the United Kingdom and the United States have begun implementing a strategy called ‘ring vaccination’ to try to halt the spread of the virus. This involves administering smallpox vaccines — which are thought to be effective against monkeypox because the viruses are related — to people who have been exposed to monkeypox through close contact with an infected person.

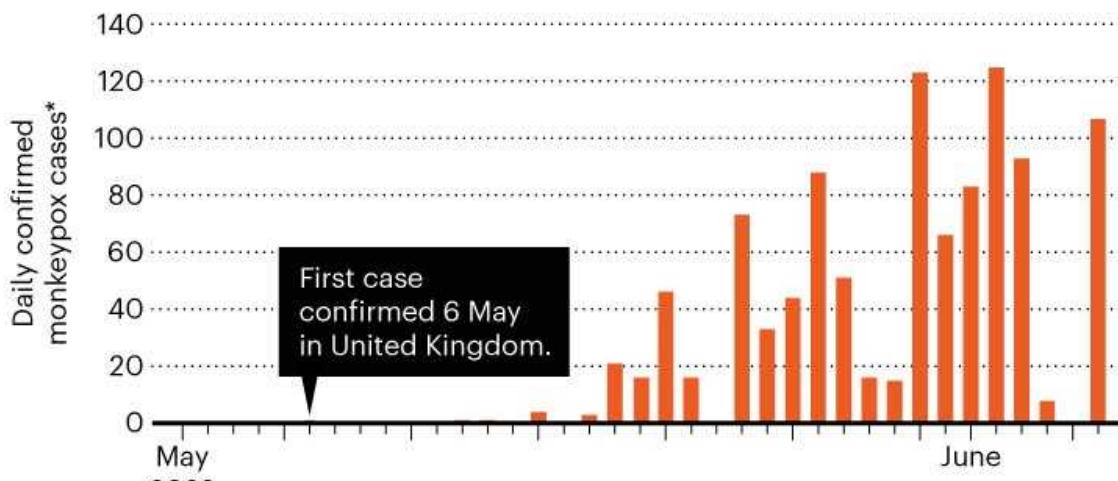
But there are unknowns and challenges that come with this strategy, says Natalie Dean, a biostatistician at Emory University in Atlanta, Georgia. Although the vaccines are considered safe and effective for use in people with smallpox infection, they have had limited testing against monkeypox. The strategy also relies on rigorous contact tracing, which might not be implemented in every country, and people must agree to be inoculated with vaccines that can trigger rare, but serious, side effects.

UNUSUAL SPREAD

Monkeypox outbreaks have been occurring in West and Central Africa for years. Occasionally, there are cases reported outside those regions — but this year has seen an explosion of monkeypox outside Africa.



More than 1,000 cases have so far been confirmed in nearly 30 countries outside Africa.



*Data as of 6 June 2022. †Data as of 26 May 2022. Nature publications remain neutral with regard to contested jurisdictional claims in published maps.

Sources: [Global health Monkeypox](#) (accessed on 2022-06-07)/WHO

Ring vaccination can be a powerful tool, Dean says, but to be effective, it needs to be used early — while case numbers are still manageable. “As the numbers crop up and you think about the number of contacts each individual has, the logistics just become more complicated.” She adds that there is a narrowing window of opportunity to prevent the virus from gaining a more permanent foothold in human or animal populations in countries where the global outbreaks are occurring.

These concerns were heightened on 3 June, when the US Centers for Disease Control and Prevention (CDC) reported genomic data showing that there are at least two strains of the monkeypox virus responsible for the outbreaks. This finding suggests that the virus might have been circulating internationally for longer than was thought. But Andrea McCollum, an epidemiologist who heads the poxvirus team at the CDC in Atlanta, Georgia, says that, although the new genomic data do not change the agency’s efforts to contain the virus, they will complicate the investigation into the outbreak’s origins.

Smallpox stockpiles

Some countries maintain stockpiles of smallpox vaccines, mainly because public-health officials have been worried that variola — the virus that causes smallpox, which was eradicated more than 40 years ago and that kills about 30% of the people who get it — could be weaponized or accidentally released from laboratories where samples are still kept. Two main types of smallpox vaccine are available today. Each contains a live poxvirus, called vaccinia virus, that is closely related to the smallpox virus. ‘Second-generation’ vaccines can cause rare but serious side effects because they contain vaccinia that can replicate in a person’s cells. ‘Third-generation’ versions have fewer side effects because they contain a weakened virus.

These smallpox vaccines are thought to be about 85% effective against monkeypox infection, according to the CDC and the WHO, which both cite “past data from Africa”, where outbreaks have occurred for decades, to support their assessments. But the highly cited figure is “shaky”, Dean cautions.

It comes from a 1988 observational study¹ carried out in Zaire (now the Democratic Republic of the Congo) involving 245 people infected with monkeypox and 2,278 of their contacts, according to McCollum. Because the second- and third-generation smallpox vaccines produce an antibody response in people that is comparable to that induced by the now-obsolete first-generation vaccines administered in the study, scientists think that the newer vaccines would have a similar efficacy against monkeypox. There is also compelling evidence from animal studies that the vaccines would work against monkeypox, but they haven't been directly tested against that disease in people, Dean says.

Unlike their response to COVID-19, public-health officials aren't currently mulling a mass-vaccination campaign for monkeypox. That's because countries have stockpiled more second-generation smallpox vaccines than third-generation versions — and the side effects of the second-generation ones prevent them from being given to children, pregnant individuals, people who are immunocompromised or those with one of a spectrum of skin conditions that are classified as 'eczema'. Third-generation vaccines, which fewer countries have access to, have fewer side effects and could therefore be given to more people.

At the moment, the risk posed by monkeypox to the general public isn't high enough to warrant mass vaccination, given the side effects and availability issues, says Daniel Bausch, the director of emerging threats and global health security at FIND, the global alliance for diagnostics in Geneva, Switzerland. But if the virus starts spreading in vulnerable populations, such as pregnant people or children, or if it turns out to have a higher fatality rate than expected, the risk–benefit calculation could change.

No deaths from monkeypox have been reported outside Africa so far this year; however, 4.7% of people who have contracted monkeypox across seven countries in West and Central Africa in 2022 have died. This makes the discussion of a ring — or even broader — vaccination campaign in nations outside Africa sting for researchers on the continent who have been fighting monkeypox outbreaks for decades, says Ifedayo Adetifa, the head of the Nigeria Centre for Disease Control in Abuja. WHO member nations have pledged more than 31 million smallpox vaccine doses to the agency for

use in smallpox emergencies, yet these doses have never been used against monkeypox in Africa.

Limited data

Usually, monkeypox causes fever, swollen lymph nodes and sometimes-painful fluid-filled skin lesions. Left untreated, the infection can clear in a few weeks — especially in those with access to health care.

Bavarian Nordic, the biotechnology firm based in Hellerup, Denmark, that created the third-generation smallpox vaccine MVA-BN, said on 30 May that it has been taking orders in response to global demand. If countries had a larger stockpile of third-generation smallpox vaccines, Raina MacIntyre, an infectious-disease epidemiologist at the University of New South Wales in Sydney, Australia, says it would be a “no-brainer” to use them for a robust ring vaccination campaign against monkeypox.

So far, the United States has been offering either a second- or third-generation smallpox vaccine regimen to people at ‘high’ or ‘intermediate’ exposure risk, which the CDC defines as a person who had “unprotected contact” with the skin or bodily fluids of a person with monkeypox, or who was within 1.8 metres (6 feet) of an infected person. Smallpox vaccines are thought to protect against monkeypox infection if administered within four days of exposure, according to the CDC.

But there are limited real-world data to support this guidance. Whereas the second-generation vaccine stockpiled in the United States is meant to be administered as a single dose, MVA-BN is a two-dose vaccine, administered with 28 days between shots. Because of a lack of testing against monkeypox in humans, it is unknown whether a single dose of MVA-BN would be enough to stop an infection, even if given within four days of exposure, McCollum says.

Challenges ahead

Even if more nations procure smallpox vaccines and begin a ring vaccination campaign, there is a large difference between theory and reality

when it comes to implementing the strategy, MacIntyre warns. In theory, monkeypox is conducive to a ring vaccination campaign because it spreads slower than most human viruses and has a long incubation period. But in reality, the success of this approach relies on robust testing and contact-tracing infrastructure, as well as the ability to quickly vaccinate any high-risk contacts, she says.

And getting people to take vaccines could be difficult. As of 24 May, only 15 of 107 community contacts and 169 of 245 health-care workers in the United Kingdom opted to take an MVA-BN vaccine after possible monkeypox exposure during the current outbreaks, according to a report in *Eurosurveillance*².

To avoid tensions and misinformation, health officials will have to communicate very clearly to the public why the campaign is necessary and why only certain individuals are receiving vaccines, says Bausch, who has worked for the WHO and the UK government to address Ebola outbreaks. Another worry is the stigma that is building up around the outbreaks: many of the cases have been in men who have sex with men. Bausch says that, if the disease continues to be stigmatized, people might not want to comply with contact-tracing efforts, which would make ring vaccination much harder.

To stop the spread of the virus, health officials will probably need to look beyond vaccination and focus on quarantine and isolation, as well as community education, he adds. As Bausch wrote in a 2021 comment about Ebola in *Nature Medicine*³, although ring vaccination has had its successes, “it is far from a panacea”.

Nature **606**, 444–445 (2022)

doi: <https://doi.org/10.1038/d41586-022-01587-1>

References

1. Jezek, Z., Grab, B., Szczeniowski, M. V., Paluku, K. M. & Mutombo, M. *Bull. World Health Organ.* **66**, 465–470 (1988).

2. Vivancos, R. *et al.* *Euro Surveill.* **27**, 2200422 (2022).

3. Bausch, D. G. *Nature Med.* **27**, 580–581 (2021).

This article was downloaded by **calibre** from <https://www.nature.com/articles/d41586-022-01587-1>

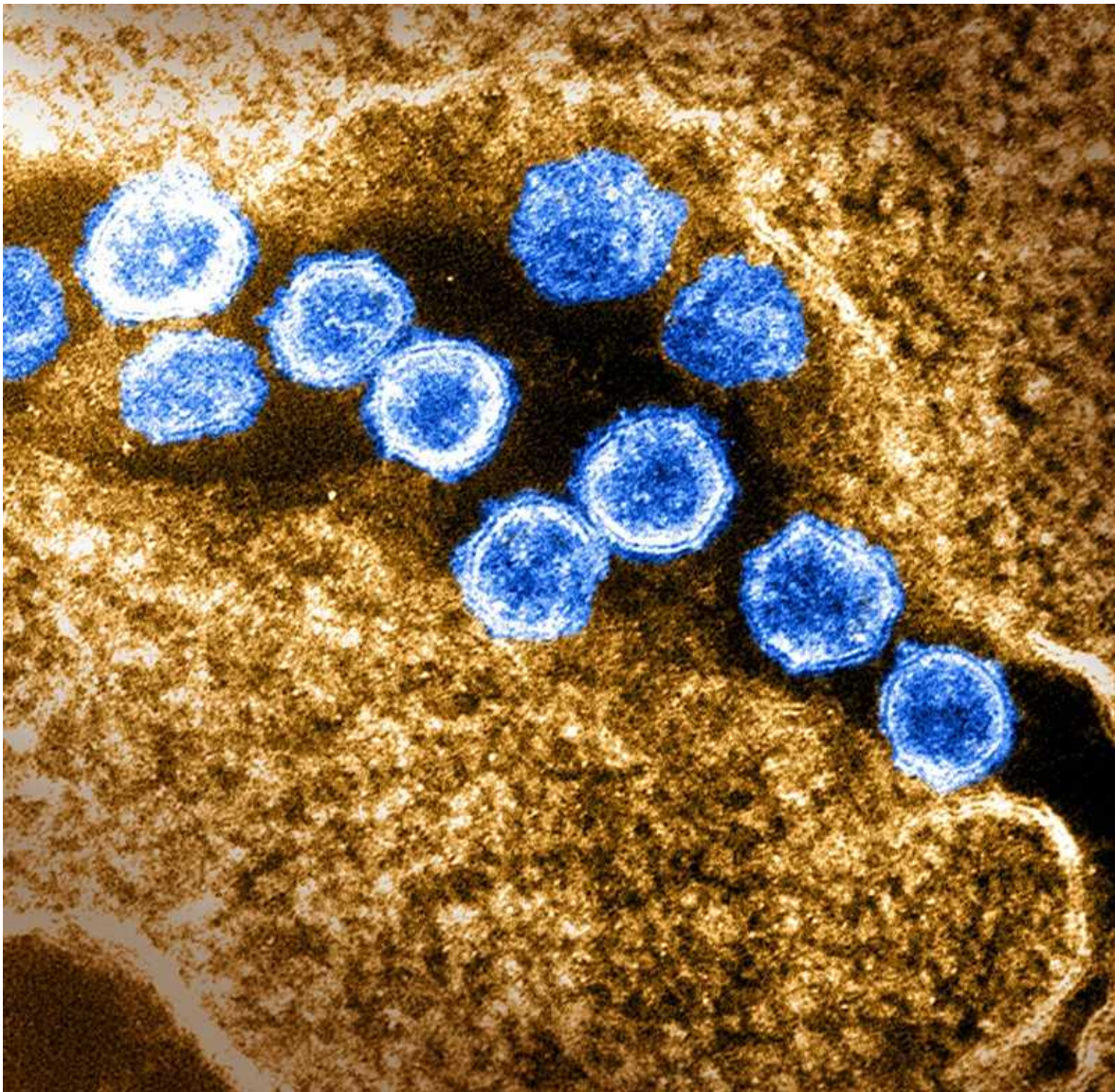
| [Section menu](#) | [Main menu](#) |

- NEWS EXPLAINER
- 27 May 2022

Why call it BA.2.12.1? A guide to the tangled Omicron family

Nature explores how subvariants are named, and why none of Omicron's family members has been upgraded to a 'variant of concern'.

- [Amy Maxmen](#)



Before naming a new variant of the SARS-CoV-2 coronavirus, researchers assess whether it represents a new lineage on the virus's family tree. Credit: National Institutes of Health/Science Photo Library

For the foreseeable future, the coronavirus SARS-CoV-2 will continue evolving into new variants that lead to waves of infections. In 2020 and 2021, the World Health Organization (WHO) announced the emergence of variants of concern by [giving them names from the Greek alphabet](#). But this year, Omicron has remained in the spotlight, with members of its family — subvariants — fuelling surges as they evade antibodies that people have generated from previous infections and vaccines. For example, the Omicron

subvariant BA.2.12.1 is gaining ground in North America, now accounting for about 26% of the SARS-CoV-2 genomes submitted to the GISAID data initiative, and BA.4 and BA.5 [are spreading rapidly in South Africa](#), comprising more than 90% of genomes sequenced.

Given the subvariants' increasing dominance, *Nature* spoke to researchers to make sense of the current wonky names, and to learn why the WHO hasn't given them Greek monikers that could spur policymakers to take stronger action.

How do scientists first identify a variant?

SARS-CoV-2 acquires mutations as it replicates in cells. Technically, this means that millions of variants probably arise every day. But the majority of mutations don't improve the virus's ability to survive and reproduce, and so these variants are lost to time — outcompeted by fitter versions.

A small portion of variants do, however, gain traction. When this happens, researchers conducting genomic surveillance flag samples that all have the same set of distinct mutations. To find out whether these samples constitute a new branch on the SARS-CoV-2 family tree, they contact bioinformaticians who have established nomenclature systems for the virus. One popular group, called Pango, consists of about two dozen evolutionary biologists and bioinformaticians who compare the samples' sequences with hundreds of others using phylogenetic software.

The group's name derives from a software program called Pangolin, originally created by bioinformatician Áine O'Toole at the University of Edinburgh, UK. If the analysis suggests that the new samples derived from the same recent common ancestor, it means that they are a distinct lineage on the coronavirus tree. In determining whether to name the lineage, Pango considers whether the variants have appeared more frequently over time, and whether their mutations are in regions of the virus that might give it a competitive edge. At this point, a lineage label doesn't indicate risk. Rather, it allows scientists to keep an eye on a variant and learn more.

“We want to name everything that jumps out at us at an early stage so that we can define it and track it, and see if it is growing quickly relative to other lineages,” says Andrew Rambaut, an evolutionary biologist at the University of Edinburgh and a member of Pango. “You probably won’t hear of most of the lineages we name,” he says, because they couldn’t compete with other versions of SARS-CoV-2 and have disappeared.

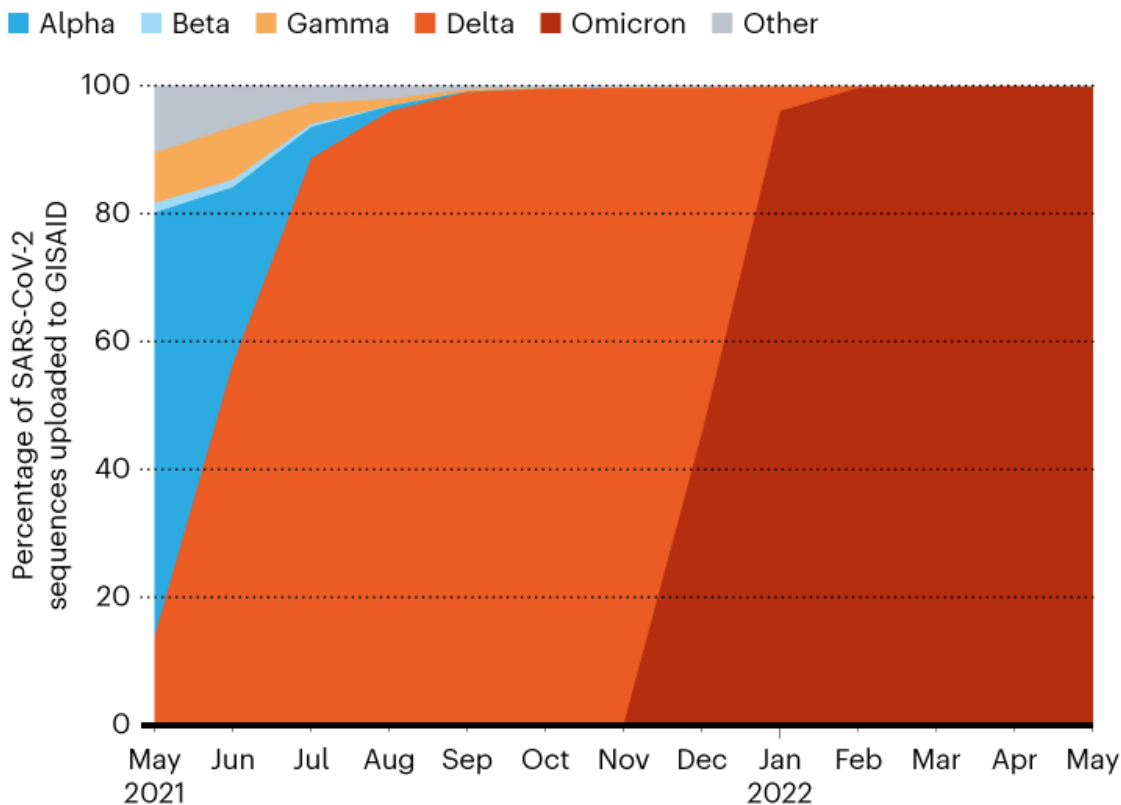
How are variants named?

When naming a variant, the Pango committee uses a hierarchical system that indicates the variant’s evolutionary history and when it was detected relative to others. The initial letters in the name reflect when Pango gave the lineage a label, following in a sequence from A to Z, then from AA to AZ, BA to BZ, and so on. Separated by a full stop, the next numbers indicate the order of branches from that lineage. For example, BA.1, BA.2, BA.3, BA.4 and BA.5 are the first five branches descending from an original Omicron ancestor. And BA.2.12.1 is the 12th lineage to branch off from BA.2, and then the first named branch on that 12th bush. All subvariants are variants, but researchers use the former term when they want to imply that the lineages belong to a larger grouping, such as Omicron.

If a variant evades the immune system much more effectively than others in circulation, causes more severe disease or is much more transmissible, the WHO might determine it to be a ‘variant of concern’ and change its name to a Greek letter (see ‘Evolution of a virus’). For instance, the multiple concerning mutations in a variant labelled as B.1.1.529 last year, coupled with its rapid rise, [prompted the WHO to change its name to Omicron](#) in November 2021. Whereas Pango’s technical names are meant to help researchers track SARS-CoV-2 evolution, the WHO’s system places a priority on the ease of communication to the public.

EVOLUTION OF A VIRUS

Variants of the SARS-CoV-2 coronavirus arise constantly as it evolves. But so far, only five have met the World Health Organization's criteria to be called variants of concern. By definition, these variants are much more transmissible, virulent or able to escape an immune response than the versions that came before them. Researchers can watch the evolution of SARS-CoV-2 by tracking genomic sequences submitted to data platforms such as GISAID.



©nature

Source: GISAID

Given all these variants, is SARS-CoV-2 evolving more rapidly than other viruses?

Not necessarily, Rambaut says. Researchers are finding an incredible amount of diversity in SARS-CoV-2, but they're also sequencing this virus at an unprecedented rate. A record 11 million SARS-CoV-2 genomes have been uploaded to the popular GISAID data platform since January 2020. By

contrast, researchers have uploaded about 1.6 million sequences of the influenza virus to GISAID's EpiFlu database since May 2008.

Still, Rambaut says, many questions remain about how SARS-CoV-2 is evolving, because sequencing is nearly absent in some parts of the world, and some countries with raging outbreaks are scaling back genomic surveillance.

Could Omicron's subvariants, such as BA.4, eventually receive Greek names?

Yes, although it hasn't happened yet. Some researchers argue that the Omicron subvariants currently fuelling surges, such as BA.4 and BA.2.12.1, deserve simpler names to aid communication with governments and the public at a time when regard for COVID-19 control measures, such as face masks, is waning. They also point out that unlike Delta's subvariants — which were not discussed much in the media — BA.4 and BA.2.12.1 can overcome immunity provided by earlier infections with other Omicron subvariants. This was unexpected, says Houriiyah Tegally, a bioinformatician at the Centre for Epidemic Response and Innovation in Stellenbosch, South Africa. "Everyone thought that only new variants would cause new waves, but now that we're seeing that Omicron can do it, maybe we should adapt the system of naming," she suggests.

But the WHO is so far resisting this idea. WHO virologist Lorenzo Subissi says that the capacity for immune evasion isn't wildly different between Omicron subvariants. He adds that the agency's assessment could change if future studies prove that an Omicron subvariant causes more severe disease than other Omicron varieties. The technical lead of the WHO's COVID-19 response, Maria Van Kerkhove, adds that the agency also doesn't recommend swapping a technical label for a Greek name in the hope of spurring leaders to take the ongoing pandemic more seriously. "This is already a scary virus, it is still killing huge numbers of people unnecessarily," she says, suggesting that world leaders should already be paying attention.

doi: <https://doi.org/10.1038/d41586-022-01466-9>

This article was downloaded by **calibre** from <https://www.nature.com/articles/d41586-022-01466-9>

| [Section menu](#) | [Main menu](#) |

- NEWS
- 07 June 2022

Indigenous knowledge reveals history of fire-prone California forest

A collaboration between scientists and Native American tribes finds tree density in parts of the Klamath Mountains is at a record high, and at risk of serious wildfires.

- [Jude Coleman](#)



Controlled fires can be used to reduce the risk of wildfires. Credit: David Hoffmann/Alamy

Indigenous oral accounts have helped scientists to reconstruct a 3,000-year history of a large fire-prone forest in California. The results suggest that parts of the forest are denser than ever before, and are at risk of severe wildfires¹. The research is part of a growing effort to combine Indigenous knowledge with other scientific data to improve understanding of ecosystem histories.

Wildfires are a substantial threat to Californian forests. Clarke Knight, a palaeo-ecosystem scientist at the US Geological Survey in Menlo Park, California, and her colleagues wanted to understand how Indigenous communities helped shape the forest by managing this risk in the state's lush western Klamath Mountains. Specifically, they studied Indigenous peoples' use of cultural burning — small, controlled fires that keep biomass low and reduce the risk of more widespread burning. The results are published in the *Proceedings of the National Academy of Science*.

“When I was a little kid, my grandmother used to burn around the house,” says Rod Mendes, fire chief for the Yurok Tribe fire department, whose family is part of the Karuk Tribe of northern California. The Karuk and Yurok tribes have called the Klamath Mountains home for thousands of years. “She was just keeping the place clean. Native people probably did some of the first prescribed fire operations in history,” says Mendes.

Understanding how Indigenous tribes used fire is essential for managing forests to reduce wildfire risk, says Knight. “We need to listen to Native people and learn and understand why they managed the landscape the way they did,” adds Mendes.

Collaboration for corroboration

To map the region’s forest history, the team drew on historical accounts and oral histories from Karuk, Yurok and Hoopa Valley Tribe members collected by study co-author Frank Lake, a US Forest Service research ecologist in Arcata, California, and a Karuk descendant, as part of his PhD thesis in

2007. These accounts described the tribes' fire and land use. For instance, members lit small fires to keep trails clear; this also reduced the amount of vegetation, preventing expansion of wildfires from lightning strikes. Larger fires, called broadcast burning, were used to improve visibility, hunting and nut-harvesting conditions in the forest. The effects of fire on the vegetation lasted for decades.

Knight says that it was important to collaborate with the tribes given their knowledge of the region. The Karuk Resources Advisory Board approved a proposal for the study before it began. "In a way, it's decolonizing the existing academic model that hasn't been very inclusive of Indigenous histories," says Lake.

The researchers also analysed sediment cores collected near two low-elevation lakes in the Klamath Mountains that are culturally important to the tribes. Layers of pollen in the cores were used to infer the approximate tree density in the area at various times, and modelling helped date the cores so they could estimate how that density changed.

The team also measured charcoal in the cores' layers, which helped to map fluctuations in the amount of fire in the region. Burn scars on tree stumps pointed to specific instances of fire in between 1700 and 1900. Because the stumps' rings serve as an ecological calendar, the researchers were able to compare periods of fire with corresponding tree-density data. They then pieced together how this density fluctuated with fire incidence. Although these empirical methods could not specifically confirm that the fires were lit by the tribes, patterns suggested when this was more probable, says Knight. For instance, increased burning in cool, wet periods, when fires caused by lightning were probably less common, suggested a human influence.

Combining multiple lines of evidence, Knight and her team show that the tree density in this region of Klamath Mountains started to increase as the area was colonized, partly because the European settlers prevented Indigenous peoples from practising cultural burning. In the twentieth century, total fire suppression became a standard management practice, and fires of any kind were extinguished or prevented — although controlled burns are currently used in forest management. The team reports that in

some areas, the tree density is higher than it has been for thousands of years, owing in part to fire suppression.

Healthy forest

A dense forest isn't necessarily a healthy one, says Knight. Douglas firs (*Pseudotsuga menziesii*), which dominate the lowland Klamath forests, are less fire resilient and more prone to calamitous wildfires. "This idea that we simply should let nature take its course is just not supported by this work," she says. She adds that one of the study's strengths is the multiple lines of evidence showing that past Indigenous burning helped to manage tree density.

Fire ecologist Jeffrey Kane at the California State Polytechnic University Humboldt in Arcata says that the study's findings of increased tree density are not surprising. He has made similar observations in the Klamath region. "There's a lot more trees than were there just 120 years ago," he says.

Dominick DellaSala, chief scientist at forest-protection organization Wild Heritage in Talent, Oregon, points out that the results suggesting record tree densities cannot be applied to the entire Klamath region, owing to the limited range of the study's lakeside data.

Knight, however, says that the results can be extrapolated to other similar low-elevation lake sites that have similar vegetation types.

More Indigenous voices

Palaeoecology studies are increasingly incorporating Indigenous knowledge — but there's still a long way to go, says physical geographer Michela Mariani at the University of Nottingham, UK. In Australia, Mariani has also found that tree density began to increase after British colonization hampered cultural burning. "It's very important that we now include Indigenous people in the discussion in fire management moving on," Mariani says. "They have a deeper knowledge of the landscape we simply don't have."

Including Indigenous voices in research is also crucial for decolonizing conventional scientific methods, Lake emphasizes. It “becomes a form of justice for those Indigenous people who have long been excluded, marginalized and not acknowledged”, he says.

Nature **606**, 447 (2022)

doi: <https://doi.org/10.1038/d41586-022-01232-x>

References

1. Knight, C. A. *et al. Proc. Natl Acad. Sci. USA* **119**, e2116264119 (2022).

This article was downloaded by **calibre** from <https://www.nature.com/articles/d41586-022-01232-x>

| [Section menu](#) | [Main menu](#) |

- NEWS FEATURE
- 14 June 2022

Why chemists can't quit palladium

A retracted paper highlights chemistry's history of trying to avoid the expensive, toxic — but necessary — catalyst.

- [Ariana Remmel](#)



Illustration by Fabio Buonocore

It's hard to find a place on Earth untouched by palladium. The silvery-white metal is a key part of catalytic converters in the world's 1.4 billion cars, which spew specks of palladium into the atmosphere. Mining and other sources add to this pollution. As a result, traces of palladium show up in some of the most remote spots on Earth, from Antarctica to the top of the Greenland ice sheet.

Palladium is also practically indispensable for making drugs. That's because catalysts with palladium atoms at their core have an unmatched ability to help stitch together carbon–carbon bonds. This kind of chemical reaction is key to building organic molecules, especially those used in medications. "Every pharmaceutical we produce at some point or another has a palladium-catalysed step in it," says Per-Ola Norrby, a pharmaceutical researcher at drug giant AstraZeneca in Gothenburg, Sweden. Palladium-catalysed reactions are so valuable that, in 2010, [their discoverers shared a Nobel prize](#).

But despite its versatility, chemists are trying to move away from palladium. The metal is more expensive than gold, and molecules that contain palladium can also be extremely toxic to humans and wildlife. Chemical manufacturers have to separate out all traces of palladium from their products and carefully dispose of the hazardous waste, which adds extra expense.

Thomas Fuchß, a medicinal chemist at the life-sciences company Merck in Darmstadt, Germany, gives the example of a reaction to make 3 kilograms of a drug molecule for which the ingredients cost US\$250,000. The palladium catalyst alone adds \$100,000; purifying it out of the product another \$30,000.

Finding less-toxic alternatives to the metal could help to reduce environmental harm from palladium waste and move the chemicals industry towards 'greener' reactions, says Tianning Diao, an organometallic chemist at New York University. Researchers hope to swap palladium for more common metals, such as iron and nickel, or invent metal-free catalysts that sidestep the issue altogether.

Several times in the past two decades, researchers have reported finding palladium-free catalysts. But in what has become a recurring pattern for the field, each heralded discovery turned out to be a mistake.

Then, last year, came an exciting result. A stunning report in January 2021 seemed to put the palladium-free dream within reach¹. Researchers in China reported that a 'carbon coupling' reaction, one of the most common carbon-bond-forming reactions in the drug industry, could be catalysed without

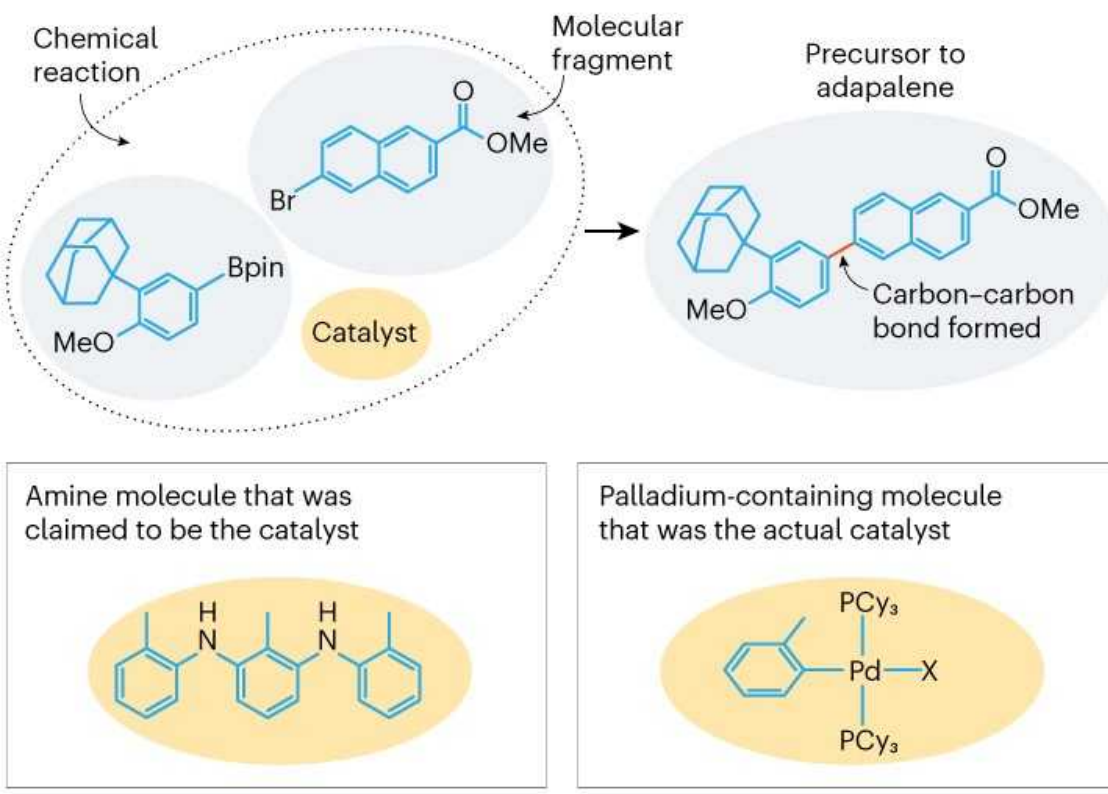
palladium or any other metal. If the findings were confirmed, the reaction would change everything we know about how carbon bonds are formed, says Norrby.

Chemists were instantly excited — and sceptical. Researchers around the world attempted to verify the extraordinary claims in their own laboratories. Within two months, three teams published preprints (working papers prior to peer review) arguing that palladium contamination was catalysing the coupling reaction.

Those critics would turn out to be right (see ‘Carbon coupling’). The discovery-that-wasn’t, and questions about how the mistake was made, has dominated discussion in some analytical and pharmaceutical chemistry circles. The saga serves as a cautionary tale about how incredibly difficult it is for chemists to keep their reactions and laboratories free from palladium contamination.

CARBON COUPLING

A common reaction in making drugs is ‘carbon coupling’: linking two molecular fragments together by a carbon–carbon bond. This process requires a catalyst that usually contains palladium (Pd). In 2021, chemists claimed to do it using an amine catalyst, but others showed that a Pd-containing molecule was responsible. This example shows part of the synthesis of an acne treatment called adapalene.



Source: Adapted from refs. 1 & 7

Cautionary tales

British chemist Nicholas Leadbeater says when he saw the new claims, the first thought that ran through his head was: “here we go again”. In 2003, Leadbeater was pursuing a palladium-free route to carbon-coupling reactions at King’s College London. His team was trying to catalyse common reactions with a combination of copper compounds and microwave heating. But when they ran a control experiment without any metals at all, the reactions still worked. Understanding what a remarkable feat this was,

Leadbeater and his colleagues took great pains to ensure that no palladium had snuck into the reaction unnoticed.

The team's papers were met with huge acclaim; Leadbeater was sure that the discovery would be the linchpin of his career. Then he moved his research group to the University of Connecticut in Storrs, and things all came apart. "We couldn't make it work no matter what we tried," he says.

After months of detective work, Leadbeater found the culprit. A common reagent bought from a UK chemical supplier had been contaminated with minute traces of palladium — around 50 parts per billion (p.p.b.) — that was absent from the same product bought in the United States. "That was enough to catalyse the reaction," he says. Leadbeater never retracted his original papers. The team instead published an analysis² showing that the metal-free reaction could yield a small amount of their desired molecule, but that palladium contamination was ultimately responsible for the previously reported results.

The same problem cropped up in 2008, when a paper by Robert Franzén at Tampere University of Technology in Finland and his colleagues reported an iron-catalysed version of another carbon-coupling reaction. A research team led by Robin Bedford at the University of Bristol, UK, found that palladium contaminants were responsible, and published a "cautionary tale" about the risks of false positives³. The Finnish team's paper was retracted. Norrby says that even his team's successful development of a nickel-catalysed reaction was initially plagued by palladium contamination that stymied progress⁴.

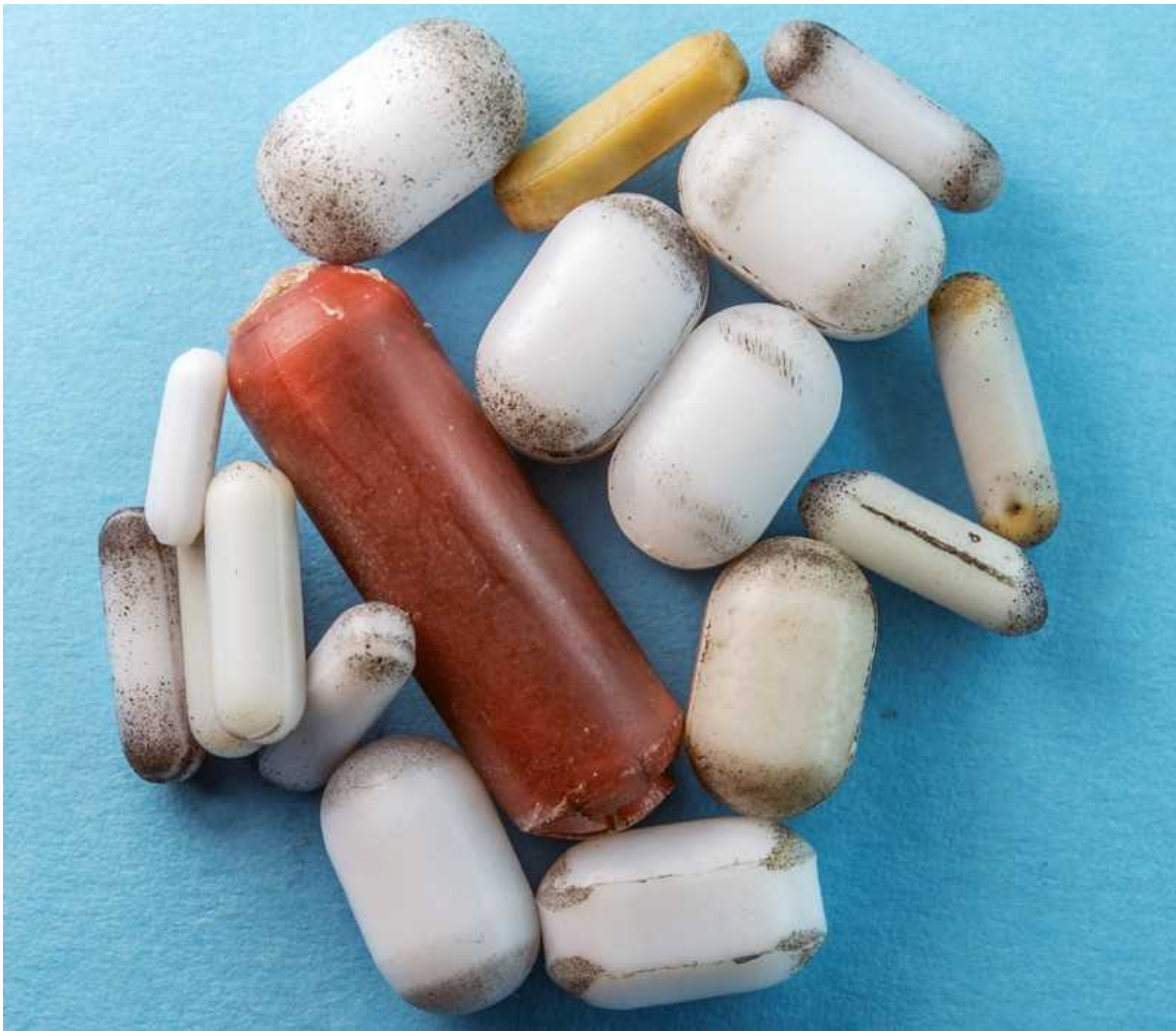
The chemistry literature is littered with palladium-related controversies such as these, researchers say: some have been definitively debunked, while suspicion lingers over others. "This has become a minefield," Leadbeater says.

Phantom catalysis

Medicinal compounds are often large, complex molecules, so chemists have to synthesize them piece by piece. Carbon-coupling reactions join those

fragments together. But the energy needed to make and break bonds in the coupling partners can render these reactions slow, if not impossible, without a catalyst, says Diao. Palladium catalysts are especially good at overcoming these energetic barriers because the metal's unique electronic structure makes it a versatile matchmaker for a huge diversity of molecular fragments, she says.

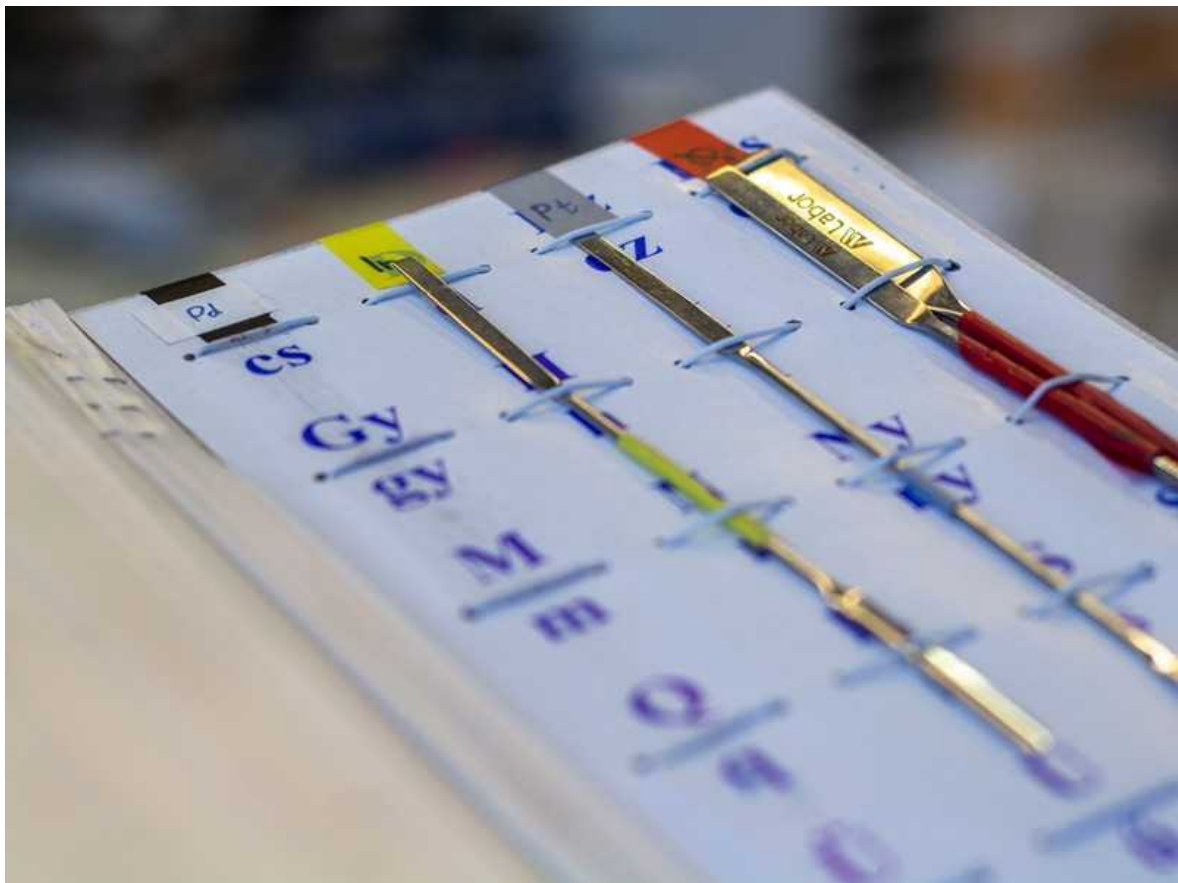
But palladium compounds are now so widely used that the metal gets everywhere. Even scratches in the whirling magnetic stir bars, used routinely to mix liquids in chemistry labs, can trap trace amounts of palladium sufficient to jump-start some reactions, according to a 2019 study led by Valentine Ananikov at the Russian Academy of Sciences in Moscow⁵. This ‘phantom catalysis’ can make it seem as if a reaction is proceeding without a catalyst, Ananikov says. “One must be extremely careful, because palladium can penetrate through contaminated labware, as well as through impurities in chemicals and solvents,” he says.



Dirty magnetic stir bars can trap trace amounts of metals, which can catalyse chemical reactions. Credit: Pentsak, E. O., *et al./ACS Catal.*

Chemists with experience of staving off unwanted palladium follow strict protocols to limit its spread. Gergely Tolnai and Zoltán Novák, synthetic organic chemists at Eötvös Loránd University in Budapest, restrict palladium use to a designated quadrant of the research lab. Tolnai's team also labels its spatulas for exclusive use with particular metals to avoid any possible cross-contamination. In Bedford's lab, researchers are prohibited from sharing glassware and they use new stir bars when palladium contamination is a concern. They even treat commercial reagents, marketed as ultra-pure, to remove any lingering palladium. Researchers analyse the final reaction mixture for contamination, too, in case an unknown agent introduced impurities along the way.

“We’re a little bit superstitious about anything related to palladium,” says Tolnai.



Spatulas labelled for use exclusively with certain metals, to prevent contamination.Credit: Gergely L. Tolnai

Three years of precautions

The chemists in China who reported a palladium-free reaction in 2021 claimed that their carbon-coupling catalyst contained no metals: only an organic molecule with nitrogen-containing structures called amines. The snag was that they used palladium to make their amine catalyst.

The team, led by Hua-Jian Xu at the Hefei University of Technology and Hai-Zhu Yu at Anhui University in Hefei, knew that palladium hanging over from this synthesis could foul their later experiments. So they went to great lengths to ensure that this didn't happen.

First, the researchers purified their amine catalyst from palladium by using a kind of chromatography, based on the principle that molecules with different polarities (a property related to the distribution of electric charge) move through a silica gel at different speeds. This aimed to separate the catalyst from any leftover metal complexes.

Then they mixed the purified amine catalyst with a scavenger complex that was supposed to bind to and remove any remaining traces of palladium.

Finally, they dunked a sample of the amine catalyst in a nitric acid solution to chew the compound up into fragments. That would liberate any residual palladium atoms tied up in organic complexes. These acid-digested parts could then be analysed using mass spectrometry to search for any signals indicating the presence of palladium on the basis of mass and charge. The technique is the gold standard for detecting metal contamination, other researchers say.

These experiments showed less than 1 p.p.b. of palladium, and any other potentially reactive metal, in the catalyst or the reaction mixture. Even when the researchers deliberately added palladium to their reactions, the product would not form without the amine catalyst, Xu wrote in February 2021 in a blog post addressing questions about the work. (The post was later taken down.) He also wrote that the team spent more than three years reproducing and validating the results before publishing its paper in *Nature Catalysis*.

These were all sensible precautions, says Bedford. When he and his colleagues tried to replicate the work by following the paper's methods, the results were consistently reproducible — until the purportedly crucial amine catalyst was made without palladium. Then, the reaction stopped working.

Setting the record straight

Attempts to independently verify the *Nature Catalysis* report began within weeks of its publication. As the paper circulated among researchers on Twitter, chemists quickly homed in on the potential complications posed by the amine catalyst synthesis. Scientific collaborations started to coalesce out

of the Twitter threads, and soon preprint manuscripts appeared critiquing the work.

By February 2021, Tolnai and Novák had reported⁶ that trace palladium impurities left over after making the amine catalyst were the true catalyst for the reaction. In March 2021, Bedford and his colleagues reported⁷ the exact palladium species involved — a compound that chemists already knew to be a highly active catalyst.

Unknown to Xu and Yu's team, the palladium left behind in the amine catalyst's synthesis formed a metal complex that was uncannily capable of evading their purification efforts. This complex has a similar polarity to the catalyst itself, so the two don't separate in the chromatography protocol the researchers used. Xu, Yu and their colleagues also chose a scavenger that's not good at binding to this particular compound. The gold-standard spectrometry technique also missed the lingering palladium because the nitric acid digest preparation wasn't harsh enough to break down the complexes, so the instrument reported no clear signal of palladium. Novák says that only by using concentrated acids at high temperatures was it possible to break apart the palladium interloper.

Then in April 2021, Kazunori Koide, an organic chemist at the University of Pittsburgh, Pennsylvania, and his colleagues published a third set of findings on the reaction⁸. Koide's team used a new detection system, developed in his lab, involving a molecular sensor that fluoresces when it reacts with dissolved palladium. The team's analysis corroborated the presence of palladium contamination. Koide is working with collaborators at Merck Research Laboratories in Rahway, New Jersey, to develop this platform as an alternative to mass spectrometry for spotting palladium adulterants.

Nature Catalysis posted an editorial expression of concern on the paper of Xu and Yu's team in March 2021, but the case was not officially closed for another nine months, when Xu and his colleagues formally retracted the paper on 8 December 2021. At the same time, *Nature Catalysis* published peer-reviewed versions of the reports by the teams of Tolnai and Novák, Bedford and Koide. In an editorial⁹ [published alongside the retraction](#), *Nature Catalysis* editors said the editors and authors involved — including critics — did not want to rush the process of examining the initial claim, and

the retraction came only after everyone involved agreed that the original conclusions were flawed.

Xu and Yu declined to answer questions, save for an e-mailed statement in which Xu acknowledged that the palladium used to make the amine was the primary cause of the “misjudgement”. Xu added: “This event and many previous reports also reflect that the challenge of non-palladium-catalysed classical coupling reaction is indeed very difficult”.

In the accompanying editorial, *Nature Catalysis* editors said the episode was a testament to the effectiveness of self-correcting science. They also noted that concerns about trace palladium had been raised during the paper’s initial peer review, but that the scientists’ tests seemed to rule out metal contamination. A spokesperson said the editorial was the journal’s full statement on the matter.

To some extent, given the layers of precautions described in the paper’s methods, the researchers were just unlucky, Bedford says. And in a study that used methods from several disciplines, such as organic synthesis, reaction kinetics and analytical chemistry, critics needed deep knowledge of many subject areas to get the bottom of the issue, Tolnai and Novák say. Novák was tipped off to problems with the spectrometry analysis only because he was reading the paper over breakfast with his wife Zsuzsanna Czégény, an analytical chemist at the Institute of Materials and Environmental Chemistry in Budapest. Although Czégény is not a specialist in metal-detecting spectroscopy, she recognized issues with the sample-preparation methods, which Novák and his colleagues later proved in their paper.

The instant discussion on Twitter, fast publication of preprints, and rapid expression of concern issued by *Nature Catalysis* did demonstrate how quickly chemists could vet palladium-free claims. Just one paper, published in *Chemical Science* in October 2021¹⁰, cited Xu and Yu’s results before their retraction. One of the paper’s authors, Bien Tan at Huazhong University of Science and Technology in Wuhan, China, said in an e-mailed statement that his team was eager to apply Xu and Yu’s “ground-breaking progress” to their own research. He says that the methods were highly reproducible, and he didn’t see the criticism on social media because he does

not use Twitter. Tan says he did not learn of concerns until after his paper was published, when editors at *Chemical Science* brought them to his attention. Tan and his team retracted their paper after a month. “This work has cost us a lot of time and money,” he says.

Forging ahead

Many researchers say they’re undeterred in their pursuit of alternative ways to build carbon-based molecules without palladium. Scientists continue to chip away at the palladium problem piece by piece — here and there finding reactions catalysed by specialized iron- or nickel-containing compounds.

But these isolated examples have so far struggled to make the transition from small batch reactions in academic labs to the massive production needs of manufacturers. Process chemists in the pharmaceutical industry are still left with only a handful of alternative catalysts to perform a small fraction of their routine reactions, says Fuchß.

Even if chemists can’t quit palladium entirely, the search for alternative catalysts could still reveal fresh ways of building molecules, says Diao. She hopes that understanding more about how successful catalysts shuffle electrons to make challenging bonds could “lead to new, revolutionary chemistries” that don’t use palladium.

Her lab has focused on designing nickel catalysts that can fill in for some palladium-catalysed reactions. And Diao has her sights set on the next frontiers of organic synthesis, such as catalysts that harness light energy to drive reactions. “I think the greatest potential for nickel is to catalyse the reactions that palladium can’t do,” she says.

Will the lessons of this failed attempt at palladium-independent coupling stick? It’s probably too soon to tell, researchers say. “I wouldn’t be surprised if this happens again ten years from now,” Koide says.

Nature **606**, 448-451 (2022)

doi: <https://doi.org/10.1038/d41586-022-01612-3>

References

1. Xu, L. *et al.* Retraction: *Nature Catal.* **4**, 71–78 (2021), retraction **4**, 1089 (2021).
2. Arvela, R. K. *et al.* *J. Org. Chem.* **70**, 161–168 (2005).
3. Bedford, R. B. *et al.* *Tetrahedron Lett.* **50**, 6110–6111 (2009).
4. Grigalunas, M., Ankner, T., Norrby, P.-O., Wiest, O. & Helquist, P. *J. Am. Chem. Soc.* **137**, 7019–7022 (2015).
5. Pentsak, E. O., Eremin, D. E., Gordeev, E. G. & Ananikov, V. P. *ACS Catal.* **9**, 3070–3081 (2019).
6. Novák, Z. *et al.* *Nature Catal.* **4**, 991–993 (2021).
7. Avanthay, M. *et al.* *Nature Catal.* **4**, 994–998 (2021).
8. Vinod, J. K., Wanner, A. K., James, E. I. & Koide, K. *Nature Catal.* **4**, 999–1001 (2021).
9. *Nature Catal.* **4**, 987–988 (2021).
10. Liu, Q., Jin, S. & Tan, B. *Chem. Sci.*
<https://doi.org/10.1039/D1SC03970A> (2021), retraction
<https://doi.org/10.1039/D1SC90250D> (2021).

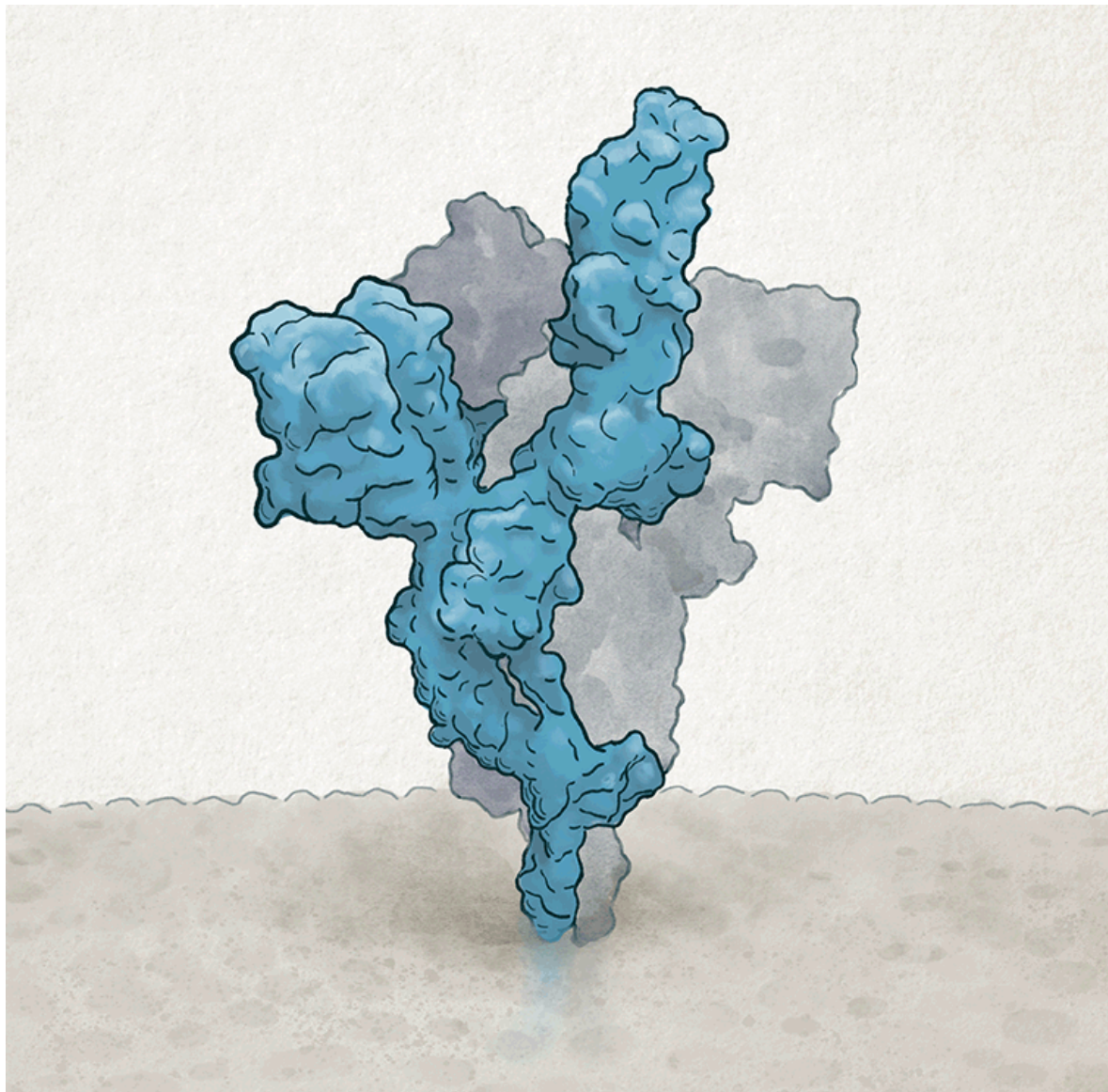
This article was downloaded by **calibre** from <https://www.nature.com/articles/d41586-022-01612-3>

- NEWS FEATURE
- 15 June 2022

How months-long COVID infections could seed dangerous new variants

Tracking SARS-CoV-2 evolution during persistent cases provides insight into the origins of Omicron and other global variants. What can scientists do with this knowledge?

- [Ewen Callaway](#)



These are mutations that accumulated in the spike protein of SARS-CoV-2 during a seven-month-long infection. Illustration by Nik Spencer/*Nature*; Source: Ref. 1

Virologist Sissy Sonnleitner tracks nearly every COVID-19 case in Austria's rugged eastern Tyrol region. So, when one woman there kept testing positive for months on end, Sonnleitner was determined to work out what was going on.

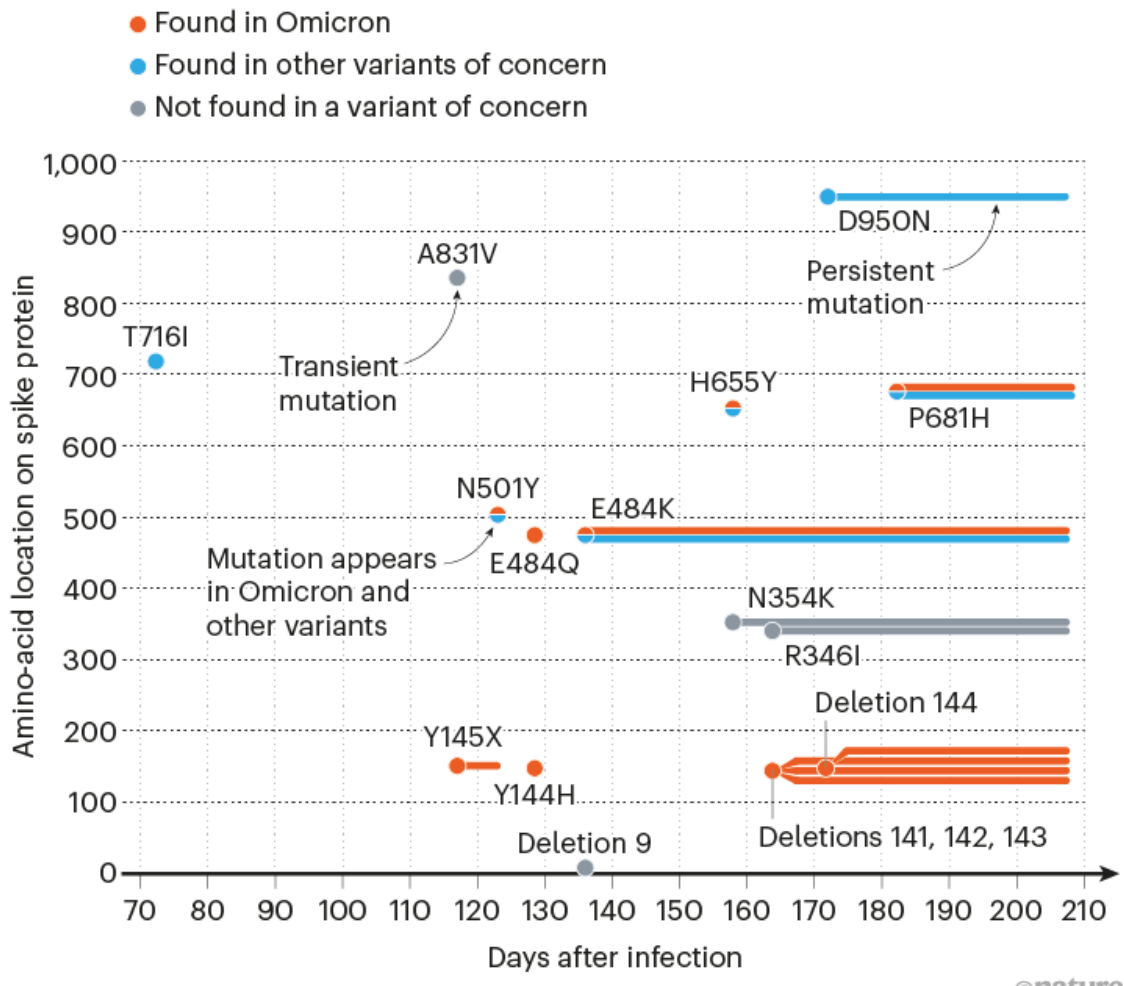
Before becoming infected with SARS-CoV-2 in late 2020, the woman, who was in her 60s, had been taking immune-suppressing drugs to treat a

lymphoma relapse. The COVID-19 infection lingered for more than seven months, causing relatively mild symptoms, including fatigue and a cough.

Sonnleitner, who is based at a microbiology facility in Außervillgraten, Austria, and her colleagues collected more than two dozen viral samples from the woman over time and found through genetic sequencing that it had picked up about 22 mutations (see ‘Tracking spike’s evolution’). Roughly half of them would be seen again in the heavily mutated Omicron variants of SARS-CoV-2 that surged around the globe months later¹. “When Omicron was found, we had a great moment of surprise,” Sonnleitner says. “We already had those mutations in our variant.”

TRACKING SPIKE'S EVOLUTION

Researchers started sequencing viruses retrieved from a person with chronic COVID-19 on day 73 of the infection. They found eight transient and nine persistent mutations appear in the virus's spike protein before the infection resolved on day 207. Many of these mirror the mutations found in Omicron and other variants of concern.



Source: Ref. 1

Omicron did not arise from the woman's infection, which doesn't seem to have spread to anyone. And although no definitive links have been made to individual cases, chronic infections such as hers are a leading candidate for the [origins of Omicron and other variants](#) that have driven COVID-19 surges globally. "I don't think there can be any doubt in anyone's mind that these are a source of new variants," says Ravindra Gupta, a virologist at the University of Cambridge, UK.

Researchers want to understand how the virus might evolve the ability to spread from person to person more easily, to evade the immune response, or to become more or less severe. Some or all of these qualities might be forged during the course of a chronic infection. “We don’t quite understand what can evolve in a single individual — and what cannot,” says Alex Sigal, a virologist at the Africa Health Research Institute in Durban, South Africa.

The odds are remote that this knowledge could help to predict the next deadly strain or even to trace variants such as Omicron to their origin. Still, virologists hope that by improving their understanding of viral evolution, they will be able to anticipate what future variants might look like — and potentially find better ways to treat chronic infections. “It’s such an important problem, given that we don’t want another variant that we can’t handle,” says Sigal.

Deadly competition

Since late 2019, scientists have sequenced the genomes of more than 11 million samples of SARS-CoV-2 taken from people. These efforts have drawn an evolutionary tree that is remarkable in its breadth, showing how the virus has changed during its march around the planet, gaining just a couple of stable mutations per month as it moves from person to person.

“But that’s only one part of the evolutionary story,” says Sarah Otto, an evolutionary biologist at the University of British Columbia in Vancouver, Canada. Each person’s infection is its own universe, where new mutations arise as the infection spreads from cell to cell. Most of these changes won’t matter to the virus, and many will do it harm. But some might give it a slight advantage over other versions of the virus in that person’s body, enhancing its ability to spread or providing some resistance to immune defences. These two traits — infectivity and immune evasion — are the main ways in which SARS-CoV-2 has evolved since it first emerged in 2019.

In acute SARS-CoV-2 infections, which generally last a week or two before being cleared by the immune system, versions of the virus with advantageous mutations have little time to outcompete those that lack them. The odds of a virus with such an advantage being transmitted to another

individual are therefore small. Studies suggest that only a few virus particles — maybe even just one — are needed to seed a new infection². “Which of those viruses happens to be in the aerosol droplet you sneeze out at the time someone walks by and breathes in is largely a matter of luck,” says Jesse Bloom, a evolutionary biologist at the Fred Hutchinson Cancer Center in Seattle, Washington. “So, most of the beneficial mutations that have arisen in a patient are lost, and then evolution has to start up all over again.”

This ‘transmission bottleneck’ is the reason SARS-CoV-2 picks up around two mutations per month globally, on average. But in chronic infections, which last for weeks to months, viruses with advantageous mutations have time to outcompete others.

Compared with acute cases, these long-term infections also allow time for much more viral diversity to develop. And through a process called recombination, which can shuffle the genomes of SARS-CoV-2 particles together, mutations that are beneficial in one part of the body, such as the upper airways, might show up in viruses bearing other useful properties, says Andrew Rambaut, an evolutionary biologist at the University of Edinburgh, UK. “If the result is a fitter virus, it can suddenly take off.”

As a result of chronic infections, globally, “this virus has opportunities not just to evolve in one way, in one direction, but literally thousands, maybe tens of thousands of directions over months”, Otto says.

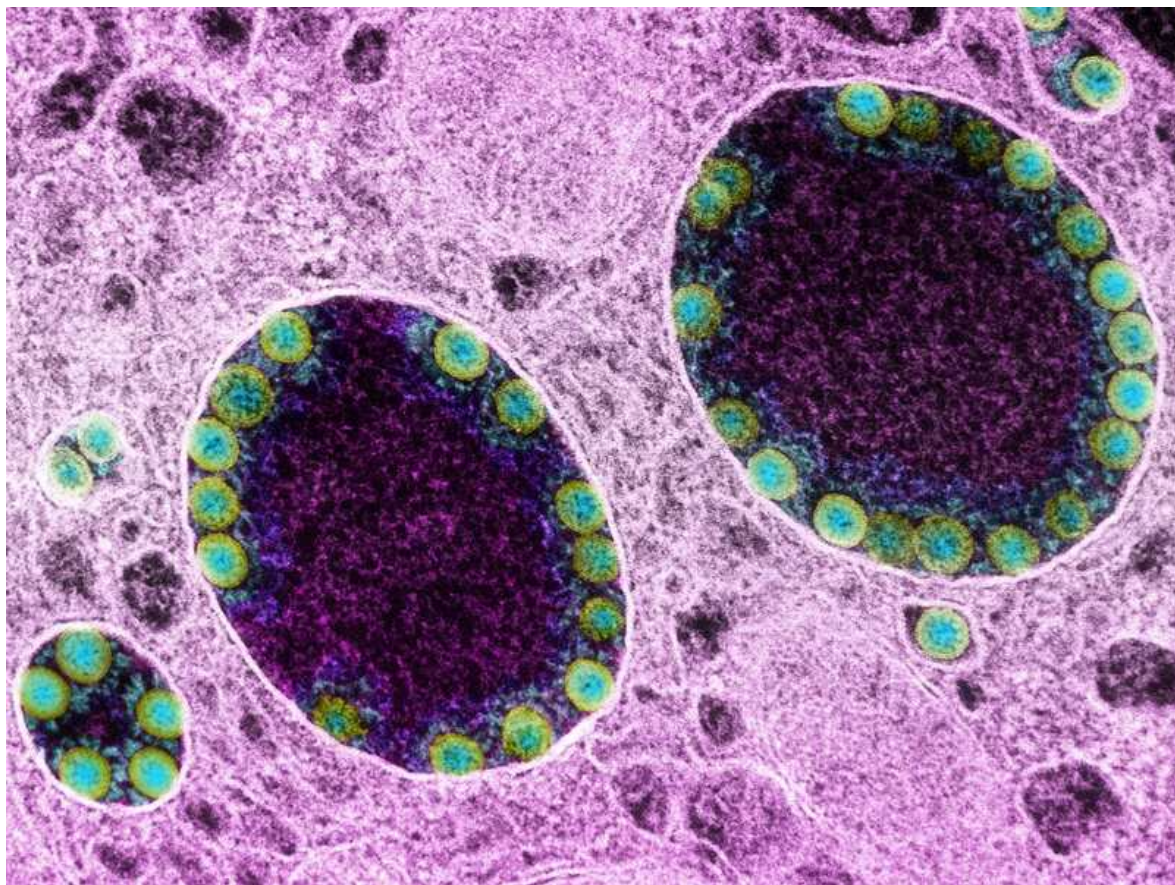
Targeting spike

No two chronic infections are identical. But in dozens of case reports, researchers have begun to identify common signatures of long-term infection. One of the most striking, says Otto, is the large number of amino-acid changes that accrue in the virus’s spike protein, which helps it to infect cells and is a primary target for the body’s immune response.

Many of these mutations map to regions of the spike that are targeted by antibodies, such as its receptor binding domain (RBD) and the N-terminal domain, which are involved in recognizing and infecting host cells. This makes sense, says Darren Martin, an evolutionary virologist at the

University of Cape Town in South Africa. If a person's immune system fails to clear an infection fully, the surviving viruses are likely to bear immunity-evasive mutations that helped them to survive the attack. One study³, which has not been peer reviewed, found that the most common mutation in chronic infections is at a position in the spike protein's RBD called E484. Changes at this site can prevent some potent infection-blocking antibodies from attaching to the virus.

Some mutations don't work particularly well on their own. Last year, Gupta and his team described a 102-day infection in a man in his 70s who had a compromised immune system, and who ultimately died from the infection⁴. After doctors had treated him with convalescent plasma — the antibody-containing portion of blood donated by people who had recovered from COVID-19 — Gupta's team found that viruses with a pair of spike-protein mutations were thriving in the man's airways.



SARS-CoV-2 particles (green) in infected olfactory epithelial cells. Credit: NIAID/NIH/SPL

One of the mutations, called D796H, conferred resistance to antibodies — but this benefit came at a cost to the virus. When the researchers engineered a non-replicating ‘pseudotype virus’ to carry the D796H mutation and measured how well it could infect cells in the lab, they found that this mutation alone made the pseudotype virus significantly less infectious. But when the pseudotype virus also contained a second mutation found in the same person — a two-amino-acid deletion at sites 69 and 70 — infectivity was restored almost completely⁴. Such compensatory mutations, which have more time to emerge in chronic infections, allow the virus to make evolutionary leaps, says Gupta. “Viruses struggle to do that when they’re jumping between hosts very quickly.”

In some cases, mutations have made sense only with hindsight. In late 2020, Jonathan Li, a physician-scientist at Brigham and Women’s Hospital in Boston, Massachusetts, and his colleagues released the first detailed report of a chronic SARS-CoV-2 infection: an ultimately fatal case in a 45-year-old man who had a rare autoimmune disease⁵. The virus developed mutations linked to antibody resistance, including E484K, and another spike mutation called N501Y, which lab studies had suggested improves the virus’s ability to bind to host-cell receptors, potentially boosting infectivity⁶.

The significance of the N501Y change became apparent when it was detected in a trio of fast-growing lineages later named the Alpha, Beta and Gamma variants of concern (VOCs). Omicron bears this mutation, as well as several others identified in the man’s infection. “He really was the harbinger of what was to come,” Li says.

Seeking variant origins

Alpha, identified in the United Kingdom in late 2020, was the first SARS-CoV-2 variant suspected to have emerged from a chronic infection. But that wasn’t the only possible explanation, says Rambaut. The variant might have arisen in a region — probably outside the United Kingdom — that had little capability to conduct genomic surveillance of SARS-CoV-2. Alternatively,

Alpha could have evolved in an animal reservoir (the variant's N501Y mutation enables it to infect mice, rats and mink).

A chance discovery nevertheless suggests that a chronic infection was the most likely source of Alpha. Rambaut and Verity Hill, an evolutionary biologist at the University of Edinburgh, reported in a March preprint the discovery of an intermediate version of Alpha in UK sequencing data⁷. The sequence was collected from a person in southeast England in July 2020, two months before Alpha was first detected in the same region.

The virus had acquired the N501Y mutation, as well as several other hallmarks of Alpha, but it lacked the full suite of changes. "It's accumulating these mutations. It was probably a bit rubbish at spreading," Hill says. Only once the Alpha intermediate gained further mutations did it have the capacity to take off, she suggests.

Combinations of mutations are seen in Omicron, too. That variant — which includes several sub-lineages with many overlapping mutations — is brimming with genetic changes linked to both immune escape and infectivity that had been spotted before. But what stood out to Martin was that the BA.1 subvariant that set off most countries' Omicron waves has a collection of 13 spike mutations that scientists had rarely seen individually, let alone all together in a single virus.

Martin and his colleagues hypothesize⁸ that, among this unique set of mutations, are some that helped to offset the evolutionary costs associated with the mutations that hastened Omicron's spread. "Those trade-offs take a long time to resolve and those require, in my opinion, chronic infections," says Martin. These could be in humans or in animals, he adds.

Another characteristic of Omicron — the reduced severity of disease — could also be a product of chronic infection. Lab studies have suggested that Omicron's relative mildness could be a result of its preference for infecting cells in the upper airways, as opposed to those in the lung⁹. The variant probably evolved from a strain that adeptly infected both upper and lower airways. Gupta suspects that Omicron's shift probably depended on the kind of coordinated evolution that occurs when a virus spends months in a single

person's body. But what's not clear are the evolutionary forces that propelled such a shift, he adds.

On the lookout

Chronic infections could be the best explanation for how variants such as Omicron and Alpha evolved. But it's not obvious how one of the defining characteristics of most variants — their ability to spread like wildfire between people — might evolve in a single individual. "That's a real mystery," says Bloom. "When something's not under selection, you often lose it. During a chronic infection there's no longer selection for transmissibility."

One possible explanation is that the same molecular mechanisms that help SARS-CoV-2 to infect a person's airways, lungs and other organs are also important for enabling the virus to spread to others. "The same transmission dynamics are required when it's inside you as when it's going from one person to another," says Martin.

But there is a difference between a virus that merely retains the ability to transmit, and one such as Omicron or Alpha that can cause a global surge in cases. A massive boost in transmissibility or the capacity to infect previously immune people might be what sets a dangerous VOC apart, says Rambaut. "It's not that all chronic infections are going to produce VOCs. It's going to be one in a million."



Isolating people with long-term infections probably won't suppress new variants of concern. Credit: Ina Fassbender/AFP/Getty

That means that surveillance is unlikely to detect a variant at its point of emergence. In a May preprint, researchers spotted an Omicron strain that had picked up other spike mutations during chronic infection in an immunocompromised individual, and showed that it had spread to several people in the same hospital, as well as in the local community¹⁰. But wider spread of such infections seems exceedingly rare. A February preprint documenting 27 people with chronic infections reports no evidence that any had spread the virus to other individuals¹¹. If VOCs so rarely emerge from chronic infections, it will be difficult to prevent them without reducing overall rates of infection around the world, says Adi Stern, an evolutionary virologist at Tel Aviv University in Israel, who led the study.

Nevertheless, there is an urgent need to understand the viral factors that contribute to chronic infections. “We need to go beyond the case reports and

understand what the virus is actually evolving during this time,” says Sigal.

Sigal and his team are tracking people with advanced HIV, whose immune systems can be severely compromised, to identify factors associated with chronic SARS-CoV-2 infection. HIV infects immune cells called CD4⁺ T cells, which also support the production of antibodies against viruses such as SARS-CoV-2. In unpublished work, Sigal and his colleagues have found that low levels of CD4⁺ T cells are associated with a risk of chronic SARS-CoV-2 infection, and that many of the cases are mild, with few or no respiratory symptoms.

On the basis of the sheer number of people living with HIV — nearly 40 million globally — and the likelihood that most people have already been infected with SARS-CoV-2, it seems likely that some cases of persistent infection are contributing to the emergence of new variants, says Otto. “From an Occam’s razor point of view, we know that should be a source.”

People with compromised immune systems aren’t the only potential source of variants. Researchers have documented SARS-CoV-2 infections lasting multiple weeks in people with healthy immune systems. From the perspective of natural selection, even a relatively short three-week infection provides exponentially more opportunities for the virus to evolve, compared with an acute infection lasting a week, says Martin.

People with relatively healthy immune systems might also provide the virus with more selection pressure than individuals who have impaired immune responses, says Hill. But how to identify people who are susceptible to such infections or what their symptoms might look like is an open question. “I would suspect they’re a lot more common than we realize,” says Hill.

Last year, Gonzalo Bello, a virologist at the Oswaldo Cruz Institute in Rio de Janeiro, Brazil, and his colleagues identified several strains of SARS-CoV-2 circulating in Amazonas state in Brazil¹². These carried some — but not all — of the mutations found in the Gamma variant that drove the region’s ferocious second wave in 2021. But each of the Gamma-like strains also had their own unique mutations: evidence, Bello says, that Gamma might have evolved not from a single chronic infection, but from

transmission chains of medium-length infections involving relatively healthy people.

Such transmission chains could have contributed to the diversity of Omicron lineages, Bello suggests. “Maybe these individuals are where some of the steps in the origin of VOCs are happening,” he says. And if chronic infections in healthy people are a likely source of VOCs, improving global vaccination rates could help to prevent new ones emerging, Hill adds. “When you’ve got these huge uncontrolled waves of infection, you’re sowing the seeds for the next.”

Antiviral drugs and other treatments taken during a chronic infection could also be playing a part in the virus’s evolution. One trait scientists are looking out for is resistance to COVID-19 drugs such as Paxlovid (nirmatrelvir-ritonavir) and molnupiravir. (Resistance to the antiviral remdesivir has already been documented in chronic infections^{[13](#)}.) The drugs affect highly conserved viral proteins — for which the barrier to drug resistance is high — but evolutionary leaps that characterize chronic infections could buy the virus time to come up with a way around that, says Gupta.

In unpublished laboratory experiments, a team led by virologist David Ho at Columbia University in New York City has found that SARS-CoV-2 can take numerous paths to Paxlovid resistance. Some involve gaining compensatory mutations that allow the virus to overcome the costs of Paxlovid resistance, allowing them to thrive, at least in the lab. Such mutations are unlikely to be behind anecdotal reports of recurring SARS-CoV-2 symptoms after Paxlovid treatment, says Ho (who himself experienced such a rebound). But if the treatment, which is normally taken for five days, is administered for a longer period to treat a chronic infection, there is a good chance resistance will emerge.

There is also an urgent need to identify effective treatments for chronic infections — particularly in people with immune-system impairments, who don’t always mount a strong response to vaccines. Most approved monoclonal antibody drugs are not effective against Omicron and its offshoots, and researchers have shown in a preprint that resistance to these therapies can emerge when they’re used to treat chronic infections^{[14](#)}.

Convalescent plasma should create a higher evolutionary barrier than monoclonal antibody therapies, says Arturo Casadevall, a microbiologist at John Hopkins Bloomberg School of Public Health in Baltimore, Maryland. Plasma that contains high levels of diverse antibodies has been shown to be effective at treating COVID-19, and some physicians are now giving it to people with compromised immune systems^{[15](#)}.

Antiretroviral drugs that target HIV can also help people living with that virus to clear chronic SARS-CoV-2 infections, but adherence to the drugs can be a challenge, Sigal notes.

Last October, UK clinicians reported a case in which a person's chronic infection was cleared after they received a COVID-19 vaccine^{[16](#)}. For the Austrian woman whom Sonnleitner and her colleagues studied, the end of her seven-month infection also followed vaccination. But it's impossible to know if the vaccine is what helped her to recover.

That outcome is rare for people with chronic infections, however; many reports end in death. "They really are heartbreaking cases," Stern says. As many parts of the world attempt to move on from the pandemic, with some healthy people shrugging their shoulders at 'mild' Omicron infections, Stern says we must do more to protect those who are most at risk of a chronic SARS-CoV-2 infection. "It's dangerous for them — and it's dangerous for us as a society."

Nature **606**, 452-455 (2022)

doi: <https://doi.org/10.1038/d41586-022-01613-2>

References

1. Sonnleitner, S. T. *et al. Nature Commun.* **13**, 2560 (2022).
2. Martin, M. A. & Koelle, K. *Sci. Transl. Med.* **13**, eabh1803 (2021).
3. Wilkinson, S. A. J. *et al.* Preprint at medRxiv
<https://doi.org/10.1101/2022.03.02.22271697> (2022).

4. Kemp, S. A. *et al.* *Nature* **592**, 277–282 (2021).
5. Choi, B. *et al.* *N. Engl. J. Med.* **383**, 2291–2293 (2020).
6. Tian, F. *et al.* *eLife* **10**, e69091 (2021).
7. Hill, V. *et al.* Preprint at bioRxiv
<https://doi.org/10.1101/2022.03.08.481609> (2022).
8. Martin, D. P. *et al.* *Mol. Biol. Evol.* **39**, msac061 (2022).
9. Meng, B. *et al.* *Nature* **603**, 706–714 (2022).
10. Gonzalez-Reiche, A. S. Preprint at medRxiv
<https://doi.org/10.1101/2022.05.25.22275533> (2022).
11. Harari, S. *et al.* Preprint at medRxiv
<https://doi.org/10.1101/2022.02.17.22270829> (2022).
12. Graf, T. *et al.* *Virus Evol.* **7**, veab091 (2021).
13. Gandhi, S. *et al.* *Nature Commun.* **13**, 1547 (2022).
14. Huygens, S. *et al.* Preprint at medRxiv
<https://doi.org/10.1101/2022.04.06.22273503> (2022).
15. Rodionov, R. N. *et al.* *Lancet Microbe* **2**, E138 (2021).
16. Bradley, R. E. *et al.* *J. Clin. Immunol.* **42**, 32–35 (2022).

This article was downloaded by **calibre** from <https://www.nature.com/articles/d41586-022-01613-2>

Books & Arts

- **[Learn from COVID: Gates's pandemic prescription](#)** [14 Jun 2022]
 - The philanthropist's life-saving ideas need insights from political science.
 - **[Female dominance, and coding for kids: Books in brief](#)** [20 May 2022]
 - Andrew Robinson reviews five of the week's best science picks.
-

- BOOK REVIEW
- 14 June 2022

Learn from COVID: Gates's pandemic prescription

The philanthropist's life-saving ideas need insights from political science.

- [Matthew M. Kavanagh](#)



The biggest barriers to preventing the next pandemic are political as much as technical. Credit: Kent Nishimura/Los Angeles Times/Shutterstock

How to Prevent the Next Pandemic *Bill Gates* Knopf (2022)

The COVID-19 pandemic was foreseen. Experts everywhere had long predicted a global viral outbreak and called for action to prevent it. World leaders, on the whole, did little. Now, with COVID-19 still raging, Bill Gates has produced a manifesto on what must be done to prevent the next pandemic. Written in accessible prose that even a busy world leader could not fail to grasp, the global-health philanthropist offers some life-saving ideas that are ambitious and achievable — if political leaders act.

“Learn from COVID” is the opening gambit. One of the book’s most important insights is how often the world’s wealthiest countries got things wrong that less well-resourced countries and communities got right. Vietnam ran outbreak simulations — something that most of Europe never did. Gates shares the example of a Vietnamese simulation that sent patient-actors into emergency rooms in the northeast of the country to test whether fictionalized cases of Middle East respiratory syndrome would be detected and correctly diagnosed. This exercise revealed gaps in sharing information about potential outbreaks, and the authorities fixed them. South Africa and Nigeria’s investment in laboratory capacity made them better able to detect variants than the United States was. The global south offers deep lessons, if US and European experts can humble themselves to learn them.

Likening a pandemic to a fire, Gates reminds us that collective action is essential. “For some 2,000 years, humans have recognized that individual families and businesses aren’t solely responsible for protecting themselves.” From financing fire departments (at a cost of US\$50 billion a year in the United States) to enacting laws that limit people’s options (no thatched roofs), government action is expected. It is an apt metaphor given that the pandemic is still ablaze — yet effective legal interventions, such as mask mandates, are being rescinded owing to unprecedented push-back from citizens and judiciaries.

Gates’s specific proposals include building a global team of expert epidemiologists, which he calls GERM (Global Epidemic Response and Mobilization). This would be managed by the World Health Organization (WHO), at a cost of about \$1 billion a year, and embedded in national governments to augment today’s fragmented and under-resourced pandemic-response teams. Gates also calls for faster development of vaccines and therapeutics, arguing for investment in research and development, delivery

technologies such as patches and pills, libraries of promising compounds, distributed manufacturing capacity and more. And he wants proactive surveillance of waste water, so that researchers can “go looking for signals in the environment” and detect viral outbreaks early.

One of the most important points is Gates’s emphasis that the capacity to track causes of death in low- and middle-income countries is a global good. For much of the early part of the COVID-19 pandemic, there was a mistaken belief that low- and middle-income countries were not as badly affected by the disease as wealthier countries were. And this opinion was sometimes used to justify decisions on the distribution of funding, vaccines and other resources. In reality, it was not low mortality that marked out these countries, but rather a lack of mortality data — and total excess deaths from COVID-19 now seem to have been highest in countries such as India ([H. Wang et al. Lancet 399, 1513–1536; 2022](#)). Indeed, all too often, global health data are useful to certain political actors but do not help local leaders to make public-health decisions. Gates profiles innovative ideas such as minimally invasive autopsies, which have been piloted in Mozambique and elsewhere to make it easier to track mortality.

How to Prevent the Next Pandemic highlights how the HIV Vaccine Trials Network was mobilized for COVID-19 vaccines, and how polio workers were key to tackling Ebola in West Africa. Fighting pandemics and outbreaks of today, such as HIV, tuberculosis and polio is excellent preparation for future challenges. As the Global Fund to Fight AIDS, Tuberculosis and Malaria seeks to replenish its financing, and the world debates new mechanisms to fund pandemic preparedness, Gates’s review of what has worked might suggest that setting up a fund for future pandemics could be less effective than expanding existing pots.

His deep, but highly readable dive into innovation, technology and policy makes sense of complex science. It also shows that the biggest barriers to stopping the next pandemic are not chiefly technical. Gates demonstrates just how much is technologically feasible, evidence-based, cost-effective, and yet not happening.

Herein lies a puzzling gap in this book. As a philanthropist, Gates has steeped himself in the scientific literature, but overlooks insights from the

study of politics that could help to reveal why many of its recommendations have not gained traction. He notes with incredulity and disapproval that some guidance on COVID-19 from the US Centers for Disease Control and Prevention was influenced by politics — yet a deep social-science literature has long explored the contours of political power in all health policymaking.

Gates urges the WHO to work with member states to secure better implementation of international health regulations and to strengthen norms on sharing outbreak information. The agency is already doing exactly this. Yet, as international-relations scholars have shown, it clearly lacks the political power, when acting alone, to compel states to act against their short-term interest (by imposing travel bans, for example). Political analysts suggest that changes in global governance — such as boosting the WHO's power to release emergency funding, or to convene governments and other international organizations beyond the health sector — might prove more important than many technological changes.

Gates calls for free vaccines around the world, but opposes a World Trade Organization waiver that would allow governments to choose which COVID-19 patents to enforce during the pandemic, partly on the grounds that it would be better if companies voluntarily shared their know-how. Yet companies have few incentives to do so without the political intervention of governments: such intervention was key to why prices of AIDS medicines fell by 99% in the first decade of this century.

The study of international relations has a great deal to tell us about governments' behaviour during the COVID-19 pandemic, and about what might change it. The COVAX initiative, for example, failed to reach its goals because countries and companies reneged on their pledges and engaged in vaccine nationalism — acting exactly as studies at the intersection of domestic and international politics would have predicted. Such analysis might have helped COVAX, which aims for equitable access to COVID-19 vaccines worldwide, to avoid assumptions that undermined its efforts to reach 2 billion people in 2021.

With this book, Gates makes a strong, evidence-based argument that the world is not yet thinking about pandemics effectively — but, rather, is missing key innovations and refusing to fund efforts that could save lives

and money. A political lens could reveal how to fix that in the world we have today.

Nature **606**, 457-458 (2022)

doi: <https://doi.org/10.1038/d41586-022-01614-1>

This article was downloaded by **calibre** from <https://www.nature.com/articles/d41586-022-01614-1>

| [Section menu](#) | [Main menu](#) |

- BOOK REVIEW
- 20 May 2022

Female dominance, and coding for kids: Books in brief

Andrew Robinson reviews five of the week's best science picks.

- [Andrew Robinson](#)

FIONA FOX

'This is how to talk about science' **Justin Webb**

BEYOND THE HYPE

*The Inside Story
of Science's
Biggest Media
Controversies*



Beyond the Hype

Fiona Fox *Elliott & Thompson* (2022)

It is 20 years since journalist Fiona Fox set up the influential Science Media Centre in London, to persuade more scientists to engage with the media. This absorbing, detailed book is her memoir of that period — not, as she makes clear, an “objective record”. Separate chapters deal with controversies such as “Climategate”, “Frankenfoods”, the politicization of science, sexism in research and how the current pandemic epitomizes an “age-old dichotomy” between the need for simple public messaging and the messy complexity of science.

Lucy
Cooke

'Rich and
compelling'
SUE PERKINS

'Deeply
important'
ALICE ROBERTS



BITCH

A revolutionary guide
to sex, evolution &
the female animal

Bitch

Lucy Cooke *Doubleday* (2022)

“Try explaining the need to be passive” to a female spotted hyena (*Crocuta crocuta*), writes zoologist and author Lucy Cooke, “and she’ll laugh in your face, after she’s bitten it off”. She is dominant in rough play, scent-marking and territorial defence. By analysing numerous animals, this sparkling attack on scientific sexism draws on many scientists — of multiple genders — to correct stereotypes of the active male versus passive female. Many such concepts were initiated by Charles Darwin, who is nevertheless Cooke’s “scientific idol”.



beyond coding

how children learn
human values
through programming

marina umaschi bers

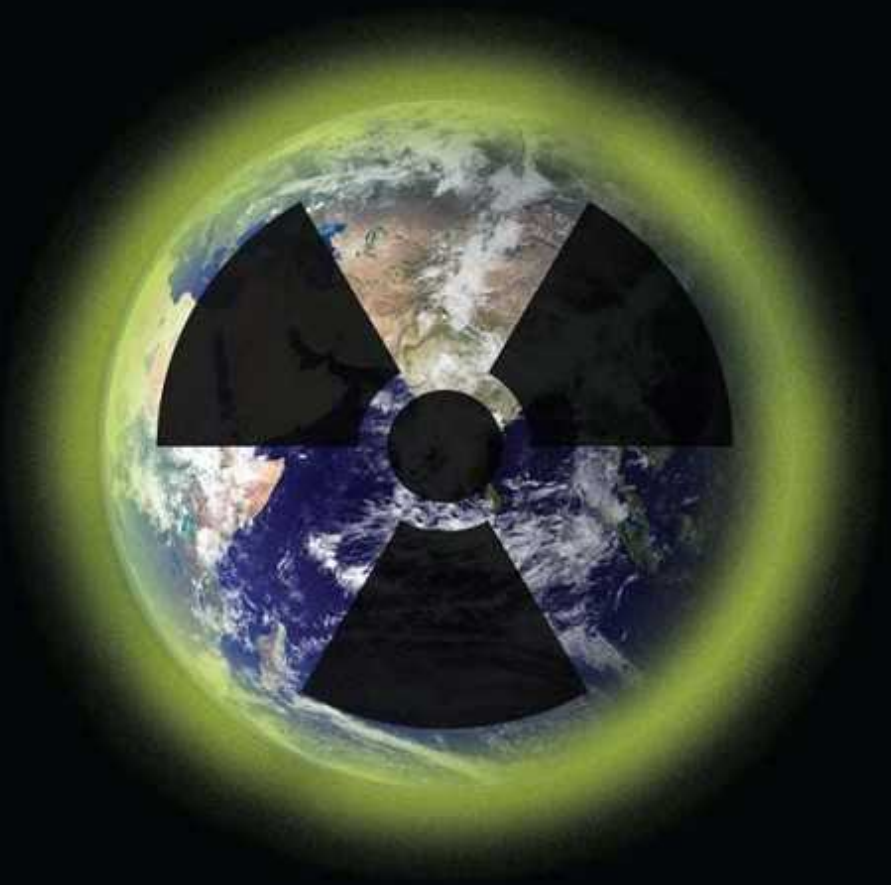


Beyond Coding

Marina Umaschi Bers *MIT Press* (2022)

Early-childhood technologist Marina Bers developed the KIBO robot, which young children can program with coloured, barcoded wooden blocks to learn computer coding. It is the chief character in her engaging book, which presents four key ways to consider coding for kids: as a “playground”; “another language”; a “palette of virtues”; and a “bridge”. The palette includes infusing ethics and moral education into programming. The bridge involves finding points of connection between diverse cultural, ethnic and religious groups.

NUCLEAR BODIES
THE GLOBAL HIBAKUSHAS
ROBERT A. JACOBS



Nuclear Bodies

Robert A. Jacobs *Yale Univ. Press* (2022)

The Japanese word *hibakusha* originally described the victims of the atomic bombs dropped on Japan in 1945. Since the 2011 Fukushima nuclear power-plant disaster, the term has been widely extended to denote worldwide victims of radiation exposure. Yet it does not appear in the *Oxford English Dictionary*: evidence that “these ‘global hibakusha’ have been largely invisible to us”, because of their relative political insignificance, notes Hiroshima-based historian Robert Jacobs in this grimly important analysis of the cold war.

TRAVELS WITH TRILOBITES

ADVENTURES IN THE
PALEOZOIC



ANDY SECHER

Forewords by Niles Eldredge, Mark Norell, and Kirk Johnson

Travels with Trilobites

Andy Secher *Columbia Univ. Press* (2022)

The fascinating marine invertebrate known as a trilobite belongs to the beginning of complex animal life. It appeared some 521 million years ago, and endured for more than 250 million years, evolving more than 25,000 recognized species. Palaeontologist Andy Secher co edits the trilobite website for the American Museum of Natural History in New York City. He owns more than 4,000 trilobite fossils, many of which are pictured in this paean to “the omnipresent monarchs of the world’s ancient seas”.

Nature **606**, 458 (2022)

doi: <https://doi.org/10.1038/d41586-022-01382-y>

This article was downloaded by **calibre** from <https://www.nature.com/articles/d41586-022-01382-y>

| [Section menu](#) | [Main menu](#) |

Opinion

- **Benjamin Mottelson (1926–2022)** [13 Jun 2022]
 - Physicist and Nobel prizewinner who revolutionized understanding of the atomic nucleus.
- **Fuel crisis: slash demand in three sectors to protect economies and climate** [13 Jun 2022]
 - Global dependence on Russian gas, oil and coal can be cut by 20–60% and greenhouse-gas emissions by 2.9% within one year, with the right policy support.
- **Fleeing Russian researchers seek Western support** [14 Jun 2022]
 -

- OBITUARY
- 13 June 2022

Benjamin Mottelson (1926–2022)

Physicist and Nobel prizewinner who revolutionized understanding of the atomic nucleus.

- [Helge Kragh](#)



Credit: Ola Jakup Joensen, Niels Bohr Institute

Benjamin Mottelson was a US-born physicist who specialized in theoretical work on the structure of the atomic nucleus. During the 1950s, in close collaboration with his Danish colleague Aage Bohr, Mottelson constructed a theory known as the collective model, which was greatly superior to previous nuclear models. The model not only stimulated fresh experiments

in nuclear physics, it also proved fertile across disciplines by relating the atomic nucleus to areas such as superconductivity and the physics of neutron stars. Mottelson and Bohr (whose father Niels won a Nobel prize in 1922) shared the 1975 Nobel Prize in Physics for their work, together with US nuclear physicist James Rainwater.

Mottelson, who has died aged 95, spent almost his entire research career in Copenhagen, where he was a leading figure in the nuclear-physics community. His work revitalized the University of Copenhagen's Institute for Theoretical Physics, founded by Niels Bohr in 1921 and renamed in 1965 as the Niels Bohr Institute. Mottelson's enthusiasm, extroversion and broad interests made him a treasured teacher and lecturer in Denmark as well as overseas.

Born in Chicago, Illinois, in 1926, Mottelson graduated from secondary school during the Second World War and was then sent by the US Navy to Purdue University in West Lafayette, Indiana, for officer training. He received his bachelor's degree from Purdue in 1947 and went on to do graduate studies in nuclear physics at Harvard University in Cambridge, Massachusetts, with Julian Schwinger, who would receive the 1965 Nobel prize for his contributions to quantum electrodynamics. Funded by fellowships from Harvard and the US Atomic Energy Commission, Mottelson then left the United States to do postgraduate work at the Institute for Theoretical Physics in Copenhagen.

Until 1950, the favoured model of the atomic nucleus was the shell model, so called because nucleons (protons and neutrons) occupied quantum levels, or shells, like the atomic electrons. However, Aage Bohr then suggested that the nucleus might rotate like a viscous liquid ellipsoid — something like a rotating raw egg. As soon as Mottelson arrived in Copenhagen and met Bohr, they began to collaborate on models of atomic nuclei. In his 1975 Nobel lecture, Mottelson described what became a life-long collaborative research programme as "a dialogue between kindred spirits that have been attuned through a long period of common experience and jointly developed understanding".

In 1953, in a 174-page essay published by the Royal Danish Academy of Sciences and Letters, Bohr and Mottelson presented what became known as

the collective, or unified, model of nuclear structure. It incorporated features of the shell model and the rival liquid-drop model, which pictured the nucleons as analogous to the molecules in a water droplet. As Mottelson was one of the first to point out, the model predicted that a phenomenon called Coulomb scattering would occur when charged particles interacted. This was confirmed by experiments in Copenhagen and elsewhere. The Bohr–Mottelson collective model stimulated a wide range of experiments in nuclear physics, such as the study of spectra generated by rotating nuclei.

In 1957, BCS — or Bardeen-Cooper-Schrieffer — theory was proposed to explain microscopic aspects of superconductivity. Bohr and Mottelson then realized that nuclear matter has properties analogous to those of superconducting solids, and published this insight in an important 1958 paper written jointly with the US physicist David Pines ([A. Bohr et al. Phys. Rev. 110, 936; 1958](#)). By extending the BCS theory to the nuclear domain, the three physicists were able to explain the difference in the stability between isotopes with even and odd numbers of nucleons. During the 1960s, Bohr and Mottelson continued their studies of nuclear structure, ambitiously aiming at a comprehensive and synthetic treatment of the entire area. The first result of their efforts appeared in 1969, with volume 1 of the monumental *Nuclear Structure*, which was completed six years later in a second volume — the same year that they received their Nobel prize. It was the most recent Nobel prize to be awarded for work in nuclear physics.

In 1953, Mottelson took up a research position in the theoretical study group that the newly established CERN, the European centre for nuclear and high-energy physics, had formed in Copenhagen at the Institute for Theoretical Physics. When the theory group moved to Geneva, Switzerland, in 1957, Mottelson was appointed professor at the nearby Nordic Institute for Theoretical Atomic Physics (Nordita) founded the same year. In 1971, Mottelson became a naturalized Danish citizen. Apart from visiting professorships, he remained at Nordita until he retired in 1994.

Although retired, he continued his research as an emeritus professor and occasional lecturer. In 2015, the 88-year-old physicist contributed to a paper on the low-temperature, low-density states of matter known as Bose-Einstein condensates ([J. C. Cremon et al. Phys. Rev. A 91, 033623; 2015](#)). Another topic that Mottelson wrestled with during his later years was the foundation

of quantum mechanics, which he investigated in papers written with Aage Bohr and Ole Ulfbeck. Mottelson and his co-authors wanted to know what quantum mechanics is really about and why its equations work so well. They argued that the proper foundation of quantum mechanics was a “principle of genuine fortuitousness” and that this principle implied a new geometric, rather than atomic, world view that had dimensions of space and time but not mass. Their radical interpretation of uncaused events, such as clicks in a detector, led them to argue that Planck’s quantum constant has no place in fundamental theory.

Ben was an active man who liked swimming, cycling and music. Every day, he biked the 12 kilometres to the Niels Bohr Institute from his home in a suburb north of Copenhagen. He will first of all be remembered for his seminal contributions to the theory of nuclear structure. But he will also be remembered, and missed, for his warm human qualities and wide interests beyond physics.

Nature **606**, 459 (2022)

doi: <https://doi.org/10.1038/d41586-022-01615-0>

This article was downloaded by **calibre** from <https://www.nature.com/articles/d41586-022-01615-0>

| [Section menu](#) | [Main menu](#) |

- COMMENT
- 13 June 2022

Fuel crisis: slash demand in three sectors to protect economies and climate

Global dependence on Russian gas, oil and coal can be cut by 20–60% and greenhouse-gas emissions by 2.9% within one year, with the right policy support.

- [Felix Creutzig](#)



Pop-up cycle lanes were installed across Germany during the COVID-19 pandemic to aid social distancing. Credit: Krisztian Bocsi/Bloomberg/Getty

The war in Ukraine has triggered an energy and resource crisis. Russian exports account for 3.6% of coal, 7.0% of natural gas and 5.8% of oil consumption globally (see Supplementary information). Much of those exports goes to Europe. Russia provides about 40% of the European Union's gas, nearly 50% of its coal and one-quarter of its oil. Russia is cutting gas exports to countries that will not pay in roubles. Prices are soaring and gas and oil are running short.

In the light of this and the economic sanctions against Russia, how can countries reduce their Russian energy imports? And, crucially, how can they do so while addressing climate change? Both require immediate action. Fortunately, the two agendas overlap.

In short, the solution is to slash energy demand: grow more food and less fodder, drive and fly less, turn down the thermostat. Demand-led solutions are efficient, quick and cheap, as Cape Town showed in 2018 when the city drastically curbed water use during extreme drought in South Africa. Designed and implemented with care, and backed by policy, such measures can lower future greenhouse-gas emissions and climate risks, as well as reducing reliance on Russian exports today.

Without such steps, governments seeking to increase or subsidize domestic supplies of gas and oil, or to burn coal or ship in liquid natural gas (LNG), might slow the fuel-price spiral in the near term. But in the long run, they — along with everyone else — will face even greater economic damage from climate change. Russia's invasion of Ukraine makes clear that propping up the old world economy will result only in more resource bottlenecks, empowered authoritarian regimes, wars and climate-related devastation.

Here I outline a set of structural, social and lifestyle changes that could reduce European reliance on fossil-fuel imports from Russia by 20–60% within one year. If this approach were adopted by member states of the Organisation for Economic Co-operation and Development (OECD) and in east Asia, it would lower global greenhouse-gas emissions by up to 2.9% over 12 months (assuming 4–9% emissions savings in end-use sectors;

further savings in industry and the power sector are possible). And, by 2050, it would cut global emissions by 40–70% relative to existing policy commitments¹.

These figures are based on reports released this year by the Intergovernmental Panel on Climate Change (IPCC)¹ and the International Energy Agency^{2,3}. Similarly, the IPCC’s latest summary for policymakers⁴ sets out how a combination of structural shifts, social choices and changes in behaviour can cut emissions from sectors that use fossil fuels: by 5% rapidly in high-income countries, and by 40–70% by mid-century.

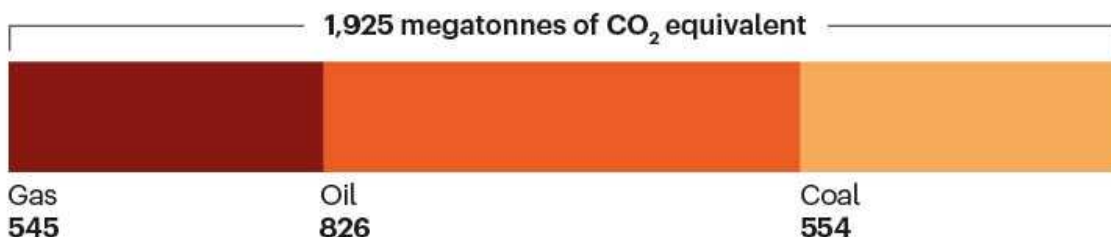
Three sectors are central: transport, buildings and food production (see ‘Cut reliance, curb emissions’). Challenges include overcoming economic inertia, changing behaviours and social norms, and ensuring policies are equitable. Some measures can be implemented straight away, such as banning cars from city centres. Others will take longer, such as overhauling food systems. The benefits of adopting new technologies and retrofitting will stack up year on year.

Such solutions aren’t new, but the war in Ukraine has made implementing them more urgent and palatable, politically and socially. It will require more than personal choice — regulation and market interventions will be needed to make low-carbon the obvious option.

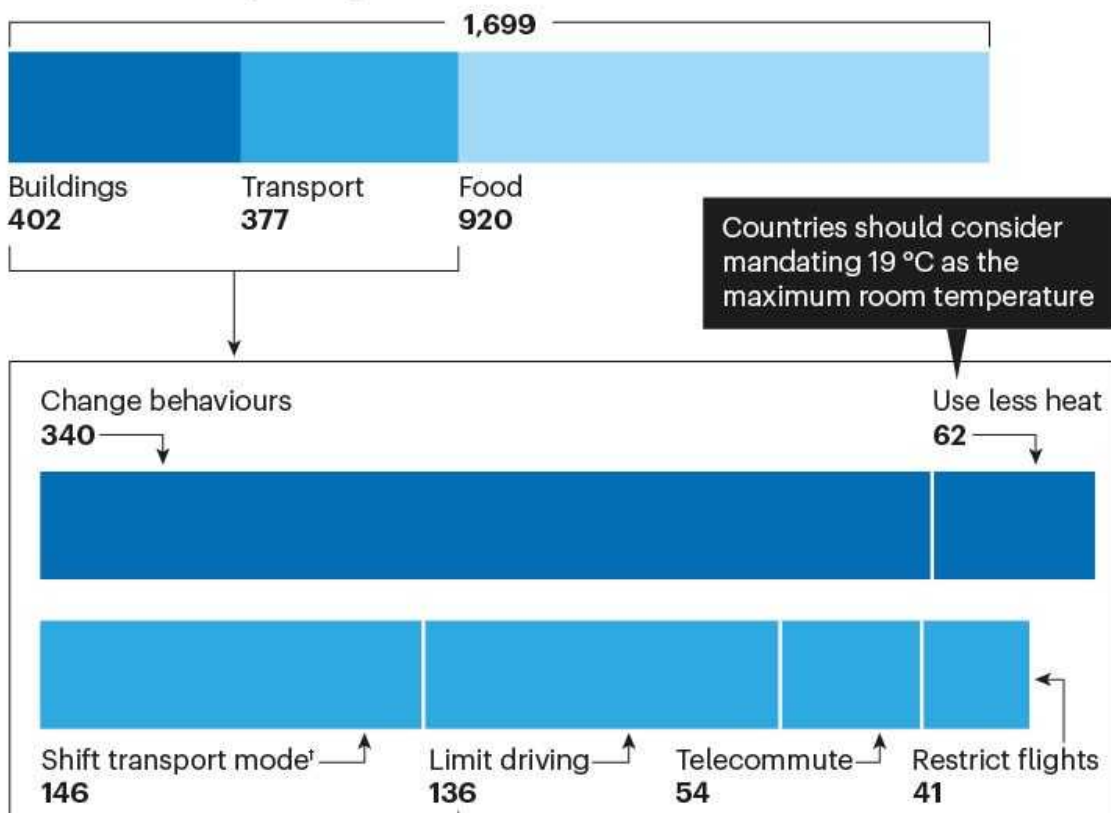
CUT RELIANCE, CURB EMISSIONS

Gas, oil and coal exports from Russia account for 7%, 5.8% and 3.6% of global consumption, respectively. Slashing energy demand would cut global emissions by 2.9% in 12 months and avert fuel shortages.

Emissions from Russian fossil fuel exports



Emissions saved by cutting demand in 3 sectors*



Lowering speed limits by 10 km h⁻¹ globally could save 430,000 barrels of oil a day

*In Organisation for Economic Co-operation and Development countries and east Asia

[†]Public transport, car pooling, cycling etc.

Source: See supplementary information

Transport

The following 5 measures (see SI for details) might, within one year, replace 60% of global oil imports from Russia (4.7 million barrels per day in 2021) and cut the transport sector's greenhouse-gas emissions by 4%. They would be most effective in OECD countries and China, nations that emit the highest share of greenhouse gases globally and have most capacity to act. They can be implemented quickly and fairly. And they support political and economic stability.

One, encourage telecommuting. During COVID-19 lockdowns, when those who could work from home did so, greenhouse-gas emissions from land-based transport fell by 40% globally⁵. Other benefits include time saved through not being stuck in traffic, a better work-life balance, fewer sick days and more freedom. In my view, governments should mandate that companies allow employees to work remotely at least half of the time, if tasks allow, with some social contact at the office.

Two, reduce speed limits. Energy consumption increases with the square of speed. On German roads where speed is unregulated, a limit of 120 kilometres per hour or 100 km h^{-1} would save up to 13% of greenhouse-gas emissions from light vehicles on highways (2.6 megatonnes of carbon dioxide equivalent or 5.4 MtCO₂e, respectively, per year; see SI). Globally, lowering speed limits for cars and heavy trucks by 10 km h^{-1} would save 430 thousand barrels of oil products per day², equivalent to Pakistan's oil consumption. It would also improve traffic safety. For example, after Seattle, Washington, reduced speed limits to 40 km h^{-1} citywide, crashes fell by 22%.

Three, ban cars from inner cities. Pontevedra in Spain and Ghent in Belgium have done so; Paris plans to; Berlin is considering it. Such a ban also lowers air pollution and noise, and revives the social nature of streets as meeting places. Restrictions, such as car-free Sundays, encourage residents to try living without cars. Implementing such measures across advanced economies could save another 82 MtCO₂e per year (see SI).

Four, adapt streets for safe cycling. In Germany, nearly 65% of all car trips, responsible for 20% of the total distance travelled by cars, are less than 10 km. Safe bicycle lanes, separated from traffic, should be expanded. Some cities tried this during the pandemic. For example, Bogotá created 84 km of temporary bicycle lanes using traffic cones. This increased the city's share of trips made by bicycle from 9% in 2020 to 13% in early 2021. One analysis of pop-up bicycle infrastructure in 2020 in 106 European cities found that extending bike lanes by 12 km per city, on average, increased the number of cycling trips by 11–48%⁶. Emissions from urban transport fell by between 0.34% and 1.87% as a result.

Five, replace short-haul flights with teleconferencing or train travel. During COVID-19 lockdowns, daily flight numbers fell by up to three-quarters⁵. France has banned domestic flights on routes that can be travelled by train in less than 2.5 hours, amounting to 12% of services. Some airlines might not object; Air France was making losses on some of those routes. In advanced economies, avoiding business air travel or replacing it with trains would save about 41 MtCO₂e per year, or about 300,000 barrels of oil per day². In academia, relocating conferences, increasing virtual participation and holding meetings every two years rather than annually could slash travel emissions by more than 90%⁷.

Social equity is an essential consideration — transport is the sector with the highest inequality in greenhouse-gas emissions. Low-income households, most of which neither have a car nor fly regularly, would hardly be impacted by bans. However, a small proportion (5–9%) of citizens in high-income countries rely on cars yet have low incomes. Policies to support them include targeted subsidies, zero-carbon shared-car and e-bike schemes, and paying climate dividends to all (see below).

Buildings

Heating accounts for one-quarter of total energy demand in buildings (see SI). Turning thermostats down by 2 °C in countries that are major importers of Russian gas, such as Germany, could save 32 billion cubic metres of gas annually (20 b.c.m. of which would be in Europe³) — about 13% of Russia's global gas exports. Lowering demand for heating should eventually reduce

energy prices, helping low-income households. Governments in OECD countries should consider mandating 19 °C as the maximum room temperature next winter. Although this would be hard to enforce, and some people might need warmer rooms for health reasons, for example, such a mandate would set a social norm that makes overheating unacceptable.



Smart meters help consumers to save electricity by displaying real-time data about their usage.Credit: Nate Pesce/The New York Times/Redux/eyevine

Behavioural interventions, such as visual prompts from ‘smart’ electricity meters, can encourage households to use less energy. Programmable devices can help them ‘game’ their energy use, by washing clothes off-peak, for instance. Social prestige should be attached to energy saving rather than large cars and housing. Utilities should roll out devices that display electricity and gas consumption, send out bills that compare customers’ energy use with neighbourhood averages, and advise on energy saving. A combination of such approaches might deliver energy savings of 4% (see SI). Making renewable-electricity providers the default for households when

they move in to a property is another effective measure — 80% of households stay with this option⁸.

Saving electricity has an immediate impact on fossil-fuel emissions and imports. The power plants that deliver peak energy loads and are switched off when demand drops often run on gas or coal.

More efficient use of industrial products can also reduce dependency on gas. For example, more than 4% of German gas imports from Russia are used to produce steel. Changing building codes can reduce the need for steel in construction by one-quarter⁹. Refurbishing old buildings or reusing parts of them is better than demolishing them to construct new ones¹⁰. Allocating floor space more efficiently can also save on materials and gas.

Food

A global food crisis is also unfolding. Russia and Ukraine are responsible for more than one-third of the world's cereal exports, mostly barley, wheat and maize. And Belarus and Russia are major exporters of fertilizer. Production of ammonia, which is used to make nitrogen-based fertilizer, consumes 120–200 b.c.m. (3–5%) of global gas output annually, comparable with Russian gas exports to the EU. Prices of cereals and fertilizer are rocketing.

What to do? Europe alone could replace lost Ukrainian grain by substituting one-third of the EU's fodder production (or the world could substitute 5% globally) with cultivation of wheat and other grains¹¹. Fodder accounts for more than half of agricultural production in the United States and the EU, and more than one-third globally¹². Yet only 12% of the calories in feed ends up as human-food calories. Such a step would reduce the pressure to deforest in other parts of the world. Rearing fewer animals would also lower emissions of methane, a potent greenhouse gas.



Harvesting cereal crops for fodder in Hungary.Credit: Sandor Ujvari/EPA/Shutterstock

Another option, taxing greenhouse emissions in the food sector, could be more effective but is harder to implement. Some analysts project¹³ that taxing food at US\$52 per tonne of CO₂ emitted would reduce emissions from the agricultural sector by 9% by incentivizing farmers to use less nitrogen fertilizer, for example.

Prices for emissions-intensive food, mostly meat, could increase by 15–40%. Those for fruits and vegetables would rise less, by less than 3%. Yet, even small price rises risk lowering access to nutrition in some parts of the world¹. The impacts of carbon taxes could be reduced by lowering value-added taxes on plant-based foods. In the long run, dietary shifts from animal protein to vegan food, and cutting food waste would, by 2050, reduce fertilizer input and emissions from agriculture by 40% compared with current national policies¹.

Overcoming obstacles

All the above actions would save up to 1,700 MtCO₂e, or 2.9% of global greenhouse gas emissions. That includes: 380 MtCO₂e from transport, 350–400 MtCO₂e from buildings and 920 MtCO₂e from food (see SI). Other measures can be deployed on top, such as the use of heat pumps, solar power and electric cars. Hurdles will need to be overcome, however.

Social equity must be addressed. One per cent of the world's population is responsible for 15% of its greenhouse-gas emissions, and yet hundreds of millions of people have inadequate access to basic services¹. In my view, climate dividends — a lump-sum transfer of several hundred dollars per year for each citizen to alleviate the burden of higher energy costs — would align climate action with social equity better than a patchwork of subsidies. Such a dividend could be financed by carbon prices, taxes or trading¹⁴. It would also protect low-income households that cannot easily shift away from fossil fuels.

Inertia and economic and political interests are the greatest barriers to change. For decades, companies and governments have spent billions on fossil-fuel infrastructure — gas pipelines, LNG terminals, petrol stations, oil platforms, diesel and petrol vehicles, and power plants. Switching them off means losing capital, expertise and investment.

Governments and others must send firm signals that the fossil-fuel industry is in decline. New oil, gas and coal infrastructure should not be built. For example, Germany will be better off saving energy than installing LNG terminals. Pension funds, banks and others should divest from oil and gas companies that still plan to expand. Commitments should be made to increase carbon pricing, and dates set for phasing out gas and oil heating and internal-combustion and diesel engines.

Revenue can be redirected to finance energy and mobility transitions, for example by taxing windfall profits of fossil-fuel companies. Taxing Russian gas imports by about 30–60% would cut the revenues of Gazprom — the giant state-owned energy firm — by 50–75%, and the tax revenues would more than compensate for surcharges incurred by consumers¹⁵. Alternatively, governments should mandate fossil-fuel companies to reinvest all income in renewable energy and other substitutes.

The barriers seem huge. But surveys show considerable public support for demand-led measures. Energy saving can create jobs and reduce energy inequity. As fossil-fuel prices keep climbing, a swift, sharp cut in energy demand is achievable and affordable, and will lead more quickly to a better future for all.

Nature **606**, 460–462 (2022)

doi: <https://doi.org/10.1038/d41586-022-01616-z>

References

1. Creutzig, F. *et al.* in *Climate Change 2022: Mitigation of Climate Change*, Ch. 5 (IPCC, 2022).
2. IEA. *A 10-Point Plan to Cut Oil Use* (2022).
3. IEA. *A 10-Point Plan to Reduce the European Union's Reliance on Russian Natural Gas* (2022).
4. Skea, J. *et al.* *Climate Change 2022: Mitigation of Climate Change, Summary for Policymakers* (IPCC, 2022).
5. Le Quéré, C. *et al.* *Nature Clim. Change* **10**, 647–653 (2020).
6. Kraus, S. & Koch, N. *Proc. Natl Acad. Sci. USA* **118**, e2024399118 (2021).
7. Klöwer, M., Hopkins, D., Allen, M. & Higham, J. *Nature* **583**, 356–359 (2020).
8. Liebe, U., Gewinner, J. & Diekmann, A. *Nature Hum. Behav.* **5**, 576–585 (2021).
9. Fennell, P., Driver, J., Bataille, C. & Davis, S. J. *Nature* **603**, 574–577 (2022).

10. Pongiglione, M. & Calderini, C. *Resour. Conserv. Recycl.* **86**, 87–92 (2014).
 11. Pörtner, L. M. *et al.* *One Earth* **5**, 470–472 (2022).
 12. Cassidy, E. S., West, P. C., Gerber, J. S. & Foley, J. A. *Environ. Res. Lett.* **8**, 034015 (2013).
 13. Springmann, M. *et al.* *Nature Clim. Change* **7**, 69–74 (2017).
 14. Budolfson, M. *et al.* *Nature Clim. Change* **11**, 1111–1116 (2021).
 15. Gros, D. How to solve Europe's Russian gas conundrum with a tariff. See <https://go.nature.com/3mb5ajt> (2022).
-

This article was downloaded by **calibre** from <https://www.nature.com/articles/d41586-022-01616-z>

| [Section menu](#) | [Main menu](#) |

- CORRESPONDENCE
- 14 June 2022

Fleeing Russian researchers seek Western support

- [Sergei M. Mirkin](#),
- [Alexander Vilenkin](#) &
- [Polina Deletic](#)

Thousands of Russian scientists initially spoke up against their country's invasion of Ukraine (see go.nature.com/3tikx92), but such expressions are now criminalized in Russia. Under these circumstances, many researchers find it morally impossible to continue working there. They have fled to neighbouring countries in the Middle East, Central Asia and the Baltics, where most are stranded without a visa, work permit or access to their savings.

These are some of the best brains of Russia. Their exodus is a massive blow to the long-term technological prowess of the oppressive regime of Vladimir Putin. Although Western governments are working to provide visas for Russians who have advanced degrees, visas alone are not enough. What is urgently needed is funding for new research positions.

When Hitler came to power in Germany in the 1930s, hundreds of German scientists relocated to the United States with emergency fellowships from the Rockefeller Foundation. Included in this group were six future Nobel laureates.

We call on government and private agencies in the United States, the European Union and the United Kingdom to set up similar emergency programmes for scholars escaping Putin's Russia.

Nature **606**, 463 (2022)

doi: <https://doi.org/10.1038/d41586-022-01622-1>

This article was downloaded by **calibre** from <https://www.nature.com/articles/d41586-022-01622-1>

| [Section menu](#) | [Main menu](#) |

Work

- **[Peer-to-peer careers advice for research managers](#)** [13 Jun 2022]
 - Six technicians and managers share tips on how their roles can be better developed and supported.
- **[Cloud labs: where robots do the research](#)** [13 Jun 2022]
 - A host of companies provide a remote, automated workforce for conducting experiments around the clock.
- **[Sniffing out forest fungi](#)** [13 Jun 2022]
 - Field mycologist Željko Zgrablić works with his dog to track how climate change affects truffles.

- CAREER FEATURE
- 13 June 2022

Peer-to-peer careers advice for research managers

Six technicians and managers share tips on how their roles can be better developed and supported.

- [Nikki Forrester](#)

[Find a new job](#)

Research technicians and laboratory managers are important for keeping scientific research moving forward. They collect data, oversee budgets and supplies, and manage research teams. Yet, these positions aren't always recognized as long-term career options and individuals in these roles often lack the resources and support needed to develop their own careers. *Nature* talked to six technicians and lab managers about how they continue to make progress towards their goals and what lab leaders and institutions can do to support them.



Takako Keida enjoys the work–life balance that the research technician role can offer.Credit: Aiko Sada

TAKAKO KEIDA: Consider your personal life

Laboratory technician at Kumamoto University in Kumamoto, Japan.

In the early years of secondary school, I enjoyed doing science experiments, so I wanted to become a pharmacist or a clinical laboratory technician. After considering the tuition and living expenses needed to go to pharmacy school, I decided on the technician route. As the daughter of divorced parents who was bought up by my aunt because neither parent had the financial resources to do so, I wanted a stable job that paid enough for me to lead an independent life and provide for my family.

I started working as a laboratory technician at Kumamoto University in December 1998 and have worked in four labs there since then. My role as a

technician is to support researchers by helping them with various protocols, such as genotyping genetically modified mice. I love the sense of accomplishment that comes with producing results in cooperation with researchers.

I was also able to earn my bachelor's degree while working as a technician. My boss at the time, cell biologist Toshio Suda, told me that improving technicians leads to improved research. He helped me and the assistant professor who was supporting me at the time to turn my research into a thesis, which was needed for my degree.

The environment for laboratory technicians has been great, not only to support my career goals, but also for raising my three children, who are now adults. Many researchers at the university have lived abroad, so they have flexible attitudes toward women who are raising children and working at the same time. I didn't have to worry about or feel guilty for taking leave when my child was sick or to attend school events. I could also adjust my work schedule as long as I achieved results during the overall project, so it was easier and less stressful to balance work and childcare.

I am grateful for the university environment, when I see my children who are now able to dedicate themselves to society. Although I have been working at the university for a long time, the atmosphere has remained the same.

JACQUELYN MOUNTCASTLE: Advocate for yourself

Staff research associate at the University of California, Los Angeles.

As a molecular-biology technician, I do a lot of genomic sequencing of native amphibians, reptiles and plant species in Los Angeles, California. I started my current position about six months ago, but worked as a technician for 4.5 years before that in a lab at Rockefeller University in New York City sequencing the genomes of vertebrate species.

In my previous lab, I felt like I got to a point at which I couldn't grow in the way I wanted to, in part because there wasn't a management position available for me to be promoted into. I also wanted to explore more applied research. I decided to join a lab at the University of California, Los Angeles, because it worked directly with local and state governments to inform conservation efforts.

I'm still not quite sure of my career path from here. I can't afford to go back to university for a PhD and I don't want to focus on a single research project, but there aren't a lot of options for people in my position to understand where to go next. To help me navigate my options, I reached out to other researchers I worked with but who were outside my lab. They helped me to weigh up the pros and cons of getting a PhD and offered perspectives on working in industry and federal agencies. About four months ago, I started working with a career coach, who helped me to identify jobs that align with my values, skills and passion for science. This has been a tremendous experience and I now have a clearer path forward than I ever had before, but it is a very expensive resource that isn't accessible for everyone.

I wish there were more mentorship services available for research technicians, but I have learnt that it's important to advocate for yourself to ensure that you get the opportunities you need to progress in your career. As a tech, it can be difficult to approach a supervisor about new opportunities and advocate for your career growth. But during my interview, I asked for the experiences that I wanted and communicated the skills I gained during my master's degree in public health to ensure that I would be compensated fairly.

We need to create more supportive environments in which technicians feel valued, because that's going to determine whether somebody stays or leaves. Lab leaders should not view technicians as just being there to pipette and go home. They should make sure that technicians feel comfortable and supported in developing their careers. Often, it feels like people view these positions as temporary roles that can be filled by undergraduates who need lab experience. But there are so many people who would like to stay in these positions for longer time periods and contribute to research in their own way.



Louis Banda in the lab.Credit: Louis Banda

LOUIS BANDA: Find your purpose

Lab manager for the Malawi Epidemiology and Intervention Research Unit in Karonga, Malawi.

I grew up in central Malawi and joined the Malawi Epidemiology and Intervention Research Unit (MEIRU) in Karonga in 2007. MEIRU is a research organization that was started in 1979 to study individuals with

leprosy. It has since expanded to conduct population studies on tuberculosis, HIV and COVID-19.

I started off as a lab technician, but always felt the need to improve myself and reach a position where I could make decisions. That inspired me to become an assistant lab manager and then the lab manager. As a technician, I worked mostly at the bench running tests on stool, blood and urine samples for various research projects. Now, I set budgets for the lab, procure reagents and consumables and manage ten assistants and technicians. I interact with a variety of people, including study leaders, a data-management team and field researchers.

Over the past 15 years, I've learnt that I need to understand the requirements of each researcher and project to ensure that I execute studies correctly. Lab managers constantly need to update their knowledge base about the latest technologies and procedures, which can be challenging because research is so dynamic. I read a lot of scientific literature and regularly ask the researchers I work with about the equipment and protocols they use or would like to use.

Although lab technicians and managers are involved in research, our contributions aren't always recognized. I'd love to lead a study about a research question I'm interested in and be first author on more scientific publications, but what keeps me motivated is the impact that I've had on people in Malawi. A lot of people have received diagnoses and treatments because of my work at MEIRU — that's why I've stayed there for so long. My advice for other lab managers is to make sure that you're benefiting other people in your community, country or region.

DEVIN LAKE: Expand your network by helping others

Lab manager and PhD student at Michigan State University in East Lansing, Michigan.

I worked as a paid laboratory technician in my current lab as an undergraduate student. During the academic year, I worked about 30 hours a

week and during the summer, I worked full time. The lab was like a second home for me. When I graduated, my supervisor offered to pay for my PhD if I took on the role of lab manager. Both positions benefit from me knowing what everyone else in the lab is doing, but that's about the only overlap. Most of my responsibilities and even my relationship with my PhD adviser differ depending on which hat I have on at the time.

As a lab manager, my main responsibility is to keep track of the undergraduate lab techs who maintain media to grow bacteria, clean and prep glassware and sterilize equipment. I train them on lab techniques, and I give them advice on navigating university and their career paths. I order equipment, make sure everyone's safety trainings are up to date and occasionally do lab work.

When I applied for graduate school, I wanted to become a professor, but managing the lab helped me realize I would much rather do this as my career. I get so much joy out of mentoring the undergraduates and helping everyone else's research projects come to fruition.

One of the toughest parts is finding a new lab-manager position when I finish my PhD and my adviser retires. I have to find either a new professor who needs help starting their research programme or an established scientist who needs help organizing their lab and can afford to hire a manager. I have my foot in 18 doors and am just waiting until someone says they've got a position available.

Thankfully, my current lab has a huge network, and many alumni have started their own labs. New professors ask me questions about different protocols and what their lab managers need to know. In June, I'm going to Texas to train a new lab manager on how to conduct experiments that we've been doing in our lab for more than 30 years. Having people come to me for help and guidance has provided opportunities for me to continue working in this role.

ELAINE FITZCHARLES: Invest in training opportunities

Senior lab manager at the British Antarctic Survey in Cambridge, UK.

I've always liked the practical side of making equipment work, which is why becoming a lab manager was probably the right decision for me. I've been at the British Antarctic Survey (BAS) since 2003, starting as a genomics technician and growing into the senior lab manager role I have today. I now oversee all of the BAS labs, including six research stations, a research ship and five laboratory suites in Cambridge.

Some days I am in constant meetings with people across the organization. Other days, I'm moving boxes, picking up orders and checking budgets. I also work with nine lab managers, so I get the team together so we can keep up to date with what people are up to and support each other.

Along with the day-to-day lab operations, I have to think about how to develop new facilities and upgrade technologies for future research projects. People in technical and lab-management roles are often looking at what's coming next across a range of scientific disciplines. I have to understand areas of science beyond my own background in marine biology and listen to people's goals for their research programmes.

Being a lab manager is about managing people as well as equipment and facilities. One of my biggest challenges is balancing the needs of different people and trying to decide who gets priority, because we have limited funds, and we need to make sure they go to the right place. Part of my role is making sure everybody's voice is heard and that I'm not just listening to the person who speaks the loudest.

You also need the right scientific skill set and personality to be a lab manager or technician, so I continue to invest in training opportunities to develop my capabilities. I've taken courses about understanding different personality types and how to have challenging conversations. I go to conferences and speak to people who are in similar roles. For instance, the Institute of Safety in Technology and Research in London hosts an annual conference, and the members e-mail group is a fantastic support network for advice on any lab management issue. The Institute of Science & Technology in Sheffield, UK, also has an annual conference that is very much aimed at the technician community and support for career development.

Becoming a lab manager is very much a career choice that I wish received the same recognition as becoming a research scientist. I had considered moving into a postdoc position and going down the researcher route, but there's a stability to lab-management positions, in part because you don't have to chase down grant funding. These roles require a different skill set from research positions, but still need a high level of knowledge and expertise.



Catherine Tuckey advises technicians and lab managers to join professional bodies. Credit: Debbie Whitmore

CATHERINE TUCKEY: Level up professionally

Professional registration specialist for the Royal Society of Chemistry and project lead of the Technician Commitment initiative in Nottingham, UK.

I manage applications to become registered science technicians and scientists that come to the Royal Society of Chemistry (RSC) in Cambridge, UK. These designations are managed by the Science Council, a UK

membership organization for professional scientific bodies, and are public awards honouring someone's skills and expertise in a professional setting. For instance, chemistry technicians must showcase their scientific knowledge as well as their skills in communication and teamwork to be eligible for registration.

As a publisher, the RSC is keen to support authorship for technicians on research papers to acknowledge their contributions. It also has funds to support technicians who want to run outreach or public-engagement events.

Sometimes technicians don't feel empowered to fight for themselves and raise their profile, but engaging in career-development opportunities can help them to build confidence. The RSC has grants specifically for technicians to develop their careers. It also funds members to undertake training courses or attend networking events, including any associated travel costs, and has a larger grant available to fund extended placements for technicians.

My advice for current and potential research technicians is to become members of a professional body. The RSC has a wealth of knowledge and a careers team that offers impartial advice, one-to-one consultations and webinars on various career paths. If you're working within a scientific field, ask technicians in your lab or department about their roles and the support resources that are available to them.

My advice for supervisors and lab managers is to take the time to understand exactly what a technician does on a daily basis, because that will allow them to tailor development opportunities to the specific needs of their staff.

Nature **606**, 609-611 (2022)

doi: <https://doi.org/10.1038/d41586-022-01617-y>

These interviews have been edited for length and clarity.

| [Section menu](#) | [Main menu](#) |

- TECHNOLOGY FEATURE
- 13 June 2022

Cloud labs: where robots do the research

A host of companies provide a remote, automated workforce for conducting experiments around the clock.

- [Carrie Arnold](#)



The automated laboratory facility at Emerald Cloud Lab in South San Francisco, California. Credit: Emerald Cloud Lab

As a chemistry PhD student, Dmytro Kolodieznyi was used to running experiments. But in early 2018, his research advisers asked him to take part in one run by robots instead.

They wanted Kolodieznyi, who was developing intracellular fluorescent probes at Carnegie Mellon University in Pittsburgh, Pennsylvania, to spend a month attempting to recreate his research at Emerald Cloud Lab (ECL). The biotechnology company in South San Francisco, California, enables scientists to perform wet-laboratory experiments remotely in an automated research environment known as a cloud lab. If the trial went well, it would help pave the way to the wider use of cloud labs at the university.

Unlike in his Pittsburgh lab, where Kolodieznyi and his fellow students conducted their own experiments, the workhorses at ECL's 1,400-square-metre headquarters were rows of machines run by lines of code issued by researchers around the world, with occasional assistance from waist-high white robots that whirred around the room. There were hundreds of machines at work, but only one or two human technicians were needed to manage the entire process.

It took just one week of hands-on time for Kolodieznyi to replicate several years of his PhD research — everything from organic synthesis of fluorescent tags to advanced microscopy. He says that he only scratched the surface of the company's capabilities, which include cell culture, DNA synthesis, liquid chromatography and structural-analysis methods, such as mass spectrometry and nuclear magnetic resonance. But the experience left its mark: in 2020, after earning his PhD, he joined the company as a scientific developer.

Kolodieznyi's positive feedback, together with disruptions to research in 2020 as a result of the COVID-19 pandemic, led Carnegie Mellon University to invest US\$40 million in a partnership with ECL to build a Pittsburgh-based cloud lab — the first such facility to be built in an academic setting. Construction of the Carnegie Mellon University Cloud Lab began in November 2021, and it is set to open in mid-2023. The university's faculty members, staff and students will have priority access to the lab, so every researcher there has the chance to use the technology, according to Rebecca Doerge, the Glen de Vries Dean of the university's Mellon College of Science.

Academics, small start-up firms and big pharma are increasingly turning to cloud labs as part of a trend to outsource work. The approach is like "having

a laboratory that is operating 24/7”, says Germano Coppola, executive director of research and development at the biotechnology firm CSL Behring in Melbourne, Australia, which is a client of ECL’s.

Cloud labs provide “tremendous potential for scientists to generate a lot of data without even having to enter a lab,” he says.

The virtual bench

ECL co-founders Brian Frezza and D. J. Kleinbaum didn’t set out to turn the lab bench virtual. Friends as children, the pair attended Carnegie Mellon, and in 2010, they founded Emerald Therapeutics in South San Francisco to focus on developing antiviral drugs. But Frezza and Kleinbaum spent much of their time trying to get the machinery in their new lab to work. Their solution was an ever-expanding set of computer codes to manage the equipment and run round-the-clock experiments. Frezza noticed not only an increase in productivity from the set-up, but also a rise in reproducibility.

“I was turning experiments into code,” Frezza says. “At the end of the day, there’s no ambiguity in this text, I can push a button and reproduce it.”

The pair realized that other labs could benefit from this virtual system, and formed ECL that same year to sell subscription access to their equipment and software. The best way to think of it, Frezza says, is like the streaming services Netflix or Spotify for the lab. Just as users of those services pay for access to a virtual library of digital content without ever purchasing a song or television episode, ECL and other cloud labs provide access to a vast warehouse of equipment without having to invest any capital.

Researchers can log on to the ECL dashboard and specify what experiments they want to conduct and when; configure the equipment to their liking; make adjustments along the way; and get live progress updates on their experiments and watch the process on video. An artificial-intelligence-based ‘expert’ acts as a highly skilled technician, giving users the ability to tweak default values and identify issues that can halt experiments.



One of the robots at a Strateos lab facility.Credit: Strateos, Inc.

ECL provides three levels of access, based on how many experiments users wish to run at once. The lowest tier allows three to run in parallel and starts at \$24,000 per month. It's not cheap, Frezza admits, but compared with the cost of buying the equipment, he says it saves researchers money in the long run. Strateos, which has a cloud lab in Menlo Park, California, customizes its access levels and pricing, allowing users to tailor their experience to their budget.

For Coppola and CSL Behring, cloud labs provide what is effectively a 24-hour service. Coppola sends his samples and reagents to ECL's headquarters or purchases them from its existing inventory, programs his commands into a point-and-click user interface and waits for the results to roll in. He can watch his experiments on a webcam and get read-outs in real time.

Cloud labs aren't the only option for research teams that lack the infrastructure or expertise to perform certain experiments: contract research

organizations (CROs) are another. But the two approaches are very different, says Daniel Rines, vice-president of Technology Enabling Services, who is based at Strateos's other facility in San Diego, California. With a cloud lab, scientists perform all of their own experiments. You might be running them from thousands of kilometres away, but they remain your ideas and your results.

By contrast, "CROs are very labour-driven," Rines says, meaning that they tend to rely on humans to do much of the work. "What we're doing is using our robotic capabilities to industrialize science and make it more reproducible and reliable."

Because of this, when experiments fail, cloud-lab users can dive back into their data to work out what went wrong, without relying on anyone else. Kolodieznyi describes the process as like having an army of highly talented, highly trained undergraduates at your beck and call. They might not be able to design studies at first, but once they are trained, they can run your experiments – and do it in the same way every time, he says.

"I cannot remember how many times I've read something in a paper, tried to do it and, not surprisingly, it didn't work. But in a cloud lab, if I just copy and paste my experiment, it will work again," Kolodieznyi says.

Advocates of cloud labs say that as well as the reproducibility advantage, providing affordable access to the equipment needed to do science helps to democratize research. "It doesn't matter who you are or where you are. You're all using the same laboratory. That's a huge thing," Frezza says.

Huaiying Zhang, a bioengineer at Carnegie Mellon, has proposed use of the university's cloud lab by high-school students in a low-income district in the state of Georgia – work for which she was awarded a grant by the US National Science Foundation. Not all students who are interested in science can get access to sophisticated equipment, she explains, but running experiments in cloud labs removes those barriers. Once the Carnegie Mellon cloud lab is up and running, she hopes to give students the chance to perform real experiments on equipment normally reserved for PhD students and postdocs.

“You’re not just memorizing facts. You’re getting real data,” Zhang says. “Students can use equipment they would not normally have been able to access.”

At University College London, researchers have teamed up with the London-based Synthace Life Sciences R&D Cloud to provide a no-code user interface that will let researchers automate tasks and create experimental workflows remotely. This partnership will enable scientists to “future-proof” their experimental designs against unexpected disruptions to their work, according to a statement from Synthace.

However, writing in the *Bulletin of the Atomic Scientists*, researchers Filippa Lentzos and Cédric Invernizzi note that, by lowering the barrier to expensive equipment, cloud labs could enable bad actors, such as terrorist groups, to misuse the technology to perform “malevolent” experiments (see go.nature.com/3nsbg9e). When asked for comment on this issue, spokespeople at both Strateos and ECL say they use the highest-level data encryption possible, and that they’ve never had any security concerns, although they do not have any active checks in place to guard against those contingencies.

For Doerge, the benefits of cloud labs outweigh such concerns — especially amid the ongoing pandemic. Much of the university’s research ground to a halt as COVID-19 took hold in early 2020. A cloud-lab facility would have allowed much of this research to continue, as well as many lab courses at the university, she says.

“This was the transformation that science needed, much like the cell phone, much like the self-driving car,” Doerge says. “The process of science hasn’t kept up with the technology.”

Nature **606**, 612–613 (2022)

doi: <https://doi.org/10.1038/d41586-022-01618-x>

| [Section menu](#) | [Main menu](#) |

- WHERE I WORK
- 13 June 2022

Sniffing out forest fungi

Field mycologist Željko Zgrablić works with his dog to track how climate change affects truffles.

- [Nic Fleming](#)



Željko Zgrablić is a field mycologist at the Ruder Bošković Institute in Zagreb, Croatia. Credit: Damir Sencar/AFP via Getty

Truffles are socially and economically important in parts of Croatia. They can be worth up to €5,000 (US\$5,300) per kilogram. The truffle industry and related tourism provides jobs, supplements incomes and boosts local

economies. It's not just about money, however; many people just love being out in the forest looking for them.

My fascination with fungi began at the age of six, when my father and grandfather began taking me out to hunt for game and to collect mushrooms near our home in Istria. Today, I focus mainly on truffles and other hypogeous fungi, which produce their fruiting bodies underground. I spend 50–100 days a year in the field with my dogs, collecting samples and data on the life cycles, ecology and geographical spread of fungi across Croatia. Here, I'm with my dog Masha. I love the work.

Thirty years ago, rainfall used to be more predictable across the year in Istria. Now, the climate is more extreme, and includes droughts. Truffles require a specific amount of water to grow. And warm winters have increased the population of wild boars, which damage the soil and eat the truffles. The truffles are becoming harder to find.

Truffle plantations could take the pressure off natural habitats. There, the soil water content can be controlled, agricultural methods can be used to enhance production and boars can be kept out. We're studying the viability of farming black truffles, in part by experimenting with different ways to inoculate tree seedlings with their spores.

We're using DNA barcoding to identify fungi in soil from their spores and root-like mycelium in protected areas. We're finding that there are often many more species present than previously thought.

Our comparisons of areas with and without truffles could help to reveal why they grow in some areas but not others. Our work is also helping to show the importance of biodiversity in places such as the Adriatic islands of Brijuni National Park.

Nature **606**, 616 (2022)

doi: <https://doi.org/10.1038/d41586-022-01619-w>

| [Section menu](#) | [Main menu](#) |

Research

- [**Measurement of the bound-electron g-factor difference in coupled ions**](#) [15 Jun 2022]
 - By trapping and crystallizing two highly charged ions of different neon isotopes in the same potential, a high-precision measurement of the bound-electron g-factor difference is obtained.
- [**Realizing the symmetry-protected Haldane phase in Fermi–Hubbard ladders**](#) [01 Jun 2022]
 - A ladder-like arrangement of an ultracold gas of lithium atoms trapped in an optical lattice enables the observation of a symmetry-protected topological phase.
- [**Graph pangenome captures missing heritability and empowers tomato breeding**](#) [08 Jun 2022]
 - A precise catalogue of more than 19 million variants from 838 tomato genomes, including 32 new reference-level genome assemblies, advances the understanding of the heritability of complex traits and demonstrates the power of the graph pangenome in crop breeding.
- [**Genome evolution and diversity of wild and cultivated potatoes**](#) [08 Jun 2022]
 - High-quality diploid assemblies of potato genomes from 24 wild and 20 cultivated potatoes provide insights into the complex evolution and diversity of potatoes, and could have applications in the breeding of hybrid potatoes.
- [**Communicating doctors' consensus persistently increases COVID-19 vaccinations**](#) [01 Jun 2022]
 - Correcting public misperceptions about the views of doctors on the COVID-19 vaccines can have lasting impacts on public uptake of the COVID-19 vaccines.
- [**An oxygen-sensing mechanism for angiosperm adaptation to altitude**](#) [01 Jun 2022]
 - Plants have adapted to grow at specific altitudes by regulating chlorophyll synthesis in response to ambient oxygen concentration, calibrated by altitude-dependent activity of GROUP VII ETHYLENE RESPONSE FACTOR.
- [**Fc_yR-mediated SARS-CoV-2 infection of monocytes activates inflammation**](#) [06 Apr 2022]
 - Antibody-mediated SARS-CoV-2 uptake by monocytes and macrophages triggers inflammatory cell death that aborts the production of infectious virus but causes systemic inflammation that contributes to COVID-19 pathogenesis.

- **Inflammasome activation in infected macrophages drives COVID-19 pathology** [28 Apr 2022]
 - A new humanized mouse model for COVID-19 demonstrates SARS-CoV-2 infection and subsequent activation of inflammasomes in human macrophages as a critical driver of disease.
- **Mechanism of mitoribosomal small subunit biogenesis and preinitiation** [08 Jun 2022]
 - Structural analysis of several small mitoribosomal subunit intermediates reveals a sequential mechanism of biogenesis, and how assembly links to initiation to form active mitoribosomes.

| [Next section](#) | [Main menu](#) | [Previous section](#) |

- Article
- Open Access
- [Published: 15 June 2022](#)

Measurement of the bound-electron g-factor difference in coupled ions

- [Tim Sailer](#),
- [Vincent Debierre](#),
- [Zoltán Harman](#),
- [Fabian Heiße](#),
- [Charlotte König](#),
- [Jonathan Morgner](#),
- [Bingsheng Tu](#),
- [Andrey V. Volotka](#),
- [Christoph H. Keitel](#),
- [Klaus Blaum](#) &
- [Sven Sturm](#)

[Nature](#) volume **606**, pages 479–483 (2022)

- 557 Accesses
- 99 Altmetric
- [Metrics details](#)

Abstract

Quantum electrodynamics (QED) is one of the most fundamental theories of physics and has been shown to be in excellent agreement with experimental results^{1,2,3,4,5}. In particular, measurements of the electron's magnetic moment (or *g* factor) of highly charged ions in Penning traps provide a

stringent probe for QED, which allows testing of the standard model in the strongest electromagnetic fields⁶. When studying the differences between isotopes, many common QED contributions cancel owing to the identical electron configuration, making it possible to resolve the intricate effects stemming from the nuclear differences. Experimentally, however, this quickly becomes limited, particularly by the precision of the ion masses or the magnetic field stability⁷. Here we report on a measurement technique that overcomes these limitations by co-trapping two highly charged ions and measuring the difference in their g factors directly. We apply a dual Ramsey-type measurement scheme with the ions locked on a common magnetron orbit⁸, separated by only a few hundred micrometres, to coherently extract the spin precession frequency difference. We have measured the isotopic shift of the bound-electron g factor of the isotopes $^{20}\text{Ne}^{9+}$ and $^{22}\text{Ne}^{9+}$ to 0.56-parts-per-trillion (5.6×10^{-13}) precision relative to their g factors, an improvement of about two orders of magnitude compared with state-of-the-art techniques⁷. This resolves the QED contribution to the nuclear recoil, accurately validates the corresponding theory and offers an alternative approach to set constraints on new physics.

Main

The theory of quantum electrodynamics (QED) describes the interaction of charged particles with other fields and the vacuum surrounding them. State-of-the-art calculations of these effects allow for stringent tests of fundamental physics, the search for physics beyond the standard model or the determination of fundamental constants^{1,2,3,4,5}. One quantity that can be used to perform such tests is the magnetic moment of an electron bound to a nucleus, expressed by the Landé or g factor in terms of the Bohr magneton. It can be both experimentally accessed and predicted by theory to high precision. In particular, hydrogen-like ions, with only a single electron left, provide a simple bound-state system that allows for testing the standard model in the extremely strong electric field of the nucleus. In this case, the g factor of a free electron is modified by the properties of the nucleus, foremost the additional electric field, but also parameters such as the nuclear mass, polarizability and the charge radius have to be considered. However, studying these effects explicitly proves to be difficult, as the QED

contributions and their uncertainties are significantly larger than many of the nuclear effects, resulting in limited visibility ('*g*-factor calculation' in Methods).

One idea to overcome this limitation is to compare the *g* factors of similar ions, by studying the isotopic shift. Here the common identical contributions and their uncertainties do not have to be considered, emphasizing the differences owing to the nucleus. In Table 1, the theoretical contributions and uncertainties to the individual *g* factors of $^{20}\text{Ne}^{9+}$ and $^{22}\text{Ne}^{9+}$ and their differences are summarized. For the calculated difference $\Delta g = g(^{20}\text{Ne}^{9+}) - g(^{22}\text{Ne}^{9+})$, the QED contribution to the nuclear recoil can be resolved and tested independently from all common QED contributions. This QED recoil effect arises from the quantized size of the momentum exchange between the electron and the nucleus, and requires a fully relativistic evaluation that goes beyond the Furry picture⁹ and the usual external-field approximation¹⁰. Understanding and confirming this contribution is essential for future *g*-factor measurements of heavier ions or when trying to improve on the precision of the fine-structure constant α (ref. 11). Furthermore, a precise measurement of the isotopic shift allows searching for physics beyond the standard model, by means of looking for a deviation from the calculated effect. In particular, a mixing of a new scalar boson and dark-matter candidate, the relaxion, of unknown mass m_Φ , with the Higgs boson would mediate an interaction between nucleons and electrons. Such a mixing with different coupling strengths y_e and y_n for electrons and nucleons, respectively, could potentially be directly observed in the isotopic shift owing to the different number of neutrons. Specifically, such a measurement would exhibit a strong sensitivity of the *g*-factor difference¹² for heavy bosons, with a specific energy range of 20 MeV to 1 GeV owing to the close proximity of the electron to the nucleus in a highly charged ion (HCI) ('Setting constraints on new physics' in Methods). The relaxion, if found, could potentially provide a solution to the long-standing electroweak hierarchy problem¹³. To explicitly study the isotopic shift with formerly unavailable resolution, we report on the application of a technique developed to measure the difference between the *g* factors directly. This method depends on coupling two ions as a well controlled ion crystal within the magnetic field of a Penning trap. In this way, the ions are close enough to be subject to the identical fluctuations of this magnetic field, which

otherwise pose strong limitations for the achievable precision. We performed such a measurement in the ALPHATRAP setup⁶. This apparatus consists of a Penning trap¹⁴ in a superconducting 4-T magnet, where the trap and all detection electronics are cooled by liquid helium to about 4.2 K. By combining the magnetic field B and a suitable electrostatic potential, ions can be stored almost indefinitely, limited only by the vacuum quality. A trapped ion's motion can be parametrized by splitting the trajectory into three independent harmonic oscillations that are related to the free cyclotron frequency $\nu_{\text{c}} = \frac{q}{m} B$, with the ion charge and mass q_{ion} and m_{ion} respectively, via¹⁴:

$$\nu_{\text{c}}^2 = \nu_{+}^2 + \nu_{-}^2 + \nu_z^2 \quad (1)$$

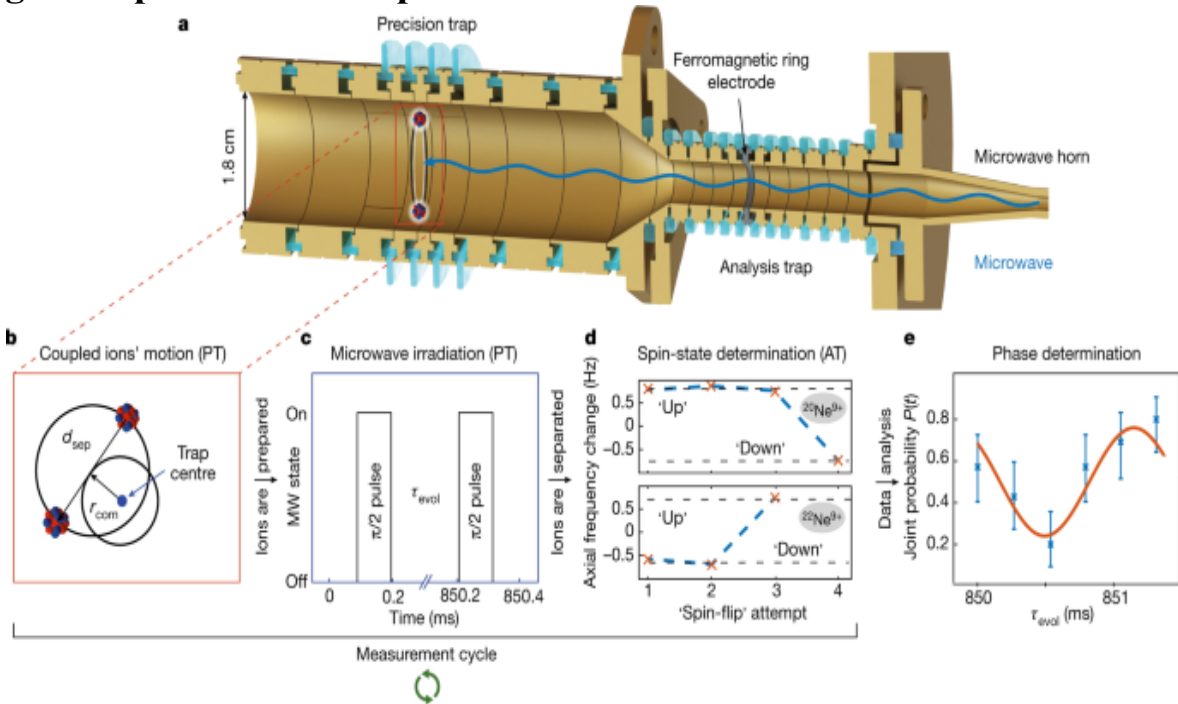
Table 1 Contributions to the g-factor difference of $^{20}\text{Ne}^{9+}$ and $^{22}\text{Ne}^{9+}$ and the final experimental result

For this measurement on $^{20}\text{Ne}^{9+}$ and $^{22}\text{Ne}^{9+}$, the modified cyclotron frequencies ν_{\pm} amount to roughly 27 MHz and 25 MHz, the axial frequencies (parallel to the magnetic field) ν_z to about 650 KHz and 620 KHz, and both magnetron frequencies ν_- to 8 kHz, respectively. These frequencies can be measured non-destructively through the image currents induced by the oscillating charged particle^{15,16}. In addition, the presence of the magnetic field results in an energy splitting $\Delta E = h\nu_L$ of the $m_s = \pm 1/2$ electronic spin states with the Larmor frequency $\nu_L = \frac{eB}{4\pi m_e}$ amounting to about 112 GHz, with the electron charge and mass e and m_e , respectively (h is Planck's constant). The orientation m_s of the spin with respect to the magnetic field can be determined by means of the continuous Stern–Gerlach effect¹⁷ in the dedicated analysis trap (AT) (Fig. 1). Here, in addition to the homogeneous magnetic field B_0 , a quadratic magnetic field gradient or magnetic bottle $B(z) = B_0 + B_1 z + B_2 z^2$ with $B_2 \approx 45 \text{ kT m}^{-2}$ is produced by a ferromagnetic ring electrode. This exerts an additional spin-dependent force on the ion that results in an instantaneous shift of the axial frequency when a

millimetre-wave (photon around ν_L is absorbed. As this magnetic bottle hinders precise frequency measurements, the spectroscopy is performed in the homogeneous magnetic field⁶ of the precision trap (PT), where also the cyclotron frequency can be measured simultaneously to the millimetre-wave excitation. The AT is then solely used for the detection of the spin state and the separation of the ions. The g factor can be extracted from the frequencies^{3,7,18}

$$\text{g} = \frac{\nu_L}{\nu_e} = \frac{m_e}{m_{\text{ion}}} \frac{q_{\text{ion}}}{q_e} \quad (2)$$

Fig. 1: Experimental setup and measurement scheme.



a, The Penning-trap setup, with the coupled ions in the centre of the precision trap. **b**, The ions are prepared on a common magnetron orbit, with a separation distance of $d_{\text{sep}} \approx 400 \mu\text{m}$ and a common mode $r_{\text{com}} < 100 \mu\text{m}$. The cyclotron radius r_p of each ion is cooled to $r_p \approx 3 \mu\text{m}$ and the axial amplitude to $r_z \approx 18 \mu\text{m}$ when in thermal equilibrium with the resonator circuit at $T = 4.2 \text{ K}$. **c**, The pulse scheme of the millimetre-wave irradiation. **d**, The change of axial frequency after each attempt to induce a spin

transition. Here $^{20}\text{Ne}^{9+}$ was found to be in the ‘up’ state and $^{22}\text{Ne}^{9+}$ was found to be in the ‘down’ state after the measurement sequence, as can be deduced from the observed change. e, After several repetitions of such cycles, the coincidental behaviour of the spin-transition rate modulation $P(t)$ is fitted, error bars represent the 68% confidence interval.

Consequently, the independently measured ion masses, as well as the electron mass, pose direct limits on the achievable precision of absolute g -factor measurements. In addition, the inherent magnetic-field fluctuations render it impossible to determine the Larmor frequency coherently on the timescales required to accurately measure the cyclotron frequency. This limits such measurements statistically to low 10^{-11} relative precision even with several months of measurement time, and renders an investigation of the small nuclear effects impractical.

Coupled ions

To overcome these limitations, we have developed a measurement technique based on the principle of the two-ion balance^{8,19}. Here the ions are first prepared separately in the AT to a known electron spin orientation and subsequently merged by placing them in the same potential well of the PT (this process takes about 10 min). After cooling the axial motion of the ions individually, they become coupled on a common magnetron orbit owing to the almost identical frequencies of this mode ($\Delta\nu_- \approx 200$ mHz), whereas the axial and modified cyclotron motions remain uncoupled owing to their large frequency discrepancy ($\Delta\nu_z \approx 30$ kHz and $\Delta\nu_+ \approx 2.5$ MHz). The combined motion, as shown in Fig. 1b, can be parametrized as a superposition of a rotation of both ions with a quasi-static separation distance d_{sep} around a common guiding centre and a rotation of this guiding centre around the trap centre on a radius r_{com} . The coupling interactions have been mathematically described and used for mass comparison measurements in ref. ⁸. Now, we determine the initial values of d_{sep} and r_{com} by measuring the axial frequency shift resulting from the Coulomb interaction of the ions, as well as the individual absolute magnetron radii (merging and determining the initial configuration takes about 10 min). Subsequently, we are able to transfer canonical angular momentum, or effectively mode radius, from the common

mode to the separation mode²⁰ (see ‘Mixing and preparing the coupled state’ in Methods), as well as directly cool the separation mode by coupling it to the axial mode. In this way, we have full control over all modes as the axial and cyclotron modes of both ions can still be addressed individually. We apply these tools to prepare the ions with a magnetron separation distance $d_{\text{sep}} \approx 400 \mu\text{m}$ and a comparably small common mode radius r_{com} (see ‘Mixing and preparing the coupled state’ in Methods; about 20 min). Now, we perform simultaneous Ramsey-type measurements on the electron spins by irradiating a single millimetre-wave $\pi/2$ pulse (see ‘Rabi frequency measurement’ in Methods) for both ions simultaneously. We then wait for the evolution time τ_{evol} , during which both magnetic moments are freely precessing with their individual Larmor frequencies and finally irradiate the second $\pi/2$ pulse (this takes about 5 min, including a determination of v_c). Subsequently, the ions are separated again (see ‘Separation of ions’ in Methods; duration 10 min). Finally, the cycle is completed by determining and comparing the spin orientation to the initial state for each ion individually in the AT again. This whole process has been fully automatized, requiring about 1 h to complete a cycle. In total, we have performed 479 cycles for the main measurement as well as 174 for the systematic uncertainty analysis. Owing to the fast Larmor precession of 112 GHz, the inherent magnetic-field fluctuations lead to decoherence of the applied millimetre-wave drive frequency with respect to the individual spin precessions already after some 10 ms, as also observed in ref. ²¹. However, as the ions are spatially close together, the spins stay coherent with respect to each other as they both experience identical fluctuations. For each evolution time τ_{evol} of the Ramsey scheme, the individual measurement points are distributed over roughly one period of the difference frequency $\Delta\nu = \nu_{\text{rm}{L1}} - \nu_{\text{rm}{L2}} \approx 758 \text{ Hz}$. The coherent difference of the precession frequencies can now be extracted from the correlated spin transition probability P . Here, the ions behave identically when their individual spins are in phase, or opposite to each other when the spins are out of phase after the evolution time. We can therefore define

$$\begin{aligned}
 \$\$P = & \{p\}_1 \{1, \{\text{rm}\{\text{SF}\}\}\} \times \{p\}_2 \{2, \{\text{rm}\{\text{SF}\}\}\} + \{p\}_1 \\
 & \{\text{rm}\{\text{noSF}\}\} \times \{p\}_2 \{2, \{\text{rm}\{\text{noSF}\}\}\}, \\
 (3)
 \end{aligned}$$

where $p_{n,\text{SF}}$ and $p_{n,\text{noSF}}$ are the probabilities for ion n to undergo or not undergo a spin transition, respectively (see ‘Fitting function for the Larmor frequency difference’ in Methods). This relation encodes the relative phases of the spins to each other but, owing to the loss of coherence with respect to the applied microwave drive, the modulation amplitude A is only $\pm 25\%$. This joint transition probability is therefore directly modulated by the differential phase of the spins and follows

$$\text{P}(t) = A \cos(2\pi(\Delta\nu_L)t + \varphi_\tau), \quad (4)$$

with an additional phase $\phi_{\tau,0}$ encoding the difference of the Larmor frequencies.

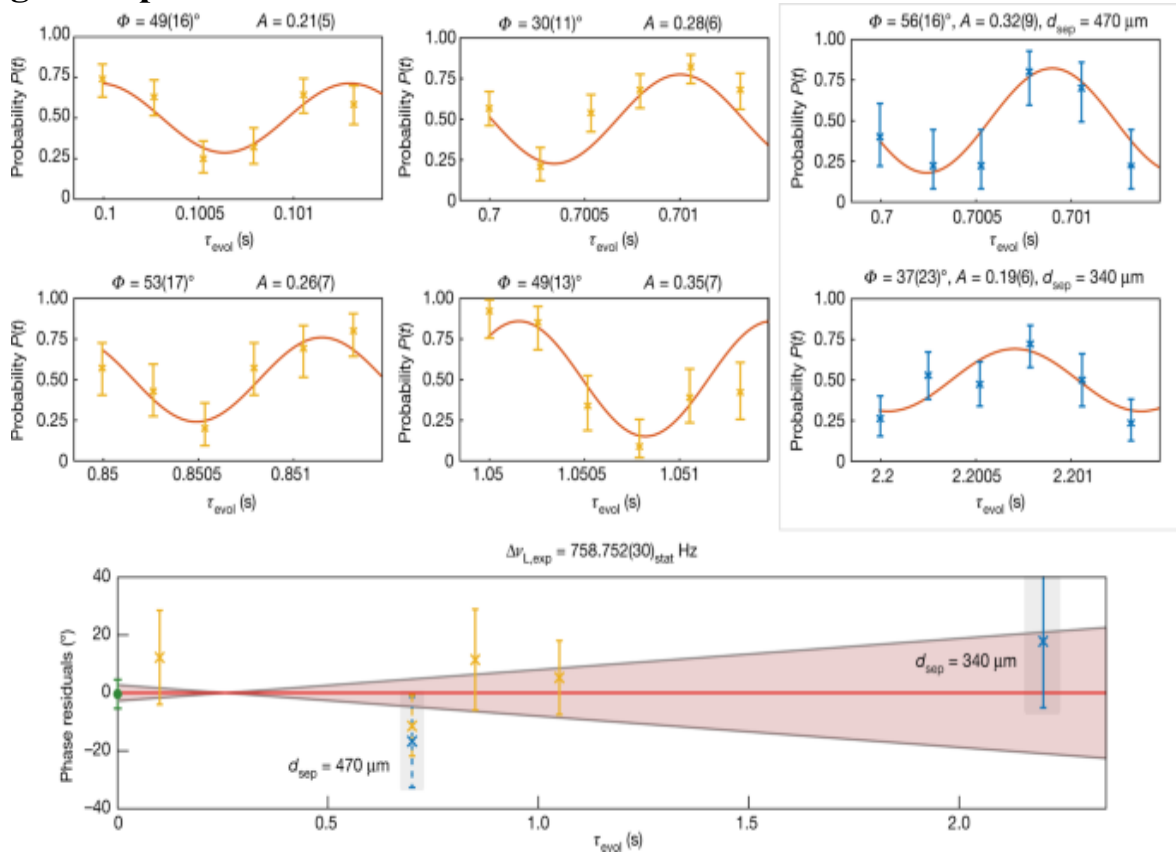
Data analysis

We have performed measurements for five different sets of evolution times and three different separation distances. Figure 2 shows the modulated probability of a coincidental spin transition occurring for all of these measurements. To extract the Larmor frequency difference, first the total accumulated phase has to be unwrapped. We perform a maximum likelihood fit with a fixed frequency difference, fitting only the phase $\phi_{\tau,0}$ and amplitude A , separately for each evolution time. For all six measurements, the observed amplitude is compatible with a modulation amplitude $A = 25\%$, which confirms the coherent behaviour of the two quantum states for at least up to $\tau_{\text{evol}} = 2.2$ s, which is more than a factor 20 longer than the coherence time of the individual spins with respect to an external drive. After unwrapping, a linear fit to those phases measured with the separation distance $d_{\text{sep}} = 411(11)$ μm as well as the calculated initial phase difference (see ‘Calculation of the initial phase difference’ in Methods) is used to determine the frequency difference and the statistical uncertainty. Systematic shifts are expected to arise owing to the small imbalance of the coupled magnetron motion, which is a consequence of the different ion masses. This causes the ions to experience slightly different magnetic fields and alters their individual Larmor frequencies. The two main contributions are: first,

this radial imbalance in combination with a residual B_2 ; and second, a slight shift of the axial equilibrium position caused by a residual deviation from the perfect symmetry of the electrostatic trapping potential, leading to an unequal change of the Larmor frequencies in the presence of a linear axial B_1 field gradient. The combined systematic shift has been evaluated (see ‘Calculation of the initial phase difference’ in Methods) as $6(5) \times 10^{-13}$ relative to the mean Larmor frequency. We specifically stress that our method, although currently experimentally limited by magnetic-field inhomogeneities, could be significantly improved by implementing active compensation coils for B_1 and B_2 (ref. 22), possibly extending the precision to the 10^{-15} regime. The bottom plot of Fig. 2 shows the residual deviation of each extracted phase with respect to the final frequency difference and uncertainty, corrected for this systematic shift. The grey highlighted data points are for the two measurements performed at a different separation distance, corrected for their expected systematic shift. The agreement of these measurements clearly confirms the systematic correction independently from the calculated correction derived from independent single-ion measurements. The frequency difference of $\Delta \nu = 758.752(30)(56)\text{ Hz}$, which corresponds to $\Delta g = 13.475(24)(53)$ (‘Calculation of the g -factor difference’ in Methods), is in agreement with the theoretical calculation of $\Delta g = 13.474(11)(11)$ (finite nuclear size) of the isotopes $\langle r^2 \rangle^{1/2} = 0.0530(34)$ fm (ref. 23). Taking theory as an input instead, our result can thus be applied to improve on the precision of the charge-radius difference by about one order of magnitude $\langle r^2 \rangle^{1/2} = 0.0533(4)$ fm. With the agreement between theory and the experimental result, we can set constraints for the scale of the $y_e y_n$ coupling constants, which appear in the new physics search in the Higgs-relaxion mixing scenario (‘Setting constraints on new physics’ in Methods). Although the bounds obtained here do not improve on already existing bounds (Fig. 3), they are derived using an alternative approach and do not rely on King plot linearity and hence offer a more direct¹² and less ambiguous^{24,25} way to search for new physics.

The obtained bounds are shown in Fig. 3, along with bounds from other fields of physics (see caption). At the present, our method and H–D spectroscopy are both dependant on charge radii determined by muonic spectroscopy^{23,26}. When combining our method with measurements on the g factor of lithium-like ions²⁷ or the ground-state energy isotope shifts of hydrogen-like ions, improved competitive bounds could be envisaged²⁸ while additionally gaining independence from assumptions on new physics coupling to muons. The $(g - 2)_e n$ bounds are independent from muonic radii, but rely on a combination of multiple neutron-scattering measurements as well as the free-electron g factor²⁹.

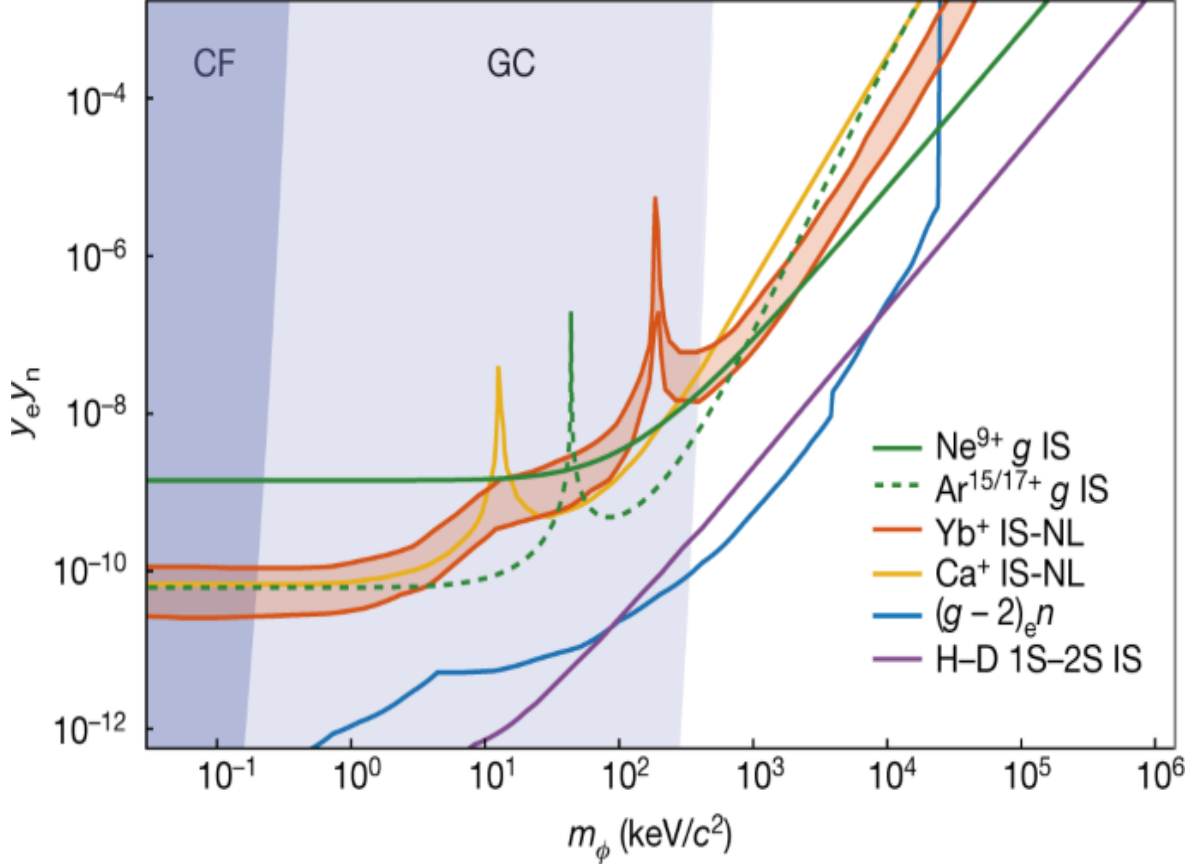
Fig. 2: Experimental results.



The top six panels show the individual measurements. The two panels highlighted in grey do not contribute to the statistical uncertainty of the final result and are used only to confirm and correct for systematic effects. The bottom panel shows the residuals with respect to the final frequency, with the 1σ statistical uncertainty being illustrated in the shaded confidence

interval (red). The initial phase (green) stems from numerical calculation. The error bars in the top six panels represent the 68% confidence interval.

Fig. 3: New physics exclusion plot.



Bounds at the 95% confidence level on the NP coupling constant (Methods) as a function of the mass of a new scalar boson. Other shown limits are derived from Casimir force (CF) measurements³³, globular cluster (GC) data³⁴, isotopic-shift measurements in Ca^+ (ref. 35) and in H–D (ref. 36), and a combination of neutron-scattering data with the free-electron g factor ($(g - 2)_e n$ (ref. 29)). The orange region indicates possible values of the coupling constant derived from isotopic-shift measurements in transition frequencies in Yb^+ (ref. 37), under the assumption that the observed King nonlinearity is caused by NP (see also refs. 38,39). The solid green line shows the limits derived in this work. The dashed green line shows a projected bound from isotopic-shift measurements of the g factor of hydrogen-like and lithium-like argon.

Conclusions and outlook

We have demonstrated and applied our method to directly measure a g -factor difference coherently to high precision. This is a direct test and validation of the hitherto untested QED contribution to the nuclear recoil and paves the way towards further high-precision measurements on heavier ions where this contribution becomes even larger. Furthermore, we are able to improve on the precision of the charge-radius difference by about one order of magnitude using this method, which could be similarly applied to other systems. In addition, we have applied the result of this single isotopic-shift measurement to strengthen the limits on the parameters for the new-physics search via the Higgs-relaxion mixing, showcasing the potential of this approach. Furthermore, this method provides a crucial step towards accessing the weighted difference of g factors^{11,30}, which has the potential to significantly improve on the precision of the fine-structure constant α . Here, the difference between two ions of different nuclear charge Z will have to be measured for both their hydrogen-like ($1s$) and lithium-like ($2s$) states using this method. In addition, a single absolute g factor of low 10^{-11} precision is required when choosing ions of the medium Z range, which has already been shown to be experimentally feasible³. However, the theoretical calculation of this g factor has to achieve similar precision, which will still require significant work and time. Finally, the possibility to directly compare matter versus antimatter with highly suppressed systematics should be investigated. This method could possibly be applied to directly compare the anti-proton and H^- g factors. In this case, the Larmor frequency difference would be mostly defined by the electronic shielding of the H^- ion, which would have to be calculated to similar precision as shown for ^3He (ref. 31). Similar to the mass comparison that was already performed³², this could enable a direct g -factor comparison with significantly reduced systematic effects. If a further comparison of proton and positive anti-hydrogen $\backslash(\{\bar{\text{rm}}\{\text{H}\}\}\}^{+}\}$ becomes experimentally feasible in the future, even the uncertainty of the shielding could be dramatically reduced as well.

Methods

Mixing and preparing the coupled state

After determining the spin orientations of the individual ions, one ion is excited to a magnetron radius $r \approx 600 \mu\text{m}$ to prepare for the coupling of the ions. They are now transported into electrodes next to each other, with only a single electrode in between to keep them separated. Subsequently, this electrode is ramped down as quickly as experimentally possible, limited by d.c. filters to a time constant of 6.8 ms to keep any voltage change adiabatic compared with the axial frequencies of several 10 kHz. The potentials are also optimized to introduce as little axial energy as possible during this mixing. Subsequently, both ions are brought into resonance with the tank circuit one at a time by adjusting the voltage to repeatedly cool their axial modes. Once thermalized, the axial frequency is automatically measured and adjusted to the resonance frequency. From the observed shift in axial frequency compared with a single cold ion, the separation distance d_{sep} of the ions can already be inferred, without gaining information about the common mode. At this point, both ions are cooled in their respective cyclotron motions via sideband coupling¹⁵. The common-mode radius r_{com} of the coupled ions can be measured by applying a C_4 field contribution, causing the axial frequency to become dependent on the magnetron radius. With the amplitudes of the axial and reduced cyclotron motion being small, this frequency shift allows for the determination of the root-mean-square (r.m.s.) magnetron radius of each ion. If the common mode is large, the modulation of the magnetron radius, owing to slightly different frequencies of separation and common mode, will lead to visible sidebands owing to the axial frequency modulation.

For small common mode radii, we will simply measure half the separation radius for each ion. In combination with the known separation distance, the common mode radius can now be determined; however, owing to limited resolution of the axial frequency shift and the quadratic dependency, $\sqrt{\frac{r_{\text{sep}}^2 + r_{\text{com}}^2}{4} - \left(\frac{d_{\text{sep}}}{2}\right)^2}$, a conservative uncertainty after the ion preparation of $r_{\text{com}} = 0(100) \mu\text{m}$ is assumed. For consistency, we have prepared the ions in the final state and again excited the common mode to a known radius that could be confirmed using this method. In case of a large initial common mode, we first have to cool it. Unfortunately, addressing it directly is complicated, as the separation mode will always be cooled as well. However, using the method described

in ref. 20, we are able to transfer the common-mode radius to the separation mode. This requires a non-harmonic trapping field with a sizeable C_4 , combined with an axial drive during this process. The axial frequency will now be modulated owing to the detuning with C_4 in combination with the modulated radius owing to the common mode. As the ion will be excited only when close to the drive, we gain access to a radius-dependant modulation force, which finally allows the coupling of the common and separation modes.

Finally, with the common mode thus sufficiently cooled, we directly address the separation mode, cooling it to the desired value. Owing to the strong axial frequency change during cooling, scaling with $\sqrt{d_{\text{sep}}}$ and typically being in the range of $\Delta\nu \approx 150$ Hz, the final radius cannot be exactly chosen but rather has a distribution that scales with the power of the cooling drive used. Therefore, one can chose to achieve more stable radii at the cost of having to perform more cooling cycles, ultimately increasing the measurement time. We choose a separation distance $d_{\text{sep}} = 411(11)$ μm , with the uncertainty being the standard deviation of all measurements as an acceptable trade-off between measurement time and final separation distance distribution. Furthermore, although a smaller separation distance directly corresponds to a decreased systematic uncertainty (Methods), the increased axial frequency shift as well as a deteriorating signal quality of the coupled ions result in a practical limit around $d_{\text{sep}} = 300$ μm .

Measurement sequence

Before irradiating the microwave pulses, the cyclotron frequency is measured via the double-dip technique using $^{22}\text{Ne}^{9+}$. This measurement is required to be accurate to only about 100 mHz, which corresponds to a microwave frequency uncertainty of about 400 Hz, which is neglectable considering a Rabi frequency of over 2 kHz for a spin transition. The microwave pulse is applied at the median of the Larmor frequencies of $^{22}\text{Ne}^{9+}$ and $^{20}\text{Ne}^{9+}$ and therefore detuned from each Larmor frequency by about 380 Hz. This detuning is taken into account when calculating the required time for a $\pi/2$ pulse.

Separation of ions

The strong magnetic bottle, or B_2 contribution, that is present in the AT gives rise to a force that is dependent on the magnetic moment of the ion. The main purpose is to allow for spin-flip detection via the continuous Stern–Gerlach effect. In addition, this B_2 can be utilized to create different effective potentials for the ions depending on their individual cyclotron radii r_+ . These give rise to the magnetic moment $\langle \{\mu\}_\text{rm{cyc}} \rangle = \{\rm{pi}\} \{\nu\}_+ \{q\}_\text{ion} \{r\}_+^2$, which then results in an additional axial force in the presence of a B_2 . To use this effect to separate the coupled ions, one of them is pulsed to $r_+ \approx 800 \mu\text{m}$ at the end of the measurement in the PT. Subsequently, both ions are cooled in their magnetron modes, resulting in a state where one ion is in the centre of the trap at thermal radii for all modes while the other is on the large excited cyclotron radius. We verify this state by measuring the radii of both ions to confirm the successful cooling and excitation. Now, we use a modified ion-transport procedure, with the electrode voltages scaled such that the ion with $r_+ > 700 \mu\text{m}$ cannot be transported into the AT but rather is reflected by the B_2 gradient, whereas the cold ion follows the electrostatic potential of the electrodes. The hot ion is transported back into the PT and can be cooled there, leaving both ions ready to determine their electron spin orientation again, completing a measurement cycle. This separation method has worked flawlessly for over 700 attempts.

Rabi frequency measurement

To determine the required $\pi/2$ -pulse duration, a single ion, in this case $^{22}\text{Ne}^{9+}$, is used. We determine the spin orientation in the AT, transport to the PT, irradiate a single microwave pulse and check the spin orientation again in the AT. Depending on the pulse duration t , the probability of achieving a change of spin orientation follows a Rabi cycle as

$$\begin{aligned} \text{P}_{\text{SF}}(t) &= \frac{\Omega}{2R} \sin^2(\Omega R t) \\ &= \frac{\Omega^2}{4R^2} \sin^2(\Omega R t) \end{aligned}$$

$$\left. \frac{\partial^2 \ln P}{\partial \Omega_R^2} \right|_{\Omega_R = 0} = \frac{1}{2} + \Delta \Omega_L^2$$

(5)

Here, Ω_R is the Rabi frequency and $\Delta\Omega_L$ is the detuning of the microwave drive with respect to the Larmor frequency. With a measured Rabi frequency of $\Omega_R = 2,465(16)$ Hz, we can irradiate the mean Larmor frequency of the two ions, with the difference being about 758 Hz. Thereby, we are able to use a single pulse simultaneously for both ions while accounting for the detuning to achieve a $\pi/2$ pulse of 101.1 μ s for both ions simultaneously. The corresponding data are shown in Extended Data Fig. 1. The fit includes a shot-to-shot jitter of the microwave offset $\delta\Omega_L$ to account for the uncertainty of the magnetic field. The measurement is performed on a magnetron radius of $r_- = 200(30)$ μ m to achieve similar conditions to those in the coupled state.

Determination of charge-radii differences

We would in principle be able to improve on any charge-radii differences, where this is the limiting factor for the theoretical calculation of g . This holds true for most differences between nuclear spin-free isotopes, as well as differences between different atoms, provided they are either light enough for theory to be sufficiently precise or close enough in nuclear charge Z such that the corresponding uncertainties are still strongly suppressed.

Fitting function for the Larmor frequency difference

To derive the fitting function of the correlated spin behaviour of the two ions, we first assume that both ions have been prepared initially in the spin-down state, indicated as \downarrow . The probability to find each ion individually in the spin-up state (\uparrow) then follows the probability of a Rabi oscillation with the frequency of the difference between the ion's Larmor frequency ω_{L1} or ω_{L2} , respectively, and the common microwave drive frequency ω_D . The probability of finding both ions after the measurement sequence in the spin-up state follows as

$$\begin{aligned}
& \text{\$\$} \begin{array}{lcc} P(\uparrow\downarrow, \uparrow\downarrow) & = & \cos \left(\frac{1}{2} (\omega_{L1} - \omega_{L2}) \right) \tau \\
& & \left(\frac{1}{2} (\rm{evol}) \right)^2 \times \cos \left(\frac{1}{2} (\omega_{L1} + \omega_{L2}) \tau \right) \\
& & \left(\frac{1}{2} (\rm{evol}) \right)^2 \times \left[\cos \left(\frac{1}{2} (\omega_{L1} - \omega_{L2}) \tau \right) \right. \\
& & \left. + \cos \left(\frac{1}{2} (\omega_{L1} + \omega_{L2}) \tau \right) \right] \end{array} \text{\$\$} \\
(6)
\end{aligned}$$

Similarly, the probability of finding both ions in the spin-down state can be written as

$$\begin{aligned}
& \text{\$\$} \begin{array}{lcc} P(\downarrow\downarrow, \downarrow\downarrow) & = & \sin \left(\frac{1}{2} (\omega_{L1} - \omega_{L2}) \right) \tau \\
& & \left(\frac{1}{2} (\rm{evol}) \right)^2 \times \sin \left(\frac{1}{2} (\omega_{L1} + \omega_{L2}) \tau \right) \\
& & \left(\frac{1}{2} (\rm{evol}) \right)^2 \times \left[\sin \left(\frac{1}{2} (\omega_{L1} - \omega_{L2}) \tau \right) \right. \\
& & \left. - \sin \left(\frac{1}{2} (\omega_{L1} + \omega_{L2}) \tau \right) \right] \end{array} \text{\$\$} \\
(7)
\end{aligned}$$

Both cases, where either both ions are in the spin-down or the spin-up state have to be considered, as we cannot perform a coherent measurement of the individual Larmor frequencies with respect to the microwave drive. As a result, the information about the Larmor frequency difference is encoded only in the common behaviour of the spins. Therefore, we have to look at the combined probability of both ions either ending up both in the spin-up or spin-down state (case 1; Extended Data Fig. 2), or the complimentary case, where the two spins behave differently, with one ion in the spin-up state and the other ending in the spin-down state. The joint probability is given by

$$\begin{aligned}
& \text{\$\$} \begin{array}{l} P(t) = P(\downarrow\downarrow) + P(\uparrow\downarrow) \\
= \frac{1}{2} \cos \left(\frac{1}{2} (\omega_{L1} - \omega_{L2}) t \right) + \frac{1}{2} \cos \left(\frac{1}{2} (\omega_{L1} + \omega_{L2}) t \right) \end{array} \text{\$\$}
\end{aligned}$$

$$\begin{aligned}
& \left. \frac{2}{2} \mathop{\mathrm{underbrace}} \left\{ \cos \left(\frac{1}{2} (\omega_{\mathrm{L1}} + \omega_{\mathrm{L2}}) t \right)^2 \right\} \right|_{t=0} = \frac{1}{2} \cos((\omega_{\mathrm{L1}} - \omega_{\mathrm{L2}}) t) + \frac{1}{2} \\
(8) \quad & \end{aligned}$$

where, owing to the loss of coherence with respect to the drive frequency, the term in the middle line of equation (8) averages to 1/2. The same formula can be derived for any known initial spin configuration.

Calculation of the g -factor difference

The g -factor difference can be directly calculated from the determined relation given by

$$\Delta g = \frac{\omega_c m_e}{m_{\mathrm{ion}} q_{\mathrm{ion}} e} \Delta \omega_L. \quad (9)$$

Although the input parameters of mass and cyclotron frequency of one of the ions are still required, the precision relative to Δg is only of about 7×10^{-5} , strongly relaxing the need for ultraprecise masses and a cyclotron frequency determination. In contrast, when measuring absolute g factors, the precision of the mass and cyclotron frequency typically limit the achievable precision to the low 10^{-11} level.

Setting constraints on new physics

Measuring the g factor allows for high-precision access to the properties of very tightly bound electrons, and hence to short-range physics, including potential new physics (NP). Bounds on NP can be set with isotopic-shift data on the g factor of hydrogen-like neon. The Higgs-relaxion mixing mechanism, in particular, involves the mixing of a potential new (massive) scalar boson, the relaxion, with the Higgs boson. It has been proposed as a solution to the long-standing electroweak hierarchy problem¹³ with the

relaxion as a dark-matter candidate⁴⁰. Constraints on this proposed extension of the standard model can be set with cosmological data, as well as with particle colliders, beam dumps and smaller, high-precision experiments (see, for example, ref. ⁴¹ and references therein).

The most common approach in atomic physics is to search for deviations from linearity on experimental isotopic-shift data in a so-called King plot analysis^{29,35,41,42,43,44}, which can be a sign of NP, although nonlinearities can also happen within the standard model^{12,24,37,44}, which limits the bounds that can be set on NP parameters. The King plot approaches also suffer from strong sensitivity on nuclear-radii uncertainties²⁵. Here we present constraints on NP from data on a single isotope pair. The influence of relaxions (scalar bosons) on atoms can be expressed^{29,41,43,44} by a Yukawa-type potential (often called the ‘fifth force’) exerted by the nucleus on the atomic electrons:

$$\begin{aligned} \text{\$}\{V\}_{\rm HR}(\text{\bf r}) &= -\hbar c \alpha \\ &\times \frac{A}{|\text{\bf r}|} e^{-m_\phi |\text{\bf r}|}, \end{aligned} \quad (10)$$

where m_ϕ is the mass of the scalar boson, $\alpha_{\rm HR} = y_e y_n / 4\pi$ is the NP coupling constant, with y_e and y_n the coupling of the boson to the electrons and the nucleons, respectively, A is the nuclear mass number and \hbar is the reduced Planck’s constant. Yukawa potentials naturally arise when considering hypothetical new forces mediated by massive particles. The corresponding correction to the hydrogen-like g factor is given by¹²

$$\begin{aligned} g_{\rm HR} &= \frac{4}{3} \alpha \\ &\times \frac{A}{|\text{\bf r}|} \left(\frac{Z\alpha}{\gamma} \right) \left(\frac{m_\phi}{2Z\alpha} \right)^2 \\ &\times \left(1 + \frac{m_\phi}{\gamma} \right)^{-2\gamma} \left[1 + 2\gamma - \frac{2\gamma}{1 + \frac{m_\phi}{\gamma}} \right], \end{aligned} \quad (11)$$

where $\gamma = \sqrt{1 - (Z\alpha)^2}$. The mass scale of the hypothetical new boson is not known⁴¹, apart from the upper bound $m_{\varphi} < 60 \text{ GeV}$. In the small-boson-mass regime $m_{\varphi} \ll Z\alpha m_e$, the contribution to the g factor simplifies to

$$\begin{aligned} g_{\rm HR} &= -\frac{4}{3} \frac{\alpha}{\gamma} A \frac{(Z\alpha)}{\gamma} \frac{1}{m_{\varphi}} \frac{1}{Z\alpha m_e}. \end{aligned} \quad (12)$$

In the large-boson-mass regime $m_{\varphi} \gg Z\alpha m_e$, we obtain

$$\begin{aligned} g_{\rm HR} &= -\frac{4}{3} \frac{\alpha}{\gamma} A \frac{(Z\alpha)(1+2\gamma)}{\gamma} \left(\frac{m_{\varphi}}{2Z\alpha m_e} \right)^{-2\gamma} \frac{1}{m_{\varphi}} \frac{1}{Z\alpha m_e}. \end{aligned} \quad (13)$$

We can set bounds on the NP coupling constant by comparing the measured and calculated values of the g -factor isotopic shift (see refs. [12,45](#) for an implementation of the same idea with transition frequencies in atomic systems). Uncertainties from theory are a source of limitation in this approach. The standard-model contributions to the isotopic shift of the g factor of hydrogen-like neon are given in Extended Data Table [1](#), as calculated in this work based on the approaches developed in the indicated references. As can be seen, the largest theoretical uncertainty comes from the leading finite nuclear-size correction, and is due to the limited knowledge of nuclear radii (the uncertainty on the finite nuclear-size correction owing to the choice of the nuclear model is negligible at this level of precision). We note that the standard source for these nuclear radii is data on X-ray transitions in muonic atoms^{[23](#)}.

In the NP relaxion scenario, the energy levels of these muonic atoms are also corrected by the relaxion exchange. Another source of r.m.s. charge radii and their differences is optical spectroscopy. The electronic transitions involved are far less sensitive to hypothetical NP than muonic X-ray transitions. The

radius difference between ^{20}Ne and ^{22}Ne extracted from optical spectroscopy⁴⁶ agrees with the one determined from muonic atom data within the respective uncertainties, which shows that NP need not be taken into account to extract nuclear radii from these experiments at their level of precision. To conclude, for our purposes, hypothetical contributions from NP do not interfere with the interpretation of muonic atom data for the extraction of nuclear radii.

Taking $\langle\Delta g\rangle_{\rm theo} \approx 1.1 \times 10^{-11}$ as the theoretical error on the isotopic shift, it can be seen from equation (12) that this corresponds to an uncertainty of $\Delta y_e y_n \approx 7.1 \times 10^{-10}$ (and a 95% bound on $y_e y_n$ twice as large as this) in the small-boson-mass regime $\langle m \varphi \rangle \ll Z \alpha m_e$, which is weaker than the current most stringent bounds coming from atomic physics (H–D 1S–2S, ref. 36). In the large-boson-mass regime $\langle m \varphi \rangle \gg Z \alpha m_e$, our bound remains weaker, but becomes more competitive and is more stringent than those of ref. 35, owing to two favourable factors. First, the nuclear charge Z in equation (13) is larger than the screened effective charge perceived by the Ca^+ valence electron, and larger than the charge of the hydrogen nuclei, which also enter the scaling of the bound obtained with these respective ions²⁹. Second, when carrying out a King analysis as done in ref. 35, one works with two different transition frequencies, and the leading term in the hypothetical NP contribution in the large-boson-mass regime, which is the equivalent of the right-hand side of equation (13), is cancelled out in the nonlinearity search, owing to its proportionality to the leading finite nuclear-size correction²⁹, leaving the next term, which scales as $\langle m \varphi \rangle / (2Z \alpha m_e)^{-1-2\gamma}$, as the first non-vanishing contribution.

In the present case, the g factor of a single electronic state is considered (for a single isotope pair), and this cancellation does not occur. This leads to competitive bounds in the large-boson-mass regime with the simple g factor isotopic shift of hydrogen-like ions, as shown in Fig. 3 (where we used the exact result, equation (11)). We compare our bounds on the coupling constant $y_e y_n = 4\pi\alpha_{\text{HR}}$, to the bounds obtained in refs. 35,36, through isotopic-

shift measurements in Ca^+ (see the curve Ca^+ IS-NL in Fig. 3) and H (with nuclear radii extracted from muonic atom spectroscopy), as well as to the bounds obtained through Casimir force measurements³³, globular cluster data³⁴ and a combination³⁵) of neutron scattering^{47,48,49,50} data and free-electron g factor¹ ($(g - 2)_e n$).

We also reproduce the preferred range for the coupling constant obtained in ref. 37, through isotopic-shift measurements in Yb^+ (Yb^+ IS-NL). This range was obtained by assuming that the observed King nonlinearity in the experimental isotopic-shift data is caused by NP. By contrast, all nuclear corrections to the g factor that are relevant at the achieved experimental precision were taken into account in our approach, allowing for an unambiguous interpretation of the experimental data.

In Fig. 3, we also indicate projected bounds that could be obtained from isotopic-shift measurements of the g factors of both hydrogen-like and lithium-like argon. Combining both measurements allows the approximate cancellation of the leading finite nuclear-size corrections through considering a weighted difference^{11,27} of hydrogen-like and lithium-like g factors. On the basis of our earlier discussion of the domination of theoretical uncertainties by the uncertainty on the leading finite nuclear-size correction (Table 1), the interest of this approach is readily understood. Our calculations indicate that argon is in the optimal range for setting bounds on α_{HR} with this approach.

The weighted difference approach is not preferred in the large-boson-mass regime, however, because of strong cancellations of the NP contribution. A similar approach based on a weighted difference of the g factor and ground-state energies of hydrogen-like ions should yield even more stringent bounds²⁸. Both these weighted-difference-based approaches are insensitive to uncertainties on the nuclear radii, as such, the bounds that they can generate are fully independent of any assumptions on NP coupling to muons.

Calculation of the initial phase difference

As our method relies on a single external drive for this specific measurement, used to drive both spins simultaneously, the drive has to be

applied at the median Larmor frequency. This results in an additional phase difference that is acquired during the $\pi/2$ pulses. We have determined this phase to be $\Phi_{\text{init}} = 35.8(50)^\circ$ using a numerical simulation. Here we use the knowledge of the Rabi frequency as well as the uncertainty of the magnetic-field determination, which leads to an effective jitter of the microwave drive from cycle to cycle. The simulation is performed for different evolution times, extrapolating to the phase that would be measured for zero evolution time. Although the phase that we can extract from the measured data as a cross-check is consistent with this prediction, we still assign an uncertainty of $\pm 5^\circ$ to the simulation.

Analysis of systematic shifts of Δg of coupled ions

Here we evaluate the total systematic shift and its uncertainty for this method, specifically for the measurement case of $^{20}\text{Ne}^{9+}$ and $^{22}\text{Ne}^{9+}$. For this approach, we consider only a separation distance and no common mode. For small common-mode radii $r_{\text{com}} \leq 100 \mu\text{m}$, which we give as an upper limit, the systematic effects discussed here are actually further reduced²⁰. We have to consider multiple individual measurements performed with single ions to characterize these frequency shifts and experimental parameters. More explanation on the methods used can be found in ref. ⁶, and the individual frequency shifts are derived in ref. ⁵¹. We define our electric potential, and specifically the coefficients C_n as

$$\begin{aligned} \Phi(r, \theta) = & \frac{V}{2} \sum_{n=0}^{\infty} \frac{C_n r^n}{d_{\text{char}}^n} P_n(\cos(\theta)), \end{aligned} \quad (14)$$

with applied ring voltage V_r , the characteristic trap size d_{char} and the Legendre polynomials P_n . The magnetic-field inhomogeneities B_1 and B_2 are defined as

$$\begin{aligned} B_1 = & \left(\frac{r}{2} \right) \left(\frac{z \bf{e}_z - r \bf{e}_r}{z^2 - r^2} \right), \\ B_2 = & \left(\frac{r}{2} \right) \left(\frac{z \bf{e}_z + r \bf{e}_r}{z^2 - r^2} \right). \end{aligned} \quad (15)$$

$$\begin{aligned} \text{\$}\$\{\{\bf B\}\}_2=\&B_2\backslash\left[\left(z^2-\frac{r^2}{2}\right)\right.\backslash\left.z\right]\text{\$}\\ (16) \end{aligned}$$

where z is the axial position with respect to the electrostatic minimum of the trap. First, we consider the two main axial frequency shifts that depend on the magnetron radius of an ion:

$$\begin{aligned} \text{\$}\$\{\frac{\Delta\nu_z}{\nu_z}\}_4=-\frac{3}{2}\frac{\frac{\partial C_2}{\partial r}}{C_2},\text{\$}\\ (17) \end{aligned}$$

$$\begin{aligned} \text{\$}\$\{\frac{\Delta\nu_z}{\nu_z}\}_3=\frac{9}{8}\frac{\frac{\partial C_3}{\partial r}}{C_2^2},\text{\$}\\ (18) \end{aligned}$$

If the shift of ν_z is measured to be zero for any radius r_- , these two shifts cancel and we can conclude that $(C_4 = \frac{3}{2}C_2)$. As it is typically not feasible to tune this for arbitrary radii, especially as higher orders will have to be considered as well for larger radii, we allow a residual $(\eta_{\rm el}(r_-))$, which includes both the residual observed shift and all neglected smaller contributions. This is a relative uncertainty, scaling with r_-^2 :

$$\begin{aligned} \text{\$}\$\begin{array}{l}\frac{\Delta\nu_z}{\nu_z}_4=\frac{3}{2}\frac{\frac{\partial C_2}{\partial r}}{C_2},\\\frac{\Delta\nu_z}{\nu_z}_3=\frac{9}{8}\frac{\frac{\partial C_3}{\partial r}}{C_2^2},\\\eta_{\rm el}(r_-)=\frac{3}{2}\frac{C_2}{r_-^2}\end{array}\text{\$}\\ (19) \end{aligned}$$

Similarly, we consider all frequency shifts that depend on the cyclotron radius r_+ of an ion:

$$\begin{aligned} \text{\$}\$\{\frac{\Delta\nu_z}{\nu_z}\}_4=-\frac{3}{2}\frac{\frac{\partial C_2}{\partial r}}{C_2},\text{\$}\\ (20) \end{aligned}$$

$$\begin{aligned} & \frac{\Delta \nu_z}{\nu_z} = \frac{9}{8} \frac{\frac{C_3^2}{C_2^2} d_{\rm char}^2}{r_+^2}, \quad (21) \end{aligned}$$

The electrostatic contributions are identical to those for the magnetron mode, and per the assumption above will also combine to the same $\frac{\eta_{\rm el}}{r_+}$, scaling with the cyclotron radius. However, we have to consider the additional terms that stem from the magnetic-field inhomogeneities, which are sizeable in this mode owing to the significantly higher frequency:

$$\begin{aligned} & \frac{\Delta \nu_z}{\nu_z} = \frac{1}{4B_0} \frac{\nu_+ + \nu_-}{\nu_+ - \nu_-} \frac{r_+^2}{2\nu_z^2} r_+^2, \quad (22) \end{aligned}$$

$$\begin{aligned} & \frac{\Delta \nu_z}{\nu_z} = - \frac{3B_1 C_3 \nu_c}{4B_0 C_2} \frac{d_{\rm char}^2}{\nu_z^2} r_+^2, \quad (23) \end{aligned}$$

In addition, for large cyclotron excitations, we have to consider the relativistic effect of the mass increase, which also slightly shifts the axial frequency:

$$\begin{aligned} & \frac{\Delta \nu_z}{\nu_z} = - \frac{3B_1 C_3 \nu_c}{4B_0 C_2} \frac{d_{\rm char}^2}{\nu_z^2} r_+^2, \quad (24) \end{aligned}$$

The combined shift depending on magnetic inhomogeneities can be expressed as

$$\begin{aligned}
& \frac{\partial}{\partial \nu} \left(\frac{\nu_z}{\nu} \right) = \frac{1}{2} \left(\frac{B_2}{B_0} \right)^2 - \frac{3}{4} \frac{B_1^2}{B_0^2} C_3 \frac{\nu_z}{\nu} + \frac{1}{4} \frac{B_1^2}{B_0^2} C_3 \frac{\nu_z}{\nu} \\
& \frac{\partial}{\partial \nu} \left(\frac{\nu_z}{\nu} \right) = \eta_{\text{mag}} . \quad (25)
\end{aligned}$$

Although we cannot currently tune these contributions actively (which could be implemented by using active compensation coils²²), we can slightly shift the ion from its equilibrium position to a more preferable position along the z axis to minimize the B_2 coefficient. Doing so, we have achieved frequency shifts of ν_z close to zero for any cyclotron excitations as well, which means these terms have to cancel as well. We will still allow for another residual error from higher orders, as well as a small residual shift, defined as η_{mag} . The observed difference in the frequency shift between cyclotron and magnetron excitations $(\eta_{\text{mag}} + \eta_{\text{el}})$, $\{r\}_{+} - \{r\}_{-}$ can be used to cancel the identical electric contributions $(\eta_{\text{el}}, \{r\}_{+})$ and $(\eta_{\text{el}}, \{r\}_{-})$ when measuring at the same radius. If we solve this combined equation for C_3 , we are left with only the magnetic-field-dependent terms B_1 and B_2 , which is what the Larmor frequency difference is sensitive to

$$\begin{aligned}
C_3 &= \frac{2}{3} \frac{B_2}{B_0} C_2 \\
&= \frac{2}{3} \frac{B_2}{B_0} \frac{C_2}{d} \frac{c}{h} \frac{a}{r} \frac{v_z^2}{B_1^2} \frac{\nu_z}{\nu} + \xi \\
&= \frac{2}{3} \frac{B_2}{B_0} C_2 d \frac{c}{h} \frac{a}{r} \frac{v_z^2}{B_1^2} \frac{\nu_z}{\nu} \quad (26)
\end{aligned}$$

where ξ summarizes the shifts depending on the radial modes of the ion. Now, instead of looking at frequency shifts of individual ions, we consider the effects on coupled ions. Owing to their mass difference, the coupled state is not perfectly symmetrical but slightly distorted owing to the centrifugal force difference. In the case of the neon isotopes, this leads to a deviation of

$\delta_{\text{mag}} = 0.87\%$, with the definition of $\langle r \rangle_1 = d_{\text{sep}}$ and $\langle r \rangle_2 = d_{\text{sep}}(1 + \delta_{\text{mag}})$ and, when choosing ion 1 to be $^{20}\text{Ne}^{9+}$ and ion 2 as $^{22}\text{Ne}^{9+}$. Consequently, the frequency difference $\langle \nu \rangle_1 - \langle \nu \rangle_2$ will be positive, as the g factor (and therefore the Larmor frequency) for $^{20}\text{Ne}^{9+}$ is larger than for $^{22}\text{Ne}^{9+}$. We now consider the axial position shift as a function of the slightly different $\langle r \rangle_1 - \langle r \rangle_2$. This is given by

$$\frac{d}{dr} \left(\frac{\partial z}{\partial r} \right) = 0 \quad (27)$$

Now we want to express all frequency shifts in terms of v_L , which is to a very good approximation dependent on only the absolute magnetic field, first considering only the effect of B_1 and all shifts along the z axis:

$$\frac{\Delta \nu_{\text{L}}}{\nu_{\text{L}}} = \frac{B_1 - B_0}{B_0}. \quad (28)$$

The difference in the shift for the individual ions can then be written as

```

$${\begin{array}{ll} \frac{\Delta (\Delta (\nu _{\rm L}))}{\nu _{\rm L}} &= \frac{\Delta (\nu _{\rm L})_1 - \Delta (\nu _{\rm L})_2}{(\nu _{\rm L})_1 + (\nu _{\rm L})_2} \\ &= \frac{B_1 - B_2}{B_1 + B_2} \\ &= \frac{3}{4} \frac{C_3 - C_2}{C_2} \frac{B_1 - B_0}{B_1 + B_0} \\ &= \left( \frac{1}{2} \frac{B_2 - B_0}{B_2} - \frac{3}{4} \frac{B_1 - B_0}{B_1} \right) \frac{C_2}{C_3} \right) \\ &= \frac{1}{2} \frac{B_2 - B_0}{B_2} \frac{C_2}{C_3} - \frac{3}{4} \frac{B_1 - B_0}{B_1} \frac{C_2}{C_3} \end{array}}. \quad (29)

```

We have now the additional uncertainties all summarized in the term scaling with the above-defined factor ξ . The final shift to consider is the same radial

difference as mentioned before in the presence of B_2 . This leads to additional individual shifts in the ν_L of the ions as

$$\frac{\Delta \nu_{\text{rmL}}}{\nu_{\text{rmL}}^2} = \frac{-B_2}{2B_0} r^2. \quad (30)$$

As a relative shift with respect to the measured Larmor frequency difference, this can be written as

$$\begin{array}{l} \frac{\Delta(\nu_L)}{\Delta(\nu_L)} = \frac{\nu_L - \nu_{L0}}{2(r_1^2 - r_2^2)} = \frac{1}{2} \frac{\nu_L - \nu_{L0}}{(B_2 - B_0)(r_1^2 - r_2^2)} \end{array}$$

Combining these shifts, $\langle \{\nu\}_{\{L\}}, \{B\}_{\{2\}}^{\{\{rel\}\}} \rangle$ and $\langle \{\nu\}_{\{L\}}, \{B\}_{\{1\}}^{\{\{rel\}\}} \rangle$, results in

$$\begin{aligned}
 & \frac{\Delta(\nu_L - \nu_{tot})}{\nu_L} = \frac{1}{\nu_L} \left(\frac{B_2}{B_0} - \frac{3}{4} \frac{\frac{B_1}{B_0} \xi_B - \frac{1}{2} \frac{d}{C_2} \text{char}}{\frac{B_2}{B_0}} \right) \\
 & - \frac{3}{4} \frac{\frac{B_1}{B_0} \xi_B - \frac{1}{2} \frac{d}{C_2} \text{char}}{\frac{B_2}{B_0}} \xi_B + \frac{3}{4} \frac{\frac{B_1}{B_0} \xi_B - \frac{1}{2} \frac{d}{C_2} \text{char}}{\frac{B_2}{B_0}} \frac{v_z^2}{\nu_L} \\
 & - \frac{3}{4} \frac{\frac{B_1}{B_0} \xi_B - \frac{1}{2} \frac{d}{C_2} \text{char}}{\frac{B_2}{B_0}} \frac{v_z^2}{\nu_L} + \frac{1}{6} \times 10^{-13}
 \end{aligned}$$

We find that, in the ideal case where neither magnetron nor cyclotron excitations produce shifts of the measured axial frequency ν_z , the final difference of the Larmor frequency is also not shifted at all. Here we use the

worst case, with a measured combined relative shift for $\frac{\eta}{\rm{mag}} \approx \frac{125}{\rm{mHz}}$ (560,). This corresponds to a systematic shift of $\Delta(\Delta\nu)_{\rm{tot}} = 6 \times 10^{-13}$, which we did correct for in the final result. This has been confirmed by performing two measurements on different separation distances, of $d_{\rm{sep}} = 340 \mu\text{m}$ and $d_{\rm{sep}} = 470 \mu\text{m}$. Both measurements have been in agreement after correcting for their respectively expected systematic shift. The uncertainty of this correction of 5×10^{-13} has been evaluated numerically by combining the uncertainties of $\eta_{\rm{mag}}$ and the radii intrinsic to its determination, an uncertainty of $\delta_{\rm{mag}}$ and the potential of a systematic suppression of the systematic shift by a residual common-mode radius.

Different axial amplitudes

The measurement is performed by first thermalizing the $^{20}\text{Ne}^{9+}$, then increasing the voltage to bring the $^{22}\text{Ne}^{9+}$ into resonance with the tank circuit. This will slightly decrease the axial amplitude of the $^{20}\text{Ne}^{9+}$, which nominally has the larger amplitude when cooled to the identical temperature, compared at the same frequency owing to its lower mass. The residual difference in amplitude will lead to a further systematic shift in the presence of a B_2 , which has been evaluated to about 3×10^{-14} and can therefore safely be neglected at the current precision.

***g*-factor calculation**

In Extended Data Table 1, the individual contributions to the *g* factors of both ions are shown. The main uncertainty, the higher-order two-loop QED contribution, is identical for both ions and does cancel in their difference and can therefore be neglected for the uncertainty of Δg . The finite nuclear size (FNS) correction gives the dominant uncertainty in Δg , which in turn is determined by the uncertainty of the r.m.s. radius²³. The next error comes from the nuclear polarization correction, which sets a hard limit for a further improvement in the determination of the r.m.s. radius. The difference in the spectra of photonuclear excitations of ^{20}Ne and ^{22}Ne defines the contribution

of the nuclear polarization to Δg . As the dominant contribution to the nuclear polarization of $^{20,22}\text{Ne}$ comes from the giant resonances, one has to estimate the isotope difference of this part of the spectrum. The measurements of the absolute yields of the various photonuclear reactions are reported in refs. [52,53](#) for ^{20}Ne and in refs. [54,55](#) for ^{22}Ne . On the basis of these data, we conclude that the integrated cross-section for the total photoabsorption between ^{20}Ne and ^{22}Ne differs by less than 20%, which we take as the relative uncertainty of the nuclear polarization contribution to Δg . The hadronic vacuum polarization (see, for example, ref. [56](#)) corresponds to the small shift of the g factor by the virtual creation and annihilation of hadrons and is largely independent of the nuclear structure. In the g -factor difference of $^{20}\text{Ne}^{9+}$ and $^{22}\text{Ne}^{9+}$, the QED contribution to the nuclear recoil can be resolved independently from all common contributions. A test of this contribution by means of an absolute g -factor measurement is possible for only the small regime from carbon to silicon and for only stable isotopes without nuclear spin. For smaller $Z \leq 6$, the QED contribution is too small to be resolved experimentally, and for $Z > 14$, the uncertainty of the two-loop QED contribution is too large to test the QED recoil. In addition, such an absolute g -factor measurement would also require the ion mass to similar precision, which is not the case for the approach via the direct difference measurement performed here.

Data availability

The datasets generated during and/or analysed during the current study are available from the corresponding author on reasonable request.

Code availability

All code used for the analysis and production of results of the current study are available from the corresponding author on reasonable request.

References

1. Hanneke, D., Fogwell, S. & Gabrielse, G. New measurement of the electron magnetic moment and the fine structure constant. *Phys. Rev.*

Lett. **100**, 120801 (2008).

2. Sturm, S. et al. *g* factor of hydrogen-like $^{28}\text{Si}^{13+}$. *Phys. Rev. Lett.* **107**, 023002 (2011).
3. Sturm, S. et al. High-precision measurement of the atomic mass of the electron. *Nature* **506**, 467–470 (2014).
4. Parker, R., Yu, C., Zhong, W., Estey, B. & Müller, H. Measurement of the fine-structure constant as a test of the standard model. *Science* **360**, 191–195 (2018).
5. Morel, L., Yao, Z., Cladé, P. & Guellati-Khélifa, S. Determination of the fine-structure constant with an accuracy of 81 parts per trillion. *Nature* **588**, 61–65 (2020).
6. Sturm, S. et al. The ALPHATRAP experiment. *Eur. Phys. J. Spec. Top.* **227**, 1425–1491 (2019).
7. Köhler, F. et al. Isotope dependence of the Zeeman effect in lithium-like calcium. *Nat. Commun.* **7**, 10246 (2016).
8. Rainville, S., Thompson, J. & Pritchard, D. An ion balance for ultra-high-precision atomic mass measurements. *Science* **303**, 334–338 (2004).
9. Furry, W. On bound states and scattering in positron theory. *Phys. Rev.* **81**, 115–124 (1951).
10. Malyshev, A., Glazov, D. & Shabaev, V. QED calculations of the nuclear recoil effect on the bound-electron *g* factor. *Phys. Rev. A* **101**, 012513 (2020).
11. Yerokhin, V., Berseneva, E., Harman, Z., Tupitsyn, I. & Keitel, C. *g*-factor of light ions for an improved determination of the fine-structure constant. *Phys. Rev. Lett.* **116**, 1–5 (2016).
12. Debierre, V., Keitel, C. & Harman, Z. Fifth-force search with the bound-electron *g* factor. *Phys. Lett. B* **807**, 135527 (2020).

13. Graham, P., Kaplan, D. & Rajendran, S. Cosmological relaxation of the electroweak scale. *Phys. Rev. Lett.* **115**, 221801 (2015).
14. Brown, L. & Gabrielse, G. Geonium theory: physics of a single electron or ion in a Penning trap. *Rev. Mod. Phys.* **58**, 233–311 (1986).
15. Cornell, E., Weisskoff, R., Boyce, K. & Pritchard, D. Mode coupling in a Penning trap: π pulses and a classical avoided crossing. *Phys. Rev. A* **41**, 312–315 (1990).
16. Sturm, S., Wagner, A., Schabinger, B. & Blaum, K. Phase-sensitive cyclotron frequency measurements at ultralow energies. *Phys. Rev. Lett.* **107**, 143003 (2011).
17. Dehmelt, H. Continuous Stern–Gerlach effect: principle and idealized apparatus. *Proc. Natl Acad. Sci. USA* **83**, 2291–2294 (1986).
18. Arapoglou, I. et al. g factor of boron-like argon $^{40}\text{Ar}^{13+}$. *Phys. Rev. Lett.* **122**, 253001 (2019).
19. Cornell, E., Boyce, K., Fygenson, D. & Pritchard, D. Two ions in a Penning trap: implications for precision mass spectroscopy. *Phys. Rev. A* **45**, 3049–3059 (1992).
20. Thompson, J. *Two-Ion Control and Polarization Forces for Precise Mass Comparisons* (Massachusetts Institute of Technology, 2003).
21. Britton, J. et al. Vibration-induced field fluctuations in a superconducting magnet. *Phys. Rev. A* **93**, 062511 (2016).
22. Rau, S. et al. Penning trap mass measurements of the deuteron and the HD^+ molecular ion. *Nature* **585**, 43–47 (2020).
23. Angeli, I. & Marinova, K. Table of experimental nuclear ground state charge radii: an update. *At. Data Nucl. Data Tables* **99**, 69–95 (2013).
24. Yerokhin, V., Müller, R., Surzhykov, A., Micke, P. & Schmidt, P. Nonlinear isotope-shift effects in Be-like, B-like, and C-like argon. *Phys. Rev. A* **101**, 1–7 (2020).

25. Müller, R., Yerokhin, V., Artemyev, A. & Surzhykov, A. Nonlinearities of King's plot and their dependence on nuclear radii. *Phys. Rev. A* **104**, L020802 (2021).
26. Pohl, R. et al. Laser spectroscopy of muonic deuterium. *Science* **353**, 669–673 (2016).
27. Shabaev, V. et al. *g* factor of high- Z lithium-like ions. *Phys. Rev. A* **65**, 062104 (2002).
28. Debierre, V., Keitel, C. & Harman, Z. Tests of physics beyond the standard model with single-electron ions. Preprint at <https://arxiv.org/abs/2202.01668> (2022).
29. Berengut, J. et al. Probing new long-range interactions by isotope shift spectroscopy. *Phys. Rev. Lett.* **120**, 091801 (2018).
30. Shabaev, V. et al. *g*-factor of heavy ions: a new access to the fine structure constant. *Phys. Rev. Lett.* **96**, 5–8 (2006).
31. Wehrli, D., Spysziewicz-Kaczmarek, A., Puchalski, M. & Pachucki, K. QED effect on the nuclear magnetic shielding of ${}^3\text{He}$. *Phys. Rev. Lett.* **127**, 263001 (2021).
32. Ulmer, S. et al. High-precision comparison of the antiproton-to-proton charge-to-mass ratio. *Nature* **524**, 196–199 (2015).
33. Bordag, M., Klimchitskaya, G., Mohideen, U. & Mostepanenko, V. *Advances in the Casimir Effect* (Oxford Univ. Press, 2009).
34. Redondo, J. & Raffelt, G. Solar constraints on hidden photons revisited. *J. Cosmol. Astropart. Phys.* **2013**, 034 (2013).
35. Solaro, C. et al. Improved isotope-shift-based bounds on bosons beyond the standard model through measurements of the ${}^2\text{D}_{3/2} - {}^2\text{D}_{5/2}$ interval in Ca^+ . *Phys. Rev. Lett.* **125**, 123003 (2020).

36. Delaunay, C., Frugueule, C., Fuchs, E. & Soreq, Y. Probing new spin-independent interactions through precision spectroscopy in atoms with few electrons. *Phys. Rev. D* **96**, 115002 (2017).
37. Counts, I. et al. Evidence for nonlinear isotope shift in Yb^+ search for new boson. *Phys. Rev. Lett.* **125**, 123002 (2020).
38. Berengut, J., Delaunay, C., Geddes, A. & Soreq, Y. Generalized King linearity and new physics searches with isotope shifts. *Phys. Rev. Res.* **2**, 1–11 (2020).
39. Figueroa, N. et al. Precision determination of isotope shifts in ytterbium and implications for new physics. *Phys. Rev. Lett.* **128**, 1–15 (2021).
40. Banerjee, A., Kim, H. & Perez, G. Coherent relaxion dark matter. *Phys. Rev. D* **100**, 115026 (2019).
41. Frugueule, C., Fuchs, E., Perez, G. & Schlaffer, M. Constraining new physics models with isotope shift spectroscopy. *Phys. Rev. D* **96**, 015011 (2017).
42. Delaunay, C., Ozeri, R., Perez, G. & Soreq, Y. Probing atomic Higgs-like forces at the precision frontier. *Phys. Rev. D* **96**, 093001 (2017).
43. Mikami, K., Tanaka, M. & Yamamoto, Y. Probing new intra-atomic force with isotope shifts. *Eur. Phys. J. C* **77**, 896 (2017).
44. Flambaum, V., Geddes, A. & Viatkina, A. Isotope shift, nonlinearity of King plots, and the search for new particles. *Phys. Rev. A* **97**, 032510 (2018).
45. Jaeckel, J. & Roy, S. Spectroscopy as a test of Coulomb's law: a probe of the hidden sector. *Phys. Rev. D* **82**, 125020 (2010).
46. Ohayon, B., Rahangdale, H., Geddes, A., Berengut, J. & Ron, G. Isotope shifts in $^{20,22}\text{Ne}$: precision measurements and global analysis in the framework of intermediate coupling. *Phys. Rev. A* **42**, 042503 (2019).

47. Barbieri, R. & Ericson, T. Evidence against the existence of a low mass scalar boson from neutron-nucleus scattering. *Phys. Lett. B* **57**, 270–272 (1975).
48. Pokotilovski, Y. Constraints on new interactions from neutron scattering experiments. *Phys. At. Nucl.* **69**, 924–931 (2006).
49. Leeb, H. & Schmiedmayer, J. Constraint on hypothetical light interacting bosons from low-energy neutron experiments. *Phys. Rev. Lett.* **68**, 1472–1475 (1992).
50. Nesvizhevsky, V., Pignol, G. & Protasov, K. Neutron scattering and extra-short-range interactions. *Phys. Rev. D* **77**, 034020 (2008).
51. Ketter, J., Eronen, T., Höcker, M., Streubel, S. & Blaum, K. First-order perturbative calculation of the frequency-shifts caused by static cylindrically-symmetric electric and magnetic imperfections of a Penning trap. *Int. J. Mass Spectrom.* **358**, 1–16 (2014).
52. Allen, P., Muirhead, E. & Webb, D. The photoneutron cross section of ^{20}Ne . *Nucl. Phys. A* **357**, 171–190 (1981).
53. Hofmann, W., Kosiek, R., Kraft, G. & Mundhenke, R. Die (γ , p)-Reaktion an einigen leichten und mittelschweren Kernen. *Z. Phys.* **225**, 303–326 (1969).
54. Veyssi  re, A. et al. A study of the photoneutron contribution to the giant dipole resonance of *s-d* shell nuclei. *Nucl. Phys. A* **227**, 513–540 (1974).
55. Varlamov, V. & Stepanov, M. Features of the $^{20,22}\text{Ne}$ dipole giant resonance decay by neutron and proton channels. *Izvestiya Akademii Nauk Rossijskaya Akademiya Nauk Seriya Fizicheskaya* **64**, 610–616 (2000).
56. Kurz, A., Liu, T., Marquard, P. & Steinhauser, M. Hadronic contribution to the muon anomalous magnetic moment to next-to-next-to-leading order. *Phys. Lett. B* **734**, 144–147 (2014).

57. Shabaev, V. Finite nuclear size corrections to the energy levels of the multicharged ions. *J. Phys. B* **26**, 1103 (1993).
58. Shabaev, V. & Yerokhin, V. Recoil correction to the bound-electron g factor in H-like atoms to all orders in $Z\alpha$. *Phys. Rev. Lett.* **88**, 091801 (2002).
59. Eides, M. & Grotch, H. Gyromagnetic ratios of bound particles. *Ann. Phys.* **260**, 191–200 (1997).
60. Michel, N., Zatorski, J., Oreshkina, N. & Keitel, C. Nonperturbative analysis of nuclear shape effects on the bound electron g factor. *Phys. Rev. A* **99**, 012505 (2019).

Acknowledgements

This work was supported by the Max Planck Society (MPG), the International Max Planck Research School for Quantum Dynamics in Physics, Chemistry and Biology (IMPRS-QD), the German Research Foundation (DFG) Collaborative Research Centre SFB 1225 (QUANT) and the Max Planck PTB RIKEN Center for Time, Constants, and Fundamental Symmetries. This project has received funding from the European Research Council (ERC) under the European Union’s Horizon 2020 research and innovation programme under grant agreement number 832848 FunI. A.V.V. acknowledges financial support by the Priority 2030 Federal Academic Leadership Program and by the Government of the Russian Federation through the ITMO Fellowship and Professorship Program. This work comprises parts of the PhD thesis work of C.K., T.S. and J.M. to be submitted to Heidelberg University, Germany.

Funding

Open access funding provided by Max Planck Society.

Author information

Authors and Affiliations

1. Max-Planck-Institut für Kernphysik, Heidelberg, Germany

Tim Sailer, Vincent Debierre, Zoltán Harman, Fabian Heiße, Charlotte König, Jonathan Morgner, Bingsheng Tu, Christoph H. Keitel, Klaus Blaum & Sven Sturm

2. Department of Physics and Engineering, ITMO University, St Petersburg, Russia

Andrey V. Volotka

3. Helmholtz–Institut Jena, Jena, Germany

Andrey V. Volotka

Contributions

The experiment was maintained and performed by T.S., B.T., C.K., F.H., J.M. and S.S. The data were analysed by T.S., F.H. and S.S. The manuscript was written by T.S. Theoretical calculations were performed by A.V.V., V.D. and Z.H. All authors discussed and approved the data as well as the manuscript.

Corresponding author

Correspondence to [Tim Sailer](#).

Ethics declarations

Competing interests

The authors declare no competing interests.

Peer review

Peer review information

Nature thanks Jonathan Sapirstein and the other, anonymous, reviewer(s) for their contribution to the peer review of this work. [Peer reviewer reports](#) are available.

Additional information

Publisher's note Springer Nature remains neutral with regard to jurisdictional claims in published maps and institutional affiliations.

Extended data figures and tables

[Extended Data Fig. 1 The measured Rabi frequency \$\Omega_R\$ on a single ion.](#)

The ion is excited to a magnetron radius of $\langle r \rangle = 200(30) \text{ nm}$, to ensure similar conditions as in the coupled state. The probability of inducing a change of spin orientation $P_{SF}(t)$ is modulated by the pulse length of the microwave irradiation time. The fit includes a varying microwave offset $\delta\Omega_L$ to account for the uncertainty of the magnetic field determination. Error bars represent the 68% CI.

[Extended Data Fig. 2 Bloch sphere representation of two of the possible outcomes of the measurement for an initial configuration with both ions in spin-down state.](#)

After both spins are rotated around the applied drive vector (orange) to the equatorial plane ($\pi/2$ pulse), they precess freely for the evolution time τ_{evol} . As the coherence with the applied drive is lost, the phase of the second time the drive is applied is completely random, leading to a reduction in visibility. The relative phase of the spins with respect to each other is encoded in their probability to behave identically, maximised when they are in phase (upper scenario) and minimal when their phase difference is 180° .

Extended Data Table 1 Contributions to the calculation of the *g*-factors of $^{20}\text{Ne}^{9+}$ and $^{22}\text{Ne}^{9+}$ and their difference and the final experimental result

Supplementary information

Peer Review File

Rights and permissions

Open Access This article is licensed under a Creative Commons Attribution 4.0 International License, which permits use, sharing, adaptation, distribution and reproduction in any medium or format, as long as you give appropriate credit to the original author(s) and the source, provide a link to the Creative Commons license, and indicate if changes were made. The images or other third party material in this article are included in the article's Creative Commons license, unless indicated otherwise in a credit line to the material. If material is not included in the article's Creative Commons license and your intended use is not permitted by statutory regulation or exceeds the permitted use, you will need to obtain permission directly from the copyright holder. To view a copy of this license, visit <http://creativecommons.org/licenses/by/4.0/>.

Reprints and Permissions

About this article

Cite this article

Sailer, T., Debierre, V., Harman, Z. *et al.* Measurement of the bound-electron *g*-factor difference in coupled ions. *Nature* **606**, 479–483 (2022).
<https://doi.org/10.1038/s41586-022-04807-w>

- Received: 27 September 2021
- Accepted: 26 April 2022

- Published: 15 June 2022
- Issue Date: 16 June 2022
- DOI: <https://doi.org/10.1038/s41586-022-04807-w>

Share this article

Anyone you share the following link with will be able to read this content:

[Get shareable link](#)

Sorry, a shareable link is not currently available for this article.

[Copy to clipboard](#)

Provided by the Springer Nature SharedIt content-sharing initiative

[**Tiny isotopic difference tests standard model of particle physics**](#)

- Gerald Gwinner
- Roshani Silwal

Nature News & Views 15 Jun 2022

This article was downloaded by **calibre** from <https://www.nature.com/articles/s41586-022-04807-w>

- Article
- Open Access
- [Published: 01 June 2022](#)

Realizing the symmetry-protected Haldane phase in Fermi–Hubbard ladders

- [Pimonpan Sompet](#),
- [Sarah Hirthe](#),
- [Dominik Bourgund](#),
- [Thomas Chalopin](#),
- [Julian Bibo](#),
- [Joannis Koepsell](#),
- [Petar Bojović](#),
- [Ruben Verresen](#),
- [Frank Pollmann](#),
- [Guillaume Salomon](#),
- [Christian Gross](#),
- [Timon A. Hilker](#) &
- [Immanuel Bloch](#)

Nature volume **606**, pages 484–488 (2022)

- 2867 Accesses
- 67 Altmetric
- [Metrics details](#)

Abstract

Topology in quantum many-body systems has profoundly changed our understanding of quantum phases of matter. The model that has played an instrumental role in elucidating these effects is the antiferromagnetic spin-1 Haldane chain^{1,2}. Its ground state is a disordered state, with symmetry-protected fourfold-degenerate edge states due to fractional spin excitations. In the bulk, it is characterized by vanishing two-point spin correlations, gapped excitations and a characteristic non-local order parameter^{3,4}. More recently it has been understood that the Haldane chain forms a specific example of a more general classification scheme of symmetry-protected topological phases of matter, which is based on ideas connected to quantum information and entanglement^{5,6,7}. Here, we realize a finite-temperature version of such a topological Haldane phase with Fermi–Hubbard ladders in an ultracold-atom quantum simulator. We directly reveal both edge and bulk properties of the system through the use of single-site and particle-resolved measurements, as well as non-local correlation functions. Continuously changing the Hubbard interaction strength of the system enables us to investigate the robustness of the phase to charge (density) fluctuations far from the regime of the Heisenberg model, using a novel correlator.

Main

Topological phases of matter often share a deep connection between their bulk and edge properties^{8,9}. In the case of the Haldane chain, the bulk exhibits a hidden antiferromagnetic (AFM) order characterized by AFM correlations interlaced with an arbitrary number of $S^z = 0$ elements, where S^z denotes the spin component in the z-direction. This pattern can only be revealed through non-local string correlations that are sensitive to the local spin states, which, however, require detection of the quantum many-body system with microscopic resolution. Although this was not possible in early experiments on spin-1 chains, evidence for a spin gap, as well as spin-1/2 localized edge states, was found using neutron scattering^{10,11} or electron resonance experiments^{12,13} while not directly probing this hidden order or spatially resolving the edge states. Recent developments in quantum simulations enable one to go beyond such solid-state bulk measurements by observing quantum many-body systems with single-site resolution^{14,15,16,17,18} and in a fully spin- and density-resolved way^{19,20}. This

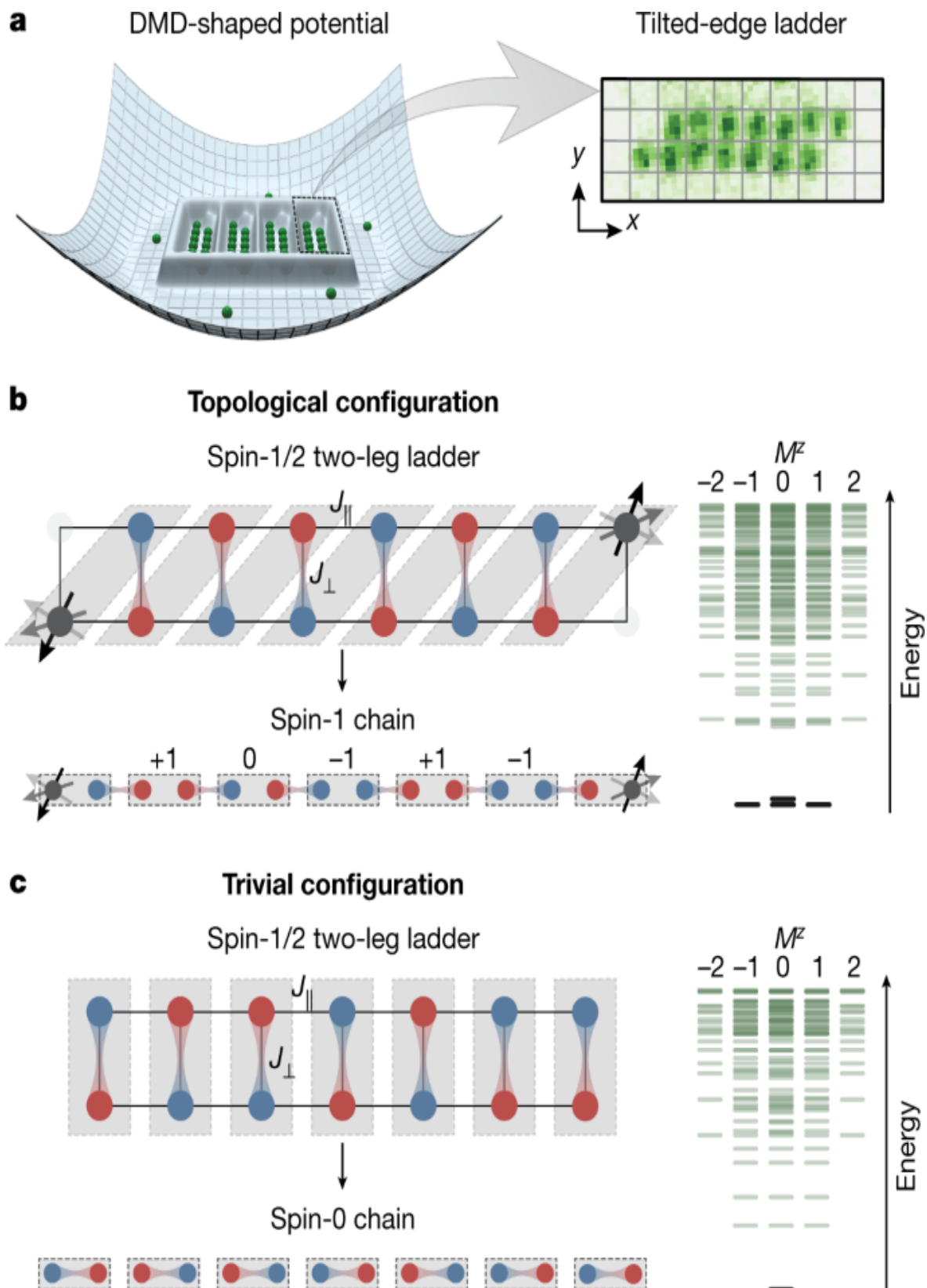
provides a rich diagnostic tool to obtain a direct microscopic picture of the hidden order in experiments^{21,22}. The power of this technique has also been demonstrated recently in a study that was able to reveal a symmetry-protected topological (SPT) phase in the hardcore boson Su–Schrieffer–Heeger (SSH) model using Rydberg atoms²³. Here we expand on those results by realizing a finite-temperature version of the Haldane phase in a spin system with tuneable coupling strength, system size and controlled charge fluctuations. We show this by measuring both topological and trivial string order parameters.

An instructive way to engineer the Haldane phase in systems of spin-1/2 fermions is on the basis of the AKLT model^{4,24}, in which a spin-1 particle is formed out of two spin-1/2 particles. Thus, spin-1/2 ladder systems emerge as an experimentally realizable platform for the Haldane phase. Whereas a natural implementation with spin-1 particles on individual rungs requires ferromagnetic rung couplings and antiferromagnetic leg couplings, a much wider variety of couplings in spin-1/2 quantum ladders feature the Haldane phase^{25,26}. This includes the antiferromagnetic Heisenberg case, which we realize here as the strong-interaction limit of the Fermi–Hubbard model.

In our experiment, we prepare such ladders by adiabatically loading a spin-balanced mixture of the two lowest hyperfine states of ${}^6\text{Li}$ into an engineered lattice potential ([Methods](#)). As illustrated in Fig. [1a](#), we realize four isolated two-leg ladders with a variable number (L) of unit cells (where L is therefore also equivalent to length), surrounded by a low-density bath of particles²⁷. The unit cells are chosen to be either along the rungs of the ladders (vertical unit cell, Fig. [1b](#)) or along the diagonals (diagonal unit cells, Fig. [1c](#)). The edges of the ladders are then engineered to match the choice of unit cell: straight edges are chosen for vertical unit cells, whereas one site is blocked on each edge in the case of diagonal unit cells. The atoms in the lowest band of the optical lattice are well described by the Fermi–Hubbard model, with tunnelling energies, $\langle\{t\}_{\{\parallel\}}\rangle$ (chain), $\langle\{t\}_{\{\perp\}}\rangle$ (rung), and on-site interactions U . For half-filling and at strong $\langle U/\{t\}_{\{\parallel,\perp\}} \rangle \approx 13$, used throughout most of our experiments (see [Methods](#) for details), density fluctuations are suppressed and the spin ladder realizes the Heisenberg model²⁸ with Hamiltonian:

$$\begin{aligned}
& \text{\$\$} \hat{H} = J_{\parallel} \sum \left\{ \begin{array}{l} \text{\bf parallel} \\ \text{\bf end} \end{array} \right\} \sum_{x \in [0, L]} \\
& y = A, B \left\{ \begin{array}{l} \text{\bf end} \\ \text{\bf begin} \end{array} \right\} \left\{ \begin{array}{l} \hat{\text{\bf S}} \\ \cdot \end{array} \right\}_{x,y} \cdot \\
& \left\{ \begin{array}{l} \hat{\text{\bf S}} \\ \cdot \end{array} \right\}_{x+1,y} + J_{\perp} \sum_{x \in [0, L]} \\
& \left\{ \begin{array}{l} \hat{\text{\bf S}} \\ \cdot \end{array} \right\}_{x,A} \cdot \left\{ \begin{array}{l} \hat{\text{\bf S}} \\ \cdot \end{array} \right\}_{x,B} \text{\$\$} \\
(1)
\end{aligned}$$

Fig. 1: Probing topological phases in spin-1/2 ladders of cold atoms.



a, Realization of tailored spin-1/2 ladders in a single plane of a 3D optical lattice with a potential shaped by a DMD. The dilute wings of the potential are well separated from the homogeneous ladder systems. Using quantum gas microscopy, we obtain fully spin- and density-resolved images of the system. The inset shows a single-shot fluorescence image of the prepared ladder without spin resolution. **b, c**, Connecting spin-1/2 ladders to integer-spin chains by grouping pairs of spins in unit cells. For diagonal unit cells (**b**) the AFM Heisenberg ladder adiabatically connects to the Haldane spin-1 chain showing spin-1/2 edge states and hidden long-range order (that is, AFM order interspersed with $S^z = 0$ unit cells). For vertical unit cells (**c**), the system is in the topologically trivial phase dominated by singlets on the rungs, forming a spin-0 chain. We adapt the edges of the system to match the respective unit cell, that is straight edges for vertical unit cells and tilted edges for diagonal unit cells, which we realize by blocking one site on each end. The energy spectra of the systems grouped by total magnetization M^z display gapped fourfold near-degenerate ground states for the topological configuration and a single ground state for the trivial one. Sketch for $L = 7$.

with positive leg and rung couplings, $\langle J_{\parallel}, J_{\perp} \rangle = 4t_{\parallel}^2 / U$ and the spin-1/2 operators $\hat{S}_{x,y}$ at site (x, y) , with A, B denoting the two legs of the ladder.

The topological properties are most easily explained in the limit $J_{\perp} \gg J_{\parallel}$, where strong spin singlets form along the rungs and the system exhibits an energy gap of $\langle J_{\perp} \rangle$. The behaviour on the edges of the ladder then depends on how the system is terminated, and therefore on which unit cells have been chosen. For diagonal unit cells (Fig. 1b), two unpaired spin-1/2 particles remain and the many-body system has a fourfold degeneracy that is only weakly lifted by an edge-to-edge coupling, which vanishes exponentially with system size (Supplementary Information). In the trivial case of vertical unit cells (Fig. 1c), all spins pair into singlets and the ground state is unique. These descriptions remain valid even for weaker $|J_{\perp}|/|J_{\parallel}|$, where the singlet alignment may change between vertical and horizontal, but any line between two rungs cuts an even number of singlets^{29,30}.

To make the analogy between the spin-1/2 ladder and the Haldane integer chain more apparent, we switch to a description in terms of total spin per k th unit cell, $\langle \hat{\{S\}}_k \rangle = \langle \hat{\{S\}}_{k,A} \rangle + \langle \hat{\{S\}}_{k,B} \rangle$, where the indices (A, B) indicate the two spin-1/2 particles in the same unit cell, making an integer spin. In the diagonal unit cell such a system shows a high ($\geq 80\%$) triplet fraction²⁶ (Supplementary Information). We note that this spin ladder can be adiabatically connected to a spin-1 chain by including ferromagnetic couplings within the unit cell²⁵. However, having a high triplet fraction is not essential for having a well-defined Haldane phase, as both systems share the same universal SPT features²⁶.

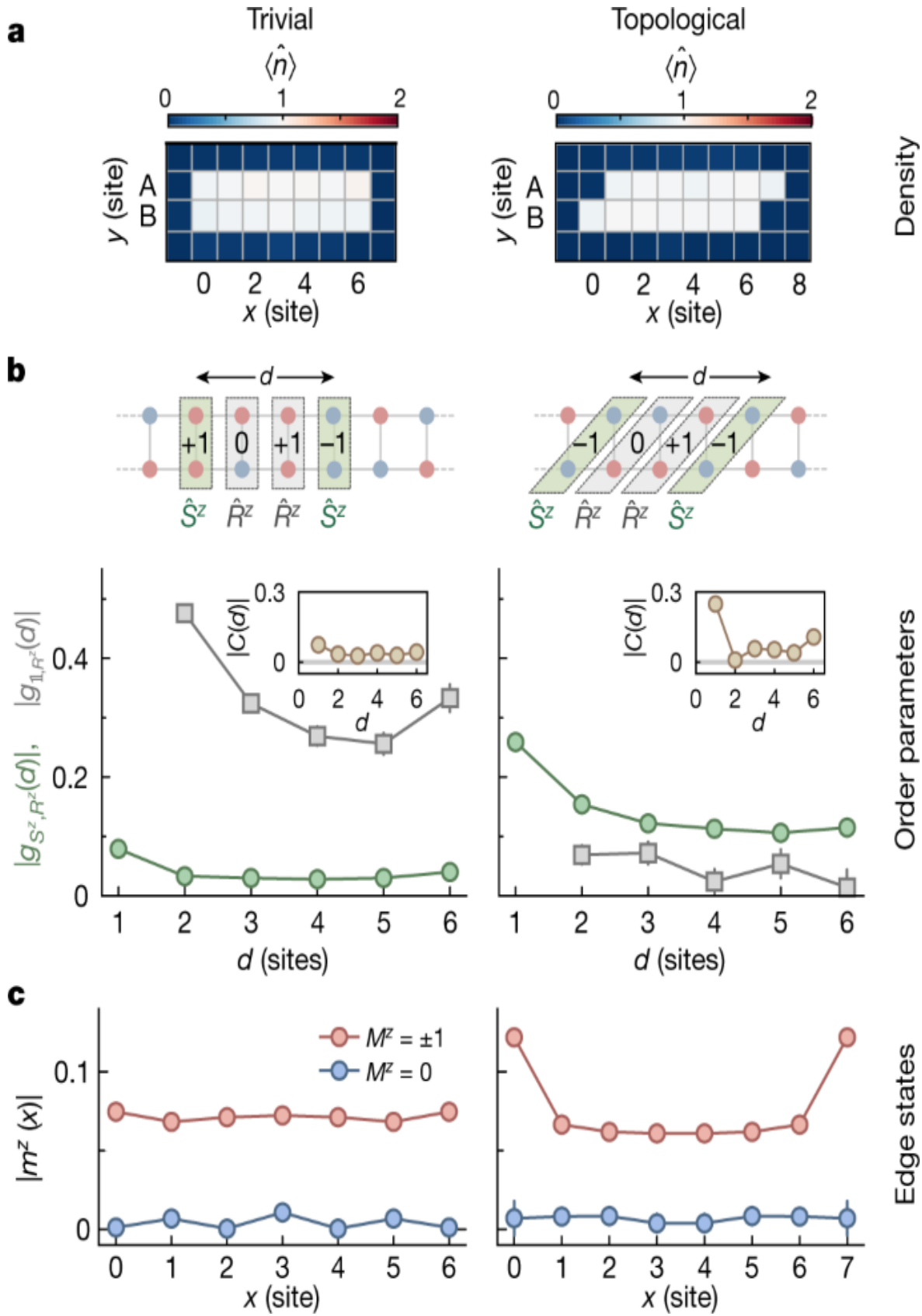
The defining property of the Haldane SPT phase is that it is an integer-spin chain with spin-1/2 edge modes: the bulk SO(3) symmetry is said to fractionalize into SU(2) symmetry at the edge. It has no spontaneous symmetry breaking and thus the spin correlation function $\langle \hat{S}_k^z \hat{S}_{k+d}^z \rangle$ is short range. Instead, the aforementioned symmetry fractionalization^{6,7} can be detected in the bulk using string order parameters^{3,31}:

$$\begin{aligned} \text{g}_{U,d} &= \langle \hat{U}_l \hat{U}_{l+d} \rangle \\ &= \langle \hat{U}_l \prod_{i=l+1}^{l+d-1} \hat{U}_i \rangle \\ &= \langle \hat{U}_d \rangle \end{aligned} \quad (2)$$

with an on-site symmetry $\langle \hat{U}_l \rangle$ and endpoint operator $\langle \hat{U}_d \rangle$, where l denotes the unit cell and d the string distance (Fig. 2 and Supplementary Information). This correlator probes the transformation behaviour of the bulk under a symmetry $\langle \hat{U}_l \rangle$; for example, a spin rotation around the z axis by π , $\langle \hat{R}_l \rangle \equiv \langle \exp(i\pi) \rangle$. The pure-string correlator $\langle g_{U,d} \rangle$, where $\langle \hat{U}_l \rangle = 1$ and $\langle \hat{U}_d \rangle = \langle \hat{R}_l \rangle$, is non-zero for $d \gg 1$ if the edge does not have half-integer spins³¹. This is the case for the topologically trivial configuration but not for the Haldane phase, in which the symmetry is fractionalized. The spin-string operator $\langle g_{U,d} \rangle$ (ref.

$\hat{O}_k = \hat{S}_k^z$, exhibits the opposite behaviour and is non-zero only in the Haldane phase (see Supplementary Information for details about the symmetries of the Haldane phase). Thus we can identify the Haldane phase by comparing the two string correlators $\langle g_{S^z, R^z} \rangle$ and $\langle g_{\mathbb{1}, R^z} \rangle$, and observe opposite behaviour in the two different regimes.

Fig. 2: Trivial versus topological configurations.



a, The atomic density distribution $\langle \langle \hat{n} \rangle \rangle$ of ladders with diagonal and vertical unit cells. **b**, The amplitudes of the spin-string correlator $\langle \{g\}_{z} \{S\}^z, \{R\}^z \rangle$ (green circles) and the string-only correlator $\langle \{g\}_{z} \{\mathbb{1}\}, \{R\}^z \rangle$ (grey squares) observed as a function of the spin distance over d unit cells. The cartoon illustrates the unit cells, the total spin S^z per unit cell and the string correlators for a subsystem with $d=3$. In the trivial configuration (rung unit cells), $\langle \{g\}_{z} \{\mathbb{1}\}, \{R\}^z \rangle(d)$ is well above zero, whereas $\langle \{g\}_{z} \{S\}^z, \{R\}^z \rangle(d)$ is rapidly vanishing at $d > 1$. By contrast, for the topological configuration (diagonal unit cells), $\langle \{g\}_{z} \{S\}^z, \{R\}^z \rangle(d)$, shows a long-range correlation, whereas $\langle \{g\}_{z} \{\mathbb{1}\}, \{R\}^z \rangle(d)$ is close to zero. In both cases, the two-point spin–spin correlation $C(d)$ decays rapidly to zero as a function of the distance d (insets). The correlators $\langle \{g\}_{z} \{\mathbb{1}\}, \{R\}^z \rangle, \langle \{g\}_{z} \{S\}^z, \{R\}^z \rangle$ and $C(d)$ are evaluated for fixed total magnetization $\langle \{m\}^z \rangle = 0$. **c**, Amplitudes of the rung- and inversion-averaged local magnetizations $\langle \{m\}^z(x) \rangle$ plotted as a function of position x along the chains for different $\langle \{m\}^z \rangle$. In the unbalanced spin sector of the topological configuration ($\langle \{m\}^z \rangle = \pm 1$), the result displays a localization of the excess spins at the edges, signalling the presence of edge states. All data were taken with $\langle \{J\}_{\perp} / \{J\}_{\parallel} \rangle = 1.3(2)$. Error bars denote one standard error of the mean (s.e.m.) and are smaller than their marker size if not visible.

[Source data](#)

Another perspective on $\langle \{g\}_{z} \{S\}^z, \{R\}^z \rangle$ can be gained by recognizing it as a normal two-point correlator at distance d , which ignores all spin-0 contributions along the way ('squeezed space'^{22,32}). In the underlying spin-1/2 system, this order stems from $N-1$ consecutive rungs dominantly consisting of $N-1$ singlets and two spin-1/2 states, which have a combined total spin of +1, 0 or -1.

To observe the characteristics of the SPT phase, we prepare a two-leg ladder of length $L=7$ and $\langle \{J\}_{\perp} / \{J\}_{\parallel} \rangle = 1.3(2)$ in both the topological and the trivial configuration. The tailored potential yields a homogeneous filling of the system with sharp boundaries (Fig. 2a), which is characterized by a remaining density variance over the system of 2×10^{-4} . To focus on the spin physics, we select realizations with $\langle \{N\}_{\uparrow} \rangle$

$\} + \{N\}_{\downarrow} = 2L$) per ladder. Additionally, we exclude ladders with an excessive number of doublon–hole fluctuations and do not consider strings with odd atom numbers in the string or the endpoints of the correlator ([Methods](#)). We characterize the spin-balanced ladder systems $((M^z) \equiv (N_{\uparrow} - N_{\downarrow})/2 = 0)$ by evaluation of the string order parameters, as defined in equation [\(2\)](#). In the topological configuration, we observe fast decay of $\langle g_S^z \rangle$, $\langle R^z \rangle$ over a distance of approximately one site and a long-range correlation up to $d = 6$, with a final value of $\langle g_S^z \rangle \approx 0.1$ (Fig. [2b](#)). In contrast, for the trivial configuration, the correlation decays rapidly to zero as a function of the string correlator length. The opposite behaviour is seen for $\langle g_{\mathbb{1}}^z \rangle$, $\langle R^z \rangle$ ($d = 6$), demonstrating the hidden correlations expected for both phases.

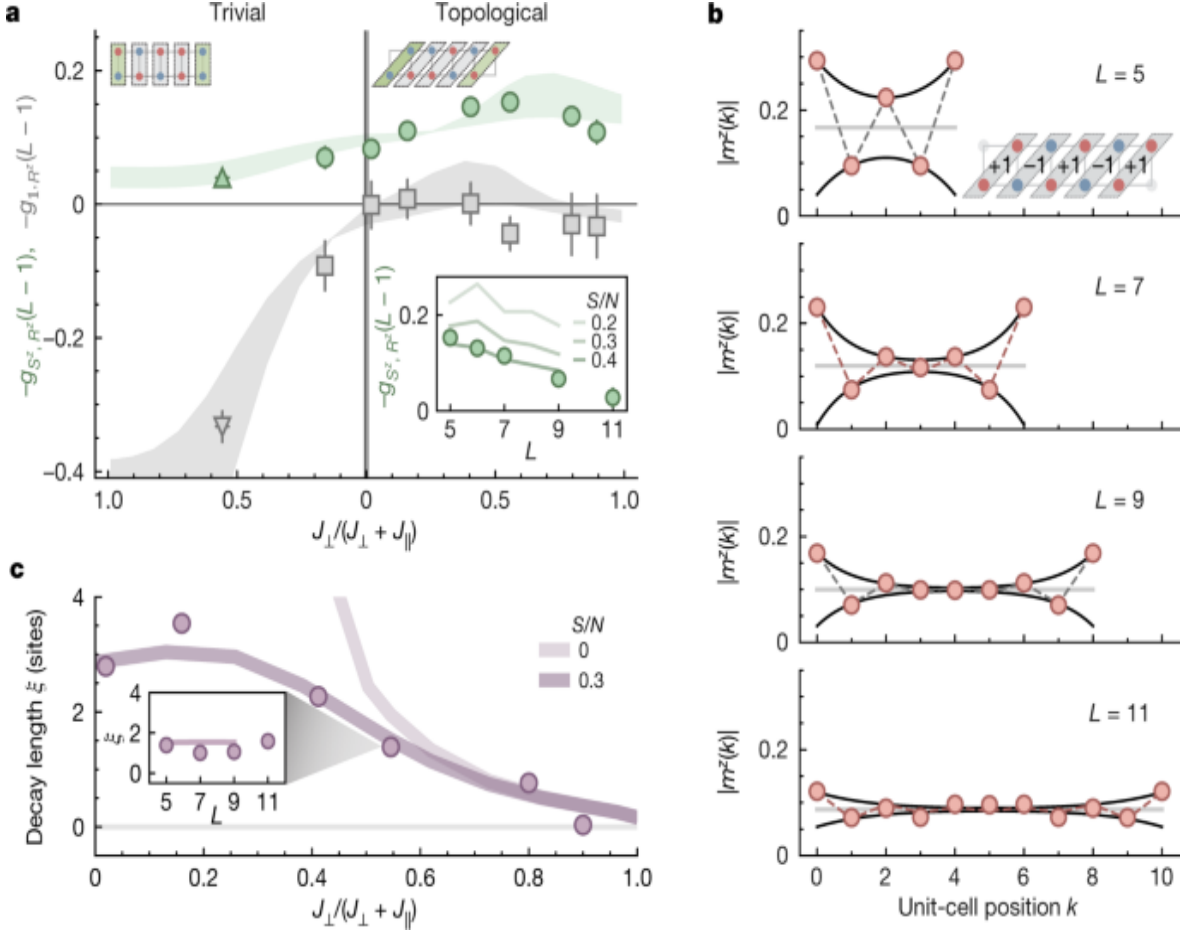
Furthermore, the two-point spin correlation, $\langle C(d) \rangle \equiv \langle g_S^z \rangle$, $\langle g_{\mathbb{1}}^z \rangle$ ($d = 6$) $\langle \langle \hat{S}_k | \hat{S}_{k+d} \rangle \rangle$ yields only the short-range AFM correlation characteristic for a gapped phase (see insets in Fig. [2b](#)). It is interesting to note that at the largest distance in the topological case, $C(d = 6)$ displays a clear (negative) correlation between the two edge spins, despite small correlations at shorter distances. This (classical) correlation confirms the existence of a non-magnetized bulk, such that spins on the edges of the system must be of opposite direction at global $M^z = 0$.

We probe the edges explicitly by measuring the amplitude of the local rung-averaged magnetization $m^z(x)$ as a function of rung position x for different sectors of the ladder magnetization M^z (Fig. [2c](#)). In the case of an imbalanced spin mixture with $M^z = \pm 1$, we see that the two end sites exhibit on average a higher magnetization than the bulk rungs in the topological configuration. This is consistent with the bulk of the ground states of both phases forming a global singlet, and only the edges of the topological phase carrying an excess spin-1/2 without energy cost. The measured bulk magnetization can be attributed to finite-temperature effects (Supplementary Information).

The SPT phase is expected to be robust^{[26](#)} on variation of the ratio $\langle J_{\perp} \rangle / \langle J_{\parallel} \rangle$, but maintains a finite gap in the system. We

realize both the trivial and topological configuration with different $\langle \{t\}_{\perp} \rangle / \langle \{t\}_{\parallel} \rangle$ at almost fixed U and study the string correlators at maximal distance ($L - 1$) versus $\langle \{J\}_{\perp} \rangle / \langle \{J\}_{\parallel} \rangle$ (Fig. 3a). For the topological configuration with diagonal unit cells, we observe $\langle \{g\}_{\{S\}^z, \{R\}^z} \rangle_{L=1} \approx 0$ and $|\langle \{g\}_{\{S\}^z, \{R\}^z} \rangle| > 0$ for all $\langle \{J\}_{\perp} \rangle / \langle \{J\}_{\parallel} \rangle$ with a maximum around $\langle \{J\}_{\perp} \rangle / \langle \{J\}_{\parallel} \rangle \approx 1.3(2)$ (that is, $\langle \{J\}_{\perp} \rangle / (\langle \{J\}_{\perp} \rangle + \langle \{J\}_{\parallel} \rangle) \approx 0.56(4)$), whereas for the trivial case the role of the correlators is reversed. Both phases continuously connect in the limit of two disconnected chains at $\langle \{J\}_{\perp} \rangle = 0$. These observations demonstrate qualitatively all the key predictions of the antiferromagnetic spin-1/2 ladder at temperature $T = 0$ (ref. 26) and the strengths of the measured correlations are consistent with exact diagonalization (ED) calculations using an entropy per particle $(S/N = (0.3 - 0.45)/k_{\text{B}})$ (shaded lines in Fig. 3a).

Fig. 3: Influence of spin-coupling strength on the string order parameters and the edge states.



a, The two string order parameters, $\langle\{g\}_{\{\{S\}^z, \{R\}^z\}}\rangle$ (green) and $\langle\{g\}_{\{\{1\}, \{R\}^z\}}\rangle$ (grey), for both trivial (left) and topological (right) configurations measured as a function of $\{J\}_\perp/\{J\}_\parallel$. Both $\langle\{g\}_{\{\{S\}^z, \{R\}^z\}}\rangle$ and $\langle\{g\}_{\{\{1\}, \{R\}^z\}}\rangle$ stay finite in their respective phases and are largely consistent with zero in the other phase. The data were taken at a chain length of $L = 5$ except for one data point marked by a triangle at $L = 7$. Shaded curves are the ED results of the two order parameters at finite entropy per particle, $S/N = (0.3-0.45) k_B$ and $L = 5$. The inset shows the measured $\langle\{g\}_{\{\{S\}^z, \{R\}^z\}}\rangle$ as a function of the chain length L at $(J_\perp/(J_\perp + J_\parallel)) = 1.3(2)$ (that is, $(J_\perp/(J_\perp + J_\parallel)) = 0.56(4)$). The decay in the magnitude of the string order parameter with length is expected at finite temperatures in quantitative agreement with ED results (lines) at $S/N \approx 0.4 k_B$. **b**, Edge state localization at $(J_\perp/(J_\perp + J_\parallel)) = 1.3(2)$. In the $(m^z) = \pm 1$ spin sectors of the topological configuration, the unit cell local magnetization $|m^z(k)|$ is plotted for $L = 5, 7, 9, 11$. **c**, Decay length ξ (sites) as a function of $J_\perp/(J_\perp + J_\parallel)$ for $S/N = 0$ (light purple) and 0.3 (dark purple). An inset shows the decay length ξ as a function of L at $J_\perp/(J_\perp + J_\parallel) = 1.3(2)$.

$\langle m \rangle^z(k) \rangle$ at chain position k shows excess magnetization localized at the edges for different lengths. The black line is a fit to our inversion-averaged data. **c**, The localization length ξ of the edge states increases with the leg coupling $\langle J \rangle_{\parallel}$ but saturates at a value set by temperature and system size $L = 5$. Lines are ED results at $S/N = 0.3 k_B$ and $0 k_B$. The inset shows the independence of ξ with respect to L extracted from the plots in **b**, as well as ED results for $S/N = 0.3 k_B$. Error bars denote one standard error of the mean (s.e.m) and are smaller than their marker size if not visible.

Source data

We reveal these features despite the finite temperature in our system, which would destroy the long-range hidden order in an infinite system. The total entropy in our system is, however, still low enough to yield a large fraction of realizations of the topological ground state. In larger systems, the total number of thermal excitations grows (at fixed entropy per particle) and the non-local correlator $\langle g_S(z), R^z(L-1) \rangle$ decreases (see inset of Fig. 3a), consistent with vanishing correlations in the thermodynamic limit, thus yielding a restriction on our system size at our level of experimental precision and entropy per particle (Supplementary Information). Finite size effects are explored in detail in the Supplementary Information. We note that the difference between the SPT phase and the trivial phase is here clearly shown by considering both $\langle g_S(z), R^z \rangle$ and $\langle g_{\mathbb{1}}(z), R^z \rangle$.

To investigate the localization length of the edge states, we evaluate our data for $\langle m \rangle^z = \pm 1$ and plot the local magnetization per unit cell $\langle m \rangle^z(k)$ for different system sizes (Fig. 3b). Because of the singlets in the bulk, the excess spin is most likely to be found at the edges of the system. This spin partly polarizes the neighbouring sites antiferromagnetically, leading to an exponentially localized net magnetization with AFM substructure³³. The data are well described by the fit function $\langle m \rangle^z(k) = m_B \left[e^{-k/\xi} + (-1)^{L-k-1} e^{-(L-k-1)/\xi} \right]$ with free bulk magnetization m_B , edge magnetization m_E and decay length ξ . In Fig. 3c, we show how this

localization length ξ decreases as we approach the limit of rung singlets, $(\{J\}_{\perp} \gg \{J\}_{\parallel})$. Comparison with ED lets us identify two regimes: at $(\{J\}_{\perp} \gtrsim \{J\}_{\parallel})$, the measured ξ drops with larger $\{J\}_{\perp}$ and coincides with theory independent of temperature, whereas at low $(\{J\}_{\parallel})$ thermal effects dominate, limiting the increase of ξ to three sites for our system (Supplementary Information).

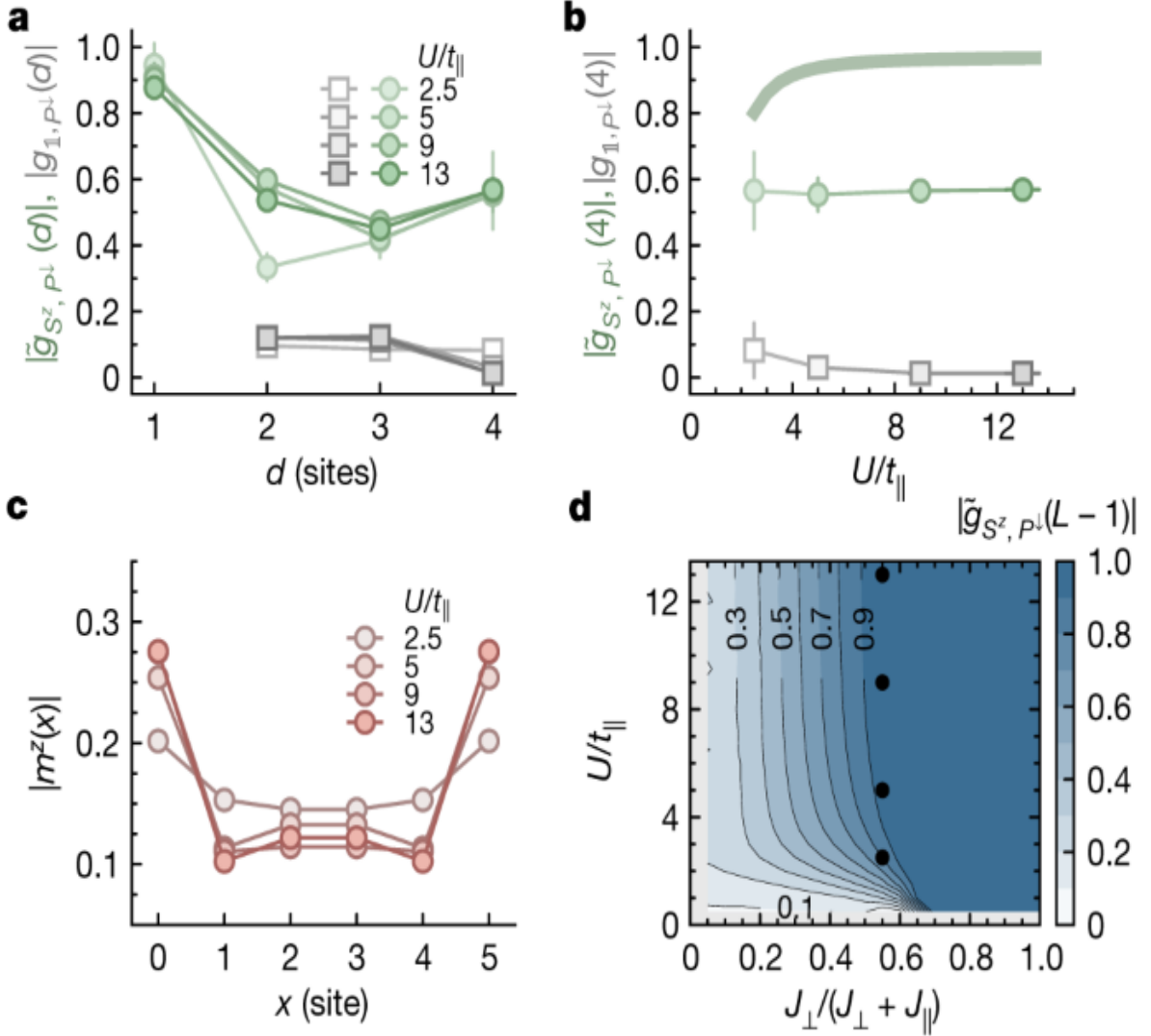
Thus far, we have worked in the Mott limit where density fluctuations can be ignored, such that the spin Hamiltonian, equation (1), is a good effective description of the Fermi–Hubbard ladder. However, it is known that the Haldane SPT phase can be unstable to density fluctuations^{34,35,36}. By reducing $(U/t)_{\parallel}$, the symmetry in the unit cell in the bulk changes from SO(3) to SU(2), as it now may contain both half-integer and integer total spin. This effectively removes the distinction between bulk and edge (Supplementary Information). This means that the edge mode and string order parameter are no longer topologically non-trivial, which is also manifested in the fact that the two phases can be adiabatically connected by tuning through a low- $(U/t)_{\parallel}$ regime if one breaks additional symmetries but preserves spin-rotation symmetry^{34,35,36}. In particular, the above string orders lose their distinguishing power: $(\{g\}_{\{S\}}^{\{z\}}, \{R\}^{\{z\}})$ and $(\{g\}_{\{\mathbb{1}\}}, \{R\}^{\{z\}})$ will both generically have long-range order away from the Mott limit³⁴.

Intriguingly, despite the breakdown of the above symmetry argument and string order parameter, the Hubbard ladder (with diagonal unit cell) remains a non-trivial SPT phase due to its sublattice symmetry. This symmetry is a direct consequence of the ladder being bipartite (see Supplementary Information for details). It is simplest to see that this protects the SPT phase in the limit $U=0$, where the two spin species decouple, such that our model reduces to two copies of the SSH chain³⁷. It is known that such a stack remains in a non-trivial SPT phase in the presence of interactions, namely $U \neq 0$ (ref. 38). Moreover, together with the parity symmetry of spin-down particles, $(\{\hat{P}\}_l)^{\downarrow} \equiv \{\exp\left[i\pi(\hat{n}_l A)\right]\}^{\downarrow} + (\hat{n}_l B)^{\downarrow}$, it then gives rise to a different string order parameter: the topological phase is characterized by long-range

order in $\langle \{g\}_{\{S\}^{\{z\}}}, \{P\}^{\{\downarrow\}} \rangle$, whereas it has vanishing correlations for $\langle \{g\}_{\{\mathbb{1}\}}, \{P\}^{\{\downarrow\}} \rangle$, with the roles being reversed in the trivial phase. This novel string order is derived in the Supplementary Information. Remarkably, in the Heisenberg limit, it coincides with the conventional string order parameter used before.

In the topological phase it is meaningful to normalize $\langle \{g\}_{\{S\}^{\{z\}}}, \{P\}^{\{\downarrow\}} \rangle$ to $\langle \{\tilde{g}\}_{\{S\}^{\{z\}}}, \{P\}^{\{\downarrow\}} \rangle = \eta$ with $\langle \{\eta\}^{\{-1\}} \rangle = \langle \hat{S}_k^z | \hat{S}_{k+d}^z \rangle$, which effectively excludes endpoints with spin $S^z = 0$. Indeed, we find unchanged string correlations $\langle \{\tilde{g}\}_{\{S\}^{\{z\}}}, \{P\}^{\{\downarrow\}} \rangle$ and $\langle \{g\}_{\{\mathbb{1}\}}, \{P\}^{\{\downarrow\}} \rangle$ down to the lowest experimentally explored value $\langle U/t \rangle_{\parallel} = 2.5(2)$ (Fig. 4a, b) and edge state signals down to $\langle U/t \rangle_{\parallel} = 5.0(3)$ (Fig. 4c). Density matrix renormalization group (DMRG) calculations for $\langle L \rangle_{\text{to inf}}$ confirm non-zero $\langle \{\tilde{g}\}_{\{S\}^{\{z\}}}, \{P\}^{\{\downarrow\}} \rangle_{(L-1)}$ at $T = 0$ and for all rung-coupling strengths (Fig. 4d), while $\langle \{g\}_{\{\mathbb{1}\}}, \{P\}^{\{\downarrow\}} \rangle_{(L-1)}$ is strictly zero. Owing to the normalization $\langle \{\tilde{g}\}_{\{S\}^{\{z\}}}, \{P\}^{\{\downarrow\}} \rangle_{(L-1)}$ goes to 1 for $\langle \{J\}_{\perp} \gg \{J\}_{\parallel} \rangle$.

Fig. 4: Robustness of the Haldane phase to density fluctuations.



a, b, The hidden SPT order is preserved even at low Hubbard interactions, as revealed by the novel string correlators $|\tilde{g}_{S^z, P^\downarrow}(d)|$ (green circles) and $|\tilde{g}_{S^z, P^\downarrow}(4)|$ (grey squares) on the basis of the spin-down parity $\langle \hat{P}^\downarrow \rangle$. $|\tilde{g}_{S^z, P^\downarrow}(d)|$ stays non-zero, whereas $|\tilde{g}_{S^z, P^\downarrow}(4)|$ is consistent with zero for $d=L-1$ over the measured interaction range. The same qualitative behaviour is seen in zero-temperature DMRG calculations (shaded line) with $L \rightarrow \infty$. **c**, Spatial distribution of excess magnetization ($|m^z(x)| = \pm 1$) for decreasing U/t_{\parallel} . Even far away from the Heisenberg regime, the edge state signal remains strong and only diminishes for very weak U/t_{\parallel} . **d**, Map of zero-temperature DMRG $(L \rightarrow \infty)$

results for the spin-string correlator in the entire parameter space of the topological phase. It shows a strictly non-zero $\langle \langle \hat{g} \rangle \rangle_{\{S\}^z}$, $\langle P \rangle^{\downarrow} \rangle \rangle$ while $\langle \{g\}_{\{mathbb{1}\}}, \langle P \rangle^{\downarrow} \rangle \rangle (L-1)=0 \rangle$ everywhere in this phase. The black circles indicate the parameters of the measurements. All experimental data were taken at $\langle \{J\}_{\{\perp\}} / \{J\}_{\{\parallel\}} = 1.3(2) \rangle$ and $L = 5$ in the tilted geometry. $\langle \{m\}^z \rangle = 0$ in **a**, **b** and **d**. Error bars denote one standard error of the mean (s.e.m.) and are smaller than their marker size if not visible.

[Source data](#)

In our work, we realized a finite-temperature version of the topological Haldane SPT phase using the full spin and density resolution of our Fermi quantum gas microscope. We demonstrated the robustness of the edge states and the hidden order of this SPT phase in both the Heisenberg and the Fermi–Hubbard regime. In the future, studies may extend the two-leg ladder to a varying number of legs, in which one would expect clear differences between even and odd numbers of legs³⁹ and topological effects away from half-filling⁴⁰, or may investigate topological phases in higher dimensions⁴¹. Furthermore, the ladder geometry holds the potential to reveal hole–hole pairing⁴² at temperatures more favourable than in a full two-dimensional system.

Methods

Experimental sequence

In each experimental run, we prepare a cold atomic cloud of ${}^6\text{Li}$ in a balanced mixture of the lowest two hyperfine states ($F=1/2$, $m_F=\pm 1/2$). For evaporation, we confine the cloud in a single layer of a staggered optical superlattice along the z direction, with spacings $a_s = 3 \mu\text{m}$ and $a_1 = 6 \mu\text{m}$ and depths $\langle \{V\}_{\{s\}} = 45 \langle E \rangle_{\{\rm{R}\}} \rangle^{\langle \{\rm{r}\{s\}\} \rangle}$ and $\langle \{V\}_{\{l\}} = 110 \langle E \rangle_{\{\rm{R}\}} \rangle^{\langle \{\rm{r}\{l\}\} \rangle}$, where E_R denotes the recoil energy of the respective lattice. The atoms are harmonically confined in the xy plane and the evaporation is performed by ramping up a magnetic gradient along the y direction²⁰. The final atom number is tuned via the evaporation parameters.

The cloud is then loaded into an optical lattice in the xy plane with spacings $a_x = 1.18 \mu\text{m}$ and $a_y = 1.15 \mu\text{m}$, which is ramped up within 100 ms to its final value, ranging from $5E_R$ to $15E_R$ depending on the chosen Hubbard parameters. The scattering length is tuned from $230 a_B$ during evaporation, with a_B being the Bohr radius, to its final value ranging between $241 a_B$ and $1,200 a_B$ using the broad Feshbach resonance of ${}^6\text{Li}$. An overview of the parameters of each dataset is given in Extended Data Table 1.

Simultaneously with the lattice loading, a repulsive potential is ramped up, which compensates for the harmonic confinement generated by the curvature of the Gaussian lattice beams and divides the resulting flat area into four disconnected ladder systems along the y direction (see ‘Potential shaping’). We achieve temperatures of $\langle k \rangle \langle \rm{rm} \{B\} \rangle T \approx 0.9(3) J_{\parallel}$ for the parameters in Fig. 2.

For detection, the configuration is frozen by ramping the xy lattices to $(43, \{E\}_{\{\rm{rm}\{R\}\}}^{xy})$ within 250 μs . A Stern–Gerlach sequence separates the two spin species into two neighbouring planes of the vertical superlattice, which are then separated to a distance of $21 \mu\text{m}$ using the charge pumping technique described in ref. 20. Finally, simultaneous fluorescence images of the two planes are taken using Raman sideband cooling in our dedicated pinning lattice⁴³, with an imaging time of 2.5 s. The fluorescence of both planes is collected through the same high-resolution objective. The light is then split into two paths using a polarizing beam splitter. One of the beams passes through a variable 1:1 telescope before both paths are recombined on a second polarizing beam splitter with a small spatial offset. This enables us to image both planes in a single exposure, with each plane in focus on a separate fixed position of our camera. We calibrated the relative position on the camera of the two imaged planes using 300 shots of a spin-split Mott insulator and the matching algorithm described in the supplement of ref. 20. The overall detection fidelity per atom was 96(1)%.

Potential shaping

The ladder systems are created by superimposing the optical lattice with a repulsive potential, which is shaped by projecting incoherent light at 650 nm

(generated from a SLED by Exalos EXS210030-03) from a digital micromirror device (DMD) through the high-resolution objective. Four ladders are created by blocking lattice sites with a potential $V = 3.5(5)U$ around each ladder. The area outside the walled ladders is lifted above the inner ladder potential, but remains below the interaction energy U . It thus serves as a reservoir for surplus atoms, which occupy this region once the lowest Hubbard band of the ladders is filled. The flatness of the potential is adjusted for each parameter setting, as the intensity of the lattice beams directly influence the curvature of the potential. This is accomplished by realizing a system with about 20% doping and returning the average density of 100–150 experimental runs as feedback to the DMD pattern. We repeat the feedback until we reach a sufficiently flat density profile with a variance $<1 \times 10^{-3}$ over the $8L$ ladder sites. To adjust for drifts in the lattice phase, we continuously track the lattice phase of each experimental run and feedback to the potential position accordingly. In Extended Data Fig. 1, the average density and occupation histograms of all four ladders and the reservoir area are shown for the dataset of $L = 7$.

Data selection

In each experimental run, four ladder systems are realized. To fulfil the criteria of the Heisenberg regime, we then select on ladder instances with atom number $N = 2L$ and restrict the total magnetization to $\langle |M|^z \rangle = 0$, $\langle |M|^z | = 1 \rangle$, or $\langle |M|^z | \leq 1 \rangle$, depending on the observable, and specify the magnetization sector whenever data points are presented. $\langle |M|^z | \leq 1 \rangle$ for 87.5% of all data. Additionally, for all measurements in the Heisenberg regime, we remove ladders with more than two doublons, as those indicate a mismatch of the DMD pattern relative to the lattice phase. To give a specific example, we here give the precise numbers for the data presented in Fig. 2. This dataset consists of 7,032 realizations with four ladders each. Out of those 28,128 ladders, 6,721 have an atom number of 14. In addition, 2,636 ladders then have a total magnetization $\langle |m|^z \rangle = 0$ and 3,094 have a magnetization of $\langle |M|^z \rangle = \pm 1$. Finally 77 of those 2,636 ladders have more than two doublon–hole pairs, which we exclude as these are most likely to be caused by drifts of the potential pattern given by the DMD. This leaves a total of 2,559 ladders out of the initial 28,128 for calculation of the string correlator.

For calculating the string correlators $\langle \{g\}_{\{\{S\}^z,\{R\}^z\}} \rangle$ and $\langle \{g\}_{\{\{\mathbb{1}\},\{R\}^z\}} \rangle$ at fixed d , we exclude realizations with an odd atom number in the bulk area (grey area in the cartoon of Fig. 2b), as those would lead to imaginary contributions to the correlators, and we also exclude odd atom numbers at the edge areas (green in the cartoon of Fig. 2b). These cases are mostly due to the finite $\langle U/\{t\}_{\{\parallel\}} \rangle$, which still allows for some particle fluctuations. We keep other particle–hole fluctuations, such as those occurring within the string. These do not alter the observed string correlation relative to the Heisenberg model.

Nearest-neighbour spin correlations

The two-leg ladder systems show strong antiferromagnetic spin correlations in which the dominant orientation depends on the ratio of couplings $\langle J_{\perp}/J_{\parallel} \rangle$ and the strength is measured by $\langle C_x \rangle$ ($d=4$) $= 4 \langle \hat{S}_i \hat{S}_{i+d} \rangle$ and $\langle C_y \rangle = 4 \left\langle \hat{S}_i \hat{S}_{i+1} \right\rangle$. For a leg coupling $\langle J_{\parallel} \rangle$ much higher than the rung coupling $\langle J_{\perp} \rangle$, the nearest-neighbour spin correlator C_y along the rung almost vanishes, whereas correlations reach $C_x(1) = -0.500(6)$ along the leg direction. For a dominating rung coupling $\langle J_{\perp} \rangle$, C_y reaches $-0.58(1)$, indicating singlet formation between the two sites of a rung. Extended Data Fig. 2a shows the measured spin correlations along both rung and leg for different values of $\langle J_{\perp}/J_{\parallel} \rangle$. The values match the finite-temperature Heisenberg model for an entropy of $S/N = (0.3–0.4) k_B$ per particle obtained from ED.

Theory simulation

In this work, we have used two different numerical methods to obtain theoretical predictions for the experimentally measured observables. The results in the Heisenberg regime were obtained using ED of our spin-1/2 ladders up to sizes of $L = 9$ (limited by computational resources). For each data point, the system size and geometry in the ED simulation are the same as in the experimental data. The finite-temperature results were obtained by

using the full spectrum. We specify the entropy per particle $s = S/N$, which we find to be approximately independent of coupling parameters in the experimental realizations. The results in the Hubbard regime are calculated using the DMRG ansatz⁴⁴ based on the TeNPy library (v.0.3.0)⁴⁵. For all calculations, we conserved the total particle number and the total magnetization. For the phase diagram in Fig. 4d we used the iDMRG technique to obtain the ground state and the values of the string order parameters in the thermodynamic limit. For this, we evaluated the ground state for each parameter and used a maximal MPS bond dimension $\chi = 1,200$. The bond dimension is increased in steps $\Delta\chi = 40$ and the simulation stopped when the difference in the ground state energy per unit cell $E(\chi + \Delta\chi) - E(\chi) < 10^{-7}$. This worked for most parameters except in the vicinity of two decoupled Hubbard chains and at small values of $|U/t|$. Nevertheless, in this regime we find that the energy per unit cell is converged up to $E(1,200) - E(1,160) < 10^{-4}$. For the experimentally accessible regime all calculations fulfil the former bound. To obtain the infinite length value of the string order parameters, we calculated it for different lengths $d \in [200, 400, \dots, 1600]$ to make sure that its final value is converged.

Data availability

The datasets generated and analysed during the current study are available from the corresponding author on reasonable request. [Source data](#) are provided with this paper.

Code availability

The code used for the analysis are available from the corresponding author on reasonable request.

References

1. Haldane, F. D. M. Nonlinear field theory of large-spin Heisenberg antiferromagnets: semiclassically quantized solitons of the one-

- dimensional easy-axis Néel state. *Phys. Rev. Lett.* **50**, 1153–1156 (1983).
2. Haldane, F. D. M. Topological quantum matter. *Int. Journ. Mod. Phys. B* **32**, 1830004 (2018).
 3. den Nijs, M. & Rommelse, K. Preroughening transistions in crystal surfaces and valence-bond phases in quantum spin chains. *Phys. Rev. B* **40**, 4709–4734 (1989).
 4. Kennedy, T. & Tasaki, H. Hidden $Z_2 \times Z_2$ symmetry breaking in Haldane-gap antiferromagnets. *Phys. Rev. B* **45**, 304–307 (1992).
 5. Schuch, N., Pérez-García, D. & Cirac, I. Classifying quantum phases using matrix product states and projected entangled pair states. *Phys. Rev. B* **84**, 165139 (2011).
 6. Pollmann, F., Turner, A. M., Berg, E. & Oshikawa, M. Entanglement spectrum of a topological phase in one dimension. *Phys. Rev. B* **81**, 064439 (2010).
 7. Chen, X., Gu, Z.-C. & Wen, X.-G. Classification of gapped symmetric phases in one-dimensional spin systems. *Phys. Rev. B* **83**, 035107 (2011).
 8. Wen, X.-G. Colloquium: zoo of quantum-topological phases of matter. *Rev. Mod. Phys.* **89**, 041004 (2017).
 9. Senthil, T. Symmetry-protected topological phases of quantum matter. *Annu. Rev. Condens. Matter Phys.* **6**, 299324 (2015).
 10. Renard, J. P. et al. Presumption for a quantum energy gap in the quasi-one-dimensional $S=1$ Heisenberg antiferromagnet $\text{Ni}(\text{C}_2\text{H}_8\text{N}_2)_2\text{NO}_2(\text{ClO}_4)$. *Europhys. Lett.* **3**, 945–952 (1987).
 11. Buyers, W. J. L. et al. Experimental evidence for the Haldane gap in a spin-1 nearly isotropic, antiferromagnetic chain. *Phys. Rev. Lett.* **56**, 371–374 (1986).

12. Hagiwara, M., Katsumata, K., Affleck, I., Halperin, B. I. & Renard, J. P. Observation of $S=1/2$ degrees of freedom in an $S=1$ linear-chain Heisenberg antiferromagnet. *Phys. Rev. Lett.* **65**, 3181–3184 (1990).
13. Glarum, S. H., Geschwind, S., Lee, K. M., Kaplan, M. L. & Michel, J. Observation of fractional spin $S=1/2$ on open ends of $S=1$ linear antiferromagnetic chains: nonmagnetic doping. *Phys. Rev. Lett.* **67**, 1614–1617 (1991).
14. Bakr, W. S., Gillen, J. I., Peng, A., Fölling, S. & Greiner, M. A quantum gas microscope for detecting single atoms in a Hubbard-regime optical lattice. *Nature* **462**, 74–77 (2009).
15. Sherson, J. F. et al. Single-atom-resolved fluorescence imaging of an atomic Mott insulator. *Nature* **467**, 68–72 (2010).
16. Haller, E. et al. Single-atom imaging of fermions in a quantum-gas microscope. *Nat. Phys.* **11**, 738–742 (2015).
17. Cheuk, L. W. et al. Quantum-gas microscope for fermionic atoms. *Phys. Rev. Lett.* **114**, 193001 (2015).
18. Parsons, M. F. et al. Site-resolved imaging of fermionic ${}^6\text{Li}$ in an optical lattice. *Phys. Rev. Lett.* **114**, 213002 (2015).
19. Boll, M. et al. Spin- and density-resolved microscopy of antiferromagnetic correlations in Fermi–Hubbard chains. *Science* **353**, 1257–1260 (2016).
20. Koepsell, J. et al. Robust bilayer charge pumping for spin- and density-resolved quantum gas microscopy. *Phys. Rev. Lett.* **125**, 010403 (2020).
21. Endres, M. et al. Observation of correlated particle–hole pairs and string order in low-dimensional Mott insulators. *Science* **334**, 200–203 (2011).
22. Hilker, T. A. et al. Revealing hidden antiferromagnetic correlations in doped Hubbard chains via string correlators. *Science* **357**, 484–487 (2017).

23. de Léséleuc, S. et al. Observation of a symmetry-protected topological phase of interacting bosons with Rydberg atoms. *Science* **365**, 775–780 (2019).
24. Affleck, S., Kennedy, E., Lieb, E. H. & Tasaki, H. Rigorous results on valence-bond ground states in antiferromagnets. *Phys. Rev. Lett.* **59**, 799–802 (1987).
25. Hida, K. Crossover between the Haldane-gap phase and the dimer phase in the spin-1/2 alternating Heisenberg chain. *Phys. Rev. B* **45**, 2207–2212 (1992).
26. White, S. R. Equivalence of the antiferromagnetic Heisenberg ladder to a single $S=1$ chain. *Phys. Rev. B* **53**, 52–55 (1996).
27. Mazurenko, A. et al. A cold-atom Fermi–Hubbard antiferromagnet. *Nature* **545**, 462–466 (2017).
28. Auerbach, A. *Interacting Electrons and Quantum Magnetism* (Springer Science & Business Media, 1994).
29. Kim, E. H., Fáth, G., Sólyom, J. & Scalapino, D. J. Phase transitions between topologically distinct gapped phases in isotropic spin ladders. *Phys. Rev. B* **62**, 14965–14974 (2000).
30. Bonesteel, N. E. Valence bonds and the Lieb–Schultz–Mattis theorem. *Phys. Rev. B* **40**, 8954–8960 (1989).
31. Pollmann, F. & Turner, A. M. Detection of symmetry-protected topological phases in one dimension. *Phys. Rev. B* **86**, 125441 (2012).
32. Ogata, M. & Shiba, H. Bethe-ansatz wave function, momentum distribution, and spin correlation in the one-dimensional strongly correlated Hubbard model. *Phys. Rev. B* **41**, 2326–2338 (1990).
33. Miyashita, S. Effects of edges in $S=1$ Heisenberg antiferromagnetic chains. *Phys. Rev. B* **48**, 913–919 (1993).

34. Anfuso, F. & Rosch, A. Fragility of string orders. *Phys. Rev. B* **76**, 085124 (2007).
35. Moudgalya, S. & Pollmann, F. Fragility of symmetry-protected topological order on a Hubbard ladder. *Phys. Rev. B* **91**, 155128 (2015).
36. Verresen, R., Bibo, J. & Pollmann, F. Quotient symmetry protected topological phenomena. Preprint at <https://arxiv.org/abs/2102.08967> (2021).
37. Su, W. P., Schrieffer, J. R. & Heeger, A. J. Solitons in polyacetylene. *Phys. Rev. Lett.* **42**, 1698–1701 (1979).
38. Verresen, R., Moessner, R. & Pollmann, F. One-dimensional symmetry protected topological phases and their transitions. *Phys. Rev. B* **96**, 165124 (2017).
39. Schulz, H. J. Phase diagrams and correlation exponents for quantum spin chains of arbitrary spin quantum number. *Phys. Rev. B* **34**, 6372–6385 (1986).
40. Nourse, H. L., McCulloch, I. P., Janani, C. & Powell, B. J. Haldane insulator protected by reflection symmetry in the doped Hubbard model on the three-legged ladder. *Phys. Rev. B* **94**, 214418 (2016).
41. Szasz, A., Motruk, J., Zaletel, M. P. & Moore, J. E. Chiral spin liquid phase of the triangular lattice Hubbard model: a density matrix renormalization group study. *Phys. Rev. X* **10**, 21042 (2020).
42. Noack, R. M., White, S. R. & Scalapino, D. J. The doped two-chain Hubbard model. *Europhys. Lett.* **30**, 163–168 (1995).
43. Omran, A. et al. Microscopic observation of Pauli blocking in degenerate fermionic lattice gases. *Phys. Rev. Lett.* **115**, 263001 (2015).
44. White, S. R. Density matrix formulation for quantum renormalization groups. *Phys. Rev. Lett.* **69**, 2863–2866 (1992).

45. Hauschild, J. & Pollmann, F. Efficient numerical simulations with tensor networks: Tensor Network Python (TeNPy). *SciPost Phys. Lect. Notes* **5**, 005 (2018).

Acknowledgements

This work was supported by the Max Planck Society (MPG), the European Union (FET-Flag 817482, PASQUANS), the Max Planck Harvard Research Center for Quantum Optics (MPHQ), the Cluster of Excellence ‘CUI: Advanced Imaging of Matter’ of the Deutsche Forschungsgemeinschaft (DFG) – EXC 2056 – project ID 390715994 and under Germany’s Excellence Strategy – EXC-2111-390814868. J.K. acknowledges funding from Hector Fellow Academy and T.C. from the Alexander v. Humboldt foundation. R.V. is supported by the Harvard Quantum Initiative Postdoctoral Fellowship in Science and Engineering and by the Simons Collaboration on Ultra-Quantum Matter (Simons Foundation, 651440, Ashvin Vishwanath). F.P. acknowledges the support of the European Research Council (ERC) under the European Union’s Horizon 2020 research and innovation program (grant agreement no. 771537). P.S. acknowledges support from the NSRF via the Program Management Unit for Human Resources & Institutional Development, Research and Innovation (grant number B05F640051).

Funding

Open access funding provided by Max Planck Society.

Author information

Author notes

1. These authors contributed equally: Pimonpan Sompet, Sarah Hirthe, Dominik Bourgund

Authors and Affiliations

1. Max-Planck-Institut für Quantenoptik, Garching, Germany

Pimonpan Sompet, Sarah Hirthe, Dominik Bourgund, Thomas Chalopin, Joannis Koepsell, Petar Bojović, Guillaume Salomon, Christian Gross, Timon A. Hilker & Immanuel Bloch

2. Munich Center for Quantum Science and Technology, Munich, Germany

Pimonpan Sompet, Sarah Hirthe, Dominik Bourgund, Thomas Chalopin, Julian Bibo, Joannis Koepsell, Petar Bojović, Frank Pollmann, Guillaume Salomon, Christian Gross, Timon A. Hilker & Immanuel Bloch

3. Department of Physics and Materials Science, Chiang Mai University, Chiang Mai, Thailand

Pimonpan Sompet

4. Department of Physics, Technical University of Munich, Garching, Germany

Julian Bibo & Frank Pollmann

5. Department of Physics, Harvard University, Cambridge, MA, USA

Ruben Verresen

6. Institut für Laserphysik, Universität Hamburg, Hamburg, Germany

Guillaume Salomon

7. The Hamburg Centre for Ultrafast Imaging, Universität Hamburg, Hamburg, Germany

Guillaume Salomon

8. Physikalisches Institut, Eberhard Karls Universität Tübingen, Tübingen, Germany

Christian Gross

9. Fakultät für Physik, Ludwig-Maximilians-Universität, München,
Germany

Immanuel Bloch

Contributions

P.S., S.H. and D.B. planned the experiment and analysed the data. P.S., S.H., D.B., T.C. and P.B. collected the data. T.C. carried out the ED calculations. J.K. and G.S. contributed to the upgrade of the experimental apparatus. J.B., R.V. and F.P. performed the DMRG simulations and analytical calculations. T.A.H., C.G. and I.B. supervised the study. All authors contributed extensively to interpretation of the data and production of the manuscript.

Corresponding authors

Correspondence to [Pimonpan Sompet](#) or [Immanuel Bloch](#).

Ethics declarations

Competing interests

The authors declare no competing interests.

Peer review

Peer review information

Nature thanks the anonymous reviewers for their contribution to the peer review of this work.

Additional information

Publisher's note Springer Nature remains neutral with regard to jurisdictional claims in published maps and institutional affiliations.

Extended data figures and tables

Extended Data Fig. 1 Density engineering.

a, Repulsive light shaped with a DMD splits the system into four independent ladders in the centre surrounded by a low-density bath. The density of the ladders is $n = 0.992$ with a standard deviation of 0.03. **b**, The occupation histograms show the normalized occurrence of total atom numbers in each ladder and the normalized occurrence in the surrounding bath for $L = 7$. Almost 25% of the ladder realizations have $N = 2L$.

Extended Data Fig. 2 Nearest-neighbour spin correlations.

The nearest-neighbour spin correlation $C(1)$ for different $\langle J_{\perp} \rangle / \langle J_{\parallel} \rangle$ in the $L = 5$ system. The brown (purple) points refer to the correlations along the rung (leg). The shaded areas correspond to the correlations in the Heisenberg model with an entropy of $S/N = (0.3–0.4) k_B$ per particle. Both theoretical and experimental values are obtained from the magnetization sector $\langle m_z \rangle = 0$.

Extended Data Table 1 Experimental parameters

Supplementary information

Supplementary Information

Supplementary text, figures, equations and references.

Source data

Source Data Fig. 2

Source Data Fig. 3

Source Data Fig. 4

Rights and permissions

Open Access This article is licensed under a Creative Commons Attribution 4.0 International License, which permits use, sharing, adaptation, distribution and reproduction in any medium or format, as long as you give appropriate credit to the original author(s) and the source, provide a link to the Creative Commons license, and indicate if changes were made. The images or other third party material in this article are included in the article's Creative Commons license, unless indicated otherwise in a credit line to the material. If material is not included in the article's Creative Commons license and your intended use is not permitted by statutory regulation or exceeds the permitted use, you will need to obtain permission directly from the copyright holder. To view a copy of this license, visit <http://creativecommons.org/licenses/by/4.0/>.

Reprints and Permissions

About this article

Cite this article

Sompet, P., Hirthe, S., Bourgund, D. *et al.* Realizing the symmetry-protected Haldane phase in Fermi–Hubbard ladders. *Nature* **606**, 484–488 (2022). <https://doi.org/10.1038/s41586-022-04688-z>

- Received: 18 March 2021
- Accepted: 24 March 2022
- Published: 01 June 2022
- Issue Date: 16 June 2022

- DOI: <https://doi.org/10.1038/s41586-022-04688-z>

Share this article

Anyone you share the following link with will be able to read this content:

[Get shareable link](#)

Sorry, a shareable link is not currently available for this article.

[Copy to clipboard](#)

Provided by the Springer Nature SharedIt content-sharing initiative

This article was downloaded by **calibre** from <https://www.nature.com/articles/s41586-022-04688-z>

| [Section menu](#) | [Main menu](#) |

- Article
- Open Access
- [Published: 08 June 2022](#)

Graph pangenome captures missing heritability and empowers tomato breeding

- [Yao Zhou](#),
- [Zhiyang Zhang](#),
- [Zhigui Bao](#),
- [Hongbo Li](#),
- [Yaqing Lyu](#),
- [Yanjun Zan](#),
- [Yaoyao Wu](#),
- [Lin Cheng](#),
- [Yuhan Fang](#),
- [Kun Wu](#),
- [Jinzhe Zhang](#),
- [Hongjun Lyu](#),
- [Tao Lin](#),
- [Qiang Gao](#),
- [Surya Saha](#),
- [Lukas Mueller](#),
- [Zhangjun Fei](#),
- [Thomas Städler](#),
- [Shizhong Xu](#),
- [Zhiwu Zhang](#),
- [Doug Speed &](#)
- [Sanwen Huang](#)

Nature volume **606**, pages 527–534 (2022)

- 12k Accesses
- 149 Altmetric
- [Metrics details](#)

Abstract

Missing heritability in genome-wide association studies defines a major problem in genetic analyses of complex biological traits^{1,2}. The solution to this problem is to identify all causal genetic variants and to measure their individual contributions^{3,4}. Here we report a graph pangenome of tomato constructed by precisely cataloguing more than 19 million variants from 838 genomes, including 32 new reference-level genome assemblies. This graph pangenome was used for genome-wide association study analyses and heritability estimation of 20,323 gene-expression and metabolite traits. The average estimated trait heritability is 0.41 compared with 0.33 when using the single linear reference genome. This 24% increase in estimated heritability is largely due to resolving incomplete linkage disequilibrium through the inclusion of additional causal structural variants identified using the graph pangenome. Moreover, by resolving allelic and locus heterogeneity, structural variants improve the power to identify genetic factors underlying agronomically important traits leading to, for example, the identification of two new genes potentially contributing to soluble solid content. The newly identified structural variants will facilitate genetic improvement of tomato through both marker-assisted selection and genomic selection. Our study advances the understanding of the heritability of complex traits and demonstrates the power of the graph pangenome in crop breeding.

Main

Missing heritability—the discrepancy between heritability estimates from family-based genetic studies and the variance explained by all of the significant variants in genome-wide association studies (GWAS)^{1,2}—compromises the use of rapidly developing genomics for understanding

biological questions and crop breeding^{5,6,7}. The resolution of missing heritability is hindered by several factors, including incomplete detection of causal genomic variants, particularly structural variants (SVs), which leads to estimation bias caused by incomplete linkage disequilibrium (LD) between genetic markers and causal variants, as well as genetic heterogeneity of causal variants, which reduces the statistical power of GWAS^{8,9,10}. To overcome these bottlenecks, an exhaustive and precise catalogue of genetic variants is required.

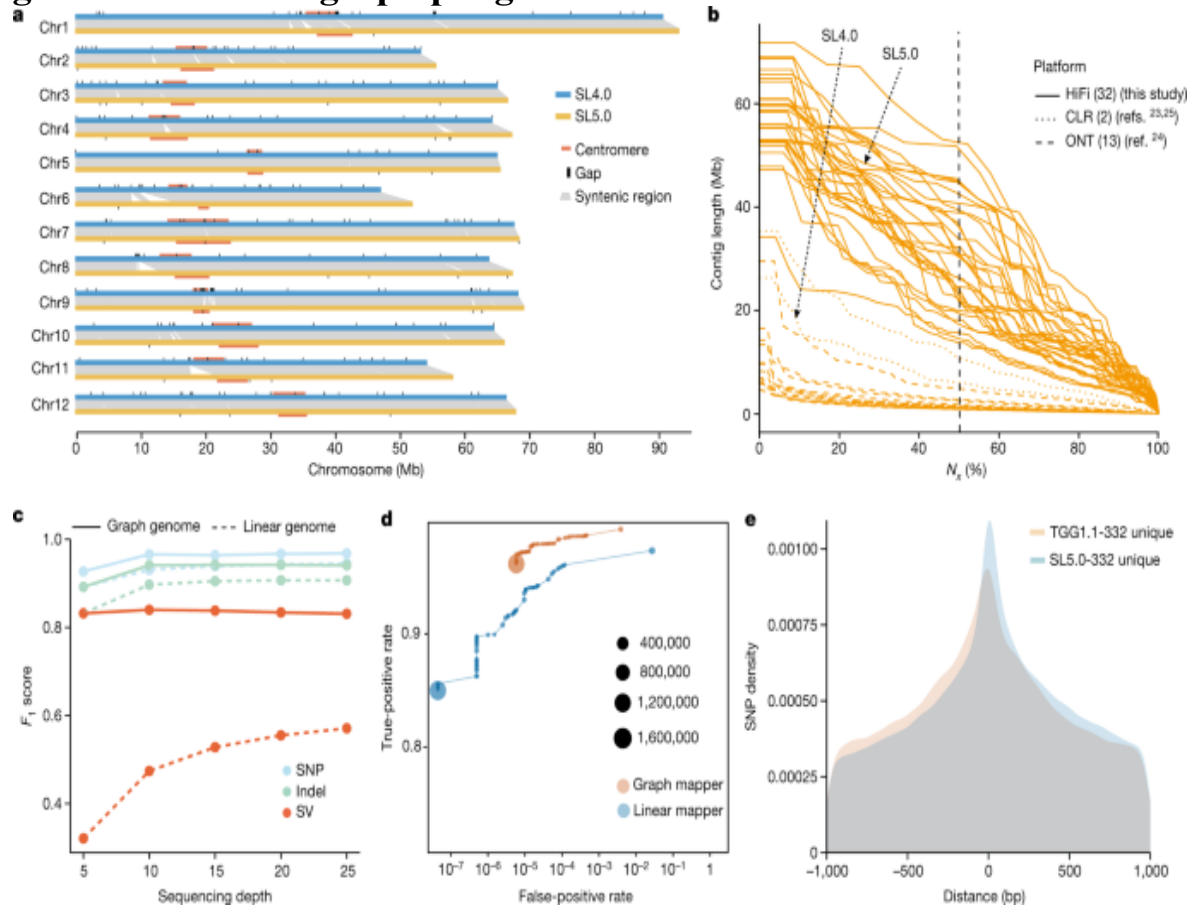
A variation map constructed by mapping sequencing reads to a single linear reference genome generates reference bias, that is, the inability to precisely map non-reference alleles^{11,12}. A pangenome comprising multiple reference genomes may more fully represent species-wide genetic diversity and, as such, retains non-reference information^{13,14,15}. However, it is challenging to incorporate coordinates of non-reference sequences into existing analysis pipelines¹⁶. Recently, graph-based structures have been used to integrate all genetic variants into a single genome graph, enabling thorough and accurate identification of genomic variants as well as data integration^{11,17,18,19}. Recent studies have demonstrated the superiority of using graph pangenomes as references in identification of SVs with short reads^{19,20,21,22}. Here we report the construction of a variant-based graph pangenome of tomato (*Solanum lycopersicum*), an important fruit crop and a model system for plant biology and breeding. We demonstrate its use in capturing missing heritability in GWAS, providing insights into a classical genetics problem and facilitating genomic breeding (Extended Data Fig. 1).

Construction of the graph pangenome

A high-accuracy and gapless linear reference genome is as critical as the backbone of a graph pangenome. To this end, we assembled a state-of-the-art backbone genome (tomato cv. Heinz 1706, Build SL5.0) using high-fidelity (HiFi) long reads and high-throughput chromosome conformation capture (Hi-C) long-range scaffolding (Extended Data Fig. 2a). The contig N_{50} size of SL5.0 is 41.7 Mb, an increase of approximately sevenfold compared with the previous build SL4.0 (ref. 23). Moreover, SL5.0 contains 19.3 Mb more sequences than SL4.0 (801.8 Mb versus 782.5 Mb), with 43

contigs (99.8% of the assembly) ordered and oriented on the 12 chromosomes (Fig. 1a and Extended Data Fig. 2b). Only 31 gaps remain in the SL5.0 pseudochromosomes, substantially fewer than in SL4.0 (259 gaps). Gaps remain mostly in highly complex regions, including subtelomeres, centromeres and rDNA repeats. Both bacterial artificial chromosome clone sequences and *k*-mer analysis support the superior quality of SL5.0 (Supplementary Table 1). We performed the annotation of SL5.0 (ITAG5.0), predicting 36,648 protein-coding genes.

Fig. 1: Genome and graph pangenome of tomato.



a, Synteny between tomato reference genome build SL4.0 (blue) and SL5.0 (yellow). The grey lines represent synteny blocks. The positions of gaps are marked with black rectangles on the chromosomes, and centromeres are represented by orange rectangles along the chromosomes. **b**, Contig N_x size of all genome assemblies. SL4.0 and SL5.0 are marked with arrows. Line types represent different sequencing platforms. CLR, PacBio continuous long reads; HiFi, high-fidelity long reads; ONT, Oxford Nanopore long

reads. The numbers in parentheses refer to the numbers of assemblies. **c**, F_1 scores (harmonic means of precision and recall) using simulated sequencing data from the genetic variants of 31 accessions with HiFi reads with different depths and genetic variants from the graph pangenome and the linear genome. **d**, Assessing false-positive (x -axis) and true-positive (y -axis) rates for the graph (Giraffe) and linear (BWA-MEM) mappers using 2,000,000 simulated reads. The size of each point represents the number of reads with mapping quality equal to 60. **e**, Density map of unique SNPs from SL5.0-332 and TGG1.1-332 located within 1 kb upstream or downstream of the SV breakpoints.

Source data

We generated reference-level genome assemblies for another 31 accessions that represent the diversity of the red-fruited clade of tomatoes, including 15 big-fruited tomato *S. lycopersicum* (BIG) accessions, eight cherry tomato (*S. lycopersicum* var. *cerasiforme*, CER) accessions and eight accessions from *S. pimpinellifolium* (PIM, considered to be the progenitor of cultivated tomatoes) (Supplementary Table 2 and Supplementary Fig. 1). The contig N_{50} sizes of these 31 assemblies range from 13.7 Mb to 52.2 Mb, with an average of 28.6 Mb, larger than any of the previously published tomato pangenome assemblies MAS2.0 (ref. 24) (Fig. 1b and Supplementary Table 3). We annotated repeats and predicted protein-coding genes for 45 assemblies: 31 from this study, 13 from MAS2.0 (eight BIG, three CER and two PIM accessions)²⁴ and 1 PIM accession from another study²⁵. The content of repetitive sequences ranges from 60.7% to 64.0%, with an average of 62.1% (Supplementary Table 4). The number of predicted protein-coding genes ranges from 33,863 to 37,237, with an average of 35,298 (Supplementary Table 5). The completeness of these assemblies was assessed by BUSCO analysis, which shows an average of 96.2% single-copy Solanales genes completely assembled (Extended Data Fig. 2c). Taken together, these high-quality genome assemblies represent a robust resource to facilitate variant detection and genomic comparison for constructing a tomato graph pangenome.

With SL5.0 serving as the backbone, single-nucleotide polymorphisms (SNPs) and small insertions and deletions (indels, 1–50 bp) identified from

the 31 accessions with HiFi reads, as well as SVs (>50 bp) from all 131 accessions with long reads (a total of 100 accessions from a previous study²⁴ and 31 accessions from this study), were integrated into a variation graph. Complex SVs were not specifically considered when constructing the graph pangenome ([Supplementary Note 4](#)). The resulting tomato graph pangenome (TGG1.0) spans 1,007,562,373 bp, including approximately 206 Mb absent from SL5.0. We mapped all predicted protein-coding genes to a graph generated from all assemblies, resulting in a tomato graph annotation (TGA1.0) with 51,155 genes, of which 14,507 are from the non-reference genomes. Previous resequencing projects accumulated 7.8 Tb of Illumina short-read data for 706 tomato accessions with a sequencing depth of greater than sixfold^{26,27,28,29,30,31}. By mapping these short reads to TGG1.0, we identified additional SNPs and indels that were not present in TGG1.0. After merging these variants with those from TGG1.0, we obtained a dataset comprising 17,898,731 SNPs, 1,499,161 indels and 195,957 SVs. Integration of this updated genetic variant dataset and the SL5.0 backbone genome resulted in the generation of a new variation graph, which we designate TGG1.1.

Simulation studies indicate that the graph pangenome outperforms the linear genome at calling all types of genetic variants (SNPs, indels and SVs) ([Supplementary Table 6](#)), consistent with a recent study on a human variation graph^{12,19}. We compared the performance metrics for SNPs, indels and SVs derived from the graph pangenome and the linear genome. From the raw output of genotypes, we obtained F_1 scores (harmonic mean of precision and recall) of 0.966 for SNPs, 0.941 for indels and 0.840 for SVs in the graph pangenome using 10× sequencing data, significantly better than those in the linear genome (0.931, 0.897 and 0.474; Wilcoxon rank sum test, $P = 6.30 \times 10^{-13}$, $P = 5.04 \times 10^{-14}$ and $P = 1.69 \times 10^{-17}$, respectively) (Fig. [1c](#)). Given that the same variant caller DeepVariant³² was used for both datasets, higher precision and recall rate is probably driven by the higher accuracy of mapping short reads using the graph mapper (Fig. [1d](#)).

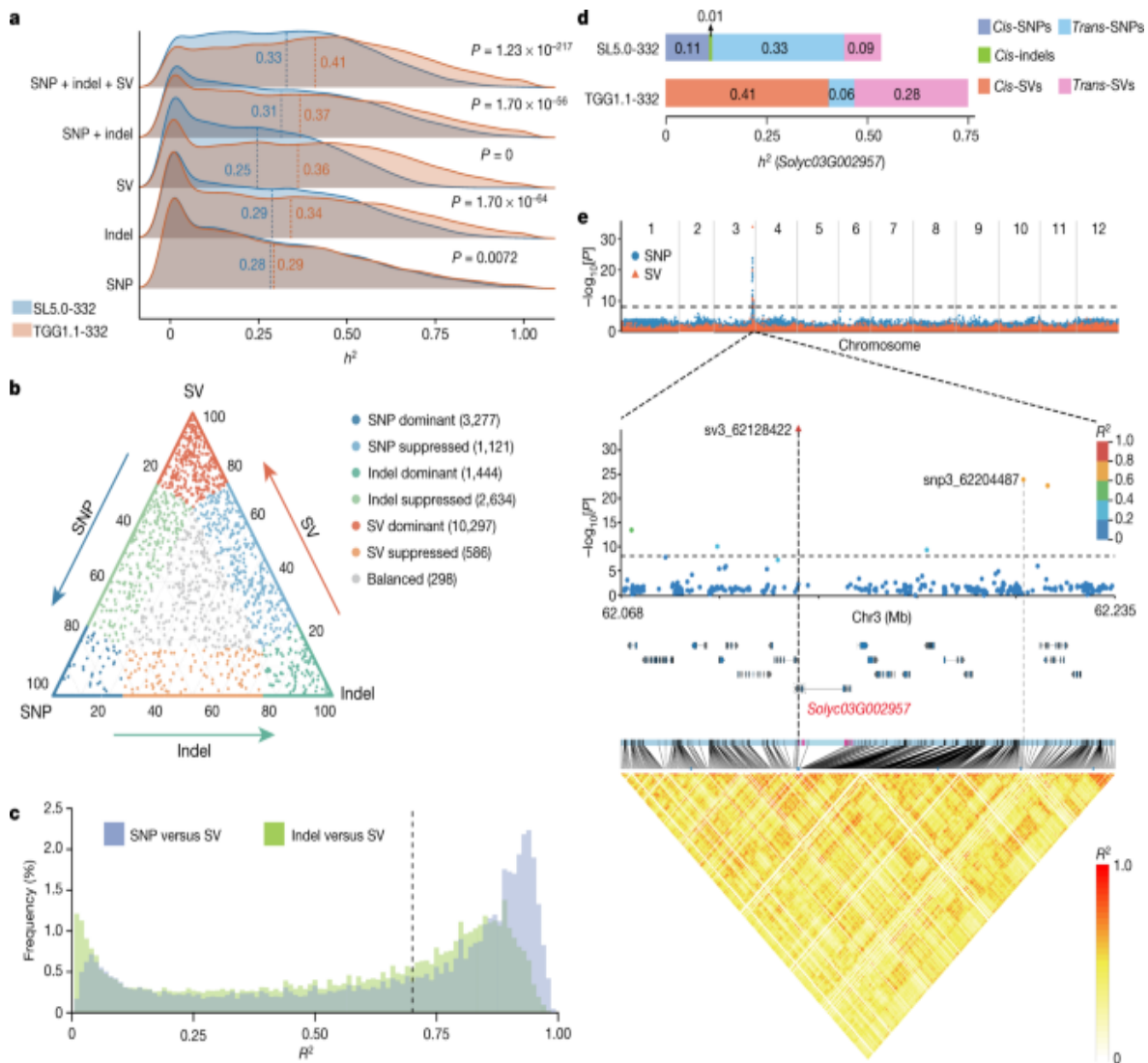
Next, we genotyped genetic variants of 332 tomato accessions by mapping their Illumina sequences onto TGG1.1, resulting in a callset designated TGG1.1-332 that comprises 6,971,059 SNPs, 657,549 indels and 54,838 SVs. We also mapped these sequences against the linear genome SL5.0 and

identified variants in a callset designated SL5.0-332 comprising 7,317,844 SNPs, 447,098 indels and 11,397 SVs. We found that SNPs that were uniquely identified by the linear reference were physically closer to their neighbouring SVs than SNPs uniquely identified by the graph pangenome (Fig. 1e), consistent with lower levels of incorrect read mapping around SVs in the latter dataset (Extended Data Fig. 3). Furthermore, TGG1.1 contains 7,197 out of the 7,720 SNPs (93.2%) that were verified in a DNA chip³³, whereas only 6,812 (88.2%) were detected using SL5.0 as the reference. Notably, the linear genome yields only 20% of the SVs called by the graph pangenome, indicating the high efficiency in detecting SVs using the graph pangenome. In summary, TGG1.1 represents one of the most comprehensive and accurate maps of tomato genome variation to date.

Capturing missing heritability

To test the power of the graph pangenome in capturing missing heritability, we used LDAK³⁴ to estimate the variant heritability of 20,323 molecular traits, comprising 19,353 expression traits and 970 metabolite traits, from fruits of the 332 tomato accessions³⁵. First, we analysed each category of genetic variants individually (that is, only SNPs, only indels or only SVs). The average heritability estimated using the graph pangenome is higher than that using the linear reference genome for all three categories (Fig. 2a and Supplementary Table 7). Higher SNP heritability (0.29 versus 0.28; Wilcoxon rank sum test, $P = 7.24 \times 10^{-3}$; Extended Data Fig. 4b) is suggested despite TGG1.1-332 comprising fewer SNPs than SL5.0-332. The results were similar when this analysis was restricted to 6,375 independent traits (square of Pearson's correlation coefficient (r^2) between the traits, <0.20) (Extended Data Fig. 4a).

Fig. 2: The contribution of genetic variants to heritability.



a, Comparison of heritability (h^2) estimated using different combinations of genetic variants from SL5.0-332 and TGG1.1-332. SNP + indel and SNP + indel + SV refer to composite models containing either two or three categories of variants. Heritability was estimated with a random effect corresponding to each category. P values were calculated using two-sided Wilcoxon rank sum tests. The vertical dashed lines indicate the mean values.

b, The proportion of heritability of traits contributed by SNPs, indels and SVs. Heritability was estimated on the basis of the SNP + indel + SV composite model (a total of 666 traits with estimated $h^2 = 0$ not shown). The numbers in parentheses represent the number of traits per group. **c**, The distribution of LD (R^2) between SVs and SNPs/indels within 50 kb of the SVs. For each SV, the maximum R^2 with adjacent SNPs/indels within 50 kb

on either side is recorded. The dashed line indicates $R^2 = 0.70$. **d**, Heritability of the expression of *Solyc03G002957* contributed by *cis* and *trans* genetic variants from SL5.0-332 and TGG1.1-332. Heritability was estimated by partitioning all genetic variants into six categories (*cis*-SNPs, *cis*-indels, *cis*-SVs, *trans*-SNPs, *trans*-indels and *trans*-SVs). **e**, Manhattan plot of the expression of *Solyc03G002957* (top). The P value of each variant was estimated using an MLM. $n = 332$ accessions. Middle, magnification of the gene region with significant variants is shown and the dot colour represents the magnitude of LD (R^2) with the leading variant sv3_62128422. The circles represent SNPs and the triangles represent SVs. Genes annotated in the magnified region are shown. Bottom, LD heatmap of the magnified region. The horizontal dashed lines represent the Bonferroni threshold ($-\log_{10}[0.05/6,423,741] = 8.11$).

Source data

We next analysed categories of genetic variants jointly. Estimated heritability increases with more categories in the model (Fig. 2a). When jointly analysing all three categories of variants in a composite model, the average heritability is 0.41 in the graph pangenome callset, 24% higher than that in the linear genome callset (0.33; Wilcoxon rank sum test, $P = 1.23 \times 10^{-217}$). We used the composite model to estimate the average heritability explained by SNPs, indels and SVs from TGG1.1-332, finding that SVs contribute the largest proportion of overall heritability (0.27, 65.9%) (Extended Data Fig. 4c). Moreover, SVs contribute the largest share of heritability for approximately half of the molecular traits (10,297 out of 20,323, 50.7%) (Fig. 2b). These data indicate that the capture of missing heritability through the graph pangenome is largely due to the inclusion of more identified SVs.

Incomplete LD between molecular markers and causal variants leads to the underestimation of heritability⁹. SVs in close proximity to genes are probably causal variants as they could lead to dysregulation of gene expression^{24,36}. We observed that a large proportion of SVs are in strong LD ($R^2 > 0.7$) with adjacent (50 kb on either side) SNPs and indels (61.2% and 45.5%, respectively), but only small fractions (3.2% and 0.6%, respectively) are in complete LD ($R^2 = 1$) (Fig. 2c), indicating that incomplete LD

between markers and causal variants is common in our population. Our simulation studies show that inclusion of causal variants captures some missing heritability (Supplementary Fig. 2). This could, at least partially, explain why the average heritability increases from 0.37 to 0.41 when SVs are included in the model compared with models that consider only SNPs and indels (Fig. 2a).

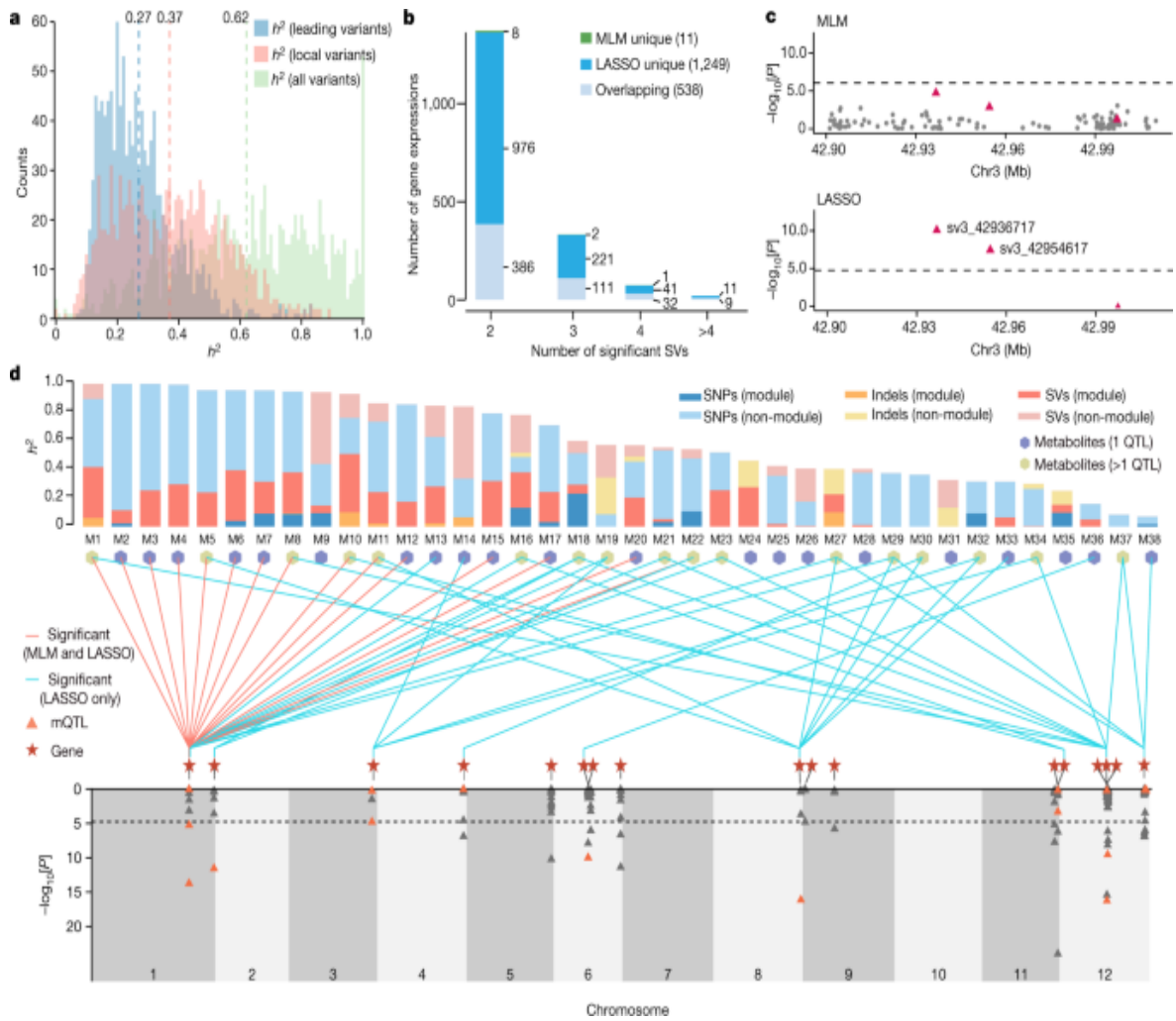
As an example, we studied the case of *Solyc03G002957*, which encodes a protein that interacts with phosphoinositides. To evaluate the effects of *cis*-variants on gene expression, we partitioned genetic variants into six categories, namely *cis*-variants (50 kb on either side of the gene) and *trans*-variants of SNPs, indels and SVs from the linear and graph pangenome callset, respectively. We found that total heritability estimated from SL5.0-332 is 0.54 (s.d. = 0.32). By contrast, total heritability estimated from TGG1.1-332 is 0.75 (s.d. = 0.51), to which *cis*- and *trans*-SVs jointly contribute the largest proportions, 0.41 (s.d. = 0.34) and 0.28 (s.d. = 0.10), respectively (Fig. 2d). This indicates that SVs around this gene, most of which can be identified only using the graph-based approach, are more likely to be causative than other variant types and contribute to the majority of total heritability.

When we performed a single-variant association study, we found that the expression of *Solyc03G002957* is probably affected by a SV, a leading variant residing at a peak on chromosome 3 (sv3_62128422, a 2,628 bp deletion causing a truncation at the end of the transcript) (Fig. 2e and Extended Data Figs. 5 and 6). This SV explains approximately 0.45 (s.d. = 0.63) of heritability and is present only in TGG1.1-322. However, a significant SNP (SNP3_62204487, located about 57.6 kb upstream from the gene) exhibits modest LD with the SV ($R^2 = 0.66$) (Fig. 2e) and explains 0.34 (s.d. = 0.48) of heritability in both SL5.0-332 and TGG1.1-332. However, given the fact that SNP3_62204487 is eight genes away from the target gene, the statistical significance of this SNP could give misleading results. These results suggest that, by addressing incomplete LD through inclusion of possibly causal SVs, the graph pangenome has the potential to capture missing heritability.

A marked discrepancy still exists between the estimated heritability and the heritability explained by GWAS significant loci². One of the important

sources is allelic heterogeneity (that is, multiple underlying genetic variants at the same locus contribute to the same phenotype), a widespread phenomenon in complex traits that tends to impair the power of GWAS^{37,38}. To assess the potential effect of allelic heterogeneity on GWAS in tomato, we analysed the effects of variants in *cis*-regions (within 50 kb on either side of genes) on their corresponding gene expression (19,353 genes). Using a single-locus mixed linear model (MLM)³⁹ on the TGG1.1-332 callset, we detected *cis*-expression quantitative trait loci (eQTLs) for 1,179 genes. Although the average estimated heritability of the expression of these genes is 0.62, the average heritability explained by leading significant variants is only 0.27 (Fig. 3a). Thus, heritability contributed by nearby genetic variants might be ‘invisible’ when considering only leading significant variants within eQTLs. When including all genetic variants in *cis*-regions of eQTLs (within 50 kb on either side of the leading variant), the average estimated heritability increases to 0.37, therefore capturing an additional 0.10 of heritability (Fig. 3a). Moreover, there is still the expression of 18,174 (93.9%) genes, some with large *cis*-heritability, without any significant *cis*-eQTLs (Extended Data Fig. 7a). Our study clearly suggests that allelic heterogeneity contributes to the missing heritability of GWAS.

Fig. 3: Resolving allelic and locus heterogeneity.



a, Histogram of heritability (h^2) explained by leading variants within QTLs, local variants (within 50 kb on either side of the leading variants) and all genetic variants. Numbers near the vertical dashed lines represent mean h^2 values contributed by different variant types. Different variant types are colour coded. **b**, Allelic heterogeneity was resolved for gene expression traits. **c**, Manhattan plots for the *cis*-region (within 50 kb upstream and downstream) of the *Solyc03G001472* gene. The grey circles represent SNPs and the red triangles represent SVs. The dashed lines represent the significance thresholds. **d**, Overview of the analysis of flavonoids. Top, h^2 of 38 flavonoid metabolites (Supplementary Table 14), estimated with a composite model using all genetic variants from TGG1.1-332 partitioned into six different categories. ‘Module’ refers to variants located within 50 kb upstream or downstream of genes in the flavonoid module, and the remaining variants are ‘non-module’ variants. The bar plots show the

contribution of each category to h^2 , indicated by unique colours. Metabolites with more than one SV QTL are coloured in green, as indicated at the top. Statistically significant SVs for metabolites identified by both MLM and LASSO and LASSO only are coloured in red and cyan, respectively. All SVs detected by the MLM were also found by LASSO. Bottom, significant *cis*-SV eQTLs for the expression of 17 genes identified using LASSO. The 16 SVs associated with flavonoids (mQTLs) are indicated by orange triangles.

Source data

Multilocus models have the potential to resolve allelic heterogeneity, but only small numbers of variants can be analysed simultaneously, limiting their applications in GWAS⁴⁰. Thus, to determine whether the graph pangenome enables capturing missing heritability by addressing allelic heterogeneity, we focused on associations between SVs within gene-proximal regions (50 kb upstream and downstream) and gene expression, motivated by the assumption that SVs are likely to be causative. Using the least absolute shrinkage and selection operator (LASSO)⁴¹, a multilocus regression model, we found that the expression of 1,787 out of the 19,353 genes is affected by at least two significantly associated SVs (false-discovery rate = 7.53×10^{-4} ; permutation test). Compared with MLM, LASSO uniquely detected 1,249 *cis*-SV eQTLs, indicating its greater power in resolving allelic heterogeneity (Fig. 3b). The *cis*-heritability of the 1,249 eQTLs ranges from 0.00 to 0.59, with an average of 0.10. By contrast, we identified only 169 *cis*-SV QTLs with at least two significant SVs using the SL5.0-332 callset, showing the need for more thorough inclusion of genetic variants to resolve allelic heterogeneity and to capture missing heritability in GWAS. Furthermore, complex SVs such as duplications, tandem repeats and copy number variants (CNVs), most of which are probably multiallelic SVs^{36,42,43}, could not be adequately addressed in this study. Thus, it is probable that allelic heterogeneity may be even more prevalent than estimated here.

By way of demonstration, we considered the gene *Solyc03G001472*, which encodes a protein of unknown function. The *cis*-heritability of this gene is 0.24 (s.d. = 0.18), contributing 52% of the total heritability. There are 646

SNPs, 46 indels and three SVs within the gene-proximal region, none of which are significantly associated with its expression when applying the MLM. Considering that the three SVs explain approximately half of the *cis*-heritability (0.12, s.d. = 0.11), we applied the LASSO model to the three SVs, and found that two of them show significant association with gene expression, one with minor allele frequency (MAF) of 0.017 (sv3_42936717) and the other with MAF of 0.032 (sv3_42954617) (Fig. 3c). The expression levels of different SV genotypes show that both SVs are associated with the expression of *SolyC03G001472* (Extended Data Fig. 7b). Overall, we show that allelic heterogeneity can be partially addressed by cataloguing of SVs exclusively identified by the graph pangenome.

Locus heterogeneity—the phenomenon that complex traits are controlled by allelic variants across multiple genes—may also decrease the statistical power of GWAS⁴⁴. In theory, the LASSO model could be used to resolve locus heterogeneity (as well as allelic heterogeneity) but, in practice, this is not feasible owing to the large number of genome-wide markers. An alternative approach is to focus on a network of genes potentially involved in regulating specific traits. The ‘omnigenic model’ postulates that all expressed genes may be involved in the regulation of complex traits⁴⁵; however, only genes with large effects can be detected with a limited sample size. For gene expression, we derived a co-expression network formed by 99 modules, including 17,592 genes, using weighted correlation network analysis (WGCNA)⁴⁶ (Supplementary Table 8). Each module consists of an average of 177.7 genes, accounting for only 0.92% of the 19,353 expressed genes. Notably, we found that variants within the proximal region of module genes on average contribute 0.22 of gene expression heritability, or 48.9% of the total estimated heritability (0.45) (Extended Data Fig. 7c). This indicates that genes in the same module, although fewer in number, may have disproportionately large effects on their corresponding module gene expression.

As a consequence, to address locus heterogeneity for complex traits, we can narrow the search space within a certain module in the co-expression network, and then focus on SVs affecting the corresponding gene expression. To assess the effectiveness of this strategy, we concentrated on flavonoid content (comprising 38 detected metabolites³⁵), an important

tomato fruit-quality trait, with heritability ranging from 0.07 to 1.00 (Fig. 3d and Supplementary Table 9). A co-expression network analysis shows that a module comprising 81 genes is related to the flavonoid pathway (hereafter, the flavonoid module) (Extended Data Fig. 8). Whole-genome SVs from TGG1.1-332 contribute on average 0.21 to the heritability of the 38 metabolite contents (range, 0.00–0.58). We found that SVs located in the proximal regions of flavonoid-module genes contribute 0.14 of heritability (Fig. 3d), suggesting that the 81 genes account for most of the genetic regulation of flavonoid content. Using LASSO, we identified 17 out of 81 genes with *cis*-SV eQTLs (Fig. 3d and Supplementary Table 10). The 171 SVs surrounding the 17 genes (*cis*-SV set) constitute the candidate dataset for evaluating the effect of locus heterogeneity on flavonoid content. We performed association analyses between the *cis*-SV set and the 38 metabolites using LASSO and identified 16 SVs surrounding nine genes associated with 31 metabolites (Supplementary Table 11). Moreover, 17 out of 31 metabolites are associated with multiple genes (Fig. 3d), suggesting that locus heterogeneity affects this complex network of flavonoids.

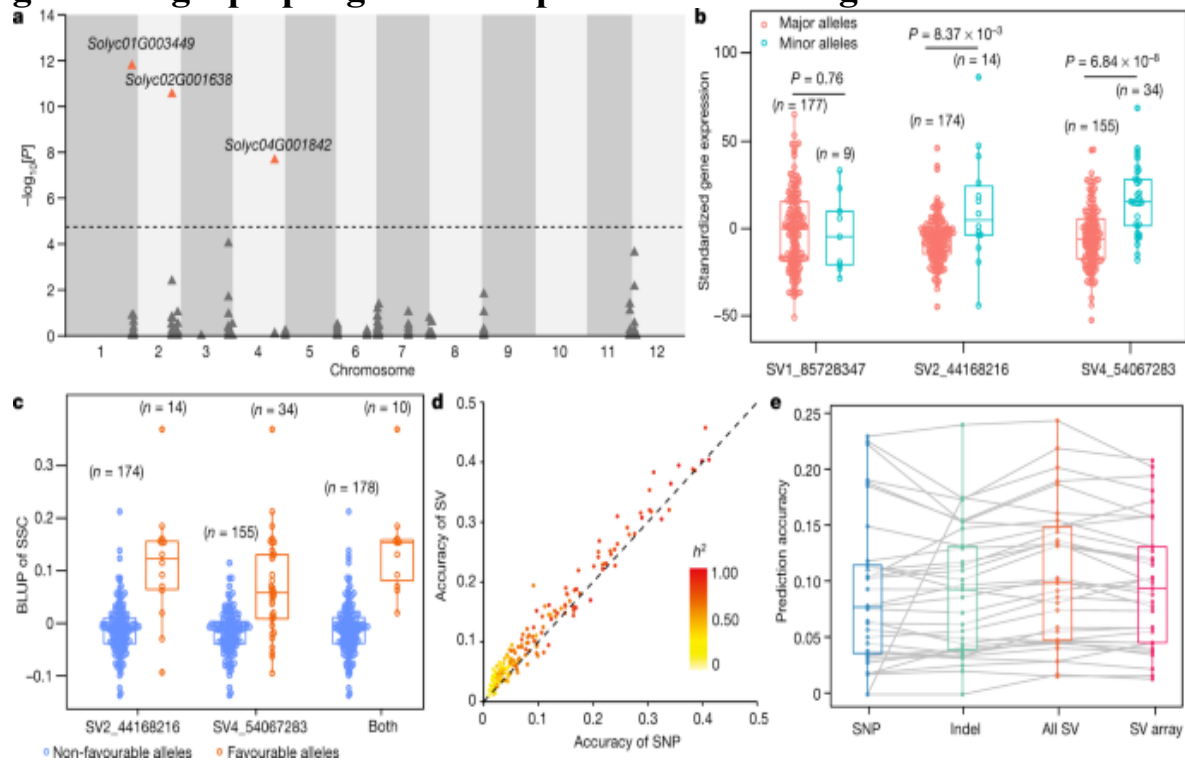
The nine genes affecting the 31 flavonoids consist of three genes with transcription factor activity (including the previously reported gene *SIMYB12*) and six enzyme-coding genes. In particular, Gene Ontology analysis shows that there are two transcription factors and two enzymes involved in the flavonoid biosynthetic process (Supplementary Table 12). This is one example demonstrating how the graph pangenome-based methodology sheds new light on recovering missing heritability by resolving locus heterogeneity.

Graph pangenome empowers tomato breeding

Optimal use of the extensive genome variants is expected to facilitate a paradigm shift in crop improvement⁴⁷. Significant genetic variants identified in GWAS are promising candidate markers for marker-assisted selection (MAS) in breeding. As a proof-of-concept study taking advantage of the added value of the graph pangenome to tomato breeding, we took fruit soluble solids content (SSC), an important yield and flavour trait, as a breeding target.

A previous study reported two QTLs underlying SSC³⁰, *Lin5* on chromosome 9 and *SSC11.1* on chromosome 11. To detect variants that potentially cause locus heterogeneity, we developed a universal pipeline by analysing SSC and gene expression simultaneously using WGCNA and identified a module containing 103 genes that are probably related to SSC. SVs in the proximal regions of these genes contribute 0.33 (s.d. = 0.21) to SSC heritability, comprising 52.9% of total heritability (0.62, s.d. = 0.68). Using LASSO, we identified *cis*-SV eQTLs in 25 genes among these module genes. Three SVs (SV1_85728347, SV2_44168216 and SV4_54067283) in physical proximity to the corresponding genes (*Solyc01G003449*, *Solyc02G001638* and *Solyc04G001842*) are significantly associated with SSC (Fig. 4a). These genes are promising candidates for dissecting the genetic architecture of SSC.

Fig. 4: The graph pangenome empowers MAS and genomic selection.



a, Association study of SSC for the *cis*-SV set using LASSO. Genes with significant associated SVs are indicated (orange triangles). **b**, SVs affecting the expression of their nearby genes. *P* values were derived from two-sided Wilcoxon rank sum tests. **c**, Selection of accessions with high SSC using SVs. For **b** and **c**, *n* represents the sample size in each group. **d**, Comparison

of genomic selection accuracies using SNPs and SVs as markers. The colour scale indicates the estimated heritability contributed by SNPs. **e**, Comparison of genomic selection accuracies using different types of genetic variants. $n = 33$ metabolic traits are plotted. ‘SV array’ denotes the SV panel for the DNA capture array. For **b**, **c** and **e**, the box and whisker plots show the median (centre line), mean (cross), upper and lower quartiles (box limits), $1.5 \times$ the interquartile range (whiskers) and outliers (solid points). Individual data points are plotted in circles.

[Source data](#)

Moreover, the significant genetic variants identified in this study can be valuable candidates for developing new markers to identify accessions with high SSC. We found that two of the three SVs (SV2_44168216 and SV4_54067283) significantly affect the expression of their nearby genes (*Solyc02G001638* and *Solyc04G001842*) (Fig. [4b](#)). *Solyc02G001638* encodes a PapD-like superfamily protein, and a previous study revealed that the expression of *Solyc04G001842* encoding a trehalose-phosphate phosphatase is negatively correlated with the contents of d-fructose and d-glucose⁴⁸. Given that SV1_85728347 is not significantly associated with the expression of *Solyc01G003449* (Fig. [4b](#)), we did not consider this variant for MAS. We found that selecting accessions with high SSC on the basis of favourable alleles of both SV2_44168216 and SV4_54067283 is more efficient than selecting on the basis of only one SV (Fig. [4c](#)). These results indicate that it is valuable to design marker assays with SVs, highlighting the superiority of the graph pangenome for future plant breeding.

Complex traits controlled by multiple small-effect loci limit the application of MAS in crop improvement. Genomic selection provides an alternative approach that takes advantage of small-effect QTLs. Genomic selection involves the selection of elite lines on the basis of genome-estimated breeding values from all markers, regardless of the magnitude of their effects. Using 191 metabolites of which the heritability estimated from SVs is larger than that from SNPs (0.60 versus 0.55; Wilcoxon rank sum test, $P = 0.032$), the accuracy (r^2 between the true phenotype and genome-estimated breeding values) of genomic selection using SVs is higher than that using SNPs (0.11 versus 0.10; Wilcoxon rank sum test, $P = 3.30 \times 10^{-32}$) (Fig. [4d](#)).

This demonstrates that capturing missing heritability using SVs improves the accuracy of genomic selection.

We next applied genomic selection to tomato flavour breeding. The estimated heritability of 33 flavour-related metabolites ranges from 0.21 to 1.00 (Supplementary Table 7). With the best linear unbiased prediction, the prediction accuracy ranges from 0.00 to 0.23, 0.00 to 0.24 and 0.02 to 0.25 using SNPs, indels and SVs, respectively, and prediction accuracy using SVs is highest for 22 of the 33 metabolites (Fig. 4e). To facilitate genomic selection in tomato breeding, we selected 20,955 candidate SVs, comprising 11,488 insertions, 9,403 deletions and 64 inversions for the design of a DNA capture array. When applied to the genomic selection of the 33 flavour-related metabolites, the SV set exhibits only limited reduction of prediction accuracy compared with the entire SV set (0.10 versus 0.11, Wilcoxon rank sum test, $P=0.693$) (Fig. 4e). As SVs can be captured by a limited number of probes (Supplementary Note), this panel potentially provides an accurate and cost-effective platform for tomato improvement. We anticipate that future studies will validate the effectiveness of the SV array in tomato breeding. These results also enable the advancement of SV-based genomic selection in other species.

Genetic variants identified from the graph pangenome will facilitate transgenic and/or genome editing-based breeding. To improve primer design in genome editing, we designed sgRNA primers with the protospacer adjacent motif of *Cas9* for all predicted genes and released them in a web-based database (<http://solomics.agis.org.cn/tomato>). This database also provides tools to search the comprehensive catalogue of SNPs, indels and SVs, and to design competitive allele-specific PCR (KASP) markers, which can benefit the tomato research and breeding communities.

Discussion

The state-of-the-art graph pangenome presented here incorporates genetic variants from a wide range of tomato germplasms. The inclusion of biodiversity from non-reference accessions will serve as an important platform for next-generation genomic studies and genome-assisted breeding. In particular, using the resources offered by the graph pangenome highlights

the importance of SVs in capturing missing heritability by addressing incomplete LD, allelic heterogeneity and locus heterogeneity.

Here we used both read mapping and assembly-based methods to detect SVs and genotype SVs in a population using short reads using a graph-based method. One limitation is that complex SVs—for example, segmental duplications, tandem repeats and CNVs—are not specifically considered in our current pipeline. Another limitation is that only SVs present in the graph could be genotyped, and the accuracy of SV genotyping is still lower than that for SNPs and indels. Methods based on high-quality genome assemblies are superior for identifying highly complex SVs^{4,49}. We believe that these problems will be addressed in the future through the development of tools that can generate a unified pangenome graph and annotation graph, reinforced by the greater availability of population-level reference-grade genome assemblies.

Some statistical tools exist that consider allelic heterogeneity, although these tools often fail to detect causal variants without high marginal *P* values⁴³. The power of these tools can probably be improved by incorporating SVs. Moreover, we have demonstrated the importance of locus heterogeneity. However, we recognize that our solution to use the LASSO is suboptimal, because it is not yet computationally feasible to consider all genetic markers at once. Ideally, multilocus tools will be developed that consider more markers. Furthermore, when it becomes feasible to genotype complex SVs, it will be necessary to develop tools that, for example, allow for multiallelic variants, and can use these variants to capture additional missing heritability and improve the accuracy of MAS and genomic selection.

Methods

Tomato sequencing and genome assembly

A total of 32 tomato accessions, including the reference cultivar Heinz 1706, were chosen from the BIG, CER and PIM groups. Genomic DNA was extracted from fresh leaves of each accession. SMRTbell libraries were constructed according to the standard protocol of PacBio (Pacific Biosciences) and sequenced on the PacBio Sequel II platform to generate

HiFi reads. Primary assemblies were generated from three assemblers (Flye v.2.7, Hicanu v.2.0 and Hifiasm v.0.13)^{50,51,52} and potential misassemblies were corrected using the GALA pipeline⁵³ ([Supplementary Note](#)). For the reference genome Heinz 1706, the Hi-C data were used to obtain a chromosome-level assembly. The remaining assemblies were anchored and oriented to chromosomes by the reference-guided software RagTag (v.1.0.1)⁵⁴ with the default parameters.

Genome annotation

Protein-coding genes were predicted for each genome assembly using the MAKER2 (ref. ⁵⁵) and PRAM⁵⁶ pipelines. RNA evidence was collected by aligning RNA-sequencing (RNA-seq) reads to the repeat-masked assembly using HISAT2 (v.2.10.2)⁵⁷ and assembling them to transcripts with StringTie (v.1.3.0)⁵⁸. TACO (v.0.7.3)⁵⁹ was applied to merge stringtie gtf (--filter-splice-juncs). Ab initio gene prediction was performed using SNAP (v.2006-07-28)⁶⁰ and AUGUSTUS (v.3.3.3)⁶¹. SNAP was trained for two rounds, and AUGUSTUS prediction was performed using the ‘tomato’ model. Proteins from SwissProt (Viridiplantae) (<https://www.uniprot.org>) and three *Solanum* species (*S. lycopersicum* cv. Heinz 1706 ITAG4.0 (ref. ²³), *Solanum pimpinellifolium* LA2093 (ref. ²⁵) and *Solanum tuberosum* DM (v.6.1)⁶² were integrated, with redundant sequences removed using CD-HIT (v.4.6)⁶³ with the parameter ‘-c 0.99’. Non-redundant proteins were used for homology-based prediction using BRAKER (v.2.1.4)⁶⁴ and GeneMark (v.4.3.8)⁶⁵. Only integrated gene models with AED values of <0.5 were retained. Furthermore, new gene models were predicted using PRAM.

SNP and indel calling using HiFi reads

The HiFi reads were first mapped to SL5.0 using minimap2 (ref. ⁶⁶) with the parameters ‘-a -k 19 -O 5,56 -E 4,1 -B 5 -z 400,50 -r 2k --eqx --secondary=no’. DeepVariant (v.1.0.0) with the pretrained PacBio mode (–model_type PACBIO) was then used for variant calling of each accession, and all individual variants were merged using glnexus_cli from DeepVariant (v.0.9.0). Finally, variants that met all of the following criteria were retained:

(1) total sequencing depth from 400 to 1,500; (2) quality score ≥ 20 ; (3) biallelic variants; (4) length ≤ 50 bp for indels.

SV detection

To detect SVs using HiFi reads from the 31 accessions, we mapped HiFi reads to SL5.0 using NGLMR (v.0.2.7)⁶⁷ with the default parameters. A total of four callers: Sniffles (v.1.0.12)⁶⁷, SVIM (v.1.2.0)⁶⁸, CuteSV (v.1.0.10)⁶⁹ and PBSV (v.2.4.0)

(<https://github.com/PacificBiosciences/pbsv>) with the default parameters were used for variant calling in each accession. We retained variants with a ‘pass’ flag and a read depth of at least three. Deletions ranging from 51 bp to 100 kb in length, and insertions ranging from 51 bp to 20 kb in length were retained. To identify SVs from the 45 genome assemblies, Assemblytics⁷⁰ was applied to the genome alignments generated using MUMmer (v.4.0)⁷¹ with the default parameters. For the 31 accessions with SVs from the five callers, we merged all SVs shorter than 100 kb using SURVIVOR (v.1.0.6)⁸ using a maximum allowed distance of 1 kb, reporting only calls supported by at least two callers and where the callers agreed regarding the type of variant. SVs longer than 100 kb detected by Assemblytics were retained. As the publicly available SVs from 100 tomatoes were identified using a different version of the reference genome (SL4.0), we transformed the coordinates to SL5.0 using the LiftOver software according to the instructions provided on the UCSC website (http://genomewiki.ucsc.edu/index.php/Minimal_Steps_For_LiftOver).

Construction of the graph pangenome

SVs from the 31 accessions with HiFi reads and previously identified SVs from the 100 tomatoes were merged, and redundant SVs were removed according to instructions provided on GitHub

(<https://github.com/vgteam/giraffe-sv-paper/blob/master/scripts/sv>). The variation graph toolkit (vg) pipeline¹⁹ was used for the construction of TGG1.0, with SNPs and indels called from the HiFi reads. The vg pipeline was also used for variant calling with short reads. To obtain genotypes of variants in TGG1.0, the GBWT index was created using the greedy path-cover algorithm and 32 paths, and the default minimizer length of 29 was

chosen in the minimizer index with a window size of 11. Short reads from 706 tomato accessions ($>6\times$) were mapped to TGG1.0 with Giraffe¹⁹ and SNPs and indels were called using DeepVariant with the NGS model. These SNPs and indels were filtered as recommended. Non-redundant SVs, SNPs and indels from both the 31 accessions with HiFi reads, the 100 accessions with ONT long reads and the 706 accessions with short reads were integrated into TGG1.1. Genotypes of SVs for the 706 accessions were called by Paragraph¹⁸ using the default parameters.

Graph annotation

To determine the coordinates of genes from non-SL5.0 assemblies, we calculated the distance of each accession from SL5.0 using Mash (v.2.2)⁷². We first generated a graph format for all assemblies by augmenting the 45 assemblies to SL5.0 using minigraph⁷³ in increasing Mash distance with the reference SL5.0, according to the instructions provided online (<https://github.com/AnimalGenomicsETH/bovine-graphs>). All of the coding sequences from the 45 accessions^{24,25} and the previous pangenome³¹ were next mapped to the graph using minigraph. Coding sequences with more than 90% coverage and sequence identity and overlapping with the SL5.0 gene models were discarded. For genes mapped to the backbone without any protein-coding gene annotation, we selected the longest one if annotated in more than one accession. For genes that were not mapped on the backbone of the graph, we removed redundant genes using CD-HIT with the parameter ‘-1 0.9’ and only genes from the accession with the lowest distance from SL5.0 were retained. Finally, the gene sets mapped to the backbone and the graph were merged, and redundant genes were removed using CD-HIT with the parameter ‘-1 0.9’.

Gene expression and metabolite contents

To quantify the expression of all genes, we used Kallisto (v.0.46.2)⁷⁴ for all 51,155 gene models in the graph pangenome. RNA-seq data from a total of 332 accessions (217 from BIG, 98 from CER and 17 from PIM) were quantified as transcripts per million (TPM). Genes with TPM values of >0.5 were defined as expressed. Only genes expressed in at least 100 accessions were retained for the downstream analyses. Raw expression levels were

normalized with quantile–quantile normalization. To remove potential batch effects and confounding factors affecting gene expression, the probabilistic estimation of expression residuals method⁷⁵ was applied with the top four factors as covariates. For metabolites with missing values in <100 accessions, the mean value of two replicates was used. Raw metabolite values were transformed using the ternary logarithm and then normalized using quantile–quantile normalization.

Heritability estimation

The LDAK-thin model⁷⁶ was used to estimate the proportion of phenotypic variance explained by genetic variants. The genetic variants were first pruned to exclude nearby SNPs in perfect LD using LDAK-thin with parameters ‘--window-prune 0.98 and --window-kb 100’. When computing the kinship matrix, it is necessary to specify the power parameter alpha, which determines the expected relationship between per-variant heritability (h_j^2) and MAF (f_j). Specifically, it is assumed that $E[h_j^2]$ is proportional to $[f_j(1 - f_j)]^{(1 + \text{alpha})}$. By trying multiple values between –1 and 0, we found that alpha = –0.5 fits best under most scenarios, indicating a tendency for per-variant heritability to decrease with lower MAF. Principal component analysis was performed using PLINK (v.2.0)⁷⁷ using SNPs and indels from TGG1.1-332, and the first four principal components were used as covariates when estimating heritability. For partitioning contributions to heritability by different types of genetic variants, we derived the kinship for each variant category and estimated the heritability using a composite model with multiple kinship matrices. For all estimations with LDAK-thin, we added the parameter ‘--constrain YES’ to ensure no negative estimates of heritability (if there was insufficient evidence to support the inclusion of a category, the estimated heritability was set to zero).

Definition of heritability category

We identified the coordinates of seven anchor dots that represent the seven categories as described in Supplementary Table 13. The proportions of heritability contributed by each type of genetic variants (SNPs, indels and SVs) were used as the coordinate of each trait. Traits with heritability of

zero were excluded as we could not determine the coordinate. We next calculated the Euclidean distance between the trait and each anchor dot, and each trait was assigned to the category with the shortest distance.

Genome-wide association study

For the MLM, we used the leave-one-chromosome-out method and the mixed model implemented in GCTA³⁹. After pruning using PLINK (v.2.0) with the parameter ‘-indep-pairwise’ set to ‘50 5 0.2’, the pruned SNPs were used for the kinship matrix (genetic relationship matrix; GRM). For SNPs and indels, the pruned dataset (-indep-pairwise 100, 1, 0.98) was used. The first four principal components were used as covariates in the model. A Bonferroni-derived threshold (0.05/total number of markers) was used as the significance threshold. For the LASSO model, the best linear unbiased prediction (BLUP) value estimate from LDAK (obtained from the composite model) was used as the response variable (new phenotype) for each trait, and the significance of genetic variants was assessed using the lassopv package⁴¹. The significance threshold of LASSO was determined by 1/number of SVs and the false-discovery rate at the threshold was estimated on the basis of permutations.

QTL definition

Significant variants were grouped into the same cluster if the correlation coefficient R^2 of two adjacent variants was >0.20 and the physical distance was <1 Mb. Clusters containing more than three significant variants were considered as candidate QTLs. For eQTL classification, *cis*-eQTLs were inferred if the leading significant variants were <50 kb from the transcription start sites or transcription end sites of the corresponding genes; otherwise, they were considered to be *trans*-eQTLs.

Co-expression network

WGCNA⁴⁶ was applied to the prefiltered expression data from 332 accessions to reconstruct gene modules exhibiting different expression patterns. Based on the criterion of approximate scale-free topology, the number nine was chosen as the proper soft-thresholding power for a signed

network. Similar expression profiles were merged to the same module with a minimum module size set to 10 and the dissimilarity set to 0.15.

Genomic selection

The rrBLUP⁷⁸ package was used for genomic prediction of metabolites. SNPs and indels with positive weight were used to calculate the kinship matrix with the A.mat function implemented in rrBLUP. The prediction accuracy was obtained by a five-fold cross-validation with five repetitions. As the kinship matrix was calculated from genomic data, the method is also called genomic best linear unbiased prediction.

Reporting summary

Further information on research design is available in the [Nature Research Reporting Summary](#) linked to this paper.

Data availability

All sequencing data generated in this study have been deposited at the Sequence Read Archive (<https://ncbi.nlm.nih.gov/sra>) under BioProject [PRJNA733299](#). Whole-genome sequencing data were downloaded from NCBI (BioProjects: [PRJNA259308](#), [PRJNA353161](#), [PRJNA454805](#) and [PRJEB5235](#)) and RNA-seq data were downloaded from the NCBI (BioProject: [PRJNA396272](#)). All assemblies with annotations, variant VCF files and graph files are available at the SolOmics database (<http://solomics.agis.org.cn/tomato/ftp>) and Sol Genomics Network (<https://solgenomics.net/ftp/genomes/TGG/>). The InterPro database was downloaded from <https://www.ebi.ac.uk/interpro/>. The UniProtKB/SwissProt database is available online (<https://www.uniprot.org>). Source data are provided with this paper.

Code availability

All code associated with this project is available at GitHub (<https://github.com/YaoZhou89/TGG>).

References

1. Maher, B. Personal genomes: the case of the missing heritability. *Nature* **456**, 18–21 (2008).
2. Manolio, T. A. et al. Finding the missing heritability of complex diseases. *Nature* **461**, 747–753 (2009).
3. Young, A. I. Solving the missing heritability problem. *PLoS Genet.* **15**, e1008222 (2019).
4. De Coster, W., Weissensteiner, M. H. & Sedlazeck, F. J. Towards population-scale long-read sequencing. *Nat. Rev. Genet.* **22**, 572–587 (2021).
5. Visscher, P. M. Sizing up human height variation. *Nat. Genet.* **40**, 489–490 (2008).
6. Hemani, G., Knott, S. & Haley, C. An evolutionary perspective on epistasis and the missing heritability. *PLoS Genet.* **9**, e1003295 (2013).
7. Brachi, B., Morris, G. P. & Borevitz, J. O. Genome-wide association studies in plants: the missing heritability is in the field. *Genome Biol.* **12**, 232 (2011).
8. Jeffares, D. C. et al. Transient structural variations have strong effects on quantitative traits and reproductive isolation in fission yeast. *Nat. Commun.* **8**, 14061 (2017).
9. Yang, J. et al. Common SNPs explain a large proportion of the heritability for human height. *Nat. Genet.* **42**, 565–569 (2010).
10. Eichler, E. E. et al. Missing heritability and strategies for finding the underlying causes of complex disease. *Nat. Rev. Genet.* **11**, 446–450 (2010).
11. Garrison, E. et al. Variation graph toolkit improves read mapping by representing genetic variation in the reference. *Nat. Biotechnol.* **36**,

875–879 (2018).

12. Martiniano, R., Garrison, E., Jones, E. R., Manica, A. & Durbin, R. Removing reference bias and improving indel calling in ancient DNA data analysis by mapping to a sequence variation graph. *Genome Biol.* **21**, 250 (2020).
13. The 1000 Genomes Project Consortium. A global reference for human genetic variation. *Nature* **526**, 68–74 (2015).
14. Jayakodi, M. et al. The barley pan-genome reveals the hidden legacy of mutation breeding. *Nature* **588**, 284–289 (2020).
15. Hufford, M. B. et al. De novo assembly, annotation, and comparative analysis of 26 diverse maize genomes. *Science* **373**, 655–662 (2021).
16. The Computational Pan-Genomics Consortium. Computational pan-genomics: status, promises and challenges. *Brief. Bioinform.* **19**, 118–135 (2018).
17. Rakocevic, G. et al. Fast and accurate genomic analyses using genome graphs. *Nat. Genet.* **51**, 354–362 (2019).
18. Chen, S. et al. Paragraph: a graph-based structural variant genotyper for short-read sequence data. *Genome Biol.* **20**, 291 (2019).
19. Sirén, J. et al. Pangenomics enables genotyping of known structural variants in 5202 diverse genomes. *Science* **374**, eabg8871 (2021).
20. Liu, Y. et al. Pan-genome of wild and cultivated soybeans. *Cell* **182**, 162–176 (2020).
21. Qin, P. et al. Pan-genome analysis of 33 genetically diverse rice accessions reveals hidden genomic variations. *Cell* **184**, 3542–3558 (2021).
22. Ebert, P. et al. Haplotype-resolved diverse human genomes and integrated analysis of structural variation. *Science* **372**, eabf7117 (2021).

23. Hosmani, P. S. et al. An improved de novo assembly and annotation of the tomato reference genome using single-molecule sequencing, Hi-C proximity ligation and optical maps. Preprint at *bioRxiv* <https://doi.org/10.1101/767764> (2019).
24. Alonge, M. et al. Major impacts of widespread structural variation on gene expression and crop improvement in tomato. *Cell* **182**, 145–161 (2020).
25. Wang, X. et al. Genome of *Solanum pimpinellifolium* provides insights into structural variants during tomato breeding. *Nat. Commun.* **11**, 5817 (2020).
26. Causse, M. et al. Whole genome resequencing in tomato reveals variation associated with introgression and breeding events. *BMC Genom.* **14**, 791 (2013).
27. Aflitos, S. et al. Exploring genetic variation in the tomato (*Solanum* section *Lycopersicon*) clade by whole-genome sequencing. *Plant J.* **80**, 136–148 (2014).
28. Bolger, A. et al. The genome of the stress-tolerant wild tomato species *Solanum pennellii*. *Nat. Genet.* **46**, 1034–1038 (2014).
29. Lin, T. et al. Genomic analyses provide insights into the history of tomato breeding. *Nat. Genet.* **46**, 1220–1226 (2014).
30. Tieman, D. et al. A chemical genetic roadmap to improved tomato flavor. *Science* **355**, 391–394 (2017).
31. Gao, L. et al. The tomato pan-genome uncovers new genes and a rare allele regulating fruit flavor. *Nat. Genet.* **51**, 1044–1051 (2019).
32. Poplin, R. et al. A universal SNP and small-indel variant caller using deep neural networks. *Nat. Biotechnol.* **36**, 983–987 (2018).
33. Sim, S.-C. et al. Development of a large SNP genotyping array and generation of high-density genetic maps in tomato. *PLoS ONE* **7**, e40563 (2012).

34. Speed, D., Hemani, G., Johnson, M. R. & Balding, D. J. Improved heritability estimation from genome-wide SNPs. *Am. J. Hum. Genet.* **91**, 1011–1021 (2012).
35. Zhu, G. et al. Rewiring of the fruit metabolome in tomato breeding. *Cell* **172**, 249–261 (2018).
36. Vinces, M. D., Legendre, M., Caldara, M., Hagihara, M. & Verstrepen, K. J. Unstable tandem repeats in promoters confer transcriptional evolvability. *Science* **324**, 1213–1216 (2009).
37. The GTEx Consortium. The GTEx Consortium atlas of genetic regulatory effects across human tissues. *Science* **369**, 1318–1330 (2020).
38. Hormozdiari, F. et al. Widespread allelic heterogeneity in complex traits. *Am. J. Hum. Genet.* **100**, 789–802 (2017).
39. Yang, J., Lee, S. H., Goddard, M. E. & Visscher, P. M. GCTA: a tool for genome-wide complex trait analysis. *Am. J. Hum. Genet.* **88**, 76–82 (2011).
40. Hormozdiari, F., Jung, J., Eskin, E. & Joo, J. W. J. MARS: leveraging allelic heterogeneity to increase power of association testing. *Genome Biol.* **22**, 128 (2021).
41. Wang, L. & Michoel, T. Controlling false discoveries in Bayesian gene networks with lasso regression *p*-values. Preprint at *arXiv* <https://arxiv.org/abs/1701.07011> (2017).
42. Sudmant, P. H. et al. An integrated map of structural variation in 2,504 human genomes. *Nature* **526**, 75–81 (2015).
43. Collins, R. L. et al. A structural variation reference for medical and population genetics. *Nature* **581**, 444–451 (2020).
44. Mancuso, N. et al. Probabilistic fine-mapping of transcriptome-wide association studies. *Nat. Genet.* **51**, 675–682 (2019).

45. Boyle, E. A., Li, Y. I. & Pritchard, J. K. An expanded view of complex traits: from polygenic to omnigenic. *Cell* **169**, 1177–1186 (2017).
46. Langfelder, P. & Horvath, S. WGCNA: an R package for weighted correlation network analysis. *BMC Bioinform.* **9**, 559 (2008).
47. Della Coletta, R., Qiu, Y., Ou, S., Hufford, M. B. & Hirsch, C. N. How the pan-genome is changing crop genomics and improvement. *Genome Biol.* **22**, 3 (2021).
48. Li, N. et al. Identification of the carbohydrate and organic acid metabolism genes responsible for brix in tomato fruit by transcriptome and metabolome analysis. *Front. Genet.* **12**, 714942 (2021).
49. Mahmoud, M. et al. Structural variant calling: the long and the short of it. *Genome Biol.* **20**, 246 (2019).
50. Kolmogorov, M., Yuan, J., Lin, Y. & Pevzner, P. A. Assembly of long, error-prone reads using repeat graphs. *Nat. Biotechnol.* **37**, 540–546 (2019).
51. Nurk, S. et al. HiCanu: accurate assembly of segmental duplications, satellites, and allelic variants from high-fidelity long reads. *Genome Res.* **30**, 1291–1305 (2020).
52. Cheng, H., Concepcion, G. T., Feng, X., Zhang, H. & Li, H. Haplotype-resolved de novo assembly using phased assembly graphs with hifiasm. *Nat. Methods* **18**, 170–175 (2021).
53. Awad, M. & Gan, X. GALA: gap-free chromosome-scale assembly with long reads. Preprint at *bioRxiv* <https://doi.org/10.1101/2020.05.15.097428> (2020).
54. Alonge, M. et al. RaGOO: fast and accurate reference-guided scaffolding of draft genomes. *Genome Biol.* **20**, 224 (2019).
55. Holt, C. & Yandell, M. MAKER2: an annotation pipeline and genome-database management tool for second-generation genome projects. *BMC Bioinform.* **12**, 491 (2011).

56. Liu, P., Soukup, A. A., Bresnick, E. H., Dewey, C. N. & Keles, S. PRAM: a novel pooling approach for discovering intergenic transcripts from large-scale RNA sequencing experiments. *Genome Res.* **30**, 1655–1666 (2020).
57. Kim, D., Paggi, J. M., Park, C., Bennett, C. & Salzberg, S. L. Graph-based genome alignment and genotyping with HISAT2 and HISAT-genotype. *Nat. Biotechnol.* **37**, 907–915 (2019).
58. Pertea, M. et al. StringTie enables improved reconstruction of a transcriptome from RNA-seq reads. *Nat. Biotechnol.* **33**, 290–295 (2015).
59. Niknafs, Y. S., Pandian, B., Iyer, H. K., Chinnaian, A. M. & Iyer, M. K. TACO produces robust multisample transcriptome assemblies from RNA-seq. *Nat. Methods* **14**, 68–70 (2017).
60. Korf, I. Gene finding in novel genomes. *BMC Bioinform.* **5**, 59 (2004).
61. Stanke, M. et al. AUGUSTUS: ab initio prediction of alternative transcripts. *Nucleic Acids Res.* **34**, W435–W439 (2006).
62. Pham, G. M. et al. Construction of a chromosome-scale long-read reference genome assembly for potato. *Gigascience* **9**, giaa100 (2020).
63. Fu, L., Niu, B., Zhu, Z., Wu, S. & Li, W. CD-HIT: accelerated for clustering the next-generation sequencing data. *Bioinformatics* **28**, 3150–3152 (2012).
64. Hoff, K., Lomsadze, A., Borodovsky, M. & Stanke, M. Whole-genome annotation with BRAKER. *Methods Mol. Biol.* **1962**, 65–95 (2019).
65. Brúna, T., Lomsadze, A. & Borodovsky, M. GeneMark-EP+: eukaryotic gene prediction with self-training in the space of genes and proteins. *NAR Genom. Bioinform.* **2**, lqaa026 (2020).
66. Li, H. Minimap2: pairwise alignment for nucleotide sequences. *Bioinformatics* **34**, 3094–3100 (2018).

67. Sedlazeck, F. J. et al. Accurate detection of complex structural variations using single-molecule sequencing. *Nat. Methods* **15**, 461–468 (2018).
68. Heller, D. & Vingron, M. SVIM: structural variant identification using mapped long reads. *Bioinformatics* **35**, 2907–2915 (2019).
69. Jiang, T. et al. Long-read-based human genomic structural variation detection with cuteSV. *Genome Biol.* **21**, 189 (2020).
70. Nattestad, M. & Schatz, M. C. Assemblytics: a web analytics tool for the detection of variants from an assembly. *Bioinformatics* **32**, 3021–3023 (2016).
71. Marçais, G. et al. MUMmer4: a fast and versatile genome alignment system. *PLoS Comput. Biol.* **14**, e1005944 (2018).
72. Ondov, B. D. et al. Mash: fast genome and metagenome distance estimation using MinHash. *Genome Biol.* **17**, 132 (2016).
73. Li, H., Feng, X. & Chu, C. The design and construction of reference pangenome graphs with minigraph. *Genome Biol.* **21**, 265 (2020).
74. Bray, N. L., Pimentel, H., Melsted, P. & Pachter, L. Near-optimal probabilistic RNA-seq quantification. *Nat. Biotechnol.* **34**, 525–527 (2016).
75. Stegle, O., Parts, L., Piipari, M., Winn, J. & Durbin, R. Using probabilistic estimation of expression residuals (PEER) to obtain increased power and interpretability of gene expression analyses. *Nat. Protoc.* **7**, 500–507 (2012).
76. Speed, D., Holmes, J. & Balding, D. J. Evaluating and improving heritability models using summary statistics. *Nat. Genet.* **52**, 458–462 (2020).
77. Purcell, S. et al. PLINK: a tool set for whole-genome association and population-based linkage analyses. *Am. J. Hum. Genet.* **81**, 559–575 (2007).

78. Endelman, J. B. Ridge regression and other kernels for genomic selection with R package rrBLUP. *Plant Genome* **4**, 250–255 (2011).
79. Kearse, M. et al. Geneious Basic: an integrated and extendable desktop software platform for the organization and analysis of sequence data. *Bioinformatics* **28**, 1647–1649 (2012).

Acknowledgements

We thank N. Stein, M. Mascher and J. Giovannoni for comments and advice; G. Zhu for providing metabolite data; and Q. Zhang for suggestions on the estimation of heritability. This work was supported by grants from the National Natural Science Foundation of China (no. 31991180 to S.H. and no. 31801441 to Y. Zhou), the National Key Research and Development Program of China (no. 2019YFA0906200 to S.H.), the Key Research and Development Program of Guangdong Province (no. 2021B0707010005 to J.Z.), the Shenzhen Science and Technology Program (no. KQTD2016113010482651 to S.H.), the Agricultural Science and Technology Innovation Program (CAAS-ZDRW202103 to S.H.) and the US National Science Foundation (IOS-1855585 to Z.F.).

Author information

Author notes

1. These authors contributed equally: Yao Zhou, Zhiyang Zhang, Zhigui Bao

Authors and Affiliations

1. Shenzhen Branch, Guangdong Laboratory of Lingnan Modern Agriculture, Genome Analysis Laboratory of the Ministry of Agriculture and Rural Affairs, Agricultural Genomics Institute at Shenzhen, Chinese Academy of Agricultural Sciences, Shenzhen, China

Yao Zhou, Zhiyang Zhang, Zhigui Bao, Hongbo Li, Yaqing Lyu, Yanjun Zan, Yaoyao Wu, Lin Cheng, Yuhan Fang, Kun Wu, Hongjun Lyu & Sanwen Huang

2. Umeå Plant Science Center, Department of Forestry Genetics and Plant Physiology, Swedish University of Agricultural Sciences, Umeå, Sweden

Yanjun Zan

3. Key Laboratory of Biology and Genetic Improvement of Horticultural Crops of the Ministry of Agriculture, Sino-Dutch Joint Laboratory of Horticultural Genomics, and Institute of Vegetables and Flowers, Chinese Academy of Agricultural Sciences, Beijing, China

Jinzhe Zhang

4. Institute of Vegetables, Shandong Academy of Agricultural Sciences, Shandong Province Key Laboratory for Biology of Greenhouse Vegetables, Shandong Branch of National Improvement Center for Vegetables, Huang-Huai-Hai Region Scientific Observation and Experimental Station of Vegetables, Ministry of Agriculture and Rural Affairs, Jinan, China

Hongjun Lyu

5. State Key Laboratory of Agrobiotechnology, College of Horticulture, China Agricultural University, Beijing, China

Tao Lin

6. Boke Biotech, Wuxi, China

Qiang Gao

7. Boyce Thompson Institute, Cornell University, Ithaca, NY, USA

Surya Saha, Lukas Mueller & Zhangjun Fei

8. Robert W. Holley Center for Agriculture and Health, US Department of Agriculture, Agricultural Research Service, Ithaca, NY, USA

Zhangjun Fei

9. Institute of Integrative Biology & Zurich, Basel Plant Science Center, ETH Zurich, Zurich, Switzerland

Thomas Städler

10. Department of Botany and Plant Sciences, University of California, Riverside, CA, USA

Shizhong Xu

11. Department of Crop and Soil Sciences, Washington State University, Pullman, WA, USA

Zhiwu Zhang

12. Quantitative Genetics and Genomics (QGG), Aarhus University, Aarhus, Denmark

Doug Speed

Contributions

S.H. and Y. Zhou conceived and designed the research. Y. Zhou, J.Z., Y.L., H. Lyu and Y.W. participated in the material preparation. S.S. and L.M. provided the Hi-C data of Heinz 1706. Y. Zhou, Z.B. and T.L. contributed to genome assembly. Z.B. contributed to genome annotation. Y. Zhou, Zhiyang Zhang and L.C. detected genetic variants. Y. Zhou and Z.B. constructed graph pangenome and annotation. Y. Zhou and Zhiyang Zhang performed gene expression and metabolites analysis. Y. Zhou, Z.B., Zhiwu Zhang, S.X. and D.S. contributed to heritability estimation and genome-wide association study. Zhiyang Zhang contributed to co-expression network analysis. Y. Zhou and Z.B. contributed to breeding analysis. Y. Zhou and Q.G. designed the SV panel of DNA capture array. K.W. and Y.W. provided metabolites

and QTL data. H. Li and Y.F. contributed to computational analysis. Y. Zan, Z.F. and T.S contributed to statistical analysis. D.S., T.S., Z.F., Zhiwu Zhang, S.X., Y. Zan, Y.F. and H. Li revised the manuscript. S.H., Y. Zhou and Zhiyang Zhang wrote the manuscript. S.H. supervised the research. All of the authors read, edited and approved the manuscript.

Corresponding author

Correspondence to [Sanwen Huang](#).

Ethics declarations

Competing interests

The authors declare no competing interests.

Peer review

Peer review information

Nature thanks Mathilde Causse, Erik Garrison and the other, anonymous, reviewer(s) for their contribution to the peer review of this work. [Peer reviewer reports](#) are available.

Additional information

Publisher's note Springer Nature remains neutral with regard to jurisdictional claims in published maps and institutional affiliations.

Extended data figures and tables

[Extended Data Fig. 1 Layout of the tomato graph pangenome study.](#)

a) Data used for constructing the tomato graph pangenome. **b**) Sketch of the tomato graph pangenome. **c**) Profiles of metabolome and transcriptome. **d–f**) Potential sources of missing heritability: incomplete linkage disequilibrium (**d**), allelic heterogeneity underlying gene expression (**e**), and locus heterogeneity represented in a co-expression network (**f**). Genes affecting the different steps of the same pathway might have the same effect on the final product. Yellow stars represent causal mutations. **g**) Practical application of genomic breeding such as genomic selection (GS), marker-assisted selection (MAS) and transgenic/gene editing.

Extended Data Fig. 2 Characteristics of tomato genome assemblies.

a) Hi-C heatmap of SL5.0. Darker red indicates higher contact probability. **b**) Structural variants between builds SL4.0 (blue) and SL5.0 (yellow). Insertions, deletions, duplications and inversions between SL4.0 and SL5.0 are labelled with unique colour for each type of variants. **c**) Benchmarking Universal Single-Copy Orthologs (BUSCO) evaluation for the tomato genome assemblies.

Extended Data Fig. 3 Read alignments to the graph pangenome and the linear genome.

Visualization of alignments of the same reads in a region by Geneious software⁷⁹ to compare differences between the graph mapper (Giraffe) (**a**) and the linear mapper (bwa) (**b**). An 81-bp deletion can be detected accurately in the graph pangenome, but soft-clipped sequences are detected in the linear genome with five false-positive SNPs (indicated by red stars).

Extended Data Fig. 4 Evaluation of contributions to heritability by different variant types.

a) Comparison of heritability estimated from different combinations of genetic variants from SL5.0-332 and TGG1.1-332. **b**) Comparison of estimated heritability based on SNPs of different groups. n = 6,375 independent traits (**a, b**) were evaluated. ‘Overlapping’ refers to SNPs found

in both TGG1.1-332 and SL5.0-332. ‘Unique’ refers to SNPs uniquely identified in either TGG1.1-332 or SL5.0-332. Box and whisker plots (**a, b**) with centre line = median, cross = mean, box limits = upper and lower quartiles, whiskers = $1.5 \times$ interquartile range and solid points = outliers. **c**) Heritability contributed by different variant categories using a composite model.

[Source data](#)

[Extended Data Fig. 5 Gene structure of *Solyc03G002957*.](#)

a) Different gene structures of *Solyc03G002957*; gene structures from three assemblies (TS12, SL5.0, and PP) are represented. The 2,628-bp deletion occurs at the end of the transcript. The 8,681-bp deletion in the LTR region results in a different annotation at the 3' end of the transcript. **b)** Graph representation of adjacent regions of *Solyc03G002957*. The graph was generated from the 46 assemblies shown in c). **c)** Linear representation of regions adjacent to *Solyc03G002957*. Multiple alignment of all assemblies was performed using pggb (<https://github.com/pangenome/pggb>). The 8,681-bp deletion in the LTR region exists in all assemblies harbouring the haplotype with the 2,628-bp deletion. Furthermore, the multiallelic LTR deletion is represented in TGG1.1 but was filtered out in TGG1.1-332 due to low frequency, implying the potential for further improvements in genotyping multiallelic SVs using short reads.

[Extended Data Fig. 6 Integrated genome viewer of gene models according to SL5.0 and SL4.0.](#)

This gene was misannotated as two separate genes in ITAG 4.0, possibly due to an LTR/Gypsy retrotransposon (12,295 bp) at the sixth intron. Blue and green lines with mRNA IDs shown represent the complete gene structure. UTRs are illustrated by thin bars, ORFs by thick bars and introns by thin lines. Arrowheads within the bars indicate transcriptional orientation. RNA-seq reads mapped to *Solyc03G002957* in SL5.0 are shown in the lower part of this figure.

[Extended Data Fig. 7 Allelic and locus heterogeneity in GWAS.](#)

a) Comparison of heritability estimated from leading significant variants (if present) and all genetic variants in the *cis* regions (within 50 kb upstream and downstream of a gene) for all expressed genes. If no significant variants are detected, $\langle\{h\}_{\{\text{cis}\}}; \text{gwas}\}^2\rangle$ is zero. **b)** Box plots of best linear unbiased prediction (BLUP) for the expression of *Solyc03G001472* in different genotypes of the two significant SVs. n represents number of accessions of each group. The total sample size is 331 (only groups with at least three accessions were analysed). The *P*-value was calculated from Kruskal-Wallis rank sum test. Box and whisker plots with centre line = median, cross = mean, box limits = upper and lower quartiles, whiskers = $1.5 \times$ interquartile range and solid points = outliers. **c)** Heritability of gene expression contributed by different types of variants (SNPs, indels and SVs) within module and non-module genes in a composite model.

[Source data](#)

[Extended Data Fig. 8 Co-expression network of expressed genes.](#)

The hub genes of each module (a total of 99) are visually magnified and coloured in black and non-hub genes are coloured in grey. The soluble solids content (SSC) and flavonoid module genes are coloured in blue and red, respectively. There are 5,520 expressed genes in the network with 190,606 links (threshold > 0.05).

Supplementary information

[Supplementary Information](#)

Supplementary Methods and Results are provided within Supplementary Notes 1–9 and Supplementary Figs. 1–20.

[Reporting Summary](#)

[Peer Review File](#)

[Supplementary Tables 1–16.](#)

Source data

[Source Data Fig. 1](#)

[Source Data Fig. 2](#)

[Source Data Fig. 3](#)

[Source Data Fig. 4](#)

[Source Data Extended Data Fig. 4](#)

[Source Data Extended Data Fig. 7](#)

Rights and permissions

Open Access This article is licensed under a Creative Commons Attribution 4.0 International License, which permits use, sharing, adaptation, distribution and reproduction in any medium or format, as long as you give appropriate credit to the original author(s) and the source, provide a link to the Creative Commons license, and indicate if changes were made. The images or other third party material in this article are included in the article's Creative Commons license, unless indicated otherwise in a credit line to the material. If material is not included in the article's Creative Commons license and your intended use is not permitted by statutory regulation or exceeds the permitted use, you will need to obtain permission directly from the copyright holder. To view a copy of this license, visit <http://creativecommons.org/licenses/by/4.0/>.

[Reprints and Permissions](#)

About this article

[**Cite this article**](#)

Zhou, Y., Zhang, Z., Bao, Z. *et al.* Graph pangenome captures missing heritability and empowers tomato breeding. *Nature* **606**, 527–534 (2022). <https://doi.org/10.1038/s41586-022-04808-9>

- Received: 04 October 2021
- Accepted: 27 April 2022
- Published: 08 June 2022
- Issue Date: 16 June 2022
- DOI: <https://doi.org/10.1038/s41586-022-04808-9>

Share this article

Anyone you share the following link with will be able to read this content:

[Get shareable link](#)

Sorry, a shareable link is not currently available for this article.

[Copy to clipboard](#)

Provided by the Springer Nature SharedIt content-sharing initiative

[**Genome evolution and diversity of wild and cultivated potatoes**](#)

- Dié Tang
- Yuxin Jia
- Sanwen Huang

Nature Article Open Access 08 Jun 2022

This article was downloaded by **calibre** from <https://www.nature.com/articles/s41586-022-04808-9>

- Article
- Open Access
- [Published: 08 June 2022](#)

Genome evolution and diversity of wild and cultivated potatoes

- [Dié Tang](#),
- [Yuxin Jia](#),
- [Jinzhe Zhang](#),
- [Hongbo Li](#),
- [Lin Cheng](#),
- [Pei Wang](#),
- [Zhigui Bao](#),
- [Zhihong Liu](#),
- [Shuangshuang Feng](#),
- [Xijian Zhu](#),
- [Dawei Li](#),
- [Guangtao Zhu](#),
- [Hongru Wang](#),
- [Yao Zhou](#),
- [Yongfeng Zhou](#),
- [Glenn J. Bryan](#),
- [C. Robin Buell](#),
- [Chunzhi Zhang](#) &
- [Sanwen Huang](#)

[Nature](#) volume 606, pages 535–541 (2022)

- 14k Accesses
- 1 Citations
- 270 Altmetric

- [Metrics details](#)

Abstract

Potato (*Solanum tuberosum* L.) is the world's most important non-cereal food crop, and the vast majority of commercially grown cultivars are highly heterozygous tetraploids. Advances in diploid hybrid breeding based on true seeds have the potential to revolutionize future potato breeding and production^{1,2,3,4}. So far, relatively few studies have examined the genome evolution and diversity of wild and cultivated landrace potatoes, which limits the application of their diversity in potato breeding. Here we assemble 44 high-quality diploid potato genomes from 24 wild and 20 cultivated accessions that are representative of *Solanum* section *Petota*, the tuber-bearing clade, as well as 2 genomes from the neighbouring section, *Etuberosum*. Extensive discordance of phylogenomic relationships suggests the complexity of potato evolution. We find that the potato genome substantially expanded its repertoire of disease-resistance genes when compared with closely related seed-propagated solanaceous crops, indicative of the effect of tuber-based propagation strategies on the evolution of the potato genome. We discover a transcription factor that determines tuber identity and interacts with the mobile tuberization inductive signal SP6A. We also identify 561,433 high-confidence structural variants and construct a map of large inversions, which provides insights for improving inbred lines and precluding potential linkage drag, as exemplified by a 5.8-Mb inversion that is associated with carotenoid content in tubers. This study will accelerate hybrid potato breeding and enrich our understanding of the evolution and biology of potato as a global staple food crop.

Main

Potato (*Solanum tuberosum* L.) belongs to the *Petota* section of the *Solanum* genus within the Solanaceae family, which contains many economically important species⁵. The *Petota* section consists of more than 100 tuber-bearing species, and is sister to the non-tuber-bearing *Etuberosum* section and the *Lycopersicon* section that comprises tomato species⁵. Commercial production of potato is dominated by autotetraploid cultivars that are

propagated using seed tubers. Reinventing potato from a clonally propagated tetraploid to a true seed-propagated diploid has the potential to considerably accelerate genetic improvement, and would enable the genome design of a crop that has been highly recalcitrant to the use of molecular breeding and genomics approaches^{3,6,7}. Diploid potatoes represent around 70% of the wild and landrace potato species⁵, and the vast diversity among them has not been fully characterized or made use of in previous breeding programs. Furthermore, the effects of the evolution of a clonal reproduction strategy on potato genomes and the evolutionary mechanisms of tuberization are largely unexplored. So far, several potato genome sequences have been released, which have been important resources for genetics and breeding^{3,8,9,10,11,12,13}. However, the minor portion of biodiversity in the *Petota* section that is captured by these genomes is insufficient to obtain a comprehensive understanding of the potato genome and tuber evolution. Here we report genome sequences and analyses of 44 diploid potatoes, as well as 2 species in the *Etuberosum* section. Our findings provide insights into the alteration of potato genomes during the evolution of tuberization, and will enable genome design for new diploid hybrids.

Pan-genome of the *Petota* section

To capture the genome diversity of the *Petota* section, we selected 44 representative accessions based on the phylogenetic relationships of 432 accessions^{7,14,15} (Supplementary Fig. 1). These comprise 20 landraces, covering 5 indigenous cultivated diploid groups (landrace), 4 accessions from *Solanum clevelandii* (CND), which is considered the progenitor of cultivated potatoes, and another 20 wild potato species (4 from clades 1 and 2; 16 from clades 3 and 4, as defined in a previous study⁵) (Supplementary Table 1). We generated an average of 24.5 Gb (approximately 30-fold relative to the estimated haploid potato genome size of around 800 Mb) high-fidelity (HiFi) reads for the 44 accessions (Supplementary Table 1); these were de-novo-assembled into raw assembled contigs with heterozygous regions retained and into monoploid assembled contigs (MTGs), with average N50 contig sizes of 9.10 Mb and 23.33 Mb, respectively (Extended Data Fig. 1a,b, Extended Data Fig. 2, Supplementary Figs. 2 and 3 and Supplementary Table 1). Among these, seven

representative genomes were assembled to chromosome level using high-throughput chromatin conformation capture (Hi-C)^{16,17} sequencing data (Supplementary Fig. 4). The raw assembly size ranged from 835.1 Mb (A6-26) to 1.71 Gb (PG6246) (Extended Data Fig. 1a); this is positively correlated to the estimated heterozygosity, which was determined using k -mer-based methods ($R^2 = 0.47$, $P = 2.5 \times 10^{-7}$) (Extended Data Fig. 1c). The completeness of assemblies was supported by BUSCO¹⁸, with an average score of 96.58% (single-copy and duplicated) in raw assembled contigs and 96.12% in MTGs (Supplementary Table 1). We predicted 44,859 (A6-26) to 88,871 (PG6002) gene models by integrating transcriptome evidence, homology-based prediction and ab initio prediction (Supplementary Table 1).

To build a comprehensive gene repertoire within the *Petota* section, we constructed a pan-genome by clustering the 2,701,787 predicted gene models from the 44 accessions and the reference genome of *S. tuberosum* Group Phureja (accession DM1-3 516 R44; hereafter referred to as DM)^{8,11} into 51,401 pan-gene clusters using the Markov clustering algorithm¹⁹. Pan-genome size increased when incorporating more genomes and nearly reached a plateau when n was close to 40 (Extended Data Fig. 1d), which suggests that our panel captures the shared gene content of potato. We next classified these clusters into four categories based on their frequency of occurrence: core clusters (present in all 45 accessions; 13,123; 25.5%), soft-core clusters (present in 42–44 accessions; 5,743; 11.2%), shell clusters (found in 2–41 individuals; 28,471; 55.4%) and accession-specific clusters (4,064; 7.9%) (Extended Data Fig. 1d, Supplementary Table 2 and Methods). A total of 89.9% and 80.7% of core and soft-core genes could be assigned to protein domains in the InterPro database—percentages nearly twice as high as those for shell and accession-specific genes (43.9% and 44.3%, respectively) (Extended Data Fig. 1e). The core and soft-core genes were expressed on average at a 2.2-fold higher level than the shell and accession-specific genes (Extended Data Fig. 1f), and showed markedly lower (1.7-fold on average) pairwise non-synonymous/synonymous substitution ratios (K_a/K_s) than did the shell genes (Extended Data Fig. 1g), suggestive of functional conservation. Functional enrichments of protein domains annotated in the InterPro database indicated that core and soft-core genes were enriched for domains that encode a wide range of functions

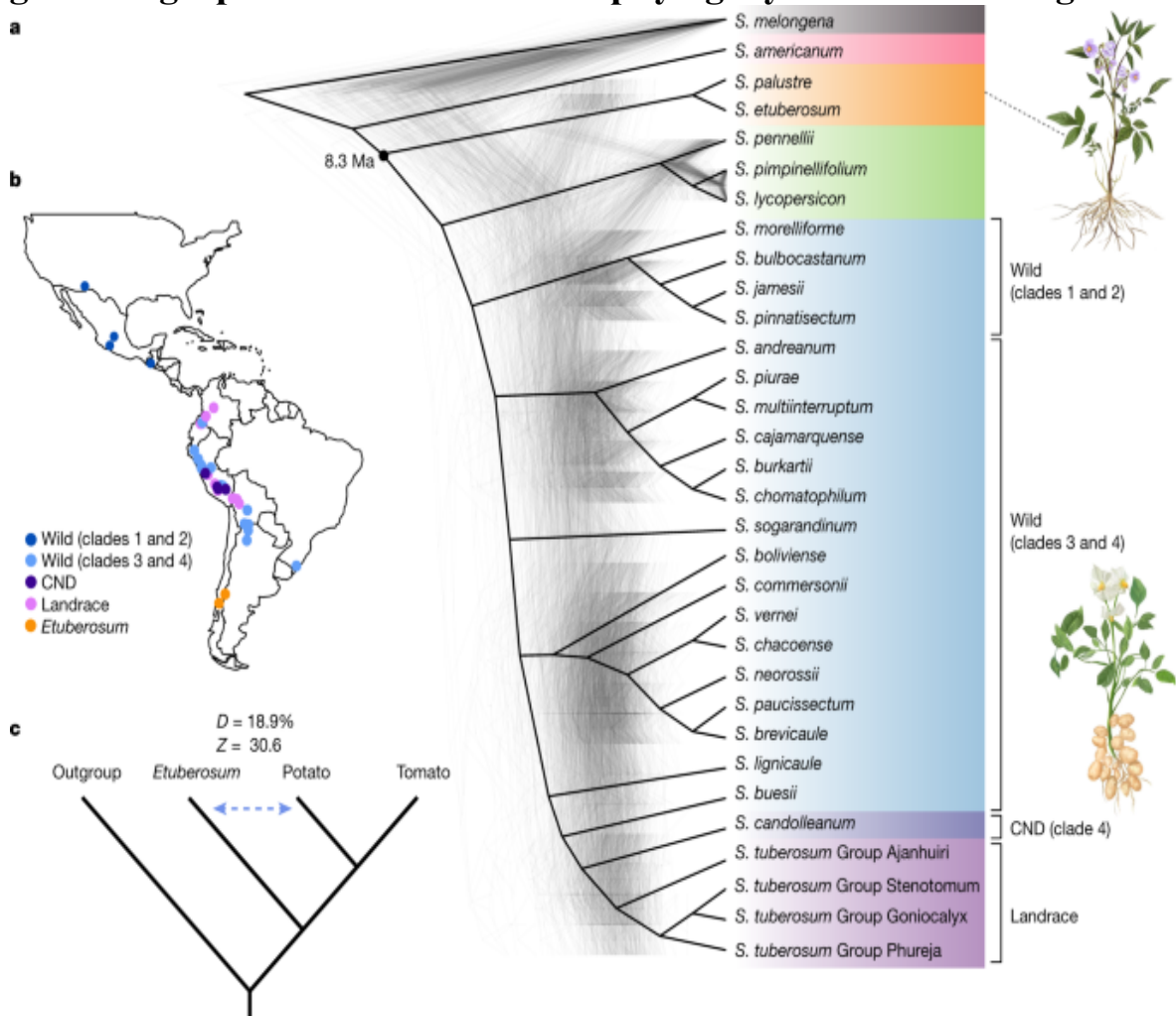
involved in plant growth and development (Extended Data Fig. [1h,i](#)), whereas domains related to retrotransposons and disease resistance were significantly enriched in shell and accession-specific genes (Extended Data Fig. [1h,i](#)). These pan-genome resources provide a starting point from which to leverage the section-wide gene pool in potato biology and breeding.

Phylogeny of *Petota* and neighbouring species

Owing to the lack of appropriate reference genomes, the evolutionary relationship among *Petota* and its sister sections *Lycopersicon* and *Etuberosum* is controversial^{[20,21](#)}. Potato stolons are underground shoots or stems that are capable of bearing tubers^{[22](#)}, whereas *Etuberosum* species generate rhizomes resembling potato stolons, which grow upwards to form new daughter plants^{[23,24](#)} (Supplementary Fig. [5](#)). *Lycopersicon* species lack both rhizomes and stolons; thus, we hypothesized that *Etuberosum* is sister to *Petota* and *Lycopersicon* is the outgroup. To infer the evolutionary relationship among *Petota*, *Etuberosum* and *Lycopersicon*, we sequenced and de-novo-assembled two *Etuberosum* species—*Solanum etuberosum* and *Solanum palustre*—using PacBio continuous long reads; this resulted in 684.6-Mb and 738.9-Mb assemblies with contig N50 sizes of 3.9 Mb and 2.5 Mb, respectively. The completeness of these assemblies was estimated to be 95.6% and 95.6% by BUSCO (Supplementary Table [1](#)).

By applying super-matrix and multispecies coalescent methods^{[25](#)}, we inferred a bifurcating species tree of 22 species from *Petota*, 2 from *Etuberosum* and 3 from *Lycopersicon*, as well as 2 outgroup species (*Solanum melongena* and *Solanum americanum*). The tree topologies were congruent, at major internal nodes, using both approaches (Fig. [1a](#), Extended Data Fig. [3a,b](#) and Supplementary Table [3](#)). We also estimated that *Etuberosum* diverged from the common ancestor of *Lycopersicon* and *Petota* at 8.30 million years ago (Ma; 95% highest posterior density interval: 7.9–8.8 Ma) (Supplementary Fig. [6](#)). These results suggest that, with the genomic data that are available at present, *Etuberosum* is sister to the common ancestor of tomato and potato—in contrast to the hypothesis that *Etuberosum* is evolutionarily more closely related to *Petota* than *Lycopersicon*.

Fig. 1: Geographical distribution and phylogeny of the *Solanum* genus.



a, Five hundred phylogenetic window trees (light grey lines) were randomly selected for visualization from 100-kb non-overlapping regions across the genome. The main cladogram shown here was built from 3,971 single-copy genes, based on 29 species (32 accessions, in which 4 are from *S. tuberosum*) (Supplementary Table 1). The number labelled beside the tree indicates the estimated divergence time. The pictures illustrate the morphological differences of tuber-bearing and non-tuber-bearing species. **b**, Geographical origin of 39 samples (Supplementary Table 1) for which the longitude and latitude information are available. The base map was generated using the function `mapBubbles()` in the R package `rworldmap`. **c**, ABBA-BABA analysis of gene flow between *Petota* and *E. tuberosum* species. Significant introgression events are detected between *Petota* and *E. tuberosum*.

Source data

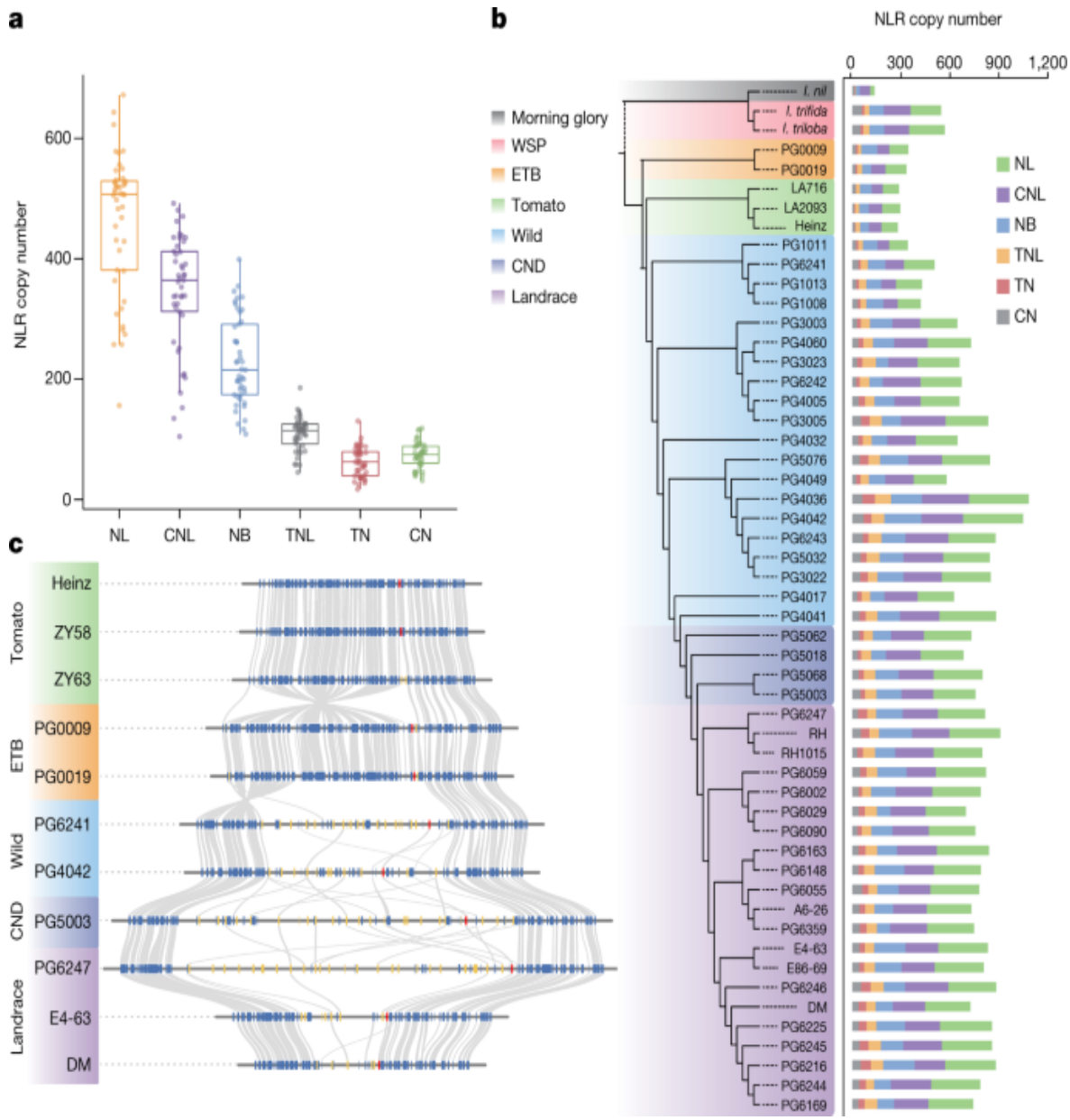
Phylogenetic topologies that are based on a single gene or genomic region may disagree with species topologies that are inferred from whole-genome markers²⁶. We then split whole-genome alignments into 100-kb non-overlapping windows and applied phylogenetic inference for each window. This resulted in 1,899 trees with distinct topologies (Supplementary Tables 4 and 5), which suggests the widespread phylogenetic discordance of tree topology across the genome. Of these, 334 (17.6%) supported *Etuberosum* being a sister clade to *Petota* (Fig. 1a and Extended Data Fig. 3c). Given the recent divergence among *Petota*, *Etuberosum* and *Lycopersicon*, the lineage sorting processes might be incomplete among species in these sections. We observed 21.6–24.7% of the potato genome exhibiting incomplete lineage sorting (ILS) by comparing allele frequencies using a previously described method²⁷. Interspecific hybridization has been prevalent among evolutionarily closely related species²⁸. Using D statistics²⁸, we detected gene flow between the species in *Petota* and *Etuberosum* sections ($D = 18.9\%$, $Z = 30.6$; Fig. 1c), and f_4 -ratio statistics²⁸ showed that 8.4% of the potato genome showed admixture between *Petota* and *Etuberosum*. Similarly, we also observed the existence of ILS (Supplementary Fig. 7) and frequent gene flow (Extended Data Fig. 3d and Supplementary Fig. 8) among species within *Petota*, which was also reported in a previous study⁵, and these may contribute to a lack of topological consensus of their evolutionary relationships (Fig. 1a). The pervasive inter- and intra-section phylogenetic discordance that we describe here suggests that potato evolution has a complex history that includes ILS and interspecific hybridization.

Expansion of the repertoire of resistance genes

Clonal propagation gave rise to the emergence of tuber-borne diseases; potato has possibly evolved an expanded repertoire of resistance genes against these diseases²⁹, which might alter the genetic landscape of the potato immune system. Genes that encode nucleotide-binding domain and leucine-rich repeat (NLR) proteins have pivotal roles in plant immune signalling³⁰. An accurate understanding of NLR evolution in potato species

requires a comprehensive NLR dataset. However, plant NLRs occur mainly in genomic clusters, which makes their annotation challenging when using conventional approaches³¹. To mitigate this problem, we developed an ‘NLR local annotation’ pipeline and benchmarked it with a tomato NLR dataset, based on resistance gene enrichment sequencing (RenSeq), resulting in comparable numbers of NLRs (Methods and Supplementary Fig. 9). This resulted in 57,683 NLR genes, with the NLR copy number varying greatly among potato species—from 478 in *Solanum morelliforme* (PG1011) to 1,976 in *Solanum chacoense* (PG4042)—implying that immune systems in potato species have a diverse evolutionary history (Fig. 2a, Extended Data Fig. 4 and Supplementary Table 6).

Fig. 2: Evolution of resistance genes in potato.



a, Canonical NLR copy number in potato. The upper and lower edges of the boxes represent the 75% and 25% quartiles, the central line denotes the median and the whiskers extend to 1.5 times the interquartile range (IQR). NL, NB-LRR; CNL, CC-NB-LRR; TNL, TIR-NB-LRR; TN, TIR-NB; CN, CC-NB; NB, NB domain only (see ‘Reannotation and classification of nucleotide-binding resistance genes’ in the Methods for detailed definitions of the abbreviations). Each NLR class contains 45 potato genomes. ETB, *Etuberosum*; WSP, wild relatives of sweet potato. **b**, Comparison of NLR copy numbers among different accessions. The NLRs from the potato monoploid assembled contigs were kept. The various colour backgrounds

indicate accessions from different clades. **c**, Synteny plots of the *R3a* locus from 11 representative accessions. Red boxes indicate *R3a* orthologues in each accession. Yellow boxes indicate for NLR gene models and blue boxes denote other genes. Grey lines identify syntenic gene pairs.

Source data

We predicted 280–344 NLRs in the *Etuberosum* and tomato genomes and observed a significant expansion of NLRs in the potato MTG assemblies (Fig. [2b](#)). We next classified NLRs from *Etuberosum*, tomato and potato, as well as 29 functionally validated NLRs, into 424 clusters, and identified 161 clusters that were putatively expanded in potato (Wilcoxon rank-sum test, $P < 0.05$; Supplementary Table [2](#)). These clusters include some well-studied potato R gene families that confer resistance to the devastating late blight pathogen *Phytophthora infestans*, such as *R3a* (Fig. [2c](#) and Supplementary Fig. [10](#)). We identified 19,241 potato-specific NLRs that are present in potato, but absent in tomato and *Etuberosum*, and around 31.4% of them were expressed in stolon or tuber, suggesting that these may contribute to protecting stolons or tubers from pathogen infection (Supplementary Table [8](#)).

Notably, we observed a similar NLR expansion event in wild relatives of the cultivated sweet potato, *Ipomoea trifida* and *Ipomoea triloba* (547 and 569 NLR genes, respectively), which are able to propagate clonally^{[32](#)}, as compared with Japanese morning glory, *Ipomoea nil* (138 NLR genes) (Fig. [2b](#) and Supplementary Table [9](#)). *I. nil* did not have a vegetative reproduction organ^{[33](#)}, and diverged from *I. trifida* around 6.4 Ma (ref. [34](#)), a similar time point to that at which potato and tomato diverged (around 7.3 Ma)^{[35](#)}, which suggests that an expansion of the NLR repertoire might have co-evolved with the emergence of a vegetative mode of propagation.

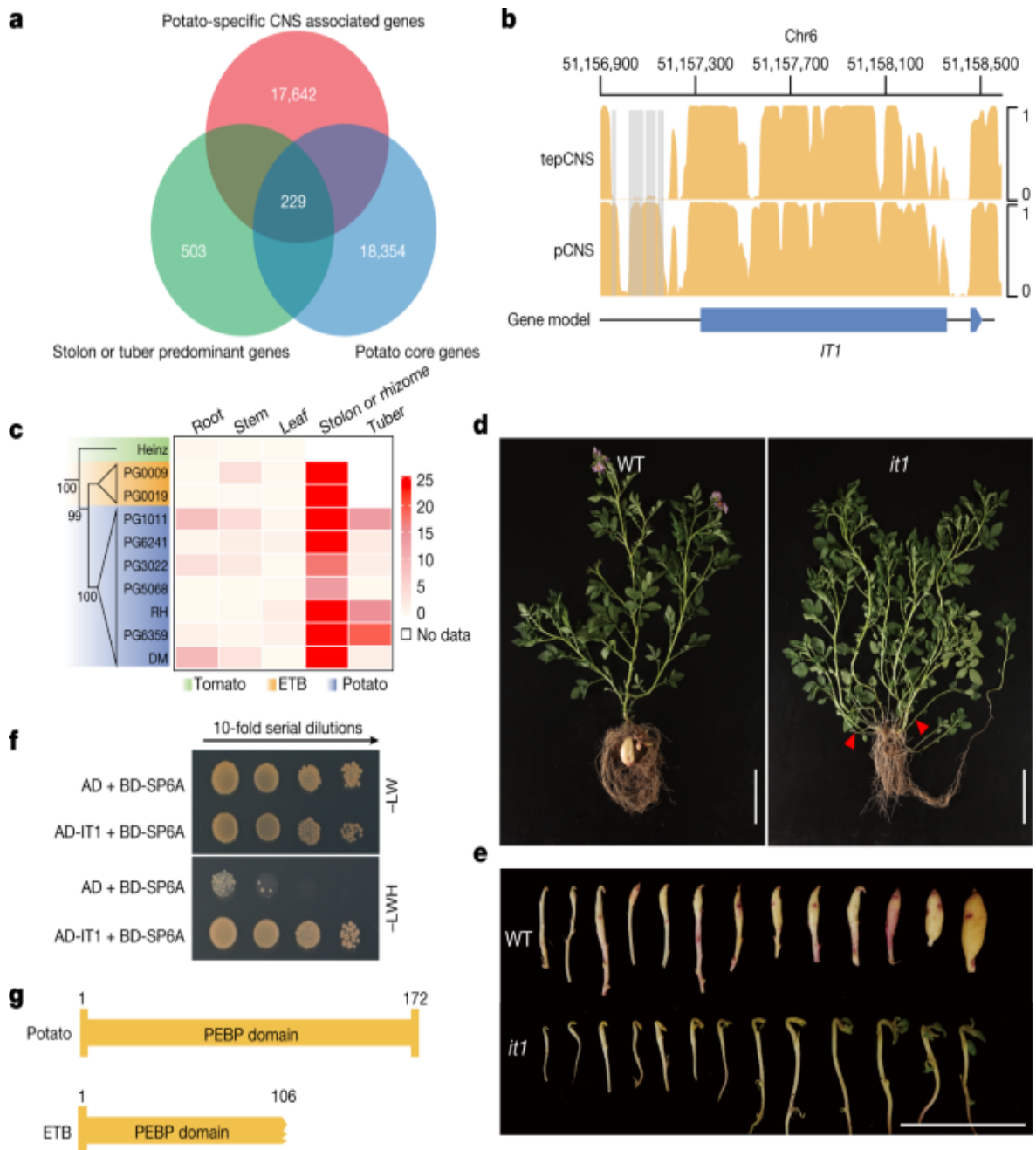
Tuber identity gene

The tuber, a storage and reproductive organ that confers a distinctive survival advantage to potato^{[36](#)}, has recently evolved throughout the divergence between tomato and potato. Despite some advances in our understanding of tuber development^{[8,37](#)}, insights into the evolution of tubers

remain elusive. Previous studies have reported that potato recruited existing genes for new pathways that contributed to tuberization, suggestive of newly evolved *cis*-regulatory elements (CREs). Given the key role of conserved non-coding sequences (CNSs), which function as CREs in regulating gene expression and organogenesis^{38,39}, we identified 149,663 potato-specific CNSs (6.9 Mb) by computing conservation scores, based on whole-genome alignment, using genome sequences of 45 potatoes (including DM), 24 tomatoes and 2 *E.tuberosum* species. A total of 54.4% of these CNSs were localized at introns, followed by promoters (18.4%), intergenic regions (14.7%), downstream regions (5.0%), 3'-untranslated regions (3'UTRs; 4.4%) and 5'-UTRs (3.0%), which could potentially affect the expression of 17,871 genes (Extended Data Fig. [5a–c](#) and Supplementary Table [10](#)).

To identify candidate pivotal genes that are involved in tuber development, we identified 732 genes that are predominantly expressed in the stolon or tuber, among which 229 were associated with potato-specific CNSs and are also conserved among the 45 potato accessions (Fig. [3a](#) and Supplementary Table [11](#)). These genes encompassed 28 transcription factors, of which only one belongs to the plant-specific TCP transcription factor family (*Soltu.DM.06G025210*) (Extended Data Fig. [5d](#)). Previous studies revealed that the TCP family is involved in the regulation of plant axillary meristem development; for example, rice tillering, maize branching and the development of cucumber tendrils^{40,41}. The associated CNSs of this TCP were found in the –376 bp to –157 bp upstream from its start codon (Fig. [3b](#) and Supplementary Fig. [11](#)), suggesting putative regulatory roles in the TCP expression. Furthermore, transcriptomic data indicated that this gene was predominantly expressed in potato stolons (Fig. [3c](#)), whereas the expression of its tomato orthologue (*Solyc06g069240.2*) could barely be detected. These findings suggest that recruitment and neofunctionalization of this gene may coincide with the emergence of tuber-bearing traits in the divergence of tomato and potato lineages.

Fig. 3: Identification of a potato tuber identity gene.



a, Venn diagram describing the identification of 229 candidate genes that are involved in regulating stolon or tuber development. **b**, Conserved CNSs around the *Identity of Tuber1 (IT1)* locus. tepCNS, conservative score for each site calculated from tomato, *Etuberosum* and potato genomes; pCNS, conservative score for each site calculated from 45 potato genomes. Grey blocks show potato-specific CNSs. **c**, Expression pattern of *IT1* and its orthologues in five tissues of *Etuberosum*, tomato and potato species. The 5-kb sequences up- and downstream of *IT1* from tomato, *Etuberosum* and

potato were used to infer the phylogenetic relationships. **d**, Phenotypes of the *it1* knockout mutant. Red arrowheads indicate several abnormally developed stolons in the *it1* mutant. Scale bars, 10 cm. WT, wild type. **e**, Comparison of potato tuber development between wild type and the *it1* mutant. Scale bar, 5 cm. **f**, IT1 directly interacts with SP6A, as validated in a yeast-two-hybrid assay. Three independent biological experiments were performed. **g**, Domain architecture of SP6A in potato and *Etuberosum* species. AD, Gal 4 activation domain; BD, Gal4 DNA-binding domain; -LW, synthetic dropout medium without Leu and Trp; -LWH, synthetic dropout medium without Leu, Trp and His.

Source data

To examine the function of *Soltu.DM.06G025210*, we generated knockout mutants by CRISPR–Cas9-based genome editing in the diploid *S. tuberosum* Group Phureja S15-65 clone (Extended Data Fig. [6a](#)). The stolons of mutants were converted into branches, instead of swelling at the sub-apical region, during tuber initiation (Fig. [3d,e](#)). Only under suitable growth conditions, and for a sufficient time, could the mutants generate a few small tubers (Extended Data Fig. [6b](#)). These data suggest that *Soltu.DM.06G025210* is key to the initiation of potato tubers; we therefore named this gene *Identity of Tuber 1* (*IT1*).

Of note, a similar non-coding sequence (identity 94.6%) was identified upstream of *IT1* orthologues in the genomes of *Etuberosum* species (*IT1^{etb}*), which are not capable of bearing tubers^{[23](#)} (Supplementary Fig. [5](#)). We then noted that *IT1^{etb}* was highly expressed in the rhizomes of *Etuberosum* species (Fig. [3c](#)), which implies that *IT1* collaborates with additional genes in regulating tuber initiation, the functions of which may have been lost in *Etuberosum*.

We next performed yeast-two-hybrid library screening to identify putative *IT1* interactors. Notably, SELF-PRUNING 6A (SP6A), the vascular-mobile signal in tuberization^{[42](#)}, was identified as interacting with *IT1*; this finding was further verified by firefly luciferase complementation imaging assays (Fig. [3f](#) and Extended Data Fig. [7a](#)), and suggests that SP6A and *IT1* might act as a protein complex in regulating tuber initiation. We then analysed *SP6A* sequence variations in potato and *Etuberosum* genomes and found that

the fourth exon in *SP6A*^{etb} was deleted, leading to an impaired phosphatidylethanolamine-binding protein (PEBP) domain (Fig. 3g and Extended Data Fig. 7b,c). Furthermore, quantitative PCR analyses did not detect any expression of *SP6A* in *Etuberosum* leaves, under either long-day or short-day conditions (Extended Data Fig. 7d). These data suggest that the impaired function of *SP6A* may contribute to the non-tuber-bearing phenotype of *Etuberosum*. Further phylogenetic analysis, using 5 kb up- and downstream sequences of *IT1*, revealed that *Etuberosum*—rather than *Lycopersicon*—was sister to potato species (Fig. 3c), suggesting that *Etuberosum* represents a transitional form during the evolution of tuberization.

Pan-genome-guided hybrid potato breeding

We previously developed the first generation of highly homozygous inbred potato lines using genome design, and the resultant hybrids showed strong heterosis^{3,43}. For successful hybrid potato breeding, more inbred lines of high homozygosity are essential, and the first set of inbred lines also require further improvement, for which this pan-genome map can offer critical guidance.

To survey the level of homozygosity of the accessions studied—a key parameter for selecting starting materials for the development of inbred lines—we localized our alternate assembled contigs (ATGs; heterozygous genomic segments) and MTGs to the DM reference genome, and defined heterozygous and homozygous regions, respectively. We found that the length of heterozygous regions varied in the 41 accessions from 103 Mb (PG1011) to 710 Mb (PG5068) (excluding inbred lines; Extended Data Fig. 8a and Supplementary Table 12). Within these heterozygous regions, we found 208–13,364 hemizygous genes in the 41 potato accessions, accounting for 0.5%–18.3% of predicted protein-coding genes, which was positively correlated to the estimated heterozygosity ($R^2 = 0.69$, $P = 1.85 \times 10^{-11}$; Supplementary Table 13). The distribution of homozygous genomic segments is a key indicator for the absence of large-effect deleterious mutations, which are less likely to be retained in the homozygous state because they are mostly recessive. In the case of tight linkage of two or more large-effect deleterious mutations in repulsion phase, some

heterozygous segments will be retained in high-generation inbred lines^{3,12}. The map of homozygous segments and gene hemizygosity, presented here, therefore offers potential targets to replace the corresponding heterozygous segments in the development of inbred lines to be used for diploid hybrid breeding.

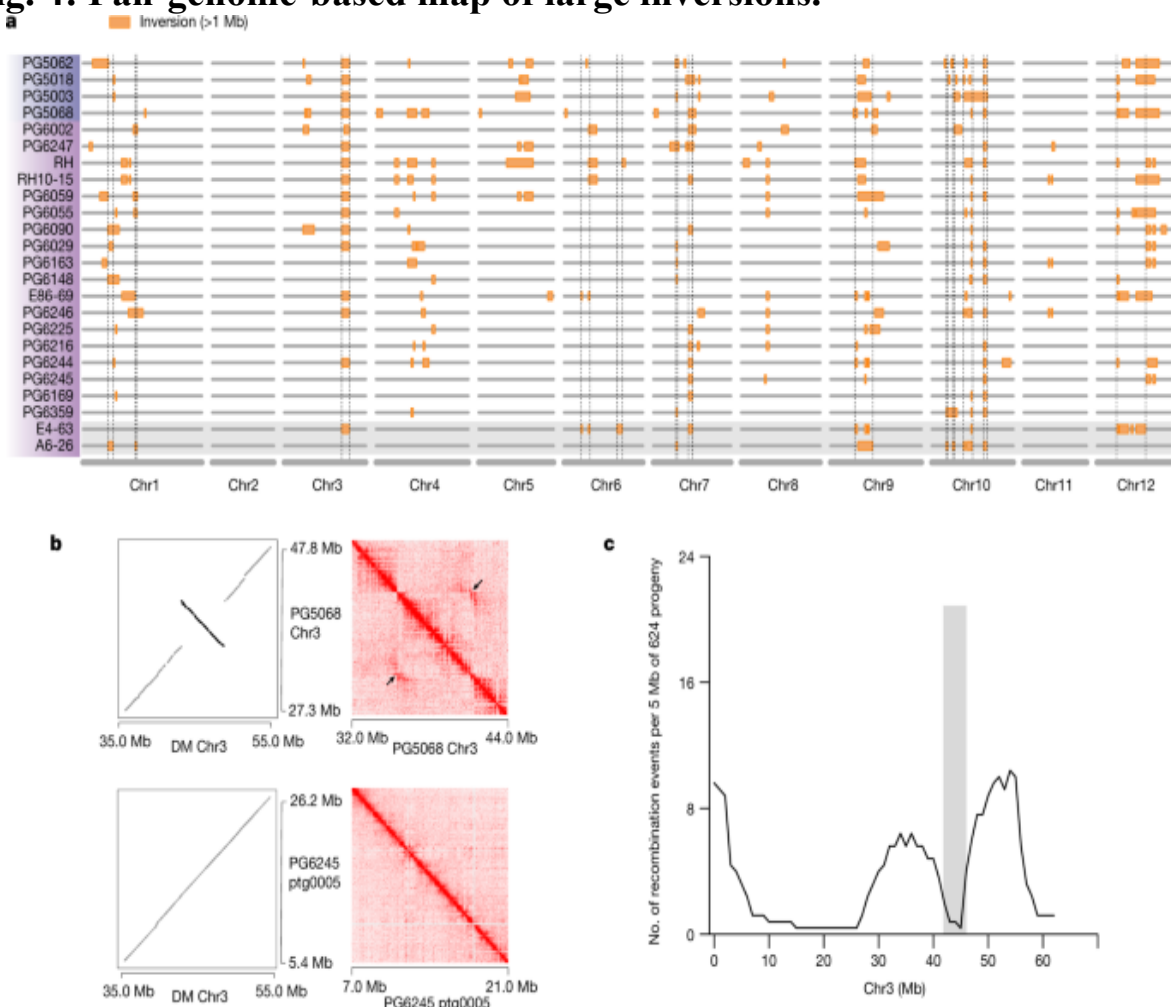
To assess the genomic divergence in *Petota*, we performed whole-genome alignments, using tomato as a control. Just 204.4 Mb (28.0% of the DM reference genome) of genomic regions shared in potato landraces were identified, in contrast to the markedly higher 675.8 Mb (87.0% of the Heinz 1706 reference genome) in cultivated tomatoes (Supplementary Table 14). The average proportion of syntenic genes among potato landraces (61.3%) was also considerably lower than that among cultivated tomatoes (91.0%; Supplementary Table 15 and Extended Data Fig. 8b,c). This indicates a loss of synteny in cultivated potatoes, a critical genomic feature with implications for hybrid breeding.

The accumulation of structural variations (SVs) may contribute to the loss of synteny. We next identified 561,433 high-confidence SVs (more than 50 bp in size), affecting 167 Mb of the DM reference genome, of which 55.5% were rare (minor allele frequency < 0.05; Extended Data Fig. 8d). SVs close to genes might lead to the alteration of expression levels⁴⁴. Most SVs (around 58.2% on average) were located in 5-kb upstream and downstream regions, followed by around 22.0% and around 13.4% overlapping intergenic and intron regions, whereas only around 6.4% affected exons (Extended Data Fig. 8e).

Among these, large inversions have been reported to suppress recombination by reducing crossing over⁴⁵; this results in severe linkage drag when conducting backcross breeding, a tool that is required to improve the first-generation inbred lines. To avoid this problem, it is necessary to select donor lines without inverted fragments that contain target genes. Therefore, we constructed a map of large-scale inversions among the 20 landraces and the 4 *S. candelleanum* accessions, comprising 224 identified inversions with sizes ranging from 1.0 Mb to 17.6 Mb (Fig. 4a). Notably, an approximately 5.8-Mb paracentric inversion on the long arm of chromosome 3 (DM chr03: 42.9–48.7 Mb)—validated by examining chromatin interaction intensity (Fig. 4b)—co-segregates with the Y locus that controls carotenoid content in

the tuber³ (yellow flesh colour), in an S₁ population of 624 individuals (Supplementary Table 16). Our analyses of genetic mapping, association study and gene expression (Extended Data Fig. 9), together with previous studies of gene silencing^{3,46,47}, indicate that *Soltu.DM.03G018410* defines the Y locus. *Soltu.DM.03G018410* encodes a β-carotene hydroxylase (BCH) that controls the accumulation of zeaxanthin, which confers yellow colour in tuber flesh⁴⁷. This gene was located around 1.5–2 kb proximal to the breakpoint of the 5.8-Mb inversion and is genetically inseparable with the inversion that contains 464 genes (Fig. 4c). Therefore, selection of individuals with yellow tuber flesh, a nutritional trait, may lead to severe linkage drag of unexpected phenotypes. With the aid of the constructed pan-genome-based inversion map, breeders could now select appropriate donor or acceptor lines for backcrossing.

Fig. 4: Pan-genome-based map of large inversions.



a, Inversion map of 20 landraces and 4 CND accessions. The orange rectangles denote megabase-scale inversions. The dashed lines mark the regions containing inversions presented in either E4-63 or A6-26. **b**, The Hi-C-validated 5.8 Mb inversion event, using DM as the reference genome. Hi-C contact maps at 25-kb resolution for accession PG5068 (wild/CND haplotype) and PG6245 (DM haplotype), using Hi-C data from the homozygous line A6-26 (DM haplotype). Wild/CND haplotype, accessions carrying the inversion; DM haplotype, accessions without the inversion. **c**, Number of recombination events per 5 Mb on chromosome 3. The grey bar indicates the region with reduced recombination around the 5.8-Mb inversion.

[Source data](#)

Discussion

The 44 high-quality genomes and the prevalent genetic variations identified herein offer useful resources for pan-genome-based potato breeding. These data are freely accessible through a comprehensive web-based Pan-Potato Database (<http://solomics.agis.org.cn/potato/>). The resources also enable the further construction of a pan-genome reference integrating the genomes and variants of the 44 diverse potato accessions, which has the potential to minimize the effect of reference bias. The discovery of IT1 and its interaction with the mobile tuberization signal, SP6A, will pave the way for further elucidation of the evolution of tuber development. We also noticed that functional complementation of *SP6A* in *Etuberosum* may not induce tuber formation, according to a study on potato and *Etuberosum* heterografts⁴⁸, which suggests that the IT1–SP6A complex is necessary but not sufficient for tuberization.

Geographical isolation between the North and South American continent may contribute to the species from clades 1 and 2 being the sister lineage to wild species in clades 3 and 4 and other landraces. This is supported by our genomic data (Fig. 1a). Previous reports indicated that diploid cultivated potatoes were domesticated from wild potatoes from clade 4 (refs. [14,15](#)). In this study, we also found that *S. candelleanum* is sister to cultivated potato, further supporting this species as the immediate progenitor of cultivated

potato. Further studies, coupled with the access to phased tetraploid potato assemblies, will allow the examination of introgression patterns from wild species, as introgression breeding was mainly conducted in these tetraploid cultivars. Considering that the endosperm balance number (EBN), a hypothetical unified prediction concept of crossability, between most of the wild species (17 out of 24) investigated here and the cultivated potatoes is the same (2EBN) (ref. ⁵), the pan-genome will motivate attempts for the introgression of favourable traits from these wild species to breed inbred lines with better disease resistance and stress tolerance.

Methods

Sample selection and sequencing

We selected 44 representative potato accessions, 3 of which are publicly accessible^{3,13}, on the basis of phylogenetic relationships of 432 accessions (PRJNA378971, PRJNA394943 and PRJNA766763; genotype information is available at http://solomics.agis.org.cn/potato/ftp/Genotype_432sp/; Supplementary Fig. 1). To infer the phylogeny of the 432 accessions, reads were mapped to the DM v4 reference genome using BWA (0.7.5a-r405)⁴⁹, and single-nucleotide polymorphisms (SNPs) were then extracted using SAMtools (v.1.9)⁵⁰ and BCFtools (v.1.9)⁴⁹. Fourfold degenerate SNPs with base quality ≥ 40 and mapping quality ≥ 30 were fed into IQ-TREE v.2.0.6 (ref. ⁵¹), with parameters ‘-st DNA -m 012345 -B 1000’. In addition, two non-tuber-bearing species from the *Etuberosum* section PG0019 (*S. etuberosum*) and PG0009 (*S. palustre*) were chosen to be used in phylogeny inference (Supplementary Table 1). Sequencing of these 44 potato accessions was performed on the Pacific Biosciences Sequel II platform, in the circular consensus sequencing (CCS) mode, and the two *Etuberosum* species were sequenced on the Pacific Biosciences Sequel II platform, in the continuous long read (CLR) mode. A total of 15.9–38.1 Gb of HiFi reads was generated using CCS (<https://github.com/PacificBiosciences/ccs>) for the 41 newly sequenced potato accessions. For the construction of Hi-C libraries, DNA was extracted from in vitro seedlings, of which PG5068, PG0019 and E86-69 were digested with the restriction enzyme MboI, and PG6359 was digested with HindIII using the previously described Hi-C

library preparation protocol⁵². These Hi-C libraries were sequenced on an Illumina HiSeq X Ten platform. The total RNA of 23 accessions (Supplementary Table 1) from the tissues of roots, stems, leaves, stolons, tubers and flowers was extracted for the library construction. These libraries were subsequently sequenced on the DNBSEQ-T7 system at Annoroad Gene Technology, which produced around 6 Gb data for each tissue in each sample.

De novo genome assembly of 44 potato and 2 *Etuberosum* accessions

Genome heterozygosity was estimated using a k -mer-based approach by GenomeScope2.0 (ref. ⁵³). Genomes of the 44 HiFi sequenced accessions were assembled by hifiasm⁵⁴ (<https://github.com/chhylp123/hifiasm>), using default parameters. The initial output of hifiasm (v.0.13) yielded a pair of assemblies: (1) the primary assembly (in hifiasm named p_ctg), representing a mosaic haplotype without purging; and (2) the alternate assembly (in hifiasm named a_ctg), which represents the alternate haplotype absent from the primary one. To facilitate downstream analyses, including inter-genomic alignment and comparison of gene copy numbers, we generated ‘monoploid’ genome assemblies, accompanied by their heterozygous assembled fragments. Haplotigs from the primary assembled contigs, with haplotypes collapsed (p_ctg.*), were then excluded using the purge_dups (v.1.01) software (https://github.com/dfguan/purge_dups) to generate the heterozygous-region-purged assemblies, which were then termed as monoploid assembled contigs (MTGs), indicative of monoploid genomes. The raw alternate assemblies from hifiasm (a_ctg.*), in addition to the contigs that have been removed by purge_dups, were concatenated as the alternate assembled contigs (ATGs) to be the heterozygous genomic segments (Supplementary Fig. 2). The two *Etuberosum* genomes PG0019 and PG0009 were assembled using CANU v1.8 (ref. ⁵⁵), and then two rounds of Pilon v.1.23 (ref. ⁵⁶) were applied for genome polishing, using available resequencing data. Pseudo-chromosomes of the seven potato accessions (A6-26, E4-63, PG6359, E86-69, RH, RH10-15 and PG5068) and one *Etuberosum* accession (PG0019) were built with Hi-C reads, using the Juicer (v.1.5) (ref. ⁵⁷) and 3D-DNA (v.180922) (ref. ⁵⁸) pipeline, with parameters ‘-m haploid -I 15000 -r 0’. The assembly completeness in genic

regions was evaluated using the solanales_odb10 database (for Solanaceae species) of BUSCO v.4.1.4 (ref. [18](#)), with default parameters.

Identification and annotation of repetitive elements

Transposable elements (TEs) were identified by the Extensive De-Novo TE Annotator (EDTA)^{[59](#)} v.1.9.4, and the non-redundant TE libraries for each accession were passed into RepeatMasker v.1.332 (<http://www.repeatmasker.org>) to mask potential genomic repeats together with simple repeats and satellites, by default parameters.

Prediction of protein-coding genes

Three distinct strategies, comprising ab initio prediction, homology search and expression evidence, were combined to generate the predicted gene models. HISAT2 (v.2.0.1-beta) (ref. [60](#)) was used to perform splice alignment of RNA-sequencing (RNA-seq) reads to the assembled genomes, with ‘--dta’ parameter. Potential transcripts were then assembled, using StringTie (v.1.3.3b) (ref. [61](#)) with parameter ‘--rf’. BRAKER2 v.2.1.6 (ref. [62](#)) was then run to use the transcript assemblies as hints to generate predicted gene models from AUGUSTUS (v.3.4.0) (<https://github.com/Gaius-Augustus/Augustus>) and to train the hidden Markov model (HMM) of GeneMark-ET (v.3.67_lic) (ref. [63](#)). The parameters set in BRAKER2 were ‘--nocleanup --softmasking’.

Non-redundant human-curated plant homologous protein sequences, downloaded from the UniProt Swiss-Prot database (<https://www.uniprot.org/downloads>), combined with published peptide sequences of tomato and potato^{[8,10,11,13,35](#)}, were used as homologous protein sequences. These and the assembled transcripts from StringTie (v.1.3.3b) were passed to MAKER2 (v.2.31.11) (ref. [64](#)). Putative gene structures were then inferred and subsequently used as the training set to generate the HMM in SNAP (v.2013-02-16) (<https://github.com/KorfLab/SNAP>). MAKER2 was then run again, combining previously generated SNAP HMM, GeneMark-ET HMM and AUGUSTUS tuned species settings, along with the predicted gene models produced from the first round of MAKER2, to

synthesize the final gene annotations. The longest transcript of each predicated gene model was considered as the representative.

For gene functional annotation, InterProScan 5.34-73.0 (ref. [65](#)) was applied to predict potential protein domains, based on sequence signatures, with parameters ‘-cli -iprlookup -tsv -appl Pfam’.

Analyses of the protein-coding-gene-based pan-genome

All-versus-all BLASTP (v.2.2.30+) (ref. [66](#)) results of 2,701,787 peptide sequences of protein-coding genes, annotated from 44 potato accessions and the DM v.6.1 reference genome^{[11](#)}, were input into OrthoFinder (v.2.5.2) (ref. [67](#)) for gene clustering, in which the MCL algorithm^{[19](#)} was enabled by setting the inflation factor to 1.5, resulting in 51,401 non-redundant pan-gene clusters. We classified those clusters into 4 categories: core gene clusters that were conserved in all the 45 individuals; soft-core gene clusters, which were present in 42–44 samples in our collection; shell gene clusters, which were found in 2–41 accessions; and accession-specific gene clusters, which contained genes from only 1 sample. To facilitate these analyses, if genes from the DM reference were present in one cluster, this gene was selected as the representative; otherwise, the gene with the longest encoded protein was chosen.

Simulation of pan-genome size in terms of number of protein-coding genes was performed by PanGP (v.1.0.1) (ref. [68](#)) using the totally random algorithm, with a number of combinations, at each given number of genomes, of 500, and with the sample replication time set to 30.

Non-synonymous/synonymous substitution ratios (K_a/K_s) within core, soft-core and shell gene clusters were computed using ParaAT (v.2.0) (ref. [69](#)), with parameters ‘-m muscle -f axt -k’. The default parameter of KaKs_Calculator was set to estimate the K_a/K_s values, which means that the K_a/K_s value was the average of the output from 15 available algorithms comprising 7 original approximate methods (NG, method from Nei and Gojobori; LWL, method from Li, Wu and Luo; MLWL, modified method from Li, Wu and Luo; LPB, method from Li, Pamilo and Bianchi; MLPB, modified method from Li, Pamilo and Bianchi; YN, method from Yang and

Nielsen; MYN, modified method from Yang and Nielsen), 7 gamma-series methods (γ -NG, γ -LWL, γ -MLWL, γ -LPB, γ -MLPB, γ -YN and γ -MYN) and one maximum likelihood method (GY, method from Goldman and Yang) (ref. ⁷⁰). To simplify the calculation, we randomly selected 1,500 clusters from clusters of core, soft-core and shell categories. Within each cluster, K_a/K_s values between gene pairs from 50 randomly chosen combinations of 2 accessions were estimated. The non-parametric multiple comparisons Kruskal–Wallis test was used to perform significance analyses for sample median, using the agricolae package in R v.4.0.3 (<https://www.r-project.org/>), as these data did not comply with a normal distribution. Multiple comparisons were performed, using the Fisher’s least significant difference. The level of significance used in the post-hoc test was 0.001. Functional enrichment was performed, using Fisher’s exact tests in R. Those functional classes with $P < 0.05$ were regarded as significantly enriched.

Whole-genome alignment of 73 *Solanum* species

Whole-genome alignment of 73 accessions, comprising 44 potato MTGs and the genomes of DM, 2 *Etuberosum* species, 24 tomato accessions (<https://solgenomics.net/projects/tomato100>, <http://caastomato.biocloud.net/page/download/>), and 2 outgroup species of *S. americanum* and *S. melongena* (<http://eggplant-hq.cn/Eggplant/home/index>)^{35,44,71,72} were performed by ProgressCactus (v.1.2.3) (ref. ⁷³). The tomato genomes investigated in this study were all built using the third-generation sequencing technique (PacBio CLR and Nanopore) and are all assembled into 12 chromosomes, indicative of their relatively high qualities. The guide tree used in ProgressCactus was inferred by IQ-TREE, v.2.0.6 (ref. ⁵¹). To reduce the computation requirement, genome sequences were soft-masked and contigs shorter than 100 kb were discarded. To facilitate downstream analyses, we next used PHAST toolkit v.1.5 (ref. ⁷⁴) to generate 73-way multi-alignment blocks in fasta format, relative to the DM genome.

Genome comparison of 44 HiFi-assembled potato accessions

The 44 MTGs were aligned to the DM reference genome, using the nucmer program in MUMmer v.4.00rc1 (ref. [75](#)) software with the ‘--mum’ parameter, and alignments with an identity of less than 90% and length shorter than 1,000 bp were discarded. We used a modified version of dotPlotly (<https://github.com/tppoorten/dotPlotly/blob/master/mummerCoordsDotPlotly.R>) for visualization. To assess the heterozygosity distribution of 41 diploids (excluding 3 homozygous inbred lines), their MTGs and ATGs were split into 5-kb fragments and were aligned to the DM reference genome, using the same approach described above, and alignments shorter than 5 kb were discarded to reduce potential noise.

Identification of syntenic genes

To identify syntenic gene pairs, BLASTP (v.2.2.30+) was used to calculate pairwise similarities (e -value $< 1 \times 10^{-5}$), and MCscanX^{[76](#)} with default parameters was then applied.

Phylogenetic analyses

To build a super-matrix tree of 29 species (32 accessions, in which 4 are from *S. tuberosum*), amino-acid sequences of the longest transcripts of their annotated gene models were first extracted from the MTG genomes of 25 potatoes, 3 tomato accessions (see Supplementary Table [1](#) for more details)^{[35,44,71,72](#)}, 2 *Etuberosum* species, *S. americanum* and eggplant^{[77](#)}. All-versus-all alignments were generated using DIAMOND (v.2.0.6.144) (ref. [78](#)). The results were then passed to OrthoFinder (v.2.5.2)^{[67](#)} to infer orthology. A total of 3,971 single-copy orthologues gene clusters were then generated and 32-way protein alignments for these genes were computed using MAFFT (v.7.471) (ref. [79](#)) with default parameters. Maximum likelihood inference of phylogenetic relationships was performed using IQ-TREE v.2.0.6 (ref. [51](#)), by automatically calculating the best-fit amino-acid substitution model via the ‘-m MFP’ parameter. The consensus tree was generated specifying the number of bootstrap replicates as 1,000 by ultrafast bootstrap approximation^{[80](#)}. We also constructed a phylogenetic tree using an additional 20 potato (including DM) and 21 tomato genomes by applying the same approach described above.

To minimize the effect of ILS, we applied a multi-species coalescent-based method incorporated in ASTRAL (v.5.7.8) (ref. [81](#)) to generate a species tree. ASTRAL took 3,971 single-copy gene trees as input and generated a species tree estimated by searching for the species tree that was most congruent with quartets garnered from the input gene trees.

To infer the local phylogeny among the 32 representative accessions, considering the diverse nucleotide evolution rate of coding and non-coding regions, we masked coding regions according to the gene prediction in DM using the maskFastaFromBed command embedded in BEDTools (v.2.29.2) (ref. [82](#)), and repetitive regions were then hard-masked. We split Cactus whole-genome alignment blocks into 100-kb non-overlapping windows and inferred tree topologies for each window, using IQ-TREE^{[51](#)} with the parameter ‘-m GTR’. Next, we filtered the window trees with three standards: (1) fully aligned length > 10 kb; (2) missing rate < 20%; (3) mean bootstrap values > 80. After filtering, we next re-estimated the tree topologies of the retained 1,899 windows, using the selected best substitution model for each window, using ModelFinder implemented into IQ-TREE (ref. [51](#)). To help with visualization, 500 window trees were randomly selected, with an R script modified from a previous report^{[83](#)} (<https://zenodo.org/record/3401692#.YNrvJ6e76XQ>). The consensus tree topology was generated by IQ-TREE^{[51](#)}, using concatenated single-copy protein-coding sequences identified by OrthoFinder^{[67](#)}.

Estimation of the divergence time

BASEML and MCMCTREE in the PAML package (v.4.9) (ref. [84](#)) were used to estimate the divergence time. To reduce the computational burden, coding sequences (CDSs) of single-copy genes from 10 representative species (*S. melongena*, *S. americanum*, PG0019, LA716, LA2093, Heinz 1706, PG6241, PG4042, PG5068 and DM) were selected for a rough estimation of the substitution rate using BASEML with model = 7. MCMCTREE was then applied to estimate the divergence time with parameters ‘model = 7, burnin = 500,000, sampfreq = 100, nsample = 20,000’. The divergence time of potato–tomato (7.3–8.0 Ma)^{[35,85](#)} and potato–eggplant (13.7–15.5 Ma)^{[85,86,87](#)} was used for calibration. The estimation was performed for two rounds and generated very similar results.

ABBA-BABA statistics

On the basis of the genome assemblies, around 20-fold short reads of the 25 representative *Petota* accessions, 2 *Etuberosum* species, 3 tomatoes and *S. americanum* were simulated using WGSc (<https://github.com/YaoZhou89/WGSc>), and reads were mapped to the outgroup reference genome *S. melongena* using BWA-mem⁴⁹ with the default parameters. Bi-allelic SNPs were then identified using SAMtools⁵⁰ and BCFtools⁴⁹. Setting *S. melongena* as the outgroup, an ABBA-BABA test was performed between all possible triplets among potato, tomato and *Etuberosum* species, using the Dtrios program within Dsuite (v.0.4 r28)⁸⁸, with the ‘-c’ parameter. The tree topology among these four species, inferred from the whole-genome data in Newick format, was also passed into Dtrios via the ‘-t’ parameter.

Inference of ILS

The level of ILS at a given bi-allelic SNP i from the above mentioned 32-way alignment was calculated as $C_{\text{ABBA}(i)}$ and $C_{\text{BABA}(i)}$ divided by the total count of segregating sites: $(C_{\text{BAAA}(i)} + C_{\text{ABAA}(i)} + C_{\text{AABA}(i)} + 2(C_{\text{BBAA}(i)} + C_{\text{BABA}(i)} + C_{\text{ABBA}(i)}))/3$, as described previously²⁷. The tree topology used was (((*Lycopersicon*, *Petota*), *Etuberosum*), *S. melongena*).

To evaluate the theta value for internal branch, which reflects the level of effective population size⁸⁹, we divided the mutation units by coalescent units. The mutation units were inferred by IQ-TREE (ref. ⁵¹) and the coalescent units were inferred by ASTRAL.

ILS simulation

Simulation of 20,000 gene trees with ILS among six potato accessions (*S. tuberosum* Group Stenotomum, *S. candelleanum*, *Solanum lignicaule*, *S. chacoense*, *Solanum cajamarquense* and *Solanum bulbocastanum*) were performed by DendroPy (ref. ⁹⁰). The branch lengths of the estimated species tree by ASTRAL were used as an input. Frequencies between the observed and simulated gene-tree topologies from all possible four-species

groups among the six potato species were plotted. The correlations were computed using the correlation function ‘cor()’ in R using the ‘pearson’ method.

Identification of SVs

Both read-mapping-based and assembly-based approaches were applied to identify SVs (≥ 50 bp in length). SVIM (v.1.4.2) (ref. [91](#)) was used to identify putative SVs, consisting of insertions, deletions, inversions, duplications and translocations. SVs with quality ≥ 10 and number of supported reads ≥ 5 were kept. Assembled genomes of each accession were first aligned to the DM v.6.1 reference using the nucmer program embedded in MUMmer v4.00rc1 (ref. [75](#)), with the following parameters: ‘--batch 1 -c 500 -b 500 -l 100’. The alignments in delta format were passed to the delta-filter program to retain highly reliable alignments with length ≥ 100 bp and identity $\geq 90\%$. Assemblytics (v.1.2.1) (ref. [92](#)) was subsequently applied to identify SVs from the filtered alignments, setting the minimum SV size to 50 bp. To make the false positive rate in our SV dataset as low as possible, we only kept SVs in terms of insertions, deletions, inversions, duplications and translocations < 10 kb in size, identified by SVIM. For $SV \geq 10$ kb, only insertions and deletions reported in Assemblytics were retained. The two SV datasets for each sample were then combined, using SURVIVOR (v.1.0.7)[93](#) merge with parameters ‘0 1 1 1 0 50’.

To detect megabase-scale inversion events among the 20 landraces and 4 CND accessions, we applied ragtag (v.2.1.0) (ref. [94](#)) with the default parameters, to order and orient the contig-level assemblies into 12 chromosomes, using the DM genome as the reference. Inversions were next identified using SyRI (v.1.4) (ref. [95](#)) with parameters ‘-k -F S’. Only those inversions that located in a single contig were retained for downstream analyses.

Identification of hemizygous genes

To identify regions present in MTGs but absent in ATGs, we mapped HiFi reads of each accession to its corresponding MTGs using minimap2 (v.2.21-r1071) (ref. [96](#)), and heterozygous deletions were detected using SVIM

(v.1.4.2) (ref. [91](#)) with default parameters (length \geq 50 bp, quality \geq 10, number of supported reads \geq 2). To identify sequences present in ATGs but absent in MTGs, we aligned ATGs to MTGs from each accession and extracted the inserted regions using Assemblytics^{[92](#)} with parameters ‘unique_anchor_length = 10,000, min_variant_size = 50, max_variant_size = 10,000,000’. These results were merged as heterozygous SVs, and genes overlapping with those SVs were considered as hemizygous genes, as applied in a previous report^{[97](#)}.

Analyses of recombination events

Breakpoints of crossing-overs were inferred based on the 624 selfing progenies of PG6359 (ref. [3](#)), using a method described previously^{[7](#)}.

Reannotation and classification of nucleotide-binding resistance genes

NLR-annotator (v.0.7) (ref. [98](#)) was first applied to identify genomic segments containing putative nucleotide-binding domain and leucine-rich repeat (NLR) genes for each accession. A total of 7,007 amino-acid sequences of high-confidence NLR gene models, downloaded from resistance gene enrichment sequencing (RenSeq)-based NLR genes of 15 tomato accessions^{[99](#)}, putative NLR genes in *Arabidopsis*^{[100](#)} (annotation version Araprot11) and experimentally validated NLR genes obtained from PRGdb 3.0 (ref. [101](#)) and RefPlantNLR^{[102](#)}, were used as homologous protein evidence. Training sets from SNAP and AUGUSTUS for each accession were then inputted to MAKER2, together with the assembled transcripts, in GFF3 format, and the homologous proteins, to predict and synthesize the final gene models. The reannotated NLR gene models were then integrated with the whole-genome annotation results, and originally predicted genes overlapping with our reannotated NLRs were removed to avoid redundancy.

To examine the completeness of NLR loci generated by our pipeline, we produced three NLR datasets of tomato accession ‘Heinz 1706’ from the predicted high-confidence and representative gene models (annotation version ITAG 4.0), predicted models using our pipeline, and previously

reported RenSeq-derived models⁹⁹, respectively. The RGAugury (v.2.2) (ref. 103) pipeline was then used to classify putative nucleotide-binding site (NB-ARC) domain-encoding genes into different subgroups, on the basis of domain and motif structures: TN (Toll/interleukin-1 receptor (TIR) and NB-ARC), CN (coiled-coil (CC) and NB-ARC), NL (NB-ARC and leucine rich repeat (LRR)), CNL (CC, NB-ARC and LRR), NB (NB-ARC), TNL (TIR, NB-ARC and LRR).

For identification of putatively expanded NLR clusters in potato, the annotated NLR loci from 45 potato, 22 tomato and 2 *Etuberosum* genomes were classified into clusters, using the method described in the pan-genome analysis. The NLR copy numbers in potato, tomato and *Etuberosum* accessions, in each cluster, were compared by Wilcoxon rank-sum test using the R package exactRankTests. The clusters with $P < 0.05$ were extracted as the expanded clusters. For the potato-specific NLR analyses, the NLR protein sequences from 2 *Etuberosum* species and 22 tomato species were merged together, as a query, to blast against those from the 45 potato species. If the best hit of a potato NLR showed an identity < 75 , the NLR was defined as potato-specific. NLRs with transcripts per kilobase of exon model per million mapped reads (TPM) ≥ 1 in potato stolon or tuber were extracted and considered as expressed in these tissues.

Gene expression profiling

RNA-seq reads of 23 accessions (Supplementary Table 1) as well as DM (SRA030516) were mapped to the corresponding assembled genome, using HISAT2 (v.2.0.1-beta) (ref. 60), with parameters ‘-x --dta’. StringTie (v.1.3.3b) (ref. 61) was applied to compute the expression level for each predicted gene in terms of TPM values, using ‘-e -G’ parameters.

Analyses of CNSs

Tools embedded in the PHAST package (v.1.5) (ref. 74) were used for CNSs analyses. The msa_view program was applied to extract fourfold degenerate synonymous sites and to prepare sufficient statistics, on the basis of multiple alignments and CDS annotation of the reference genome. PhyloFit was then used to train the un-conserved model, with sufficient statistics generated by

msa_view.phastCons, with the parameter ‘--most-conserved’ used to identify conserved regions and assign an odds score for each site. Finally, conserved regions containing gaps and overlapping with CDS were removed to generate CNSs shared among potato species. To further remove CNSs shared within outgroup species, we identified CNSs from genomes of 45 potato, 24 tomato and 2 *Etuberosum* species, using the same pipeline presented above. The potato conserved CNSs that shared sequences with tomato and *Etuberosum* species were removed. In addition, short sequences (<5 bp) were excluded and sequences that were located within 10 bp of each other were merged to generate the final potato-specific CNSs. ChIPseeker v.1.24.0 (ref. [104](#)) was adopted to annotate these CNSs, in which sequences 3 kb upstream from the start codon or 3 kb downstream from the stop codon of a certain gene were defined as promoter or downstream regions. Genes possessing CNSs within their promoters, introns, upstream regions, downstream regions or UTRs were defined as CNS-associated genes. pyGenomeTracks v.3.6 was applied to visualize the CNS region^{[105](#)}. Sequences flanking *IT1* CNS regions were extracted from the 71-way multiple alignment and were imported into MView (v.1.67) (ref. [106](#)) to generate the multiple comparisons figure.

Generation of *it1* mutants

The diploid *S. tuberosum* Group Phureja S15-65 clone was used for gene editing in this study. The 19-nucleotide single-guide RNA sequence for *IT1* from the S15-65 clone was incorporated into the CRISPR–Cas9 vector pKSE401 (ref. [107](#)). Three-week-old plantlets were used for transformation. *Agrobacterium*-mediated transformation of potato internodes was conducted as previously described^{[6](#)}: after two days of pre-culture, the explants were co-cultured with *Agrobacterium* containing pKSE401 with the target sequence for two days, in the presence of 2 mg l⁻¹ α-naphthaleneacetic acid and 1 mg l⁻¹ zeatin, followed by callus induction and regeneration mediated by 0.01 mg l⁻¹ α-naphthaleneacetic acid and 2 mg l⁻¹ zeatin until shoot proliferation. Positive transformants were screened on the basis of growth on the medium containing 50 mg l⁻¹ kanamycin.

Yeast-two-hybrid library screening

The cDNA of S15-65 stolons was used to construct the cDNA library for yeast-two hybrid by using the CloneMiner II cDNA Library Construction Kit. The library was screened, with the *IT1* as bait, according to the Matchmaker Gold Yeast Two-Hybrid System User Manual. To further validate the interaction between *IT1* and *SP6A*, the CDSs of *IT1* and *SP6A* were inserted into pGADT7 and pGBKT7 vectors, respectively, and co-transfected into the yeast strain AH109, and the yeast cells were then plated on SD/-Leu/-Trp medium and SD/-Leu/-Trp/-His medium and cultivated at 30 °C for 5 days.

Firefly luciferase complementation imaging assay

The CDSs of *SP6A* and *IT1* were fused in the pCAMBIA-nLUC-GW and pCAMBIA-cLUC-GW vectors, respectively¹⁰⁸. The vectors were transformed into *Agrobacterium* strain GV3101, and infiltrated into *Nicotiana benthamiana* leaves. After 3 days, the detached leaves were sprayed with 100 mM luciferin and kept in the dark for 10 min. The leaves were observed under a low-light cooled charge-coupled device imaging apparatus, Lumazone 1300B (Roper Bioscience).

Quantitative PCR analysis of *SP6A* expression

The seeds of potato inbred line E4-63 and *Etuberosum* species PG0019 were planted in soil and cultivated under long-day conditions (16-h light, 8-h dark) for one month, and then half of the plants were transferred to short-day (8-h light, 16-h dark) conditions. When flower buds developed in the long-day plants (usually two months after sowing), the fourth leaf of both long-day and short-day plants was harvested at ZT4 to investigate *SP6A* gene expression. The total leaf RNA was extracted using an RNAPrep Pure Plant Kit (DP441), and a PrimeScript RT Reagent Kit (RR047A) was used to reversely transcribe the RNA to cDNA. Quantitative PCR was performed using SYBR Premix Ex Taq II (RR820A) on a 7500 Fast Real-Time PCR system (Applied Biosystems), according to standard instructions. *EF1A* was used as the internal reference. The specific primers used are listed in Supplementary Table [17](#).

Syntenic analyses of *R3a* and *SP6A* loci

To plot synteny relationships around the *R3a* locus, collinear blocks between the given two species were identified by MCScanX (Python version)¹⁰⁹. Syntenic genes around *R3a* loci were extracted and plotted using in-house R scripts. For a synteny plot of the *SP6A* loci, the *SP6A* genomic sequences from different species were extracted and aligned using MAFFT, with ‘--auto’ parameter⁷⁹. In-house Python scripts were used to transfer aligned regions between two species to the BED format required by MCScanX. The micro-synteny plot between the two species was then generated. Finally, synteny plots among different species were merged using Adobe Illustrator.

Reporting summary

Further information on research design is available in the [Nature Research Reporting Summary](#) linked to this paper.

Data availability

All PacBio sequence data, transcriptome data and Hi-C data in this study have been deposited at the National Center for Biotechnology Information (NCBI) Sequence Read Archive (SRA), with BioProject accession number [PRJNA754534](#), and the National Genomics Data Center (NGDC) Genome Sequence Archive (GSA) (<https://ngdc.cncb.ac.cn/gsa/>), with BioProject accession number [PRJCA006011](#). Genome assemblies, annotation, sequence variation and gene expression data for the 46 accessions and the genotype information of 432 lines that were used for sample selection are hosted in the Pan-Potato Database (<http://solomics.agis.org.cn/potato/>, <http://218.17.88.60/potato/>). Publicly available sequencing data were downloaded from the NCBI with BioProject accession numbers [PRJNA641265](#), [PRJNA573826](#), [PRJNA378971](#), [PRJNA394943](#) and [PRJNA766763](#).

References

1. Lindhout, P. et al. Towards F₁ hybrid seed potato breeding. *Potato Res.* **54**, 301–312 (2011).

2. Li, Y., Li, G., Li, C., Qu, D. & Huang, S. Prospects of diploid hybrid breeding in potato. *Chinese Potato J.* **27**, 96–99 (2013).
3. Zhang, C. et al. Genome design of hybrid potato. *Cell* **184**, 3873–3883 (2021).
4. Stokstad, E. The new potato. *Science* **363**, 574–577 (2019).
5. Spooner, D. M., Ghislain, M., Simon, R., Jansky, S. H. & Gavrilenko, T. Systematics, diversity, genetics, and evolution of wild and cultivated potatoes. *Bot. Rev.* **80**, 283–383 (2014).
6. Ye, M. et al. Generation of self-compatible diploid potato by knockout of S-RNase. *Nat. Plants* **4**, 651–654 (2018).
7. Zhang, C. et al. The genetic basis of inbreeding depression in potato. *Nat. Genet.* **51**, 374–378 (2019).
8. The Potato Genome Sequencing Consortium. Genome sequence and analysis of the tuber crop potato. *Nature* **475**, 189–195 (2011).
9. Aversano, R. et al. The *Solanum commersonii* genome sequence provides insights into adaptation to stress conditions and genome evolution of wild potato relatives. *Plant Cell* **27**, 954–968 (2015).
10. Leisner, C. P. et al. Genome sequence of M6, a diploid inbred clone of the high glycoalkaloid-producing tuber-bearing potato species *Solanum chacoense*, reveals residual heterozygosity. *Plant J.* **94**, 562–570 (2018).
11. Pham, G. M. et al. Construction of a chromosome-scale long-read reference genome assembly for potato. *Gigascience* **9**,giaa100 (2020).
12. van Lieshout, N. et al. Solyntus, the new highly contiguous reference genome for potato (*Solanum tuberosum*). *G3* **10**, 3489–3495 (2020).
13. Zhou, Q. et al. Haplotype-resolved genome analyses of a heterozygous diploid potato. *Nat. Genet.* **52**, 1018–1023 (2020).

14. Hardigan, M. A. et al. Genome diversity of tuber-bearing *Solanum* uncovers complex evolutionary history and targets of domestication in the cultivated potato. *Proc. Natl Acad. Sci. USA* **114**, E9999–E10008 (2017).
15. Li, Y. et al. Genomic analyses yield markers for identifying agronomically important genes in potato. *Mol. Plant* **11**, 473–484 (2018).
16. Burton, J. N. et al. Chromosome-scale scaffolding of de novo genome assemblies based on chromatin interactions. *Nat. Biotechnol.* **31**, 1119–1125 (2013).
17. Kaplan, N. & Dekker, J. High-throughput genome scaffolding from in vivo DNA interaction frequency. *Nat. Biotechnol.* **31**, 1143–1147 (2013).
18. Simao, F. A., Waterhouse, R. M., Ioannidis, P., Kriventseva, E. V. & Zdobnov, E. M. BUSCO: assessing genome assembly and annotation completeness with single-copy orthologs. *Bioinformatics* **31**, 3210–3212 (2015).
19. Enright, A. J., Van Dongen, S. & Ouzounis, C. A. An efficient algorithm for large-scale detection of protein families. *Nucleic Acids Res.* **30**, 1575–1584 (2002).
20. Rodriguez, F., Wu, F. N., Ane, C., Tanksley, S. & Spooner, D. M. Do potatoes and tomatoes have a single evolutionary history, and what proportion of the genome supports this history? *BMC Evol. Biol.* **9**, 191 (2009).
21. Szinay, D. et al. Chromosome evolution in *Solanum* traced by cross-species BAC-FISH. *New Phytol.* **195**, 688–698 (2012).
22. Struik, P. C. in *Potato Biology and Biotechnology: Advances and Perspectives* (eds Vreugdenhil, D. et al.) Ch. 11 (Elsevier, 2007).
23. Contreras, M. A. & Spooner, D. M. in *Solanaceae IV* (eds Nee, M. et al.) 227–245 (Royal Botanic Gardens, Kew, 1999).

24. Guo, L., Plunkert, M., Luo, X. & Liu, Z. C. Developmental regulation of stolon and rhizome. *Curr. Opin. Plant Biol.* **59**, 101970 (2021).
25. Zhang, L. et al. The water lily genome and the early evolution of flowering plants. *Nature* **577**, 79–84 (2020).
26. Hahn, M. W. & Nakhleh, L. Irrational exuberance for resolved species trees. *Evolution* **70**, 7–17 (2016).
27. Scally, A. et al. Insights into hominid evolution from the gorilla genome sequence. *Nature* **483**, 169–175 (2012).
28. Green, R. et al. A draft sequence of the Neandertal genome. *Science* **328**, 710–722 (2010).
29. Simmonds, N. W. A review of potato propagation by means of seed, as distinct from clonal propagation by tubers. *Potato Res.* **40**, 191–214 (1997).
30. Feehan, J. M., Castel, B., Bentham, A. R. & Jones, J. D. Plant NLRs get by with a little help from their friends. *Curr. Opin. Plant Biol.* **56**, 99–108 (2020).
31. Barragan, A. C. & Weigel, D. Plant NLR diversity: the known unknowns of pan-NLRomes. *Plant Cell* **33**, 814–831 (2021).
32. Wu, S. et al. Genome sequences of two diploid wild relatives of cultivated sweetpotato reveal targets for genetic improvement. *Nat. Commun.* **9**, 4580 (2018).
33. Hoshino, A. et al. Genome sequence and analysis of the Japanese morning glory *Ipomoea nil*. *Nat. Commun.* **7**, 13295 (2016).
34. Isobe, S., Shirasawa, K. & Hirakawa, H. Current status in whole genome sequencing and analysis of *Ipomoea* spp. *Plant Cell Rep.* **38**, 1365–1371 (2019).
35. The Tomato Genome Consortium. The tomato genome sequence provides insights into fleshy fruit evolution. *Nature* **485**, 635–641

(2012).

36. Suttle, J. C. Physiological regulation of potato tuber dormancy. *Am. J. Potato Res.* **81**, 253–262 (2004).
37. Zierer, W., Ruscher, D., Sonnewald, U. & Sonnewald, S. Tuber and tuberous root development. *Annu. Rev. Plant Biol.* **72**, 551–580 (2021).
38. Haudry, A. et al. An atlas of over 90,000 conserved noncoding sequences provides insight into crucifer regulatory regions. *Nat. Genet.* **45**, 891–898 (2013).
39. Wang, K. et al. African lungfish genome sheds light on the vertebrate water-to-land transition. *Cell* **184**, 1362–1376 (2021).
40. Yang, X. et al. Regulation of plant architecture by a new histone acetyltransferase targeting gene bodies. *Nat. Plants* **6**, 809–822 (2020).
41. Danisman, S. TCP transcription factors at the interface between environmental challenges and the plant's growth responses. *Front. Plant Sci.* **7**, 1930 (2016).
42. Navarro, C. et al. Control of flowering and storage organ formation in potato by *FLOWERING LOCUS T*. *Nature* **478**, 119–122 (2011).
43. Li, D. et al. The multi-omics basis of potato heterosis. *J. Integr. Plant Biol.* **64**, 671–687 (2022).
44. Alonge, M. et al. Major impacts of widespread structural variation on gene expression and crop improvement in tomato. *Cell* **182**, 145–161 (2020).
45. Wellenreuther, M. & Bernatchez, L. Eco-evolutionary genomics of chromosomal inversions. *Trends Ecol. Evol.* **33**, 427–440 (2018).
46. Eck, J. V. et al. Enhancing beta-carotene content in potato by RNAi-mediated silencing of the beta-carotene hydroxylase gene. *Am. J. Potato Res.* **84**, 331 (2007).

47. Kloosterman, B. et al. From QTL to candidate gene: genetical genomics of simple and complex traits in potato using a pooling strategy. *BMC Genomics* **11**, 158 (2010).
48. Plantenga, F. D. M. et al. The tuberization signal *StSP6A* represses flower bud development in potato. *J. Exp. Bot.* **70**, 937–948 (2019).
49. Li, H. & Durbin, R. Fast and accurate short read alignment with Burrows–Wheeler transform. *Bioinformatics* **25**, 1754–1760 (2009).
50. Li, H. et al. The Sequence Alignment/Map (SAM) format and SAMtools. *Bioinformatics* **25**, 2078–9 (2009).
51. Nguyen, L. T., Schmidt, H. A., von Haeseler, A. & Minh, B. Q. IQ-TREE: a fast and effective stochastic algorithm for estimating maximum-likelihood phylogenies. *Mol. Biol. Evol.* **32**, 268–274 (2015).
52. Belton, J. M. et al. Hi-C: a comprehensive technique to capture the conformation of genomes. *Methods* **58**, 268–276 (2012).
53. Ranallo-Benavidez, T. R., Jaron, K. S. & Schatz, M. C. GenomeScope 2.0 and smudgeplot for reference-free profiling of polyploid genomes. *Nat. Commun.* **11**, 1432 (2020).
54. Cheng, H., Concepcion, G. T., Feng, X., Zhang, H. & Li, H. Haplotype-resolved de novo assembly using phased assembly graphs with hifiasm. *Nat. Methods* **18**, 170–175 (2021).
55. Koren, S. et al. Canu: scalable and accurate long-read assembly via adaptive k -mer weighting and repeat separation. *Genome Res.* **27**, 722–736 (2017).
56. Walker, B. J. et al. Pilon: an integrated tool for comprehensive microbial variant detection and genome assembly improvement. *PLoS One* **9**, e112963 (2014).
57. Durand, N. C. et al. Juicer provides a one-click system for analyzing loop-resolution Hi-C experiments. *Cell Syst.* **3**, 95–98 (2016).

58. Dudchenko, O. et al. De novo assembly of the *Aedes aegypti* genome using Hi-C yields chromosome-length scaffolds. *Science* **356**, 92–95 (2017).
59. Xie, D. et al. The wax gourd genomes offer insights into the genetic diversity and ancestral cucurbit karyotype. *Nat. Commun.* **10**, 5158 (2019).
60. Kim, D., Landmead, B. & Salzberg, S. L. HISAT: a fast spliced aligner with low memory requirements. *Nat. Methods* **12**, 357–360 (2015).
61. Pertea, M. et al. StringTie enables improved reconstruction of a transcriptome from RNA-seq reads. *Nat. Biotechnol.* **33**, 290–295 (2015).
62. Hoff, K. J., Lange, S., Lomsadze, A., Borodovsky, M. & Stanke, M. BRAKER1: unsupervised RNA-seq-based genome annotation with GeneMark-ET and AUGUSTUS. *Bioinformatics* **32**, 767–769 (2016).
63. Lomsadze, A., Ter-Hovhannisyan, V., Chernoff, Y. O. & Borodovsky, M. Gene identification in novel eukaryotic genomes by self-training algorithm. *Nucleic Acids Res.* **33**, 6494–6506 (2005).
64. Holt, C. & Yandell, M. MAKER2: an annotation pipeline and genome-database management tool for second-generation genome projects. *BMC Bioinformatics* **12**, 491 (2011).
65. Blum, M. et al. The InterPro protein families and domains database: 20 years on. *Nucleic Acids Res.* **49**, D344–D354 (2021).
66. Altschul, S. F., Gish, W., Miller, W., Myers, E. W. & Lipman, D. J. Basic local alignment search tool. *J. Mol. Biol.* **215**, 403–410 (1990).
67. Emms, D. M. & Kelly, S. OrthoFinder: solving fundamental biases in whole genome comparisons dramatically improves orthogroup inference accuracy. *Genome Biol.* **16**, 157 (2015).
68. Zhao, Y. et al. PanGP: a tool for quickly analyzing bacterial pan-genome profile. *Bioinformatics* **30**, 1297–1299 (2014).

69. Zhang, Z. et al. ParaAT: a parallel tool for constructing multiple protein-coding DNA alignments. *Biochem. Biophys. Res. Commun.* **419**, 779–781 (2012).
70. Wang, D., Zhang, Y., Zhang, Z., Zhu, J. & Yu, J. KaKs_Calculator 2.0: a toolkit incorporating gamma-series methods and sliding window strategies. *Genom. Proteom. Bioinform.* **8**, 77–80 (2010).
71. Bolger, A. et al. The genome of the stress-tolerant wild tomato species *Solanum pennellii*. *Nat. Genet.* **46**, 1034–1038 (2014).
72. Wang, X. et al. Genome of *Solanum pimpinellifolium* provides insights into structural variants during tomato breeding. *Nat. Commun.* **11**, 5817 (2020).
73. Armstrong, J. et al. Progressive Cactus is a multiple-genome aligner for the thousand-genome era. *Nature* **587**, 246–251 (2020).
74. Hubisz, M. J., Pollard, K. S. & Siepel, A. PHAST and RPHAST: phylogenetic analysis with space/time models. *Brief. Bioinform.* **12**, 41–51 (2011).
75. Marcais, G. et al. MUMmer4: a fast and versatile genome alignment system. *PLoS Comput. Biol.* **14**, e1005944 (2018).
76. Wang, Y. et al. MCScanX: a toolkit for detection and evolutionary analysis of gene synteny and collinearity. *Nucleic Acids Res.* **40**, e49 (2012).
77. Wei, Q. et al. A high-quality chromosome-level genome assembly reveals genetics for important traits in eggplant. *Hortic. Res.* **7**, 153 (2020).
78. Buchfink, B., Xie, C. & Huson, D. H. Fast and sensitive protein alignment using DIAMOND. *Nat. Methods* **12**, 59–60 (2015).
79. Katoh, K. & Standley, D. M. MAFFT multiple sequence alignment software version 7: improvements in performance and usability. *Mol. Biol. Evol.* **30**, 772–780 (2013).

80. Minh, B. Q., Nguyen, M. A. T. & von Haeseler, A. Ultrafast approximation for phylogenetic bootstrap. *Mol. Biol. Evol.* **30**, 1188–1195 (2013).
81. Mirarab, S. et al. ASTRAL: genome-scale coalescent-based species tree estimation. *Bioinformatics* **30**, i541–i548 (2014).
82. Quinlan, A. R. & Hall, I. M. BEDTools: a flexible suite of utilities for comparing genomic features. *Bioinformatics* **26**, 841–842 (2010).
83. Edelman, N. B. et al. Genomic architecture and introgression shape a butterfly radiation. *Science* **366**, 594–599 (2019).
84. Yang, Z. PAML 4: phylogenetic analysis by maximum likelihood. *Mol. Biol. Evol.* **24**, 1586–1591 (2007).
85. Sarkinen, T., Bohs, L., Olmstead, R. G. & Knapp, S. A phylogenetic framework for evolutionary study of the nightshades (Solanaceae): a dated 1000-tip tree. *BMC Evol. Biol.* **13**, 214 (2013).
86. Wang, Y. et al. Sequencing and comparative analysis of a conserved syntenic segment in the Solanaceae. *Genetics* **180**, 391–408 (2008).
87. Wu, F. & Tanksley, S. D. Chromosomal evolution in the plant family Solanaceae. *BMC Genomics* **11**, 182 (2010).
88. Malinsky, M., Matschiner, M. & Svardal, H. Dsuite—fast *D*-statistics and related admixture evidence from VCF files. *Mol. Ecol. Resour.* **21**, 584–595 (2021).
89. Cai, L. et al. The perfect storm: gene tree estimation error, incomplete lineage sorting, and ancient gene flow explain the most recalcitrant ancient angiosperm clade, malpighiales. *Syst. Biol.* **70**, 491–507 (2021).
90. Sukumaran, J. & Holder, M. T. DendroPy: a Python library for phylogenetic computing. *Bioinformatics* **26**, 1569–1571 (2010).
91. Heller, D. & Vingron, M. SVIM: structural variant identification using mapped long reads. *Bioinformatics* **35**, 2907–2915 (2019).

92. Nattestad, M. & Schatz, M. C. Assemblytics: a web analytics tool for the detection of variants from an assembly. *Bioinformatics* **32**, 3021–3023 (2016).
93. Jeffares, D. C. et al. Transient structural variations have strong effects on quantitative traits and reproductive isolation in fission yeast. *Nat. Commun.* **8**, 14061 (2017).
94. Alonge, M. et al. Automated assembly scaffolding elevates a new tomato system for high-throughput genome editing. Preprint at *bioRxiv* <https://doi.org/10.1101/2021.11.18.469135> (2021).
95. Goel, M., Sun, H., Jiao, W. B. & Schneeberger, K. SyRI: finding genomic rearrangements and local sequence differences from whole-genome assemblies. *Genome Biol.* **20**, 277 (2019).
96. Li, H. Minimap2: pairwise alignment for nucleotide sequences. *Bioinformatics* **34**, 3094–3100 (2018).
97. Zhou, Y. et al. The population genetics of structural variants in grapevine domestication. *Nat. Plants* **5**, 965–979 (2019).
98. Steuernagel, B. et al. The NLR-Annotator tool enables annotation of the intracellular immune receptor repertoire. *Plant Physiol.* **183**, 468–482 (2020).
99. Seong, K., Seo, E., Witek, K., Li, M. & Staskawicz, B. Evolution of NLR resistance genes with noncanonical N-terminal domains in wild tomato species. *New Phytol.* **227**, 1530–1543 (2020).
100. Cheng, C. Y. et al. Araport11: a complete reannotation of the *Arabidopsis thaliana* reference genome. *Plant J.* **89**, 789–804 (2017).
101. Osuna-Cruz, C. M. et al. PRGdb 3.0: a comprehensive platform for prediction and analysis of plant disease resistance genes. *Nucleic Acids Res.* **46**, D1197–D1201 (2018).
102. Kourelis, J., Sakai, T., Adachi, H. & Kamoun, S. RefPlantNLR is a comprehensive collection of experimentally validated plant disease

- resistance proteins from the NLR family. *PLoS Biol.* **19**, e3001124 (2021).
103. Li, P. et al. RGAugury: a pipeline for genome-wide prediction of resistance gene analogs (RGAs) in plants. *BMC Genomics* **17**, 852 (2016).
 104. Yu, G. C., Wang, L. G. & He, Q. Y. ChIPseeker: an R/Bioconductor package for ChIP peak annotation, comparison and visualization. *Bioinformatics* **31**, 2382–2383 (2015).
 105. Lopez-Delisle, L. et al. pyGenomeTracks: reproducible plots for multivariate genomic datasets. *Bioinformatics* **37**, 422–423 (2021).
 106. Brown, N. P., Leroy, C. & Sander, C. MView: a web-compatible database search or multiple alignment viewer. *Bioinformatics* **14**, 380–381 (1998).
 107. Xing, H. L. et al. A CRISPR/Cas9 toolkit for multiplex genome editing in plants. *BMC Plant Biol.* **14**, 327 (2014).
 108. Zhang, J. et al. The Arabidopsis RING-type E3 ligase TEAR1 controls leaf development by targeting the TIE1 transcriptional repressor for degradation. *Plant Cell* **29**, 243–259 (2017).
 109. Tang, H. et al. Synteny and collinearity in plant genomes. *Science* **320**, 486–488 (2008).

Acknowledgements

We thank N. Stein, Y. Zhang, S. Dong, L. Wang, S. Zhou, L. Liu, Y. Wu and Y. Yang for discussion and comments on the project, and the AGIS CAAS-YNNU Joint Academy of Potato Sciences for greenhouse assistance. This work was supported by the National Key Research and Development Program of China (grant 2019YFA0906200), the Agricultural Science and Technology Innovation Program (CAAS-ZDRW202101), the Shenzhen Science and Technology Program (grant KQTD2016113010482651), the Special Funds for Science Technology Innovation and Industrial

Development of Shenzhen Dapeng New District (grant RC201901-05), the National Natural Science Foundation of China (31902027), Shenzhen Outstanding Talents Training Fund and the China National Key Research and Development Program to C.Z. (2019YFE0120500).

Author information

Author notes

1. These authors contributed equally: Dié Tang, Yuxin Jia, Jinzhe Zhang, Hongbo Li

Authors and Affiliations

1. Shenzhen Branch, Guangdong Laboratory of Lingnan Modern Agriculture, Genome Analysis Laboratory of the Ministry of Agriculture and Rural Affairs, Agricultural Genomics Institute at Shenzhen, Chinese Academy of Agricultural Sciences, Shenzhen, China

Dié Tang, Yuxin Jia, Hongbo Li, Lin Cheng, Pei Wang, Zhigui Bao, Zhihong Liu, Dawei Li, Yao Zhou, Yongfeng Zhou, Chunzhi Zhang & Sanwen Huang

2. Key Laboratory of Biology and Genetic Improvement of Horticultural Crops of the Ministry of Agriculture, Sino-Dutch Joint Laboratory of Horticultural Genomics, Institute of Vegetables and Flowers, Chinese Academy of Agricultural Sciences, Beijing, China

Jinzhe Zhang & Shuangshuang Feng

3. Graduate School Experimental Plant Sciences, Laboratory of Plant Breeding, Wageningen University and Research, Wageningen, The Netherlands

Hongbo Li

4. The AGISCAAS-YNNU Joint Academy of Potato Sciences, Yunnan Normal University, Kunming, China

Xijian Zhu & Guangtao Zhu

5. Department of Integrative Biology, University of California Berkeley, Berkeley, CA, USA

Hongru Wang

6. Cell and Molecular Sciences, The James Hutton Institute, Invergowrie, UK

Glenn J. Bryan

7. Center for Applied Genetic Technologies, University of Georgia, Athens, GA, USA

C. Robin Buell

Contributions

S.H. conceived and designed the project. D.T., Y.J., H.L. and S.H. wrote the manuscript. D.T., Y.J. and H.L. performed the bioinformatics analyses. L.C. and Z.B. assisted in bioinformatics analyses. J.Z., Z.L., S.F. and X.Z. performed the molecular work on *IT1*. P.W. and D.L. contributed to the greenhouse work. G.Z. provided the computing platform. H.W., Yao Zhou, Yongfeng Zhou, G.J.B., C.R.B. and C.Z. coordinated the project.

Corresponding author

Correspondence to [Sanwen Huang](#).

Ethics declarations

Competing interests

The authors declare no competing interests.

Peer review

Peer review information

Nature thanks Martin Mascher and the other, anonymous, reviewer(s) for their contribution to the peer review of this work. [Peer reviewer reports](#) are available.

Additional information

Publisher's note Springer Nature remains neutral with regard to jurisdictional claims in published maps and institutional affiliations.

Extended data figures and tables

[Extended Data Fig. 1 Pan-genome of 45 potato accessions.](#)

a, Assembled size of monoploid assembled contigs (MTGs) and alternate assembled contigs (ATGs). **b**, Contig N50 of raw assembled contigs and improved contig N50 of MTGs. **c**, Correlation between raw assembly size and heterozygosity. The grey shaded region indicates the 95% confidence interval using a linear model ('lm'). **d**, Simulation of pan- and core-genome sizes, in terms of number of gene clusters and pan-genome composition. At each given number of genomes, the number of combinations is 500 with 30 times of replication. **e**, Percentage of genes in core, soft-core, shell and accession-specific gene subsets with annotated InterPro protein domains. Orange bars show the proportion of genes with InterPro domains, whereas red bars depict the genes without those domains. **f**, Expression profiles of genes belonging to core (13,123), soft-core (5,732), shell (5,009) and accession-specific (134) gene families. **g**, Non-synonymous/synonymous substitution ratios (K_a/K_s) within core, soft-core, and shell genes. Kruskal-Wallis test was used to determine significance. Multiple comparisons were performed, using the Fisher's least significant difference. The level of

significance used in the *post hoc* test was 0.001. Number of gene pairs used in core, soft-core and shell genes are 52,148, 28,363 and 31,654, respectively. The upper and lower edges of the boxes represent the 75% and 25% quartiles, the central line denotes the median and the whiskers extend to $1.5 \times \text{IQR}$ in **d**, **f** and **g**. **h**, InterPro protein domain enrichments of core and soft-core (upper panel) and shell and accession-specific (lower panel) genes relative to pan genes. **i**, Pfam protein families enriched in core and soft-core (upper panel) and shell and accession-specific (lower panel) genes, relative to pan genes.

[Source data](#)

[**Extended Data Fig. 2 Genome-wide alignments among 45 genome accessions.**](#)

Whole-genome alignments of 44 MTGs to DM reference genome. Alignments with length greater than 10 kb and showing greater than 90% identity are kept for visualization. Black dashed rectangles indicate the specially focused regions.

[**Extended Data Fig. 3 Phylogenetic analysis of the 32 representative accessions.**](#)

a, Maximum likelihood super-matrix tree based on 3,971 single-copy ortholog genes. The scale bar represents branch lengths, which corresponds to the mean number of substitutions per site in the alignments. **b**, Coalescent tree based on 3,971 single-copy ortholog genes, accounting for ILS. **c**, The proportion of different tree topologies among 1,899 non-overlapping window trees. **d**, Heat map of the most significant *D* scores observed between two given potato accessions (P2 and P3) across all possible individuals in P1 species. *D* scores and $\log_{10}(p)$ values are shown in different colour schemes. *Lycopersicon*, *Etuberosum*, *S. americanum* and *S. melongena* are used as an outgroup. The *P* values are calculated using a standard block-jackknife procedure as in ref. [28](#).

[Source data](#)

Extended Data Fig. 4 Landscape of NLRs in the potato genome.

a, NLR copy number in six canonical classes. NL: NB-LRR, CNL: CC-NB-LRR, NB: NB domain only, TNL: TIR-NB-LRR, TN: TIR-NB, CN: CC-NB. **b**, Proportion of each NLR class in 45 potato genomes.

[Source data](#)

Extended Data Fig. 5 Features of potato-specific CNSs and categories of 229 candidate genes.

a, CNS length distribution. **b**, Summary of CNSs in potato. **c**, Pie chart shows the distribution of CNSs in potato genome. **d**, Functional categories of 229 CNS-associated potato core genes displaying stolon or tuber predominant expression.

[Source data](#)

Extended Data Fig. 6 Phenotypes of the *it1* knockout mutant.

a, The *IT1* CRISPR/Cas9 knockout mutant. **b**, The *it1* mutant shows an impaired tuberization phenotype. The main stems were removed. Red arrows indicate *it1* stolons that convert to branches. The white arrow shows a small tuber formed on *it1*.

Extended Data Fig. 7 Interaction, sequence synteny and expression of *SP6A*.

a, Interaction between IT1 and SP6A revealed by the firefly luciferase complementation imaging assay. Three independent experiments are performed. **b**, Synteny plot of *SP6A* genomic sequences from representative *Etuberosum* and potato species. Blue boxes indicate the exons of *SP6A*, and grey blocks show collinear regions among these genomes. **c**, The protein sequence alignment of SP6A between DM and PG0019. **d**, The *SP6A* expression in potato (E4-63) and *Etuberosum* (PG0019) leaves at ZT4. ** *P*-value = 1.59e-04 in two-sided Student's *t*-test. ETB: *Etuberosum*. LD: long-

day. SD: short-day. Data presented in mean \pm SD, $n = 3$. Three independent experiments are carried out.

[Source data](#)

Extended Data Fig. 8 Genome-wide sequence variation of the 44 potato genomes.

a, Genomic architecture of heterozygosity distribution in 44 diploid potato genomes revealed by alignment to the DM reference genome; heterozygous (blue) and homozygous (pink) regions, respectively. **b**, Local synteny (DM chr12: 53.57–54.31 Mb) illustration surrounding the *GLYCOALKALOID METABOLISM 4 (GAME4)* locus. **c**, Local synteny (DM chr01: 0.65–1.13 Mb) illustration surrounding *FLAVIN-BINDING KELCH REPEAT F-BOX PROTEIN (FKF1)*. Genes from four potato landraces (DM, A6-26, E4-63, and RH) and four cultivated tomatoes (Heinz 1706, BGV006865, EA00371 and M82) are shown. **d**, SV allele frequency among the 44 potatoes. **e**, Number of SVs localized at regulatory, genic and intergenic regions. The upper and lower edges of the boxes represent the 75% and 25% quartiles, the central line denotes the median and the whiskers extend to $1.5 \times$ IQR. The number of genomes investigated in each category is 44.

[Source data](#)

Extended Data Fig. 9 Association between tuber flesh colour, *BCH* expression level and the presence of the 5.8-Mb inversion.

a, Phenotypes of tuber colour for accessions E4-63, A6-26, PG6359 and PG5068. **b**, Expression level (\log_2 TPM) of *BCH* in five tissues of wild, CND and landrace accessions/haplotypes. Orange dot denotes DM haplotype, and grey dot denotes wild/CND haplotype. DM haplotype: accessions without the inversion; Wild/CND haplotype: accessions carrying the inversion. **c**, Expression level (TPM) of *BCH* in tubers of 22 accessions/haplotypes, including 4 DM haplotypes, and 18 wild/CND haplotypes. *** P -value = 1.462e-07 in two-sided Student's *t*-test.

[Source data](#)

Supplementary information

Supplementary Information

This file includes Supplementary Figs. 1–11.

Reporting Summary

Peer Review File

Supplementary Tables

This file includes Supplementary Tables 1–17.

Source data

Source Data Fig. 1

Source Data Fig. 2

Source Data Fig. 3

Source Data Fig. 4

Source Data Extended Data Fig. 1

Source Data Extended Data Fig. 3

Source Data Extended Data Fig. 4

Source Data Extended Data Fig. 5

Source Data Extended Data Fig. 7

[Source Data Extended Data Fig. 8](#)

[Source Data Extended Data Fig. 9](#)

Rights and permissions

Open Access This article is licensed under a Creative Commons Attribution 4.0 International License, which permits use, sharing, adaptation, distribution and reproduction in any medium or format, as long as you give appropriate credit to the original author(s) and the source, provide a link to the Creative Commons license, and indicate if changes were made. The images or other third party material in this article are included in the article's Creative Commons license, unless indicated otherwise in a credit line to the material. If material is not included in the article's Creative Commons license and your intended use is not permitted by statutory regulation or exceeds the permitted use, you will need to obtain permission directly from the copyright holder. To view a copy of this license, visit <http://creativecommons.org/licenses/by/4.0/>.

[Reprints and Permissions](#)

About this article

Cite this article

Tang, D., Jia, Y., Zhang, J. *et al.* Genome evolution and diversity of wild and cultivated potatoes. *Nature* **606**, 535–541 (2022).
<https://doi.org/10.1038/s41586-022-04822-x>

- Received: 04 October 2021
- Accepted: 28 April 2022
- Published: 08 June 2022
- Issue Date: 16 June 2022

- DOI: <https://doi.org/10.1038/s41586-022-04822-x>

Share this article

Anyone you share the following link with will be able to read this content:

[Get shareable link](#)

Sorry, a shareable link is not currently available for this article.

[Copy to clipboard](#)

Provided by the Springer Nature SharedIt content-sharing initiative

Further reading

- [**Potato genomes pave the way to crop improvement**](#)

- Juanita Gutiérrez-Valencia
- Tanja Slotte

Nature (2022)

[**Graph pangenome captures missing heritability and empowers tomato breeding**](#)

- Yao Zhou
- Zhiyang Zhang
- Sanwen Huang

Nature Article Open Access 08 Jun 2022

[**Potato genomes pave the way to crop improvement**](#)

- Juanita Gutiérrez-Valencia
- Tanja Slotte

Nature News & Views 08 Jun 2022

This article was downloaded by **calibre** from <https://www.nature.com/articles/s41586-022-04822-x>

| [Section menu](#) | [Main menu](#) |

- Article
- Open Access
- [Published: 01 June 2022](#)

Communicating doctors' consensus persistently increases COVID-19 vaccinations

- [Vojtěch Bartoš](#) ,
- [Michal Bauer](#),
- [Jana Cahlíková](#) &
- [Julie Chytilová](#)

Nature volume **606**, pages 542–549 (2022)

- 15k Accesses
- 1 Citations
- 735 Altmetric
- [Metrics details](#)

Abstract

The reluctance of people to get vaccinated represents a fundamental challenge to containing the spread of deadly infectious diseases^{1,2}, including COVID-19. Identifying misperceptions that can fuel vaccine hesitancy and creating effective communication strategies to overcome them are a global public health priority^{3,4,5}. Medical doctors are a trusted source of advice about vaccinations⁶, but media reports may create an inaccurate impression that vaccine controversy is prevalent among doctors, even when a broad

consensus exists^{7,8}. Here we show that public misperceptions about the views of doctors on the COVID-19 vaccines are widespread, and correcting them increases vaccine uptake. We implement a survey among 9,650 doctors in the Czech Republic and find that 90% of doctors trust the vaccines. Next, we show that 90% of respondents in a nationally representative sample ($n = 2,101$) underestimate doctors' trust; the most common belief is that only 50% of doctors trust the vaccines. Finally, we integrate randomized provision of information about the true views held by doctors into a longitudinal data collection that regularly monitors vaccination status over 9 months. The treatment recalibrates beliefs and leads to a persistent increase in vaccine uptake. The approach demonstrated in this paper shows how the engagement of professional medical associations, with their unparalleled capacity to elicit individual views of doctors on a large scale, can help to create a cheap, scalable intervention that has lasting positive impacts on health behaviour.

Main

COVID-19 is a salient example of a disease with profound economic, social and health impacts, which can be controlled by large-scale vaccination if enough people choose to be vaccinated. Nevertheless, a large percentage of people are hesitant to get a vaccine, preventing many countries from reaching the threshold necessary to achieve herd immunity^{9,10}. Consequently, rigorous evidence on scalable approaches that can help to overcome people's hesitancy to take a COVID-19 vaccine is a global policy priority^{3,4,5}. Existing research has made important progress in documenting the roles of providing financial incentives^{11,12}, reminders^{4,5}, information about the efficacy of the vaccines^{13,14}, the role of misinformation¹⁵ on the intentions of the public to get vaccinated and, more recently, also on their actual decisions to get a vaccine⁵ shortly after an intervention. However, little is known about whether cheap, scalable strategies with the potential to cause lasting increases in people's vaccination demand and uptake exist. A focus on the persistence of the impacts of interventions is especially important for vaccines such as those against COVID-19, which are often distributed in phases to different demographic groups due to capacity

constraints, and multiple doses spaced over time are required to avoid declines in protection.

In many surveys across the globe, people report that they strongly trust the views of doctors⁶. This makes it crucial to understand how people perceive doctors' views about the COVID-19 vaccine. In this paper, we pursue the hypothesis that reluctance to adopt the vaccine originates, in part, in misperceptions about the distribution of aggregate views of the medical community: many people may fail to recognize that there is a broad consensus in favour of the vaccine among doctors. Furthermore, we argue and show that professional associations can serve as aggregators of individual views in a medical community, by helping to implement surveys eliciting the views of doctors on a large scale. Disseminating information of a broad consensus, when one exists, can lead to people updating their perceptions of doctors' views and, in turn, may induce lasting changes in vaccination demand and uptake.

Our focus on public misperceptions of the views of doctors is motivated by a widespread concern that media coverage can create uncertainty and polarization in how people perceive expert views, even when a broad consensus actually exists. In terms of traditional media, a desire to appear neutral often motivates journalists to provide a 'balanced' view by giving roughly equal time to both sides of an argument^{7,16}, creating an impression of controversy and uncertainty⁸. Such 'falsely balanced' reporting has been shown to be a characteristic element of policy debates ranging from climate change^{7,16} to health issues, including links between tobacco and cancer, and potential side effects of vaccines^{8,17}. In the context of the COVID-19 vaccines, casual observation suggests that media outlets often feature expert opinions that highlight the efficacy of approved COVID-19 vaccines together with skeptical experts who voice concerns about rapid vaccine development and untested side effects. The media usually do not specify which claims are supported by the wider medical community, leading the World Health Organization to warn media outlets against engaging in false-balance reporting¹⁸. Furthermore, polarization of beliefs can arise due to echo chambers—people choosing to be exposed to expert opinions or opinion programmes that fuel their fears of the vaccine or, alternatively, to those who strongly approve of it^{19,20,21}.

We study these issues in the Czech Republic, which is a suitable setting, given the observed level of vaccine hesitancy among a large share of its population, similar to the situation in many other countries. At the time of data collection, the acceptance rate of the vaccine in the Czech Republic was around 65%, compared to 55–90% in other countries globally. At the same time, the Czech Republic ranks close to the median level of trust and satisfaction with medical doctors, based on a comparison of 29 countries⁶. We provide more background in Section 3.1 of the [Supplementary Information](#).

We start by documenting and quantifying public misperceptions about the views of doctors on the COVID-19 vaccines. Shortly before the COVID-19 vaccine rollout began, we implemented a short online survey among 9,650 doctors. We found strong evidence of consensus: 90% of doctors intend to get vaccinated themselves and 89% trust the approved vaccines. At the same time, we found evidence of systemic and widespread misperceptions of the views held by the medical community among a nationally representative sample of the adult population ($n = 2,101$): more than 90% of people underestimate doctors' trust in the vaccines and their vaccination intentions, with most people believing that only 50% of doctors trust the vaccines and intend to be vaccinated.

These findings set the stage for our main experiment, in which we tested whether randomized provision of information about the actual views of doctors can recalibrate public beliefs and, more importantly, cause a lasting increase in vaccination uptake. The experimental design aimed to make progress on two important empirical challenges that are common in experiments on the determinants of demand for COVID-19 vaccines. First, as an intention–behaviour gap has been documented in the context of flu vaccines and other health behaviours²², measuring both vaccination intentions and actual vaccination uptake allows us to test whether treatment effects on vaccination intentions translate into behavioural changes of a similar magnitude. The initial set of studies on COVID-19 vaccination, typically implemented before the vaccines became available, only tested impacts on intentions^{11,14,15}, although recent exceptions exist^{5,23}.

Second, most experiments designed to correct misperceptions about the views of others, and other information provision experiments in various

domains, including migration, health and political behaviour, document treatment effects to be substantially smaller when measured with a delay^{24,25}. In theory, the worry is that individual perceptions about the views of doctors might shift between the time when the treatment takes place and when people decide whether to actually get vaccinated, for reasons including regression of perceptions to the mean, biased recall or motivated memory²⁶. Conversely, researchers have suggested that providing facts about a widely shared consensus of trustworthy experts might be resilient to these forces¹⁷, as the treatment may reduce incentives to seek new information, and condenses complex information into a simple fact ('90% of doctors trust the approved vaccines'), which is easy to remember. Understanding whether providing information about medical consensus has temporary or lasting effects on vaccination demand is informative for policy, in terms of whether a one-off information campaign is sufficient, or whether the timing of messages needs to be tailored for different groups of people who become eligible for a vaccine at different points in time, and also whether such an information campaign needs to be repeated in cases of multiple-dose vaccines.

To address these issues, our experiment is integrated into longitudinal data collection with low attrition rates. The treatment was implemented in March 2021. We used data from 12 consecutive survey waves collected from March to November 2021, covering the early period when the vaccine was scarce, later when it gradually became available to more demographic groups, and finally for several months when it was easily available to all adults. This is reflected in the vaccination rates, which increased in our sample from 9% in March to 20% in May and to nearly 70% in July. Then, it grew slowly to 77% at the end of November. This longitudinal, data-collection-intensive approach allows us to estimate: (1) whether disseminating information on the consensus view of the medical community has immediate effects on people's beliefs and their intentions to get the vaccination shortly after the intervention; (2) whether the effects translate into actually getting vaccinated, even though most of the participants became eligible for the vaccine only many weeks after the intervention; and (3) whether the effects on vaccine uptake are persistent or whether the vaccination rate of untreated individuals eventually catches up, perhaps due to ongoing governmental

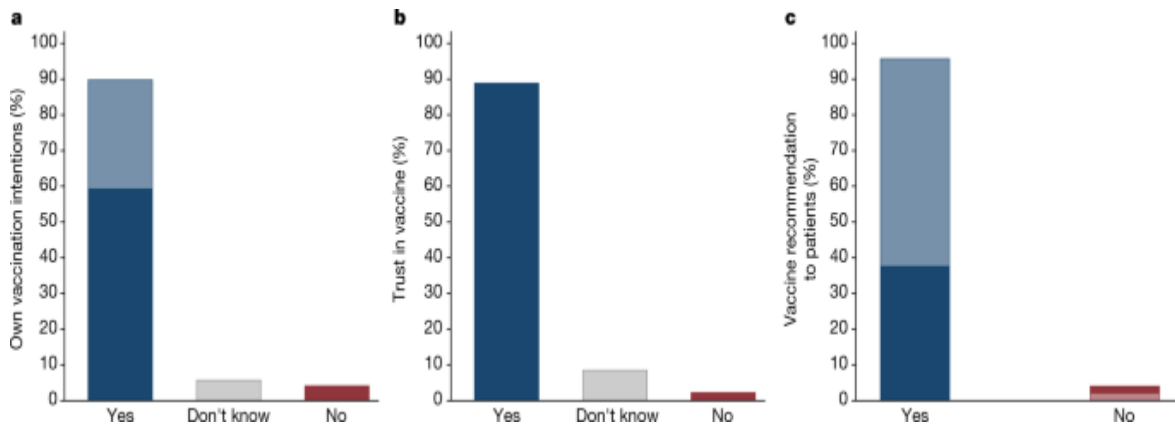
campaigns, stricter restrictions for individuals who are not vaccinated, or greater potential life disruptions during severe epidemiological periods.

Consensus of the medical community

We conducted a supplementary survey to gather the views of doctors on COVID-19 vaccines in February 2021. The survey was implemented in partnership with the Czech Medical Chamber (CMC), whose contact list includes the whole population of doctors in the country, because membership is compulsory. All doctors who communicate with the CMC electronically (70%) were asked to participate and 9,650 (24% of those contacted) answered the survey. Supplementary Table 1 provides summary statistics and documents that the sample is quite similar, in terms of age, gender, seniority and location, to the overall population of medical doctors in the Czech Republic.

Figure 1 shows the distribution of doctors' responses. A clear picture arises, suggesting that a broad consensus on COVID-19 vaccines exists in the medical community: 89% trust the vaccine (9% do not know and 2% do not trust it), 90% intend to get vaccinated (6% do not know and 4% do not plan to get vaccinated) and 95% plan to recommend that their patients take a vaccine (5% do not). These responses are broadly similar across gender, age, years of medical practice and size of the locality in which the doctors live: for all sub-groups, we found the share of positive answers to all questions ranges between 85% and 100% (Supplementary Table 2). Using probability weights based on observable characteristics of the entire population of doctors in the country makes very little difference in the estimated distribution of opinions in our survey. Reassuringly, the opinions in our survey are in line with high actual vaccination rates (88%) observed among Czech doctors when vaccines became available²⁷, despite vaccination not being compulsory for any profession, including for doctors.

Fig. 1: The views of doctors on COVID-19 vaccines.



Supplementary study among the members of the CMC ($n = 9,650$). **a**, Distribution of responses to the question “Will you personally be interested in getting vaccinated, voluntarily and free of charge, with an approved vaccine against COVID-19?”. Among participants who answered yes, the dark blue refers to those who reported already being vaccinated, whereas the light blue refers to those who plan to get vaccinated. **b**, Responses to the question “Do you trust COVID-19 vaccines that have been approved by the European Medicines Agency (EMA) approval process?”. **c**, Responses to the question “Will you recommend COVID-19 vaccination to your healthy patients to whom you would recommend other commonly used vaccines?” Among participants who answered yes, the dark blue refers to those who would recommend the vaccines even without being asked, whereas the light blue refers to those who would recommend only when asked. In [Supplementary Table 2](#), we show that the distribution of views is similar across various demographic groups and level of seniority.

Longitudinal experiment

Our main sample consists of participants in the longitudinal online data collection ‘Life during the pandemic’, organized by the authors in cooperation with PAQ Research; the data were collected by the NMS survey agency (Methods and [Supplementary Methods](#)). The information intervention was implemented on 15 March 2021 (wave 0). We used data from 12 consecutive waves of data collection regularly conducted from March to November 2021. This time span covers the period when the vaccination was gradually rolled out and eligibility rules changed regularly, making the vaccine available for more demographic groups (until June

2021), and a period when vaccination was freely available for the entire adult population (from July 2021).

The sample from wave 0 is our ‘base sample’ ($n = 2,101$). By design, the sample is broadly representative of the adult Czech population in terms of a host of observable characteristics (for summary statistics, see Extended Data Table 1). In addition, the vaccination rate reported in our sample closely mimics the levels and dynamics of the overall adult vaccination rate in the country (Extended Data Fig. 1). This comparison suggests that attitudes to vaccination in our sample are likely to be representative of the larger population, in contrast to surveys based on convenience samples²⁸. Although this pattern is reassuring, we cannot test and fully rule out a possibility that our sample might not be representative in terms of unobservable characteristics affecting receptivity to the information treatment studied. Furthermore, the response rate in the follow-up waves is high, ranging between 76% and 92%. A large portion of participants ($n = 1,212$; the ‘fixed sample’) took part in all 12 waves of data collection.

The participants were randomly allocated to either the Consensus condition ($n = 1,050$) or Control condition ($n = 1,051$) in wave 0. In the Consensus condition, they were provided with a summary of the survey among medical doctors, including three charts that displayed the distribution of doctors’ responses regarding their trust in the vaccines, willingness to get vaccinated themselves and intentions to recommend the vaccine to patients. In the Control condition, the participants did not receive any information about the survey of medical doctors and only filled the regular part of the longitudinal survey.

In all 12 waves, we asked whether respondents got vaccinated against COVID-19. The main outcome variable ‘vaccinated’ is equal to one if the respondent reported having obtained at least one dose of a vaccine against COVID-19. We also elicited prior beliefs on the views of doctors about the vaccines in wave 0 shortly before the information intervention, and posterior beliefs in wave 1 2 weeks afterwards.

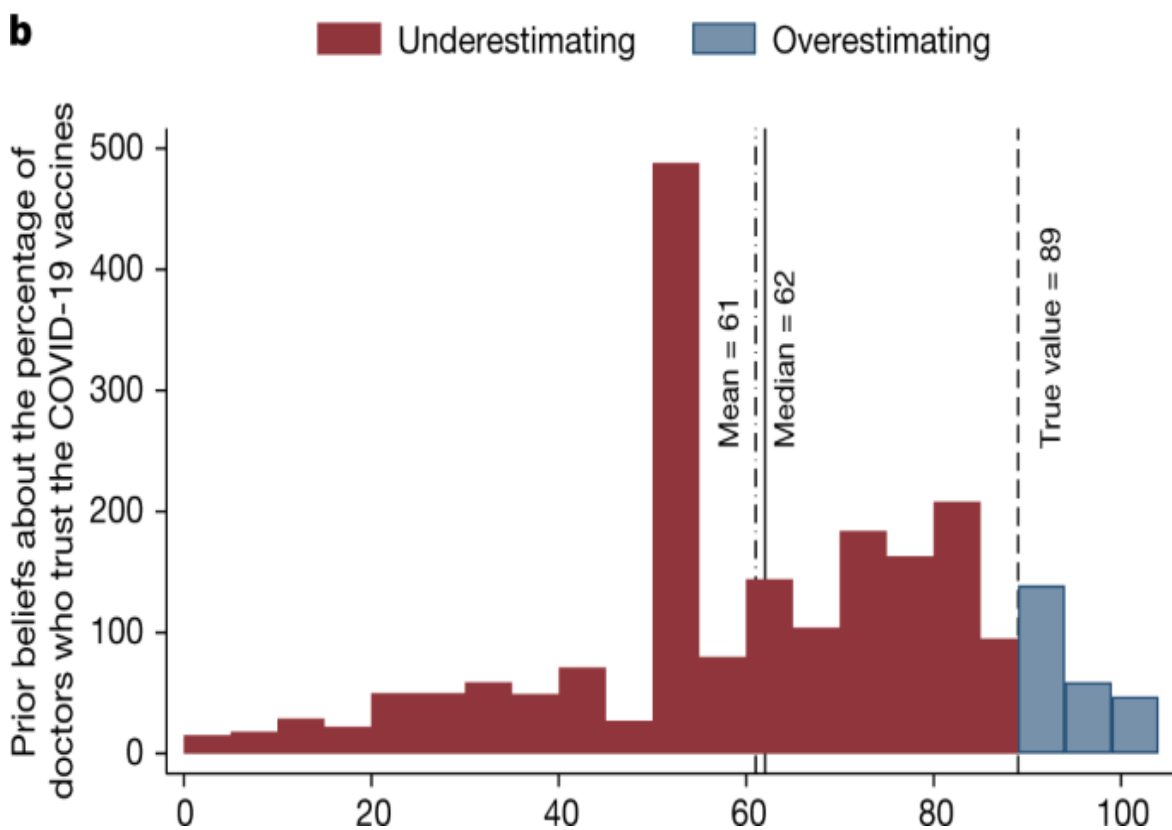
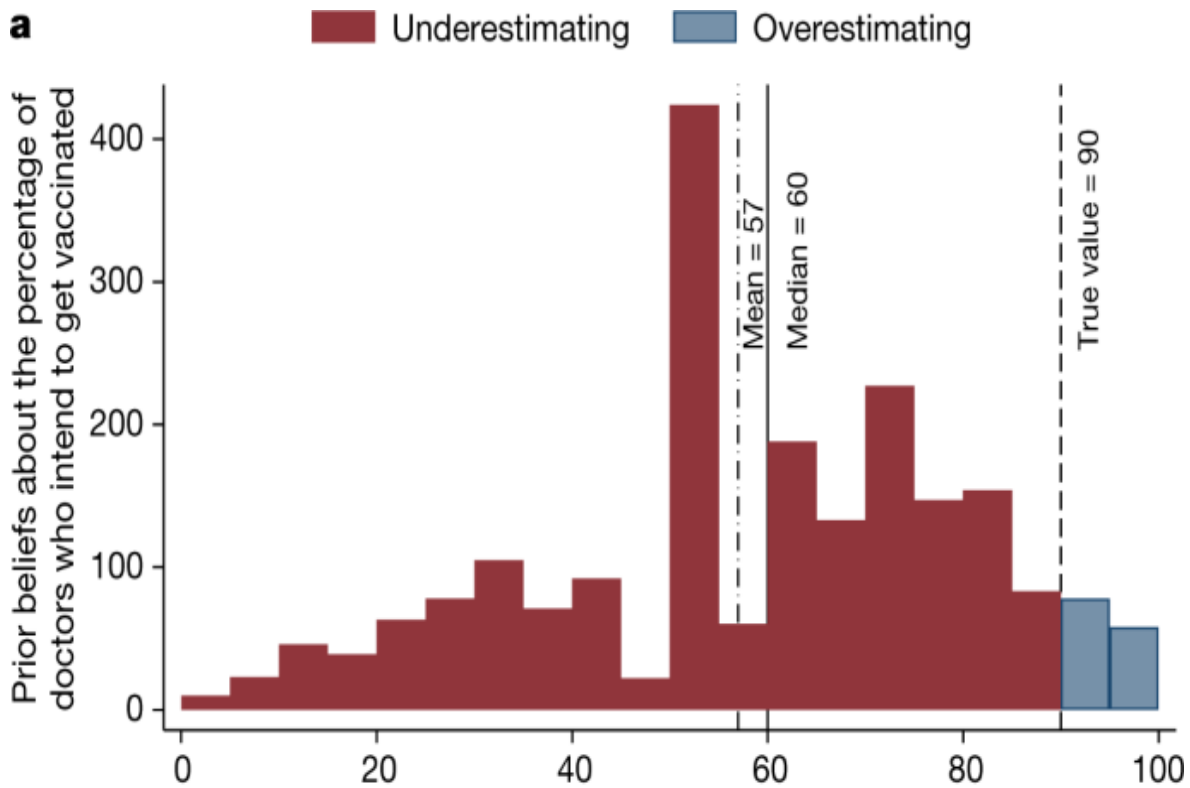
Extended Data Table 1 and Supplementary Table 3 show no systematic differences in the set of baseline characteristics pre-registered as control variables. Nevertheless, because the randomization was not stratified on

baseline covariates, there are random imbalances in some covariates, as expected. Some of the larger differences are for variables not included in the set of pre-registered control variables. Specifically, before the intervention, compared to participants in the Control condition, the individuals in the Consensus condition were slightly less likely to be vaccinated themselves (standardized mean difference (SMD) = 0.069), and expected a smaller percentage of doctors to trust the vaccine (SMD = 0.072) or to intend to get vaccinated (SMD = 0.090). As these three variables are highly predictive of vaccination uptake, we report two main regression specifications: (1) with the pre-registered set of control variables, and (2) with control variables selected by the LASSO procedure²⁹. To document robustness, we also report estimates with no control variables and with alternative sets of control variables.

Misperceptions about doctors' views

To quantify misperceptions about the views of doctors on COVID-19 vaccines, we compared the prior beliefs of participants about doctors' views, measured before the intervention, with the actual views of the doctors from the CMC survey. We found strong evidence of misperceptions. The average, median and modal guesses are that 57%, 60% and 50% of doctors, respectively, want to be vaccinated (Fig. 2a), whereas in reality 90% of doctors do. The average, median and modal guesses about the percentage of doctors who trust the vaccines are 61%, 62% and 50%, respectively (Fig. 2b), whereas in practice 89% of doctors report trusting the vaccines. A vast majority of participants underestimate the percentage of doctors who want to be vaccinated (90%) and those who trust the vaccines (88%).

Fig. 2: Perceptions of doctors' views on COVID-19 vaccines.



A sample of the adult Czech population ($n = 2,101$). **a**, Distribution of the prior beliefs of respondents about what percentage of doctors would like to get vaccinated. **b**, Distribution of the beliefs of respondents about what percentage of doctors trust approved COVID-19 vaccines. The dashed line shows the true value, based on the responses of doctors in the Supplementary study. The red and blue colours show the percentage of those who underestimate and overestimate, respectively, doctors' own vaccination intentions (**a**) and trust in the COVID-19 vaccines (**b**).

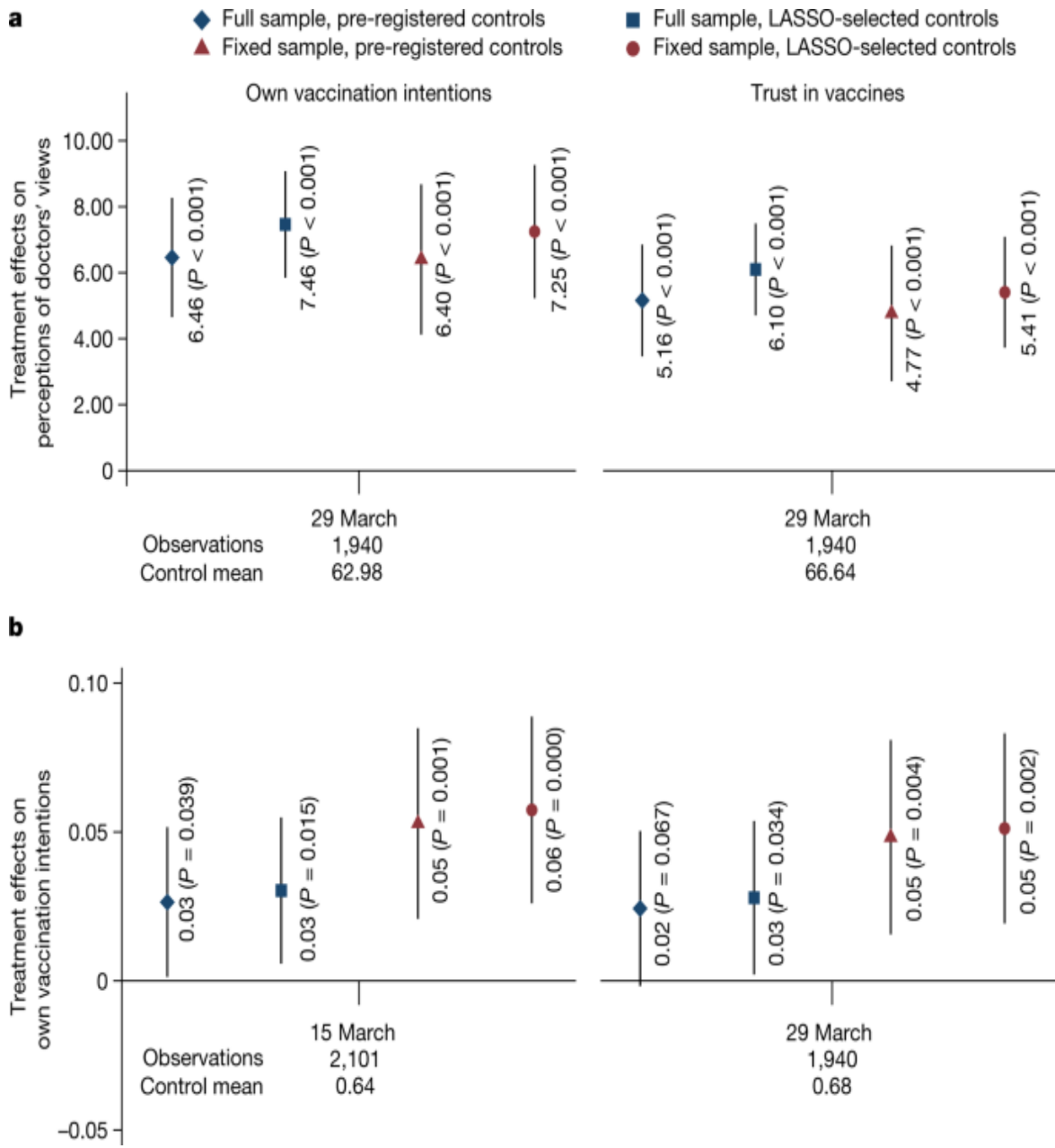
The distribution of beliefs reveals that the large underestimation does not originate in two distinct groups of participants holding opposite views of the medical consensus—one group thinking that most doctors have positive views about the vaccines and the other group thinking that most doctors are skeptical about them. Instead, most people expect a wide diversity of attitudes across individual doctors. Of participants, 81% believe that the percentage of doctors who want to be vaccinated is between 20% and 80%. For beliefs about doctors' trust in the vaccines, this number is 76%. Furthermore, these misperceptions are widespread across all demographic groups based on age, gender, education, income and geographical regions (Supplementary Table 4).

We found several intuitive descriptive patterns that increase confidence in our measures of beliefs. First, beliefs about the vaccination intentions of doctors and their trust in the vaccines are strongly positively correlated ($r(2,099) = 0.60$, $P < 0.001$). Second, beliefs about doctor's trust and vaccination intentions are highly predictive of respondents' own intentions and uptake (Supplementary Table 4). In the next sub-section, we explore whether this relationship is causal. Third, in Supplementary Fig. 1, we show that misperceptions about the doctor's views are unlikely to arise due to the inattention of participants to the questions. The results are very similar when we excluded the 4% of participants who did not pass all of the attention checks embedded in the survey, and when we excluded the 10% of participants with the shortest response times.

Intervention impacts on vaccination

We first established the effects of the intervention on posterior beliefs about the views and vaccination intentions of doctors shortly after the intervention. We found that the information provided shifts expectations about the views of doctors (Fig. 3a and Supplementary Table 5). Two weeks after the intervention (in wave 1), the Consensus condition increased beliefs about the share of doctors who trust the vaccines by 5 percentage points (p.p.) ($P < 0.001$) and beliefs about the share of doctors who want to get vaccinated by 6 p.p. ($P < 0.001$). Next, the Consensus condition increased the prevalence of people intending to get vaccinated by around 3 p.p. ($P = 0.039$; Fig. 3b and Supplementary Table 6). When we restricted the sample to those who participated in all waves, we found the point estimate to be slightly larger (5 p.p., $P = 0.001$).

Fig. 3: Effects of the Consensus condition on posterior beliefs about doctors' views and vaccination intentions.

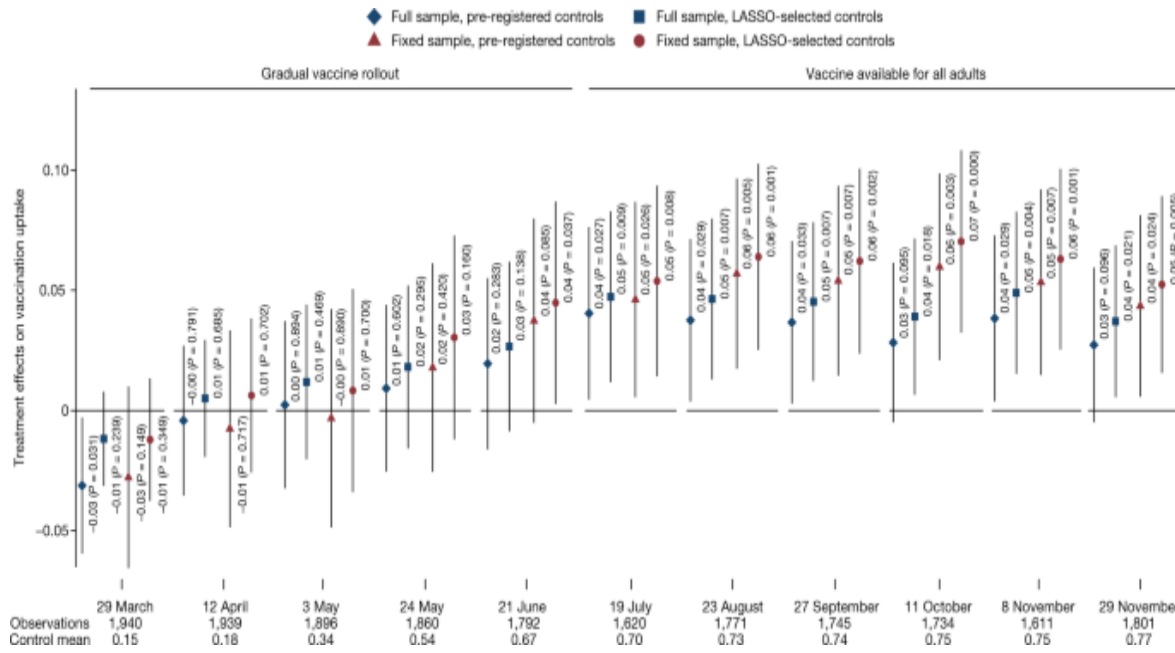


A sample of the adult Czech population. **a**, Estimated effects of the Consensus condition on beliefs about the percentage of medical doctors who plan to get vaccinated (left panel) and on beliefs about the percentage of doctors who trust approved COVID-19 vaccines (right panel), measured in wave 1 (29 March; Consensus condition $n = 970$; Control $n = 970$). **b**, The dependent variable is an indicator for an intention to be vaccinated with a vaccine against COVID-19, measured in wave 0 (15 March; Consensus condition $n = 1,050$; Control $n = 1,051$) and wave 1 (29 March; Consensus condition $n = 970$; Control $n = 970$). We report the results of two

specifications: (1) a linear probability regression controlling for pre-registered covariates: gender, age category (6 categories), household size, number of children, region (14 regions), town size (7 categories), education (4 categories), economic status (7 categories), household income (11 categories) and baseline vaccination intentions, and (2) a double-selection LASSO linear regression selecting from a wider set of controls in Extended Data Table 1, including prior vaccine uptake and beliefs about the views of doctors. Markers show the estimated effects and the whiskers denote the 95% confidence interval based on Huber–White robust standard errors. The estimated effects and Student's *t*-test (two-sided) *P* values are reported in the figure. No adjustments were made for multiple comparisons. We report estimates for (1) all observations, full sample (diamond and square), and (2) for a sub-sample of participants who took part in all 12 waves (Consensus condition $n = 614$; Control $n = 598$), fixed sample (triangle and circle). In the lower part of the figure, we report the timing, the total number of observations and the Control mean for each wave. See [Supplementary Section 3.5](#) for further specification details. [Supplementary Tables 5 and 6](#) show the regression results for **a** and **b** in detail, respectively.

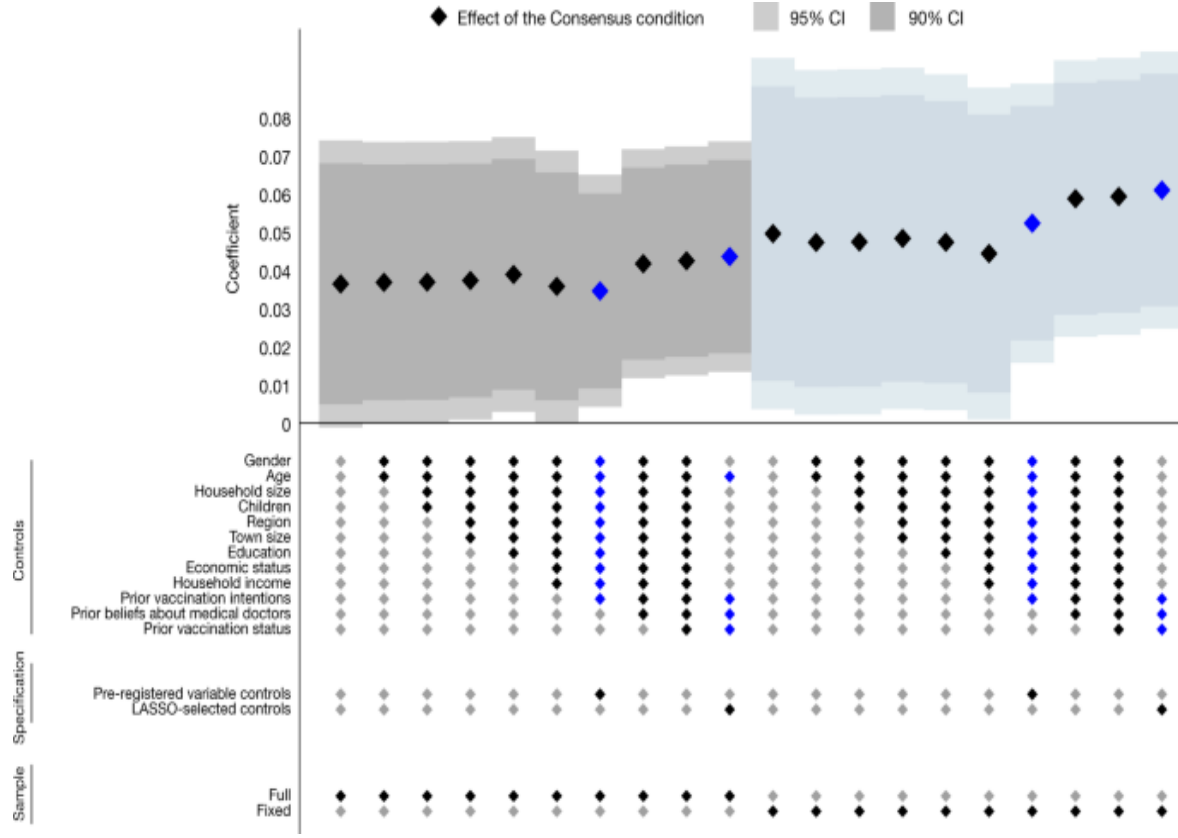
Next, we found a systematic, robust and lasting treatment effect on vaccine uptake. Four months after the intervention, when vaccines became available to all adults, we found that participants in the Consensus condition were around 4 p.p. more likely to be vaccinated than those in the Control condition (Figs. 4 and 5). As expected, owing to the gradual rollout of the vaccine during the March to June period, the effect emerged gradually (Extended Data Table 2 provides more information about changes in vaccine eligibility rules). The difference in the uptake rates between the Consensus and Control conditions steadily increased to 4–5 p.p. in July and remained relatively stable thereafter (Fig. 4 and Extended Data Table 3).

Fig. 4: Effects of the Consensus condition on vaccination uptake.



A sample of the adult Czech population. Estimated effects of the Consensus condition by survey wave on getting at least one dose of a vaccine against COVID-19. We report the same four specifications as in Fig. 3 (linear probability model with pre-registered controls using full (diamond) and fixed (triangle) samples, and double-selection LASSO linear regression selecting from controls in [Extended Data Table 1](#) using full (square) and fixed (circle) samples). Markers show the estimated effects and the whiskers denote the 95% confidence interval based on Huber–White robust standard errors. The estimated effects and Student's t -test (two-sided) P values are reported in the figure. No adjustments were made for multiple comparisons. We report estimates for (1) all observations, full sample (diamond and square), and (2) for a sub-sample of participants who took part in all 12 waves, fixed sample (triangle and circle). In the lower part of the figure, we report the timing, the total number of observations and the Control mean for each wave. Full sample: Consensus condition $n = 807\text{--}970$, Control $n = 800\text{--}973$; see [Extended Data Table 2](#) for exact n per wave. Fixed sample: Consensus condition $n = 614$; Control $n = 598$. [Extended Data Table 3](#) shows the regression results in detail.

Fig. 5: Effects of the Consensus condition on vaccine uptake: robustness.



A sample of the adult Czech population. This specification chart plots the estimated effects of Consensus on the likelihood of vaccine uptake for a pooled sample across waves 6–11 (when the vaccine was available for all adults). All specifications include wave fixed effects. Markers show the estimated effects, the darker or lighter whiskers denote the 90% or 95% confidence interval, respectively, based on standard errors clustered at the respondent level. No adjustments were made for multiple comparisons. We report a range of linear probability model specifications by sequentially adding sets of control variables in Extended Data Table 1. The main specifications are marked by blue diamonds. We report all specifications for both the full sample (left-hand side) and the fixed sample (right-hand side). Full sample: Consensus condition $n = 5,145$ (981 clusters = respondents); Control $n = 5,137$ (983 clusters = respondents). Fixed sample: Consensus $n = 3,684$ (614 clusters = respondents); Control $n = 3,588$ (598 clusters = respondents). Extended Data Table 4 shows the regression results in detail.

In Fig. 5 and Extended Data Table 4, we report results from pooled regressions to utilize data from all six waves implemented in July to

November, include wave fixed effects and cluster standard errors at the individual level. The estimated treatment effect is significant for both main specifications—when we control for a set of variables selected by the LASSO procedure ($P = 0.005$) and when we control for the pre-registered set of variables ($P = 0.026$). The effect is similar when estimated in each of these waves separately (Fig. 4).

The estimated effect size is slightly larger (4.4 p.p.) when we used the specification with LASSO-selected control variables than when we used the specification with pre-registered control variables (3.5 p.p.). Figure 5 shows that this is because the LASSO procedure selects baseline beliefs and vaccination status as relevant control variables, whereas these variables are not included in the pre-registered set. Consequently, both approaches document robust positive treatment effect between 3.5 and 4.4 p.p. Readers who believe that researchers should control for random imbalances in important baseline variables may favour the upper bound, whereas readers concerned about departures from pre-registered analyses may favour the lower bound.

Our finding of a positive treatment effect does not rely on a specific choice of control variables or estimation strategy. First, the effect is very similar when we controlled for various sets of baseline variables other than the pre-registered and LASSO-selected sets, as well as when we controlled for none (Fig. 5 and Extended Data Table 4). Second, the effect is significant at conventional levels when we calculated P values using the randomization inference method (Extended Data Tables 3 and 5). Third, the estimated treatment effect is 5.4 p.p. ($P = 0.008$) when we used baseline data about vaccination rates, and used a difference-in-difference estimation (Supplementary Table 7). Furthermore, the results are robust to excluding participants who arguably paid less attention (Extended Data Table 5). As in the analysis of vaccination intentions, the estimated effects on uptake are slightly larger when we restricted the analysis to those who participated in all 12 waves.

Differential attrition cannot explain our findings. First, we found that the participation rate is relatively high and does not differ across the Consensus and Control conditions on average. There is also no evidence of differential attrition by baseline covariates, suggesting that different types of individuals

were not participating in the Consensus and Control conditions (Supplementary Table 8). We found this pattern for participation in each of the 11 follow-up waves separately as well as when we focused on participation in all waves (being in the fixed sample). As a sensitivity test, we imputed missing vaccination status for those who did not participate in some of the waves and assumed either that (1) their vaccination status has not changed since the last wave for which the data are available, or that (2) their status is the same as the one reported in the earliest next wave for which the data are available. The first approach allowed us to impute all the missing information because we know the vaccination status of each participant in the initial wave. The second approach allowed us to impute the missing information, except in cases when a respondent did not participate in the last wave. The effects are robust (Extended Data Table 5).

The effect of the Consensus condition on uptake is lasting. First, although in the main estimates we focused on the likelihood of respondents getting at least one vaccine dose, a qualitatively similar and significant effect emerges when we focused on the likelihood of participants getting two doses (Extended Data Fig. 2). Second, the treatment effect emerges during a 3-month period, due to availability restrictions, and then is stable across all six follow-up waves covering the July to November period (Fig. 4). Thus, the main effect is not driven by differences in the timing of getting vaccinated. Last, in the September and November waves, we asked about the intentions of participants to get a booster dose. The estimated effect is very similar in magnitude as the effect on uptake of the first dose (around 4 p.p.), suggesting that the information intervention elevates vaccination demand even 9 months after it was implemented (Extended Data Fig. 2).

Documenting such persistence has interesting implications. As the demand for vaccination in the Control condition does not catch up with the Consensus condition over such a long period, the results suggest that the type of vaccine hesitancy reduced by the Consensus condition is resilient to policies, campaigns or any life disruptions that participants were exposed to during the period studied. This includes a severe COVID-19 wave that took place in November 2021 in the Czech Republic, which resulted in one of the highest national mortality rates in global comparisons (see Section 3.1 of the [Supplementary Information](#) and Extended Data Fig. 3).

The point estimates of around 4 p.p. imply a relatively large effect size, especially in light of the low costs of the intervention. As the vaccination rate in the Control condition was 70–75% during the July to November period, the Consensus condition reduces the number of those who are not vaccinated by 13–16%. To compare, providing truthful information about the vaccination intentions of other people was shown to increase intentions to get vaccinated by 1.9 p.p.^{[30](#)}. Nudging health workers to get vaccinated by referring to vaccinated colleagues has been shown to increase the likelihood of their registering for vaccination by around 3 p.p.^{[31](#)}. More generally, the most successful, low-cost behavioural nudges with documented effect on uptake have estimated effect sizes up to 5 p.p.^{[4,5](#)}, which is quite similar to the effect of providing information about consensus in doctors' opinions studied here. In addition, a noteworthy aspect of our study is the documented persistence of the effects, which is another crucial margin for assessing the intervention effectiveness.

The [Supplementary Information](#) describes exploratory analyses of how the treatment effect differs across different sub-samples of respondents (Supplementary Table [5](#) and Extended Data Table [5](#)). Reassuringly, we found that the positive effect on vaccine uptake is concentrated among those who underestimated doctors' trust and vaccination intentions, whereas no systematic effect was observed among overestimators. In addition, the effect is driven by those who initially did not intend to get vaccinated, in line with the interpretation that the intervention changed the views of individuals who were initially skeptical about the vaccine. Nevertheless, the analysis of heterogenous effects should be treated as tentative because the differences in coefficients are not always significant and we did not adjust for testing of multiple hypotheses.

Given that vaccination status is self-reported, we provide several tests documenting that the observed effect does not arise due to priming or the experimenter demand motivating some people in the Consensus condition to report being vaccinated even when they were not. We begin by noting that the observed treatment effect is lasting and emerged only gradually over several months, as more people became eligible to get vaccinated. By contrast, priming and experimenter demand effects are typically thought to be relevant mainly for responses shortly after a treatment^{[25,32](#)}.

To probe more directly, we used two distinct approaches to verify the reported vaccination status in the main dataset. First, inspired by existing work^{25,33}, we used additional data about vaccination status collected for us by a third, independent party among the same sample. As the survey agency, graphical interface and topic of the survey were different from our main data collection, the experimenter demand effect that might be potentially associated with treatment in our main survey is unlikely to affect responses in the third-party verification survey. Only two respondents (one in the Consensus condition and one in the Control condition) reported being vaccinated in the main survey, but reported the opposite in the verification survey (Extended Data Table 6), so mismatch in reporting of being vaccinated is very rare in general and not related to treatment. We arrive at a similar conclusion using the second verification approach that links reported vaccination status with an official proof of vaccination: an EU Digital COVID certificate issued by the Czech Ministry of Health. We showed that respondents in the Consensus condition compared to the Control condition are not less willing or able to provide verifiable information from the certificate (Extended Data Table 6). Finally, we showed that the effect of the Consensus condition on lower prevalence of those reporting not being vaccinated in the main survey is almost fully explained by greater prevalence of those reporting being vaccinated and having their vaccination status verified (Supplementary Table 9). More details about the methods and results of both verifications appear in the Methods section and in Section 3.4 of the [Supplementary Information](#).

Discussion

Our results shed light on the role that misperceptions of the distribution of expert views have in vaccine hesitancy, and also show how this barrier can be lifted by providing accurate information. We provide evidence that (1) the vast majority of medical doctors in the Czech Republic trust the approved COVID-19 vaccines, (2) the vast majority of respondents in a nationally representative survey substantially underestimate the percentage of doctors with positive views of the vaccine, and (3) correcting these misperceptions has lasting positive effects on vaccine uptake. Although existing experiments have made progress in identifying low-cost strategies to increase vaccination intentions^{4,13,14,15} and uptake⁵ measured shortly after

the intervention, this paper integrates the experiment in longitudinal online data collection and contributes by identifying a low-cost, scalable treatment that has lasting effects on behaviour.

Scientists, and the medical community as a whole, have invested enormous efforts to develop and deliver COVID-19 vaccines. However, much less collective effort has been directed at informing the public of the high levels of trust in the vaccine across the broad medical community. Here we show that professional medical associations can serve as aggregators of individual doctors' views, by facilitating opinion polls among doctors. Resulting data can be used in campaigns to tackle vaccine hesitancy and also as input for media reports. Although we cannot empirically pin down the sources of the misperceptions observed in our study, we suspect that they originate, at least in part, in a journalistic norm in which balance is often considered a mark of objective and impartial reporting, and a way to attract the attention of news consumers³⁴. Our results strengthen the case for supplementing contrasting views on controversial issues with information about how prevalent such views are³⁵.

To guide efforts to scale up this intervention, we discuss what types of factors may affect its efficiency and how we view the boundary conditions in terms of the applicability of the intervention beyond the context that we studied. We estimate the effects of a one-time intervention, among a sample in which most people probably paid attention to the information. Understanding whether the efficiency of the intervention can be fostered by repeated provision of information, as some research has suggested³⁶, and which modes of delivery, such as media advertisements, text messages or informational mail flyers, can best attract a sufficient degree of attention is an important next step for future research. Next, in many settings, implementing such information campaigns by governments, health insurance companies or healthcare providers may help to facilitate access to the contacts of large numbers of individuals^{4,5} and to address the need for a trusted source to provide the information intervention. Furthermore, in theory, this type of intervention should have larger effects: (1) the greater the trust in medical doctors in a given country is, and (2) the greater the prevalence of misperceptions about the views of doctors towards a vaccine is. We studied this intervention in a country with an approximately median

level of trust in doctors⁶, which provides some confidence that our findings from the Czech Republic may extend to other settings. At the same time, to our knowledge, because this is the first paper to provide direct evidence of the prevalence and size of misperceptions about the views of doctors on COVID-19 vaccines, we can only speculate how widespread such misperceptions are in other settings. Given that the likely sources of the misperceptions—false-balance reporting and echo chambers—are not specific to the Czech Republic, and given that misperceptions about scientific consensus have been documented in other countries in other domains, including health and climate change^{24,37}, we suspect that this bias in beliefs about COVID-19 vaccines is relatively widespread. We hope to see more research on this front.

Methods

Supplementary survey among doctors

To gather the views of doctors on COVID-19 vaccines, we implemented a survey in partnership with the CMC, to maximize coverage of the medical community. The survey was implemented online in February 2021. Because membership in the CMC is compulsory, the CMC has a list of contacts for the whole population of doctors in the country. The CMC approached all doctors who communicate with the CMC electronically (70%) and asked them to participate in a short survey, using the Qualtrics platform. Of doctors contacted, 9,650 (24%) answered the survey. The doctors in our sample work in all regions of the country, are on average 52 years of age, 64% are female individuals and 62% have more than 20 years of experience. A comparison of characteristics of doctors in our sample and of all doctors in the Czech Republic is presented in Supplementary Table 1.

Main experiment

Sample

Our main sample consisted of 2,101 participants of the longitudinal online data collection ‘Life during the pandemic’, organized by the authors in

cooperation with PAQ Research and the NMS survey agency. In March 2020, the panel began to provide real-time data on developments in economic, health and social conditions during the COVID-19 pandemic. We used data from 12 consecutive waves of data collection conducted at 3–4-week intervals between mid-March and the end of November 2021.

The information intervention was implemented on 15 March 2021, which we labelled as wave 0. The sample from wave 0 is the ‘base sample’ ($n = 2,101$, 1,052 female participants and 1,049 male participants, mean age of 52.9 years (s.d. = 15.98), youngest 18 years of age, oldest 92 years of age). The base sample is broadly representative of the adult Czech population in terms of sex, age, education, region, municipality size, employment status before the COVID-19 pandemic, age \times sex, and age \times education. Prague and municipalities with more than 50,000 inhabitants are oversampled (boost 200%). Sample statistics are presented in Extended Data Table 1. The sample is close to being representative of the adult Czech population in terms of attitudes to COVID-19 vaccines. The development of the proportion of people getting vaccinated in the Control condition very closely mimics the actual vaccination rates in the Czech Republic (Extended Data Fig. 1), when we weighted the observations in our sample to be representative in terms of observable characteristics.

An important feature of the panel is that participants agreed to be interviewed regularly, and the response rate is high throughout the study: it ranges between 76% and 92% in individual follow-up waves, and is 86% for the last wave, implemented at the end of November 2021. Of participants, 1,212 (58%) took part in all 12 waves of data collection: they form the ‘fixed sample’. Consequently, in the analysis, we report the main results for (1) all participants from the base sample who responded in a given wave, which we denote ‘full sample’, and for (2) the ‘fixed sample’, composed of individuals who participated in all 12 waves, eliminating the potential role of differences in samples across waves and making it easier to gauge the dynamics of treatment effects.

Information intervention

In wave 0, the participants were randomly assigned to either the Consensus condition ($n = 1,050$) or the Control condition ($n = 1,051$). In the Consensus condition, they were informed that the CMC conducted a large survey of almost 10,000 doctors from all parts of the country to collect their views on COVID-19 vaccines. They were also informed that the views were similar for doctors of different genders, ages and regions. Then, the participants were shown three charts displaying the distribution of responses of doctors regarding their trust in the vaccines, willingness to get vaccinated themselves and intentions to recommend the vaccine to their patients. Each of the charts was supplemented by a short written summary. The exact wording and the charts are provided in Section 3.3 of the [Supplementary Information](#). In the Control condition, the participants did not receive any information about the survey of medical doctors.

Data

Before the information intervention in wave 0, we elicited prior beliefs about doctor's views to quantify misperceptions about doctors' opinions.

Specifically, the participants were asked to estimate (1) the percentage of doctors in the Czech Republic who trust the approved vaccines, and (2) the percentage of doctors who are either vaccinated or intend to get vaccinated themselves. Later, in wave 1, we elicited posterior beliefs to estimate whether people in the Consensus condition actually updated their beliefs about doctors' views based on the information provided. In each of the 12 waves, we asked respondents to report whether they got vaccinated against COVID-19. The main outcome variable 'vaccinated' is equal to one if the respondent reported having obtained at least one dose of a vaccine against COVID-19.

In the analysis, we report two main regression specifications: (1) a linear probability regression controlling for pre-registered covariates: gender, age (6 categories), household size, number of children, region (14 regions), town size (7 categories), education (4 categories), economic status (7 categories), household income (11 categories) and prior vaccination intentions, and (2) a double-selection LASSO linear regression selecting from a wider set of controls in Extended Data Table 1, including prior vaccine uptake and beliefs about the views of doctors.

Additional data to verify vaccination status

We collected two sets of additional data to verify the reported vaccination status in the main dataset.

Third-party verification

First, we used data collected for us by a third, independent party. We took advantage of the fact that different survey agencies have access to the panel our respondents are sampled from (the Czech National Panel). Although the main data collection was implemented by one agency (NMS), we partnered with another agency (STEM/MARK) to include a question on vaccination status in a survey implemented on its behalf among the same sample. As the survey agency, graphical interface and topic of the survey were different from our main data collection, we believe that respondents considered the two surveys to be completely independent of each other, and thus experimenter demand unlikely had a role in the second survey. The response rate was high (92.8%) and independent of the treatment (Extended Data Table 6). Out of 1,801 participants in wave 11, 1,672 also took part in the third-party verification survey implemented 2 weeks later. This allowed us to compare reported vaccination status at the individual level for a vast majority of our sample, and to test whether Consensus affects the level of consistency in reporting of being vaccinated across surveys.

Certificate verification

The second verification links the reported vaccination status with an official proof of vaccination. We exploited the fact that all vaccinated people receive an EU Digital COVID certificate issued by the Czech Ministry of Health, which was often used as a screening tool at the time of data collection. We collected the data on vaccination certificates among respondents from our full sample who (1) participated in wave 11, and (2) reported to have at least one dose of the COVID-19 vaccine in wave 11 ($n = 1,414$). We asked respondents whether they had the certificate with them. Of participants, 96% confirmed that they had the certificate with them, and this proportion is very similar across the Consensus and Control conditions ($\chi^2(1,n = 1,414) = 0.999, P = 0.318$). Those with a certificate were asked to type in several

specific pieces of information about the applied vaccine that are unlikely to be known by someone without a certificate (for example, the correct answer for those who got a vaccine from Pfizer/Biontech is ‘SARS-CoV-2 mRNA’). Assessment of the typed text by independent raters suggests that, conditional on their having the certificate, more than 94% of respondents actually looked at the certificate when responding to our detailed questions. This rate is again very similar across conditions ($\chi^2(1,n = 1,364) = 0.473$, $P = 0.492$).

More details about both verification procedures and results are in the [Supplementary Information](#).

Ethics approval

The research study was approved by the Commission for Ethics in Research of the Faculty of Social Sciences of Charles University. Participation was voluntary and all respondents provided their consent to participate in the survey.

Reporting summary

Further information on research design is available in the [Nature Research Reporting Summary](#) linked to this paper.

Data availability

The experiment and analyses were pre-registered on the AEA RCT Registry (AEARCTR-0007396). The dataset generated and analysed for the main experiment is available in the Harvard Dataverse repository (<https://doi.org/10.7910/DVN/RH0T6R>). The availability of the dataset from the supplementary survey with medical doctors is subject to the approval of the CMC.

Code availability

The code to replicate the analyses and figures is available in the Harvard Dataverse repository (<https://doi.org/10.7910/DVN/RH0T6R>).

References

1. Greenwood, B. The contribution of vaccination to global health: past, present and future. *Phil. Trans. R. Soc. B* **369**, 20130433 (2014).
2. Banerjee, A. et al. *Selecting the Most Effective Nudge: Evidence from a Large-Scale Experiment on Immunization*. Working Paper 28726 (NBER, 2021).
3. Jarrett, C. et al. Strategies for addressing vaccine hesitancy—a systematic review. *Vaccine* **33**, 4180–4190 (2015).
4. Milkman, K. L. et al. A megastudy of text-based nudges encouraging patients to get vaccinated at an upcoming doctor’s appointment. *Proc. Natl Acad. Sci. USA* **118**, 10–12 (2021).
5. Dai, H. et al. Behavioral nudges increase COVID-19 vaccinations. *Nature* **597**, 404–409 (2021).
6. Blendon, R. J., Benson, J. M. & Hero, J. O. Public trust in physicians—U.S. medicine in international perspective. *N. Engl. J. Med.* **371**, 1570–1572 (2014).
7. Shapiro, J. M. Special interests and the media: theory and an application to climate change. *J. Public Econ.* **144**, 91–108 (2016).
8. Dixon, G. & Clarke, C. The effect of falsely balanced reporting of the autism-vaccine controversy on vaccine safety perceptions and behavioral intentions. *Health Educ. Res.* **28**, 352–359 (2013).
9. Lazarus, J. V. et al. A global survey of potential acceptance of a COVID-19 vaccine. *Nat. Med.* **27**, 225–228 (2021).
10. McDermott, A. Herd immunity is an important—and often misunderstood—public health phenomenon. *Proc. Natl Acad. Sci. USA* **118**, e2107692118 (2021).

11. Serra-Garcia, M. & Szech, N. Choice architecture and incentives increase COVID-19 vaccine intentions and test demand. *SSRN Electron. J.* <https://doi.org/10.2139/ssrn.3818182> (2021).
12. Klüver, H., Hartmann, F., Humphreys, M., Geissler, F. & Giesecke, J. Incentives can spur COVID-19 vaccination uptake. *Proc. Natl Acad. Sci. USA* **118**, e2109543118 (2021).
13. Alsan, M. & Eichmeyer, S. *Experimental Evidence on the Effectiveness of Non-Experts for Improving Vaccine Demand*. Working Paper 28593 (NBER, 2021).
14. Ashworth, M., Thunström, L., Cherry, T. L., Newbold, S. C. & Finnoff, D. C. Emphasize personal health benefits to boost COVID-19 vaccination rates. *Proc. Natl Acad. Sci. USA* **118**, e2108225118 (2021).
15. Loomba, S., de Figueiredo, A., Piatek, S. J., de Graaf, K. & Larson, H. J. Measuring the impact of COVID-19 vaccine misinformation on vaccination intent in the UK and USA. *Nat. Hum. Behav.* **5**, 337–348 (2021).
16. Boykoff, M. T. & Boykoff, J. M. Balance as bias: global warming and the US prestige press. *Glob. Environ. Chang.* **14**, 125–136 (2004).
17. Van Der Linden, S. L., Clarke, C. E. & Maibach, E. W. Highlighting consensus among medical scientists increases public support for vaccines: evidence from a randomized experiment. *BMC Public Health* **15**, 1207 (2015).
18. World Health Organization. *COVID-19: an informative guide: advice for journalists* (WHO, 2021).
19. Haidt, J. Why social media is terrible for multiethnic democracies. *Vox* <https://www.vox.com/policy-and-politics/2016/11/15/13593670/donald-trump-social-media-culture-politics> (2016).
20. Jennings, W. et al. Lack of trust, conspiracy beliefs, and social media use predict COVID-19 vaccine hesitancy. *Vaccines* **9**, 593 (2021).

21. Bursztyn, L., Rao, A., Roth, C. & Yanagizawa-Drott, D. *Misinformation During a Pandemic*. Working Paper 27417 (NBER, 2021).
22. Bronchetti, E. T., Huffman, D. B. & Magenhein, E. Attention, intentions, and follow-through in preventive health behavior: field experimental evidence on flu vaccination. *J. Econ. Behav. Organ.* **116**, 270–291 (2015).
23. Campos-Mercade, P. et al. Monetary incentives increase COVID-19 vaccinations. *Science* **374**, 879–882 (2021).
24. Bursztyn, L. & Young, D. Misperceptions about others. *Annu. Rev. Econom.* (in the press).
25. Haaland, I., Roth, C. & Wohlfart, J. Designing information provision experiments. *J. Econ. Lit.* (in the press).
26. Bordalo, P., Gennaioli, N. & Shleifer, A. Memory, attention, and choice. *Q. J. Econ.* **135**, 1399–1442 (2020).
27. Czech News Agency (CTK). Mezi lékaři je očkováno 88 procent, více než polovina lékařů má posilující dávku [88 percent of doctors is vaccinated, more than one half have booster dose]. *České Noviny* <https://www.ceskenoviny.cz/zpravy/mezi-lekari-je-ockovano-88-procent-vice-nez-polovina-lekaru-ma-posilujici-davku/2129777> (2021).
28. Bradley, V. C. et al. Unrepresentative big surveys significantly overestimated US vaccine uptake. *Nature* **600**, 695–700 (2021).
29. Bloniarz, A., Liu, H., Zhang, C. H., Sekhon, J. S. & Yu, B. Lasso adjustments of treatment effect estimates in randomized experiments. *Proc. Natl Acad. Sci. USA* **113**, 7383–7390 (2016).
30. Moehring, A. et al. Surfacing norms to increase vaccine acceptance. *SSRN Electron. J.* <https://doi.org/10.2139/ssrn.3782082> (2021).
31. Santos, H. C., Goren, A., Chabris, C. F. & Meyer, M. N. Effect of targeted behavioral science messages on COVID-19 vaccination

registration among employees of a large health system: a randomized trial. *JAMA Netw. Open* **4**, e2118702 (2021).

32. Cohn, A. & Maréchal, M. A. Priming in economics. *Curr. Opin. Psychol.* **12**, 17–21 (2016).
33. Haaland, I. & Roth, C. Labor market concerns and support for immigration. *J. Public Econ.* **191**, 104256 (2020).
34. Dunwoody, S. in *Communicating Uncertainty: Media Coverage of New and Controversial Science* (eds Friedman, S. M., Dunwoody, S. & Rogers, C. L.) 59–79 (Lawrence Erlbaum, 1999).
35. Schmid, P., Schwarzer, M. & Betsch, C. Weight-of-evidence strategies to mitigate the influence of messages of science denialism in public discussions. *J. Cogn.* **3**, 36 (2020).
36. Milkman, K. L. et al. A 680,000-person megastudy of nudges to encourage vaccination in pharmacies. *Proc. Natl Acad. Sci. USA* **119**, e2115126119 (2022).
37. Van Linden, S. L. D., Leiserowitz, A. A., Feinberg, G. D. & Maibach, E. W. The scientific consensus on climate change as a gateway belief: experimental evidence. *PLoS ONE* **10**, e0118489 (2015).
38. Komenda, M. et al. Complex reporting of coronavirus disease (COVID-19) epidemic in the Czech Republic: use of interactive web-based application in practice. *J. Med. Internet Res.* **22**, e19367 (2020).

Acknowledgements

We thank PAQ Research (especially D. Prokop) and NMS Market Research (especially L. Rambousek) for implementing the longitudinal data collection; STEM/MARK for implementing the third-party verification; the CMC, M. Kubek, D. Valášek, M. Matoušek, R. Mounajjed and J. Studený for implementing the supplementary survey of medical doctors and providing further statistics; and D. Cantoni, F. Matějka, G. Veramendi and J. Zápal for feedback. V.B. thanks the German Research Foundation (CRC

TRR 190 and 444754857). M.B. and J.Chytilová thank the Czech Science Foundation (20-11091S). J.Cahlíková thanks the Max Planck Institute for Tax Law and Public Finance for generous funding of the project. This project has received funding from the European Research Council (grant agreement no. 101002898). The funders had no role in the design of the study, data collection and analysis, decision to publish or preparation of the manuscript. D. Korlyakova, T. Bielaková, M. Pospíšil, I. Burianová and D. Nováková provided excellent assistance.

Author information

Authors and Affiliations

1. Department of Economics, University of Munich, Munich, Germany

Vojtěch Bartoš

2. Department of Economics, Management and Quantitative Methods,
University of Milan, Milan, Italy

Vojtěch Bartoš

3. CERGE-EI, a joint workplace of Charles University and the Economics
Institute of the Czech Academy of Sciences, Prague, Czech Republic

Michal Bauer & Julie Chytilová

4. Institute of Economic Studies, Faculty of Social Sciences, Charles
University, Prague, Czech Republic

Michal Bauer & Julie Chytilová

5. Department of Public Economics, Max Planck Institute for Tax Law
and Public Finance, Munich, Germany

Jana Cahlíková

Contributions

V.B., M.B., J.Cahlíková and J.Chytilová contributed equally to the preparation of the design, implementation and interpretation of the findings from the main experiment. V.B. initiated the project, organized and implemented the survey among doctors, and had a lead role in the data analyses. M.B. and J.Chytilová wrote the manuscript. J.Cahlíková secured most of the funding.

Corresponding author

Correspondence to [Vojtěch Bartoš](#).

Ethics declarations

Competing interests

The authors declare no competing interests.

Peer review

Peer review information

Nature thanks Dean Eckles and the other, anonymous, reviewer(s) for their contribution to the peer review of this work. [Peer reviewer reports](#) are available.

Additional information

Publisher's note Springer Nature remains neutral with regard to jurisdictional claims in published maps and institutional affiliations.

Extended data figures and tables

[Extended Data Fig. 1 Comparison of development of vaccination rate in the Control group \(Sample of adult Czech population\) and the Czech adult population.](#)

The horizontal axis represents a timeline. Population data means are for a Tuesday following the start of the data collection (Mondays) at a respective wave denoted by diamonds. The weighted Control group means are denoted by triangles. Control condition n = 800–1,051, depending on survey wave. Source of population data: Opendatalab, a website set up by the Faculty of Information Technologies at the Czech Technical University in Prague using open data from the Czech Ministry of Health (<https://ockovani.opendatalab.cz/statistiky>), ISSN 2787-9925 - http://aleph.techlib.cz/F/?func=direct&doc_number=000017426&local_base=STK02 (accessed on January 12, 2022)³⁸.

Extended Data Fig. 2 Effects of the Consensus condition on the second dose uptake and on intentions to uptake a third (booster) dose (Main Experiment, Sample of adult Czech population).

This figure plots estimated treatment effects on 1) the second dose uptake (two doses were designed as a complete vaccination cycle for the most commonly used vaccines), and on 2) intentions to uptake a third (booster) dose. Markers show the estimated effects, the whiskers denote the 95%-confidence interval based on standard errors clustered at the individual level. Estimated effects and t-test (two-sided) p-values are reported in the Figure. No adjustments for multiple comparisons. Diamonds and triangles report estimates from a linear probability regression that controls for the pre-registered set of control variables. Squares and circles report estimates from a double-selection LASSO linear regression (dsregress command in Stata 17) selecting from a set of covariates in Extended Data Table 1. All regressions include wave fixed effects. In the upper part of the Figure we report the timing and control mean. We report estimates for the full sample (diamonds and squares) and for a restricted sample of respondents participating in all 11 waves (triangles and circles). Full sample: Consensus condition n = 807–904, Control condition n = 800–897, depending on survey wave. Fixed sample: Consensus condition n = 614; Control condition n = 598.

Extended Data Fig. 3 Weekly average of newly confirmed Covid-19 cases per 100,000 population.

Case data source: The Czech Ministry of Health (<https://onemocneni-aktualne.mzcr.cz/api/v2/covid-19/osoby.csv>, Accessed on January 12, 2022).

Population data source: The Czech Statistical Office (<https://www.czso.cz/csu/czso/obyvatelstvo-podle-petiletych-vekovych-skupin-a-pohlavi-v-krajich-a-okresech>, Accessed on January 12, 2022) and ref. ³⁸.

Extended Data Table 1 Demographic characteristics: summary statistics and randomization check for the full sample (Main Experiment, Sample of adult Czech population)

Extended Data Table 2 Timeline of the Main Experiment (Sample of adult Czech population)

Extended Data Table 3 Effect of the Consensus condition on respondents' vaccination uptake

Extended Data Table 4 Effect of the Consensus condition on respondents' vaccination uptake: Robustness

Extended Data Table 5 Effect of the Consensus condition on respondents' vaccination uptake: additional results

Extended Data Table 6 Third party and certificate verification

Supplementary information

Supplementary Information

This Supplementary Information file contains the following sections: 1. Supplementary Figure 1; 2. Supplementary Tables 1–9; 3. Supplementary Methods; 4. Populated Pre-Analysis Plan.

Reporting Summary

Peer Review File

Rights and permissions

Open Access This article is licensed under a Creative Commons Attribution 4.0 International License, which permits use, sharing, adaptation,

distribution and reproduction in any medium or format, as long as you give appropriate credit to the original author(s) and the source, provide a link to the Creative Commons license, and indicate if changes were made. The images or other third party material in this article are included in the article's Creative Commons license, unless indicated otherwise in a credit line to the material. If material is not included in the article's Creative Commons license and your intended use is not permitted by statutory regulation or exceeds the permitted use, you will need to obtain permission directly from the copyright holder. To view a copy of this license, visit <http://creativecommons.org/licenses/by/4.0/>.

Reprints and Permissions

About this article

Cite this article

Bartoš, V., Bauer, M., Cahlíková, J. *et al.* Communicating doctors' consensus persistently increases COVID-19 vaccinations. *Nature* **606**, 542–549 (2022). <https://doi.org/10.1038/s41586-022-04805-y>

- Received: 03 October 2021
- Accepted: 26 April 2022
- Published: 01 June 2022
- Issue Date: 16 June 2022
- DOI: <https://doi.org/10.1038/s41586-022-04805-y>

Share this article

Anyone you share the following link with will be able to read this content:

[Get shareable link](#)

Sorry, a shareable link is not currently available for this article.

[Copy to clipboard](#)

Provided by the Springer Nature SharedIt content-sharing initiative

Further reading

- [**Give physicians' views to improve COVID vaccine uptake**](#)

◦ Nina Mažar

Nature (2022)

[**Robot exercises shoulder cells for better tissue transplants**](#)

- Benjamin Thompson
- Nick Petrić Howe

Nature Nature Podcast 01 Jun 2022

[**Give physicians' views to improve COVID vaccine uptake**](#)

- Nina Mažar

Nature News & Views 01 Jun 2022

This article was downloaded by **calibre** from <https://www.nature.com/articles/s41586-022-04805-y>.

- Article
- Open Access
- [Published: 01 June 2022](#)

An oxygen-sensing mechanism for angiosperm adaptation to altitude

- [Mohamad Abbas](#),
- [Gunjan Sharma](#),
- [Charlene Dambire](#),
- [Julietta Marquez](#),
- [Carlos Alonso-Blanco](#),
- [Karina Proaño](#) &
- [Michael J. Holdsworth](#)

Nature volume 606, pages 565–569 (2022)

- 7953 Accesses
- 428 Altmetric
- [Metrics details](#)

Abstract

Flowering plants (angiosperms) can grow at extreme altitudes, and have been observed growing as high as 6,400 metres above sea level^{1,2}; however, the molecular mechanisms that enable plant adaptation specifically to altitude are unknown. One distinguishing feature of increasing altitude is a reduction in the partial pressure of oxygen (pO_2). Here we investigated the relationship between altitude and oxygen sensing in relation to chlorophyll biosynthesis—which requires molecular oxygen³—and hypoxia-related gene expression. We show that in etiolated seedlings of angiosperm species,

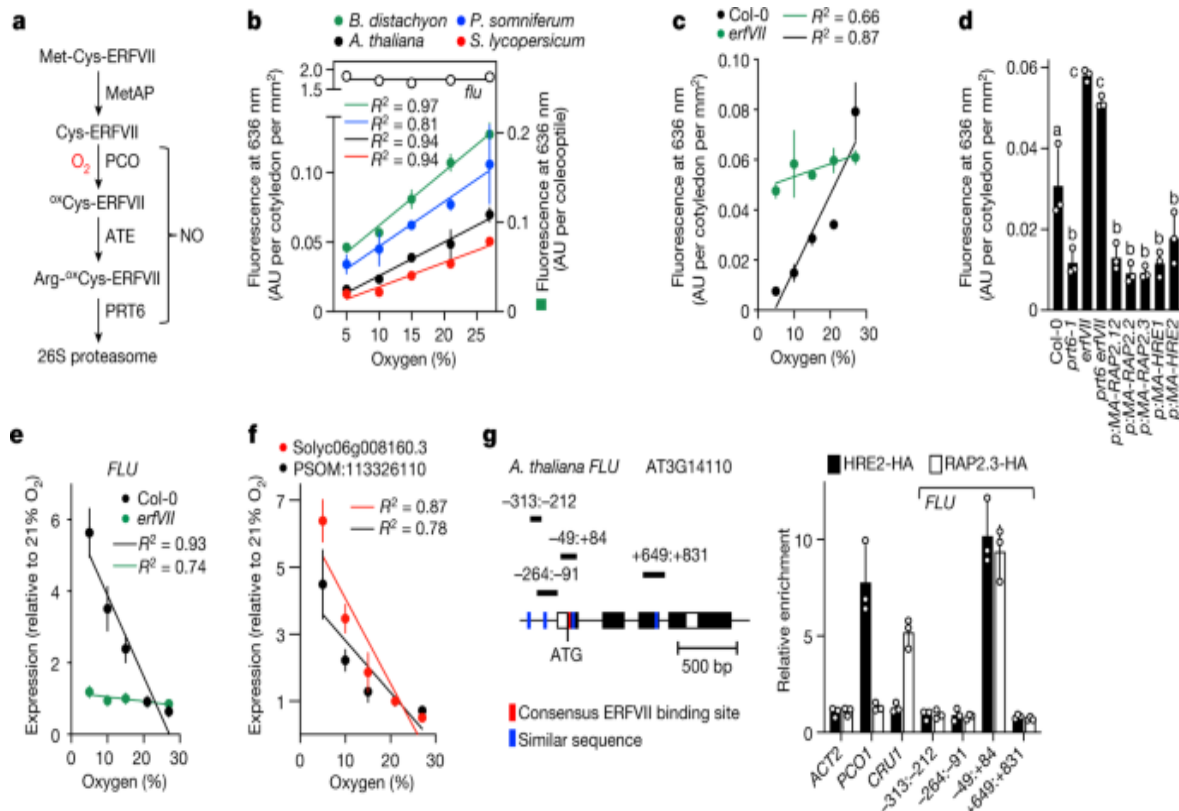
steady-state levels of the phototoxic chlorophyll precursor protochlorophyllide are influenced by sensing of atmospheric oxygen concentration. In *Arabidopsis thaliana*, this is mediated by the PLANT CYSTEINE OXIDASE (PCO) N-degron pathway substrates GROUP VII ETHYLENE RESPONSE FACTOR transcription factors (ERFVIIIs). ERFVIIIs positively regulate expression of *FLUORESCENT IN BLUE LIGHT (FLU)*, which represses the first committed step of chlorophyll biosynthesis, forming an inactivation complex with tetrapyrrole synthesis enzymes that are negatively regulated by ERFVIIIs, thereby suppressing protochlorophyllide. In natural populations representing diverse angiosperm clades, we find oxygen-dependent altitudinal clines for steady-state levels of protochlorophyllide, expression of inactivation complex components and hypoxia-related genes. Finally, *A. thaliana* accessions from contrasting altitudes display altitude-dependent ERFVII activity and accumulation. We thus identify a mechanism for genetic adaptation to absolute altitude through alteration of the sensitivity of the oxygen-sensing system.

Main

Around 25% of the Earth's land surface, containing at least 30% of plant species diversity⁴, is mountainous. Although the altitude at which an individual plant grows may never change, it is critical that individuals (and populations) are adapted to survive at that altitude, and this is an important component of plant ecology⁴. Altitude and latitude have been considered collectively to impart a syndrome of developmental and physiological characteristics linked mostly to climatic adaptation (including dwarfism, resistance to ultra-violet light, low temperature tolerance, flowering time and others^{4,5}). However, no consistent trait has been associated with specific environmental components of altitude, such as pO_2 , which might reveal mechanisms underlying direct altitudinal adaptation. Here we investigate the idea that adaptation to altitude involves direct sensing of oxygen concentration across altitudinal ranges. Mammalian adaptation to very high altitude involved mutation of components of the hypoxia-inducible factor (HIF) oxygen-sensing system^{6,7,8} (which is mechanistically different to the plant oxygen-sensing pathway⁹), indicating the importance of matching metabolism with altitude. Oxygen sensing in plants through Met1–Cys2

ERFVII transcription factors is mediated by the PCO branch of the PROTEOLYSIS 6 (PRT6) N-degron pathway^{10,11}. Following Met1 removal, the amino-terminal cysteine is oxidized by PCOs¹² using molecular O₂, arginylated by arginyl transferase¹³ and recognized by the E3 ligase PRT6 for ubiquitin-mediated destruction (Fig. 1a).

Fig. 1: Atmospheric oxygen sensing regulates tetrapyrrole synthesis via FLU.



a, Schematic representation of the PCO branch of the PRT6 N-degron pathway²⁸. MetAP, methionine amino-peptidase; ATE, arginyl transferase; ^{ox}Cys, oxidized cysteine. The position of oxygen and possible positions of nitric oxide (NO) in the pathway are shown. Oxygen is used by PCOs to oxidize amino-terminal Cys of ERFVIIIs. **b**, Steady-state Pchlide, measured by fluorescence at 636 nm, in etiolated seedlings of different species grown at different ambient O₂ concentrations. **c**, **d**, Steady-state Pchlide in Col-0 and *erfVII* at different ambient O₂ concentrations (**c**) with expression of individual stabilized Cys2Ala mutant ERFVIIIs controlled by their native promoters (**d**)¹⁸ (p). **e**, Amount of *FLU* RNA transcript in Col-0 and *erfVII*

grown at different ambient O₂ concentrations. **f**, Regulation of *FLU* orthologue mRNA in *P. somniferum* (PSOM) and *S. lycopersicum* (Solyc) grown at various ambient O₂ concentrations. **g**, Schematic of the *A. thaliana* *FLU* gene, showing potential ERFVII binding sites (left) and chromatin immunoprecipitation (ChIP) analysis of RAP2.3–HA and HRE2–HA occupancy of *FLU* gene regions (range indicated by colons); including known positive and negative regulatory sequences^{20,29} using anti-HA antibody. All experiments were carried out using etiolated seedlings after 5 days growth at pO₂ 21.2 kPa (48 m a.s.l.) unless otherwise stated. Data are mean ± s.d.; one-way ANOVA. Significantly different groups are indicated by letters in **d**. *n* = 3 biologically independent experiments. AU, arbitrary units; *R*², coefficient of determination.

Source data

We reasoned that plant biochemical pathways that require oxygen may be subject to evolutionary pressure in relation to altitude. Tetrapyrrole synthesis, which leads to chlorophyll, is dependent on ambient O₂ at several points (Extended Data Fig. [1a](#)). Following germination, during etiolated growth in the dark, the chlorophyll biosynthesis intermediate protochlorophyllide (Pchlide) accumulates because angiosperms possess only a light-activated chloroplast enzyme for Pchlide reduction¹⁴ (light-dependent NADPH-protochlorophyllide oxidoreductase (L-POR, hereafter POR)). We set out to determine whether differences in pO₂ with altitude could influence the flux through the tetrapyrrole pathway through oxygen sensing and be a target for evolutionary adaptation. We first investigated whether the ambient O₂ concentration regulates steady-state Pchlide levels in plant species representing diverse angiosperm clades, *A. thaliana* (rosid), *Solanum lycopersicum* (asterid), *Papaver somniferum* (basal dicot) and *Brachypodium distachyon* (monocot) (Fig. [1b](#)). This showed that decreasing ambient O₂ levels from 27% (hyperoxia) to 5% (hypoxia) decrease Pchlide levels in etiolated seedlings. To show that this is not just the result of hypoxia-related flux restrained by O₂-requiring enzymes of the pathway we also analysed steady-state Pchlide levels for the *A. thaliana* *flu* mutant. *FLU* directly inhibits the first committed enzyme of tetrapyrrole synthesis, glutamyl tRNA reductase (GluTR)—the major form of which is encoded by

HEMA1—thereby inhibiting synthesis of 5-aminolevulinic acid (ALA), the precursor of all tetrapyrroles¹⁵, which results in prevention of accumulation of free Pchlide (Extended Data Fig. 1a). The proposed mechanism for FLU activity involves POR, Pchlide, GluTR and CHL27 (a component of the tetrapyrrole synthesis enzyme Mg-protoporphyrin monomethylester cyclase³); in the dark, free Pchlide (which cannot be converted to chlorophyllide without light) binds POR as part of a complex with CHL27 and FLU. This inactivation complex enables FLU to interact with and inhibit GluTR activity, reducing ALA synthesis and therefore Pchlide levels^{16,17}. Under mild hypoxia, compared with normoxia and hyperoxia, steady-state Pchlide levels were unrestrained in the *flu* mutant, indicating that the observed oxygen-associated Pchlide levels in different species are regulated by oxygen sensing (Fig. 1b, Extended Data Fig. 1b–d). In *A. thaliana* accession Col-0 (originally collected less than 100 m above sea level (a.s.l.)) grown at 48 m a.s.l. ($pO_2 = 21.2$ kPa), this decrease was largely abolished in the absence of all 5 ERFVII transcription factors (using the pentuple *related to apetala (rap)* and *hypoxia responsive erf (hre)* mutant¹⁸ *rap2.12 rap2.2 rap2.3 hrel hre2* (hereafter referred to as *erfVII*) (Fig. 1c), demonstrating that oxygen sensing via ERFVIIIs is required for this response. A Cys-to-Ala mutation (Cys2Ala) (which removes the Cys N-degron) in all ERFVIIIs significantly reduced Pchlide levels in etiolated seedlings, similar to *prt6* seedlings (in which all ERFVIIIs are stable) (Fig. 1d). Mutation of either *PRT6* or ERFVII genes led to opposite stable changed steady-state Pchlide levels (lower in *prt6*, higher in *erfVIIs*); mutation of *RAP2.3* had the largest effect, indicating that all ERFVIIIs contribute to this function and that *RAP2.3* may have a predominant role (Extended Data Fig. 2a, b). A *prt6 flu* double mutant showed high levels of Pchlide equivalent to those in the *flu* mutant, indicating that stabilized ERFVIIIs act upstream of *FLU* (Extended Data Fig. 2c). Because hypoxia suppressed Pchlide levels, we analysed the role of ERFVIIIs in regulating expression of genes encoding components of the inactivating complex—including *FLU*, *HEMA1*, *CHL27* and *POR* (which is encoded by three genes, two of which (*PORA* and *PORB*) are expressed in etiolated seedlings¹⁹)—and *CHLM*, which encodes a chlorophyll synthesis enzyme previously shown to be regulated by oxygen sensing¹⁸. Accumulation of *FLU* transcripts was positively regulated by ERFVIIIs via *PRT6*, whereas *CHL27*, *PORA*, *PORB* and *CHLM* were negatively regulated, and *HEMA1* was not regulated, by this pathway.

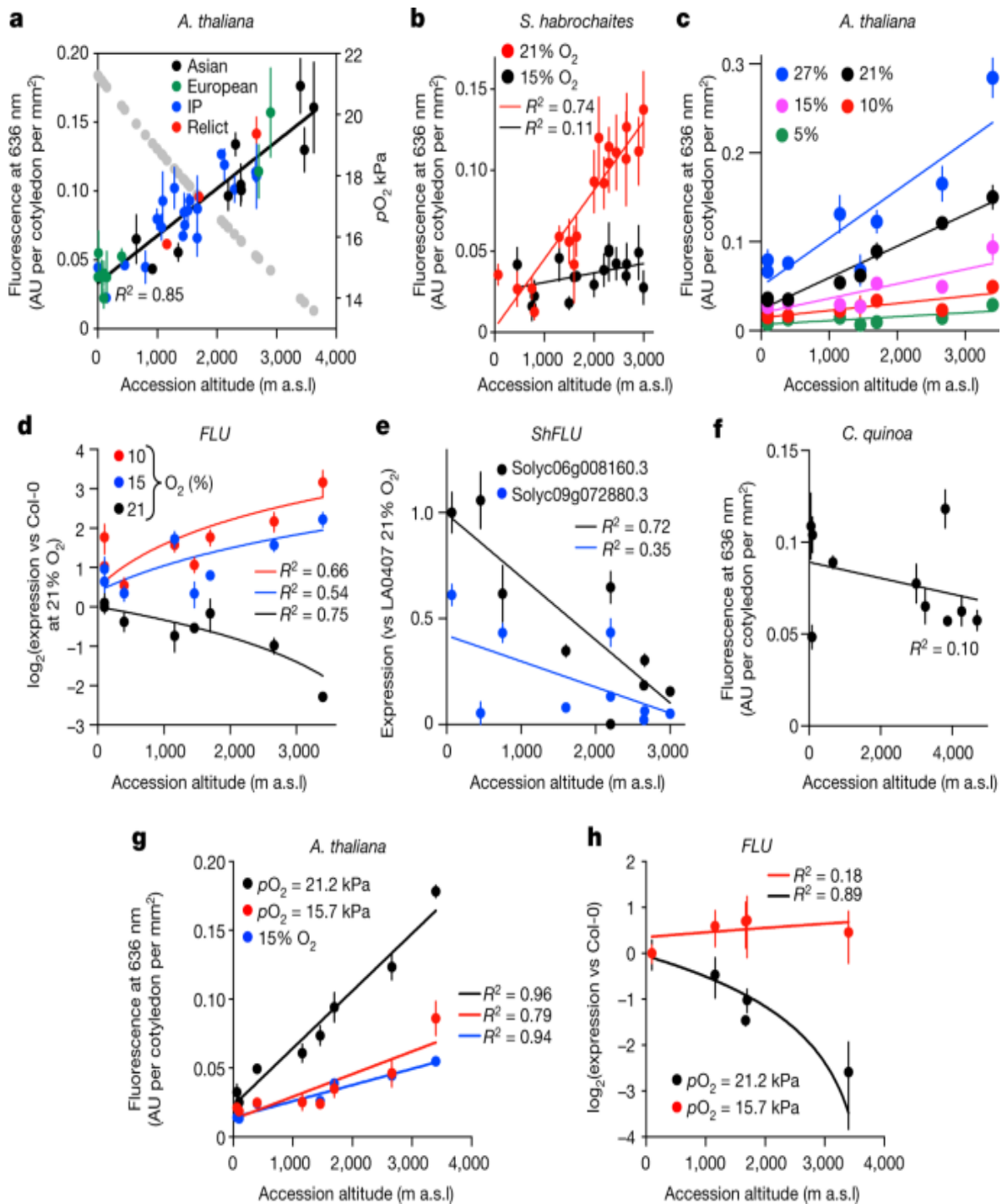
(Extended Data Fig. 2d). The amount of *FLU* RNA increased strongly with increasing hypoxia, a response that was abolished in the *erfVII* mutant, whereas expression of tetrapyrrole synthesis genes showed the opposite trend (Fig. 1e, Extended Data Fig. 2e). Reflecting the transcript data, *FLU* protein levels were enhanced by hypoxia via ERFVIIIs, whereas POR protein accumulation was repressed by hypoxia through ERFVIIIs (Extended Data Fig. 2f). Oxygen-controlled repression of *FLU*-orthologous RNA accumulation was conserved in *S. lycopersicum* and *P. somniferum* (Fig. 1f).

In *A. thaliana*, the C-terminally haemagglutinin (HA)-tagged ERFVIIIs HRE2 and RAP2.3 associated with the *FLU* gene in a region containing an evolutionarily-conserved ERFVII binding site²⁰, adjacent to the initiating ATG (similar binding was previously observed for HRE2 at the *FLU* locus during the response of light-grown seedlings to hypoxia²⁰). HRE2–HA and RAP2.3–HA also showed differential binding to two genes (*PCO1* and *CRUI*) previously shown to be regulated by ERFVIIIs. HRE2 similarly associated with ATG-proximal regions of *CHL27* and *CHLM* genes, and also with gene regions of *PORA* and *PORB* but not with *HEMA1* (Fig. 1g, Extended Data Fig. 3). These data demonstrate that O₂ regulation of Pchlide synthesis occurs via oxygen sensing of the PCO N-degron pathway through ERFVII-regulated control of expression of components of the GluTR inactivation complex, in particular the negative regulator *FLU*.

Because *pO*₂ decreases with altitude (Fig. 2a), and could thus affect steady-state Pchlide levels, we investigated the relationship between Pchlide levels and altitude. We analysed Pchlide in accessions of *A. thaliana* (collected from Eurasia and Africa), *Solanum habrochaites* (collected from South America), *Solanum cheesmaniae* (collected from the Galapagos Islands) and *B. distachyon* (collected from Turkey) from natural populations growing at different altitudes from sea level to more than 3,000 m a.s.l. with different latitudinal ranges (Fig. 2a, b, Extended Data Fig. 4a, b, Supplementary Table 1a). When analysed at 48 m a.s.l. (*pO*₂ 21.2 kPa), all species showed a positive correlation between altitude of accession collection and Pchlide steady state level. Furthermore, the amount of Pchlide in *A. thaliana* and *S. habrochaites* was dependent on the ambient O₂ concentration, and hypoxia resulted in greater reduction of Pchlide levels in accessions from higher altitudes (Fig. 2b, c). In *A. thaliana*, the steady-state Pchlide level was not

related to submergence tolerance (Extended Data Fig. 4c, Supplementary Table 1c). As a result of increased Pchlido (which produces singlet oxygen under light), following transfer to light, dark-grown seedlings of accessions collected at higher altitude accumulated substantially more reactive oxygen species (ROS) at 48 m a.s.l. than those collected at a lower altitude; this effect was dependent on the ambient O₂ level and functional PRT6 (Extended Data Fig. 5). These results show that there is a relationship between Pchlido accumulation and the altitude of accession collection, suggesting adaptation of oxygen sensing and/or downstream signalling through the PCO N-degron pathway that fine-tunes steady-state Pchlido level to local atmospheric O₂ levels, potentially avoiding damaging light-associated singlet-oxygen ROS production. Consistent with such a relationship, we found that accumulation of FLU transcript in *A. thaliana* grown at 48 m a.s.l. ($pO_2 = 21.2$ kPa) was strongly influenced by the altitude at which the accession was collected (that is, there was less FLU transcript in high-altitude accessions) and by ambient O₂ level (Fig. 2d). There was a similar relationship between altitude of collection and FLU expression for *S. habrochaites* (FLU expression was lower in high-altitude accessions) (Fig. 2e). Conversely, the amounts of PORA, PORB and CHLM (but not CHL27 or HEMA1) transcripts were higher in accessions from higher elevations, and lower at 15% oxygen compared with those grown in 21% oxygen (Extended Data Fig. 6a). POR protein accumulated to higher levels in the high-altitude *A. thaliana* accession Sha (originally collected in Tajikistan at 3,400 m a.s.l, $pO_2 = 13.9$ kPa) than in the low-altitude Col-0, and by introgressing the *prt6-1* transfer-DNA insertion mutation from Col-0 through eight back-crosses into Sha (*prt6^{Sha}*), we showed that this increase was controlled through the oxygen-sensing pathway; conversely FLU protein accumulation was increased in *prt6^{Sha}* compared with Sha (Extended Data Fig. 6b). In contrast to the observed relationship between the steady-state Pchlido level and elevation in wild species, an altitudinal cline of cultivated *Chenopodium quinoa* (quinoa, recently domesticated in the high Andes²¹) did not show altitude-dependent Pchlido accumulation (Fig. 2f).

Fig. 2: Steady-state levels of Pchlido and FLU expression are determined by altitude.



a, Pchlide levels in *A. thaliana* accessions collected at different altitudes and geographic locations³⁰, grown at a pO_2 of 21.2 kPa. Grey dots show pO_2 at the different altitudes from which the accessions were collected. Genomic groups are indicated in different colours. IP, Iberian Peninsula **b**, Pchlide levels in *S. habrochaites* grown at 48 m a.s.l. with 21% and 15% ambient

O_2 . **c**, Effect of ambient O_2 concentration on Pchlide levels in *A. thaliana* accessions grown at 48 m a.s.l. (R^2 values from Supplementary Table [1b](#)). **d**, **e**, Effect of ambient O_2 concentration on amount of *FLU* mRNA in *A. thaliana* (**d**) and *S. habrochaites* (**e**) grown at 48 m a.s.l. **f**, Pchlide levels in cultivated domesticated *C. quinoa* accessions obtained from different altitudes grown at pO_2 21.2 kPa. **g**, Comparison of Pchlide levels in *A. thaliana* accessions collected at different altitudes and grown at 48 m a.s.l. with pO_2 = 21.2 kPa or 15% ambient O_2 , or at 2,479 m a.s.l. (pO_2 = 15.7 kPa). **h**, *FLU* RNA accumulation in *A. thaliana* accessions collected at different altitudes and grown at 48 m a.s.l. (pO_2 = 21.2 kPa) or at 2,479 m a.s.l. (pO_2 = 15.7 kPa). All experiments were carried out using etiolated seedlings after 5 days growth. Data are mean \pm s.d. Accessions used are listed in Supplementary Table [1a](#). $n = 3$ biologically independent experiments.

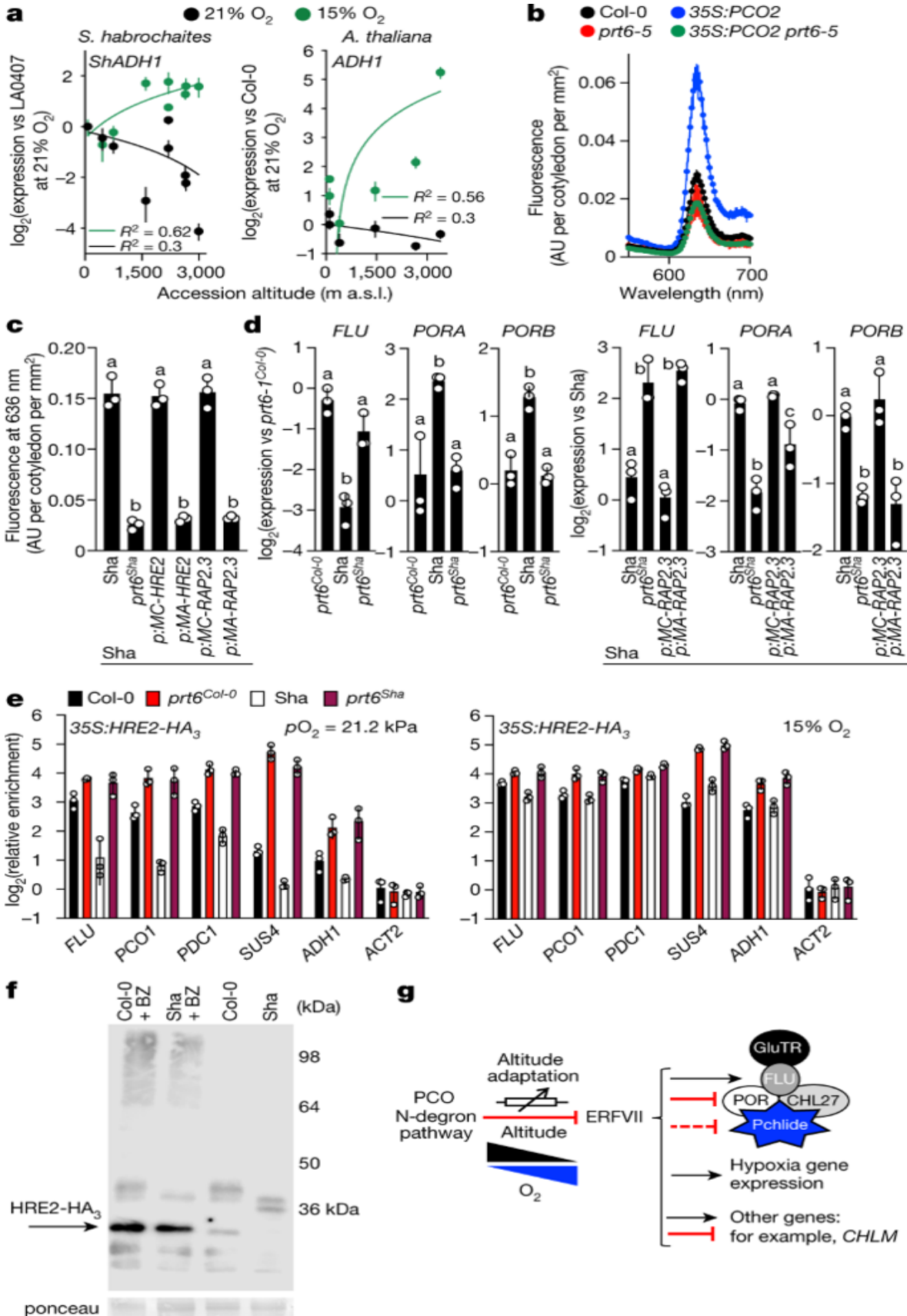
Source data

Reduced pO_2 is just one altitude-dependent parameter: others include atmospheric pressure. We therefore assessed steady-state Pchlide levels and *FLU* expression in etiolated seedlings at two sites located at extreme altitudes (site SB: 52.829809° N –1.249732° E, 48 m a.s.l., pO_2 = 21.2 kPa; and site ESPE: –0.312917° N –78.445157° E, 2,479 m a.s.l., pO_2 = 15.7 kPa) (Extended Data Fig. [7](#)). The Pchlide level was much lower in the high-altitude accession Sha when it was grown at the high-altitude site ESPE compared with the low-altitude site SB, whereas in the *erfVII* mutant Pchlide level remained similar at both sites (Extended Data Fig. [8a](#)). Steady state levels of Pchlide in an *A. thaliana* altitudinal cline were reduced at ESPE, compared to SB at pO_2 21.2 kPa, and were similar to accumulation at SB in 15% ambient O_2 (Fig. [2g](#)). The amount of *FLU* transcript was also increased in plants grown under ambient O_2 concentration at ESPE compared with SB, particularly in high-altitude accessions, and was similar to the amount of *FLU* transcript in plants grown at SB under 15% O_2 (Fig. [2d,h](#)), whereas the amounts of *PORA*, *PORB* and *CHLM* transcripts were lower in the plants grown under atmospheric O_2 concentration at ESPE compared with SB (Extended Data Fig. [8b](#)). These data demonstrate that O_2 is the major

component sensed by altitudinal clines when controlling steady-state Pchlide levels. They also indicate that high-altitude populations have adapted to lower ambient O₂ through increased O₂ sensitivity, and that this has occurred in phylogenetically distant angiosperm species. Reduced accumulation of *FLU* transcripts in high-altitude accessions at pO₂ 21.2 kPa further suggests that they exhibit lower ERFVII activity compared with low-altitude accessions. In summary, the sensitivity to O₂ determines downstream Pchlide level, which is tailored to the local ambient pO₂ via regulation of *FLU* expression mediated by ERFVIIIs.

Since the analyses carried out at different altitudes showed that the sensitivity to atmospheric O₂—as indicated by accumulation of Pchlide and its regulatory component *FLU*—increases with altitude, we examined the expression of classical hypoxia-associated genes. The expression of *ADH1*, *PDC1*, *PGB1* and *SUS4* transcripts (members of the core 49 conserved hypoxia-induced genes²² that are regulated by ERFVIIIs through the PCO N-degron pathway²³) was highly dependent on both the altitude of accession collection and ambient oxygen level in both *A. thaliana* and *S. habrochaites* (Fig. 3a, Extended Data Figs. 8c, d). This indicates that altitude adaptation is not restricted to Pchlide accumulation and is a central conserved feature of oxygen sensing in angiosperms. Furthermore, it suggests that—similar to *FLU* regulation—at high oxygen levels, ERFVIIIs are more active in low-altitude accessions than in high-altitude accessions. We next tested whether ERFVIIIs are active in etiolated seedlings of the low-altitude accession Col-0 at pO₂ 21.2 kPa. Pchlide level in Col-0 was intermediate between those in *prt6* and *erfVII* mutants (Fig. 1d), indicating ERFVII repressive activity. Increasing PCO₂ activity in Col-0 led to increased levels of Pchlide, suggesting that active ERFVIIIs can be destabilized, but this over-accumulation was inhibited by removal of *PRT6* activity (Fig. 3b).

Fig. 3: Genetic mechanisms linking oxygen sensing to altitude adaptation.



a, Effect of ambient O₂ on RNA accumulation of hypoxia-associated *ADH1* in *S. habrochaites* and *A. thaliana* accessions. **b**, Pchlide levels in *prt6-5*, 35S:PCO2, *prt6-5* 35S:PCO2 and Col-0. **c, d**, Pchlide level and *FLU*, *PORA* and *PORB* transcript expression in *prt6-1* mutants and transgenic plants expressing wild-type or Cys2Ala mutant Col-0 RAP2.3 or HRE2 (driven by their own promoters) in Sha and Col-0 genetic backgrounds. **e**, ChIP analysis of HRE2–HA occupancy at *FLU* -49:+84 and hypoxia-related genes in Col-0 and Sha seedlings grown with pO₂ 21.2 kPa or 15% ambient oxygen. **f**, Western blot analysis of HRE2–HA in Sha and Col-0 accessions grown at pO₂ 21.2 kPa. The experiment was repeated independently three times with similar results. BZ, bortezomib. **g**, A model for angiosperm adaptation to altitude through oxygen sensing. Wedges indicate decreasing pO₂ with increasing altitude. Blocked arrows indicate repression. Arrow-crossed box is international standard symbol for a rheostat. The inactivation complex model is adapted from ref. [16](#). All experiments were carried out using etiolated seedlings after 5 days growth at 48 m a.s.l. Data are mean ± s.d.; one-way ANOVA. Significantly different groups are indicated by letters in **c, d**. *n* = 3 biologically independent experiments.

[Source data](#)

To understand the genetic mechanisms involved in altitude adaptation through oxygen sensing, we investigated the influence of components of the ERFVII–PCO N-degron pathway in the high-altitude *A. thaliana* accession Sha. We transformed wild-type and Cys2Ala stable versions of the Col-0 ERFVIIIs RAP2.3 and HRE2 (expression driven by their own promoters) into Sha. In *prt6*^{Sha}, RAP2.3(Cys2Ala)-expressing Sha and HRE2(Cys2Ala)-expressing Sha (but not in Sha expressing wild-type Col-0 RAP2.3), *FLU*, *PORA* and *PORB* expression were markedly affected, resulting in reduced Pchlide (Fig. [3c, d](#)). In addition, expression of hypoxia-related genes was enhanced in *prt6*^{Sha} and RAP2.3(Cys2Ala)-expressing Sha (Extended Data Fig. [9a, b](#)). This indicates that constitutively stabilized ERFVIIIs reduce Pchlide as effectively in Sha as in Col-0. Therefore, components downstream of stabilized ERFVIIIs, including *FLU* function, are unaltered in Sha (as otherwise altering upstream components would not affect the high Pchlide level in Sha). Expression of components of the PCO branch of the PRT6 N-degron pathway were not significantly different

between Col-0 and Sha, and the sequences of Col-0 and Sha *FLU* genes were identical (Extended Data Fig. 9c, d). Etiolated seedlings from Sha × *erfVII* reciprocal crosses showed low Pchlide steady-state levels, indicating that ERFVII activity (in repressing Pchlide levels) in Sha has the potential to be as strong as that in Col-0 (Extended Data Fig. 10). This result also suggests the presence of dominant repressor(s) of oxygen sensing in the low-altitude accession Col-0. We further analysed ERFVII activity in Col-0 and Sha by measuring HRE2–HA occupancy on *FLU* and hypoxia-related genes (which have been shown to bind HRE2 (ref. 20)). At a pO_2 of 21.2 kPa, HRE2–HA occupancy of these genes was high in the *prt6* mutant in both Sha and Col-0 backgrounds (in which HRE2 is stabilized), whereas in the wild type, HRE2–HA displayed lower occupancy of these genes in Sha than in Col-0 (Fig. 3e). Occupancy increased in Sha and Col-0 when grown in 15% ambient O_2 . Thus, at high ambient oxygen ERFVII occupancy is higher in the low-altitude genetic background, but HRE2 activity in both low- and high-altitude genetic backgrounds responds to hypoxia. Finally, Western blot analysis showed that at pO_2 21.2 kPa, HRE2–HA abundance was higher in Col-0 than in Sha, but treatment with the proteasome inhibitor bortizomib resulted in equivalent markedly higher HRE2–HA abundance in both accessions (Fig. 3f).

Here we demonstrate that altitude adaptation involves genetic modifications of the sensitivity to atmospheric O_2 through oxygen sensing, mediated by ERFVII accumulation and activity. We show that this adaptation, through ERFVII regulation, influences two distinct features: hypoxia-related gene expression and steady-state levels of Pchlide (mainly via oxygen-regulated expression of *FLU* and *POR*). Prevention of free Pchlide accumulation is a result of the regulated rate of ALA synthesis, mediated by the POR–Pchlide–CHL27 complex that triggers *FLU* inactivation of GluTR²⁴. Coupling of *POR* expression to the ambient oxygen concentration may enable matching of POR protein to Pchlide levels, allowing POR to bind to free Pchlide. It may be ecologically important to match tetrapyrrole flux (which requires molecular O_2) to the ambient O_2 concentration to provide the most effective Pchlide level once seedlings arrive at the soil surface and chlorophyll synthesis commences in the light. Altitude adaptation involves fine-tuning the activity of the oxygen-sensing system, which acts like a rheostat measuring altitude (Fig. 3g), perhaps through negative regulation of

the PCO N-degron pathway. Oxygen sensing is transduced by ERFVIIIs to influence outputs including expression of hypoxia-related genes, steady-state Pchlide levels (through regulation of ALA synthesis by inactivation complex components) and potentially other biochemical pathways that require molecular oxygen. Altitude adaptation enables decoding of the ambient oxygen level (determined by the local pO_2) to provide equivalent outputs at different altitudes, resulting in, for example, equivalent Pchlide levels in a low-altitude (high pO_2)-adapted accession grown at low altitude to those in a high-altitude (low pO_2)-adapted accession grown at high altitude.

Although this study only investigated etiolated seedlings, other stages of development (including analogous stages such as subsurface rhizome-derived etiolated shoots) may also be subject to a similar adaptive mechanism, as the steady-state Pchlide level is an important regulator of chlorophyll synthesis and FLU has been shown to influence the chlorophyll supply in light conditions²⁴. Notably, regulation of tetrapyrrole synthesis by oxygen sensing also occurs in cyanobacteria, which share a common ancestor with chloroplasts²⁵. Previous studies have shown that oxygen sensing is an important feature of skotomorphogenesis¹⁸. Here we demonstrate that oxygen sensing during this important developmental stage is associated with genetic adaptation to altitude. We show that local ambient absolute O_2 concentration regulates expression of hypoxia-related genes and steady-state levels of Pchlide—a biochemical intermediate of chlorophyll biosynthesis—in altitudinal clines of diverse species through the oxygen-sensing system. This provides a general mechanism for adaptation to absolute elevation that is likely to be conserved throughout angiosperms. In addition, as this mechanism appears to not have been selected in breeding of quinoa, it may represent an untapped trait for crop improvement at unadapted altitude²⁶. It also represents a component that deserves investigation in relation to plant ecological adaptation. The relevance of this mechanism will be of increasing importance as global warming leads to displacement of wild and crop plants to higher altitudes²⁷.

Methods

No statistical methods were used to predetermine sample size. Experiments were not randomized. The investigators were not blinded to allocation during experiments and outcome assessment.

Plant materials

Information on *A. thaliana*, *S. habrochaites*, *S. cheesmaniae*, *B. distachyon* *P. somniferum* and *C. quinoa* accessions (Supplementary Table 1): *A. thaliana* accessions were obtained from NASC, UK. The *A. thaliana* *prt6-1*, *-5*, *erfVII* and individual mutant *ERFVII* lines (all in Col-0 accession background) were described previously^{18,31}. The *flu-1* (Col-0 background) mutant³² was obtained from M. Terry. The 35S:*PCO2-FLAG*¹² transgenic (Col-0 background) was obtained from F. Licausi. *Solanum* accessions were obtained from TGRC, UC Davis, USA. *C. quinoa* cultivated accessions and *B. distachyon* accessions were obtained from the US National Plant Germplasm Collection Germplasm Resources Information Network (GRIN), Beltsville, US Department of Agriculture, Agricultural Research Service (<http://www.ars-grin.gov/>), and the *B. distachyon* accession Bd21 was provided by L. Mur. *P. somniferum* ('Lauren's grape') seeds were obtained from Mr. Fothergill's seeds, UK, and tomato *Solanum lycopersicum* (Marmande) were obtained from Sutton Seeds, UK. The Col-0 accession *prt6-1* T-DNA insertion was introgressed through eight back-crosses into the Sha accession following BASTA resistance conferred by the transgene. The 35S:*HRE2-3× HA* transgene¹⁰ from Col-0 was introgressed into Sha through five back-crosses following BASTA resistance conferred by the transgene, genotyping across all five chromosomes was used to confirm absence of detectable Col-0 genomic DNA away from both transgenes.

Growth conditions for etiolated seedlings

As previously described¹⁸, surface-sterilized seeds were plated on 0.5× MS media (including 1% w/v sucrose) and chilled for 4 days at 4 °C before being exposed to constant white light at 20 °C for 8 h to activate germination. Subsequently, unless indicated otherwise, plates were incubated in darkness at 20 °C for 5 days. For experiments using different oxygen levels, open plates were placed in a methacrylate chamber (1,120 × 180 × 270 mm) (Epica) and flushed until equilibrium with water-saturated

premixed gas combinations (BOC) and left for 5 days in the dark. Oxygen levels in the chamber were measured at the beginning and end of the experiment using an oxygen meter attached to the outlet pipe (KANE 250 Compact Flue Gas Analyzer-Kane International).

Generation of transgenic plants

Individual C2A and WT ERFVII transgenes, including 2 kbp of sequence upstream of the initiating ATG and introns in accession Col-0 were described previously¹⁸. These were transformed into *A. thaliana* accession Sha as previously described³³.

Biochemical analyses

Measurements of Pchlido and ROS

Pchlido was assayed from cotyledons isolated from etiolated seedling as described³⁴. Cotyledons (or whole coleoptiles of *B. distachyon*) of etiolated seedlings were homogenized in 1 ml ice-cold 80% (v/v) acetone overnight at 4 °C. Extractions were vortexed and centrifuged, 800 µl was aliquoted into a fresh tube and 200 µl was used to measure the relative fluorescence at room temperature (excitation: 440 nm; emission: 550–750 nm) using either a Varioskan Flash (Thermo Fisher Scientific) for measurements at SB, or BioTek Cytation 5 Multi-Mode Reader (for measurements at ESPE). To account for differences in cotyledon size between accessions, images of 20 representative cotyledons for each accession in each experiment were taken using a Leica MZ75 and the area was measured using Fiji (<https://imagej.net/>). Reported Pchlido values represent the florescence (either from 550 to 700 nm or at 636 mn (arbitrary units)) per cotyledon in a 1 mm² area.

ROS were detected in 5 days old etiolated seedlings 1 day after transfer to light, 10 µM 2',7'-dichlorodihydrofluorescein diacetate (H₂DCFDA) was incubated with seedlings for 30 min and then washed in 10 mM MES, 0.1 mM CaCl₂, pH 6, for 1 h at 22 °C. Dye excitation was at 480 nm and emitted

light was detected at 535–550 nm with a Leica DM5000 B. ROS and chlorophyll quantification was carried out using Fiji.

ChIP, gene expression and protein analyses

ChIP was performed as described³⁵. Chromatin was extracted from ~3.5 g of etiolated seedlings. Ten microgrammes of anti-HA (Sigma, H3663-200UL) was used for immunoprecipitation. *EUKARYOTIC TRANSLATION INITIATION FACTOR 4A1* (*EIF4A1*, AT3G13920) and *ACTIN 2* (*ACT2*, AT3G18780) were used as negative targets. *CRUCIFERINA* (*CRU1*, AT5G44120) and *PLANT CYSTEINE OXIDASE 1* (*PCO1*, AT5G15120) served as a known positive targets for RAP2.3 and HRE2 (refs. [20,29](#)). Chromatin was purified using QIAquick PCR Purification Kit (Qiagen). Quantitative PCR values of the immunoprecipitation product were normalized against the no-antibody samples. Data presented shows the average of three independent biological repeats. Oligonucleotide primers for ChIP are listed in Supplementary Table [2](#). For quantitative real time (QrtPCR), RNA was extracted from etiolated seedlings using a RNeasy mini kit (Qiagen) and DNase I on-column digestion (Sigma). First strand cDNA was synthesized using a qScript cDNA Synthesis Kit (Quantabio) from 0.8 µg RNA. rtPCR was performed using PerfeCTa SYBR Green FastMix (Quantabio) and the BioRad CFX96 qPCR system. Relative values were normalized over housekeeping genes in the appropriate species. Data presented shows the average of three independent biological repeats. Oligonucleotide primers used for rtPCR are shown in Supplementary Table [2](#).

Western blots were carried out as previously described³⁶. The mouse anti-HA antibody (Sigma-Aldrich) was used at a concentration of 1:1,000 dilution, anti-POR (Agrisera AS05 067-10) was used at 1:4,000 dilution, and anti-FLU (obtained from B. Grimm) was used at 1:2,000 and the secondary antibody, goat anti-mouse IgG1 horseradish peroxidase conjugate (Thermo Fisher Scientific) was used at 1:20,000 dilution. Proteins were extracted from 5-day-old etiolated seedlings under green light as previously described³⁷. Bortezomib treatment was carried out in 6-well tissue culture plates (Fisher Scientific); a total reaction volume of 3 ml of 50 µM Bortezomib (Santa Cruz Biotechnology) was added to each well. Negative

controls contained an equivalent volume of DMSO (Sigma-Aldrich) (DMSO was used to reconstitute the Bortezomib powder). Five-day-old etiolated seedlings were transferred to each well by laying the seedlings on top of the solution in each well gently ensuring that the roots of each seedlings were immersed in the reaction solution. The plate was covered with aluminium foil and placed on a flatbed shaker (60 rpm) for 2 h, after which material was dried with paper towel to remove excess water and frozen in liquid nitrogen immediately.

Phylogenetic analyses

Genomic DNA and CDS sequences for *FLU*, *CHLM* and hypoxia-related gene orthologues were obtained from KEGG: Kyoto Encyclopedia of Genes and Genomes (<https://www.kegg.jp/kegg/>). *FLU*, *CHLM* genomic sequences were searched manually for potential ERFVII binding sites and HRPE-like sequences²⁰.

Statistics

For experimental analysis of Pchlide and quantitative reverse transcription PCR, three independent replicates with different biological material are reported for each experiment. For ChIP, three independent replicates with different biological material were used per experiment. Each experiment was repeated at least twice. For analysis of ROS via staining and microscopy 8–15 seedlings were analysed and images taken for representative samples, experiment was repeated at least three times. In all cases measurements were taken from distinct samples. Differences in ROS content were tested by general linear model (GLM) with two factors (genotype and oxygen) with fixed effects. GLM tests were carried out with SPSS v.27. All graphs were produced using Graphpad software (Version 8), also used to calculate standard deviation of the mean for all samples tested. Relationships between dependent and independent variables were assessed by linear regression analysis using standard parameters for coefficient of determination (R^2) in Graphpad.

Reporting summary

Further information on research design is available in the [Nature Research Reporting Summary](#) linked to this paper.

Data availability

Full versions of all blots are provided in Supplementary Fig 1. Unique identifiers for genes from all species analysed are listed in the text. Where appropriate, seeds of accessions and transgenic lines are available from the corresponding author. [Source data](#) are provided with this paper.

References

1. Angel, R. et al. The root-associated microbial community of the world's highest growing vascular plants. *Microb. Ecol.* **72**, 394–406 (2016).
2. Dentant, C. The highest vascular plants on Earth. *Alp. Bot.* **128**, 97–106 (2018).
3. Brzezowski, P., Richter, A. S. & Grimm, B. Regulation and function of tetrapyrrole biosynthesis in plants and algae. *Biochim. Biophys. Acta* **1847**, 968–985 (2015).
4. Körner, C. The use of ‘altitude’ in ecological research. *Trends Ecol. Evol.* **22**, 569–574 (2007).
5. Bomblies, K. The high life: alpine dwarfism in *Arabidopsis*. *Plant Physiol.* **168**, 767 (2015).
6. Beall, C. M. Adaptation to high altitude: phenotypes and genotypes. *Annu. Rev. Anthropol.* **43**, 251–272 (2014).
7. Huerta-Sánchez, E. et al. Altitude adaptation in Tibetans caused by introgression of Denisovan-like DNA. *Nature* **512**, 194–197 (2014).
8. Lorenzo, F. R. et al. A genetic mechanism for Tibetan high-altitude adaptation. *Nat. Genet.* **46**, 951–956 (2014).

9. Holdsworth, M. J. & Gibbs, D. J. Comparative biology of oxygen sensing in plants and animals. *Curr. Biol.* **30**, R362–R369 (2020).
10. Gibbs, D. J. et al. Homeostatic response to hypoxia is regulated by the N-end rule pathway in plants. *Nature* **479**, 415–418 (2011).
11. Licausi, F. et al. Oxygen sensing in plants is mediated by an N-end rule pathway for protein destabilization. *Nature* **479**, 419–422 (2011).
12. Weits, D. A. et al. Plant cysteine oxidases control the oxygen-dependent branch of the N-end-rule pathway. *Nat. Commun.* **5**, 3425 (2014).
13. White, M. D. et al. Plant cysteine oxidases are dioxygenases that directly enable arginyl transferase-catalysed arginylation of N-end rule targets. *Nat. Commun.* **8**, 14690 (2017).
14. Schoefs, B. & Franck, F. Protochlorophyllide reduction: mechanisms and evolution. *Photochem. Photobiol.* **78**, 543–557 (2003).
15. Meskauskiene, R. et al. FLU: a negative regulator of chlorophyll biosynthesis in *Arabidopsis thaliana*. *Proc. Natl Acad. Sci. USA* **98**, 12826–12831 (2001).
16. Kauss, D., Bischof, S., Steiner, S., Apel, K. & Meskauskiene, R. FLU, a negative feedback regulator of tetrapyrrole biosynthesis, is physically linked to the final steps of the Mg⁺⁺-branch of this pathway. *FEBS Lett.* **586**, 211–216 (2012).
17. Hou, Z. W., Pang, X. Q., Hедтke, B. & Grimm, B. In vivo functional analysis of the structural domains of FLUORESCENT (FLU). *Plant J.* **107**, 360–376 (2021).
18. Abbas, M. et al. Oxygen sensing coordinates photomorphogenesis to facilitate seedling survival. *Curr. Biol.* **25**, 1483–1488 (2015).
19. Oosawa, N. et al. Identification and light-induced expression of a novel gene of NADPH-protochlorophyllide oxidoreductase isoform in *Arabidopsis thaliana*. *FEBS Lett.* **474**, 133–136 (2000).

20. Lee, T. A. & Bailey-Serres, J. Integrative analysis from the epigenome to translatome uncovers patterns of dominant nuclear regulation during transient stress. *Plant Cell* **31**, 2573–2595 (2019).
21. Jarvis, D. E. et al. The genome of *Chenopodium quinoa*. *Nature* **542**, 307–312 (2017).
22. Mustroph, A. et al. Cross-kingdom comparison of transcriptomic adjustments to low-oxygen stress highlights conserved and plant-specific responses. *Plant Physiol.* **152**, 1484–1500 (2010).
23. van Dongen, J. T. & Licausi, F. Oxygen sensing and signaling. *Annu. Rev. Plant Biol.* **66**, 345–367 (2015).
24. Hou, Z. W., Yang, Y. Y., Hedtke, B. & Grimm, B. Fluorescence in blue light (FLU) is involved in inactivation and localization of glutamyl-tRNA reductase during light exposure. *Plant J.* **97**, 517–529 (2019).
25. Ludwig, M. et al. ChlR protein of *Synechococcus* sp PCC 7002 is a transcription activator that uses an oxygen-sensitive 4Fe–4S cluster to control genes involved in pigment biosynthesis. *J. Biol. Chem.* **289**, 16624–16639 (2014).
26. Moat, J. et al. Resilience potential of the Ethiopian coffee sector under climate change. *Nat. Plants* **3**, 17081 (2017).
27. Lenoir, J., Gegout, J. C., Marquet, P. A., de Ruffray, P. & Brisson, H. A significant upward shift in plant species optimum elevation during the 20th century. *Science* **320**, 1768–1771 (2008).
28. Holdsworth, M. J., Vicente, J., Sharma, G., Abbas, M. & Zubrycka, A. The plant N-degron pathways of ubiquitin-mediated proteolysis. *J. Integr. Plant Biol.* **62**, 70–89 (2020).
29. Marin-de la Rosa, N. et al. Large-scale identification of gibberellin-related transcription factors defines group VII ETHYLENE RESPONSE FACTORS as functional DELLA partners. *Plant Physiol.* **166**, 1022–1032 (2014).

30. Alonso-Blanco, C. et al. 1,135 genomes reveal the global pattern of polymorphism in *Arabidopsis thaliana*. *Cell* **166**, 481–491 (2016).
31. Holman, T. J. et al. The N-end rule pathway promotes seed germination and establishment through removal of ABA sensitivity in *Arabidopsis*. *Proc. Natl Acad. Sci.* **106**, 4549–4554 (2009).
32. Wagner, D. et al. The genetic basis of singlet oxygen-induced stress responses of *Arabidopsis thaliana*. *Science* **306**, 1183–1185 (2004).
33. Clough, S. J. & Bent, A. F. Floral dip: a simplified method for *Agrobacterium*-mediated transformation of *Arabidopsis thaliana*. *Plant J.* **16**, 735–743 (1998).
34. Terry, M. J. & Kacprzak, S. M. in *Phytochromes: Methods and Protocols* (ed. Hiltbrunner, A.) 169–177 (Springer, 2019).
35. Song, L., Koga, Y. & Ecker, J. R. Profiling of transcription factor binding events by chromatin immunoprecipitation sequencing (ChIP-seq). *Curr. Protoc. Plant Biol.* **1**, 293–306 (2016).
36. Vicente, J. et al. The Cys-Arg/N-end rule pathway is a general sensor of abiotic stress in flowering plants. *Curr. Biol.* **27**, 3183–3190 (2017).
37. Gibbs, D. J. et al. Nitric oxide sensing in plants is mediated by proteolytic control of group VII ERF transcription factors. *Mol. Cell* **53**, 369–379 (2014).
38. Gasch, P. et al. Redundant ERF-VII transcription factors bind to an evolutionarily conserved *cis*-motif to regulate hypoxia-responsive gene expression in *Arabidopsis*. *Plant Cell* **28**, 160–180 (2016).
39. Vashisht, D. et al. Natural variation of submergence tolerance among *Arabidopsis thaliana* accessions. *New Phyt.* **190**, 299–310 (2011).

Acknowledgements

Solanum sp. accessions were obtained from the UC Davis/C.M. Rick Tomato Genetics Resource Center maintained by the Department of Plant Sciences, University of California, Davis, USA; *A. thaliana* accessions were obtained from NASC, Nottingham, UK; and quinoa and *B. distachyon* altitudinal cline accessions were provided by the US Department of Agriculture's National Plant Germplasm System, Plant Introduction Research Station, Ames, Iowa, USA. We thank M. Baldeon and O. Barreiro for generous use of equipment; B. Grimm for FLU antibody; G. Miño for technical support; and N. Crout and M. Blazquez for many helpful discussions. The work was funded by a Marie Curie CASCADE fellowship (600181) to M.A. and a Leverhulme Trust Research Project Grant (RPG-2018-172) to M.J.H. and was supported by the Biotechnology and Biological Sciences Research Council (grant number BB/R002428/1) to M.J.H. C.A.-B. was funded by grant PID2019-104249GB-I00 from the Agencia Estatal de Investigación of Spain (AEI)/10.13039/501100011033.

Author information

Authors and Affiliations

1. School of Biosciences, University of Nottingham, Nottingham, UK
Mohamad Abbas, Gunjan Sharma, Charlene Dambire, Julietta Marquez & Michael J. Holdsworth
2. Centro Nacional de Biotecnología, Consejo Superior de Investigaciones Científicas, Madrid, Spain
Carlos Alonso-Blanco
3. Laboratorio de Biotecnología Vegetal, Departamento de Ciencias de la Vida y la Agricultura, Universidad de las Fuerzas Armadas ESPE, Sangolquí, Ecuador
Karina Proaño

Contributions

M.J.H., M.A., C.A.-B. and K.P. designed the experiments. M.J.H., M.A., G.S., C.D. and J.M. carried out the experiments. M.A., C.A.-B. and M.J.H. conducted statistical analyses. M.J.H. and C.A.-B. wrote the manuscript with inputs from all co-authors. All co-authors read and approved the submitted manuscript.

Corresponding author

Correspondence to [Michael J. Holdsworth](#).

Ethics declarations

Competing interests

The authors declare no competing interests.

Peer review

Peer review information

Nature thanks Nico Dissmeyer, Bernhard Grimm, Margret Sauter and the other, anonymous reviewer(s) for their contribution to the peer review of this work.

Additional information

Publisher's note Springer Nature remains neutral with regard to jurisdictional claims in published maps and institutional affiliations.

Extended data figures and tables

[Extended Data Fig. 1 Tetrapterrole synthesis and Pchlide steady state levels in etiolated seedlings.](#)

a, Schematic of tetrapyrrole synthesis showing points of oxygen requirement³. Blue, enzymes, black metabolites. Blocked arrows indicate repression. ALA, 5-aminolevulinic acid; Mg-Proto, Mg-protoporphyrin; GluTR, glutamyl-tRNA reductase; CHLM, MAGNESIUM-PROTOPORPHYRIN IX METHYLTRANSFERASE; HY1, HEME OXYGENASE1; POR, Light requiring PCHLIDE OXIDOREDUCTASE; FLU, FLOURESCENT IN BLUE LIGHT. Constituents of the GluTR inactivation complex are shown, diagram after¹⁶. b, Linearity of the measurement of Pchlido peak fluorescence at 636 nm, measured as arbitrary units (a.u.) per cotyledon per mm² (to account for differing cotyledon sizes between accessions of the same species), using the Pchlido over-accumulating Col-0 mutant *flu*. c, Pchlido levels in Col-0 (wild type) and *flu*. d, Levels of Pchlide in *A. thaliana* during 7 days of etiolated growth of Col-0 (wild-type) and *flu*. Experiments carried out using etiolated seedlings after 5 days growth at pO_2 21.2 kPa (48 m a.s.l) unless otherwise stated. Means are plotted, error bars report SD. For each n = 3 biologically independent experiments.

Source data

Extended Data Fig. 2 The influence of the PRT6 N-degron pathway and ERFVIIIs on Pchlido levels.

a, Pchlide steady state levels in *A. thaliana* during 7 days of etiolated growth of Col-0 (wild-type) and N-degron pathway mutant *prt6-1* and *erfVII* combinations. b, Pchlido levels at pO_2 21.2 kPa (48 m a.s.l) in *A. thaliana* N-degron pathway mutant *prt6-1* and *erfVII* combinations and individual *ERFVII* mutants. c, Pchlido levels in *prt6*, *flu* and *prt6 flu*. d, Analysis of RNA expression of *FLU* and genes of tetrapyrrole synthesis in Col-0 (wild type) and *erfVII* and *prt6* mutants. e, Transcript levels in Col-0 and *erfVII* at different ambient oxygen levels. f, Accumulation of proteins for POR and FLU in Col-0 (wild type) and PRT6 N-degron pathway mutants at pO_2 21.2 kPa (48 m a.s.l), and in Col-0 and *erfVII* at different ambient oxygen levels, repeated independently three times with similar results. All experiments carried out using etiolated seedlings after 5 days growth at pO_2 21.2 kPa (48 m a.s.l) unless otherwise stated. Means are plotted, error bars report SD.

Significant differences denoted with letters for one-way ANOVA ($p < 0.05$). Coefficient of determination (R^2) is given. For each $n = 3$ biologically independent experiments.

[Source data](#)

Extended Data Fig. 3 ChIP analysis of HRE2 interaction with tetrapyrrole synthesis-related genes.

a, Conservation of ERFVII binding site (also known as EBP, GC box) and related HRPE (Hypoxia-Responsive Promoter Element³⁸)-like element in the first coding exon of *A. thaliana FLU* and orthologues from selected angiosperms (initiating ATG highlighted). b, Schematic of the *CHLM* gene (repressed by ERFVIIIs) showing ERFVII-binding sites and ChIP analysis of RAP2.3-3xHA and HRE2-3xHA occupancy of *CHLM* gene regions (including known positive and negative sequences²⁹). c,d Conservation of ERFVII binding site in the first coding exons of *CHLM* and *CHL27* respectively. e, ChIP analysis of HRE2-3xHA occupancy of gene regions of *CHL27*, *PORA*, *PORB* and *HEMA1*. f, Schematics of genes showing positions of ERFVII and ERFVII-like binding sites. White boxes untranslated and black boxes translated regions. All experiments carried out using etiolated seedlings after 5 days growth at pO_2 21.2 kPa (48 m a.s.l). Means are plotted, error bars report SD. For each $n = 3$ biologically independent experiments.

[Source data](#)

Extended Data Fig. 4 Pchlide steady state levels and submergence tolerance for species accessions used in this study.

a, b, Pchlide levels at pO_2 21.2 kPa in *S. cheesmaniae* and *B. distachyon* accessions collected at different altitudes and geographic locations. c, Relationship between *A. thaliana* accession and submergence tolerance, LT50 is defined as the number of days after which 50% of the plant population (for a particular accession) dies and was calculated from survival curves for each accession (data replotted from³⁹), original data in

Supplementary Table [1c](#). Coefficient of determination (R^2) is given. Means are plotted, error bars report SD. For each n = 3 biologically independent experiments.

[Source data](#)

Extended Data Fig. 5 ROS and chlorophyll accumulation in 5 day old etiolated seedlings after one day of light in *A. thaliana*.

a. Relative fluorescence of ROS and chlorophyll. b. Example images of fluorescence of ROS and chlorophyll in different accessions at 21% and 15% ambient oxygen. Differences in ROS content were tested by GLM (General Linear Model) with two factors (Genotype and Oxygen) with fixed effects, both factors as well as the interaction where highly significant (Supplementary Table [1d](#)). At least 8 seedlings were measured per accession, representative cotyledons are shown. For box and whisker plots whiskers go down to the minimum and up to the maximum values, boxes represent from 25th to 75th percentile and bars equal the median values.

[Source data](#)

Extended Data Fig. 6 Expression of RNA and protein for FLU, CHLM, HEMA1 and PORs in *A. thaliana* accessions.

a, Analysis of RNA expression in accessions collected at increasing altitude at pO_2 21.2 kPa and 15% ambient oxygen. b, Accumulation of proteins for POR and FLU in Col-0 (wild type) and Sha, *prt6* (Col-0 background) and Sha *prt6*, repeated independently three times with similar results. All experiments were carried out using etiolated seedlings after 5 days growth at 48 m a.s.l unless otherwise stated. Means are plotted, error bars report SD. Coefficient of determination (R^2) is given. For each n = 3 biologically independent experiments.

[Source data](#)

Extended Data Fig. 7 Locations of sites used for reciprocal transplantation experiments.

Relationship between altitude and partial pressure of oxygen (pO_2 kPa), showing positions of sites Sutton Bonington (SB): Latitude 52.829809° N longitude –1.249732° E pO_2 21.2 kPa: 48 m a.s.l, and Sangolquí (ESPE): Latitude –0.312917° N longitude –78.445157° E pO_2 15.7 kPa: 2479 m a.s.l. Maps obtained from <http://www.ginkgomaps.com/>.

Extended Data Fig. 8 Influence of ambient O₂ on expression of hypoxia-induced RNAs in *A. thaliana* and *S. habrochaites* accessions.

a, Pchlde in *A. thaliana* high-altitude accession Sha, and *erfVII* (pentuple mutant obtained from the low altitude accession Col-0), measured at 48 m a.s.l. (SB, pO_2 21.2 kPa) and 2479 m a.s.l. (ESPE, pO_2 15.7 kPa). b, *PORA/B*, *CHLM* gene expression in *A. thaliana* accessions collected at different altitudes measured at 48 m a.s.l. (pO_2 21.2 kPa, SB) or at 2479 m a.s.l. (pO_2 15.7 kPa, ESPE). c, Hypoxia-related gene expression in *A. thaliana* accessions Col-0 (low altitude) and Sha (high altitude), at 48 m a.s.l. in different ambient levels of oxygen. d, Expression of *S. habrochaites* hypoxia-related genes at 15% and 21% ambient oxygen in accessions from different altitudes measured at 48 m a.s.l. Carried out using etiolated seedlings after 5 days growth (48 m a.s.l.). Means are plotted, error bars report SD, coefficient of determination (R^2) is given. For each n = 3 biologically independent experiments. For a, Sha (SB) was measured once.

Source data

Extended Data Fig. 9 Comparisons of genomic DNA and RNA expression patterns in *A. thaliana* accessions Col-0 and Sha.

a,b Introduction of the *prt6-1* mutation (by introgression from low altitude accession Col-0) or C2A-RAP2.3 (by transformation) into *A. thaliana* high altitude accession Sha enhances the expression of hypoxia-related genes. c, Expression of RNAs for PCO PRT6 N-degron pathway components in accessions Sha and Col-0. RNA was extracted using etiolated seedlings after 5 days growth at pO_2 21.2 kPa (48 m a.s.l.). d, Comparison of DNA

sequence of the first coding exon of *FLU* in accessions Col-0 and Sha. DNA sequence information was obtained from Arabidopsis 1001 web site: <http://signal.salk.edu/atg1001/2.0/gebrowsr.php>. Shown are ERFVII binding site (also known as EBP, GCC box) and related HRPE (Hypoxia-Responsive Promoter Element²)-like element in the first coding exon of *A. thaliana* *FLU* (initiating ATG highlighted). All experiments carried out using etiolated seedlings after 5 days growth. Means are plotted, error bars report SD. Significant differences denoted with letters for one-way ANOVA ($p < 0.05$). For each $n = 3$ biologically independent experiments.

[Source data](#)

Extended Data Fig. 10 Pchlde steady state levels in reciprocal genetic crosses between *A. thaliana* high altitude accession Sha and erVII (Col-0 accession).

Experiments carried out using etiolated seedlings after 5 days growth at pO_2 21.2 kPa (48 m a.s.l). Means are plotted, error bars report SD. Significant differences denoted with letters for one-way ANOVA ($p < 0.05$). For each $n = 3$ biologically independent experiments.

[Source data](#)

Supplementary information

Supplementary Figure 1

All uncropped western blots

Reporting Summary

Supplementary Table 1

Lists of accessions for species used, R^2 values for Fig. 2c, relationship between altitude of collection of *A. thaliana* accessions and submergence survival and comparison of ROS content among all *A. thaliana* genotypes

Supplementary Table 2

List of oligonucleotide primers used in this study.

Source data

Source Data Fig. 1

Source Data Fig. 2

Source Data Fig. 3

Source Data Extended Data Fig. 1

Source Data Extended Data Fig. 2

Source Data Extended Data Fig. 3

Source Data Extended Data Fig. 4

Source Data Extended Data Fig. 5

Source Data Extended Data Fig. 6

Source Data Extended Data Fig. 8

Source Data Extended Data Fig. 9

Source Data Extended Data Fig. 10

Rights and permissions

Open Access This article is licensed under a Creative Commons Attribution 4.0 International License, which permits use, sharing, adaptation,

distribution and reproduction in any medium or format, as long as you give appropriate credit to the original author(s) and the source, provide a link to the Creative Commons license, and indicate if changes were made. The images or other third party material in this article are included in the article's Creative Commons license, unless indicated otherwise in a credit line to the material. If material is not included in the article's Creative Commons license and your intended use is not permitted by statutory regulation or exceeds the permitted use, you will need to obtain permission directly from the copyright holder. To view a copy of this license, visit <http://creativecommons.org/licenses/by/4.0/>.

Reprints and Permissions

About this article

Cite this article

Abbas, M., Sharma, G., Dambire, C. *et al.* An oxygen-sensing mechanism for angiosperm adaptation to altitude. *Nature* **606**, 565–569 (2022).
<https://doi.org/10.1038/s41586-022-04740-y>

- Received: 25 June 2021
- Accepted: 07 April 2022
- Published: 01 June 2022
- Issue Date: 16 June 2022
- DOI: <https://doi.org/10.1038/s41586-022-04740-y>

Share this article

Anyone you share the following link with will be able to read this content:

[Get shareable link](#)

Sorry, a shareable link is not currently available for this article.

[Copy to clipboard](#)

Provided by the Springer Nature SharedIt content-sharing initiative

This article was downloaded by **calibre** from <https://www.nature.com/articles/s41586-022-04740-y>.

| [Section menu](#) | [Main menu](#) |

- Article
- [Published: 06 April 2022](#)

Fc γ R-mediated SARS-CoV-2 infection of monocytes activates inflammation

- [Caroline Junqueira](#),
- [Ângela Crespo](#),
- [Shahin Ranjbar](#),
- [Luna B. de Lacerda](#),
- [Mercedes Lewandrowski](#),
- [Jacob Ingber](#),
- [Blair Parry](#),
- [Sagi Ravid](#),
- [Sarah Clark](#),
- [Marie Rose Schrimpf](#),
- [Felicia Ho](#),
- [Caroline Beakes](#),
- [Justin Margolin](#),
- [Nicole Russell](#),
- [Kyle Kays](#),
- [Julie Boucau](#),
- [Upasana Das Adhikari](#),
- [Setu M. Vora](#),
- [Valerie Leger](#),
- [Lee Gehrke](#),
- [Lauren A. Henderson](#),
- [Erin Janssen](#),
- [Douglas Kwon](#),
- [Chris Sander](#),
- [Jonathan Abraham](#),

- [Marcia B. Goldberg](#),
- [Hao Wu](#),
- [Gautam Mehta](#),
- [Steven Bell](#),
- [Anne E. Goldfeld](#),
- [Michael R. Filbin](#) &
- [Judy Lieberman](#)

Nature volume **606**, pages 576–584 (2022)

- 103k Accesses
- 13 Citations
- 1487 Altmetric
- [Metrics details](#)

Abstract

SARS-CoV-2 can cause acute respiratory distress and death in some patients¹. Although severe COVID-19 is linked to substantial inflammation, how SARS-CoV-2 triggers inflammation is not clear². Monocytes and macrophages are sentinel cells that sense invasive infection to form inflammasomes that activate caspase-1 and gasdermin D, leading to inflammatory death (pyroptosis) and the release of potent inflammatory mediators³. Here we show that about 6% of blood monocytes of patients with COVID-19 are infected with SARS-CoV-2. Monocyte infection depends on the uptake of antibody-opsonized virus by Fc γ receptors. The plasma of vaccine recipients does not promote antibody-dependent monocyte infection. SARS-CoV-2 begins to replicate in monocytes, but infection is aborted, and infectious virus is not detected in the supernatants of cultures of infected monocytes. Instead, infected cells undergo pyroptosis mediated by activation of NLRP3 and AIM2 inflammasomes, caspase-1 and gasdermin D. Moreover, tissue-resident macrophages, but not infected epithelial and endothelial cells, from lung autopsies from patients with COVID-19 have activated inflammasomes. Taken together, these findings

suggest that antibody-mediated SARS-CoV-2 uptake by monocytes and macrophages triggers inflammatory cell death that aborts the production of infectious virus but causes systemic inflammation that contributes to COVID-19 pathogenesis.

Main

SARS-CoV-2 causes severe COVID-19 marked by acute respiratory distress that can progress to multiorgan failure and death in older individuals and patients with comorbidities¹. Increased chronic inflammation is associated with ageing (inflammaging) and the comorbidities linked to severe disease⁴, and severe disease is linked to signs of inflammation². When myeloid cells sense invasive infection, they activate inflammasomes to sound an innate immune alarm³. Inflammasome activation is required to process and release interleukin-1 (IL-1)-family cytokines, arguably the most potent inflammatory mediators⁵. However, activation of NF-κB, the TNF receptor superfamily and T helper 17 (T_H17) cell cytokines can also cause severe inflammation. When inflammasomes sense infection, they recruit the ASC adaptor and assemble into large complexes that recruit and activate caspase-1, which in turn processes IL-1 pro-cytokines and the pore-forming gasdermin D (GSDMD) to disrupt the cell membrane, leading to cell death and cytokine release³. Pyroptotic cell membrane rupture releases cytokines, chemokines and other alarmins that recruit immune cells to infection sites. LDH release is pathognomonic for pyroptosis and other forms of necrotic cell death³ and elevated LDH is one of the best correlates of severe COVID-19⁶.

COVID-19 blood shows signs of pyroptosis

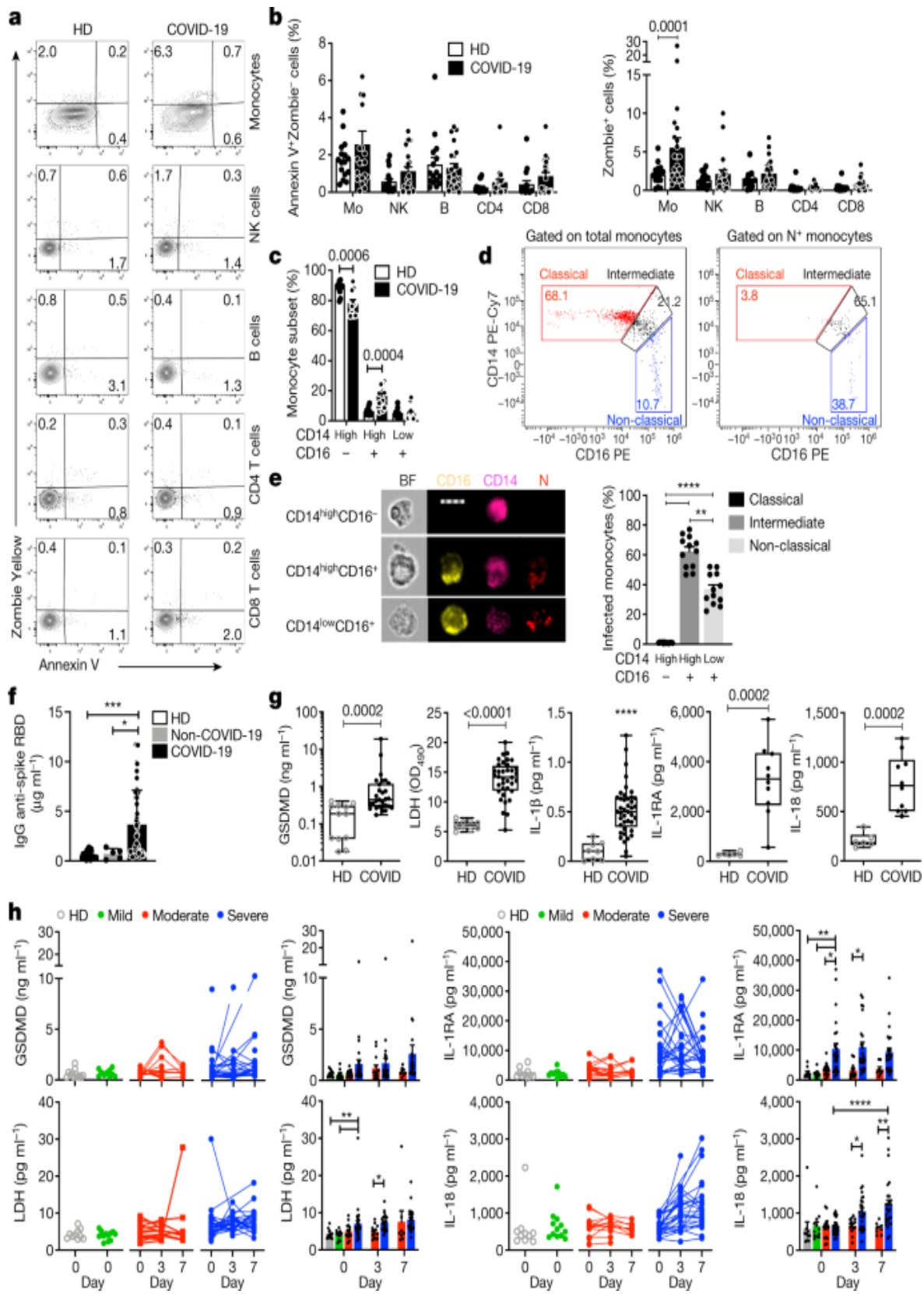
As inflammasome activation is a major mediator of inflammation⁷, we examined the blood of patients infected with SARS-CoV-2 for inflammasome activation and pyroptosis. Freshly isolated mononuclear cells from 19 healthy donor individuals (HDs) and 22 patients with COVID-19 in the emergency department were stained for haematopoietic cell markers; with a small fixable dye (Zombie Yellow) that enters cells with damaged

plasma membranes; and for annexin V, an indicator of programmed cell death (Fig. [1a](#), [b](#), Extended Data Fig. [1a](#) and Supplementary Table [1](#)).

Annexin V⁺Zombie⁻ apoptotic cells did not increase in any subpopulation in samples from patients with COVID-19. However, around 6% of monocytes of patients with COVID-19 on average took up Zombie dye, a sign of membrane damage consistent with pyroptosis. None of the lymphocyte subsets in samples from patients with COVID-19 showed increased pyroptosis. Monocyte flow cytometry analysis indicated that there was a reduced frequency of classical monocytes (CD14^{high}CD16⁻) in 15 patients with COVID-19 compared with 13 HDs, whereas intermediate monocytes (CD14^{high}CD16⁺) were significantly increased, but there was no change in the non-classical subset (CD14^{low}CD16⁺) (Fig. [1c](#) and Extended Data Fig. [1b](#)). Many intermediate (about 60%) and non-classical (about 40%), but none of the more abundant classical, monocytes had taken up SARS-CoV-2 virus as they stained for nucleocapsid (N) (Fig. [1d](#), [e](#)). As only monocytes that expressed CD16—an important mediator of antibody-dependent phagocytosis—took up virus, anti-spike RBD IgG plasma titres were measured in plasma samples of 64 patients with COVID-19 that were obtained at presentation at the emergency department, 20 HDs and 5 patients who presented with COVID-19-like symptoms but were SARS-CoV-2 PCR negative (hereafter, non-COVID-19 patients) (Fig. [1f](#)). Most patients with COVID-19, but not HDs or non-COVID-19 controls, had elevated anti-spike RBD IgG, suggesting that they had been infected for approximately a week^{[8](#)}. Plasma samples from patients with COVID-19 with diverse disease outcomes and HDs were compared for pyroptosis-specific markers (GSDMD, IL-1 β , IL-1RA, IL-18 and LDH activity) (Fig. [1g](#)), inflammatory markers not specific for pyroptosis (inflammatory cytokines IL-6, TNF and IL-17/17A; growth factors IL-7 and G-CSF; and chemokines CCL7, CXCL9 and CXCL10) and interferons (IFN β and IFN γ). Consistent with published data^{[9,10](#)}, all inflammation markers that are not specific for pyroptosis were significantly elevated in the plasma of patients with COVID-19 (except for IL-17/17A) and IFNs were not detected above the baseline (data not shown). All pyroptosis markers were significantly elevated in the plasma of patients with COVID-19 compared with HDs. Although significantly higher in samples from patients with COVID-19, plasma IL-1 β was low, which was not surprising as it is rapidly cleared and is usually not detected even in patients with pyroptosis-mediated diseases. However, its antagonist IL-1RA,

used as a surrogate⁵, was greatly increased in samples from patients with COVID-19. Note that IL-1 cytokines and pyroptosis potently activate the other elevated inflammation markers¹¹.

Fig. 1: Monocytes of patients with COVID-19 undergo pyroptosis.



a, b, Representative flow cytometry plots (**a**) and the percentage of lymphocyte subset and monocyte (Mo) staining for annexin V only or Zombie dye (**b**) in fresh blood from HDs ($n = 16$) and patients with COVID-19 ($n = 22$). NK, natural killer cells. **c**, The frequency of monocyte subsets (classical, CD14^{high}CD16⁻; intermediate, CD14^{high}CD16⁺; and non-classical, CD14^{low}CD16⁺) in freshly isolated blood from HDs ($n = 11$) and patients with COVID-19 ($n = 12$). **d, e**, Imaging flow cytometry analysis of SARS-CoV-2 infection in monocyte subsets of patients with COVID-19 ($n = 12$). Monocytes from patients with COVID-19 were enriched by negative selection and stained for CD14, CD16 and SARS-CoV-2 N. **d**, Representative dot plots of monocyte subsets gated on all monocytes (left) or N⁺ monocytes. **e**, Representative images of imaging flow cytometry (left) and quantification of infection (N⁺) in the monocyte subsets (right). BF, bright field. Scale bar, 7 μ m. **f**, The concentration of anti-spike RBD IgG in the plasma of HDs ($n = 20$), non-COVID-19 patients (with COVID-19-like symptoms but PCR negative for SARS-CoV-2; $n = 5$) and patients with COVID-19 ($n = 68$) at presentation. **g**, The concentration of pyroptosis biomarkers and cytokines in HD and COVID-19 plasma. GSDMD ($n = 12$ (HD), $n = 29$ (COVID-19)); LDH activity ($n = 10$ (HD), $n = 36$ (COVID-19)); IL-1 β ($n = 8$ (HD), $n = 41$ (COVID-19)); IL-1RA and IL-18 ($n = 6$ (HD), $n = 10$ (COVID-19)). A description of the samples is provided in Supplementary Table 1. OD₄₉₀, optical density at 490 nm. **h**, Plasma pyroptosis biomarkers at presentation (day 0) and during hospitalization (day 3 and 7) in patients with COVID-19 with mild ($n = 12$), moderate ($n = 16$) and severe ($n = 32$) COVID-19 Acuity scores (the samples are described in Supplementary Table 2). Left, individual patient data. Right, grouped data. For **b, c, e, f, h**, data are mean \pm s.e.m. The plots in **g** show the median (centre line), the interquartile range between the 25th and 75th percentiles (box), and the 25th percentile value $- 1.5 \times$ the interquartile range (lower whisker) and the 75th percentile value $+ 1.5 \times$ the interquartile range (upper whisker). Statistical analysis was performed using two-tailed nonparametric unpaired *t*-tests (**b, c**), one-way analysis of variance (ANOVA) with Tukey multiple-comparisons test (**e, f**), two-tailed nonparametric unpaired *t*-tests (**g**) and two-way ANOVA with Tukey multiple-comparisons test (**h**); * $P < 0.05$, ** $P < 0.01$, *** $P < 0.001$, **** $P < 0.0001$.

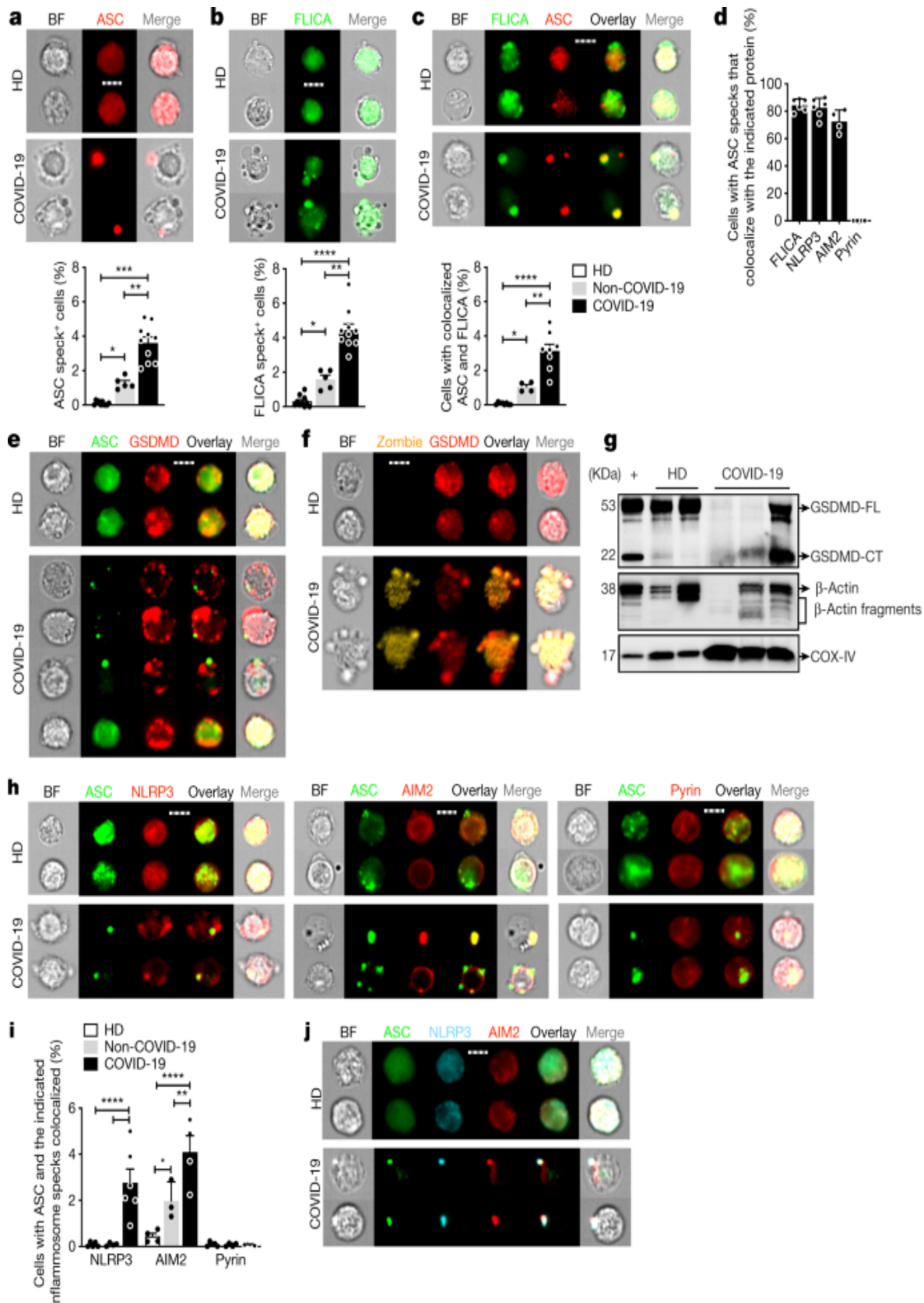
To determine whether pyroptosis biomarkers correlate with COVID-19 disease severity, plasma from 10 HDs and 60 patients with COVID-19 was analysed for GSDMD, LDH, IL-1RA and IL-18 at presentation and on days 3 and 7 for hospitalized patients (Fig. [1h](#) and Supplementary Table [2](#)). The patients were grouped into mild, moderate or severe disease using the MGH COVID Acuity scale^{[12](#)}. Plasma GSDMD, LDH, IL-1RA and IL-18 were all elevated in the samples from patients with severe disease compared with those with mild or moderate disease, but the increase in GSDMD was not significant. Taken together, these results suggest ongoing pyroptosis in COVID-19 blood that was more prominent in severe disease.

Monocytes have activated inflammasomes

These data suggested that monocytes in patients with COVID-19 might die of pyroptosis and release inflammatory cytokines to contribute to poor outcome. Not much is known about how viruses interact with the 27 potential human canonical inflammasome sensors^{[3](#)}. The NLRP3 inflammasome, which detects K⁺ efflux generated by a variety of stimuli, could be activated by specific viral proteins^{[13,14](#)}. Three SARS-CoV-2 proteins—Orf3a, Orf8 and envelope (E)—are thought to be ‘viroporins’ (ion channels) that potentially activate K⁺ efflux, as previously described for SARS-CoV^{[15](#)}. Orf3 and Orf8 are encoded only by pathogenic human coronaviruses. Interestingly, bats, which are the natural hosts of SARS-CoV and SARS-CoV-2, have a dampened NLRP3 response to multiple viruses, including MERS-CoV, which might explain their toleration of these infections despite high viral loads^{[16](#)}. To examine whether monocytes of patients with COVID-19 undergo pyroptosis, freshly isolated, enriched monocytes from HDs, patients with COVID-19 of mixed disease severity (Supplementary Table [1](#)) and non-COVID-19 patients were analysed using imaging flow cytometry for the expression and intracellular distribution of the common inflammasome adaptor ASC, activated caspase-1 (using the fluorochrome-labelled inhibitor of caspases assay (FLICA)) and GSDMD. Activated canonical inflammasomes form large micrometre-sized inflammasome–ASC–caspase-1 specks^{[3](#)}. About 4% of monocytes from patients with COVID-19, 1% of monocytes from non-COVID-19 patients, but no monocytes from HDs, had caspase-1 and ASC specks (Fig. [2a–c](#) and

Extended Data Fig. [2a](#), [b](#)). These results suggest that other causes of respiratory distress activate monocyte inflammasomes, but activation is more extensive in SARS-CoV-2 infection. Most cells with ASC specks (about 80%) from patients with COVID-19 also had colocalized caspase-1 specks (Fig. [2d](#)).

Fig. 2: Monocytes of patients with COVID-19 have activated inflammasomes, caspase-1 and GSDMD.



Monocytes from HDs, non-COVID-19 patients or patients with COVID-19 at the time of presentation were analysed by imaging flow cytometry for ASC, GSDMD, caspase-1 activation (FLICA) and/or Zombie dye uptake. **a–c**, The percentage of monocytes with activated ASC (**a**) or caspase-1 (**b**) ($n = 8$ (HD), $n = 5$ (non-COVID-19), $n = 10$ (COVID-19)) or colocalized ASC/caspase-1 specks (**c**) ($n = 8$ (HD), $n = 4$ (non-COVID-19), $n = 8$ (COVID-19)) (**c**). Representative images (top) and quantification of all samples (bottom) are shown. **d**, The percentage of ASC-speck-containing monocytes with colocalized activated caspase-1, NLRP3, AIM2 or pyrin specks. $n = 6$. **e, f**, Representative images of ASC (**e**) or Zombie dye (**f**) and GSDMD co-stained monocytes. $n = 4$ independent experiments. **g**, Lysates of purified monocytes of HDs and patients with COVID-19, and of LPS- and nigericin-treated monocytes of HDs (+) probed with a monoclonal antibody that recognizes full length GSDMD (GSDMD-FL) and the C-terminal of GSDMD (GSDMD-CT) (top), β -actin (middle) and COX-IV (bottom). Representative of $n = 4$ independent experiments. **h, i**, Representative images of ASC co-staining with NLRP3 (left; $n = 5$ (HD), $n = 4$ (non-COVID-19), $n = 6$ (COVID-19)), AIM2 (middle; $n = 4$ (HD), $n = 3$ (non-COVID-19), $n = 4$ (COVID-19)) and pyrin (right; $n = 4$ (HD), $n = 4$ (non-COVID-19), $n = 5$ (COVID-19)) (**h**), and quantification of monocytes showing ASC specks colocalized with the indicated inflammasomes (**i**). **j**, Representative images of co-staining of ASC, NLRP3 and AIM2. $n = 3$ independent experiments. For **a–c, e, f, h, j**, scale bars, 7 μ m. For **a–d, i**, data are mean \pm s.e.m. Statistical analysis was performed using one-way ANOVA with Tukey multiple-comparisons test (**a–d**) and two-way ANOVA with Tukey multiple-comparisons test (**i**); * $P < 0.05$, ** $P < 0.01$, *** $P < 0.001$, **** $P < 0.0001$.

COVID-19 monocytes with ASC specks showed ballooning plasma membranes, GSDMD redistribution from the cytoplasm to cell membrane puncta and Zombie dye uptake, consistent with GSDMD pore formation and pyroptosis, but cells without ASC specks did not (Fig. [2e, f](#) and Extended Data Fig. [2b, e](#)). Most Zombie⁺ cells had ASC specks ($62 \pm 9\%$), suggesting that most COVID-19 monocyte death is due to inflammasome activation. However, only $28 \pm 5\%$ of cells with ASC specks had taken up Zombie dye. This difference could be because cell membrane permeabilization is delayed after ASC activation and dying cells with damaged membranes are rapidly

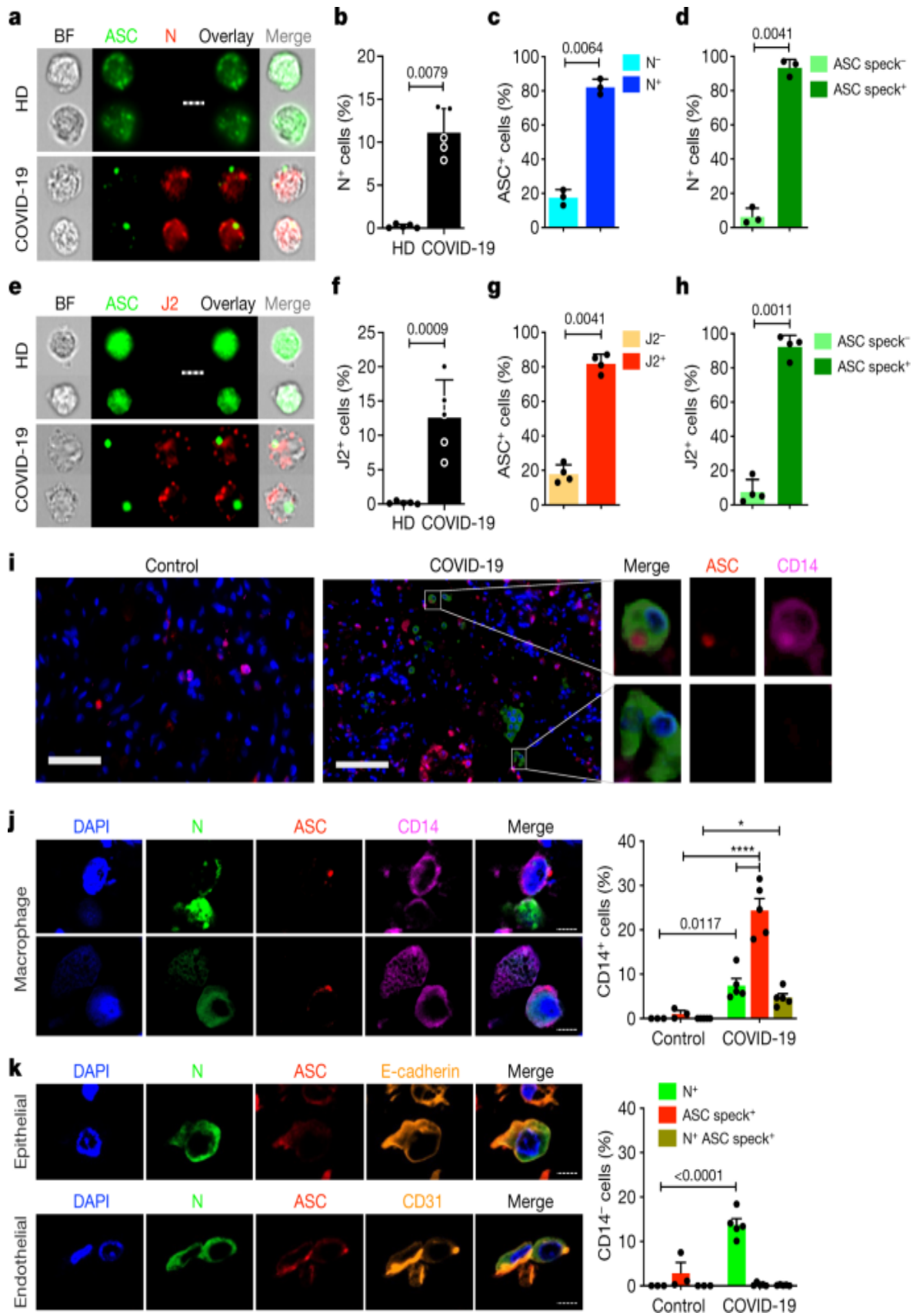
removed from the blood. Immunoblots of monocyte lysates of HDs and patients with COVID-19 were probed for full-length GSDMD (GSDMD-FL) and its C-terminal fragment (GSDMD-CT) and housekeeping proteins, β -actin and COX-IV (Fig. 2g and Extended Data Fig. 2g). During pyroptosis, cleaved GSDMD and actin are released and the actin cytoskeleton disintegrates, whereas membrane-bound proteins, such as COX-IV, are mostly retained^{3,17}. GSDMD-FL was detected in all of the HD samples, but in only 1 out of 3 samples from patients with COVID-19. GSDMD-CT was detected in monocytes of patients with COVID-19 and the positive control (LPS + nigericin-treated HD monocytes). Although COX-IV was detected in all of the samples, full-length β -actin was not detected in one COVID-19 sample, but β -actin fragments were detected in all of the samples from patients with COVID-19 and in nigericin-activated HD monocytes. Thus, monocytes of patients with COVID-19 are undergoing pyroptosis.

To identify the activated inflammasome, monocytes of HDs and patients with COVID-19 were co-stained for ASC and three canonical inflammasomes (NLRP3, AIM2 (activated by cytoplasmic DNA) and pyrin (activated by bacterial toxins))¹⁴ (Fig. 2d, h–j and Extended Data Fig. 2c–f). In monocytes of patients with COVID-19, ASC specks colocalized with NLRP3 and AIM2, but there were no pyrin specks. AIM2 activation was unexpected, although AIM2 is activated by RNA viruses in rare cases by an unclear mechanism¹⁸. AIM2 might sense host mitochondrial DNA as mitochondrial membranes are damaged during pyroptosis¹⁹. Almost all ASC-speck-positive monocytes had colocalized NLRP3 and AIM2 specks (Fig. 2d), and ASC, NLRP3 and AIM2 colocalized (Fig. 2j). We did not expect to find more than one inflammasome stimulated in the same cell, although colocalization of two distinct inflammasomes has been reported²⁰. Confocal microscopy confirmed ASC, caspase-1, NLRP3 and AIM2 colocalization in inflammasomes selectively in COVID-19 monocytes (Extended Data Fig. 2f). These data showing inflammasome specks and GSDMD membrane localization and cleavage, together with the detection of dying annexin V[−]Zombie⁺ monocytes and plasma GSDMD and IL-1 cytokines (Fig. 1), indicate that COVID-19 monocytes die of pyroptosis.

Monocyte infection triggers pyroptosis

We next examined what activates inflammasomes in COVID-19 monocytes. As inflammasomes sense invasive infection, monocyte infection might be the trigger. A few reports suggest that monocytes^{10,21} and macrophages can be infected by SARS-CoV-2, and we detected nucleocapsid in patient monocytes (Fig. 1d, e). However, monocytes do not express ACE2, the viral entry receptor²². Indeed, ACE2 was undetected or barely detected by flow cytometry and quantitative PCR with reverse transcription (RT–qPCR) analysis of monocytes of patients with COVID-19 and HDs (Extended Data Fig. 3a, b). Monocytes of HDs and patients with COVID-19 expressed similar levels of CD147 (also known as basigin and EMMPRIN), which is reported to bind to the SARS-CoV-2 spike protein and facilitate viral uptake, although this finding is controversial^{23,24,25} (Extended Data Fig. 3c, d). Monocytes express three Fc γ receptors—CD64 (Fc γ RI) and CD32 (Fc γ RII), which is expressed on most blood monocytes, and CD16 (Fc γ RIIIa), which is expressed on a small minority of blood monocytes (around 10% in HDs)^{26,27}—that are increased in COVID-19⁹. These receptors could recognize antibody-opsonized virions and mediate uptake through antibody-dependent phagocytosis²⁸. Anti-SARS-CoV-2 spike antibodies are detected early in SARS-CoV-2 infection, about when patients develop inflammatory symptoms^{8,29}, as in our cohort (Fig. 1f). To examine whether monocytes of patients with COVID-19 are infected, we co-stained monocytes of HDs and patients with COVID-19 for nucleocapsid (N) (Fig. 3a–d) or double-stranded RNA (dsRNA) (anti-J2 antibodies) (Fig. 3e–h) and ASC. N staining indicates virus internalization, but J2 staining indicates active infection³⁰. Monocytes of HDs did not stain for N, dsRNA or ASC. About 10% of monocytes from patients with COVID-19 stained for N or dsRNA (Fig. 3b, f) and around 95% of N⁺ monocytes were also J2 positive, indicating viral replication. Almost all infected cells showed ASC specks (Fig. 3c, g) and all ASC-speck-positive cells were infected (Fig. 3d, h). Thus, SARS-CoV-2 monocyte infection activates inflammasomes and pyroptosis.

Fig. 3: SARS-CoV-2-infected monocytes and lung macrophages have activated inflammasomes.



a–h, Monocytes of HDs and patients with COVID-19 were stained for SARS-CoV-2 N ($n = 5$) (**a–d**) or dsRNA (anti-J2 antibodies) ($n = 4$) (**e–h**) and ASC. **a, e**, Representative imaging flow cytometry images. **b, f**, Quantification of infected cells on the basis of N (**b**) or J2 (**f**) staining. **c, g**, Uninfected or infected cells that showed ASC specks. **d, h**, The percentage of cells with or without ASC specks that were infected. For **a, e**, scale bars, 7 μm . **i–k**, Lung autopsies from five patients with COVID-19 (the samples are described in Supplementary Table 3) and three control individuals who have experienced trauma were stained for N (green), ASC (red) and CD14 (magenta), and with DAPI (blue). **i**, Digital scanner images of a representative patient who experienced trauma (left) and a patient with COVID-19 (middle), showing a magnified image of representative infected CD14 $^{+}$ (top) and CD14 $^{-}$ (bottom) cells from the lungs of the patient with COVID-19 (right). Scale bars, 50 μm (left), 100 μm (middle). **j, k**, Representative confocal microscopy COVID-19 lung images of infected CD14 $^{+}$ (**j**) and CD14 $^{-}$ (**k**) cells (left). Right, quantification of CD14 $^{+}$ (**j**) and CD14 $^{-}$ (**k**) cells that are N positive and/or have ASC specks in the lungs of patients with COVID-19 ($n = 5$) and control individuals ($n = 3$). In **k**, representative images of CD14 $^{-}$ N $^{+}$ cells (left) were co-stained for ASC and E-cadherin, an epithelial marker (top), or CD31, an endothelial marker (bottom). For **j, k**, scale bars, 7 μm . For **b–d, f–h, j, k**, data are mean \pm s.e.m. Statistical analysis was performed using two-tailed nonparametric unpaired *t*-tests (Mann–Whitney *U*-tests) (**b–d, f–h**) and two-way ANOVA with Tukey multiple-comparisons test (**j, k**); * $P < 0.05$, ** $P < 0.01$, *** $P < 0.001$, **** $P < 0.0001$.

Lung macrophages have inflammasome specks

As the respiratory tract is the main infection site, we next assessed whether macrophages in lung autopsies were infected with SARS-CoV-2 and had active inflammasomes. Fixed lung slides from five individuals with SARS-CoV-2 infection (Supplementary Table 3) and three uninfected individuals who have experienced trauma were co-stained for CD14, ASC, N and DAPI (Fig 3*i–k*). In the lungs of patients with COVID-19, $15.1 \pm 2.9\%$ of CD14 $^{-}$ cells and $8.3 \pm 4.2\%$ of CD14 $^{+}$ cells stained for N, but N was not detected in the unaffected individuals who have experienced trauma (Fig 3*i–k*). As

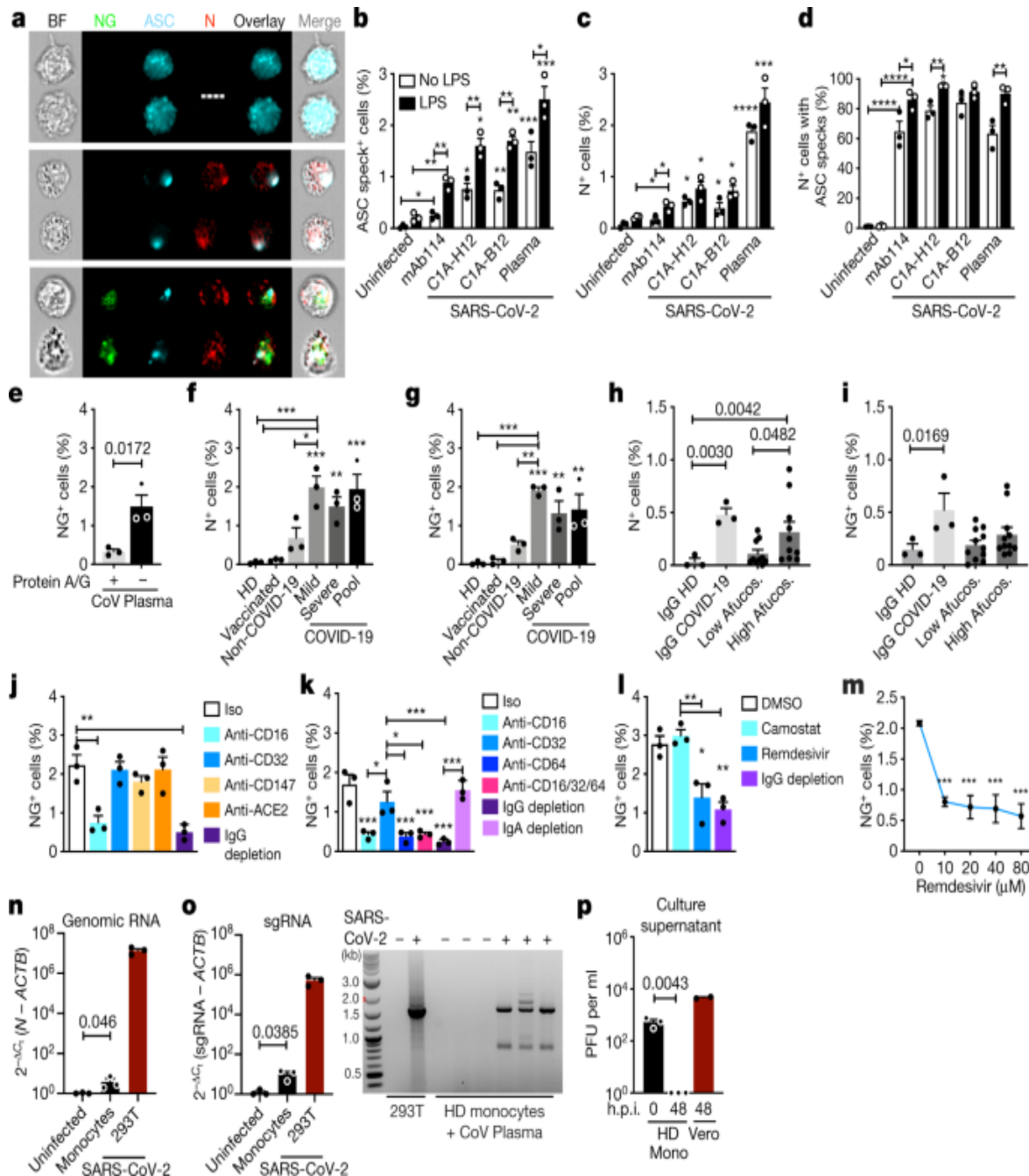
expected, both E-cadherin⁺ epithelial and CD31⁺ endothelial CD14⁻ cells stained for N (Fig. 3k). However, ASC specks were detected only in CD14⁺, but not in CD14⁻, COVID-19 lung cells, indicating that tissue-resident macrophages have activated ASC-containing inflammasomes, but infected lung epithelial and endothelial cells do not. Most CD14⁺N⁺ cells had ASC specks (Fig. 3j). ASC specks were not seen in control autopsies. About a quarter of CD14⁺ lung cells had ASC specks, although only approximately 8% were N positive, suggesting that danger-associated molecular patterns, released from infected or otherwise damaged lung cells, may have activated inflammasomes in uninfected macrophages.

CD16 mediates infection of opsonized virus

To confirm that monocytes can be infected, monocytes of HDs were infected with an engineered infectious clone (icSARS-CoV-2-mNG) encoding a Neon Green (NG) fluorescent reporter of viral replication³¹. Monocytes, primed or not with LPS, were infected (multiplicity of infection of 1) with reporter virus preincubated with IgG1 isotype control antibodies (mAb114), anti-spike monoclonal antibodies (non-neutralizing (C1A-H12) or neutralizing (C1A-B12))³² or pooled plasma (heat-inactivated or not) from HDs or patients with COVID-19. Antibodies and plasma were also present during culture. After 48 h, monocytes were analysed for N, dsRNA and ASC by imaging flow cytometry (Fig. 4a–g and Extended Data Fig. 4). Without LPS, anti-spike antibodies or COVID-19 pooled plasma, few monocytes of HDs took up or replicated the virus, but infection increased significantly in the presence of anti-spike monoclonal antibodies or plasma from patients with COVID-19. Antibody-neutralizing activity and plasma heat-inactivation did not affect infection (Extended Data Fig. 4a–e), suggesting that complement was not involved. IgG-depletion of plasma from patients with COVID-19 nearly abrogated viral infection, assessed by NG fluorescence, but IgA depletion had no effect on infection (Fig. 4e, j, k). These results suggest that infection is mediated by virus opsonized by anti-spike antibodies. Nonetheless, N-, J2- and NG-positive monocytes were detected at low levels after infection of HD monocytes with virus preincubated with isotype control monoclonal antibodies or with HD plasma, suggesting possible inefficient anti-SARS-CoV-2 antibody-

independent monocyte infection. The highest in vitro infection rate was around 3% in HD monocytes that were pretreated with LPS and incubated with patient plasma. N and J2 staining were comparable, with a low background of around 0.1% in uninfected samples; fewer cells were NG fluorescent (about half as many) and there was no background NG fluorescence. More J2⁺ or N⁺ cells in samples with the highest infection rates (treated with LPS and patient plasma or anti-spike antibodies) were also NG fluorescent, indicating viral replication (Extended Data Fig. 4e). NG may be detected less often than N or dsRNA because it is expressed late in the viral lifecycle and/or is more difficult to detect. ASC specks were barely detected in uninfected HD monocytes but increased with SARS-CoV-2 infection (Fig. 4c and Extended Data Fig. 4d). ASC-speck-positive cells increased when SARS-CoV-2 was preincubated with anti-spike antibodies and still more when preincubated with patient plasma. HD monocyte infection with the fluorescent molecular clone was similar to infection with the parental Washington (WA) strain or a Delta variant clinical isolate but, as expected, the molecular clone less efficiently infected A549-ACE2 cells compared with the WA strain or the more infectious Delta variant (Extended Data Fig. 4f,g). The similarity of HD monocyte infection for all three viruses suggested that monocyte viral entry might be ACE2-independent.

Fig. 4: HD monocytes take up antibody-opsonized SARS-CoV-2 through an FcγR but viral replication is aborted.



a-d, HD monocytes ($n = 3$) were primed (black bars) or not (white bars) with LPS, infected with icSARS-CoV-2-mNG and stained 48 h later for N and ASC. Virus was preincubated with IgG1 control mAb114, non-neutralizing anti-spike (C1A-H12) or neutralizing anti-RBD (C1A-B12), or with pooled plasma from patients with COVID-19, and these were retained throughout culture. **a**, Representative imaging flow cytometry images of uninfected (top), N⁺NG⁻ (middle) or N⁺NG⁺ (bottom) monocytes. Scale bar,

7 μm. **b–d**, Quantification of the percentage of ASC speck⁺ (**b**) or N⁺ (**c**) monocytes, and of N⁺ monocytes with ASC specks (**d**). $n = 3$. **e–i**, LPS-activated HD monocytes were infected with icSARS-CoV-2-mNG preincubated with pooled COVID-19 plasma, depleted or not depleted of immunoglobulins using protein A/G beads ($n = 3$; **e**), or preincubated with pooled plasma from HDs, recipients of a COVID-19 mRNA vaccine, non-COVID-19 patients or patients with COVID-19 with mild and/or severe disease ($n = 3$; **f, g**); or with purified IgG from HDs ($n = 3$), pooled from patients with COVID-19 of mixed severity ($n = 3$) or patients with COVID-19 with low (about 8%) or high (about 30%) afucosylated (Afucos.) anti-spike IgG ($n = 11$) (**h, i**). Infection was quantified by N staining (**f, h**) or NG fluorescence (**e, g, i**). **j–m**, LPS-treated HD monocytes were infected with icSARS-CoV-2-mNG, preincubated with pooled plasma from patients with COVID-19, depleted or not depleted of IgG or IgA as indicated, in the presence of the indicated blocking or isotype control (Iso) antibodies ($n = 3$; **j, k**) or antiviral drugs (**l** (10 μM remdesivir), **m**), and infection was assessed 48 h later by NG fluorescence. The statistical analysis in **m** compared drug with no drug. **n, o**, RT–qPCR analysis of genomic SARS-CoV-2 *N* RNA (**n**) and sgRNA (**o**, left) in uninfected or infected HD monocytes ($n = 3$), normalized to *ACTB* mRNA. Infected HEK293T cells were used as a positive control ($n = 3$). Agarose gel electrophoresis of ethidium-bromide-stained RT–qPCR-amplified sgRNA is shown (**o**, right). The approximately 1,600-bp band in the samples from patients with COVID-19 was sequenced and confirmed to be *N* sgRNA. **p**, SARS-CoV-2 plaque-forming units (PFU) in culture supernatants of infected monocytes (Mono) or Vero E6 cells collected at the indicated hours post-infection (h.p.i.). For **b–p**, data are mean ± s.e.m. Statistical analysis was performed using two-way ANOVA with Sidak multiple-comparisons test (**b–d**), two-tailed nonparametric unpaired *t*-tests (**e**) and one-way ANOVA with Tukey multiple-comparisons test (**f–p**); * $P < 0.05$, ** $P < 0.01$, *** $P < 0.001$, **** $P < 0.0001$. Data are representative of $n = 3$ replicate experiments.

To assess whether disease severity or antibodies raised by vaccination increased monocyte virus uptake, LPS-activated monocytes were infected in the presence of pooled plasma from uninfected donors, mRNA vaccine recipients or patients with COVID-19 with mild or severe disease. Importantly, uninfected HD and post-vaccination plasma did not facilitate

virus uptake or replication, even though plasma anti-RBD IgG was around twofold higher in HD vaccine recipients ($6.5 \pm 1.1 \mu\text{g ml}^{-1}$) than in patients with COVID-19 ($3.6 \pm 0.5 \mu\text{g ml}^{-1}$) (Fig. 4f,g). However, pooled plasma from non-COVID-19 patients slightly increased infection, but the increase was not significant, suggesting possible inefficient viral uptake by some non-COVID plasma component. Disease severity did not affect infection by the plasma of patients with COVID-19 as pooled mild and/or severe plasma similarly facilitated infection.

Patients with severe acute COVID-19 have increased antiviral IgGs that are afucosylated in their Fc region and bind better to CD16^{33,34,35}. To test whether afucosylation affects HD monocyte infection, HD monocyte infection by virus preincubated with purified IgG from pooled plasma from HDs or patients with COVID-19, or from patients with COVID-19 with relatively low (about 8%) or high (about 30%) afucosylation (2 patients of each) was compared (Fig. 4h,i). As expected, purified HD plasma IgG did not lead to N staining or NG fluorescence, whereas IgG from pooled plasma from patients with COVID-19 did. Low afucosylated IgG did not significantly increase infection compared to HD IgG, but more highly afucosylated COVID-19 IgGs modestly, but significantly, increased N⁺ cells. However, NG fluorescence did not increase significantly after adding either low- or high-afucosylated IgG from patients with COVID-19 compared to HD IgG, perhaps because this assay is less sensitive than N staining. Purified IgG enhanced HD monocyte infection less than patient plasma (compare Fig. 4l,m with Fig. 4f,g), suggesting that an Ig-independent plasma component might facilitate infection.

To identify the viral receptor on monocytes, purified HD monocytes were infected with the reporter virus in the presence of plasma of patients with COVID-19 that was or was not depleted of IgG or in the presence of blocking antibodies to potential monocyte receptors—ACE2, CD147 and the three monocyte Fc γ Rs, CD16, CD32 and CD64 (Fig. 4j,k and Extended Data Fig. 5a,b). Blocking CD16 or CD64 or IgG depletion strongly inhibited infection, whereas blocking the other receptors had no significant effect. The combination of anti-CD16 and anti-CD64 blocking antibodies did not inhibit virus uptake more than either blocking antibody on its own.

Thus, SARS-CoV-2 infection of monocytes is mostly mediated by CD16 and/or CD64 uptake of opsonized virus.

CD16 is also expressed on neutrophils and cytotoxic T and natural killer cells, which could be infected by a similar antibody-dependent mechanism. We did not observe increased cell death in patient lymphocytes (Fig. 1a) and therefore did not study them further. However, neutrophils contribute to SARS-CoV-2 immunopathology and inflammation³⁶. To determine whether neutrophils are infected, HD neutrophils and monocytes were infected side by side in the presence of COVID-19 plasma (Extended Data Fig. 5b,c). Infection of HD neutrophils was low compared with monocyte infection (around 0.2% versus almost 3% in monocytes) and not significantly increased above background. To assess whether neutrophils are infected *in vivo*, the frequency of *in vivo* neutrophil infection in samples from COVID-19 patients of mixed disease severity and HDs was assessed by N staining negatively selected, fresh blood neutrophils (Extended Data Fig. 5d). Infection was not detected in neutrophils of patients with COVID-19.

SARS-CoV-2 monocyte infection is aborted

dsRNA and NG detection strongly suggested that monocytes replicate SARS-CoV-2. To confirm viral replication and further assess whether uptake is ACE2 mediated, HD monocytes were infected in the presence of plasma from patients with COVID-19 and the antiviral drugs remdesivir, an inhibitor of the viral RNA-dependent RNA polymerase, and camostat mesylate, an inhibitor of TMPRSS2, which primes the spike protein for ACE2-mediated entry³⁷ (Fig. 4l,m and Extended Data Fig. 5e–g). Monocyte infection, assessed by N or NG positivity, was unaffected by camostat, but significantly and comparably inhibited by Ig depletion or remdesivir, confirming antibody-dependent entry and viral replication. A lack of inhibition by camostat and anti-ACE2 antibodies suggests that ACE2 is unlikely to be a dominant receptor for viral entry into monocytes but does not rule out a small role in monocyte infection or a more prominent role in the infection of ACE2⁺ macrophages. Early in viral replication, a series of positive-strand subgenomic RNAs (sgRNAs) is transcribed with a common leader sequence that specifically indicates viral replication¹⁶. RT-qPCR was used to detect SARS-CoV-2 genomic RNAs (gRNAs) and sgRNAs using

primers targeting the N1 region of the *N* gene and the shared leader sequence and 3' UTR sequences of the sgRNAs, respectively. gRNA and sgRNA were detected only in SARS-CoV-2-infected HD monocytes (Fig. [4n](#),[o](#)). The most abundant amplified sgRNA fragment migrated on agarose gels at the size of the *N* sgRNA (1,560 nucleotides), and its identity was confirmed by sequencing.

Although multiple assays indicated monocytes begin viral replication, we next assessed whether infected monocytes produce infectious virus. Infectious SARS-CoV-2 is detected in plasma of patients with COVID-19 only with especially sensitive assays, and we did not detect infectious virus by plaque assay in plasma samples from nine patients with COVID-19. Although infected HD monocyte culture supernatants formed plaques in Vero cells when culture supernatants were collected immediately after infection (probably detecting input virus), no infectious virus was detected when culture supernatants were collected 48 h after infection (Fig. [4p](#)). By contrast, plaques were easily detected in culture supernatants from infected Vero cells collected at 48 h after infection. Thus, monocyte infection did not produce infectious virus.

Discussion

Here we show antibody-opsonized SARS-CoV-2 infects and replicates in blood monocytes and lung macrophages. About 10% of monocytes and 8% of lung macrophages in patients with COVID-19 were SARS-CoV-2-infected. We found a one-to-one correspondence between monocyte infection and inflammasome caspase-1 activation and pyroptosis. Most dying monocytes in the blood of patients with COVID-19 had activated inflammasomes, suggesting that monocytes are dying of pyroptosis. This is a large number, considering that dying cells are rapidly eliminated in vivo. It may be surprising that monocyte infection and cell death has not been widely recognized. However, this may be because (1) many COVID-19 studies use thawed, frozen cells, and dying cells do not survive freeze–thawing; (2) investigation of whether circulating mononuclear cells are dying is lacking in published studies; and (3) few researchers have looked for monocyte infection because monocytes do not express ACE2. A few previous studies have shown increased IL-1 cytokines in the plasma of

patients with COVID-19, in vitro SARS-CoV-2 entry in myeloid cells or NLRP3 inflammasome caspase-1 activation in blood cells of patients with COVID-19^{9,10,21,38}. However, no previous study showed that SARS-CoV-2 infection of monocytes is antibody mediated, identified the monocyte receptor, showed that viral replication does not produce infectious virions, identified monocyte infection as the cause of inflammasome activation or showed evidence of pyroptosis. However, two previous studies suggested that monocyte-derived macrophages can be abortively infected³⁸. In contrast to our findings, monocyte-derived macrophages weakly express ACE2 and their infection may be partly mediated by ACE2, as in vitro infection in the absence of anti-spike is blocked by anti-ACE2³⁸.

Fc γ R-mediated uptake of antibody-coated virus into monocytes is a double-edged sword. Pyroptosis, which occurs rapidly, probably aborts viral infection before infectious virions are fully assembled.

Monocyte/macrophage infection is a dead end for the virus—it removes virions from the extracellular milieu, blocks them from producing infectious progeny and prevents them from disseminating. Pyroptosis in infected monocytes/macrophages also sounds a potent immune alarm to recruit and activate innate and adaptive immune cells to infection sites to mobilize immune defence. By contrast, the inflammatory mediators released from pyroptotic monocytes and macrophages can cause a cytokine storm. It may not be a coincidence that clinical deterioration coincides temporally with the detection of SARS-CoV-2 antibody responses^{8,29,39}. In fact, some recent studies suggest that higher antibody titres correlate with disease severity^{29,39}.

Pyroptotic myeloid cells are probably a major cause of the serious inflammatory sequelae that lead to acute lung injury, multiorgan damage, vascular leak and respiratory distress in patients with severe disease. In particular, patients with severe COVID-19 had increased plasma biomarkers of pyroptosis compared with patients with mild or moderate COVID-19. However, neither antibody titres nor the proportion of infected ASC-speck-positive monocytes at presentation correlated with severe disease, perhaps because of the small number of samples. Larger cohorts are needed to better assess the relative importance of monocyte/macrophage pyroptosis in severe COVID-19 pathogenesis. The large numbers of infected monocytes and

macrophages, the fact that a quarter of lung macrophages have activated inflammasomes, and that myeloid cells are the major source of IL-1 and other inflammatory cytokines make it probable that monocyte/macrophage infection and inflammasome activation are important in severe COVID-19 pathogenesis. Although neutrophils could potentially be infected, infection of freshly isolated COVID-19 neutrophils or in vitro-infected HD neutrophils was not detected. Thus, neutrophil infection is probably not a major contributor to pathogenesis, although neutrophil activation of GSDMD-dependent NETosis (a cell death process involving neutrophil extracellular traps (NETs)) or other features of neutrophil activation may well be important drivers. It will be worthwhile to study other infected cells as potential sources of inflammation, and to understand what aspects of monocyte/macrophage activation enhance infection.

Four times as many lung-resident macrophages had activated inflammasomes as were infected. Further studies are needed to identify what stimulates inflammation in uninfected macrophages, but alarmins released by lung tissue damage are probably culprits. Although inflammasome activation was detected in almost every infected monocyte and macrophage, it was not detected in lung epithelial cells. Why lung epithelial cells resist inflammasome activation will require further study. It is worth examining whether infection might activate inflammasome-independent pyroptosis by other gasdermins in non-myeloid cells in the lungs. NLRP3 and AIM2 inflammasomes that recognize cell membrane damage and cytosolic DNA, respectively, formed in SARS-CoV-2-infected monocytes. Further work is needed to understand how SARS-CoV-2 activates these inflammasomes, whether activation is restricted to virulent coronaviruses, and whether other inflammasomes are activated, such as NLRP1 and NLRP6, which sense dsRNA^{40,41}.

In this study, blocking antibodies against two Fc γ Rs, CD16 and CD64, inhibited monocyte infection. CD64 is expressed on all monocytes, including the dominant classical subtype that is not infected, whereas CD16 is more selectively expressed, and all the infected patient monocytes are CD16 positive. This means that CD16 is probably the major Fc receptor that mediates viral entry into monocytes. Blocking infection by anti-CD64 antibodies may be indirect, as CD64 and CD16 use the same signalling adaptors and associate on the cell surface.

At diagnosis, plasma biomarkers of pyroptosis, including IL-1RA, IL-18, LDH and GSDMD, were increased in patients who developed severe disease—suggesting that they might help to predict prognosis—and who would benefit from immune-modulating therapy. Repurposing FDA-approved drugs that inhibit inflammatory cytokines or GSDMD is worth assessing but, so far, controlled clinical trials evaluating inhibiting inflammatory cytokines (anti-IL-1 β (canakinumab), anti-IL-1RA (anakinra), anti-IL-6 and anti-IL-6R) have shown at best weak protection, which may be due to suboptimal timing or because any cytokine is only one of many inflammatory mediators. Two FDA-approved inhibitors of GSDMD, disulfiram (antabuse)⁴² and dimethyl fumarate (tecfidera)⁴³ are currently being evaluated in clinical studies (NCT04485130, NCT04594343 and NCT04381936). In mouse models of sepsis, which has overlapping features with severe COVID-19 disease, these drugs strongly improved survival and reduced plasma IL-6 and TNF.

Our findings, which implicate opsonizing antibodies in monocyte infection and inflammasome activation, suggest that antibodies may contribute to deleterious immune reactions associated with severe disease⁴⁴. Fc γ R-mediated monocyte infection is an example of antibody-mediated enhancement of infection. Nonetheless, overwhelming evidence shows that vaccine-generated neutralizing antibodies prevent infection and improve the clinical outcome of breakthrough infections, suggesting that anti-spike antibodies are highly beneficial. Plasma from vaccinated individuals did not promote monocyte infection, indicating that antibody-mediated enhancement is not a concern with respect to vaccination. However, therapeutically administered anti-spike neutralizing monoclonal antibodies only improve the clinical outcome if given early, before hospitalization^{45,46}, and antibody-containing convalescent sera have not shown clinical benefit⁴⁷. Thus, it is worth considering whether some antibodies might have both protective and deleterious effects⁴⁸. Antibodies are clearly beneficial for blocking infection of ACE2-expressing lung and airway epithelia, in which the virus completes replication to produce infectious progeny. However, antibody properties that affect Fc-receptor-mediated cellular uptake, phagocytosis, cytotoxicity and complement activation can affect disease pathogenesis²⁸.

Early development of afucosylated anti-spike antibodies promotes alveolar macrophage inflammation and is associated with COVID-19 severity^{33,34,35}. Afucosylated antibodies are increased during acute infection with enveloped viruses like SARS-CoV-2 but are not abundant after COVID-19 vaccination⁴⁹ or other types of antigen exposure³⁴. IgG isolated from patients with COVID-19 with a higher proportion of afucosylated antibodies significantly, but weakly, increased in vitro monocyte infection but IgG from patients with fewer afucosylated antibodies did not. The increased pathogenicity of afucosylated antibodies could be secondary to antibody-mediated infection and downstream inflammasome activation in monocytes and macrophages. However, our findings about afucosylation are preliminary and more work is needed to make this association. Characterizing how antibody features, such as afucosylation, sialylation and choice of constant region, alter protective versus deleterious functions of anti-spike antibodies will be important not only for understanding SARS-CoV-2 pathogenesis, but also for choosing the best preparations of convalescent patient plasma and monoclonal antibodies for therapy and/or prevention of severe disease.

Methods

Human participants

Fresh PBMCs and plasma cohort

The study was approved by the Investigation Review Boards of Boston Children's Hospital and Massachusetts General Hospital (MGH), and all of the enrolled patients signed an informed consent. A total of 73 patients aged 18 years or older with clinical symptoms suggestive of COVID-19 infection were enrolled at the time of presentation to the MGH emergency department (ED) from 9 July 2020 to 15 October 2021. A 10-ml EDTA blood sample was transported to Boston Children's Hospital and processed within 2 h of collection. Samples from patients with COVID-19 were all RT-qPCR verified for SARS-CoV-2 infection on the day on which blood was drawn. Patients who presented to the ED with COVID-19-like symptoms, but were PCR negative, were used as non-COVID-19 samples. Patients who had

received SARS-CoV-2 vaccination before presentation were excluded from the study. A summary of demographic and clinical data is provided in Supplementary Table 1. HD samples were processed and analysed in parallel with the patient samples. The participants were enrolled from 9 July 2020 to 10 January 2021 at Boston Children's Hospital (BCH) with IRB-approved waiver of informed consent. Vaccinated HDs ($n = 6$), who received two doses of the Pfizer-BioNtech mRNA vaccine, were enrolled 3 weeks after the second dose and their plasma was pooled to evaluate whether it promoted monocyte infection.

Frozen plasma cohort

A total of 60 patients aged 18 years or older with clinical symptoms suggestive of COVID-19 infection were enrolled in the MGH ED from 15 March 2020 to 15 April 2020 with an IRB-approved waiver of informed consent. The enrolled patients had at least one of the following: (1) tachypnea, ≥ 22 breaths per minute; (2) oxygen saturation, $\leq 92\%$ on room air; (3) requirement for supplemental oxygen; and (4) positive-pressure ventilation. A 10-ml EDTA tube was obtained with the initial clinical blood draw in the ED ($n = 60$). Blood was also obtained on days 3 ($n = 42$) and 7 ($n = 35$) if the patient was hospitalized on those dates. Clinical course was followed for 28 days after enrolment or until hospital discharge if after 28 days. SARS-CoV-2-confirmed patients (by RT-qPCR) were assigned a maximum acuity score (A1–A5) (A1, died; A2, required mechanical ventilation; A3, hospitalized requiring supplemental oxygen; A4, hospitalized but not requiring supplemental oxygen; and A5, discharged and not requiring hospitalization)¹². Patients were grouped on the basis of their worst acuity score over 28 days and divided into three groups for comparison (A1 and A2, severe disease; A3, moderate disease; and A4 and A5, mild disease). Only 1 patient was in A4; most of the mild patients therefore represent those who were discharged immediately from the ED and therefore have only a day-0 sample. A summary of the demographic and clinical data for each outcome group is provided in Supplementary Table 2.

Lung tissue samples

Lung samples from five individuals who died from COVID-19 (Supplementary Table 3) and three individuals who died from trauma and without lung disease were obtained from MGH. The study was approved by the institutional review board of MGH IRB 2020P001147. Informed consent was obtained from the relatives of study participants. Lung tissue specimens were obtained within 24 h of autopsy and immediately formalin-fixed and embedded in paraffin.

Reagents and antibodies

A list of reagents and antibodies and their sources is provided in Supplementary Table 4.

Plasma, PBMC, neutrophil and monocyte isolation

Samples were processed using the recommended safety precautions in a BSL-2+ facility. Blood tubes were centrifuged at 2,000 rpm for 10 min to separate the plasma from blood cells. The plasma was collected in a new tube and incubated or not with 1% Triton X-100 for 1 h on ice before aliquoting and freezing at -80 °C. Blood cells were resuspended in PBS and layered over Ficoll for density centrifugation. PBMCs were collected from the interface and subjected to red blood cell lysis (if necessary) with Red Blood Cell Lysing Buffer Hybri-Max for 5 min on ice, followed by quenching with RPMI medium supplemented with 10% FBS and 1% penicillin-streptomycin. PBMCs were washed once more with RPMI and one fraction was stained for flow cytometry, while the remaining cells were used for monocyte purification by negative selection using the RosetteSep Human Monocyte Enrichment Cocktail. Neutrophils of patients with COVID-19 were isolated from the whole blood by immunomagnetic negative selection using the EasySep Direct Human Neutrophil Isolation Cocktail, according to the manufacturer's instructions. HD monocytes for in vitro infection were purified from PBMCs by positive selection with CD14⁺ magnetic beads. The red blood cell pellet from the Ficoll density centrifugation was used to isolate neutrophils from the same HD samples. Neutrophils were separated from the RBC pellet by hypotonic lysis.

Cell lines

The THP-1 monocytic cell line and Vero E6 cells were obtained from ATCC. A549 cells and HEK293T cells overexpressing *ACE2* were obtained from the MassCPR variants repository at Ragon Institute. *ACE2* expression was validated by RT-qPCR and anti-*ACE2* flow cytometry. All cells were tested for mycoplasma contamination.

Multiplex luminex, immunoassay and LDH activity assay

IL-1RA, IL-2, IL-4, IL-5, IL-6, IL-7, IL-10, IL-12, IL-13, IL-17, IL-18, IL-21, IL-23, CCL3, CCL7, CCL9, CXCL10, G-CSF, TNF, IFN β and IFN γ were measured in plasma samples using a custom Luminex assay (R&D Systems) according to the manufacturer's instructions. Sample data were acquired using the Luminex xPONENT 4.2 for MAGPIX Analyzer at the Analytical Instrumentation Core Lab of Boston University and analysed with Milliplex Analyst v5. The plasma levels of IL-1 β were measured using the Simple Plex cartridge Ella (ProteinSimple) according to the manufacturer's instructions at the BCH. All of the samples were diluted 1:3 with the dilution buffer and the analytical performance was conducted on the ProteinSimple Ella automated immunoassay platform (Bio-Techne). The samples were acquired using the Simple Plex Runner v.3.7.2.0 software and analysed using Simple Plex Explorer 3.7.2.0. GSDMD was measured in the same samples using the Human GSDMD ELISA kit (MyBiosource) according to the manufacturer's instructions and LDH activity was measured using the CytoTox 96 Non-Radioactive Cytotoxicity Assay (Promega). Results from the latter assays were analysed using the Biotek Synergy 2 analyzer; GSDMD absorbance was measured at 450 nm and LDH absorbance was measured at 490 nm. Absorbance levels were quantified by linear regression based on the standard curve.

Anti-spike RBD ELISA

The enzyme-linked immunosorbent assay (ELISA) anti-spike RBD kit (BioLegend) was used to quantify antigen-specific IgG in the plasma from HDs, non-COVID-19 patients and patients with COVID-19. ELISA was performed according to the manufacturer's instructions. Anti-spike RBD absorbance was measured at 450 nm and 570 nm and quantified by linear regression based on the standard curve.

Intracellular staining for imaging flow cytometry and confocal microscopy

Fixed monocytes were permeabilized with 0.1% Triton X-100 for 10 min and washed twice with PBS + 3% FBS. Monocytes were then blocked for 30 min with PBS + 5% FBS, washed twice and then stained with unconjugated primary antibodies against ASC (1:200, mouse or rabbit), NLRP3 (1:200, goat), AIM2 (1:200, mouse), GSDMD (1:200, mouse), pyrin (1:200, rabbit), dsRNA (J2, mouse) (1:500) or SARS-CoV-2 nucleocapsid protein (1:500, rabbit) for 2 h, followed by three washes with PBS + 3% FBS. The cells were then stained with secondary antibodies (donkey anti-mouse, rabbit or goat conjugated with Alexa Fluor 488, 546 or 647, at 1:1,000) for 1 h in PBS + 3% FBS, followed by three washes. Untreated THP-1 cells, THP-1 cells treated with LPS + nigericin or transfected with Poly(dA:dT) using Lipofectamine 2000, and HEK293T cells (negative control) were stained with anti-NLRP3 and anti-AIM2 antibodies for antibody validation.

For microscopy analysis, cells were fixed and then stained with DAPI (1:1,000) for 10 min, washed three times and cytospun onto glass slides (VWR), and sealed using polyvinyl alcohol and 1.5 mm coverslips (VWR). Confocal images were acquired using the Zeiss LSM 800 system with 405-nm, 488-nm, 561-nm and 633-nm lasers (emission filters, 465 nm, 509 nm, 561 nm and 668 nm, respectively) and a $\times 40$ or $\times 63$ 1.4 NA oil-immersion objective. Images were acquired using Zen Black 2.0 and processed using Zen Blue 3.2.

For imaging flow cytometry, cells were resuspended in PBS + 3% FBS for analysis. Data were acquired using the ImageStream X MKII system with $\times 60$ magnification (Amnis), the INSPIRE v.2 acquisition software and were analysed using IDEAS v.6.2 (Amnis). Monocytes were gated based on area/aspect ratio. ASC, NLRP3, AIM2 and pyrin specks were gated and quantified on the basis of fluorophore intensity/maximum pixels.

Flow cytometry

PBMCs were washed and stained for viability with Zombie Yellow in PBS (1:200) for 15 min on ice. Cells were washed with PBS, centrifuged and then stained with anti-annexin V PE (1:200) antibodies in 1× annexin buffer for 15 min on ice. After washing with 1× annexin V buffer, cells were blocked for 10 min with anti-CD32 (1:100) in PBS + 3% FBS, and then stained for 15 min on ice with a cocktail of antibodies to identify lymphocyte and myeloid cell subsets (all 1:200 except CD19 BV650, CD123 PerCP-Cy5.5 and CD56 APC-Cy7, 1:100). Purified monocytes and an A549 cell line overexpressing *ACE2* were blocked with anti-CD32, then stained with primary antibodies for ACE2 (1:100) for 15 min on ice. The secondary anti-goat AF488 antibody was co-incubated with anti-CD14 PE-Cy7 (1:200) and anti-CD147 APC (1:100) antibodies. After the last wash, cells were resuspended in 2% PFA and kept at 4 °C until flow cytometry analysis. In vitro-infected monocytes were fixed and permeabilized with 0.1% Triton X-100, then blocked with PBS + 5% FBS. Cells were stained with primary antibodies for dsRNA (J2, mouse) (1:500), then stained with secondary antibodies (donkey anti-mouse conjugated with Alexa Fluor 647, at 1:500) and anti-CD14 PE-Cy7 antibodies. Cells were acquired using the FACS Canto II or LSR II using the FACSDiva v7 acquisition software, and data were analysed using FlowJo v.10.7.1.

FLICA assay

Freshly isolated monocytes were washed and resuspended in RPMI 10% FBS with FLICA substrate (BioRad FAM-FLICA Caspase-1 kit) and cultured for 1 h at 37 °C. Cells were then washed twice with 1× apoptosis buffer (from the kit) and fixed with 1× fixative (from the kit). Cells were kept at 4 °C until further staining and analysis.

Immunoblot analysis

Lysates of enriched monocytes from HDs and patients with COVID-19, the former treated or not for 16 h at 37 °C with 100 ng ml⁻¹ LPS and 20 µM nigericin, were resolved on 12% SDS-PAGE gels, transferred to nitrocellulose membranes and blotted to detect GSDMD using (Abcam ab210070) primary rabbit monoclonal antibodies and secondary anti-rabbit IgG. The membranes were also blotted for β-actin and COX-IV.

Immunofluorescence analysis of lung samples

Formalin-fixed and paraffin-embedded lung parenchymal samples were stained for SARS-CoV-2 N, ASC and CD14, and immunofluorescence was analysed on the Leica Bond RX automated staining platform using the Leica Biosystems Refine Detection Kit (Leica). The antibody for SARS nucleocapsid (Novus) was run with citrate antigen retrieval and tagged with Alexa Fluor 488 Tyramide (Life). After citrate stripping, the antibody for CD14 (Cell Signaling) was incubated and tagged with Alexa Fluor 594 Tyramide (Life). After EDTA stripping, staining for ASC (Santa Cruz) was analysed using antibodies tagged with Alexa Fluor 647 Tyramide (Life). EDTA stripping was performed before anti-CD31 or anti-E-cadherin staining tagged to Alexa Fluor 555 Tyramide (Life). The samples were counterstained with DAPI. The slides were scanned using the Aperio Versa Digital Pathology Scanner (Leica) and analysed using Aperio ImageScope v.12.4.3 (Leica). The slides were also analysed by confocal microscopy as described above.

In vitro SARS-CoV-2 infection

icSARS-CoV-2-mNG (a molecular clone of SARS-CoV-2 expressing Neon Green (NG) fluorescent protein) was a gift to A.E.G. from S. P. Yong and the World Reference Center for Emerging Viruses and Arboviruses)³¹. The NG fusion protein is expressed only during viral replication. The SARS CoV-2 US-WA1/2020 ancestral (WA) variant was obtained from BEI Resources. The B.1.617.1/Delta variant isolate was obtained from the MassCPR variant repository. In brief, the variant was isolated at the Ragon BSL3 by rescue on Vero-E6 cells from primary clinical specimens. The whole genome of subsequent viral stocks was sequenced to confirm that no additional mutation arose during virus expansion. HD monocytes/neutrophils were purified from apheresis leukoreduction collars collected at Brigham and Women's Hospital. Monocytes were incubated overnight with medium or 100 ng ml⁻¹ LPS, and then infected with icSARS-CoV-2-mNG, SARS-CoV-2 (WA) and SARS CoV-2 B.1.617.1/Delta (multiplicity of infection (MOI) = 1) in a BSL-3 facility. Infection of A549-ACE2 cells at an MOI of 0.01 was used as a control. The viral inoculum was treated with 10 µg ml⁻¹ of antibody (isotype control mAb114, anti-spike

C1A-H12, or anti-spike C1A-B12), or 5% pooled plasma (heat-inactivated or not; Ig-depleted or not, as indicated) from HDs ($n = 3$), patients with COVID-19 of mixed disease severity ($n = 12$ (total), $n = 4$ (mild), $n = 4$ (moderate), $n = 4$ (severe)) or vaccinated HDs ($n = 6$) before infection with SARS-CoV-2 for 30 min at room temperature. Treated virus (100 μ l) was added to monocytes (2×10^6 cells per well) in 48-well plates. Infected cells were incubated at 37 °C under 5% CO₂ with gentle shaking every 10 min for 1 h, after which the culture volume was increased to 500 μ l with RPMI supplemented with 5% heat-inactivated normal AB human serum and 10 μ g ml⁻¹ of the aforementioned antibodies, or 5% pooled plasma from HDs or patients with COVID-19. Cultures were then incubated at 37 °C under 5% CO₂ for 48 h, at which time the cells were collected and fixed for 20 min with 4% PFA and then stained.

IgG from the pooled plasma of patients with COVID-19 was depleted by protein A/G agarose resin and IgA depleted by peptide M agarose. Control samples were incubated with agarose resin without coupled protein. C1A-B12 and C1A-H12, two SARS-CoV-2 spike-targeting human monoclonal antibodies, were produced as previously described³². For blocking experiments, cells were incubated with 10 μ g ml⁻¹ monoclonal antibodies, anti-CD16, anti-CD32 (clone IV.3 (Fig. 4j and Extended Data Fig. 5a), clone 6C4 (Fig. 4k and Extended Data Fig. 5b,c)), anti-CD64, anti-ACE2 and anti-CD147 for 30 min, before virus infection. For antiviral drug treatment, monocytes were incubated at 37 °C under 5% CO₂ for 1 h with 10 μ M remdesivir (GS-5734) or camostat mesylate before infection. To find an appropriate remdesivir concentration, serial dilutions between 10 and 80 μ M were analysed. To compare plasma obtained from patients with different disease severity, plasma was pooled on the basis of the MGH acuity score (A1–A5), as described above.

To test the role of IgG afucosylation, IgG purified from serum samples of patients with COVID-19 was analysed by mass spectrometry to define the percentage of afucosylation as described previously³³. Low afucosylated samples, provided by T. Wang, contained $8.4 \pm 0.7\%$ afucosylated IgG and high afucosylated samples, $30.1 \pm 1.5\%$ afucosylated IgG. IgG was also purified from pooled plasma from HDs and patients with COVID-19 using the Melon gel IgG Spin Purification Kit (Thermo Fisher Scientific)

according to the manufacturer's instructions. Virus was preincubated with $10 \mu\text{g ml}^{-1}$ of purified IgG and the infection was performed as described above.

RT-qPCR

RNA was extracted using Trizol reagent (Invitrogen) from monocytes of patients with COVID-19 or from uninfected or infected HD monocytes (stimulated or not with LPS (100 ng ml^{-1} for 16 h)), then reverse-transcribed using the High-Capacity cDNA Reverse Transcription Kit (Applied Biosystems). Random primers were used to generate cDNA for detection of cellular RNAs (*ACE2*, *BSG* and *ACTB*) and SARS-CoV-2-specific primers were used to generate cDNA to detect viral genomic RNAs (N1 region of *N* gene)⁵⁰. cDNA was analysed by RT-qPCR using the SsoFast EvaGreen Supermix (BioRad) (30 s at 95°C ; then 40 cycles of 3 s at 95°C and 3 s at 54°C) in the CFX96 Touch Real-Time PCR Detection System (BioRad) using the CFX Manager v.1.6 acquisition/analysis software. To detect SARS-CoV-2 sgRNA, RT-qPCR was performed using a primer pair with the forward primer annealing to the 5' leader region of the viral genome and the reverse primer annealing to the 3' UTR. With the cycling conditions used (30 s at 95°C ; then 40 cycles of 30 s at 95°C , 30 s at 60°C and 90 s at 72°C), full-length gRNA was not amplified, but small sgRNA segments (<3 kb) could be amplified^{16,51,52}. For each sample, C_t values were normalized to the *ACTB* C_t value. Primer sequences are provided in Supplementary Table 4. sgRNA qPCR products were also analysed by electrophoresis on 1% agarose gels stained with ethidium bromide and visualized on the Chemidoc imager (BioRad). The approximately 1,600 nucleotide band was excised and sequenced to confirm its origin as the SARS-CoV-2 sgRNA encoding *N*.

Plaque assays

Vero E6 cells were seeded as monolayers in 24-well plates 1 day before infection. Virus-infected sample culture supernatants were serially diluted in DMEM. The plates were washed once with DPBS and then infected with $100 \mu\text{l}$ of diluted sample and incubated at 37°C under 5% CO_2 for 1 h with

rocking every 15 min. After 1 h, the inoculum was removed and an overlay of 1% methylcellulose (Sigma-Aldrich) in complete MEM (Gibco) was applied to each well. The plates were incubated at 37 °C until plaques were observable in positive control wells. To visualize plaques, the overlay was removed, and the cell monolayer was fixed with 4% PFA and stained with crystal violet. Plaques were then counted to quantify the virus titre in PFU per ml.

Statistical analysis

Statistical analysis was performed using GraphPad Prism v.9.0. Normal distribution of the data was evaluated using the D'Agostino and Pearson normality test before applying statistical methods. Distributions were considered to be normal if $P \leq 0.05$. Parametric or nonparametric (Mann–Whitney *U*-test) two-tailed unpaired *t*-tests were used to compare two unpaired groups. Multiple-group comparisons were analysed using one-way ANOVA with Sidak or Tukey multiple-comparisons tests, or nonparametric Kruskal–Wallis with Dunn post-test. Multiple groups were compared using two-way ANOVA with additional Sidak or Tukey multiple-comparisons test. Mean plasma values from hospitalized patients with COVID-19 on each day were compared between severity groups by multiple unpaired *t*-tests. Correlations of plasma levels were determined by simple linear regression and Pearson correlation coefficient.

Reporting summary

Further information on research design is available in the [Nature Research Reporting Summary](#) linked to this paper.

Data availability

The data and materials supporting the findings of this study are available from the corresponding authors on request.

References

1. Hu, B., Guo, H., Zhou, P. & Shi, Z. L. Characteristics of SARS-CoV-2 and COVID-19. *Nat. Rev. Microbiol.* **19**, 141–154 (2021).
2. Del Valle, D. M. et al. An inflammatory cytokine signature predicts COVID-19 severity and survival. *Nat. Med.* **26**, 1636–1643 (2020).
3. Liu, X., Xia, S., Zhang, Z., Wu, H. & Lieberman, J. Channelling inflammation: gasdermins in physiology and disease. *Nat. Rev. Drug Discov.* **20**, 384–405 (2021).
4. Akbar, A. N. & Gilroy, D. W. Aging immunity may exacerbate COVID-19. *Science* **369**, 256–257 (2020).
5. Dinarello, C. A. Interleukin-1 in the pathogenesis and treatment of inflammatory diseases. *Blood* **117**, 3720–3732 (2011).
6. Wu, C. et al. Risk factors associated with acute respiratory distress syndrome and death in patients with coronavirus disease 2019 pneumonia in Wuhan, China. *JAMA Intern. Med.* **180**, 934–943 (2020).
7. Vora, S. M., Lieberman, J. & Wu, H. Inflammasome activation at the crux of severe COVID-19. *Nat. Rev. Immunol.* **21**, 694–703 (2021).
8. Long, Q. X. et al. Antibody responses to SARS-CoV-2 in patients with COVID-19. *Nat. Med.* **26**, 845–848 (2020).
9. Hadjadj, J. et al. Impaired type I interferon activity and inflammatory responses in severe COVID-19 patients. *Science* **369**, 718–724 (2020).
10. Rodrigues, T. S. et al. Inflammasomes are activated in response to SARS-CoV-2 infection and are associated with COVID-19 severity in patients. *J. Exp. Med.* **218**, e20201707 (2021).
11. Chan, A. H. & Schroder, K. Inflammasome signaling and regulation of interleukin-1 family cytokines. *J. Exp. Med.* **217**, e20190314 (2020).
12. Filbin, M. R. et al. Longitudinal proteomic analysis of severe COVID-19 reveals survival-associated signatures, tissue-specific cell death, and cell-cell interactions. *Cell Rep. Med.* **2**, 100287 (2021).

13. Pan, P. et al. SARS-CoV-2 N protein promotes NLRP3 inflammasome activation to induce hyperinflammation. *Nat. Commun.* **12**, 4664 (2021).
14. Sharma, D. & Kanneganti, T. D. The cell biology of inflammasomes: mechanisms of inflammasome activation and regulation. *J. Cell Biol.* **213**, 617–629 (2016).
15. Fung, S.-Y., Yuen, K.-S., Ye, Z.-W., Chan, C.-P. & Jin, D.-Y. A tug-of-war between severe acute respiratory syndrome coronavirus 2 and host antiviral defence: lessons from other pathogenic viruses. *Emerg. Microbes Infect.* **9**, 558–570 (2020).
16. Irving, A. T., Ahn, M., Goh, G., Anderson, D. E. & Wang, L. F. Lessons from the host defences of bats, a unique viral reservoir. *Nature* **589**, 363–370 (2021).
17. Davis, M. A. et al. Calpain drives pyroptotic vimentin cleavage, intermediate filament loss, and cell rupture that mediates immunostimulation. *Proc. Natl Acad. Sci. USA* **116**, 5061–5070 (2019).
18. Spel, L. & Martinon, F. Detection of viruses by inflammasomes. *Curr. Opinion Virol.* **46**, 59–64 (2021).
19. Rogers, C. et al. Gasdermin pores permeabilize mitochondria to augment caspase-3 activation during apoptosis and inflammasome activation. *Nat. Commun.* **10**, 1689 (2019).
20. Swanson, K. V. et al. A noncanonical function of cGAMP in inflammasome priming and activation. *J. Exp. Med.* **214**, 3611–3626 (2017).
21. Zheng, J. et al. Severe acute respiratory syndrome coronavirus 2-induced immune activation and death of monocyte-derived human macrophages and dendritic cells. *J. Infect. Dis.* **223**, 785–795 (2021).
22. Song, X. et al. Little to no expression of angiotensin-converting enzyme-2 on most human peripheral blood immune cells but highly

expressed on tissue macrophages. *Cytometry A*, <https://doi.org/10.1002/cyto.a.24285> (2020).

23. Ragotte, R. J. et al. Human basigin (CD147) does not directly interact with SARS-CoV-2 spike glycoprotein. *mSphere* **6**, e0064721 (2021).
24. Shilts, J., Crozier, T. W. M., Greenwood, E. J. D., Lehner, P. J. & Wright, G. J. No evidence for basigin/CD147 as a direct SARS-CoV-2 spike binding receptor. *Sci. Rep.* **11**, 413 (2021).
25. Wang, K. et al. CD147-spike protein is a novel route for SARS-CoV-2 infection to host cells. *Signal Transduct. Target. Ther.* **5**, 283 (2020).
26. Bruhns, P. & Jonsson, F. Mouse and human FcR effector functions. *Immunol. Rev.* **268**, 25–51 (2015).
27. Ong, S.-M. et al. A novel, five-marker alternative to CD16–CD14 gating to identify the three human monocyte subsets. *Front. Immunol.* **10**, 1761 (2019).
28. Bournazos, S., Gupta, A. & Ravetch, J. V. The role of IgG Fc receptors in antibody-dependent enhancement. *Nat. Rev. Immunol.* **20**, 633–643 (2020).
29. Li, K. et al. Dynamic changes in anti-SARS-CoV-2 antibodies during SARS-CoV-2 infection and recovery from COVID-19. *Nat. Commun.* **11**, 6044 (2020).
30. Weber, F., Wagner, V., Rasmussen, S. B., Hartmann, R. & Paludan, S. R. Double-stranded RNA is produced by positive-strand RNA viruses and DNA viruses but not in detectable amounts by negative-strand RNA viruses. *J. Virol.* **80**, 5059–5064 (2006).
31. Xie, X. et al. An infectious cDNA clone of SARS-CoV-2. *Cell Host Microbe* **27**, 841–848 (2020).
32. Clark, S. A. et al. Molecular basis for a germline-biased neutralizing antibody response to SARS-CoV-2. Preprint at *bioRxiv* <https://doi.org/10.1101/2020.11.13.381533> (2020).

33. Chakraborty, S. et al. Proinflammatory IgG Fc structures in patients with severe COVID-19. *Nat. Immunol.* **22**, 67–73 (2021).
34. Larsen, M. D. et al. Afucosylated IgG characterizes enveloped viral responses and correlates with COVID-19 severity. *Science* **371**, eabc8378 (2021).
35. Hoepel, W. et al. High titers and low fucosylation of early human anti-SARS-CoV-2 IgG promote inflammation by alveolar macrophages. *Sci. Transl. Med.* **13**, eabf8654 (2021).
36. Ackermann, M. et al. Patients with COVID-19: in the dark-NETs of neutrophils. *Cell Death Differ.* **28**, 3125–3139 (2021).
37. Hoffmann, M. et al. SARS-CoV-2 cell entry depends on ACE2 and TMPRSS2 and is blocked by a clinically proven protease inhibitor. *Cell* **181**, 271–280 (2020).
38. Hui, K. P. Y. et al. Tropism, replication competence, and innate immune responses of the coronavirus SARS-CoV-2 in human respiratory tract and conjunctiva: an analysis in ex-vivo and in-vitro cultures. *Lancet Respir. Med.* **8**, 687–695 (2020).
39. Garcia-Beltran, W. F. et al. COVID-19-neutralizing antibodies predict disease severity and survival. *Cell* **184**, 476–488 (2021).
40. Shen, C. et al. Phase separation drives RNA virus-induced activation of the NLRP6 inflammasome. *Cell* **184**, 5759–5774 (2021).
41. Bauernfried, S., Scherr, M. J., Pichlmair, A., Duderstadt, K. E. & Hornung, V. Human NLRP1 is a sensor for double-stranded RNA. *Science* **371**, eabd0811 (2021).
42. Hu, J. J. et al. FDA-approved disulfiram inhibits pyroptosis by blocking gasdermin D pore formation. *Nat. Immunol.* **21**, 736–745 (2020).
43. Humphries, F. et al. Succination inactivates gasdermin D and blocks pyroptosis. *Science* **369**, 1633–1637 (2020).

44. Iwasaki, A. & Yang, Y. The potential danger of suboptimal antibody responses in COVID-19. *Nat. Rev. Immunol.* **20**, 339–341 (2020).
45. Weinreich, D. M. et al. REGN-COV2, a neutralizing antibody cocktail, in outpatients with COVID-19. *N. Engl. J. Med.* **384**, 238–251 (2021).
46. Gupta, A. et al. Early treatment for COVID-19 with SARS-CoV-2 neutralizing antibody sotrovimab. *N. Engl. J. Med.* **385**, 1941–1950 (2021).
47. Korley, F. K. et al. Early convalescent plasma for high-risk outpatients with COVID-19. *N. Engl. J. Med.* **385**, 1951–1960 (2021).
48. Zhou, Y. et al. Enhancement versus neutralization by SARS-CoV-2 antibodies from a convalescent donor associates with distinct epitopes on the RBD. *Cell Rep.* **34**, 108699 (2021).
49. Chakraborty, S. et al. Early non-neutralizing, afucosylated antibody responses are associated with COVID-19 severity. *Sci. Transl. Med.* **14**, eabm7853 (2022).
50. Division of Viral Diseases, NCIRD. *2019-Novel Coronavirus (2019-nCoV) Real-Time rRT-PCR Panel Primer and Probes*, <https://www.cdc.gov/coronavirus/2019-ncov/lab/rt-pcr-panel-primer-probes.html> (CDC, 2020).
51. Kim, D. et al. The architecture of SARS-CoV-2 transcriptome. *Cell* **181**, 914–921 (2020).
52. Perera, R. et al. SARS-CoV-2 virus culture and subgenomic RNA for respiratory specimens from patients with mild coronavirus disease. *Emerg. Infect. Dis.* **26**, 2701–2704 (2020).

Acknowledgements

We thank members of the MGH COVID-19 collection and the processing team (K. Lavin-Parsons, B. Lilley, C. Lodenstein, B. McKaig, N. Charland, H. Khanna, A. Gonye, I. Gushterova, T. Lasalle, N. Sharma, B. C. Russo, M.

Rojas-Lopez, M. Sade-Feldman, K. Manakongtreeecheep, J. Tantivit and M. Fisher Thomas) for plasma samples; T. Wang for providing the high and low afucosylated IgGs from donors with COVID-19; the members of the Analytical Instrumentation Core Lab of Boston University for running and analysing the Luminex Multiplex assay; D. Briscoe and L. Sheward for analysing IL-1 β ; the staff at the Specialized Histopathology Core of the Dana-Farber/Harvard Cancer Center (supported in part by an NIH P30CA06516) for histology and immunohistochemistry; the staff at the MassCPR variants repository (funded by the Massachusetts Consortium on Pathogen Readiness) for providing viral strains and ACE2-overexpressing cell lines; and the staff at the Ragon Institute BSL3 laboratory (funded by the Harvard Center for AIDS Research (NIH P30AI060354)) and the Massachusetts Consortium on Pathogen Readiness. This research was supported by the Lemann Brazil Research Fund (to J.L. and C.J.); the National Institutes of Health grant R01AI124491 (to H.W.); the National Institutes of Health grant U19AI131135 (to L.G.); the Annenberg Foundation and FAST grants and a gift from J. Sullivan (to A.E.G.); the American Lung Association (to M.B.G. and M.R.F.); the British Heart Foundation Programme grant RG/16/4/32218 (to S.B.); a Conselho Nacional de Desenvolvimento Científico e Tecnológico (CNPq) fellowship (to C.J.); a Coordenação de Aperfeiçoamento de Pessoal de Nível Superior (CAPES) fellowship (to L.B.d.L.); and the National Institutes of Health training grant T32AI007245-31A1 (to M.L.).

Author information

Author notes

1. These authors contributed equally: Caroline Junqueira, Ângela Crespo, Shahin Ranjbar

Authors and Affiliations

1. Program in Cellular and Molecular Medicine, Boston Children's Hospital, Boston, MA, USA

Caroline Junqueira, Ângela Crespo, Shahin Ranjbar, Luna B. de Lacerda, Mercedes Lewandrowski, Jacob Ingber, Sagi Ravid, Marie Rose Schrimpf, Felicia Ho, Setu M. Vora, Hao Wu, Anne E. Goldfeld & Judy Lieberman

2. Department of Pediatrics, Harvard Medical School, Boston, MA, USA

Caroline Junqueira, Ângela Crespo, Luna B. de Lacerda, Mercedes Lewandrowski, Jacob Ingber, Sagi Ravid, Marie Rose Schrimpf, Felicia Ho, Lauren A. Henderson, Erin Janssen, Hao Wu & Judy Lieberman

3. Instituto René Rachou, Fundação Oswaldo Cruz, Belo Horizonte, Brazil

Caroline Junqueira & Luna B. de Lacerda

4. Department of Medicine, Harvard Medical School, Boston, MA, USA

Shahin Ranjbar & Anne E. Goldfeld

5. Emergency Medicine, Institute for Patient Care, Massachusetts General Hospital, Boston, MA, USA

Blair Parry, Caroline Beakes, Justin Margolin, Nicole Russell, Kyle Kays & Michael R. Filbin

6. Department of Microbiology, Blavatnik Institute, Harvard Medical School, Boston, MA, USA

Sarah Clark, Lee Gehrke, Jonathan Abraham & Marcia B. Goldberg

7. Ragon Institute, Massachusetts General Hospital, Massachusetts Institute of Technology, Harvard Medical School, Cambridge, MA, USA

Julie Boucau, Upasana Das Adhikari & Douglas Kwon

8. Department of Biological Chemistry and Molecular Pharmacology, Harvard Medical School, Boston, MA, USA

Setu M. Vora

9. Institute for Medical Engineering and Science, Massachusetts Institute of Technology, Cambridge, MA, USA

Valerie Leger, Lee Gehrke & Hao Wu

10. Division of Immunology, Boston Children's Hospital, Boston, MA, USA

Lauren A. Henderson & Erin Janssen

11. cBio Center, Dana-Farber Cancer Institute and Department of Cell Biology, Harvard Medical School, Boston, MA, USA

Chris Sander

12. Center for Bacterial Pathogenesis, Department of Medicine, Division of Infectious Diseases, Massachusetts General Hospital, Boston, MA, USA

Marcia B. Goldberg

13. Institute for Liver and Digestive Health, University College London, London, UK

Gautam Mehta

14. Institute of Hepatology, Foundation for Liver Research, London, UK

Gautam Mehta

15. Department of Clinical Neurosciences, University of Cambridge, Cambridge, UK

Steven Bell

Contributions

All of the authors contributed to preparing the manuscript. Conceptualization: J.L., C.J., A.C. and H.W. Experimentation: C.J., A.C., S. Ranjbar, L.B.d.L., M.L., J.I., S. Ravid, F.H., M.R.S., J.B., S.H., S.M.V., L.A.H., E.J., V.L., B.P., G.M. and S.B. Patient recruitment: C.B., J.M., N.R., U.D.A., D.K., M.R.F., M.B.G. and K.K. Data analysis: C.J., A.C., J.I., S.B. and C.S. Reagents: S.C. and J.A. Supervision: J.L., C.J., A.C., L.G. and A.E.G. Manuscript writing: C.J., A.C., J.I. and J.L.

Corresponding authors

Correspondence to [Caroline Junqueira](#), [Michael R. Filbin](#) or [Judy Lieberman](#).

Ethics declarations

Competing interests

The authors declare no competing interests.

Peer review

Peer review information

Nature thanks Stanley Perlman, Gestur Vidarsson and the other, anonymous, reviewer(s) for their contribution to the peer review of this work.

Additional information

Publisher's note Springer Nature remains neutral with regard to jurisdictional claims in published maps and institutional affiliations.

Extended data figures and tables

[Extended Data Fig. 1 Identification of lymphocyte and monocyte subsets in healthy donors and COVID-19 patients.](#)

Flow cytometry gating strategy for identifying lymphocytes and monocytes in Fig. [1a](#),[b](#) (**a**) and for identifying monocyte subpopulations in Fig. [1c](#) (**b**). Monocyte subpopulations: CL - classical CD14^{hi}CD16⁻; ITM - intermediate CD14^{hi}CD16⁺; NCL - non-classical CD14^{lo}CD16⁺.

Extended Data Fig. 2 Inflammasome imaging and GSDMD cleavage analysis.

a, Gating strategy for imaging flow cytometry analysis of isolated monocytes. **b**, Representative imaging flow cytometry images of GSDMD and ASC staining in COVID-19 patient monocytes that lacked ASC specks. **c, d**, Representative imaging flow cytometry images of HEK293T cells (negative control) and THP-1 cells untreated or treated with LPS+nigericin or transfected with poly(dA:dT), then stained with anti-NLRP3 (**c**) and anti-AIM2 (**d**). **e**, Single staining controls for antibody staining. Representative images of monocytes from COVID-19 patients shown were stained with 1° ASC - 2° AF488; 1° NLRP3 - 2° AF568; 1° GSDMD, Pyrin, AIM2, J2, N - 2° AF647; or FAM FLICA Caspase-1 fluorescence, and Zombie Yellow dye. FLICA⁺ and Zombie⁺ cells in cells undergoing pyroptosis; GSDMD, Pyrin, AIM2 and NLRP3 in non-pyroptotic cells (diffuse staining); J2⁺ and N⁺ in infected monocytes. Scale bar, 7 μm (**b–e**). **f**, Representative confocal image z-stacks and plane projections of monocytes of HD and COVID-19 patients, stained for the same markers as in Figure [2](#). Scale bars, 5 μm. **g**, Full scan images for blots shown in Fig. [2g](#).

Extended Data Fig. 3 ACE2 and CD147 expression on circulating monocytes.

Purified blood monocytes from HD ($n = 3$), COVID-19 patients ($n = 4$) and A549-ACE2 ($n = 3$) were analysed by flow cytometry (**a, c**) and RT-qPCR (**b, d**) for expression of ACE2 (**a, b**) or CD147 (*BSG*) (**c, d**). HD monocytes were treated or not with LPS before analysis. A549-ACE2 cells were used as positive control. Mean ± S.E.M. is shown. * $p < 0.05$, ** $p < 0.001$, *** $p < 0.0001$ relative to isotype (Iso) control antibody-stained, LPS-activated HD monocytes (**a,c**) by one-way ANOVA with Tukey's multiple comparisons test. Data are representative of 2 independent experiments.

Extended Data Fig. 4 Effect of anti-spike monoclonal antibodies or pooled COVID-19 plasma on in vitro infection of healthy donor purified monocytes with icSARS-CoV-2-mNG.

a–e, HD monocytes ($n = 3$) were primed with LPS, infected with icSARS-CoV-2-mNG (MOI, 1), then stained 48 h later for nucleocapsid (N) or dsRNA (J2) and ASC and analysed by imaging flow cytometry. Before infection, virus was preincubated with indicated monoclonal antibodies (IgG1 isotype control mAb114 (Iso)), non-neutralizing anti-spike (C1A-H12 (H12)) or neutralizing anti-RBD (C1A-B12 (B12)) or with pooled HD or COVID-19 patient plasma that had been heat-inactivated (HI) or not. U, uninfected. Quantification of HD monocyte staining for N (**a**), J2 (**b**), NG (**c**, **e**) or ASC specks (**d**). (**e**) Shows the percentage of N^+ cells that were also NG fluorescent. **f**, **g**, A5490-ACE2 ($n = 3$) (**f**) or LPS-primed HD monocytes ($n = 3$) (**g**) were infected at the indicated MOI with icSARS-CoV-2-mNG (NG), a molecular clone of the Washington (WA) strain, or with clinical WA and Delta strains. Infection was measured by N staining and flow cytometry. Mean \pm S.E.M. is shown. * $p < 0.05$, ** $p < 0.01$, *** $p < 0.001$, **** $p < 0.0001$ by one-way ANOVA with Tukey's multiple comparisons test, relative to Iso or as indicated (**a–g**). Data are representative of 2 independent experiments.

Extended Data Fig. 5 In vitro infection of healthy donor monocytes and neutrophils.

a–c, LPS-primed HD monocytes ($n = 3$) (**a**, **b**) or purified HD neutrophils ($n = 3$) (**c**) were infected with icSARS-CoV-2-mNG (MOI, 1), then stained 48 h later for nucleocapsid (N) or analysed for NG fluorescence (**c**, right). Before infection, virus was preincubated with COVID-19 plasma, depleted or not of IgG as indicated, and infection was carried out in the presence of indicated blocking or isotype (Iso) control antibodies (**a–c**). The monocyte and neutrophil infections in (**b**) and (**c**) were performed with cells isolated from the same HDs. **d**, Freshly isolated neutrophils, enriched by negative selection, from HD ($n = 3$) and COVID-19 patients of mixed disease severity ($n = 4$) were stained for N and analysed by flow cytometry to assess in vivo infection. **e**, Infection of LPS-primed HD monocytes ($n = 3$) with icSARS-CoV-2-mNG in the presence of pooled COVID-19 patient plasma, depleted or not of IgG as indicated, and antiviral drugs, Camostat and Remdesivir. **f**,

Infection of A549-ACE2 ($n = 3$) with icSARS-CoV-2-mNG to verify the inhibitory activity of 10 μ M Remdesivir. Infection was measured by N staining and flow cytometry. **g**, Infection of A549-ACE2 ($n = 3$) and HD monocytes ($n = 3$) with icSARS-CoV-2-mNG in the presence of anti-ACE2 blocking antibody at different concentrations. Infection was measured by NG fluorescence. Mean \pm S.E.M. is shown. * $p < 0.05$, ** $p < 0.01$, *** $p < 0.001$, by one-way ANOVA with Tukey's multiple comparisons test (**a–c, g**), nonparametric unpaired *t*-test (**d, f**) and two-tailed nonparametric unpaired multiple *t*-test (**e**). Data are representative of 2 replicate experiments.

Supplementary information

Reporting Summary

Supplementary Table 1

Demographic and clinical information of the fresh PBMCs and plasma cohort. Age, race and ethnicity, body mass index, co-morbidities, symptoms, MGH Acuity score, hospitalization details and clinical information of the patients in the fresh PBMCs and plasma cohort.

Supplementary Table 2

Demographic and clinical information of the frozen plasma cohort. Age, body mass index, co-morbidities, symptoms, MGH Acuity score, hospitalization details and clinical information of the patients in the frozen plasma cohort.

Supplementary Table 3

Clinical information of COVID-19 lung autopsies. Gender, age, onset of symptoms, date and time of death, autopsy date, comorbidity and clinical notes.

Supplementary Table 4

Reagents and materials used for this manuscript. Antibodies, chemicals and commercial kits (with sources and catalogue numbers) described in the Methods.

Rights and permissions

[Reprints and Permissions](#)

About this article

Cite this article

Junqueira, C., Crespo, A., Ranjbar, S. *et al.* Fc γ R-mediated SARS-CoV-2 infection of monocytes activates inflammation. *Nature* **606**, 576–584 (2022). <https://doi.org/10.1038/s41586-022-04702-4>

- Received: 22 January 2021
- Accepted: 29 March 2022
- Published: 06 April 2022
- Issue Date: 16 June 2022
- DOI: <https://doi.org/10.1038/s41586-022-04702-4>

Share this article

Anyone you share the following link with will be able to read this content:

[Get shareable link](#)

Sorry, a shareable link is not currently available for this article.

[Copy to clipboard](#)

Provided by the Springer Nature SharedIt content-sharing initiative

Further reading

- [What triggers severe COVID? Infected immune cells hold clues](#)

- Smriti Mallapaty

Nature (2022)

- [Immune response in COVID-19: what is next?](#)

- Qing Li
- Ying Wang
- Yufang Shi

Cell Death & Differentiation (2022)

This article was downloaded by **calibre** from <https://www.nature.com/articles/s41586-022-04702-4>

| [Section menu](#) | [Main menu](#) |

- Article
- [Published: 28 April 2022](#)

Inflammasome activation in infected macrophages drives COVID-19 pathology

- [Esen Sefik](#),
- [Rihao Qu](#),
- [Caroline Junqueira](#),
- [Eleanna Kaffe](#),
- [Haris Mirza](#),
- [Jun Zhao](#),
- [J. Richard Brewer](#),
- [Ailin Han](#),
- [Holly R. Steach](#),
- [Benjamin Israelow](#),
- [Holly N. Blackburn](#),
- [Sofia E. Velazquez](#),
- [Y. Grace Chen](#),
- [Stephanie Halene](#),
- [Akiko Iwasaki](#),
- [Eric Meffre](#),
- [Michel Nussenzweig](#),
- [Judy Lieberman](#),
- [Craig B. Wilen](#),
- [Yuval Kluger](#) &
- [Richard A. Flavell](#)

Nature volume **606**, pages 585–593 (2022)

- 22k Accesses

- 3 Citations
- 343 Altmetric
- [Metrics details](#)

Abstract

Severe COVID-19 is characterized by persistent lung inflammation, inflammatory cytokine production, viral RNA and a sustained interferon (IFN) response, all of which are recapitulated and required for pathology in the SARS-CoV-2-infected MISTRG6-hACE2 humanized mouse model of COVID-19, which has a human immune system^{[1,2,3,4,5,6,7,8,9,10,11,12,13,14,15,16,17,18,19,20](#)}. Blocking either viral replication with remdesivir^{[21,22,23](#)} or the downstream IFN-stimulated cascade with anti-IFNAR2 antibodies in vivo in the chronic stages of disease attenuates the overactive immune inflammatory response, especially inflammatory macrophages. Here we show that SARS-CoV-2 infection and replication in lung-resident human macrophages is a critical driver of disease. In response to infection mediated by CD16 and ACE2 receptors, human macrophages activate inflammasomes, release interleukin 1 (IL-1) and IL-18, and undergo pyroptosis, thereby contributing to the hyperinflammatory state of the lungs. Inflammasome activation and the accompanying inflammatory response are necessary for lung inflammation, as inhibition of the NLRP3 inflammasome pathway reverses chronic lung pathology. Notably, this blockade of inflammasome activation leads to the release of infectious virus by the infected macrophages. Thus, inflammasomes oppose host infection by SARS-CoV-2 through the production of inflammatory cytokines and suicide by pyroptosis to prevent a productive viral cycle.

Main

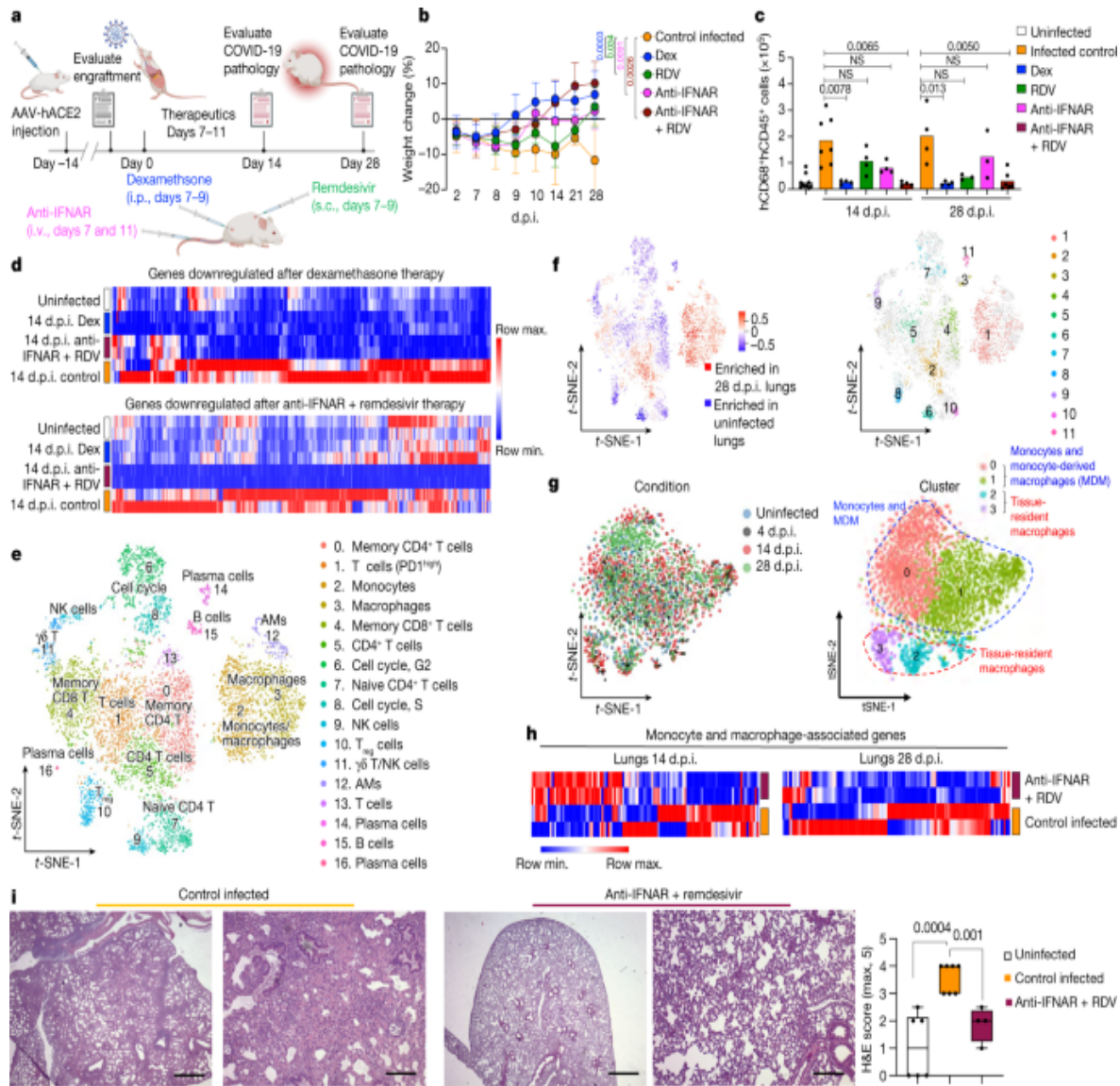
Acute SARS-CoV-2 infection resolves in most patients but becomes chronic and sometimes deadly in about 10–20% of patients^{[1,2,3,4,5,6,7,14,15,16,20,24,25,26,27](#)}. Two hallmarks of severe COVID-19

are a sustained IFN response and viral RNA persisting for months^{1,2,3,4,5,6,7,8,9,10,11,12,13,14,15,16,17,20,24,25,26,27,28}. This chronicity is recapitulated in SARS-CoV-2-infected MISTRG6-hACE2 humanized mice¹⁹. High levels of IL-1 β , IL-18 and lactate dehydrogenase (LDH) are correlated with COVID-19 severity in patients, suggesting a role for inflammasome activation and pyroptosis in pathology^{5,6,7,14,15,16,17,18,29}. Here we show that human lung macrophages are infected by SARS-CoV-2. Replicating SARS-CoV-2 in these human macrophages activates inflammasomes and initiates an inflammatory cascade with a unique transcriptome, results in pyroptosis, and contributes to the downstream type-I IFN response. Blocking viral replication, the downstream IFN response or inflammasome activation *in vivo* during the chronic phase of the disease attenuates many aspects of the overactive immune inflammatory response (especially the inflammatory macrophage response) and disease.

Viral replication and the IFN response

Chronic interferon is associated with disease severity and impaired recovery in influenza infection³⁰. To test whether a viral-RNA-dependent type-I IFN response was a driver of chronic disease, we treated SARS-CoV-2-infected MISTRG6-hACE2 mice with remdesivir^{21,22,23} and/or anti-IFNAR2 antibodies (Fig. 1a) to inhibit viral replication and/or the IFN response downstream of chronic infection, respectively. As a control, we used dexamethasone, which reverses many aspects of immunopathology in infected MISTRG6-hACE2 mice¹⁹ and in humans³¹. Although remdesivir and anti-IFNAR2 alone were partially therapeutic, combined therapy achieved more rapid weight recovery and suppression of the immune inflammatory response, especially macrophages, as effectively as dexamethasone (Fig. 1b–c and Extended Data Fig. 1a–f), suggesting that remdesivir and anti-IFNAR2 antibodies have a combinatorial effect in chronic infection.

Fig. 1: Targeting viral replication and downstream interferon signalling ameliorates chronic COVID-19.



a, Schematic of therapy: SARS-CoV-2-infected MISTRG6-hACE2 mice were treated with dexamethasone (Dex) and remdesivir (RDV) at 7, 8 and 9 d.p.i., and with anti-IFNAR2 antibodies at 7 and 11 d.p.i., and analysed at 14 or 28 d.p.i. i.p., intraperitoneal; i.v., intravenous; s.c., subcutaneous. **b**, Weight changes after infection. 28 d.p.i.: $n = 5$ (control infected), $n = 4$ (Dex; anti-IFNAR2 + RDV) and $n = 3$ (RDV; anti-IFNAR2) mice were examined over at least two experiments. Data are mean \pm s.d. **c**, Human macrophages in the lungs. $n = 10$ (uninfected); 14 d.p.i.: $n = 7$ (control infected), $n = 4$ (Dex; RDV; anti-IFNAR; anti-IFNAR + RDV); 28 d.p.i.: $n = 4$ (control infected; Dex), $n = 3$ (RDV; anti-IFNAR) and $n = 6$ (anti-IFNAR + RDV) mice were examined over three experiments. Mean values are shown with error bars. NS, not significant. **d**, Genes downregulated after dexamethasone therapy. **e**, t-SNE plot of cell types. **f**, t-SNE plots of monocytes/macrophages. **g**, t-SNE plot of monocyte/macrophage-associated genes. **h**, Heatmaps of monocyte/macrophage-associated genes. **i**, Histology and H&E scores.

data points. NS, not significant. **d**, Heat map of human genes suppressed by therapy in the lungs ($\log_2[\text{fold change}] > 1$; adjusted P with Bonferroni correction < 0.05). Differential expression was determined using DESeq2. Statistical analysis was performed using Wald tests. Transformed (minimum–maximum) normalized counts of duplicates. Hierarchical clustering (1 – Pearson). **e**, t -Distributed stochastic neighbour embedding (t -SNE) plot of human immune cells from uninfected or infected lungs (28 d.p.i.). Pooled duplicates. Cluster marker genes were identified using Wilcoxon rank-sum tests (Extended Data Fig. 2e). $n = 3,655$ (uninfected) and $n = 3,776$ (28 d.p.i.) cells analysed. NK, natural killer; T_{reg} , T regulatory. **f**, t -SNE plots highlighting differentially abundant (DA) human immune cell populations identified by DA-seq⁶¹. Top, distribution/enrichment of DA populations. Bottom, DA clusters. **g**, t -SNE plots of human monocyte/macrophage clusters from 4 d.p.i., 14 d.p.i. and 28 d.p.i., and uninfected lungs. Left, d.p.i. Right, clusters. Different conditions were integrated as described in the [Methods](#) (ref. 62). Marker genes were identified using Wilcoxon rank-sum tests (Extended Data Fig. 3a,b). P values were adjusted with Bonferroni correction. $n = 438$ (uninfected), $n = 336$ (4 d.p.i.), $n = 793$ (14 d.p.i.) and $n = 1,368$ (28 d.p.i.) cells analysed. **h**, Heat map visualizing the response to the combined therapy based on differentially expressed genes associated with human monocytes and macrophages. Transformed (minimum–maximum) normalized expression of duplicates. Hierarchical clustering (1 – Pearson). **i**, Representative haematoxylin and eosin (H&E) staining and box plot of histopathological scores. $n = 6$ (uninfected), $n = 7$ (control infected) and $n = 4$ (anti-IFNAR2 + RDV) mice were examined over three experiments. The centre line shows the median value, the box limits show the 25th–75th percentiles, and the whiskers show the lowest (minimum) to the highest (maximum) value. Scale bars, 1 mm (first and third), 0.1 mm (second and fourth). For **b**, **c** and **i**, statistical analysis was performed using unpaired two-tailed t -tests. The data associated with dexamethasone used here as a control were reported previously¹⁹.

[Source data](#)

We assessed the effect of therapeutics on the lung transcriptome. Both dexamethasone and the combined therapy reversed overactive immune

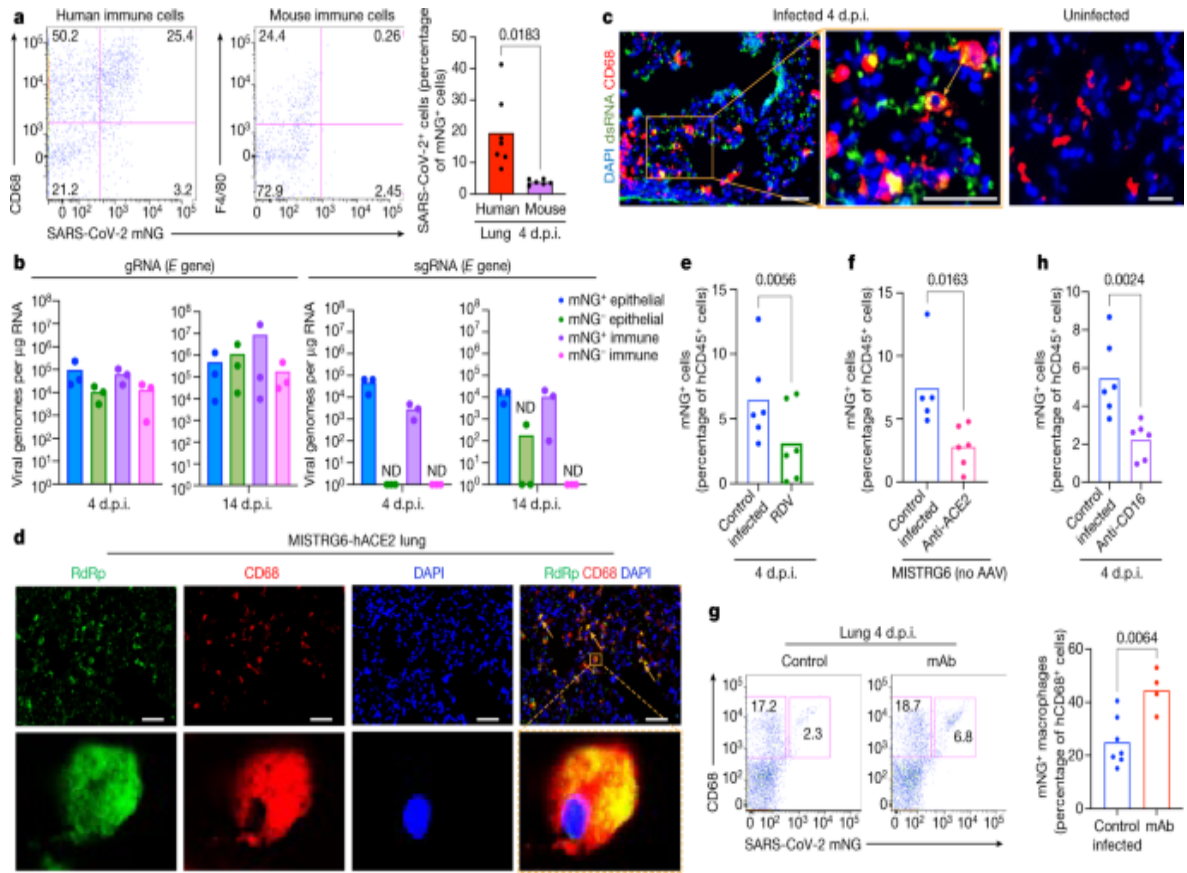
transcripts to the levels in uninfected animals (Fig. 1d, Extended Data Fig. 2a,b and Supplementary Table 1). The reduced transcripts were enriched for chemokine and cytokine networks (*CXCL10*, *CXCL8*, *CCL2*), inflammatory (*TLR7*, *NLRP3*, *CASPI*) and anti-viral (*MPO*, *OASI*, *OAS2*) response, and interferon-stimulated genes (ISGs) (*IFITM3*, *IFITM2*, *IRF7*) (Supplementary Table 1 and Extended Data Fig. 2c,d), emphasizing the central role of IFN signalling and inflammatory cytokine-chemokines in chronic COVID-19. Comparison of single-cell transcriptomes of human immune cells from infected mice with their uninfected counterparts (Fig. 1e–g and Extended Data Fig. 2e) showed tissue-resident macrophages, such as alveolar macrophages (AMs), activated at the peak of infection, followed by an inflammatory response with infiltrating monocytes and monocyte-derived macrophages (MDM)(Fig. 1g, Extended Data Fig. 3a–c and Supplementary Table 2). As macrophages differentiated, they maintained their inflammatory signature and activated status throughout infection (Extended Data Fig. 3a–c and Supplementary Table 2). All macrophage subsets were enriched for ISGs at all timepoints (Extended Data Fig. 3c). These ISGs were suppressed after combination therapy with anti-IFNAR2 antibodies and remdesivir (Fig. 1h, Extended Data Fig. 4 and Supplementary Table 3). However, key anti-viral responses such as *IFNG* primarily produced by cytotoxic T cells were spared (Extended Data Fig. 5a), highlighting the selective effects of combined anti-IFNAR2–remdesivir therapy on the pathology of chronic COVID-19. Consistent with the fibrosis seen both in patients^{32,33,34,35,36} and humanized mice¹⁹, alveolar self-renewal and differentiation programs were inhibited, resulting in the accumulation of the pre-alveolar type 1 transitional cell state program in pneumocytes^{7,37,38,39}. This state was reversed in infected MISTRG6-hACE2 mice by anti-IFNAR2–remdesivir combination therapy, restoring self-renewal and differentiation programs (Extended Data Fig. 5b). Overall, reducing chronic inflammation enhanced lung tissue recovery and prevented transition to fibrosis seen in humanized mice¹⁹ and humans^{32,33,34,35,36} (Fig. 1i and Extended Data Fig. 5c).

SARS-CoV-2 replicates in human macrophages

To determine the cellular source of persistent viral RNA and replication, we measured genomic RNA (gRNA) and subgenomic viral RNA (sgRNA)⁴⁰ in

lung tissue or in sorted lung epithelial cells or human immune cells from infected MISTRG6-hACE2 mice (Extended Data Fig. 6a–d). Notably, epithelial cells and human immune cells had similar levels of viral RNA (Extended Data Fig. 6d). Although gRNA was abundant, we could not discern sgRNA in either cell type. We tracked infected cells in MISTRG6-hACE2 mice using a reporter strain of virus—SARS-CoV-2-mNG⁴¹, which encodes the fluorescent protein mNG in infected cells. On the basis of this assay, most epithelial cells in the bronchioalveolar lavage (BAL) but only a few total lung epithelial cells were infected with SARS-CoV-2 (Extended Data Fig. 6e). Notably, human macrophages were strongly mNG positive throughout disease (Fig. 2a and Extended Data Fig. 6f,g). No mouse immune cells expressed mNG (Fig. 2a and Extended Data Fig. 6f). To address whether the SARS-CoV-2 viral RNA replicates in these cells or is acquired by phagocytosis, we measured the mNG signal in human macrophages from infected MISTRG6 mice untransduced with hACE2. In these mice, epithelial cells were not infected or infected poorly with SARS-CoV-2^{19,42} (Extended Data Fig. 6h). However, these mice had similar levels of mNG⁺ human macrophages to AAV-hACE2 mice, suggesting that viral uptake by macrophages is independent of infected epithelial cells (Extended Data Fig. 6i). To determine whether SARS-CoV-2 replicates in human macrophages, we quantified gRNA and sgRNA⁴⁰ in mNG⁺ versus mNG⁻ epithelial or human immune cells at 4 days post-infection (d.p.i.) or 14 d.p.i. (Extended Data Fig. 6j). Only mNG⁺, and not mNG⁻, epithelial and immune cells had sgRNA (Fig. 2b). Second, we stained for double-stranded RNA (dsRNA), a diagnostic indicator of viral replication (Fig. 2c). As expected, mNG and dsRNA were detected/colocalized in human macrophages (Fig. 2c and Extended Data Fig. 7a). Third, we detected viral RNA-dependent RNA polymerase (RdRp) in human macrophages, which colocalized with a viral spike protein supporting specificity (Fig. 2d, Extended Data Fig. 7b and 8a–c). Viral RdRp and spike were also present in the human macrophages of autopsies of human lungs with SARS-CoV-2 pneumonia (Extended Data Fig. 9). Thus, the mouse model observations reflected the human disease. Remdesivir reduced the mNG signal and viral titres by the same amount in infected MISTRG6-hACE2 mice (Fig. 2e and Extended Data Fig. 10a). Thus, SARS CoV-2 appeared to replicate in human immune cells.

Fig. 2: SARS-CoV-2 replicates in human macrophages.



a, Representative flow cytometry plots and frequencies of mNG⁺ human (CD68⁺) or mouse (F4/80⁺) lung macrophages in SARS-CoV-2-mNG infected MISTRG6-hACE2 mice. $n = 7$ (human) and $n = 6$ (mouse) mice over at least three experiments. **b**, Quantification of gRNA and sgRNA (*E* gene)^{40,63} in sorted mNG⁺ or mNG⁻ epithelial cells or human immune cells. $n = 3$ mice over 2 experiments. Mean values are shown with data points. ND, not detected. **c**, Representative fluorescence microscopy images of dsRNA (rJ2), CD68 and DAPI staining in fixed lung tissues from SARS-CoV-2-infected MISTRG6-hACE2 mice. Representative of $n = 5$ mice examined over 3 experiments. The yellow rectangle indicates the region magnified on the right. The yellow arrow indicates colocalization of CD68 with dsRNA. Pseudocolours were assigned. **d**, Representative fluorescence microscopy images of RdRp, CD68 and DAPI staining in fixed lung tissues from SARS-CoV-2-infected MISTRG6-hACE2 mice. Representative of $n = 5$ mice examined over 3 experiments. The yellow arrows indicate colocalization of human CD68 with dsRNA. The yellow rectangle indicates the region magnified above. Pseudocolours were assigned. For **c** and **d**, scale bars are present in the bottom left corner of each panel.

e, **f**, **g**, Bar graphs showing mNG⁺ cells (percentage of hCD45⁺ cells) in Control, Infected (RDV), Infected (Anti-ACE2), and Infected (Anti-CD16) groups. $n = 5$ mice examined over 3 experiments. Mean values are shown with data points. Statistical significance is indicated by brackets.

Group	Control	Infected (RDV)	Infected (Anti-ACE2)	Infected (Anti-CD16)
mNG ⁺ cells (percentage of hCD45 ⁺ cells)	~6.5	~13.5	~4.5	~2.5

h, Bar graph showing mNG⁺ cells (percentage of hCD45⁺ cells) in Control and Infected groups. $n = 5$ mice examined over 3 experiments. Mean values are shown with data points. Statistical significance is indicated by brackets.

Group	Control	Infected
mNG ⁺ cells (percentage of hCD45 ⁺ cells)	~5.5	~45.5

bars, 50 µm. **e**, The frequencies of mNG⁺ human immune cells in remdesivir-treated (1–3 d.p.i.) or control MISTRG6-hACE2 mice infected with SARS-CoV-2-mNG. $n = 6$ mice were examined over 3 experiments. Mean values are shown with data points. **f**, The frequencies of mNG⁺ human immune cells after ACE2 blockade (1–3 d.p.i.) in MISTRG6 (no AAV) mice infected with SARS-CoV-2-mNG. $n = 5$ (control infected) and $n = 6$ (anti-ACE2 treated) mice were examined over 2 experiments. Mean values are shown with data points. **g**, Representative flow cytometry plots and frequencies of mNG⁺ macrophages in infected MISTRG6-hACE2 mice treated with monoclonal antibodies (mAbs)^{19,45,64} at 35 h.p.i. $n = 7$ (control infected) and $n = 4$ (treated) mice were examined over 2 experiments. Mean values are shown with data points. **h**, The frequencies of mNG⁺ human immune cells in MISTRG6-hACE2 mice after CD16 blockade (2 d.p.i.). $n = 6$ mice were examined over 3 experiments. Mean values are shown with data points. Statistical analysis was performed using unpaired (**a** and **g**) and paired (**e**, **f** and **h**) two-tailed *t*-tests.

Source data

SARS-CoV-2 infects through ACE2 and CD16

The ACE2 receptor used by SARS-CoV-2 to infect the lung epithelium can be expressed in macrophages⁴³. We measured ACE2 expression using flow cytometry and immunofluorescence staining in mouse epithelial cells and human lung macrophages (Extended Data Fig. [10b–f](#)). Human lung macrophages of both MISTRG6 and MISTRG6-hACE2 mice, as well as the epithelial cells of only MISTRG6-hACE2 mice, expressed human ACE2 (Extended Data Fig. [10b–e](#)). Interestingly, ACE2 expression was higher in both infected (mNG⁺) human macrophages and epithelial cells (Extended Data Fig. [10b–e](#)). We treated SARS-CoV-2-infected MISTRG6 mice with a blocking antibody against human ACE2. In these mice, SARS-CoV-2 infects epithelial cells poorly^{19,42}, as the mice did not receive AAV-ACE2 and only human macrophages express human ACE2 (Extended Data Fig. [6h](#)). ACE2 blockade significantly diminished infected human macrophages (Fig. [2f](#)), suggesting that ACE2 can mediate viral entry in human lung macrophages.

Antibodies can also mediate viral uptake by macrophages (for example, Dengue virus⁴⁴). To test the role of antibody-mediated viral entry to macrophages, we treated infected mice with monoclonal antibodies⁴⁵ against SARS-CoV-2 spike protein early (35 h post-infection (h.p.i.)) when the effects of endogenous antibodies are minimal or late (7 d.p.i.) (Extended Data Fig. 10g). Indeed, monoclonal antibody treatments increased infected lung macrophages (Fig. 2g and Extended Data Fig. 10h). Immune cells express a wide range of surface Fcγ receptors (FcγRs) that interact with the Fc moiety of antibodies. These interactions lead to multiple protective or pathological effector functions^{44,46}. The severity of COVID-19 correlates with high serum IgG levels and specific IgG-Fc structures and interactions^{47,48,49}. One such Fc interaction is mediated by CD16, which is expressed at high levels in mNG⁺ macrophages. We treated mice early (2 d.p.i., low antibody levels) as a proof of concept, or late (7 d.p.i. and 11 d.p.i., high antibody levels) as a possible therapeutic with anti-CD16 antibodies. Anti-viral antibody levels in the lung tissue were sufficient to mediate viral uptake and were positively correlated with mNG levels at 4 d.p.i. (Extended Data Fig. 10g,i). When dosing was optimized, CD16 blockade did not alter the distribution of macrophages, although it resulted in significantly fewer infected human macrophages at both timepoints (Fig. 2h and Extended Data Fig. 10j).

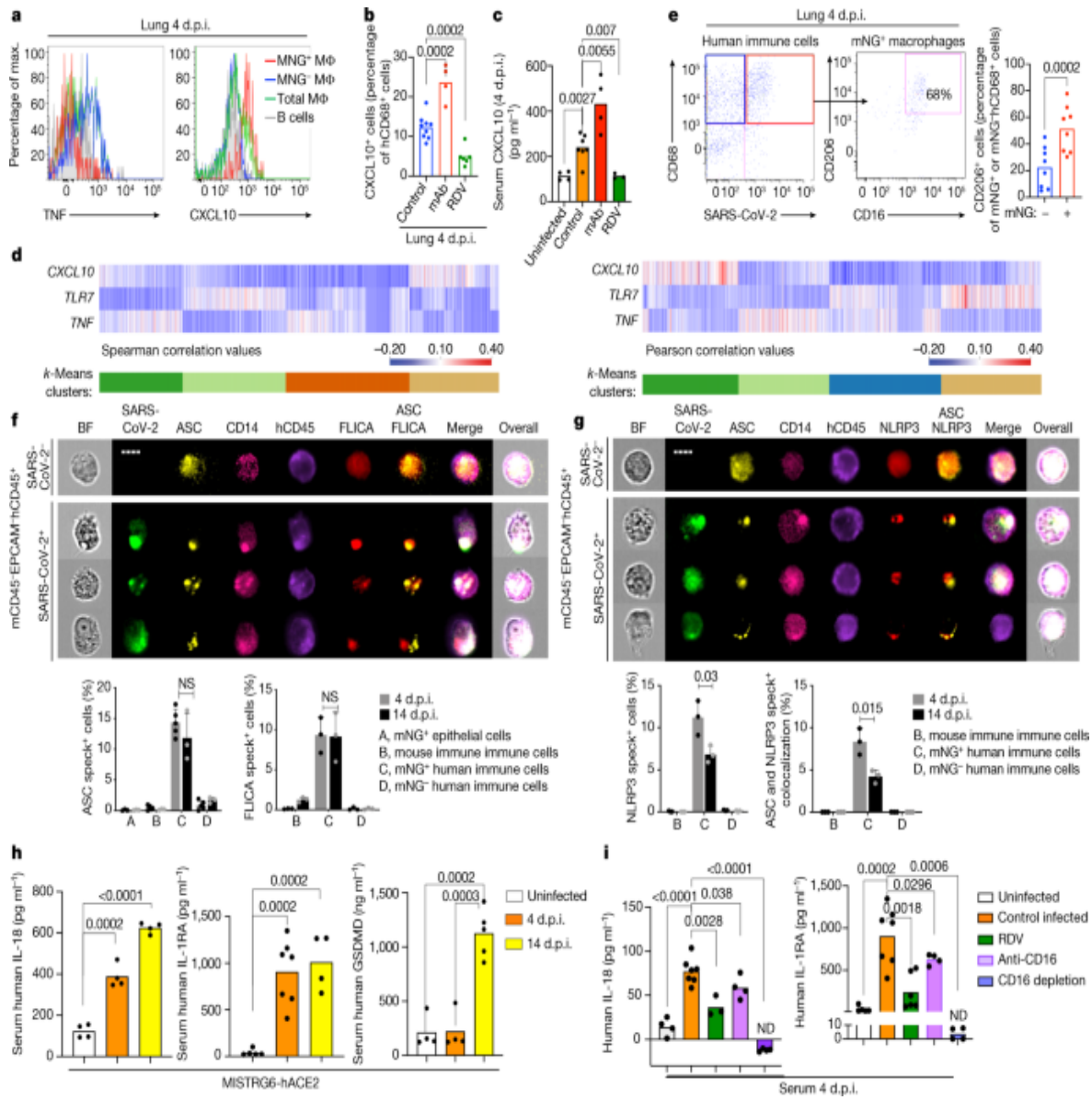
To elucidate whether viral replication products are the result of bona fide infection, we cultured human bone-marrow-derived macrophages (BMDMs, differentiated from bone-marrow cells of immune-reconstituted MISTRG6 mice) with SARS-CoV-2 in vitro. Indeed, SARS-CoV-2 was taken up by BMDMs and replicated in these cells, as measured by mNG signal (Extended Data Fig. 10k) and high levels of sgRNA (Extended Data Fig. 10l). This was true for multiple types of macrophage (Extended Data Fig. 10m). As in vivo, in vitro macrophage infection enhanced by antibodies (convalescent plasma or monoclonal antibodies) was reduced by CD16, ACE2 or RdRp blockade (Extended Data Fig. 10n,o). sgRNA levels in these macrophages were also reduced by these treatments (Extended Data Fig. 10l), further supporting a role for both ACE2 and CD16 in viral uptake and RdRp in viral replication. SARS-CoV-2 infection in human macrophages was not productive or produced very little as indicated by undetectable infectious virus, titrated in culture, from sorted immune cells from infected

mice at 4 d.p.i. and in vitro infected macrophages at 48 h.p.i. (Extended Data Fig. [10p–r](#)).

The transcriptome of infected macrophages

We next determined the consequences of infection of human macrophages by SARS-CoV-2. Infected macrophages preferentially produced CXCL10, a chemokine that recruits many types of immune cells (Fig. [3a](#)), but not TNF. Similar to mNG positivity, CXCL10 production by human macrophages was also enhanced by antibodies and inhibited by remdesivir, also reflected in serum levels and in vitro (Fig. [3b,c](#) and Extended Data Fig. [11a–c](#)). Thus, we used CXCL10 as a proxy for SARS-CoV-2-infected macrophages and identified a unique transcriptional signature enriched for genes encoded by tissue-resident macrophages, in particular AMs^{[50](#)} (*APOC1*, *MRC1*, *ALOX5AP*, *FABP5*, *INHBA*), chemokines of interstitial macrophages (*CCL18*, *CCL3*, *CCL7*, *CCL8*, *CCL20*, *CXCL8*), inflammatory cytokines (*IL1A*, *IL18*, *IL27*), complement genes (*C1QA*, *C1QB*) and ISGs (*ISG20*, *IFI27*) (Fig. [3d](#), Extended Data Figs. [11d,e](#) and [12a,b](#), and Supplementary Table [4](#)). Further flow cytometry characterization of mNG⁺ cells also confirmed enrichment for CD16⁺ AMs, which produced more CXCL10 (Fig. [3e](#) and Extended Data Fig. [12c](#)). Consistent with our findings, CD14^{high}CD16^{high} cells and AMs enriched with viral RNA in autopsies of the lungs of patients with COVID-19^{[7,20](#)} also had distinct transcriptomes that were largely recapitulated in what we construe as CXCL10-associated genes (*CXCL11*, *CCL18*, *CCL8*, *ISG15*, *CD83*). Interestingly, this strong network of CXCL10-specific gene signature was no longer restricted to AMs later in infection as different macrophage subsets continuously differentiate, as evidenced by the high *IL7R* expression of developing lung macrophages^{[50](#)} (CXCL10⁺ and AMs) at all timepoints (Figs. [1g](#) and [3d](#) and Extended Data Fig. [12d](#)).

Fig. 3: SARS-CoV-2 infection of human macrophages activates inflammasomes and pyroptosis.



a, CXCL10⁺ or TNF⁺ human macrophages (MΦ). Representative of $n = 6$ mice over 3 experiments. **b**, CXCL10⁺ lung macrophage frequencies after monoclonal antibody or remdesivir therapy. $n = 9$ (control infected), $n = 4$ (monoclonal antibodies) and $n = 6$ (RDV) mice over 2 experiments. Mean values are shown with data points. **c**, Serum CXCL10 levels after monoclonal antibody or remdesivir therapy. Mean values are shown with data points. $n = 4$ (uninfected; monoclonal antibodies); $n = 7$ (control infected) and $n = 3$ (RDV) mice examined over 2 experiments. **d**, Correlation (Pearson and Spearman) of each gene with CXCL10, TNF or TLR7 in human lung monocytes and macrophages. *k*-means clustering. P

values were calculated based on a *t*-distribution with $\text{length}(x) - 2$ d.f. or algorithm AS 89 with exact = TRUE; two-tailed. **e**, Representative plots and AM frequencies within mNG⁺ or mNG⁻ macrophages. $n = 8$ mice examined over 4 experiments. **f**, ASC speck visualization/quantification and colocalization with active caspase-1 (FLICA) in mNG⁺ or mNG⁻ human immune cells from MISTRG6-hACE2 mouse lungs. Cells were sorted as shown in Extended Data Fig. 6j. $n = 1,000$ cells were analysed per condition. ASC⁺ specks: $n = 3$ (A, 4 d.p.i.), $n = 5$ (B–D, 4 d.p.i.) and $n = 3$ mice (14 d.p.i.); FLICA: $n = 3$ mice examined over at least 2 experiments. Data are mean \pm s.d. with data points. BF, bright field. NS, not significant. **g**, ASC speck visualization/quantification and colocalization with NLRP3 oligomerization in sorted mNG⁺ or mNG⁻ human lung immune cells. $n = 1,000$ cells were analysed per condition. $n = 3$ mice over 2 experiments. Data are mean \pm s.d. with data points. For **f** and **g**, scale bars 7 μm . BF, bright field. **h**, Serum IL-18, IL-1RA and GSDMD levels. IL-18: $n = 4$ mice were examined over 2 experiments; IL-1RA: $n = 5$ (uninfected), $n = 7$ (4 d.p.i.) and $n = 4$ (14 d.p.i.) mice were examined over 3 experiments; GSDMD: $n = 4$ (uninfected; 4 d.p.i.) and $n = 5$ (14 d.p.i.) mice over 3 experiments. Mean values are shown with data points. $P < 0.0001$ represents $P = 3.32 \times 10^{-7}$. **i**, Serum IL-18 and IL-1RA levels in mice treated with CD16-blocking or CD16-depleting antibodies or remdesivir. IL-18: $n = 4$ (uninfected; CD16 blocking; CD16 depleting), $n = 7$ (control infected) and $n = 3$ (RDV); IL-1RA: $n = 5$ (uninfected), $n = 7$ (control infected), $n = 6$ (RDV), $n = 4$ (CD16 blocking; CD16 depleting) mice were examined over at least 2 experiments. Mean values are shown with data points. $P < 0.0001$; uninfected, $P = 3.28 \times 10^{-5}$; CD16 depletion, $P = 7.92 \times 10^{-7}$. For **b**, **c** and **f–i**, statistical analysis was performed using unpaired two-tailed *t*-tests.

[Source data](#)

SARS-CoV-2 activates inflammasomes

Morphological analysis of sorted mNG⁺ cells revealed the appearance of membrane bubbles—a characteristic of pyroptosis—prompting us to investigate inflammasome activation as part of the inflammatory cascade initiated by infection. Inflammasomes are dynamic multiprotein complexes

in which specific NOD-like receptors and adaptor molecules are assembled to activate caspases—the central effector proteins. We sorted mNG⁺ and mNG⁻ human immune cells, mNG⁺ epithelial cells and mouse immune cells (Extended Data Fig. 6j), and assayed for sensors, adaptors and effectors of the inflammasome pathway. First, focusing on adaptor molecule apoptosis-associated speck-like protein containing a CARD (ASC) as the common adaptor molecule with an essential role in inflammasome assembly and activation, we found that infected (mNG⁺) human cells exclusively showed substantial inflammasome activation, quantified by ASC speck formation (Fig. 3f and Extended Data Fig. 13a,b). ASC specks co-localized with both NLRP3 and active caspase-1 (visualized by fluorochrome-labelled inhibitor of caspases assay (FLICA)) (Fig. 3f,g and Extended Data Fig. 13a–d). Inflammasome activation in infected human macrophages was sustained during disease (4–14 d.p.i.; Fig. 3f,g and Extended Data Fig. 13c).

Once inflammasome complexes are formed, active caspase-1 cleaves and proteolytically activates the pro-inflammatory IL-1-family cytokines IL-1 β and IL-18, which are typically elevated and characteristic of severe COVID-19 in patients. IL-18 levels in the blood and lungs were significantly elevated in SARS-CoV-2-infected mice and correlated well with the proportions of infected (mNG⁺) macrophages (Fig. 3h and Extended Data Fig. 13e). Although IL-1 β levels in serum in vivo were not detectable, we measured IL-1RA. This specific receptor antagonist, induced by IL-1 β , served as a proxy of IL-1 β and it paralleled enhanced IL-18 levels and correlated with mNG⁺ cells (Fig. 3h and Extended Data Fig. 13f).

Finally, we assayed for pyroptosis by detecting LDH and gasdermin D (GSDMD) in the serum. GSDMD, which is a substrate of active caspase-1 and a pore-forming executor of pyroptosis, and LDH, released by pyroptosis, were particularly enriched in the serum of infected mice at the late timepoints (14 d.p.i.; Fig. 3h and Extended Data Fig. 13g), further supporting continuous inflammasome activation during infection. Moreover, infected lung macrophages showed higher incorporation of a small fixable dye (Zombie Aqua) that enters dying cells with a compromised cell membrane, consistent with the pore-forming function of GSDMD and pyroptosis (Extended Data Fig. 13h).

All aspects of inflammasome activation were also recapitulated in vitro when BMDMs were infected in vitro with SARS-CoV-2. Active caspase-1 in infected BMDMs, which was dependent on viral replication, was inhibited by remdesivir (Extended Data Fig. [13i](#)). High levels of the inflammasome products IL-18, IL-1 β and IL-1RA (in response to IL-1 β) and two measures of pyroptosis, GSDMD and LDH, that were detected at high levels in the supernatants of infected BMDMs were also inhibited by remdesivir (Extended Data Fig. [13j–n](#)). In vitro infected cells also had higher incorporation of Zombie Aqua, consistent with pyroptosis (Extended Data Fig. [13o](#)).

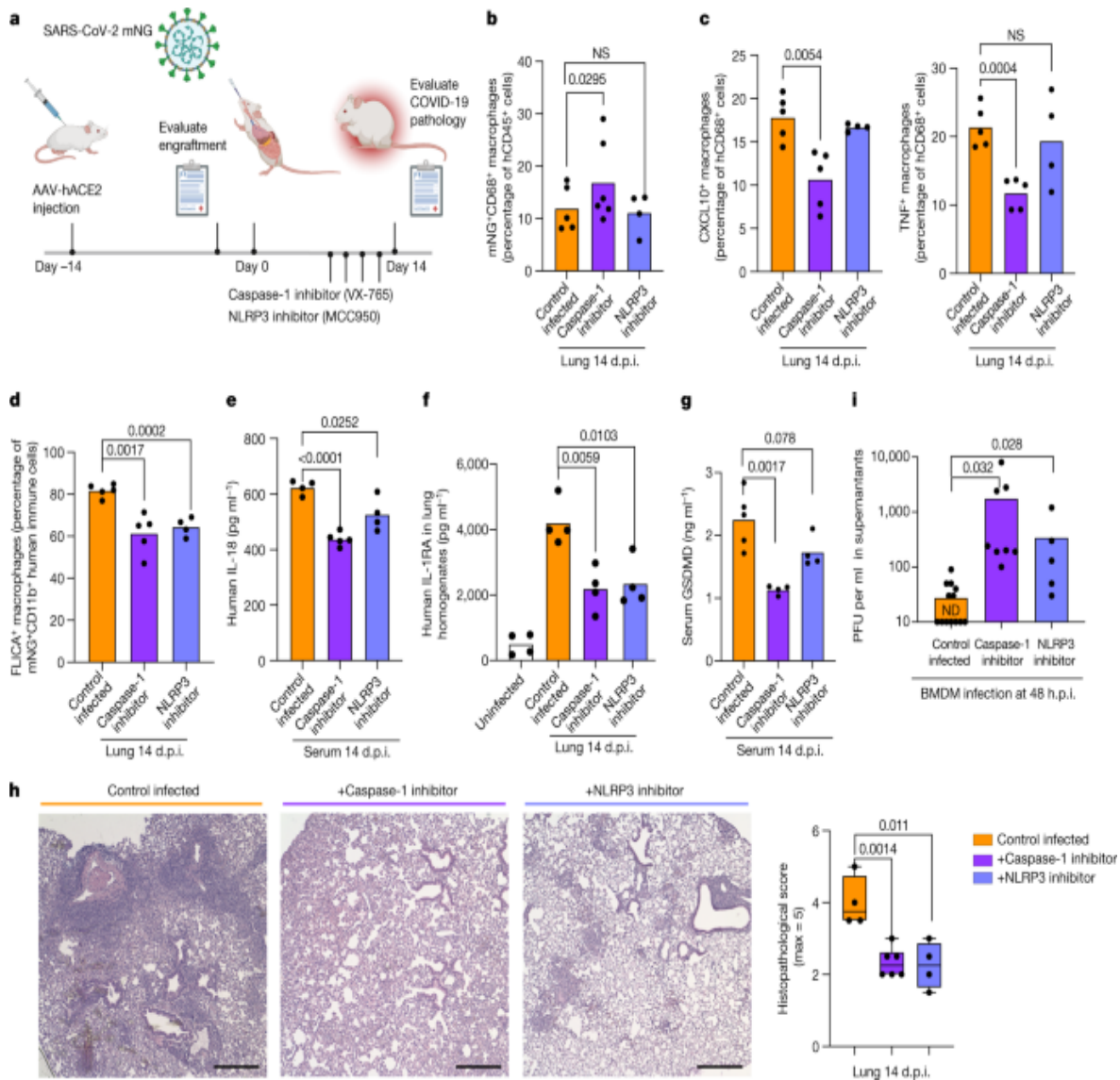
Infection affects the macrophage response

To determine the role of viral infection on the inflammatory macrophage response, we first blocked viral entry and replication in vivo and measured inflammatory cytokines and chemokines. Blocking viral entry (CD16 or ACE2 blockade) or inhibiting viral replication (remdesivir) all reduced IL-18, IL-1RA and CXCL10 levels, paralleling mNG levels (Fig. [3i](#) and Extended Data Fig. [14a–e](#)). Depletion of CD16 $^+$ cells in vivo (Extended Data Fig. [14f,g](#)) resulted in the complete loss of IL-18 and IL-1RA in the serum, consistent with the concept that viral replication and inflammasome activation occurred mainly in myeloid cells (Fig. [3i](#)). By contrast, monoclonal antibodies promoting viral infection in human macrophages (Fig. [2g](#) and Extended Data Fig. [10h](#)) enhanced systemic IL-18, IL-1RA and CXCL10, particularly during early disease (Extended Data Fig. [14h–k](#)). Nonetheless, despite changes in the levels of the inflammatory cytokines and chemokines, neither monoclonal antibodies nor CD16 blockade affected lung pathology, potentially owing to the conflicting role of these antibodies on viral titres versus inflammation (Extended Data Fig. [14l,m](#)). Consistent with the in vivo studies, IL-18, IL-1 β , IL-1RA and CXCL10 levels were also reduced in the supernatants of in vitro infected BMDMs after CD16, ACE2 or RdRp inhibition, again paralleling the reduced viral replication inferred from mNG levels (Extended Data Figs. [10o](#) and [14n–q](#)).

Inflammasome inhibition in COVID-19

Finally, to assess the causal role of NLRP3 and caspase-1 activation in inflammasome-mediated inflammation and disease, we treated mice with caspase-1 and NLRP3 inhibitors (Fig. 4a). As expected, the proportion of infected cells did not diminish, but the inflammatory profile of these cells and other lung macrophages was considerably attenuated (Fig. 4b,c). In inhibitor-treated mice, mNG⁺ cells produced less CXCL10, which was also reflected in reduced serum levels (Fig. 4c and Extended Data Fig. 15a–c). Lung macrophages (mNG⁻) also produced less TNF (Fig. 4c and Extended Data Fig. 15a). Overall, inhibitor-treated mice had lower levels of caspase-1 activation and lower levels of IL-18, IL-1RA and GSDMD (Fig. 4d–g). The cumulative decrease in proinflammatory cytokines and chemokines after inflammasome inhibition reversed the immune-pathological state of the lungs, measured by scoring lung histopathology (Fig. 4h). Inflammasome inhibition reduced immune cell infiltration and enhanced tissue recovery to homeostasis in the lungs, despite persistently high levels of mNG⁺ human immune cells in the lungs.

Fig. 4: Inflammasome inhibition ameliorates inflammation and disease in infected MISTRG6-hACE2 mice.



a, Schematic of inflammasome inhibition in vivo. SARS-CoV-2-infected MISTRG6-hACE2 mice were treated with caspase-1 or NLRP3 inhibitors at 6–12 d.p.i. **b**, The frequencies of mNG⁺ human immune cells after inflammasome inhibition. $n = 5$ (control infected), $n = 6$ (caspase-1 inhibitor) and $n = 4$ (NLRP3 inhibitor) mice were examined over at least 2 experiments. Mean values are shown with data points. **c**, The frequencies of CXCL10⁺ or TNF⁺ human lung macrophages after inflammasome inhibition. $n = 5$ (control infected), $n = 5$ (caspase-1 inhibitor), $n = 4$ (NLRP3 inhibitor) mice were examined over at least 2 experiments. Mean values are shown with data points. **d**, Quantification of active caspase-1 in mNG⁺ human macrophages after inflammasome inhibition. $n = 5$ (control infected), $n = 5$ (caspase-1 inhibitor) and $n = 4$ (NLRP3 inhibitor) mice were examined over at least 2 experiments. Mean values are shown with data points.

$n = 5$ (caspase-1 inhibitor), $n = 4$ (NLRP3 inhibitor) mice examined over at least 2 experiments. Mean values are shown with data points. **e**, Serum human IL-18 levels after inflammasome inhibition. $n = 4$ (control; NLRP3), $n = 5$ (caspase-1) mice were examined over 2 experiments. Mean values are shown with data points. $P < 0.0001$ represents $P = 1.00114 \times 10^{-5}$. **f**, Human IL-1RA levels in lung homogenates after inflammasome inhibition. $n = 4$ mice were examined over 2 experiments. Mean values are shown with data points. **g**, Serum GSDMD levels after inflammasome inhibition. $n = 5$ (control infected) and $n = 4$ (caspase-1 inhibitor; NLRP3 inhibitor) mice were examined over 2 experiments. Mean values are shown with data points. **h**, Representative H&E staining (left) and histopathological scores (right) after inflammasome inhibition. $n = 4$ (control infected), $n = 6$ (caspase-1 inhibitor), $n = 4$ (NLRP3 inhibitor) independent mice over at least 2 experiments. For the box plots, the centre line shows the median value, the box limits show the 25th–75th percentiles, and the whiskers show the lowest (minimum) to the highest (maximum) value. Scale bars, 0.2 mm. **i**, Viral titres from the supernatants of BMDMs infected with SARS-CoV-2-mNG in vitro and treated with caspase-1 or NLRP3 inhibitors. $n = 13$ (control infected), $n = 8$ (caspase-1 inhibitor) and $n = 5$ (NLRP3 inhibitor) independent data points collected over 3 experiments. Mean values are shown with data points. Statistical analysis was performed using paired (**b**) and unpaired (**c–i**) two-tailed *t*-tests.

Source data

Caspase-1 and NLRP3 inhibitors blocked inflammasomes in vitro but did not affect macrophage infection, measured as mNG⁺ macrophage frequency, and reduced the inflammatory response to infection (Extended Data Fig. [15d](#)). All parameters of inflammasome activation, including active caspase-1, IL-1 β , IL-18, GSDMD and LDH, were significantly reduced after caspase-1 and NLRP3 inhibition in vitro (Extended Data Fig. [15e–i](#)). Consistent with decreased pyroptosis, inflammasome blockade significantly reduced Zombie Aqua⁺ cells (Extended Data Fig. [15j](#)). As seen in vivo, in vitro infected bone marrow macrophages produced less CXCL10 and IL-1RA (Extended Data Fig. [15k,l](#)).

Finally, we tested whether inflammasome activation translated to any changes in the levels of infectious virus. We therefore first measured viral

titres in the lungs of mice treated with caspase-1 inhibitor. Indeed, mice treated with caspase-1 inhibitor had a higher viral load at 14 d.p.i. *in vivo* (Extended Data Fig. 15m). Given that a reduced inflammatory response could result in deficient viral clearance, we infected macrophages *in vitro* and treated them with caspase-1 or NLRP3 inhibitors to test the direct effect of inflammasome activation on infectious virus. An analysis of the supernatants of these cultures showed that inhibitor-treated cells produce substantially higher amounts of virus compared with the uninhibited controls (Fig. 4i and Extended Data Fig. 15n). Thus, the activation of inflammasomes in infected macrophages has two protective functions—it attenuates virus production and signals infection to the immune system by releasing inflammatory cues to recruit and activate more immune cells at the site of infection.

Overall, these findings suggest that infection of macrophages by SARS-CoV-2 activates inflammasomes and drives pyroptosis. Pyroptosis interrupts the viral replication cycle and prevents viral amplification; in parallel it releases immune cell activators and recruiters. Viral RNA/pathogen-associated molecular patterns and proinflammatory cytokines released from these cells probably shape the hyperinflammatory macrophage response sustained by infiltrating monocytes and MDMs and drive immunopathology.

Discussion

The MISTRG6 COVID-19 model faithfully reflects many of the chronic immunoinflammatory features of the human disease, such as chronic viral RNA, IFN response and the inflammatory state in macrophages¹⁹. Overall, our mechanistic study of this model defines a cascade of events that initiates with the infection of lung macrophages generating replicative intermediates and products, including RdRp, dsRNA and sgRNA. SARS-CoV-2 replication activates an inflammatory program with activation of inflammasomes, production and release of inflammatory cytokines and chemokines, and pyroptosis. We established all steps of inflammasome activation by visualizing ASC oligomerization, colocalization with active caspase-1 and NLRP3, maturation of inflammasome-mediated cytokines IL-1 β and IL-18, and pyroptosis assayed by GSDMD and LDH release. Inhibitors of both caspase-1 and NLRP3 blocked the downstream aspects of

inflammasome activation and the inflammatory cascade both *in vivo* and *in vitro*. Notably, targeting inflammasome-mediated hyperinflammation, or the combined targeting of viral replication and the downstream interferon response in the chronic phase of the disease, prevented immunopathology associated with chronic SARS-CoV-2 infection *in vivo*.

In contrast to epithelial cells, infected macrophages produce little virus. However, inhibition of the inflammasome pathway led to a substantial increase in infectious virus produced by infected macrophages, although the degree to which these macrophages contribute, if at all, to high titres of virus production is unclear. Notably, inflammasome activation denies the virus the opportunity to replicate productively in these sentinel immune cells and, instead, broadcasts inflammatory signals that inform the immune system of the infection. Although this is potentially beneficial, excessive inflammation occurring through this mechanism coupled with the dysregulated interferon response may be the key factor leading to the excessive inflammation that typifies chronic COVID-19^{2,5,51,52,53,54}. Indeed, attenuation of the inflammasome *in vivo* blocks the inflammatory infiltrates in the lungs of infected mice *in vivo*. We speculate that, by contrast, an early interferon response, as may occur in the majority of patients who rapidly clear infection, as well as in the acute mouse models of infection in which human immune cells that can be infected are not present, leads to viral elimination before this inflammatory chain reaction can occur.

Viral RNA and particles can be detected by a variety of innate immune sensors. The inflammasome sensor NLRP3 is both upregulated and activated by replicating SARS-CoV-2. The NLRP3 inflammasome can directly sense viral replication/RNA or can rely on other viral RNA sensors such as MDA5 or RIG-I^{55,56,57}. The loss of IL-18/IL-1 β production after remdesivir treatment in our studies strongly suggests that viral replication is involved. Recent reports have also identified a possible role for NLRP3-driven inflammasome activation in SARS-CoV-2 infected myeloid cells in post-mortem tissue samples and PBMCs⁵⁸. Although many candidates have been proposed (lytic cell death after infection, N protein⁵⁹, ORF3A⁶⁰), the exact mechanism of NLRP3 activation is still poorly understood²⁹. Activation of other NOD-like receptors may also contribute to the process, as inhibition of caspase-1 was stronger than NLRP3 alone. Finally, there may be other

mechanisms that enhance SARS-CoV-2 infection or the downstream inflammatory response in human macrophages that are unexplored here.

A role for inflammasome-driven hyperinflammation in COVID-19 pathophysiology in patients is now recognized^{5,6,7,14,15,16,17,18}. Targeting inflammasome pathways in patients may provide alternative therapeutic options for resolving chronicity in COVID-19. However, the increased virus production seen after inflammasome blockade could pose a significant risk to the benefit of wholesale inhibition of the pathway. The findings from our study and its implications provide alternative therapeutic options to be investigated in the clinic and may guide new therapeutic developments and prompt clinical trials to investigate combinatorial therapies that target viral RNA, inflammasome activation or its products and sustained IFN response.

Methods

Mice

MISTRG6 mice were generated by the R. Flavell laboratory by combining mice generated by this laboratory, the laboratory of M. Manz and Regeneron Pharmaceuticals based on the *Rag2*^{-/-}*IL2rg*^{-/-} 129xBalb/c background supplemented with genes encoding human M-CSF, IL-3, SIRPa, thrombopoietin, GM-CSF and IL-6 knocked into their respective mouse loci^{65,66}. MISTRG6 mice are deposited at Jackson Laboratories and have been made available to academic, non-profit and governmental institutions under a Yale-Regeneron material transfer agreement (already approved and agreed to by all parties). Instructions on obtaining the material transfer agreement for this mouse strain will be available along with strain information and on request. The CD1 strain of mice acquired from Charles River Laboratories was used for cross-fostering of MISTRG6 pups after birth to stabilize healthy microbiota. All mice were maintained under specific-pathogen free conditions in our animal facilities (biosafety level 1, 2 or 3) under our Animal Studies Committee-approved protocol.

Unconstituted MISTRG6 mice were maintained with cycling treatment with enrofloxacin in the drinking water (Baytril, 0.27 mg ml⁻¹). All animal experimentation was performed in compliance with Yale Institutional Animal Care and Use Committee protocols. For SARS-CoV-2-infected

mice, all procedures were performed in a biosafety level 3 (BSL-3) facility with approval from the Yale Institutional Animal Care and Use Committee and Yale Environmental Health and Safety.

Transplantation of human CD34⁺ haematopoietic progenitor cells into mice

Fetal liver samples were cut into small fragments, treated for 45 min at 37 °C with collagenase D (Roche, 200 µg ml⁻¹), and prepared into a cell suspension. Human CD34⁺ cells were purified by performing density-gradient centrifugation (Lymphocyte Separation Medium, MP Biomedicals), followed by positive immunomagnetic selection using the EasySep Human CD34 Positive Selection Kit (StemCell). For intrahepatic engraftment, newborn 1–3-day-old pups were injected with 20,000 fetal liver CD34⁺ cells in 20 µl of PBS into the liver with a 22-gauge needle (Hamilton Company). All use of human materials was approved by the Yale University Human Investigation Committee. At least three fetal liver samples (purchased) were used to account for variability and at least 8–10 gender-mixed mice were transplanted and analysed to account for reproducibility. Humanized mice that had lower than 30% humanization (percentage of human immune cells out of total (mouse and human combined) immune cells) in blood were excluded from the study or data collection.

AAV-hACE2 administration

AAV9 encoding hACE2^{19,67} was purchased from Vector Biolabs (AAV9-CMV-hACE2). Animals were anaesthetized using isoflurane. The rostral neck was shaved and disinfected. A 5 mm incision was made, and the trachea was visualized. Using a 32-gauge insulin syringe, a 50 µl injection dose of 10¹¹ genomic copies per ml of AAV-CMV-hACE2 was injected into the trachea. The incision was closed with 4–0 Vicryl suture and/or 3M Vetbond tissue adhesive. After administration of analgesic, the animals were placed into a heated cage until full recovery. The mice were then moved to BSL-3 facilities for acclimatization.

In vivo SARS-CoV-2 infection

The SARS-CoV-2 isolate USA-WA1/2020 was obtained from BEI reagent repository. SARS-CoV-2 mNG was obtained from P. Y. Shi⁴¹. All infection experiments were performed in a BSL-3 facility, licensed by the State of Connecticut and Yale University. Mice were anaesthetized using 20% (v/v) isoflurane diluted in propylene glycol. Using a pipette, 50 µl of SARS-CoV-2-WA1 or SARS-CoV-2-mNG ($1\text{--}3 \times 10^6$ plaque-forming units (PFU)) was delivered intranasally.

Therapeutics

SARS-CoV-2-infected MISTRG6-hACE2 were treated intraperitoneally daily with dexamethasone at 10 mg kg^{-1} for 3 days starting at 7 d.p.i. Mice were treated subcutaneously with remdesivir at 25 mg kg^{-1} dosing as has been previously described²² for 3 consecutive days starting at 7 d.p.i. (Fig. 1) or 1 d.p.i. (Fig. 2; for human macrophage infection studies mice were treated twice, daily). Mice were treated with anti-IFNAR2 antibodies at 1.5 mg kg^{-1} dosing at 7 and 11 d.p.i. Weight changes post-infection were plotted as the percentage change compared with preinfection weight.

Infected MISTRG6-hACE2 mice were treated with two different clones of anti-human CD16 antibodies. For CD16 blockade experiments, mice were treated with anti-CD16 (Abcam, SP175) antibodies early and late. For early CD16 blockade studies, the mice were treated with anti-CD16 antibodies at 2 d.p.i. with a single dose (20 µg per mouse) and euthanized at 4 d.p.i. For late CD16 blockade studies, the mice were treated with anti-CD16 antibodies at 7 d.p.i. and 11 d.p.i. and euthanized at 14 d.p.i. For depletion experiments, the mice were treated with anti-CD16 (Thermo Fisher Scientific, 3G8) antibodies with a daily dose of 20 µg for 3 days starting 1 d.p.i. Rabbit IgG, monoclonal (EPR25A) isotype control (ab172730) and mouse IgG1 kappa isotype control (P3.6.2.8.1) were used.

Infected MISTRG6 (without AAV-hACE2) mice were treated with monoclonal antibodies against human ACE2 (MM0073-11A31, Abcam, ab89111) for 3 days i.p. with a daily dose of 20 µg starting at 1 d.p.i. In these mice only, epithelial cells were not infected or infected poorly with SARS-CoV-2 with undetectable titres using standard plaque assays¹⁹, presumably

due to differences between mouse and human ACE2 that limit viral entry and replication⁴². Mouse IgG2 isotype was used as a control.

Infected MISTRG6-hACE2 mice received a mixed cocktail of monoclonal antibody clone 135 (m135) and clone 144 (m144) at 20 mg kg⁻¹ at 35 h.p.i. or 7 d.p.i. Monoclonal recombinant antibodies used in this study were cloned from the convalescent patients (whose plasma was used for in vitro studies infecting BMDMs) and had high neutralizing activity against SARS-CoV-2 in vitro and in vivo in mouse adapted SARS-CoV-2 infection and ancestral strain of SARS-CoV-2/WA1^{19,45,64}.

For NLRP3-inhibitor experiments, infected MISTRG6-hACE2 mice were treated with MCC950 (R&D Systems) at a dose of 8 mg kg⁻¹ i.p. on days 6, 8, 10 and 12 after infection and euthanized on day 14^{68,69,70}. For caspase-1-inhibitor experiments, infected MISTRG6-hACE2 mice were treated with VX-765 (Invivogen) at a dose of 8 mg kg⁻¹ on days 6, 8, 10 and 12 after infection and euthanized on day 14⁷⁰. Control infected mice were treated with PBS.

Viral titres

Mice were euthanized in 100% isoflurane. Approximately half of the right lung lobe was placed into a bead homogenizer tube with 1 ml of DMEM + 2% FBS. After homogenization, 300 µl of this mixture was placed in 1 ml Trizol (Invitrogen) for RNA extraction and analysis. The remaining volume of lung homogenates was cleared of debris by centrifugation (3,900g for 10 min). Infectious titres of SARS-CoV-2 were determined by plaque assay in Vero E6 (standard) or Vero ACE2⁺TMPRSS2⁺ (sensitive) cells in DMEM 4% FBS and 0.6% Avicel RC-581⁷¹. Plaques were resolved at 48 h after infection by fixing in 10% formaldehyde for 1 h followed by staining for 1 h in 0.5% crystal violet in 20% ethanol. Plates were rinsed in water to visualize plaques. Multiple dilutions of lung homogenates were used to quantify infectious titres (the minimum number of plaques that can be quantified is 10 per ml of lung homogenate or ml of supernatant). Viral titres from supernatants of BMDM cultures were determined by plaque assay in Vero ACE2⁺TMPRSS2⁺ (sensitive) cells according to the same protocols described for lung homogenates. VERO C1008 (Vero 76, clone E6, Vero E6)

were obtained from ATCC. Vero ACE2⁺TMPRSS2⁺ cells were obtained from B. Graham. None of the cell lines were authenticated or tested for mycoplasma contamination.

Viral RNA analysis

RNA was extracted using the RNeasy mini kit (Qiagen) according to the manufacturer's protocol. SARS-CoV-2 RNA levels were quantified using the Luna Universal Probe Onestep RT-qPCR kit (New England Biolabs) and US CDC real-time RT-PCR primer/probe sets for 2019-nCoV_N1. For each sample, 1 µg of RNA was used. Subgenomic viral RNA was quantified using primer and probe sets targeting the *E* gene as previously described^{40,63}. The primer/probe sequences were as follows: E_Sarbeco_F primer, ACAGGTACGTTAATAGTTAATAGCGT (400 nM per reaction); E_Sarbeco_probe_P1, FAM-ACACTAGCCATCCTTACTGCGCTTCG-BBQ (200 nM per reaction); E_Sarbeco_R primer ATATTGCAGCAGTACGCACACA (400 nM per reaction); E leader specific primer sgLead-F, CGATCTCTTAGATCTGTTCTC (400 nM per reaction).

Histology and immunofluorescence

Yale pathology provided assistance with embedding and sectioning of lung tissue. A pulmonary pathologist reviewed the slides in a blinded manner and identified immune cell infiltration and other related pathologies. Paraffin-embedded lung tissue (fixed in 4% paraformaldehyde (PFA) for no more than 24 h) sections were deparaffinized in xylene and rehydrated. After antigen retrieval with 10 mM sodium citrate (pH 6) and permeabilization with 0.1% Triton-X for 10 min, the slides were blocked with 5% BSA in PBS with 0.05% Tween-20 for 1 h. The samples were next stained with primary antibodies against SARS-CoV-2-dsRNA, SARS-CoV2-RNA-dependent RNA polymerase, SARS-CoV-2 spike, human CD68, human ACE2 and their isotype controls diluted in 1% BSA overnight at 2–8 °C. The next day, the samples were washed and incubated with fluorescent secondary antibodies. After washes, the samples were treated with TrueBlack lipofuscin autofluorescence quencher for 30 s and mounted onto DAPI mounting medium (Sigma-Aldrich). Images were acquired using the

Keyence BZ-X800 Fluorescence Microscope or Nikon ECLIPSE Ti Series Confocal Microscope. Pseudocolours were assigned for visualization. All histopathological assessment and scoring of H&E, trichrome and immunofluorescence staining were performed on blinded samples by a board-certified pathologist.

Isolation of cells and flow cytometry

All mice were analysed at approximately 9–14 weeks of age. Single-cell suspensions were prepared from blood, spleen, bronchioalveolar lavage and lungs. Mice were euthanized with 100% isoflurane. Bronchioalveolar lavage was performed using standard methods with a 22G Catheter (BD). Blood was collected either retro-orbitally or by cardiac puncture after euthanasia. Bronchioalveolar lavage was performed using standard methods with a 22G Catheter (BD)⁷². Lungs were collected, minced and incubated in a digestion cocktail containing 1 mg ml⁻¹ collagenase D (Sigma-Aldrich) and 30 µg ml⁻¹ DNase I (Sigma-Aldrich) in RPMI at 37 °C for 20 min with gentle shaking. Tissue was then filtered through a 70 or 100 µm filter. Cells were treated with ammonium-chloride-potassium buffer and resuspended in PBS with 1% FBS. Mononuclear cells were incubated at 4 °C with human (BD) and mouse (BioxCell, BE0307) Fc block for 10 min. After washing, primary antibody staining was performed at 4 °C for 20 min. After washing with PBS, cells were fixed using 4% PFA. For intracellular staining, cells were washed with BD permeabilization buffer and stained in the same buffer for 45 min at room temperature. Samples were analysed on an LSRII flow cytometer (BD Biosciences). Data were analysed using FlowJo software. Experimenters were not blinded to group allocation during sample collection of flow cytometric studies but were blinded during data analysis.

For cell sorting experiments, single-cell suspensions from digested lungs were stained with antibodies against human CD45, mouse CD45, mouse EPCAM and sorted using the BD FACS Aria II contained within a Baker BioProtect IV Biological Safety Cabinet. Cell viability was assessed with DAPI when applicable.

For imaging flow cytometry, cells from SARS-CoV-2-infected humanized mice were sorted on the basis of human immune cells (hCD45⁺); mouse

immune cells (mCD45^+) or epithelial mouse cells (EPCAM^+). A $^-$ mNG^+ epithelial cells (SARS-CoV-2-mNG $^+$ mCD45(PE) $^-$ EPCAM(APC) $^+$ hCD45(PB) $^-$; B-total mouse immune cells ($\text{mCD45(PE)}^+\text{EPCAM(APC)}^-\text{hCD45(PB)}^-$; C $^-$ mNG^+ human immune cells (SARS-CoV-2-mNG $^+$ mCD45(PE) $^-$ EPCAM(APC) $^-$ hCD45(PB) $^+$); D $^-$ mNG^- human immune cells (SARS-CoV-2-mNG $^-$ mCD45(PE) $^-$ EPCAM(APC) $^-$ hCD45(PB) $^+$). These sorted cells (epithelial or immune cells) were fixed in 4% PFA for at least 30 min. Fixed sorted cells (epithelial or immune cells) were permeabilized, stained with unconjugated primary antibodies against ASC (1:200, rabbit), NLRP3 (1:200, goat), then stained with secondary antibodies (donkey anti-rabbit or goat conjugated with AlexaFluor 546 or 647, at 1:1,000). Cells data were acquired using the ImageStream X MKII (Amnis) system with $\times 63$ magnification and analysed using Ideas software (Amnis). ASC, NLRP3 specks were gated and quantified on the basis of fluorophore intensity/maximum pixels. For FLICA–caspase-1 colocalization, macrophages were pretreated with FLICA before sorting.

In vitro infection of human macrophages with SARS-CoV-2

Using aseptic techniques under sterile conditions, bone marrow cells were isolated from femurs of immune-reconstituted MISTRG6 mice. For differentiation into human macrophages in vitro, bone marrow cells were incubated in medium supplemented with 10% FBS, 1% penicillin-streptomycin and recombinant human M-CSF (50 ng ml $^{-1}$), GM-CSF (50 ng ml $^{-1}$) and IL-4 (20 ng ml $^{-1}$) at 1×10^6 per ml concentration for 6 days in an incubator under 5% CO $_2$ and at 37 °C. Medium supplemented with 10% FBS was replenished with new medium every 3–4 days. Before infection with SARS-CoV-2, these bone-marrow-derived macrophages were monitored for granularity, elongated morphology and stronger adherence to the plate. Purity of cultures was confirmed by flow cytometry. Human macrophages were then cultured with SARS-CoV-2-mNG in the presence or absence of the plasma of patients with COVID-19 or healthy individuals, monoclonal antibodies (mix of clones 135 and 144, described as therapeutics), remdesivir, anti-CD16 antibodies, anti-ACE2 antibodies, control isotype antibodies, caspase-1 inhibitor (VX-765⁷³) or NLRP3 inhibitor (MCC950).

Human BMDMs in vitro or human lung macrophages ex vivo were cultured with a viral inoculum at 10^4 PFU of SARS-CoV-2-mNG (multiplicity of infection of around 0.1). These macrophage cultures were then incubated at 37 °C under 5% CO₂ for 24, 48 and 72 h at which time cells were collected. Cells were dissociated from the culture plate with 10 mM EDTA or Accutase (Thermo Fisher Scientific) cell dissociation reagent (10–20 min). For studies pertaining to the mechanism of viral entry, viral replication and inflammasome activation, infected macrophages were treated with remdesivir (10 µM), anti-CD16 (Abcam clone, 10 µg ml⁻¹) and anti-ACE2 (10 µg ml⁻¹), caspase-1 inhibitor (VX765, 20 µM) and NLRP3 inhibitor (MCC950, 20 µg ml⁻¹) in culture. Cells were stained when applicable and fixed for 30 min with 4% PFA. Convalescent plasma samples from the top 30 neutralizers in a cohort of 148 individuals were pooled to create a mixture with an NT₅₀ titre of 1,597 against HIV-1 pseudotyped with SARS-CoV-2 S protein⁴⁵. We used this pooled serum at a concentration of 5 µl plasma per ml for in vitro experiments and refer to it as plasma from patients with COVID-19. Healthy plasma was collected from healthy volunteers and pooled before the COVID-19 pandemic and was used at a concentration of 5 µl plasma per ml. Monoclonal antibodies (a mix of clones 135 and 144) were used at 4 µg per ml concentration.

Zombie Aqua and annexin V staining

Single-cell suspensions from in vitro cultures or enzymatically dissociated lungs were washed and stained for viability with Zombie Aqua (BioLegend, 423101) in PBS (1:400) for 15 min at 4 °C. Without washing the cells, cell surface antibody cocktail was added, and cells were incubated for another 15 min. Cells were then washed with PBS twice and resuspended in annexin V binding buffer. Cells were stained with annexin V PE (1:400) in binding buffer for 15 min at 4 °C. Cells were then washed with annexin V buffer and fixed in 4% PFA.

FLICA assay

Single-cell suspensions from in vitro cultures or enzymatically dissociated lungs were resuspended in RPMI 10% FBS with FLICA substrate (BioRad-

FLICA 660 caspase-1 kit- ICT9122) and cultured for 1 h (for microscopy) or 30 min (for flow cytometry) at 37 °C. Cells were then washed twice with PBS and stained with Zombie Aqua and annexin V as described. Cells were then fixed with 1× Fixative (provided in the BioRad-FLICA caspase-1 kit) for at least 1 h, but not exceeding 16 h. Cells were kept at 4 °C until further staining and analysis. The FLICA 660 caspase-1 kit uses a target sequence (YVAD) sandwiched between a far-red fluorescent 660 dye (excitation max 660 nm, emission max 685 nm).

LDH measurement

LDH levels were measured from freshly collected supernatant of infected cells (BMDMs) or freshly collected serum using the CyQUANT LDH Cytotoxicity Assay (Thermo Fisher Scientific, C20300) according to the manufacturer's instructions under BSL3 conditions.

Human samples

For this study we acquired six control uninfected, and two SARS-CoV-2-infected deidentified lung (4 different cuts) samples as paraffin-embedded tissues from autopsies of individuals admitted to Yale New Haven Hospital. Lungs were fixed in 10% formalin (details of patient samples are provided in Supplementary Table 5).

Cytokine, chemokine and IgG quantification

Human IL-18 (Sigma-Aldrich or RND), human CXCL10 (RND), human IL-1RA (Abcam), human gasdermin D (MyBioSource) were quantified from supernatants of BMDMs infected (or not) with SARS-CoV-2-mNG or from serum or lung homogenates of SARS-CoV-2-mNG-infected (or not) MISTRG6 or MISTRG6-hACE2 mice according to the manufacturer's instructions. Human IL-1 β was quantified from supernatants of BMDMs infected with SARS-CoV-2-mNG using the cytometric bead array for human IL-1B (BD) according to the manufacturer's instructions. Human anti-spike-RBD IgG (BioLegend) was quantified from sera and lung homogenates of infected or uninfected MISTRG6-hACE2 mice.

Antibodies

Flow cytometry

All antibodies used in flow cytometry were obtained from BioLegend, unless otherwise specified.

Antibodies against the following antigens were used for characterization or isolation of cells by flow cytometry. Mouse antigens: CD45 (30-F11, 103130), CD45 (30-F11, 103108), CD45 (30-F11, 103147), CD326 (G8.8, 118218), F4/80 (BM8, 123117). Human antigens: CD45 (H130, 304044), CD45 (H130, 304029), CD3 (UCHT1, 300408), CD14 (HCD14, 325620), CD16 (3G8, 302030), CD16 (3G8, 302006), CD19 (HIB19, 302218), CD19 (HIB19, 302226), CD33 (WM53, 983902), CD20 (2H7, 302313), CD20 (2H7, 302322), CD206 (Clone15-2, 321106), CD206 (15-2, 321109), CD86 (BU63, 374210), CD123 (6H6, 306006), CD11B (M1/70, 101242), CD11C (3.9, 301608), HLA-DR (LN3, 327014), HLA-DR (LN3, 327020), HLA-DR (LN3, 327005), CD183 (G025H7, 353720), CD335-NKp46 (9E2, 331916), CD4 (OKT4, 317440), CD8 (SK1, 344718), CD8 (SK1, 344748), CD68 (YI/82A, 333828).

Immunofluorescence

Anti-dsRNA antibodies (rJ2) were purchased from Sigma-Aldrich (MABE1134) or Antibodies online (Ab01299-23.0). Polyclonal SARS-CoV-2 RNA-dependent RNA polymerase antibodies were purchased from Cell Signaling (67988S). Monoclonal SARS-CoV-2 RNA-dependent RNA polymerase antibodies were purchased from Kerafest (ESG004). Anti-spike (spike 1) antibodies (1A9, GTX632604) were obtained from GeneTex. Anti-spike (spike 2) antibodies (T01Khu, 703958) were obtained from Thermo Fisher Scientific.

Imaging flow cytometry

Mouse anti-human PE-Cy7 CD16 (3G8) was purchased from BioLegend (302016). Rabbit anti-human ASC (polyclonal) was purchased from Santa

Cruz (sc-22514-R). Goat anti-human NLRP3 (polyclonal) was purchased from Abcam (ab4207). Donkey anti-rabbit IgG (H+L) highly cross-adsorbed secondary antibody (Polyclonal) was purchased from Thermo Fisher Scientific (A-31573). Donkey anti-rabbit IgG (H+L) cross-adsorbed secondary antibody (polyclonal) was purchased from Thermo Fisher Scientific (A-10040). Donkey anti-goat IgG (H+L) cross-adsorbed secondary antibody (polyclonal) was purchased from Thermo Fisher Scientific (A-21447).

Therapeutic antibodies

Monoclonal antibodies against human CD16 used in blocking experiments were purchased from Abcam (SP175). Monoclonal antibodies against human ACE2 were purchased from Abcam. Anti-CD16 antibodies used in depletion experiments was purchased from Thermo Fisher Scientific (3G8). Monoclonal antibodies (clones 135 and 144) were acquired from M. Nussenzweig as previously described⁴⁵. Anti-IFNAR2 antibodies were purchased from PBL Assay science (21385-1).

Gene expression

RNA was extracted using the RNeasy mini kit (Qiagen) according to the manufacturer's protocol. The High-Capacity cDNA Reverse Transcription Kit was used to make cDNA. Quantitative PCR with reverse transcription was performed using the SYBR FAST universal qPCR kit (KAPA Biosystems). Predesigned KiCqStart primers for *DDX58*, *IL6*, *IFITM3*, *IRF7*, *IFIH1*, *IFNA6*, *IFNG* and *HPRT1* were purchased from Sigma-Aldrich.

Bulk whole-tissue RNA-seq analysis

RNA isolated from homogenized lung tissue, also used for viral RNA analysis, was prepared for whole-tissue transcriptome analysis using low input (14 d.p.i.) or conventional (28 d.p.i.) bulk RNA sequencing (RNA-seq). Libraries were generated with the help of the Yale Center for Genomic Analysis. In brief, libraries were prepared using the Illumina rRNA depletion kit and sequenced on a NovaSeq system. Raw sequencing reads

were aligned to the human–mouse combined genome with STAR⁷⁴, annotated and counted with HTSeq⁷⁵, normalized using DESeq2⁷⁶ and graphed using the Broad Institute Morpheus web tool. Heat maps visualize normalized counts of duplicates as minimum–maximum-transformed values, calculated by subtracting the row mean and diving by the s.d. for each gene. Rows (genes) were clustered by hierarchical clustering (1 – Pearson) or k -means clustering as indicated in the figure legends. Differential expression analysis was also performed with DESeq2. For IFN-stimulated gene identification, <http://www.interferome.org> was used with parameters -In Vivo, -Mus musculus or Homo sapiens -fold change up 2 and down 2.

10x Genomics scRNA-seq

Sorted human lung immune cells (hCD45⁺ in uninfected, 14 d.p.i. and 28 d.p.i.) were stained with TotalSeq (TotalSeq, B0251, anti-human hashtag 1 antibody, GTCAACTCTTAGCG; TotalSeq, B0252, anti-human hashtag 2 antibody, TGATGGCCTATTGGG) antibodies (BioLegend) before processing for droplet-based single-cell RNA-seq (scRNA-seq). Single-cell transcriptomes and associated protocols of 4 d.p.i. lungs (total lung cells as opposed to sorted human immune cells analysed) were previously described¹⁹. Duplicates from each condition/time point were pooled in equal numbers to ensure 10,000 cells were encapsulated into droplets using 10x Chromium GEM technology. Libraries were prepared in house using the Chromium Next GEM Single Cell 3' Reagent Kits v.3.1 (10x Genomics). scRNA-seq libraries were sequenced using the Nova-Seq system. Raw sequencing reads were processed with Cell Ranger v.3.1.0 using a human–mouse combined reference to generate a gene–cell count matrix. To distinguish between human and mouse cells, we counted the number of human genes (nHuman) and mouse genes (nMouse) with non-zero expression in each cell, and selected cells with nHuman > 20 × nMouse as human cells. The count matrix of human cells and human genes was used in the downstream analysis using Seurat (v.3.2)⁶². Specifically, this matrix was filtered to remove low-quality cells, retaining cells with >200 and <5,000 detected genes and <20% mitochondrial transcripts. We then log-normalized each entry of the matrix by computing $\log[CPM/100 + 1]$, where CPM is the counts per million. To visualize the cell subpopulations in two dimensions, we applied principal component analysis followed by t-SNE, a nonlinear

dimensionality reduction method, to the log-transformed data. Graph-based clustering was then used to generate clusters that were overlaid on the *t*-SNE coordinates to investigate cell subpopulations. Marker genes for each cluster of cells were identified using the Wilcoxon test (two-tailed, rank-sum) with Seurat. For adjusted *P* values, Bonferroni correction was used. In this analysis, 438 cells (uninfected), 336 cells (4 d.p.i.), 793 cells (14 d.p.i.) and 1,368 (28 d.p.i.) cells were included.

To identify DA subpopulations that were not restricted to clusters, we applied DA-seq⁶¹, a targeted, multiscale approach that quantifies a local DA measure for each cell for comprehensive and accurate comparisons of transcriptomic distributions of cells. DA measure defined by DA-seq shows how much a cell's neighbourhood is enriched by the cells from either uninfected or infected lungs. DA-seq analysis of our data revealed that T cells, monocytes and macrophages were responsible for most of the chronic infection driven changes. Red colouring marks enrichment at 28 d.p.i. lungs and blue colouring marks enrichment in uninfected lungs.

To combine cells from different d.p.i. (uninfected, 4 d.p.i., 14 d.p.i., 28 d.p.i.), we applied the integration method⁶² in Seurat to remove batch effects. We then performed principal component analysis and retained the top 30 PCs as the input to *t*-SNE, a nonlinear dimensionality reduction method, to embed the data onto two-dimensional space for visualization. Graph-based clustering with a resolution of 0.8 was then used to generate clusters that were overlaid on the *t*-SNE coordinates to investigate cell subpopulations. Marker genes for each cluster of cells were identified using the Wilcoxon test (two-tailed, rank-sum) with Seurat (for the adjusted *P* values, Bonferroni correction was used). After cell type identification, we separated out macrophage populations from all d.p.i., and applied the same procedures as described above to reprocess and visualize the data. Clusters were redefined based on a resolution of 0.3.

Statistics and reproducibility

Unpaired or paired *t*-tests (always two-tailed) were used to determine statitical significance for changes in immune cell frequencies and numbers while comparing infected mice with uninfected control mice or treated mice with

untreated mice. To determine whether the viral RNA quantification was statistically significant across treatment groups or timepoints, two-tailed Mann–Whitney *U*-tests were used. Unpaired *t*-tests (two-tailed) or ratio paired *t*-tests (two-tailed) were used to determine whether the viral titre quantification of the untreated condition was significantly different from the treated groups. For the Pearson test, significance was deemed using *t*-test. The test statistic is based on Pearson's product-moment correlation coefficient $\text{cor}(x, y)$ and follows a *t*-distribution with $\text{length}(x) - 2$ d.f. For Spearman tests, *P* values were computed using algorithm AS 89 with exact = TRUE. All micrographs presented in the study were representative of at least 3 animals or samples. Each experiment was repeated independently at least twice. All attempts yielded similar results. In the *in vivo* studies, each dot represents a biologically independent mouse.

Reporting summary

Further information on research design is available in the [Nature Research Reporting Summary](#) linked to this paper.

Data availability

All data supporting the findings of this study are available within the Article and the [Supplementary Information](#). All 10x Genomics single-cell RNA-seq and bulk RNA-seq data supporting the findings of this study have been deposited at the Gene Expression Omnibus (GEO) under accession codes [GSE186794](#) and [GSE199272](#). [Source data](#) are provided with this paper.

References

1. Gaebler, C. et al. Evolution of antibody immunity to SARS-CoV-2. *Nature* **591**, 639–644 (2021).
2. Acharya, D., Liu, G. & Gack, M. U. Dysregulation of type I interferon responses in COVID-19. *Nat. Rev. Immunol.* **20**, 397–398 (2020).
3. Pairo-Castineira, E. et al. Genetic mechanisms of critical illness in COVID-19. *Nature* **591**, 92–98 (2020).

4. Nienhold, R. et al. Two distinct immunopathological profiles in autopsy lungs of COVID-19. *Nat. Commun.* **11**, 5086 (2020).
5. Zhou, Z. et al. Heightened innate immune responses in the respiratory tract of COVID-19 patients. *Cell Host Microbe* **27**, 883–890 (2020).
6. Dolan, M. E. et al. Investigation of COVID-19 comorbidities reveals genes and pathways coincident with the SARS-CoV-2 viral disease. *Sci. Rep.* **10**, 20848 (2020).
7. Delorey, T. M. et al. COVID-19 tissue atlases reveal SARS-CoV-2 pathology and cellular targets. *Nature* **595**, 107–113 (2021).
8. Singanayagam, A. et al. Duration of infectiousness and correlation with RT-PCR cycle threshold values in cases of COVID-19, England, January to May 2020. *Euro Surveill.* **25**, 2001483 (2020).
9. Decker, A. et al. Prolonged SARS-CoV-2 shedding and mild course of COVID-19 in a patient after recent heart transplantation. *Am. J. Transplant.* **20**, 3239–3245 (2020).
10. Jeong, H. W. et al. Viable SARS-CoV-2 in various specimens from COVID-19 patients. *Clin. Microbiol. Infect.* **26**, 1520–1524 (2020).
11. Liu, W. D. et al. Prolonged virus shedding even after seroconversion in a patient with COVID-19. *J. Infect.* **81**, 318–356 (2020).
12. van Kampen, J. J. A. et al. Duration and key determinants of infectious virus shedding in hospitalized patients with coronavirus disease-2019 (COVID-19). *Nat. Commun.* **12**, 267 (2021).
13. Folgueira, M. D., Luczkowiak, J., Lasala, F., Perez-Rivilla, A. & Delgado, R. Prolonged SARS-CoV-2 cell culture replication in respiratory samples from patients with severe COVID-19. *Clin. Microbiol. Infect.* **27**, 886–891 (2021).
14. Lucas, C. et al. Longitudinal analyses reveal immunological misfiring in severe COVID-19. *Nature* **584**, 463–469 (2020).

15. Del Valle, D. M. et al. An inflammatory cytokine signature predicts COVID-19 severity and survival. *Nat. Med.* **26**, 1636–1643 (2020).
16. Wu, C. et al. Risk factors associated with acute respiratory distress syndrome and death in patients with coronavirus disease 2019 pneumonia in Wuhan, China. *JAMA Intern. Med.* **180**, 934–943 (2020).
17. Rodrigues, T. S. et al. Inflammasomes are activated in response to SARS-CoV-2 infection and are associated with COVID-19 severity in patients. *J. Exp. Med.* **218**, e20201707 (2021).
18. Henry, B. M. et al. Lactate dehydrogenase levels predict coronavirus disease 2019 (COVID-19) severity and mortality: a pooled analysis. *Am. J. Emerg. Med.* **38**, 1722–1726 (2020).
19. Sefik, E. et al. A humanized mouse model of chronic COVID-19. *Nat. Biotechnol.* <https://doi.org/10.1038/s41587-021-01155-4> (2021).
20. Grant, R. A. et al. Circuits between infected macrophages and T cells in SARS-CoV-2 pneumonia. *Nature* **590**, 635–641 (2021).
21. Beigel, J. H. et al. Remdesivir for the treatment of COVID-19—final report. *N. Engl. J. Med.* **383**, 1813–1826 (2020).
22. Pruijssers, A. J. et al. Remdesivir inhibits SARS-CoV-2 in human lung cells and chimeric SARS-CoV expressing the SARS-CoV-2 RNA polymerase in mice. *Cell Rep.* **32**, 107940 (2020).
23. Yin, W. et al. Structural basis for inhibition of the RNA-dependent RNA polymerase from SARS-CoV-2 by remdesivir. *Science* **368**, 1499–1504 (2020).
24. Havervall, S. et al. Symptoms and functional impairment assessed 8 months after mild COVID-19 among health care workers. *JAMA* **325**, 2015–2016 (2021).
25. Nasserie, T., Hittle, M. & Goodman, S. N. Assessment of the frequency and variety of persistent symptoms among patients with COVID-19: a systematic review. *JAMA Netw. Open* **4**, e2111417 (2021).

26. Ginestra, J. C., Mitchell, O. J. L., Anesi, G. L. & Christie, J. D. COVID-19 critical illness: a data-driven review. *Annu. Rev. Med.* **73**, 95–111 (2022).
27. Phetsouphanh, C. et al. Immunological dysfunction persists for 8 months following initial mild-to-moderate SARS-CoV-2 infection. *Nat. Immunol.* **23**, 210–216 (2022).
28. Basile, K. et al. Cell-based culture of SARS-CoV-2 informs infectivity and safe de-isolation assessments during COVID-19. *Clin. Infect. Dis.* <https://doi.org/10.1093/cid/ciaa1579> (2020).
29. Vora, S. M., Lieberman, J. & Wu, H. Inflammasome activation at the crux of severe COVID-19. *Nat. Rev. Immunol.* **21**, 694–703 (2021).
30. Major, J. et al. Type I and III interferons disrupt lung epithelial repair during recovery from viral infection. *Science* **369**, 712–717 (2020).
31. The RECOVERY Collaborative Group. Dexamethasone in hospitalized patients with Covid-19—preliminary report. *N. Engl. J. Med.* **384**, 693–704 (2020).
32. Polak, S. B., Van Gool, I. C., Cohen, D., von der Thesen, J. H. & van Paassen, J. A systematic review of pathological findings in COVID-19: a pathophysiological timeline and possible mechanisms of disease progression. *Mod. Pathol.* **33**, 2128–2138 (2020).
33. Tian, S. et al. Pathological study of the 2019 novel coronavirus disease (COVID-19) through postmortem core biopsies. *Mod. Pathol.* **33**, 1007–1014 (2020).
34. Menter, T. et al. Postmortem examination of COVID-19 patients reveals diffuse alveolar damage with severe capillary congestion and variegated findings in lungs and other organs suggesting vascular dysfunction. *Histopathology* **77**, 198–209 (2020).
35. Barton, L. M., Duval, E. J., Stroberg, E., Ghosh, S. & Mukhopadhyay, S. Covid-19 autopsies, Oklahoma, USA. *Am. J. Clin. Pathol.* **153**, 725–733 (2020).

36. Xu, Z. et al. Pathological findings of COVID-19 associated with acute respiratory distress syndrome. *Lancet Respir. Med.* **8**, 420–422 (2020).
37. Strunz, M. et al. Alveolar regeneration through a Krt8⁺ transitional stem cell state that persists in human lung fibrosis. *Nat. Commun.* **11**, 3559 (2020).
38. Kobayashi, Y. et al. Persistence of a regeneration-associated, transitional alveolar epithelial cell state in pulmonary fibrosis. *Nat. Cell Biol.* **22**, 934–946 (2020).
39. Choi, J. et al. Inflammatory signals induce AT2 cell-derived damage-associated transient progenitors that mediate alveolar regeneration. *Cell Stem Cell* **27**, 366–382 e367 (2020).
40. Wolfel, R. et al. Virological assessment of hospitalized patients with COVID-2019. *Nature* **581**, 465–469 (2020).
41. Xie, X. et al. An infectious cDNA clone of SARS-CoV-2. *Cell Host Microbe* **27**, 841–848 (2020).
42. Hassan, A. et al. A SARS-CoV-2 infection model in mice demonstrates protection by neutralizing antibodies. *Cell* **182**, 744–753 (2020).
43. Muus, C. et al. Single-cell meta-analysis of SARS-CoV-2 entry genes across tissues and demographics. *Nat. Med.* **27**, 546–559 (2021).
44. Bournazos, S., Gupta, A. & Ravetch, J. V. The role of IgG Fc receptors in antibody-dependent enhancement. *Nat. Rev. Immunol.* **20**, 633–643 (2020).
45. Davide, F. R. et al. Convergent antibody responses to SARS-CoV-2 in convalescent individuals. *Nature* **584**, 437–442 (2020).
46. Bournazos, S. & Ravetch, J. V. Fc γ receptor function and the design of vaccination strategies. *Immunity* **47**, 224–233 (2017).
47. Chakraborty, S. et al. Proinflammatory IgG Fc structures in patients with severe COVID-19. *Nat. Immunol.* **22**, 67–73 (2021).

48. Hoepel, W. et al. High titers and low fucosylation of early human anti-SARS-CoV-2 IgG promote inflammation by alveolar macrophages. *Sci. Transl. Med.* **13**, eabf8654 (2021).
49. Larsen, M. D. et al. Afucosylated IgG characterizes enveloped viral responses and correlates with COVID-19 severity. *Science* **371**, eabc8378 (2021).
50. Evren, E. et al. Distinct developmental pathways from blood monocytes generate human lung macrophage diversity. *Immunity* **54**, 259–275 (2021).
51. Hadjadj, J. et al. Impaired type I interferon activity and inflammatory responses in severe COVID-19 patients. *Science* **369**, 718–724 (2020).
52. Chua, R. L. et al. COVID-19 severity correlates with airway epithelium-immune cell interactions identified by single-cell analysis. *Nat. Biotechnol.* **38**, 970–979 (2020).
53. Lei, X. et al. Activation and evasion of type I interferon responses by SARS-CoV-2. *Nat. Commun.* **11**, 3810 (2020).
54. Zhang, J. Y. et al. Single-cell landscape of immunological responses in patients with COVID-19. *Nat. Immunol.* **21**, 1107–1118 (2020).
55. Allen, I. C. et al. The NLRP3 inflammasome mediates in vivo innate immunity to influenza A virus through recognition of viral RNA. *Immunity* **30**, 556–565 (2009).
56. Thomas, P. G. et al. The intracellular sensor NLRP3 mediates key innate and healing responses to influenza A virus via the regulation of caspase-1. *Immunity* **30**, 566–575 (2009).
57. Pothlichet, J. et al. Type I IFN triggers RIG-I/TLR3/NLRP3-dependent inflammasome activation in influenza A virus infected cells. *PLoS Pathog.* **9**, e1003256 (2013).
58. Ferreira, A. C. et al. SARS-CoV-2 engages inflammasome and pyroptosis in human primary monocytes. *Cell Death Discov.* **7**, 43

(2021).

59. Pan, P. et al. SARS-CoV-2 N protein promotes NLRP3 inflammasome activation to induce hyperinflammation. *Nat. Commun.* **12**, 4664 (2021).
60. Xu, H. et al. SARS-CoV-2 viroporin encoded by ORF3a triggers the NLRP3 inflammatory pathway. *Virology* **568**, 13–22 (2022).
61. Zhao, J. et al. Detection of differentially abundant cell subpopulations in scRNA-seq data. *Proc. Natl Acad. Sci. USA* **118**, e2100293118 (2021).
62. Stuart, T. et al. Comprehensive integration of single-cell data. *Cell* **177**, 1888–1902 (2019).
63. Corman, V. M. et al. Detection of 2019 novel coronavirus (2019-nCoV) by real-time RT-PCR. *Euro Surveill.* **25**, 2000045 (2020).
64. Schäfer, A. et al. Antibody potency, effector function, and combinations in protection and therapy for SARS-CoV-2 infection *in vivo*. *J. Exp. Med.* **218**, e20201993 (2020).
65. Yu, H. et al. A novel humanized mouse model with significant improvement of class-switched, antigen-specific antibody production. *Blood* **129**, 959–969 (2017).
66. Rongvaux, A. et al. Development and function of human innate immune cells in a humanized mouse model. *Nat. Biotechnol.* **32**, 364–372 (2014).
67. Israelow, B. et al. Mouse model of SARS-CoV-2 reveals inflammatory role of type I interferon signaling. *J. Exp. Med.* **217**, e20201241 (2020).
68. Coll, R. C. et al. A small-molecule inhibitor of the NLRP3 inflammasome for the treatment of inflammatory diseases. *Nat. Med.* **21**, 248–255 (2015).

69. Perera, A. P. et al. MCC950, a specific small molecule inhibitor of NLRP3 inflammasome attenuates colonic inflammation in spontaneous colitis mice. *Sci. Rep.* **8**, 8618 (2018).
70. Dixon, K. O. et al. TIM-3 restrains anti-tumour immunity by regulating inflammasome activation. *Nature* **595**, 101–106 (2021).
71. Wei, J. et al. Genome-wide CRISPR screens reveal host factors critical for SARS-CoV-2 infection. *Cell* **184**, 76–91 (2020).
72. Sun, F., Xiao, G. & Qu, Z. Murine bronchoalveolar lavage. *Bio Protoc.* **7**, e2287 (2017).
73. Stack, J. H. et al. IL-converting enzyme/caspase-1 inhibitor VX-765 blocks the hypersensitive response to an inflammatory stimulus in monocytes from familial cold autoinflammatory syndrome patients. *J. Immunol.* **175**, 2630–2634 (2005).
74. Dobin, A. et al. STAR: ultrafast universal RNA-seq aligner. *Bioinformatics* **29**, 15–21 (2013).
75. Anders, S., Pyl, P. T. & Huber, W. HTSeq-a Python framework to work with high-throughput sequencing data. *Bioinformatics* **31**, 166–169 (2015).
76. Love, M. I., Huber, W. & Anders, S. Moderated estimation of fold change and dispersion for RNA-seq data with DESeq2. *Genome Biol.* **15**, 550 (2014).

Acknowledgements

The generation of the original MISTRG6 model was supported by the Bill and Melinda Gates Foundation. We thank G. Yancopoulos, D. Valenzuela, A. Murphy, and W. Auerbach at Regeneron Pharmaceuticals who generated, in collaboration with our groups, the individual knockin alleles combined in MISTRG; M. Chiorazzi, I. Odell and W. Philbrick and all of the other members of the Flavell laboratory for discussions and comments; J. Alderman, B. Cadugan and E. Hughes-Picard for administrative assistance;

B. Cadugan and E. Eynon for manuscript editing; P. Ranney, C. Hughes for mouse colony management; D. Urbanos for human CD34⁺ cell isolation; L. Devine and E. Manet for help with cell sorting; B. Fontes and M. Schniederberend for biosafety guidance and training; R. Filler for help with viral stocks and cell lines. E. Sefik is a HHMI Fellow of the Damon Runyon Cancer Research Foundation (DRG-2316-18). H.R.S was supported by an NSF Graduate Research Fellowship Program under DGE1752134. This work was funded by the Howard Hughes Medical Institute (to R.A.F., M.N. and A.I.). This study was also supported in part by awards from National Institute of Health grants R35 GM142687 (to Y.G.C.), R01AI157488 (to A.I.), 2T32AI007517 (to B.I.), R01 AI061093 (to E.M.), AI118855 (to E.M.), CA016359 (to E.M.), K08 AI128043 (to C.B.W.), U01 CA260507 (to S.H.), Animal Modeling Core of the Yale Cooperative Center of Excellence in Hematology at Yale University School of Medicine U54 DK106857 (S.H., R.A.F.), R01 GM131642 and GM135928 (to R.A.F. and Y.K.), the Burroughs Wellcome Fund (to C.B.W.), the Patterson Foundation (to C.B.W.), a Fast Grant from Emergent Ventures at the Mercatus Center (to A.I. and C.B.W.), the Mathers Foundation (to A.I., C.B.W. and E.M.), the Ludwig Family Foundation (to A.I. and C.B.W.), the Harvard Lemann Brazil Research Fund (to J.L.) and the Rita Allen Foundation (to Y.G.C.).

Author information

Authors and Affiliations

1. Department of Immunobiology, Yale University School of Medicine, New Haven, CT, USA

Esen Sefik, Rihao Qu, Eleanna Kaffe, Haris Mirza, Jun Zhao, J. Richard Brewer, Ailin Han, Holly R. Steach, Benjamin Israelow, Holly N. Blackburn, Sofia E. Velazquez, Y. Grace Chen, Akiko Iwasaki, Eric Meffre, Craig B. Wilen & Richard A. Flavell

2. Department of Pathology, Yale University School of Medicine, New Haven, CT, USA

Rihao Qu, Haris Mirza, Jun Zhao, Stephanie Halene & Yuval Kluger

3. Computational Biology and Bioinformatics Program, Yale University,
New Haven, CT, USA

Rihao Qu

4. Program in Cellular and Molecular Medicine, Boston Children's
Hospital, Boston, MA, USA

Caroline Junqueira & Judy Lieberman

5. Department of Pediatrics, Harvard Medical School, Boston, MA, USA

Caroline Junqueira & Judy Lieberman

6. Instituto René Rachou, Fundação Oswaldo Cruz, Belo Horizonte,
Brazil

Caroline Junqueira

7. Department of Surgery, Yale University School of Medicine, New
Haven, CT, USA

Holly N. Blackburn

8. Section of Hematology, Yale Cancer Center and Department of Internal
Medicine, Yale University School of Medicine, New Haven, CT, USA

Stephanie Halene

9. Howard Hughes Medical Institute, Yale University School of Medicine,
New Haven, CT, USA

Akiko Iwasaki & Richard A. Flavell

10. Laboratory of Molecular Immunology, The Rockefeller University,
New York, NY, USA

Michel Nussenzweig

11. Howard Hughes Medical Institute, The Rockefeller University, New York, NY, USA

Michel Nussenzweig

12. Department of Laboratory Medicine, Yale University School of Medicine, New Haven, CT, USA

Craig B. Wilen

13. Program of Applied Mathematics, Yale University, New Haven, CT, USA

Yuval Kluger

Contributions

E.S. conceived the project, performed experiments, analysed the data and wrote the manuscript. R.Q. and J.Z. performed bioinformatics analysis. C.J. performed imaging flow cytometry experiments for characterization of the NLRP3 inflammasome. E.K. prepared samples for histopathological assessment and performed all immunofluorescence staining. H.M. performed histopathological assessment of lung pathology, quantification of immunofluorescence staining and offered essential conceptual insights in interpreting lung pathology. B.I. helped to establish the model in biosafety level 3. M.N. provided monoclonal antibodies used in the study. H.N.B. helped with tissue preparation and immunofluorescence staining. S.V. provided help with IL-1 quantification protocols. Y.G.C. provided protocols and insights on dsRNA staining. J.R.B., A.H., H.R.S., S.H., A.I., E.M., M.N., J.L., C.B.W. and Y.K. offered conceptual insights, contributed to the overall interpretation of this work and helped with writing the manuscript. R.A.F. co-conceived and supervised the project, helped to interpret the work and supervised the writing of the manuscript.

Corresponding author

Correspondence to [Richard A. Flavell](#).

Ethics declarations

Competing interests

R.A.F. is an advisor to Glaxo Smith Kline, Zai Labs and Ventus Therapeutics. J.L. is an advisor of Ventus Therapeutics. S.H. is a consultant for FORMA Therapeutics. The other authors declare no competing interests.

Peer review

Peer review information

Nature thanks Stanley Perlman, Gestur Vidarsson and the other, anonymous, reviewer(s) for their contribution to the peer review of this work.

Additional information

Publisher's note Springer Nature remains neutral with regard to jurisdictional claims in published maps and institutional affiliations.

Extended data figures and tables

Extended Data Fig. 1 Targeting viral replication and the downstream interferon response attenuates the hyperactive immune/inflammatory response (matched to figure 1).

a. Representative gating strategy of human immune cells in the lungs of SARS-CoV-2 infected MISTRG6-hACE2 mice. Cells isolated from lungs or bronchioalveolar lavage (BAL) were stained with antibodies against human CD45, HLA-DR, CD68, CD16, CD14, CD206, CD86, CD11B, CD11C, CD123, CD3, and mouse CD45. Cell numbers were calculated using counting beads. **b.** Human immune cells (numbers) in BAL (14 d.p.i.) or lungs (14 and 28 d.p.i.) of SARS-CoV-2 infected MISTRG6-hACE2 mice treated with dexamethasone (Dex), Remdesivir (RDV), anti-IFNAR2 or a combined therapy of Remdesivir (RDV) and anti-IFNAR2. 14 d.p.i., BAL: CTRL-infected n = 5; Dex, RDV, anti-IFNAR2 n = 3; anti-IFNAR2+RDV n = 4 biologically independent mice examined over 2 independent experiments. 14 d.p.i., Lung: CTRL-infected n = 7; Dex, RDV, anti-IFNAR2, anti-IFNAR2+RDV n = 4 biologically independent mice examined over 3 independent experiments. 28 d.p.i., Lung: CTRL infected n = 5, Dex n = 4, RDV n = 3, anti-IFNAR2 n = 3, anti-IFNAR2+RDV n = 6 biologically independent mice examined over 3 independent experiments. Means with individual datapoints plotted. Unpaired, two-tailed t-test. $P < 0.0001 = 8.19 \times 10^{-5}$. **c.** Representative flow cytometry plots and frequencies of alveolar macrophages (AMs) (middle: hCD206^{hi}hCD86⁺hCD68⁺) or inflammatory macrophages (bottom: hCD206^{lo/-}hCD86⁺hCD68⁺) in 14 d.p.i. or 28 d.p.i. lungs of treated or untreated MISTRG6-hACE2 mice. 14 d.p.i.: CTRL infected n = 5, Dex n = 4, RDV n = 4, anti-IFNAR2 n = 4, anti-IFNAR2+RDV n = 4 biologically independent mice examined over at least 2 independent experiments. 28 d.p.i.: CTRL infected n = 5, Dex n = 4, RDV n = 3, anti-IFNAR2 n = 3, anti-IFNAR2+RDV n = 6 biologically independent mice examined over 3 independent experiments. Means with individual datapoints. Unpaired, two-tailed t-test. $P < 0.0001 = 4.67 \times 10^{-5}$. **d.** Frequencies (left) and numbers (right) of lung pDCs at 14 d.p.i. CTRL-infected n = 6, Dex n = 4, RDV, anti-IFNAR2 n = 3, anti-IFNAR2+RDV n

= 6 mice examined over at least 2 experiments. Means with datapoints. Unpaired, two-tailed t-test. $P < 0.0001 = 7.29 \times 10^{-5}$. **e** *IFNA* transcript levels measured by qPCR in treated or control untreated MISTRG6-hACE2 mice infected with SARS-CoV-2: Uninfected n = 5; CTRL infected: 4 d.p.i. n = 8, 14 d.p.i. n = 9, 28 d.p.i. n = 6; Dex: 14 d.p.i. n = 4, 28 d.p.i. n = 4; RDV 14 and 28 d.p.i. n = 3; anti-IFNAR2 14 and 28 d.p.i. n = 3; anti-IFNAR2+ Remdesivir 14 and 28 d.p.i. n = 4 biologically independent mice examined over at least 2 independent experiments. Normalized to *HPRT1*. Violin plots with individual datapoints. Unpaired, two-tailed t test.
f. Representative histograms and frequencies of HLA-DR⁺ activated T cells in treated or control mice. 14 d.p.i.: CTRL-infected n = 5, Dex, RDV, anti-IFNAR2, anti-IFNAR2+RDV n = 4; 28 d.p.i.: CTRL infected, Dex, anti-IFNAR2+RDV n = 4, RDV, anti-IFNAR2 n = 3 biologically independent mice examined over 3 independent experiments. Means with datapoints. Unpaired, two-tailed t-test. Some of the data associated with dexamethasone therapy used here as a control have been reported^{[19](#)}.

Source data

Extended Data Fig. 2 Anti-IFNAR2 and Remdesivir therapy reverses infection induced transcriptional changes (matched to figure 1).

a. Similarity comparison of uninfected, infected, and therapeutically manipulated lungs based on dexamethasone suppressed genes. Pearson correlation. Duplicates analysed for each condition. **b.** Genes suppressed by both dexamethasone and combined therapy of Remdesivir and anti-IFNAR2 (\log_2 , foldchange < -1 , P adj < 0.05). P adj: For the adjusted P values the Bonferroni correction was used. Duplicates analysed for each condition. Dexamethasone suppressed genes significantly overlapped with genes significantly suppressed by combined anti-IFNAR2 and Remdesivir therapy (64% overlap). See Supplementary Table [1](#) for a full list of genes and their normalized expression. **c.** Network analysis (STRING v11.0) of genes suppressed by both dexamethasone and combined therapy of Remdesivir and anti-IFNAR2 (as shown in Extended Data Fig. [2b](#)). Duplicates analysed for each condition. K- means clustering (n = 4).

d. Pathway (Ingenuity) analysis of genes suppressed by both dexamethasone and combined therapy of Remdesivir and anti-IFNAR2 (as shown in Extended Data Fig. 2b). Duplicates analysed for each condition. Fisher's Exact Test was used to determine statistical significance in the overlap between the dataset genes and the genes suppressed by therapy. **e.** Transcriptional landscape of human immune cells at single cell level in uninfected or infected (28 d.p.i.) MISTRG6-hACE2 mice. Cluster identifying genes comparing human immune cells from infected (28 d.p.i.) or uninfected lungs for 17 clusters shown in Fig. 1e. Marker genes for each cluster of cells were identified using the Wilcoxon rank-sum test with Seurat. Pooled duplicates analysed for each condition.

[Source data](#)

Extended Data Fig. 3 Deeper characterization of monocyte/macrophage clusters at early (4 d.p.i.) or late (14 and 28 d.p.i.) SARS-CoV-2 infection (matched to figure 1).

a. Heatmap visualizing cluster identifying genes comparing human monocytes and macrophages from infected (4, 14 or 28 d.p.i.) or uninfected lungs (as shown in Fig. 1g). Pooled duplicates. Uninfected: 438 cells, 4 d.p.i.: 336 cells, 14 d.p.i.: 793 cells, 28 d.p.i.: 1368 cells were analysed. This analysis allowed step by step characterization of the inflammatory macrophage response. Marker genes for each cluster of cells were identified using the Wilcoxon rank-sum test (two-tailed) with Seurat. **b.** Temporal distribution of transcriptional changes associated with monocytes and macrophages in infected (4, 14 or 28 d.p.i.) or uninfected lungs (as shown in Fig. 1g). Pooled duplicates analysed. Uninfected: 438 cells, 4 d.p.i.: 336 cells, 14 d.p.i.: 793 cells, 28 d.p.i.: 1368 cells included in analysis. **c.** Top: Heatmap of representative genes that are differentially regulated (DEGs) in human macrophages from 4, 14, 28 d.p.i. lungs compared with uninfected lungs. Uninfected: 438 cells, 4 d.p.i.: 336 cells, 14 d.p.i.: 793 cells, 28 d.p.i.: 1368 cells included in analysis. Bottom: Distribution of interferon stimulated genes within these DEGs. Pooled duplicates analysed.

[Source data](#)

Extended Data Fig. 4 Therapeutics reduced expression of a representative list of interferon stimulated genes- ISGs (*DDX58*, *IFIH1*, *IFITM3*, *IRF7*) or inflammatory markers (*IL6*) (matched to figure 1).

Relative expression of interferon inducible or inflammatory genes in treated or untreated MISTRG6- hACE2 mice infected with SARS-CoV-2 mice at 14 d.p.i. or 28 d.p.i. Uninfected baseline expression values are presented as reference. The distribution of cells that preferentially express these genes is overlayed on the tSNE plots showing 14 d.p.i. and 28 d.p.i. human immune cells. *IFITM3* and *IL6* were particularly enriched in human macrophage/monocyte clusters, while *IRF7*, *DDX58* and *IFIH1* were enriched in multiple human immune cells such as T cells, B cells, and myeloid cells. Normalized to *HPRT1*. *DDX58*: uninfected n = 3; CTRL-infected: 14 d.p.i. n = 8, 28 d.p.i. n= 5; Dex 14 d.p.i. n = 3, 28 d.p.i. n = 6; RDV 14 and 28 d.p.i. n = 3; anti-IFNAR2 14 and 28 d.p.i. n = 3, anti-IFNAR2+ Remdesivir 14 and 28 d.p.i. n = 5 biologically independent mice examined over at least 2 independent experiments. *IFIH1*: uninfected n = 5; CTRL-infected: 14 d.p.i. n = 11, 28 d.p.i. n= 3; Dex 14 and 28 d.p.i. n = 4; RDV 14 and 28 d.p.i. n = 3; anti-IFNAR2 14 and 28 d.p.i. n = 3, anti-IFNAR2+ Remdesivir 14 d.p.i. n = 4 and 28 d.p.i. n = 5 biologically independent mice examined over at least 2 independent experiments. *IFITM3*: uninfected n = 4; CTRL-infected: 14 d.p.i. n = 7, 28 d.p.i. n=: 4; Dex 14 and 28 d.p.i. n = 4; RDV 14 and 28 d.p.i. n = 3; anti-IFNAR2 14 and 28 d.p.i. n = 3, anti-IFNAR2+ Remdesivir 14 and 28 d.p.i. n = 4 biologically independent mice examined over at least 2 independent experiments. *IRF7*: uninfected n = 4; CTRL-infected: 14 d.p.i. n = 7, 28 d.p.i. n=: 5; Dex 14 and 28 d.p.i. n = 4; RDV 14 and 28 d.p.i. n = 3; anti-IFNAR2 14 and 28 d.p.i. n = 3, anti-IFNAR2+ Remdesivir 14 d.p.i. n = 4, 28 d.p.i. n = 5 biologically independent mice examined over at least 2 independent experiments. *IL6*: uninfected n = 5; CTRL-infected: 14 d.p.i. n = 9, 28 d.p.i. n=: 4; Dex 14 d.p.i. n = 3, 28 d.p.i. n = 4; RDV 14 and 28 d.p.i. n = 3; anti-IFNAR2 14 and 28 d.p.i. n = 3, anti- IFNAR2+ Remdesivir 14 d.p.i. n = 4, 28 d.p.i. n = 5 biologically independent mice examined over at least 2 independent experiments. Unpaired, two-tailed t-test.

[Source data](#)

Extended Data Fig. 5 Anti-IFNAR2 and Remdesivir combined therapy reverses fibrotic transcriptional signature and prevents the transition to fibrosis seen in the infected mice (matched to figure 1).

a. Relative expression of *IFNG* in treated or untreated MISTRG6-hACE2 mice infected with SARS-CoV-2 mice at 14 d.p.i. or 28 d.p.i. Uninfected baseline expression values are presented as reference. Normalized to *HPRT1*. Uninfected n = 7; CTRL infected: 14 d.p.i. n = 7, 28 d.p.i. n=: 6; Dex 14 d.p.i. = 3, 28 d.p.i. = 5; anti-IFNAR2+ Remdesivir 14 d.p.i. n = 4, 28 d.p.i. n = 6 biologically independent mice examined over at least 2 independent experiments. Unpaired, two-tailed t-test. **b.** Heatmap of AT2 cell self-renewal and AT1 differentiation and pre-alveolar type 1 transitional cell state (PATS) associated genes at in uninfected or infected (14 d.p.i.) lungs in response to therapeutics. AT2 cell self-renewal and AT1 differentiation gene signature was inhibited while PATS gene signature was enriched in autopsy lungs of patients with severe COVID-19⁷. Top differentially expressed genes in epithelial cluster 7 of autopsy lungs⁷ were used in the analysis. Duplicates were analysed for each condition. Normalized counts of duplicates visualized as min-max transformed values, calculated by subtracting row mean and diving by SD for each gene. Rows (genes) clustered by hierarchical clustering (one-minus Pearson). **c.** Representative images of trichrome staining and box and whisker plot (min to max, with all datapoints) of the trichrome scoring of MISTRG6-hACE2 mice treated with a combined therapy of Remdesivir and anti-IFNAR2 or not (CTRL infected). The whiskers go down to the smallest value (minimum) and up to the largest value (maximum). The box extends from the 25th to 75th percentiles. The median is shown as a line in the center of the box. N = 4 biologically independent mice examined over 2 independent experiments. Unpaired, two-tailed t-test.

Source data

Extended Data Fig. 6 Cellular source of persistent SARS-CoV-2 viral RNA and sustained viral replication in lungs (matched to figure 2).

a. Quantification of genomic (gRNA) and subgenomic (sgRNA) viral RNA (E-gene) in whole homogenized lung tissue at 4, 14 and 28 d.p.i. 4 d.p.i.: n = 7, 14 d.p.i. n = 5, 28 d.p.i. n = 4 biologically independent mice examined over 3 independent experiments. Means with all datapoints and SD. **b.** Quantification of genomic (gRNA) and subgenomic (sgRNA) viral RNA (E-gene) in whole homogenized lung tissue at 14 d.p.i. in mice treated with combined therapy of Remdesivir and anti-IFNAR2. CTRL: n = 4, anti-IFNAR2+RDV: n = 4 biologically independent mice examined over 2 independent experiments. N.D.= not detected. **c.** Quantification of genomic (gRNA) and subgenomic (sgRNA) viral RNA (E-gene) in whole homogenized lung tissue at 28 d.p.i. in mice treated with Remdesivir, anti-IFNAR2 or combined therapy of Remdesivir and anti-IFNAR2. N = 3 biologically independent mice representative of 2 independent experiments. N.D.= not detected. **d.** Representative gating strategy for sorting human immune cells (human CD45⁺) or mouse epithelial cells (mouse EPCAM⁺) from lungs of mice infected with SARS-CoV-2 and quantification of viral RNA (E and N genes) in these sorted cells. N gene: 4 d.p.i. n = 3, 14 d.p.i. n = 6(epithelial), n = 5 (immune), 28 d.p.i. n = 4 (epithelial) n = 3 (immune) biologically independent mice analysed over 3 independent experiments. E gene: 4 d.p.i. n = 3, 14 d.p.i. n = 7 (epithelial), n = 6 (immune), 28 d.p.i. n = 4 (epithelial) n = 3 (immune) biologically independent mice analysed over 3 independent experiments. **e.** mNG signal in epithelial (EPCAM⁺) cells from lungs and BAL of mice infected with reporter SARS-CoV-2-mNG or control wild type SARS-CoV-2/WA1. mNG is expressed in infected cells following viral replication. Representative of n = 4 biologically independent mice examined over 2 independent experiments. **f.** Representative histograms of mNG expression in human or mouse lung macrophages isolated from BAL of infected MISTRG6-hACE2 mice at 4 d.p.i. Representative of n = 3 biologically independent mice examined over 2 independent experiments. **g.** Frequencies of mNG+ cells within human lung immune cells (hCD45⁺) of SARS-CoV-2-mNG infected MISTRG6-ACE2 mice at 4 d.p.i. and 14 d.p.i. 4 d.p.i. n = 4, 14 d.p.i. n = 6 biologically independent mice examined over at least 2 experiments. Unpaired, two-tailed t-test. P value = 0.066. **h.** Viral titres measured as PFU using Vero ACE2⁺TMRSS2⁺ cells that over express human ACE2 from lung homogenates of MISTRG6 mice transduced with AAV-hACE2 (+AAV) or not (-AAV) and infected with SARS-CoV-2. MISTRG6-hACE2 (+AAV):

2 d.p.i. n = 2, 4 d.p.i. n = 5, 7 d.p.i. n = 2, 14 d.p.i. n = 6 MISTRG6(-AAV): 2 d.p.i. n = 4, 4 d.p.i. n = 10 and 7, 14 d.p.i. n = 2, biologically independent mice representative of at least 2 independent experiments. Viral titres using standard Vero E6 cells do not have any detectable titres (previously reported¹⁹) in MISTRG6 mice without AAV-hACE2. Some of the MISTRG6-hACE2 data presented here have been previously reported as part of the characterization of the model¹⁹. **i.** Frequencies of mNG⁺ cells within human macrophages (human CD68⁺) isolated from lungs of infected MISTRG6 mice transduced with AAV-hACE2 (AAV+) or not (AAV-). MISTRG6 mice with and without AAV-hACE2 were reconstituted with human progenitor cells from the same donor. AAV+ n = 6, AAV- n = 5 biologically independent mice examined over 3 independent experiments. **j.** Representative gating strategy for sorting mNG⁺ and mNG⁻ human immune cells, mNG⁺ and mNG⁻ mouse epithelial cells and mouse immune cells. Lung cells from SARS-CoV2-mNG infected MISTRG6-hACE2 mice were stained with antibodies against human CD45, mouse CD45, and mouse EPCAM. Sorted cells were used for viral RNA quantification (Fig. 2) and characterization of the inflammasome pathway (Fig. 3).

Source data

Extended Data Fig. 7 Viral replication products are detected in human lung macrophages of infected MISTRG6-hACE2 mice (matched to figure 2).

- a.** Representative fluorescent microscopy images showing colocalization of double stranded RNA (dsRNA, clone rJ2) staining, mNG signal and DAPI staining in fixed lung tissue at 4 d.p.i. Representative of n = 4 biologically independent mice examined over 2 independent experiments. **b.** Representative fluorescent microscopy images of RNA dependent RNA polymerase (RdRp), anti- human CD68 and DAPI staining in fixed lung tissue from SARS-CoV-2 infected or control MISTRG6-hACE2 mice (Non-SARS-CoV-2 pneumonia). Representative of n = 7 biologically independent SARS-CoV-2 infected mice examined over 3 independent experiments. Yellow arrows mark RdRp⁺ human macrophages. Blue arrows mark RdRp⁻ human macrophages. Isotype controls (bottom panels) and non- COVID

pneumonia lungs (bacterial infection, top panels) n = 3 biologically independent mice are presented as controls. Pseudo-colours were assigned for visualization.

Extended Data Fig. 8 Viral RNA dependent RNA polymerase (RdRp) and Spike in human lung macrophages of MISTRG6-hACE2 mice infected with SARS-CoV-2 (matched to figure 2).

a. Representative fluorescent microscopy images of Spike (S), human CD68, and DAPI staining in fixed lungs of SARS-CoV-2- infected MISTRG6-hACE2 mice. Yellow rectangle provides a higher magnification view of the selected area. Pseudo-colours were assigned for visualization. Representative of n = 5 biologically independent mice examined over 3 independent experiments. **b.** Quantification of viral replication products or machinery in human lung macrophages from SARS-CoV-2 infected MISTRG6-hACE2 mice measured by immunofluorescence staining. Quantification was performed based on representative high-power images (40x) in areas showing diffuse alveolar damage. Frequencies of dsRNA, mNG, RdRp, and Spike positive human macrophages out of hCD68⁺DAPI⁺ cells are plotted. dsRNA: 20, 81, 133, 135, 52 human macrophages were counted. mNG: 30, 103, 110 human macrophages were counted. RdRp monoclonal: 187, 59, 85, 106, 142, 63, 59 human macrophages were counted. RdRp polyclonal: 134, 21, 22, 218, 44 human macrophages were counted. Spike (antibody 1): 21, 22, 218, 44 total human macrophages were counted. Spike (antibody 2): 63, 83, 163, 101, 57 human macrophages were counted. N = 5 (dsRNA⁺), N = 3 (mNG), N = 7 (RdRp⁺, monoclonal), N = 5 (RdRp⁺, polyclonal), N = 4 (Spike⁺-1), N = 5 (Spike⁺-2) biologically independent mice representative of at least 2 independent experiment. Means with all datapoints are shown. See Methods for details of antibodies used. **c.** Representative fluorescent microscopy images and quantification of colocalization of Spike (S), RNA dependent RNA polymerase (RdRp), human CD68, and DAPI staining in fixed lungs of SARS-CoV-2- infected MISTRG6-hACE2 mice. Top panel: isotype control staining of SARS-CoV-2- infected lungs. Middle panel: control lungs with Non-SARS-CoV-2, bacterial pneumonia. Bottom panels: SARS-CoV-2- infected MISTRG6-hACE2 mice. Yellow rectangle provides a higher magnification view of the

selected area. Pseudo-colours are assigned for visualization. Representative of n = 5 biologically independent mice over 3 independent experiments.

[Source data](#)

Extended Data Fig. 9 Viral RNA dependent RNA polymerase (RdRp) and Spike in human macrophages of human autopsy lungs with SARS-CoV-2 pneumonia (matched to figure 2).

Representative fluorescent microscopy images and quantification of colocalization of Spike (S), RNA dependent RNA polymerase (RdRp), human CD68 and DAPI staining in fixed human autopsy lungs with SARS-CoV-2 pneumonia or non-SARS-CoV-2 pneumonia. Quantification was performed based on representative high-power images (40x) in areas showing diffuse alveolar damage. Top panels: Representative of RdRp staining with human CD68; middle panels: Representative of Spike staining with CD68; bottom panels: RdRp and Spike staining in SARS-CoV-2-infected autopsy lungs. Yellow rectangle provides a higher magnification view of the selected area. Pseudo-colours are assigned for visualization. SARS-CoV-2 pneumonia n = 4, non-SARS-CoV-2 pneumonia n = 3 biologically independent specimens.

[Source data](#)

Extended Data Fig. 10 Human macrophage infection was enhanced by antibodies and reduced by CD16, ACE2, or RdRp blockade *in vivo* and *in vitro* (matched to figure 2).

- a. Viral titres in lung homogenates of Remdesivir (RDV) treated or control untreated MISTRG6-hACE2 mice infected with SARS-CoV-2-mNG. CTRL infected n = 6, RDV treated n = 6 biologically independent mice examined over 3 independent experiments.
- b. Representative histograms and mean fluorescent intensity (MFI) for human ACE2 expression in mNG⁺ or mNG⁻ epithelial cells from MISTRG6-hACE2 (AAV+) mice or total epithelial cells from MISTRG6 (AAV-) mice infected with SARS-CoV-2-mNG. AAV+ n = 10, AAV- n = 6 biologically independent mice examined

over at least 3 independent experiments. Paired, two-tailed t-test. **c.**

Representative histograms for human ACE2 expression in mNG⁺ or mNG⁻ human macrophages, human B cells (CD19⁺) or mouse immune cells isolated from MISTRG6-hACE2 mice infected with SARS-CoV-2-mNG.

Representative of N = 10 mice for epithelial cells, n = 7 mice for human macrophages examined over at least 3 independent experiments. **d.** MFI of human ACE2 expression in mNG⁺ or mNG⁻ human macrophages or mouse epithelial cells isolated from SARS-CoV-2-mNG infected MISTRG6-hACE2 mice. Epithelial cells n = 10, human macrophages n = 7 biologically independent mice examined over at least 3 independent experiments.

Paired, two-tailed t-test. **e.** MFI of human ACE2 expression in mNG⁺ or mNG⁻ human macrophages isolated from MISTRG6 (AAV-) mice infected with SARS-CoV-2-mNG. Epithelial cells are virtually not infected with SARS-CoV-2-mNG in MISTRG6 mice without transduced human ACE2. N = 8 biologically independent mice examined over at least 3 independent experiments. Paired, two-tailed t-test. **f.** Representative fluorescent microscopy images showing colocalization of human ACE2 and human CD68 cells in SARS-CoV-2 infected MISTRG6-hACE2 mice.

Representative of 3 independent mice over 2 independent experiments. **g.**

Anti-Spike (RBD) IgG levels measured by ELISA in serum or lung homogenates of SARS-CoV-2 infected (4 and 14 d.p.i.) or uninfected MISTRG6-hACE2 mice treated therapeutically with monoclonal antibodies (mAbs) against SARS-CoV-2 spike protein (treated at 35 h.p.i. or 7 d.p.i.) or not. Lung homogenates: Uninfected n = 5, 4 d.p.i. n = 8, 14 d.p.i. n = 8, 4 d.p.i.+mAb n = 2, 14 d.p.i.+mAb n = 2 biologically independent mice representative of at least 2 experiments. Serum: Uninfected n = 3, 4 d.p.i. n = 3, 14 d.p.i. n = 3, 4 d.p.i.+mAb n = 3, 14 d.p.i.+mAb n = 2 biologically independent mice representative of at least 2 experiments. Unpaired, two-tailed t-test. **h.** Frequencies of mNG signal in human immune cells in infected mice (14 d.p.i.) treated therapeutically with monoclonal

antibodies^{45,64} (mAb) at 7 d.p.i. CTRL infected n = 5, mAb treated n = 4 biologically independent mice examined over 2 independent experiments. Means with datapoints and SD. Paired, two-tailed t-test. **i.** Two-way plot showing anti-Spike (RBD) IgG levels and corresponding mNG⁺ human immune cell proportions in lungs of infected MISTRG6-hACE2 mice at 4 d.p.i. Pearson's correlation value = 0.70. N = 8 biologically independent

mice examined over 4 independent experiments. **j.** Frequencies of mNG⁺ human macrophages in human immune cells in SARS-CoV-2-mNG infected MISTRG6-hACE2 mice treated with anti-CD16 antibody (Abcam-clone SP175) at 7 d.p.i. and 11 d.p.i. and analysed at 14 d.p.i. n = 6 biologically independent mice examined over 3 independent experiments. Unpaired, two-tailed t-test. **k.** Representative histograms and frequencies of mNG⁺ cells in human BMDMs cultured (or not) with SARS-CoV-2-mNG for 48 h. Human BMDMs were differentiated in vitro from bone marrow cells of immune-reconstituted uninfected MISTRG6 mice. BMDMs were treated with pooled plasma from healthy controls (prior to COVID-19 pandemic) or convalescent COVID-19⁴⁵ patients during the course of SARS-CoV-2 infection in vitro. Uninfected n = 3, infected+ healthy plasma n = 7, infected+ COVID plasma n = 10 independent samples cultured and analysed over at least 3 experiments. Means with datapoints. Unpaired t-test. P < 0.0001 = 1.57x10⁻⁵. **l.** Quantification of genomic (gRNA) and subgenomic (sgRNA) viral RNA (E gene) in infected BMDMs at 48 h.p.i. Cells were treated with plasma from healthy controls or convalescent COVID-19 patients. Healthy plasma: n = 4, COVID plasma n = 6, RDV: n = 6, anti-CD16+anti-ACE2 n = 4 independent samples analysed over at least 2 independent experiments. Means with datapoints. Mann-Whitney, two-tailed, t-test. **m.** Representative histograms and frequencies of mNG⁺ cells in BMDMs and lung macrophages cultured with SARS-CoV-2 in presence of plasma of convalescent COVID-19 patients. mNG⁺ macrophages were analysed at 48 h.p. BMDMs n= 6, Lung macrophages n = 4 independent samples analysed over 2 independent experiments. Unpaired, two-tailed t-test. **n.** Frequencies of mNG⁺ cells in BMDMs cultured with SARS-CoV-2 or not in presence of healthy patient plasma, COVID plasma, monoclonal antibodies (clones 135 and 144) or no antibodies. COVID plasma n = 5, mAb n = 4, healthy plasma n = 4, no Ab n = 5 independent samples analysed over 2 independent experiments. Means with datapoints and SD. The same monoclonal antibody cocktail used was used in vivo (Figs. 2 and 3). Unpaired, two-tailed t-test. **o.** Representative histograms and frequencies of mNG⁺ cells in BMDMs cultured with SARS-CoV-2-mNG (or not) in presence or absence of COVID plasma. Cultures were treated with Remdesivir, anti-human CD16 antibody and/or anti-human ACE2 antibody. Healthy plasma n = 5, COVID plasma n = 10, RDV n = 5,

anti-CD16 n = 6, anti-ACE2 n = 4, anti-CD16+ACE2 n = 4 independent samples analysed over at least 2 independent experiments. Means with datapoints. Unpaired two-tailed t-test. P values < 0.0001: anti-CD16 vs. COVID plasma=1.98x10⁻⁵, RDV vs. COVID plasma = 5.24x10⁻⁶. **p.** Viral titres and representative plaque images from supernatants of human or mouse BMDMs infected with SARS-CoV-2 mNG in vitro (without COVID plasma). Infectious virus from supernatants of infected macrophage cultures collected at 24, 48 and 72 h.p.i. was plaqued using Vero ACE2⁺TMPRSS2⁺ cells. Supernatant collected from Vero E6 cell cultures were provided as reference. Human: 24 h.p.i. n = 9, 48 h.p.i. n = 13, 72 h.p.i. n = 4. Mouse: 24 h.p.i. n = 6 independent samples analysed over at least 2 independent experiments. **q.** Viral titres from supernatants of BMDMs infected with SARS-CoV-2 mNG in vitro and treated with Remdesivir (RDV) or a combination of anti-CD16 and anti-ACE2 antibodies. Cultures were not supplemented with COVID plasma. Infectious virus from supernatants of infected macrophage cultures collected at 24 h.p.i. was plaqued using Vero ACE2⁺TMPRSS2⁺ cells. CTRL n = 9, RDV n = 4, anti-CD16 and anti-ACE2 n = 4 independent samples representative of 2 independent experiments. Means with datapoints. **r.** Viral titres measured as PFUs using supernatants containing concentrations of Remdesivir (1 μm) or anti-ACE2 (1 μg/ml) and anti-CD16 antibodies diluted to (1:10) allow quantification of PFUs at 24 h.p.i. from macrophage cultures. Supernatants were applied on Vero ACE2⁺TMPRSS2⁺ cells which were then infected with a matched inoculum of SARS-CoV-2 mNG (10³ PFU quantified in Vero-E6 cells) to test carry over effect in plaque quantification. Untreated N = 9, RDV N = 6, anti-ACE2+anti-CD16 n = 4 independent datapoints collected over 3 independent experiments. Means with datapoints. Unpaired, two-tailed, t-test.

Source data

Extended Data Fig. 11 SARS-CoV-2 infected human macrophages have a unique transcriptional signature (matched to figure 3).

a. Representative gating strategy of CXCL10 or TNF producing human macrophages in MISTRG6-hACE2 mice infected with SARS-CoV-2-mNG.
b. Representative flow cytometry plots of CXCL10 and TNF staining in mice therapeutically treated with mAb or control untreated mice.
Representative of n = 4 biologically independent mice examined over 2 independent experiments. **c.** CXCL10 production measured by ELISA in supernatants of BMDMs infected with SARS-CoV-2 in vitro. Infected BMDM cultures were supplemented with pooled plasma from COVID-19 patients and were treated with Remdesivir or not. Uninfected n = 5, CTRL infected n = 12, RDV n = 4 over 3 independent experiments. Means with individual values are plotted. Unpaired, two-tailed t-test. **c.** Spearman correlation values of each gene based on its correlation with *CXCL10* or *TNF* or *TLR7*. **d.** Expression and distribution of *CXCL10*, *TNF* and *TLR7* in human immune cells from infected (4, 14 and 28 d.p.i.) MISTRG6-hACE2 mice.

[Source data](#)

[Extended Data Fig. 12 CXCL10-associated genes \(matched to figure 3\).](#)

a. Network (STRING v11.0) analysis of top *CXCL10*-associated genes (top 200 genes). K-means clustering. Clusters and their corresponding pathway analysis are available as source files. Top genes that correlate with CXCL10 (4 d.p.i., Pearson and Spearmen correlation combined) are enriched for distinct inflammatory molecules. **b.** Network (STRING) analysis of genes that are preferentially associated with *CXCL10* but not with *TLR7* or *TNF*. Disconnected nodes in the network are not displayed. K-means clustering. Clusters and their corresponding pathway analysis are presented as source files. **c.** Proportions of TNF or CXCL10 producing macrophages among alveolar ($CD206^{hi}CD68^+$) macrophages. Unpaired, two-tailed t-test. N = 6 biologically independent mice examined over 3 independent experiments. MISTRG6-hACE2 mice were infected with SARS-CoV-2-mNG and lungs were analysed at 4 d.p.i. **d.** Distribution of *CXCL10* or *TNF* associated genes at 4, 14, 28 d.p.i. in lungs infected with SARS-CoV-2 or not. Analysis performed on macrophages of 4 d.p.i. lungs in Fig. [3d](#) was extended to more timepoints. Pearson (top) and Spearman (bottom) correlation values were

calculated for each gene for its correlation with *CXCL10* or *TNF* in human monocytes and macrophages isolated from uninfected and infected (4, 14 and 28 d.p.i.) lungs of MISTRG6-hACE2 mice. K-means clustering analysis.

Source data

Extended Data Fig. 13 SARS-CoV-2 infection of human macrophages activates inflammasomes and leads to death by pyroptosis *in vivo* and *in vitro* (matched to figure 3).

a. Representative images of single stained cells for ASC specks, NLRP3, human CD14, human CD45, mouse CD45 and mouse EPCAM. Cells from SARS-CoV-2 infected humanized mice were sorted based on (Extended Data Fig. 6j): human immune cells (hCD45^+); mouse immune cells (mCD45^+) or epithelial mouse cells (EPCAM^+). Sorted cells were stained with single antibodies against ASC, CD14 or NLRP3. Left panel shows human immune cells and right panel shows mouse immune cells (mCD45^+) and mouse epithelial cells (EPCAM^+). Representative of $n = 5$ independent mice examined over 3 independent experiments. **b.** Visualization of ASC specks as a measure of inflammasome activation in mNG^+ (SARS-CoV-2 $^+$) or mNG^- (SARS-CoV-2 $^-$) human immune cells at 4 d.p.i. Human immune cells were sorted from SARS-CoV-2 infected humanized mice were sorted based on expression of human CD45 and mNG and lack of mouse CD45 and EPCAM expression (Extended Data Fig. 6j). Representative of $n = 5$ biologically independent mice examined over 3 independent experiments. **c.** Left: Representative flow cytometry plot displaying SARS-CoV-2-mNG and Casp1-FLICA staining of CD11b^+ human immune cells. Right: quantification of FLICA^+ cells (%) as a measure of active caspase-1 in infected (mNG^+) and uninfected (mNG^-) human lung macrophages ($\text{CD11b}^+\text{hCD45}^+$) at 4 d.p.i. and 14 d.p.i. 4 d.p.i.: $n = 3$ biologically independent mice examined over 2 independent experiments, 14 d.p.i. $n = 5$ biologically independent mice examined over 3 independent experiments. Lung cells were incubated with FLICA-Casp1 substrate for 30 min. Means with individual datapoints plotted. Paired, two-tailed t-test. $P < 0.0001 = 4.29 \times 10^{-9}$. **d.** Quantification of Casp1-FLICA staining as a measure of

active caspase-1 in infected (mNG^+) human or total mouse CD11b $^+$ cells at 4 d.p.i. Mouse cells: mCD45 $^+$ CD11b $^+$ hCD45 $^-$. Human cells:

mCD45 $^-$ CD11b $^+$ hCD45 $^+$ mNG^+ . N = 6 biologically independent mice examined over 3 independent experiments. Means with individual datapoints plotted. Paired, two-tailed t-test. P < 0.0001 = 1.79×10^{-9} .

e. Human IL-18 (measured by ELISA) in lungs and serum and corresponding mNG levels (measured as percent within human immune cells by flow cytometry) in lungs of infected MISTRG6-hCE2 mice at 4 d.p.i. Lung: Pearson's correlation value = 0.69. N = 8 biologically independent mice examined over 3 independent experiments. Serum: Pearson's correlation value = 0.75. n = 7 biologically independent mice examined over 3 independent experiments. Unpaired, two-tailed t-test. **f.**

Human IL-1RA (measured by ELISA) in lungs and serum and corresponding mNG levels (measured as percent within human immune cells by flow cytometry) in lungs of infected MISTRG6-hCE2 mice at 4 d.p.i. Lung: Pearson's correlation value = 0.82 n = 8 biologically independent mice examined over 3 independent experiments. Serum:

Pearson's correlation value = 0.46 n = 8 biologically independent mice examined over 3 independent experiments. Unpaired t-test, two-tailed. **g.**

LHD levels measured as absorbance at OD 490nm in serum of uninfected or infected MISTRG6-hACE2 mice at 4 d.p.i. and 14 d.p.i. Fresh serum was assayed for LDH. Uninfected n = 3, 4 d.p.i. n = 4, 14 d.p.i. n = 4 biologically independent mice examined over 2 independent experiments. Means with individual datapoints. Unpaired, two-tailed t-test. **h.** Zombie Aqua

incorporation in infected (mNG^+) or uninfected (mNG^-) CD16 $^+$ CD11b $^+$ or CD16 $^-$ CD11b $^+$ human myeloid cells. Frequencies of Zombie $^+$ cells were measured in Annexin V $^-$ cells. N = 5 biologically independent mice examined over 2 independent experiments. Means with individual datapoints. Paired, two-tailed t-test. **i.** Representative histograms and

quantification of Casp1-FLICA staining as a measure of active caspase-1 in bone marrow derived macrophages (BMDMs) infected with SARS-CoV-2 in vitro or not for 48 h. BMDM cultures were either supplemented with healthy or COVID plasma or monoclonal antibodies for the duration of the infection. Cultures were treated with Remdesivir, anti-ACE2 and anti-CD16 to block viral replication or viral entry. Colouring on the histograms matches the bar graph legend. Uninfected n = 4; healthy plasma CTRL

infected n = 9, anti-ACE2 n = 4, RDV n = 4; mAb n = 4; COVID plasma CTRL infected n = 12, anti-ACE2+anti-CD16 n = 6, RDV n = 5 independent datapoints collected over at least 2 independent experiments. Means with all datapoints. Unpaired, two-tailed t-test. P- values < 0.0001: COVID plasma vs. RDV: 5.85×10^{-6} . j. Representative histograms and quantification of IL-1 β in supernatants of BMDMs infected with (or not) SARS-CoV-2 *in vitro* for 48 or 72 h. Uninfected n = 7, 48 h.p.i. n = 10, 72 h.p.i. n = 5 independent datapoints collected over 3 independent experiments. Means with SD and individual datapoints. Unpaired, two-tailed t-test. P- values < 0.0001: uninfected vs. 72 h.p.i. = 4.96×10^{-7} , 48 h.p.i. vs. 72 h.p.i. = 1.17×10^{-8} . k. Human IL-18 levels at 48 h.p.i. in supernatants of BMDMs infected or not with SARS-CoV-2 *in vitro*. BMDM cultures were supplemented with COVID plasma for the duration of the infection. Uninfected n = 4, 48 h.p.i. n = 7 independent datapoints collected over at least 2 independent experiments. Unpaired, two-tailed t-test. Means with individual datapoints. Unpaired, two-tailed t-test. l. Human IL-1RA levels at 48 h.p.i in supernatants of BMDMs infected with SARS-CoV-2 *in vitro* or not. Uninfected n = 3, infected n = 7 independent datapoints collected over at least 2 independent experiments. Means with individual datapoints. Unpaired, two-tailed t-test. m. Gasdermin D (GSDMD) levels in supernatants of BMDMs infected with (or not) SARS-CoV-2 *in vitro* for 48 h. BMDM cultures were supplemented with COVID plasma for the duration of the infection. Cultures were treated with Remdesivir to block viral replication. Uninfected N = 3, CTRL infected n = 10, RDV n = 3 independent datapoints collected over at least 2 independent experiments. Means with individual datapoints. Unpaired, two-tailed t-test. n. LHD levels measured by absorbance at OD 490 nm in supernatants of infected or uninfected BMDMs. Uninfected n = 6, Infected n = 11 independent datapoints collected over 3 independent experiments. Means with individual datapoints. Unpaired, two-tailed t-test. P-value = 7.38×10^{-6} . o. Zombie Aqua incorporation in uninfected or SARS-CoV-2-mNG infected BMDMs. Frequencies of Zombie $^+$ cells within Annexin V $^-$ population at 48 h.p.i. are presented. Uninfected n = 4, infected n = 7 independent datapoints collected over 3 independent experiments. Means with individual datapoints. Unpaired, two-tailed t-test.

[Source data](#)

Extended Data Fig. 14 Promoting or blocking viral entry or replication in human macrophages in vivo and in vitro impacts inflammatory profile of macrophages (matched to figure 3).

a. Human IL-18 levels measured in lung homogenates of infected (4 d.p.i.) MISTRG6-hACE2 mice treated (or not) with CD16 blocking antibody (Abcam). CTRL infected n = 7, anti-CD16 n = 5 biologically independent mice examined over 3 independent experiments. Means with datapoints. Unpaired, two-tailed t-test. **b.** Human IL-1RA levels measured in lung homogenates of infected (4 d.p.i.) MISTRG6-hACE2 mice treated (or not) with CD16 blocking antibody (Abcam). N = 4 biologically independent mice examined over 2 independent experiments. Means with all datapoints. Unpaired, two-tailed t-test. **c.** Human CXCL10 levels measured in serum of infected (4 d.p.i.) MISTRG6-hACE2 mice treated (or not) with CD16 blocking antibody (Abcam). CTRL infected n = 7, anti-CD16 n = 4 biologically independent mice examined over at least 2 experiments. Means with individual datapoints. Unpaired, two-tailed t-test. **d.** Human IL-18 levels measured in serum of infected (14 d.p.i.) MISTRG6-hACE2 mice treated (or not) with CD16 blocking antibody (Abcam). Mice were treated with anti-CD16 blocking antibody at 7 d.p.i. and 11 d.p.i. CTRL infected n = 4, anti-CD16 n = 4 biologically independent mice examined over 2 independent experiments. Means with individual datapoints. Unpaired, two-tailed t-test. **e.** Human IL-18 levels measured in serum of infected (4 d.p.i.) MISTRG6 mice treated (or not) with anti-ACE2 antibody (Abcam). Mice were treated with anti-ACE2 antibody at 1,2,3 d.p.i. Uninfected n = 4, CTRL infected n = 5, anti-ACE2 n = 4 biologically independent mice examined over 2 independent experiments. Means with individual datapoints. Unpaired, two-tailed t-test. P < 0.0001 = uninfected vs. CTRL-infected = 1.43×10^{-5} , CTRL-infected vs. anti-ACE2 = 6.95×10^{-5} . **f.** Representative flow cytometry plots of CD14 staining on total human immune cells (hCD45+) as a proxy for myeloid cells in infected MISTRG6-hACE2 mice (4 d.p.i.) treated (or not) with a depleting antibody against CD16 (ThermoFisher, clone 3G8). MISTRG6-hACE2 mice were infected with SARS-CoV-2-mNG. Representative of n = 4 biologically independent mice examined over 2 independent experiments. **g.** Frequencies of mNG⁺ cells in infected MISTRG6-hACE2 mice at 4 d.p.i. treated (or not) with a

depleting antibody against CD16 (ThermoFisher, clone 3G8). N = 4 biologically independent mice examined over 2 independent experiments. Means with datapoints. Unpaired, two-tailed t-test. **h.** Human IL-18 levels in serum of infected or uninfected MISTRG6-hACE2 mice that were therapeutically treated with monoclonal antibodies (mAb) at 36 h.p.i. or not. Sera from infected mice were analysed at 4 d.p.i. N = 4 biologically independent mice examined over 2 independent experiments. Means with datapoints. Unpaired, two-tailed t-test. **i.** Human IL-1RA levels in serum of infected (4 d.p.i.) or uninfected MISTRG6-hACE2 mice that were therapeutically treated with mAb at 36 h.p.i. or not. Uninfected and mAb treated n = 4, CTRL infected n = 3 (matched to mAb treatment) biologically independent mice examined over 2 independent experiments. Means with datapoints. Paired, two-tailed t-test. **j.** Human IL-18 levels measured in serum of infected (14 d.p.i.) MISTRG6-hACE2 mice treated (or not) with mAb (clone 135+ clone 144) at 7 d.p.i. and analysed at 14 d.p.i. N = 3 biologically independent mice examined over 2 independent experiments. Mean with individual datapoints. Unpaired, two-tailed t-test. **k.** Frequencies of CXCL10⁺ macrophages within total human macrophages (hCD45⁺hCD68⁺) in lungs of infected MISTRG6-hACE2 mice treated (or not) with mAb (clone 135, clone 144) at 7 d.p.i. and analysed at 14 d.p.i. Mean with individual values. Unpaired, two-tailed t-test, not significant (ns). CTRL-infected n = 5, mAb n = 4 biologically independent mice examined over 2 independent experiments. **l.** Box and whisker plot (min to max, with all datapoints) of the histopathological scoring of the H&E staining of infected MISTRG6-hACE2 lungs at 4 d.p.i. Mice were either treated with monoclonal antibodies at 35 h.p.i. or anti-CD16 at 2 d.p.i. CTRL infected n = 9, mAb treated n = 6, anti-CD16 treated n = 3 biologically independent mice examined over at least 2 independent experiments. The whiskers go down to the smallest value (minimum) and up to the largest value (maximum). The box extends from the 25th to 75th percentiles. The median is shown as a line in the center of the box. Unpaired t-test not significant. **m.** Box and whisker plot (min to max, with all datapoints) of the histopathological scoring of the H&E staining of infected MISTRG6-hACE2 lungs at 14 d.p.i. Mice were either treated with monoclonal antibodies at 7 d.p.i. or anti-CD16 at 7 and 11 d.p.i. CTRL infected n = 4, mAb treated n = 4, anti-CD16 treated n = 4 biologically independent mice examined over 2 independent experiments. The whiskers

go down to the smallest value (minimum) and up to the largest value (maximum). The box extends from the 25th to 75th percentiles. The median is shown as a line in the center of the box. Unpaired, two-tailed t-test, not significant. **n.** Human IL-18 levels in supernatants of SARS-CoV-2 infected BMDMs treated with anti-CD16 and anti-ACE2 antibodies to block viral entry or with Remdesivir to block viral replication. CTRL infected n = 8, anti-CD16+anti-ACE2 n = 5, RDV n = 5 independent datapoints over 3 independent experiments. Means with all datapoints. Unpaired, two-tailed t-test. P < 0.0001 = 5.0×10^{-5} . **o.** Human IL-1 β levels in supernatants of SARS-CoV-2 infected BMDMs treated with anti-CD16 and anti-ACE2 antibodies to block viral entry or with Remdesivir to block viral replication. N = 4 independent datapoints over 2 independent experiments. Means with all datapoints. Unpaired, two-tailed, t-test. **p.** Human IL-1RA in supernatants of SARS-CoV-2 infected BMDMs treated with anti-CD16 and anti-ACE2 antibodies to block viral entry or with Remdesivir to block viral replication. CTRL infected n = 7, anti-CD16+anti-ACE2 n = 3, RDV n = 3 independent datapoints over 2 independent experiments. Means with all datapoints. Unpaired, two-tailed, t-test. **q.** Human CXCL10 levels in supernatants of BMDMs infected in vitro in presence or absence of anti-CD16 and anti-ACE2 antibodies to block viral entry. CTRL infected N = 12, anti-ACE2+ anti-CD16 treated n = 6 independent datapoints over 2 independent experiments. Means with all datapoints. Unpaired, two-tailed, t-test.

[Source data](#)

[Extended Data Fig. 15 Blockade of inflammasome activation leads to reduced cytokine production in vitro \(matched to figure 4\).](#)

a. Representative flow cytometry plots of CXCL10 and TNF staining in total human macrophages and histograms of CXCL10 expression in infected (mNG^+) and uninfected (mNG^-) macrophages from lungs of SARS-CoV-2- mNG infected MISTRG6-hACE2 mice treated with caspase-1 (Casp1) or NLRP3 inhibitors in vivo. Mice were treated on days 6,8,10,12 post-infection and analysed at 14 d.p.i. Representative of n = 5 biologically independent mice. **b.** Mean fluorescent intensity (MFI) of CXCL10

expression in human macrophages isolated from infected MISTRG6-hACE2 mice treated with caspase-1 inhibitor or left untreated. N = 3 biologically independent mice. Representative of 3 independent experiments. Means with all datapoints and SD. Unpaired, two-tailed t-test. **c.** CXCL10 levels in serum of SARS-CoV-2-mNG infected MISTRG6-hACE2 mice (14 d.p.i.) treated with caspase-1 or NLRP3 inhibitors. N = 4 biologically independent mice examined over 2 independent experiments. Means with all datapoints and SD. Unpaired, two-tailed t-test. **d.**

Frequencies of mNG⁺ bone marrow-derived macrophages (BMDMs) infected with SARS-CoV-2-mNG in vitro. BMDMs were treated with caspase-1 (Casp1) or NLRP3 inhibitors or left untreated and analysed at 48 h.p.i. CTRL infected n = 22, Casp1 inhibitor-treated n = 17, NLRP3 inhibitor-treated n = 6 independent datapoints collected over at least 3-experiments. Means with all datapoints and SD. Unpaired, two-tailed t-test.

e. Frequencies of FLICA⁺ BMDMs infected with SARS-CoV-2 in vitro for 48 h. BMDMs were treated with caspase-1 or NLRP3 inhibitors or left untreated. CTRL infected n = 13, Casp1 inhibitor-treated n = 12, NLRP3 inhibitor-treated n = 6 independent datapoints collected over at least 3 independent experiments. Means with all datapoints. Unpaired, two-tailed t-test. P < 0.0001 = 3.33x10⁻⁵. **f.** Human IL-18 levels in supernatants of SARS-CoV-2-mNG infected BMDMs treated with caspase-1 (Casp1) inhibitor or left untreated. CTRL infected n = 8, Casp1 inhibitor-treated n = 6 independent datapoints collected over 2 independent experiments. Means with all datapoints and SD. Unpaired, two-tailed t-test. **g.** Representative histograms and quantification of IL-1 β in supernatants of BMDMs infected with SARS-CoV-2 in vitro. Cultures were treated with caspase-1 (Casp1) inhibitor. Uninfected n = 7; 48 h.p.i. CTRL infected n = 10, Casp1 inhibitor-treated n = 9, NLRP3 inhibitor-treated n = 3; 72 h.p.i. CTRL infected n = 5 Casp1 inhibitor-treated n = 3, NLRP3 inhibitor-treated n = 3 independent datapoints collected over at least 2 experiments. Means with all datapoints and SD. Unpaired, two-tailed t-test. P < 0.0001 = 4.96x10⁻⁷.

h. Human Gasdermin D (GSDMD) levels at 48 h.p.i. in supernatants of SARS-CoV-2-mNG infected BMDMs treated with caspase-1 inhibitor or left untreated. CTRL infected n = 10, Casp1 inhibitor-treated n = 6 independent datapoints collected over at least 3 independent experiments. Means with all datapoints. Unpaired, two-tailed t-test. **i.** LDH levels measured as absorbance at OD 490nm in supernatants of uninfected or SARS-CoV-2-

mNG infected BMDMs treated with Casp1 or NLRP3 inhibitor or left untreated in vitro. Uninfected n = 6, CTRL infected (48 h.p.i.) n = 11, Casp1 inhibitor-treated (48 h.p.i.) n = 9, NLRP3 inhibitor-treated (48 h.p.i.) n = 5 independent datapoints collected over 2 independent experiments. Means with all datapoints and SD. Unpaired, two-tailed t-test. P < 0.0001 = 7.38x10⁻⁶. **j.** Zombie Aqua incorporation in SARS-CoV-2-mNG infected BMDM treated with caspase-1 or NLRP3 inhibitors or left untreated (CTRL infected). Frequencies of Zombie⁺ cells within Annexin V⁻ population at 48 h.p.i. are reported. Uninfected n = 4, CTRL infected n = 7, Casp1 inhibitor n = 4, NLRP3 inhibitor n = 3 over 2 experiments. Means with all datapoints. Unpaired, two-tailed t-test. **k.** Human CXCL10 levels in supernatants of infected BMDMs treated with caspase-1 or NLRP3 inhibitors or left untreated. Supernatants were collected at 48 h.p.i. Uninfected n = 5, CTRL infected n = 12, Casp1 inhibitor n = 5, NLRP3 n = 4 independent datapoints over at least 2 independent experiments. Means with all datapoints and SD. Unpaired, two-tailed t-test. **l.** Human IL-1RA levels in supernatants of SARS-CoV-2-mNG infected BMDMs treated with caspase-1 inhibitor or not. Supernatants were collected at 48 h.p.i. CTRL infected n = 7, Casp1 inhibitor-treated n = 6, NLRP3 inhibitor-treated n = 4 independent datapoints collected over at least 2 independent experiments. Means with all datapoints. Unpaired, two-tailed t-test. **m.** Viral titres measured as PFU in lung homogenates of MISTRG6-hACE2 mice infected with SARS-CoV-2 and treated with caspase-1 inhibitor in vivo. Infected MISTRG6-hACE2 mice were treated with caspase-1 inhibitor on days 6,8,10,12 post-infection and analysed at 14 d.p.i. Lung homogenates were plaqued using Vero ACE2⁺TMPRSS2⁺ cells. of CTRL infected: n = 7, Casp1 inhibitor-treated: n = 6 biologically independent mice examined over 3 independent experiments. Box and whisker plot (min to max, with all datapoints) The whiskers go down to the smallest value (minimum) and up to the largest value (maximum). The box extends from the 25th to 75th percentiles. The median is shown as a line in the center of the box. Ratiopaired, two-tailed t-test. **n.** Representative images of plaque assays used to quantify infectious virus in supernatants of BMDMs infected with SARS-CoV-2-mNG and treated with caspase-1 or NLRP3 inhibitors. Supernatants of infected macrophage cultures were collected at 48 h.p.i. and plaqued using Vero ACE2⁺TMPRSS2⁺ cells. Plaques were resolved at 48 h.p.i. Representative of CTRL infected: n = 13, Casp1 inhibitor-treated:

$n = 8$, NLRP3 inhibitor-treated: $n = 5$ independent datapoints collected over 3 independent experiments.

[Source data](#)

Supplementary information

[Supplementary Information](#)

Supplementary Discussion, a guide for Supplementary Tables 1–5 and Supplementary References.

[Reporting Summary](#)

[Supplementary Table 1](#)

Human genes that are differentially regulated in lungs of infected MISTRG6-hACE2 in response to therapeutics. Genes that are upregulated in response to infection and downregulated in response to therapeutics (dexamethasone, anti-IFNAR + remdesivir) in these infected mice at 14 d.p.i. were included in the analysis (matched to Fig. 1d). Normalized expression of duplicates. $n = 2$ biologically independent mice examined over two independent experiments. Differential expression analysis was performed using DESeq2 and statistical significance was determined using the Wald test.

[Supplementary Table 2](#)

Cluster identifying markers and markers that identify temporal transcriptional changes associated with monocytes and macrophages in infected (4, 14 or 28 d.p.i.) or uninfected lungs of MISTRG6-hACE2 mice (matched to Fig. 1g). $n = 2$ biologically independent mice for each condition were pooled. Marker genes for each cluster of cells were identified using the Wilcoxon rank-sum tests with Seurat. For the adjusted P values, Bonferroni correction was used.

Supplementary Table 3

Expression of human genes that are enriched in macrophages (clusters identified as part of Fig. 1g) during SARS-CoV-2 infection and their response to anti-IFNAR2 and remdesivir therapy (matched to Fig. 1h). Normalized expression of duplicates was analysed. $n = 2$ biologically independent mice examined over two independent experiments. Differential expression analysis was performed using DESeq2 and statistical significance was determined using the Wald test.

Supplementary Table 4

Pearson and Spearman correlation values were calculated for each gene for its correlation with CXCL10, TNF or TLR7 in human monocytes and macrophages at 4 d.p.i. (based on Fig. 1g, matched to Fig. 3d) For the Pearson test, significance was based on the *t*-test with statistics based on Pearson's product-moment correlation coefficient $\text{cor}(x, y)$ and following a *t* distribution with $\text{length}(x)-2$ d.f. For Spearman's test, *P* values were recomputed using algorithm AS 89 with exact = TRUE. Correlation values, *P* values (two-tailed) and FDR-adjusted *P* values are presented.

Supplementary Table 5

The patient samples used for immunofluorescence staining. Details of patient demographics for specimens used in immunofluorescence staining, including age, gender, medication, time of death post-symptom onset (dps), co-morbidities, cause of death and histopathological findings. This table is presented as part of the Supplementary Methods.

Source data

Source Data Fig. 1

Source Data Fig. 2

Source Data Fig. 3

[**Source Data Fig. 4**](#)

[**Source Data Extended Data Fig. 1**](#)

[**Source Data Extended Data Fig. 2**](#)

[**Source Data Extended Data Fig. 3**](#)

[**Source Data Extended Data Fig. 4**](#)

[**Source Data Extended Data Fig. 5**](#)

[**Source Data Extended Data Fig. 6**](#)

[**Source Data Extended Data Fig. 8**](#)

[**Source Data Extended Data Fig. 9**](#)

[**Source Data Extended Data Fig. 10**](#)

[**Source Data Extended Data Fig. 11**](#)

[**Source Data Extended Data Fig. 12**](#)

[**Source Data Extended Data Fig. 13**](#)

[**Source Data Extended Data Fig. 14**](#)

[**Source Data Extended Data Fig. 15**](#)

Rights and permissions

[**Reprints and Permissions**](#)

About this article

Cite this article

Sefik, E., Qu, R., Junqueira, C. *et al.* Inflammasome activation in infected macrophages drives COVID-19 pathology. *Nature* **606**, 585–593 (2022). <https://doi.org/10.1038/s41586-022-04802-1>

- Received: 30 July 2021
- Accepted: 25 April 2022
- Published: 28 April 2022
- Issue Date: 16 June 2022
- DOI: <https://doi.org/10.1038/s41586-022-04802-1>

Share this article

Anyone you share the following link with will be able to read this content:

[Get shareable link](#)

Sorry, a shareable link is not currently available for this article.

[Copy to clipboard](#)

Provided by the Springer Nature SharedIt content-sharing initiative

Further reading

- [**Immune response in COVID-19: what is next?**](#)
 - Qing Li
 - Ying Wang
 - Yufang Shi

Cell Death & Differentiation (2022)

This article was downloaded by **calibre** from <https://www.nature.com/articles/s41586-022-04802-1>

| [Section menu](#) | [Main menu](#) |

- Article
- Open Access
- [Published: 08 June 2022](#)

Mechanism of mitoribosomal small subunit biogenesis and preinitiation

- [Yuzuru Itoh](#),
- [Anas Khawaja](#),
- [Ivan Laptev](#),
- [Miriam Cipullo](#),
- [Ilian Atanassov](#),
- [Petr Sergiev](#),
- [Joanna Rorbach](#) &
- [Alexey Amunts](#)

Nature volume **606**, pages 603–608 (2022)

- 8870 Accesses
- 257 Altmetric
- [Metrics details](#)

Abstract

Mitoribosomes are essential for the synthesis and maintenance of bioenergetic proteins. Here we use cryo-electron microscopy to determine a series of the small mitoribosomal subunit (SSU) intermediates in complex with auxiliary factors, revealing a sequential assembly mechanism. The methyltransferase TFB1M binds to partially unfolded rRNA h45 that is promoted by RBFA, while the mRNA channel is blocked. This enables binding of METTL15 that promotes further rRNA maturation and a large

conformational change of RBFA. The new conformation allows initiation factor mtIF3 to already occupy the subunit interface during the assembly. Finally, the mitochondria-specific ribosomal protein mS37 (ref. ¹) outcompetes RBFA to complete the assembly with the SSU–mS37–mtIF3 complex² that proceeds towards mtIF2 binding and translation initiation. Our results explain how the action of step-specific factors modulate the dynamic assembly of the SSU, and adaptation of a unique protein, mS37, links the assembly to initiation to establish the catalytic human mitoribosome.

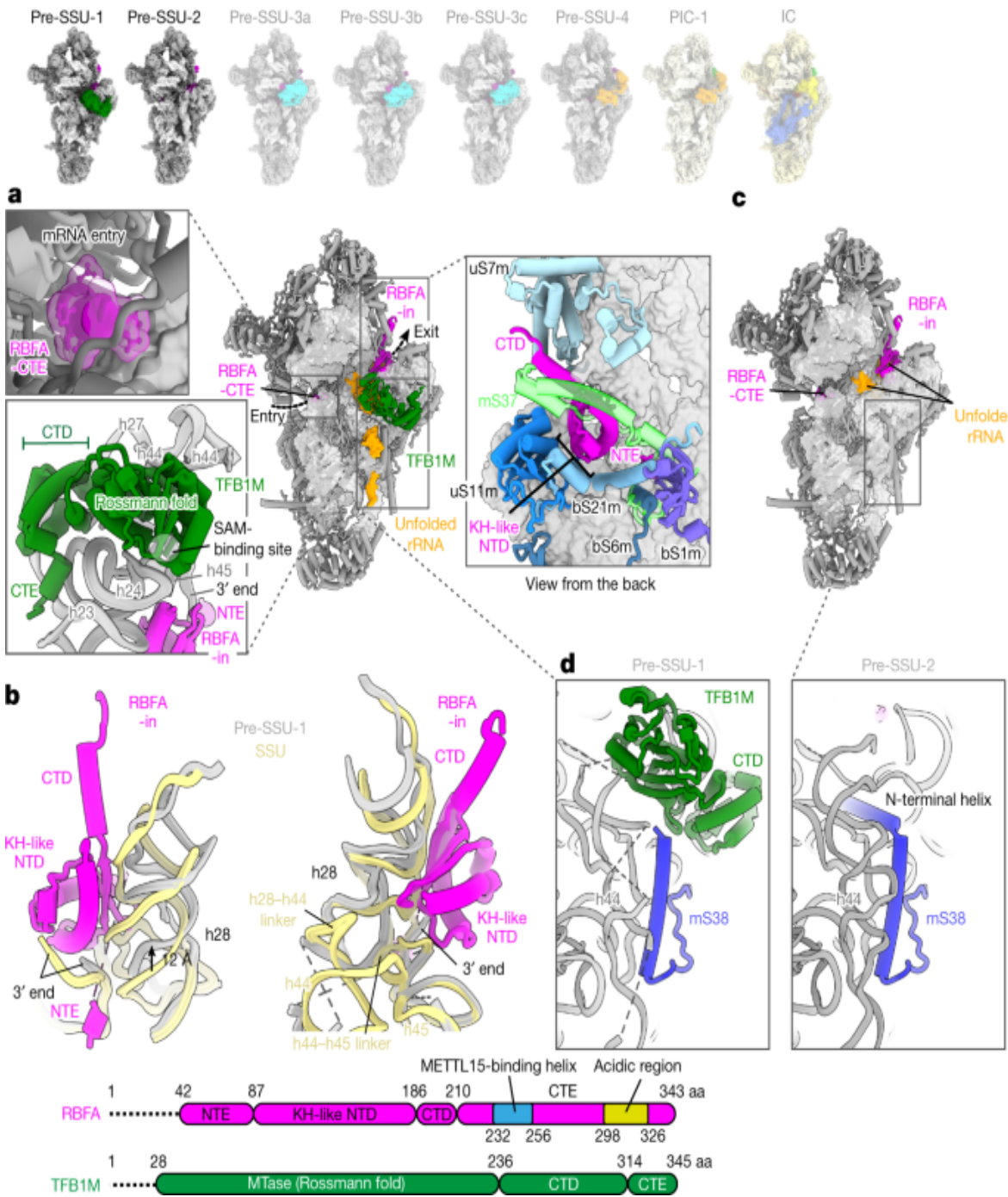
Main

The human mitoribosome consists of the SSU that binds mRNA and tRNA to ensure accurate initiation and decoding, and the large subunit (LSU) that secures a nascent polypeptide arrival to the inner mitochondrial membrane via the OXA1L insertase^{1,2,3,4}. Although recent structural studies have deepened our understanding of the mitoribosome structure, function and antibiotic binding^{1,2,3,4,5,6,7,8,9}, we still lack information on the assembly of the mitoribosomal components that would explain how they cooperatively reach the first functional state to initiate translation. In bacteria and the cytosol of eukaryotic cells, the assembly steps for the SSU include a series of alternating RNA conformations that rearrange in a stepwise manner into a native structure with a fully folded decoding region^{10,11,12,13,14}. However, no structural data exist on any of the assembly steps of the SSU in mammalian mitochondria, and it remains unclear to what extent they are shared with the bacterial counterpart, and what are the tasks of mitochondria-specific components in ensuring a correct placement and folding of the rRNA. This is particularly important as defects in the assembly are linked to severe pathologies that manifest as a broad range of developmental disorders¹⁵. In this study, we determined sequential cryo-electron microscopy (cryo-EM) structures of stable assembly intermediates and initiation complexes at 2.8–3.2 Å resolution that involve six factors: RBFA, TFB1M, METTL15, mtIF3, mS37 and mtIF2 (Extended Data Figs. ^{1–4}, Supplementary Tables ¹ and ², Supplementary Video ¹ and Supplementary Figs. ¹ and ²).

As several rRNA methyltransferases are required for the assembly, to stall the process, we first depleted the enzyme TRMT2B, responsible for the

formation of 5-methyluridine^{16,17} ([Methods](#)), which produced a viable cell line with stable rRNA and allowed to purify intermediate pre-SSU particles in different states. Judged by the proportion of the unfolded rRNA, the earliest intermediate pre-SSU-1 (3.2 Å resolution) is represented by partially disordered rRNA helices (h44 and h45) and two disordered linkers (h28–h44 and h44–h45) (Fig. [1a](#) and Extended Data Figs. [1](#) and [2](#)). It lacks the peripheral mitoribosomal protein mS37, and instead contains the assembly factors RBFA and dimethyladenosine transferase TFB1M (Fig. [1a](#) and Extended Data Fig. [1](#)). RBFA has a KH-like N-terminal domain (NTD), followed by a short C-terminal domain (CTD), which remained unresolved in the previous structures^{10,18} (Fig. [1](#)). Mitochondria-specific extensions nearly double the protein size (Extended Data Fig. [5](#)), and we identified their specific functions. The association of RBFA leads to a vertical displacement of uS7m in the head by approximately 12 Å up, and the entire head is rotated approximately 10° towards the A site, compared to the mature SSU, thereby exposing the P site region (Extended Data Fig. [6a](#)). Such an arrangement of RBFA occupies a position on the SSU, which is incompatible with mS37 (Fig. [1a](#), Extended Data Fig. [6b](#) and Supplementary Video [2](#)), and mitochondrial C-terminal extension (CTE) has a specific role by stretching over 60 Å through the entire mRNA channel to block its entry (Fig. [1a](#)). RBFA further acts as a local rRNA scaffolder that promotes maturation by predisposing the hotspot modification region for TFB1M, and we detected two functional RBFA–rRNA contacts (Fig. [1b](#) and Extended Data Fig. [6c](#)): (1) binding of otherwise free rRNA 3' end, which in the mature SSU is associated with the missing mS37; and (2) binding of rRNA h28 through a 30 Å-long surface, correlated with a dislocation of h28 by 12 Å towards the h44–h45 linker.

Fig. 1: Structures of pre-SSU-1 and pre-SSU-2 states.



a, Pre-SSU-1 with RBFA and TFB1M. Unfolded rRNA is in orange. RBFA-CTE (surface model) blocking the mRNA channel (upper left), TFB1M binding (bottom left), and superposition of pre-SSU-1 with mature SSU showing clashes of RBFA with mS37 (right) are displayed. **b**, Superposition of pre-SSU-1 with mature SSU rRNA shows an upwards displacement of h28 due to extended association with RFBA that also interacts with the

rRNA 3' end. **c**, Pre-SSU-2 with RBFA. **d**, Comparison of pre-SSU-1 and pre-SSU-2 shows that the mS38 N-terminal helix is disordered in pre-SSU-1. aa, amino acid; NTE, N-terminal extension.

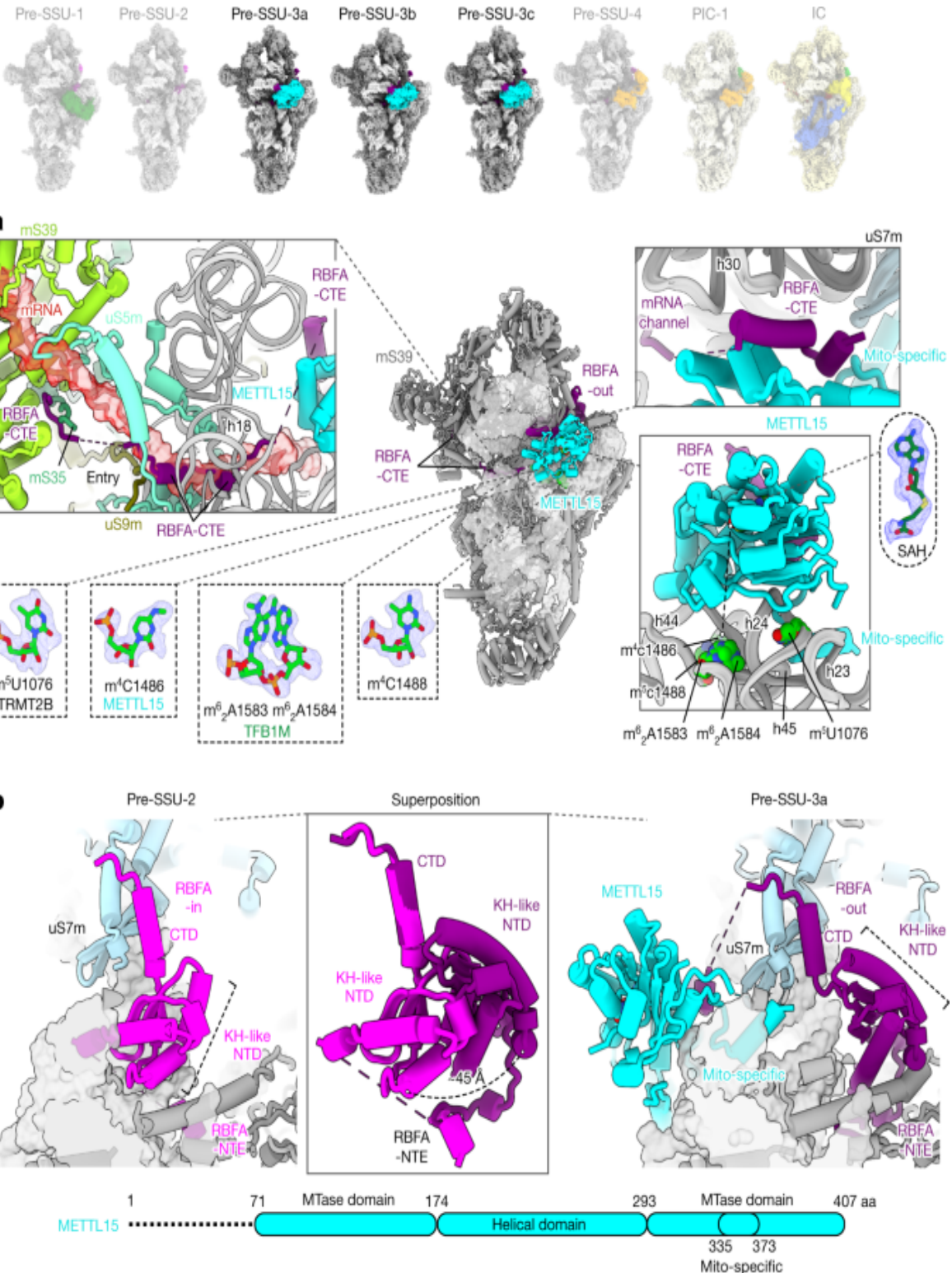
TFB1M is the methyltransferase that uses *S*-adenosylmethionine (SAM) to dimethylate two adjacent adenosine residues, A937 and A938 (mouse numbering, equivalent to human A1583 and A1584) (Supplementary Table 3), in the hairpin loop of h45. It has a CTD (residues 237–314), followed by a CTE (residues 315–345), forming an additional α -helix that together make a large interface of $2,077 \text{ \AA}^2$ with the rRNA h23, h24, h27 and h45 (Fig. 1a and Extended Data Fig. 7a). The C-terminal α -helix, which is disordered in the crystal structures^{19,20}, further links TFB1M from h24 to the platform rRNA h23 (Extended Data Fig. 7a). In the SSU body, the N-terminal helix of the mitoribosomal protein mS38 is disordered, and its mature conformation would clash with TFB1M.

Comparison of our pre-SSU-1 and pre-SSU-2 (3.1 \AA resolution) structures shows that TFB1M is missing in the latter, whereas rRNA is more ordered (Fig. 1a–c, Extended Data Figs. 1 and 7b and Supplementary Video 2). In addition, the N-terminal helix of mS38 is inserted into the rRNA groove, adopting its mostly mature conformation (Fig. 1d and Extended Data Fig. 7b). Thus, RBFA prepares pre-SSU-2 for a subsequent accommodation of the next assembly factor, and also prevents a premature association of mRNA and mS37.

In the same dataset, we also observed a class with a subset of particles with folded rRNA and the additional density that is different from TFB1M, suggesting a later sequential assembly intermediate. To explore how the SSU progresses through the mitoribosomal assembly pathway after maturation of TFB1M, we reasoned that an inhibition of the corresponding LSU assembly would allow the SSU to proceed towards later stages up to the subunit joining. Therefore, we knocked out the enzyme mitochondrial rRNA methyltransferase 3 (MRM3), which is responsible for a late assembly of the LSU²¹, and collected cryo-EM data of the accumulated SSU and LSU particles (Extended Data Figs. 3, 4 and 8 and Supplementary Figs. 2 and 3). Approximately 7% of the SSU particles in this cryo-EM data showed identical structural features and the presence of the same additional density that were also detected in the particles from the TRMT2B-depleted

cells, and the latter was identified as the N^4 -methylcytidine methyltransferase METTL15 (Extended Data Figs. 1, 2a and 3a). METTL15 is the mitochondrial orthologue of the bacterial RsmH and is responsible for the methylation of C1486 in the SSU rRNA decoding centre^{22,23,24}. We resolved this state (pre-SSU-3) at 2.8 Å resolution (Extended Data Fig. 1 and Supplementary Fig. 2). In pre-SSU-3, the rRNA h28, h44 and h45 are folded and all known rRNA modifications are observed (Fig. 2a). The improved resolution allowed us to reveal how mito-specific RBFA-CTE blocks mRNA binding: residues 278–298 fill the A site, residues 299–326 that are enriched with 13 Asp/Glu residues (see 'acidic region' in Fig. 1) is located at the mRNA entry and further interact with mS35 and mS39 to prevent recruitment of mRNA.

Fig. 2: Structures of pre-SSU-3a,b,c states.



a, Pre-SSU-3 with RBFA-out and METTL15. RBFA-CTE blocks the mRNA path on mS39, the channel entry (uS5m and uS9m) and the A site (uS5m) (upper left); mRNA is superimposed in red. RBFA-CTE interacts with

METTL15 (upper right). rRNA modifications are observed in the density (bottom left). S-adenosylhomocysteine (SAH) with its density is away from the target residue ($\text{m}^4\text{C}1486$), indicating a post-catalytic state (bottom right); the dashed line shows the 40 Å distance. **b**, Superposition of pre-SSU-2 with pre-SSU-3 shows that RBFA adopts a conformational change.

In coordination with METTL15 binding and rRNA maturation, RBFA adopts a large conformational change in pre-SSU-3 (from in to out) (Fig. 2b and Supplementary Video 2), which is enabled by a pivot point between the KH-like domain and CTD. The conformational change appears to be a unique feature of RBFA, which was not reported for bacterial counterparts^{10,25}. METTL15 would clash with RBFA-in from pre-SSU-2 (Extended Data Fig. 9a), but forms direct interactions with RBFA-out through an α -helix (residues 232–256 in RBFA-CTE) (Fig. 2a), which is consistent with the report that METTL15 coprecipitates with RBFA²³. Therefore, the association of METTL15 triggers the conformational change from RBFA-in to RBFA-out. This implies that METTL15, in addition to its enzymatic activity, has an important structural role in guiding the biogenesis pathway and stabilizing the conformation that excludes the RBFA from the mitoribosomal core. The conformational change allows the head to rotate approximately 6° back from the A site towards the E site, and the associated uS7m is now placed approximately 8 Å below its initial position in pre-SSU-2 (Supplementary Video 2).

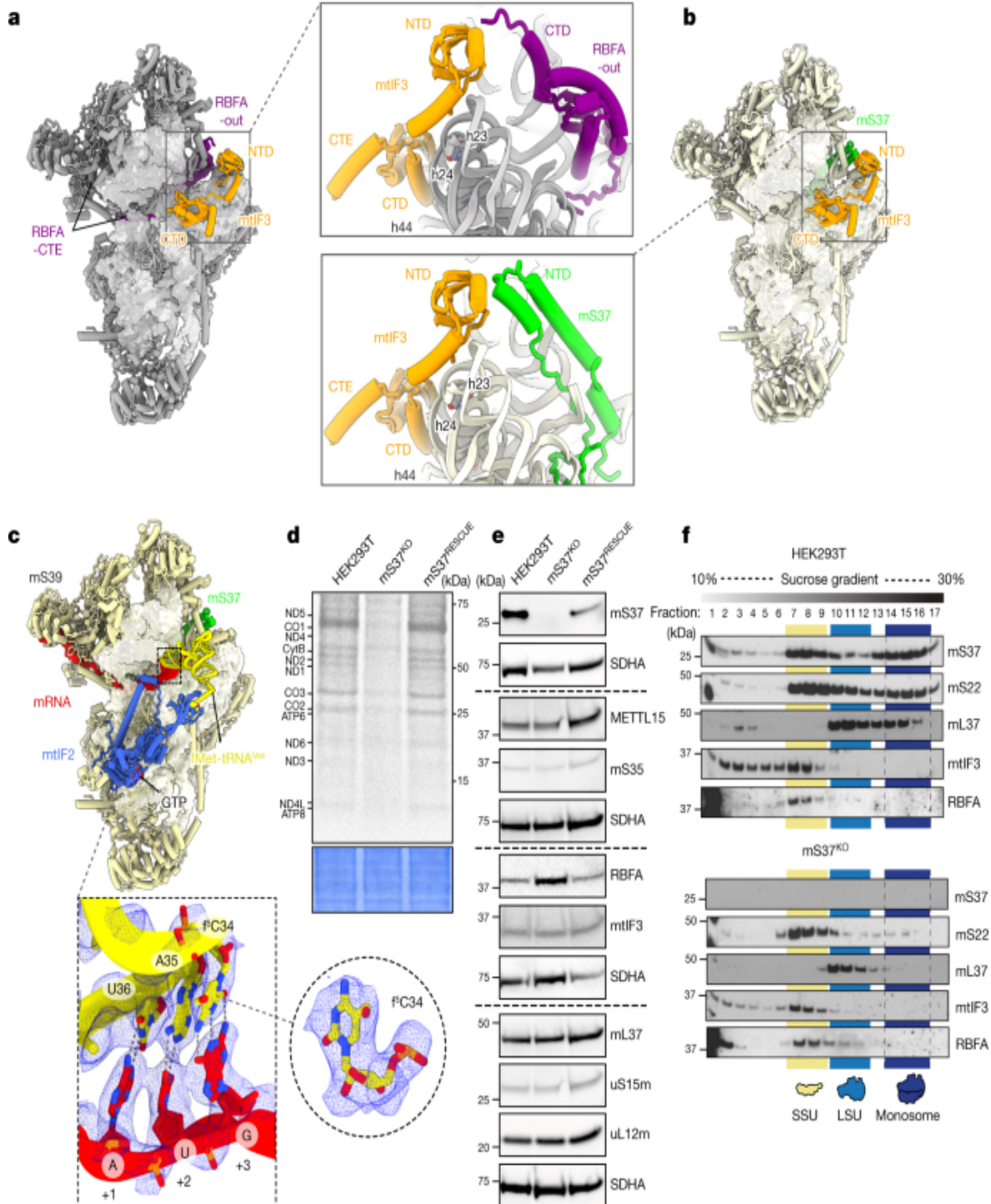
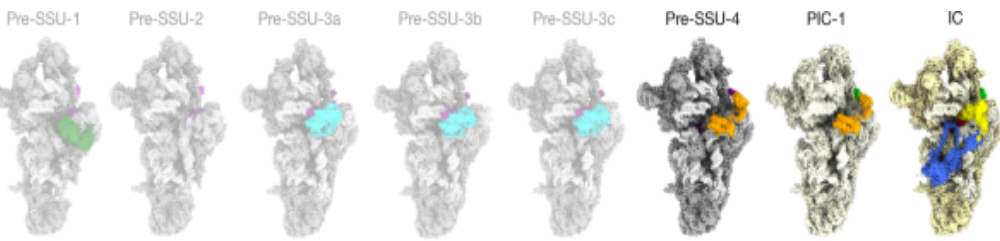
Structure prediction of RBFA by AlphaFold2 (ref. 26) provides a conformation that is different from RBFA-in, which, to our knowledge, has been the only known conformation before this work (Extended Data Fig. 9b). We also generated the RBFA–METTL15 complex structure with AlphaFold2 by connecting the two sequences with a linker without the SSU, and the interaction through the RBFA-CTE helix was also predicted (Extended Data Fig. 9c).

To better characterize the interactions, we further classified the pre-SSU-3 particles and obtained three conformations at 2.8–3.1 Å resolution (pre-SSU-3a,b,c) that differ from each other with respect to the rRNA conformation of h23 and h24 and the METTL15–SSU interactions (Extended Data Figs. 1 and 9d and Supplementary Video 3). In pre-SSU-3a, the mito-specific

insertion (residues 335–373) forms an α -helix and interacts with h23, h24 and h45 (Extended Data Fig. 9e), and these interactions move the tip of h24 by approximately 6 Å, compared to the mature SSU, which opens the space between h24 and h44, and shifts the entire SSU platform by approximately 4 Å (Extended Data Fig. 9d,e and Supplementary Video 3). In pre-SSU-3b, the mito-specific insertion is mostly disordered, and the methyltransferase domain has looser contact to h24. As a result, h24 adopts its mature conformation, whereas h23 is extended and detached from the tip of h24 (Extended Data Fig. 9d). Finally, the pre-SSU-3c structure represents the completely folded rRNA (Extended Data Figs. 1 and 9d). Therefore, METTL15 has the additional role that facilitates rRNA folding and ultimately leads to a productive assembly pathway.

Upon completion of rRNA folding, METTL15 is released and replaced by the initiation factor mtIF3. This leads to the next assembly state pre-SSU-4 (2.9 Å resolution) (Fig. 3a, Extended Data Fig. 1 and Supplementary Video 4). Mitochondrial mtIF3 has diverged considerably from its bacterial counterpart and it was not found colocalized on the SSU with mRNA and tRNA². Yet, the heart and skeletal muscle-specific loss of mtIF3 leads to cardiomyopathy, and the constitutive knockout in mice is embryonic lethal²⁷. In pre-SSU-4, mtIF3 adopts a conformation with its CTD bound to rRNA h24 and h44 that blocks the premature association of LSU and fMet-tRNA^{Met} (Fig. 3a). The NTD contacts RBFA-CTD, whereas the association of mS37 remains sterically precluded (Fig. 3a). Consistently, knockout of the gene encoding mtIF3 shows a reduction of steady-state levels of mS37 (Supplementary Figs. 7 and 8). RBFA keeps occupying the mRNA path, and therefore the binding of mRNA remains prevented. Thus, the binding of mtIF3 during the assembly process is in stark contrast to the mechanism in bacteria, where it associates after all of the ribosomal components have been assembled to further secure the fidelity of translation initiation²⁸. Recent structural studies in trypanosomes have also suggested an involvement of mitochondrial initiation factors during the assembly²⁹.

Fig. 3: Structures of pre-SSU-4, PIC-1 and IC states.



a, Pre-SSU-4 with RBFA-out and mtIF3. **b**, PIC-1 with mS37 and mtIF3. **c**, IC SSU–mtIF2–GTP–fMet-tRNA^{Met}–mRNA with the density showing codon–anticodon interactions at the P site and modification (^{f5}C) on tRNA^{Met}. **d**, Metabolic labelling with [³⁵S]-methionine of mitochondrial translation products in the wild-type, mS37^{KO} and mS37^{RESCUE} cells. Coomassie blue-stained gel was used as the loading control. **e**, Steady-state levels of mitoribosomal proteins, assembly and initiation factors in the wild-type, mS37^{KO} and mS37^{RESCUE} cells analysed by immunoblotting. SDHA was the loading control. **f**, Mitoribosomal sedimentation on a 10–30% sucrose gradient. For **d–f**, representative gels from three independent biological experiments are shown. For source data, see Supplementary Figs. [4](#) and [5](#).

We also identified a class with mS37 and mtIF3 without RBFA and refined it to 2.9 Å resolution (Fig. [3b](#), Extended Data Figs. [1](#) and [3](#), Supplementary Fig. [2](#) and Supplementary Video [4](#)). It represents pre-initiation complex (PIC-1)². Therefore, the arrival of mS37 disrupts the RBFA–mtIF3 contact, and RBFA is eliminated to finalize the assembly. Unlike typical peripheral mitoribosomal proteins, mS37 is unusually conserved and can also be found in the mitoribosomal structures from trypanosomes^{[30](#)}, fungi^{[31](#)} and ciliates^{[32](#)}. To further investigate the special role of mS37, we generated its knockout cell line that showed a decrease in protein synthesis in mitochondria (Fig. [3d](#) and Extended Data Fig. [10a](#)). Moreover, increased steady-state levels of RBFA were observed, which supports an equilibrium shift towards assembly, as earlier states are accumulated and no monosomes were formed (Fig. [3e,f](#)).

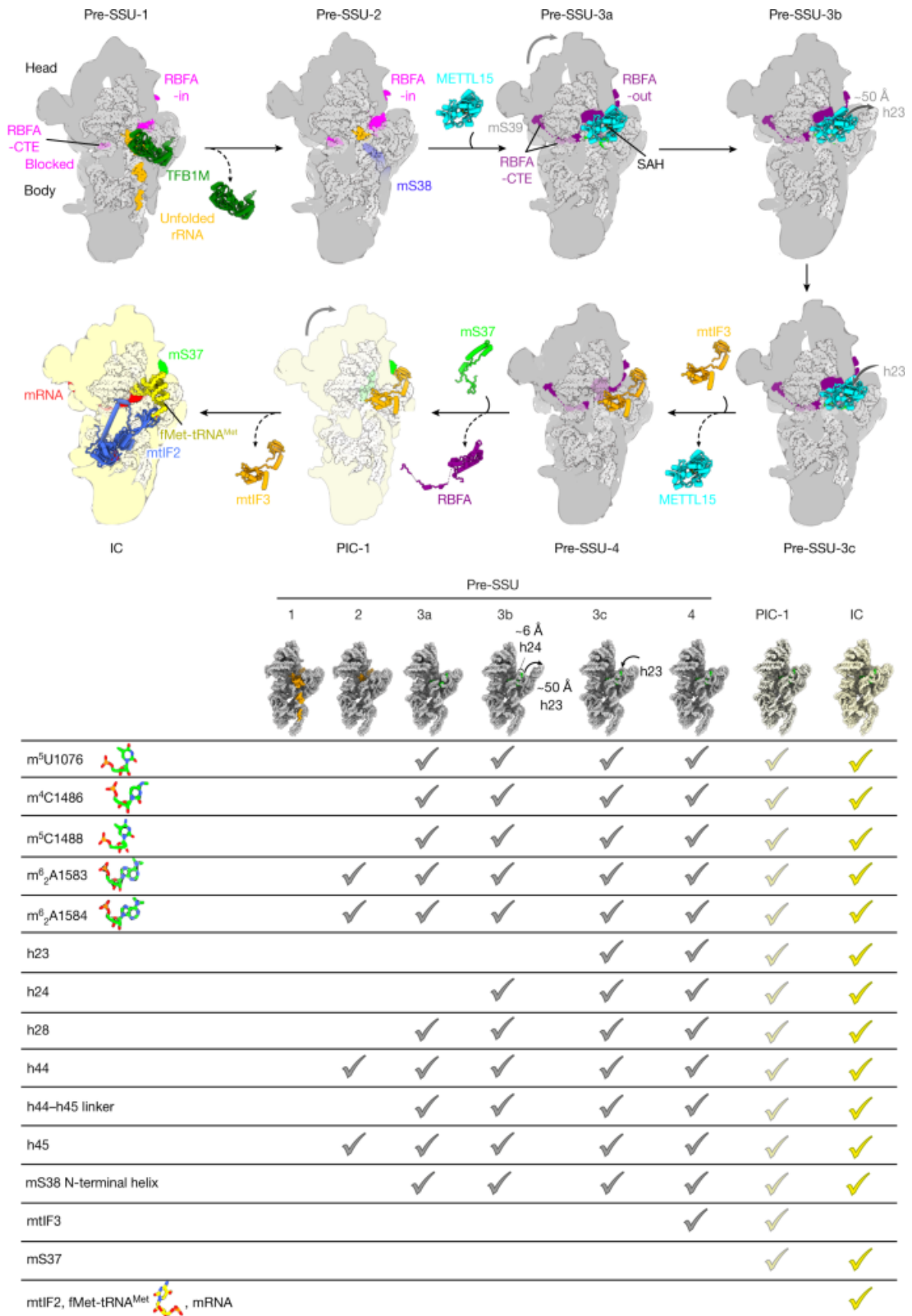
The structural analysis of the SSU assembly intermediates obtained from the *MRM3*-knockout model suggests that disruption of the LSU assembly affects maturation of SSUs. To strengthen the structural data, we performed metabolic labelling of the nascent polypeptides in the *MRM3*-knockout cells and gradient analysis, which detected no mitochondrial translation or monosome formation (Extended Data Fig. [10a–c](#)). We observed an accumulation of RBFA and decreased levels of mS37 in the mitoribosome (Extended Data Figs. [10c](#) and [11a](#)), consistent with our structural studies. Furthermore, the overall steady-state levels showed a downregulation of mS37 and increased abundance of RBFA compared to the wild type

(Extended Data Fig. 11a,b). These observations were further validated by an additional analysis of cells with a knockout of the gene encoding another LSU assembly factor, GTPBP10 (refs. 33,34). Similarly to the *MRM3*-knockout cells, an attenuation of translation and monosome formation are correlated with decreased levels of mS37 and accumulation of RBFA (Extended Data Figs. 10a–c and 11a), supporting coordination between the assembly pathways of both subunits.

Finally, a subpopulation of 3.5% particles in our data that represents an initiation complex (IC) resolved at 3.1 Å resolution (Extended Data Fig. 1 and Supplementary Fig. 2). It has hallmark features of the initiation factor mtIF2 and initiator-tRNA that together form the complex SSU–mtIF2–GTP–fMet-tRNA^{Met}–mRNA (Fig. 3c, Extended Data Fig. 12a and Supplementary Video 4). In addition, for the tRNA^{Met} bound to the P site, we identified a modification at position 34 with 5-formylcytidine (f⁵C) (Fig. 3c), which is essential for mitochondrial translation³⁵. The relative location of mtIF2 and the SSU head rotational state in our native complex are in a similar configuration to the reconstituted monosome IC³, and mS37 facilitates the binding of mtIF2 (Extended Data Fig. 12b). However, the current complexes do not explain how an mRNA is delivered to the mitoribosome, thus leaving open the question of the activation mechanism of mitochondrial translation.

In conclusion, the model for the SSU progression through the assembly pathway includes a sequence of binding factors as an integrated network, with RBFA serving as a regulator through its allosteric control mechanism (Fig. 4), which was not reported in a bacterial counterpart. The finding of the mtIF3 as an assembly factor features a new paradigm of a unique protein, mS37, that links the assembly to the initiation of translation, and additional transient intermediates are likely to exist. The role of mS37 is confirmed biochemically, and we have shown that it is reduced when the LSU is not fully assembled, supporting the special function for this protein in mitochondria.

Fig. 4: Mitoribosomal SSU biogenesis.



SSU progression showing the major biogenesis states. A table of specific biogenesis events and stages when they occur is also displayed; models of rRNA are shown in insets.

Methods

Generation and maintenance of mammalian cell lines

The Flp-In-TREx human embryonic kidney 293T (HEK293T) cell line (Invitrogen) was cultured in Dulbecco's modified eagle medium (DMEM) supplemented with 10% (v/v) tetracycline-free FBS, 2 mM Glutamax (Gibco), 1× penicillin–streptomycin (Gibco), 50 µg ml⁻¹ uridine, 10 µg ml⁻¹ Zeocin (Invitrogen) and 100 µg ml⁻¹ blasticidin (Gibco) at 37 °C under 5% CO₂ atmosphere. Cell lines have been routinely tested for mycoplasma contamination.

For SILAC-based quantitative proteomic analysis, cells were grown in Iscove's modified Dulbecco's medium (IMDM) for Stable Isotope Labeling by Amino acids in Cell culture (SILAC) supplemented with 'heavy' (¹⁵N-labelled and ¹³C-labelled) or 'light' Arg, Lys and Pro and 10% dialysed FCS (Thermo Scientific HyClone).

The *Trmt2b*-knockout cell line was cultured in RPMI 1640 medium (Gibco) supplemented with 10% FBS (Gibco), GlutaMAX (Gibco) and penicillin–streptomycin (Gibco) at 37 °C, 5% CO₂. Large cell culture volumes were grown in Thomson OptimumGrowth 1.6-l and 5-l flasks in a shaker incubator at 110 rpm. For the cryo-EM sample, approximately 10 bln cells of the *Trmt2b*-knockout cell line were used.

Trmt2b gene inactivation

For the mitoribosome preparation, we used an NS0 mouse cell line with an inactivated *Trmt2b* gene that has been characterized in ref. [16](#). In brief, guide RNA (gRNA) for Cas9 targeting the first coding exon of *Trmt2b* was inserted into the pX458 vector (Addgene #48138). NS0 cells were transfected with the pX458 plasmid containing the gRNA sequence using a

Lipofectamine 3000 reagent (Thermo Scientific). Twenty-four hours after transfection, GFP-positive cells were sorted using BD FACS Aria III in 96-well plates containing 0.2 ml of RPMI medium per well. Individual clones were analysed by PCR amplification of an approximately 250-bp *Trmt2b* fragment (5'-TCAAGAGTCCTAAATGCACAACC-3' and 5'-CCAGGAGTCATCTCTACAATGC-3') and sequencing of the amplicon. For off-target analysis, we chose five off-targets with the highest score according to the Benchling CRISPR gRNA designing tool (<https://benchling.com>). Each off-target was analysed by PCR amplification of approximately 250 bp and sequencing.

***MRM3*, *mS37* and *GTPBP10* gene inactivation**

To generate the *MRM3*-knockout and *mS37*-knockout cell lines, two pairs of gRNAs targeting exon 1 of *MRM3* or *mS37* (Supplementary Table 4) were designed and cloned into the pSpCas9(BB)-2A-Puro (pX459) V2.0 vector to generate out-of-frame deletions. Cells were transfected with the pX459 variants using Lipofectamine 3000 according to the manufacturer's recommendations. Transfected cell populations were selected by puromycin treatment at a final concentration of 1.5 µg ml⁻¹ for 48 h. Subsequent to this, cells were diluted to achieve single-cell-derived clones on 96-well plates. Resultant clones were screened by Sanger sequencing to assess knockout, and loss of *MRM3* and *mS37* in selected clones was confirmed by western blotting. The *GTPBP10*-knockout cell line was generated as previously described³⁴.

Generation of the rescue cell lines

To generate knockout cell lines stably re-expressing the protein of interest (*mS37*, *MRM3* and *GTPBP10*), the HEK293T cell line that permits doxycycline-inducible expression of the gene of interest in a dose-dependent manner was used. HEK293T cells were cultured at 37 °C under 5% CO₂ in DMEM supplemented with 10% (v/v) tetracycline-free FBS, 1× penicillin–streptomycin (Gibco), 50 µg ml⁻¹ uridine, 100 µg ml⁻¹ zeocin (Invitrogen) and 10 µg ml⁻¹ blasticidin S (Gibco). Knockout cells were seeded in a 10-cm dish, 1 day before transfection, to achieve 70–90% confluence. Co-transfection of the expression plasmid pcDN5/FRT/TO (with *mS37*, *MRM3*–

Flag and GTPBP10-Flag) and the Flp-recombinase plasmid pOG44 was carried out using Lipofectamine 3000 (Invitrogen), according to the manufacturer's instructions. Selective antibiotics, 100 µg ml⁻¹ of hygromycin (Invitrogen) and 10 µg ml⁻¹ blasticidin S were added 48 h post-transfection and culture media were replaced every 2–3 days. To induce expression of the protein of interest, cells were incubated with 50 ng ml⁻¹ doxycycline for 48 h before analysis.

Mitoribosome preparation

Cells were harvested by centrifugation at 1,000g for 7 min. Cells were resuspended in MIB buffer (50 mM HEPES-KOH, pH 7.5, 10 mM KCl, 1.5 mM MgCl₂, 1 mM EDTA, 1 mM EGTA and 1 mM DTT) and allowed to swell by stirring on ice. SM4 buffer (0.28 M sucrose, 0.84 M mannitol, 50 mM HEPES-KOH, pH 7.5, 10 mM KCl, 1.5 mM MgCl₂, 1 mM EDTA, 1 mM EGTA and 1 mM DTT) was added to adjust the final concentrations of sucrose and mannitol to 70 mM and 0.21 M, respectively. Lysis of the cells was done in a nitrogen cavitation chamber at 500 psi for 20 min on ice. Lysate was cleared by centrifugation at 800g for 15 min. Supernatant was collected and the pellet was resuspended in half of the volume of the MIBSM buffer (70 mM sucrose, 0.21 M mannitol, 50 mM HEPES-KOH, pH 7.5, 10 mM KCl, 1.5 mM MgCl₂, 1 mM EDTA, 1 mM EGTA and 1 mM DTT) used at the previous step and homogenized in teflon Dounce homogenizer. Homogenate was centrifuged 800g for 15 min and supernatant was collected. The procedure with the pellet was repeated using half of the MIBSM buffer volume in the previous step. All supernatants were combined. Mitochondria were pelleted from cell lysates by centrifugation at 10,000g for 15 min at 4 °C, resuspended in MIBSM buffer and loaded on top of the step sucrose gradient (1.0 M and 1.5 M sucrose in 20 mM HEPES-KOH pH 7.5, and 1 mM EDTA) in SW40 tubes (Beckman Coulter) and centrifuged in a SW40 Ti rotor at 28,000 rpm (139,000g) for 1 h at 4 °C. Mitochondria were collected from tubes, resuspended in equal volume of 20 mM HEPES-KOH pH 7.5, and centrifuged at 10,000g for 10 min at 4 °C. Pellets of mitochondria were snap-frozen in liquid nitrogen and stored at –80 °C.

Purified mitochondria were defrosted and lysed in two volumes of lysis buffer (25 mM HEPES-KOH pH 7.5, 100 mM KCl, 20 mM Mg(OAc)₂, 2% Triton X-100, 2 mM DTT, 1X cOmplete EDTA-free protease inhibitor cocktail (Roche) and 40 U μ l⁻¹ RNase inhibitor (Invitrogen) for 10 min on ice. Lysates were cleared by centrifugation at 15,871g for 10 min at 4 °C, then each 1 ml was loaded on top of a 0.4-ml sucrose cushion (0.6 M sucrose, 25 mM HEPES-KOH pH 7.5, 50 mM KCl, 10 mM Mg(OAc)₂, 0.5% Triton X-100 and 2 mM DTT) and centrifuged in a TLA 120.2 rotor (Beckman Coulter) at 100,000 rpm (436,000g) for 1 h at 4 °C. The pellet was resuspended in resuspension buffer (25 mM HEPES-KOH pH 7.5, 50 mM KCl, 10 mM Mg(OAc)₂, 0.05% *n*-dodecyl β -d-maltoside (β -DDM) and 2 mM DTT), loaded on top of 10 ml of a 15–30% sucrose gradient (25 mM HEPES-KOH pH 7.5, 50 mM KCl, 10 mM Mg(OAc)₂, 0.05% β -DDM and 2 mM DTT) and centrifuged in a TLS-55 rotor (Beckman Coulter) at 39,000 rpm (130,000g) for 2 h 15 min. Mitoribosome gradients were fractionated into approximately 100- μ l fractions and absorbance of each fraction was measured. Fractions corresponding to SSU and LSU peaks were gathered and the buffer was changed to resuspension buffer using centrifugal concentrator Vivaspin MWCO 30,000 PES (Sartorius). Obtained SSU and LSU solutions were used for grid preparation.

SDS-PAGE and western blot analysis

To assess the steady-state levels of the individual proteins, total cell extracts or purified mitochondria were analysed using the SDS-PAGE and western blotting. Cell pellets from the wild-type HEK293T cells and *MRM3*-knockout, *mS37*-knockout and *GTPBP10*-knockout lines were lysed (50 mM Tris-HCl pH 7.4, 150 mM NaCl, 5 mM MgCl₂, 1 mM EDTA, 1% Triton X-100 and 1× PIC (Roche). Protein concentration was measured using the Pierce BCA Protein Assay Kit (Thermo Fisher Scientific). Equal amounts (approximately 30 μ g) of total cell extracts or mitochondrial proteins (approximately 10 μ g) were separated by SDS-PAGE and subsequently wet transferred to the polyvinylidene difluoride (PVDF) membranes for western blotting. The membranes were blocked for 1 h with 5% non-fat milk (Semper) in PBS and further incubated overnight with specific primary antibody at 4 °C. The next day, the blots were incubated with the horseradish

peroxidase (HRP)-conjugated secondary antibody and visualized using enhanced chemiluminescence (ECL; Bio-Rad). The primary and secondary antibodies are summarized in Supplementary Table 4.

[³⁵S]-metabolic labelling of mitochondrial proteins

To label newly synthesized mitochondrial DNA-encoded proteins, cells were seeded into a six-well dish at 80–90% confluence. First, two washing steps of 5 min each in methionine/cysteine-free DMEM were performed.

Subsequently, cells were incubated with fresh methionine/cysteine-free DMEM supplemented with Glutamax 100X (Gibco), sodium pyruvate 100X (Gibco), 10% dialysed FBS and 100 µg ml⁻¹ emetine (Sigma-Aldrich) for 20 min at 37 °C. Labelling was performed with the addition of 166,7 µCi ml⁻¹ of EasyTag EXPRESS [³⁵S] protein labelling mix (methionine and cysteine) (Perkin Elmer) for 30 min at 37 °C. Following labelling, cells were washed with 1 ml of PBS three times and the final pellets were collected by centrifugation. Cells were lysed in 1× PBS-PIC with the addition of 50 units of benzonase (Life Technologies) with incubation on ice for 20 min, followed by the addition of SDS to 1% final concentration, and further incubation on ice for 30 min. After cell lysis, 30 µg total protein was separated on Bolt 12% Bis-Tris Plus (Invitrogen) SDS-PAGE gels. Gels were then incubated in Imperial Protein Stain (Thermo Fisher) for 1 h and with fixing solution (20% methanol, 7% acetic acid and 3% glycerol) for 1 h. Next, gels were vacuum-dried at 65 °C for 2 h. The resultant gel was exposed to storage phosphor screens and visualized with Typhoon FLA 7000 Phosphorimager.

Sucrose gradient centrifugation analysis

Isolation of mitochondria and sucrose gradient centrifugation was performed as previously described². In brief, 1 mg of mitochondria was lysed in lysis buffer (10 mM Tris-HCl pH 7.5, 100 mM KCl or 50 mM KCl, 20 mM MgCl₂, 1× PIC, 260 mM sucrose and 1% Triton X-100) freshly supplemented with 0.4 U µl⁻¹ final concentration of RNase Block Ribonuclease Inhibitor (Agilent), loaded onto a linear sucrose gradient (10–30%, 11 ml total volume) in 1× gradient buffer (20 mM Tris-HCl pH 7.5, 50

mM KCl, 20 mM MgCl₂ and 1× PIC) and centrifuged for 15 h at 79,000g at 4 °C (Beckman Coulter SW41-Ti rotor). A total of 25 fractions with a volume of 450 µl each were collected via pipetting from the top of the gradient, and 15 µl of each fraction was used for western blot analysis. For fractions 1 and 2, and for fractions 18 and 19, 7.5 µl of each fraction was combined and resolved together.

For SILAC-based proteomics, HEK293T-knockout or MRM3-knockout cells were grown in ‘heavy’, containing ¹⁵N-labelled and ¹³C-labelled Arg and Lys, or ‘light’-labelled media for more than seven doublings. Cell lines were pooled together, and mitochondrial isolation and sucrose gradient analysis were performed as described above.

Mass spectrometry analysis

Peptides from SILAC sucrose gradient centrifugation experiments were prepared from fractions 1 and 2 joined, 3 and 4 joined, and 5 to 17 individually. Collected fractions were precipitated in 20× 100% ice-cold ethanol overnight at –20 °C. Pelleted proteins were resuspended in 6 M GuHCl/Tris pH 8.0 solution and sonicated for 5 min at maximum output (10-s on/off cycles). After a 5-min incubation at room temperature, samples underwent a second round of sonication and were later centrifuged at maximum speed for 10 min. DTT, at a final concentration of 5 mM, was added to the obtained supernatants and incubated for 30 min at 55 °C followed by incubation with 15 mM chloroacetamide for 15 min at room temperature in the dark. Before digestion, protein quantification was performed and trypsin (Pierce, trypsin protease MS-grade, Thermo Fisher Scientific) was added accordingly. Protein digestion was performed at 37 °C overnight, mildly shaking. After 12–14 h, trypsin was inactivated using 1.2% formic acid and samples were spun down at 3,000g for 10 min at room temperature. Samples were desalted, using desalting columns (Thermo Fisher Scientific) previously equilibrated and washed respectively with 100% acetonitrile and 0.5% formic acid, and eluted (0.5% formic acid and 50% acetonitrile). Peptides were consequently dried using SpeedVac Vacuum Concentrator and resuspended in 0.5% formic acid for mass spectrometry.

For liquid chromatography with tandem mass spectrometry analysis, peptides were separated on a 25-cm, 75- μ m internal diameter PicoFrit analytical column (New Objective) packed with 1.9- μ m ReproSil-Pur 120 C18-AQ media (Dr. Maisch) using an EASY-nLC 1000 (Thermo Fisher Scientific). The column was maintained at 50 °C. Buffer A and buffer B were 0.1% formic acid in water and 0.1% formic acid in 80% acetonitrile. Peptides were separated on a segmented gradient from 6% to 31% buffer B for 57 min and from 31% to 44% buffer B for 5 min at 250 nl min⁻¹. Eluting peptides were analysed on an Orbitrap Fusion Tribrid mass spectrometer (Thermo Fisher Scientific). Peptide precursor *m/z* measurements were carried out at 60,000 resolution in the 350–1,500 *m/z* range. The most intense precursors with charge state from 2 to 7 only were selected for higher-energy collisional dissociation (HCD) fragmentation using 27% normalized collision energy. The *m/z* values of the peptide fragments were measured at a resolution of 50,000 using an automatic gain control (AGC) target of 2×10^{-5} and 86-ms maximum injection time. The cycle time was set to 1 s. Upon fragmentation, precursors were put on a dynamic exclusion list for 45 s.

For protein identification and quantification, the raw data were analysed with MaxQuant version 1.6.1.0 (ref. ³⁶) using the integrated Andromeda search engine³⁷. Peptide fragmentation spectra were searched against the canonical sequences of the human reference proteome (proteome ID UP000005640, downloaded September 2018 from UniProt). Methionine oxidation and protein N-terminal acetylation were set as variable modifications; cysteine carbamidomethylation was set as fixed modification. The digestion parameters were set to 'specific' and 'Trypsin/P'. The minimum number of peptides and razor peptides for protein identification was 1; the minimum number of unique peptides was 0. Protein identification was performed at a peptide spectrum matches and protein false discovery rate of 0.01. The 'second peptide' option was on. Successful identifications were transferred between the fractions using the 'Match between runs' option. Differential expression analysis was performed using limma, version 3.34.9 (ref. ³⁸) in R, version 3.4.3.

Cryo-EM data collection and image processing

For cryo-EM analysis, 3 µl of approximately 100 nM mitoribosome was applied onto a glow-discharged (20 mA for 30 s) holey-carbon grid (Quantifoil R2/1 or R2/2, copper, mesh 300) coated with continuous carbon (of approximately 3-nm thickness) and incubated for 30 s in a controlled environment of 100% humidity at 4 °C. The grids were blotted for 3 s, followed by plunge-freezing in liquid ethane, using a Vitrobot MKIV (FEI/Thermo Fisher). The datasets were collected on a FEI Titan Krios (FEI/Thermo Fisher) transmission electron microscope operated at 300 keV with a slit width of 20 eV on a GIF quantum energy filter (Gatan). A K2 Summit detector (Gatan) was used at a pixel size of 0.81 Å or 0.83 Å (magnification of ×165,000) with a dose of 30–32 electrons per Å² fractionated over 20 frames. A defocus range of 0.8–3.8 µm was used. Detailed parameters are listed in Supplementary Tables 1 and 2.

Beam-induced motion correction was performed for all datasets using RELION 3.0 (ref. 39). Movie stacks were motion corrected and dose weighted using MotioCor2 (ref. 40). Motion-corrected micrographs were used for contrast transfer function (CTF) estimation with GCTF⁴¹. Particles were picked by Gautomatch (<https://www.mrc-lmb.cam.ac.uk/kzhang>) with reference-free, followed by reference-aided particle picking procedures. The reference-based pickings of SSU and LSU particles were done separately, using their corresponding picking references. Reference-free 2D classification was carried out to sort useful particles from falsely picked objects, which were then subjected to 3D refinement, followed by a 3D classification with local-angular search. UCFS Chimera⁴² was used to visualize and interpret the maps. 3D classes corresponding to unaligned or low-quality particles were removed. Well-resolved classes were pooled and subjected to 3D refinement and CTF refinement (beam-tilt, per-particle defocus and per-micrograph astigmatism) by RELION 3.1 (ref. 43), followed by Bayesian polishing. Particles were separated into multi-optics groups based on acquisition areas and date of data collection. A second round of 3D refinement and CTF refinement (beam-tilt, trefoil and fourth-order aberrations, magnification anisotropy, per-particle defocus and per-micrograph astigmatism) were performed, followed by 3D refinement.

To classify the SSU states, non-align focus 3D classifications with particle-signal subtraction using the mask covering the factor binding were done

with RELION 3.1 (Extended Data Figs. 2 and 3). The particles of each state were pooled, the subtracted signal was reverted and 3D refinement was done with the corresponding solvent mask. To improve the local resolution, the several local masks were prepared and used for local-masked 3D refinements (Extended Data Figs. 2 and 3 and Supplementary Tables 1 and 2). Nominal resolutions are based on gold standard, applying the 0.143 criterion on the Fourier shell correlation between reconstructed half-maps. Maps were subjected to B-factor sharpening and local-resolution filtering by RELION 3.1, superposed to the overall map and combined for the model refinement.

Model building, refinement and analysis

The starting models for SSU was Protein Data Bank (PDB) ID 6RW4 (ref. 2), whereas those of LSU were PDB IDs 6ZM5 (ref. 4) and 5OOM⁴⁴. These SSU and LSU models were rigid body fitted into the maps, followed by manual revision. Initial models of RBFA, TFB1M and METTL15 were generated by SWISS-MODEL⁴⁵ using PDB IDs 2E7G, 4GC9 and 1WG8, respectively, as templates. Ligands and specific extensions or insertions were built manually based on the density. Secondary-structure information prediction by PSIPRED⁴⁶ was also considered for low-resolution regions. mtIF3 and mtIF2 models were modified from previous work² (PDB IDs 6RW4 and 6RW5). fMet-tRNA^{Met} was from PDB ID 6GAZ (ref. 3) with the addition of the modification of f⁵C, whereas the mRNA was manually built into the density. The CTD of bL12m was generated from PDB ID 1CTF. Coot 0.9 with Ramachandran and torsion restraints⁴⁷ was used for manual fitting and revision of the model.

Water molecules were automatically picked by Coot, followed by manual revision. Geometrical restraints of modified residues and ligands were calculated by Grade Web Server (<http://grade.globalphasing.org>) or obtained from the library of CCP4 7.0 (ref. 48). Hydrogens were added to the molecules except for waters by REFMAC5 (ref. 49).

Final models were subjected to refinement of energy minimization and atomic displacement parameters (ADP) estimation by Phenix.real_space_refine v1.18 (ref. 50) with rotamer restraints without

Ramachandran restraints, against the composed maps with B-factor sharpening and local-resolution filtering. Reference restraints were also applied for non-modified protein residues, using the input models from Coot as the reference. Metal-coordination restraints were generated by ReadySet in the PHENIX suite and used for the refinement with some modifications. Non-canonical covalent bond restraints between non-modified residues and modified residue or ligand were prepared manually and used. Refined models were validated with MolProbity⁵¹ and EMRinger⁵² in the PHENIX suite. Model refinement statistics are listed in Supplementary Tables 1 and 2. UCSF ChimeraX 0.91 (ref. ⁵³) was used to make the figures.

Reporting summary

Further information on research design is available in the [Nature Research Reporting Summary](#) linked to this paper.

Data availability

The atomic coordinates have been deposited in the RCSB PDB and the EM maps have been deposited in the Electron Microscopy Data Bank under the following accession numbers, respectively: [7PNT](#) and [EMD-13551](#) (pre-SSU-1), [7PNU](#) and [EMD-13552](#) (pre-SSU-2), [7PNV](#) and [EMD-13553](#) (pre-SSU-3c), [7PNW](#) and [EMD-13554](#) (mature SSU), [7PNX](#) and [EMD-13555](#) (pre-SSU-3a), [7PNY](#) and [EMD-13556](#) (pre-SSU-3b), [7PNZ](#) and [EMD-13557](#) (pre-SSU-3c), [7PO0](#) and [EMD-13558](#) (pre-SSU-4), [7PO1](#) and [EMD-13559](#) (PIC-1), [7PO2](#) and [EMD-13560](#) (IC), [7PO3](#) and [EMD-135561](#) (mature SSU), [7PO4](#) and [EMD-135562](#) (pre-LSU). The following atomic coordinates were used in this study: [7BOG](#) (*Escherichia coli* small ribosomal subunit), [6RW4](#) (human SSU with mitochondrial IF3), [6RW5](#) (human SSU with mitochondrial IF3 and IF2), [6ZM5](#) (human mitoribosome in complex with OXA1L), [5OOM](#) (assembly intermediate of human LSU), [2E7G](#) (RBFA from human mitochondrial precursor), [4GC9](#) (TFB1M in complex with SAM), [1WG8](#) (SAM-dependent methyltransferase from *Thermus thermophilus*), [6GAZ](#) (mammalian mitochondrial translation IC) and [1CTF](#) (L7/L12 protein). Mass spectrometry data are available via ProteomeXchange with identifier PXD031678.

References

1. Amunts, A., Brown, A., Toots, J., Scheres, S. H. & Ramakrishnan, V. The structure of the human mitochondrial ribosome. *Science* **348**, 95–98 (2015).
2. Khawaja, A. et al. Distinct pre-initiation steps in human mitochondrial translation. *Nat. Commun.* **11**, 2932 (2020).
3. Kummer, E. et al. Unique features of mammalian mitochondrial translation initiation revealed by cryo-EM. *Nature* **560**, 263–267 (2018).
4. Itoh, Y. et al. Mechanism of membrane-tethered mitochondrial protein synthesis. *Science* **371**, 846–849 (2021).
5. Aibara, S., Singh, V., Modelska, A. & Amunts, A. Structural basis of mitochondrial translation. *eLife* **9**, e58362 (2020).
6. Desai, N. et al. Elongational stalling activates mitoribosome-associated quality control. *Science* **370**, 1105–1110 (2020).
7. Kummer, E. & Ban, N. Structural insights into mammalian mitochondrial translation elongation catalyzed by Mt efg1. *EMBO J.* **39**, e104820 (2020).
8. Kummer, E., Schubert, K. N., Schoenhet, T., Scaiola, A. & Ban, N. Structural basis of translation termination, rescue, and recycling in mammalian mitochondria. *Mol. Cell* **81**, 2566–2582.e6 (2021).
9. Itoh, Y. et al. Structural basis of streptomycin off-target binding to human mitoribosome. Preprint at *bioRxiv* <https://doi.org/10.1101/2022.02.02.478878> (2022).
10. Schedlbauer, A. et al. A conserved rRNA switch is central to decoding site maturation on the small ribosomal subunit. *Sci. Adv.* **7**, eabf7547 (2021).

11. Stephan, N. C., Ries, A. B., Boehringer, D. & Ban, N. Structural basis of successive adenosine modifications by the conserved ribosomal methyltransferase KSGA. *Nucleic Acids Res.* **49**, 6389–6398 (2021).
12. Du, Y. et al. Cryo-EM structure of 90S small ribosomal subunit precursors in transition states. *Science* **369**, 1477–1481 (2020).
13. Cheng, J. et al. 90S pre-ribosome transformation into the primordial 40S subunit. *Science* **369**, 1470–1476 (2020).
14. Singh, S., Vanden Broeck, A., Miller, L., Chaker-Margot, M. & Klinge, S. Nucleolar maturation of the human small subunit processome. *Science* **373**, eabj5338 (2021).
15. Lopez Sanchez, M. I., Krüger, A., Shiriaev, D. I., Liu, Y. & Rorbach, J. Human mitoribosome biogenesis and its emerging links to disease. *Int. J. Mol. Sci.* **22**, 3827 (2021).
16. Laptev, I. et al. Mouse Trmt2b protein is a dual specific mitochondrial methyltransferase responsible for m⁵U formation in both tRNA and rRNA. *RNA Biol.* **17**, 441–450 (2019).
17. Powell, C. A. & Minczuk, M. TRMT2B is responsible for both tRNA and rRNA m⁵U-methylation in human mitochondria. *RNA Biol.* **17**, 451–462 (2020).
18. Datta, P. P. et al. Structural aspects of RBFA action during small ribosomal subunit assembly. *Mol. Cell* **28**, 434–445 (2007).
19. Guja, K. E. et al. Structural basis for S-adenosylmethionine binding and methyltransferase activity by mitochondrial transcription factor B1. *Nucleic Acids Res.* **41**, 7947–7959 (2013).
20. Liu, X. et al. Structural insights into dimethylation of 12S rRNA by TFB1M: indispensable role in translation of mitochondrial genes and mitochondrial function. *Nucleic Acids Res.* **47**, 7648–7665 (2019).
21. Rorbach, J. et al. MRM2 and MRM3 are involved in biogenesis of the large subunit of the mitochondrial ribosome. *Mol. Biol. Cell* **25**, 2542–

2555 (2014).

22. Haute, L. V. et al. METTL15 introduces N4-methylcytidine into human mitochondrial 12S rRNA and is required for mitoribosome biogenesis. *Nucleic Acids Res.* **47**, 10267–10281 (2019).
23. Laptev, I. et al. METTL15 interacts with the assembly intermediate of murine mitochondrial small ribosomal subunit to form m4c840 12S rRNA residue. *Nucleic Acids Res.* **48**, 8022–8034 (2020).
24. Chen, H. et al. The human mitochondrial 12S rRNA m⁴C methyltransferase METTL15 is required for mitochondrial function. *J. Biol. Chem.* **295**, 8505–8513 (2020).
25. Maksimova, E. M. et al. Rbfa is involved in two important stages of 30S subunit assembly: formation of the central pseudoknot and docking of helix 44 to the decoding center. *Int. J. Mol. Sci.* **22**, 6140 (2021).
26. Jumper, J. et al. Highly accurate protein structure prediction with alphafold. *Nature* **596**, 583–589 (2021).
27. Rudler, D. L. et al. Fidelity of translation initiation is required for coordinated respiratory complex assembly. *Sci. Adv.* **5**, eaay2118 (2019).
28. Hussain, T., Llácer, J. L., Wimberly, B. T., Kieft, J. S. & Ramakrishnan, V. Large-scale movements of IF3 and tRNA during bacterial translation initiation. *Cell* **167**, 133–144.e13 (2016).
29. Lenarčič, T. et al. Mitoribosomal small subunit maturation involves formation of initiation-like complexes. *Proc. Natl Acad. Sci. USA* **119**, e2114710118 (2022).
30. Ramrath, D. J. et al. Evolutionary shift toward protein-based architecture in trypanosomal mitochondrial ribosomes. *Science* **362**, eaau7735 (2018).
31. Itoh, Y., Naschberger, A., Mortezaei, N., Herrmann, J. M. & Amunts, A. Analysis of translating mitoribosome reveals functional

characteristics of translation in mitochondria of fungi. *Nat. Commun.* **11**, 5187 (2020).

32. Tobiasson, V. & Amunts, A. Ciliate mitoribosome illuminates evolutionary steps of mitochondrial translation. *eLife* **9**, e59264 (2020).
33. Maiti, P., Kim, H.-J., Tu, Y.-T. & Barrientos, A. Human GTPBP10 is required for mitoribosome maturation. *Nucleic Acids Res.* **46**, 11423–11437 (2018).
34. Lavdovskaia, E. et al. The human OBG protein GTPBP10 is involved in mitoribosomal biogenesis. *Nucleic Acids Res.* **46**, 8471–8482 (2018).
35. Van Haute, L., Powell, C. A. & Minczuk, M. Dealing with an unconventional genetic code in mitochondria: the biogenesis and pathogenic defects of the 5-formylcytosine modification in mitochondrial tRNA^{Met}. *Biomolecules* **7**, 24 (2017).
36. Cox, J. & Mann, M. MaxQuant enables high peptide identification rates, individualized P.P.B.-range mass accuracies and proteome-wide protein quantification. *Nat. Biotechnol.* **26**, 1367–1372 (2008).
37. Cox, J. et al. Andromeda: a peptide search engine integrated into the maxquant environment. *J. Proteome Res.* **10**, 1794–1805 (2011).
38. Ritchie, M. E. et al. Limma powers differential expression analyses for RNA-sequencing and microarray studies. *Nucleic Acids Res.* **43**, e47 (2015).
39. Zivanov, J. et al. New tools for automated high-resolution cryo-EM structure determination in Relion-3. *eLife* **7**, e42166 (2018).
40. Zheng, S. Q. et al. Motioncor2: anisotropic correction of beam-induced motion for improved cryo-electron microscopy. *Nat. Methods* **14**, 331–332 (2017).
41. Zhang, K. GCTF: real-time CTF determination and correction. *J. Struct. Biol.* **193**, 1–12 (2016).

42. Pettersen, E. F. et al. UCSF Chimera—a visualization system for exploratory research and analysis. *J. Comput. Chem.* **25**, 1605–1612 (2004).
43. Zivanov, J., Nakane, T. & Scheres, S. H. Estimation of high-order aberrations and anisotropic magnification from Cryo-EM data sets in Relion-3.1. *IUCrJ* **7**, 253–267 (2020).
44. Brown, A. et al. Structures of the human mitochondrial ribosome in native states of assembly. *Nat. Struct. Mol. Biol.* **24**, 866–869 (2017).
45. Waterhouse, A. et al. Swiss-model: homology modelling of protein structures and complexes. *Nucleic Acids Res.* **46**, W296–W303 (2018).
46. Buchan, D. W. & Jones, D. T. The PSIPRED protein analysis workbench: 20 years on. *Nucleic Acids Res.* **47**, W402–W407 (2019).
47. Emsley, P., Lohkamp, B., Scott, W. G. & Cowtan, K. Features and development of Coot. *Acta Crystallogr. D* **66**, 486–501 (2010).
48. Winn, M. D. et al. Overview of the CCP4 suite and current developments. *Acta Crystallogr. D* **67**, 235–242 (2011).
49. Murshudov, G. N. et al. REFMAC5 for the refinement of macromolecular crystal structures. *Acta Crystallogr. D* **67**, 355–367 (2011).
50. Liebschner, D. et al. Macromolecular structure determination using X-rays, neutrons and electrons: recent developments in Phenix. *Acta Crystallogr. D* **75**, 861–877 (2019).
51. Williams, C. J. et al. Molprobity: more and better reference data for improved all-atom structure validation. *Protein Sci.* **27**, 293–315 (2017).
52. Barad, B. A. et al. Emringer: side chain-directed model and map validation for 3D cryo-electron microscopy. *Nat. Methods* **12**, 943–946 (2015).

53. Goddard, T. D. et al. UCSF ChimeraX: meeting modern challenges in visualization and analysis. *Protein Sci.* **27**, 14–25 (2017).
54. Nowinski, S. M., Van Vranken, J. G., Dove, K. K. & Rutter, J. Impact of mitochondrial fatty acid synthesis on mitochondrial biogenesis. *Curr. Biol.* **28**, R1212–R1219 (2018).
55. Masud, A. J., Kastaniotis, A. J., Rahman, M. T., Autio, K. J. & Hiltunen, J. K. Mitochondrial acyl carrier protein (ACP) at the interface of metabolic state sensing and mitochondrial function. *Biochim. Biophys. Acta Mol. Cell Res.* **1866**, 118540 (2019).

Acknowledgements

We thank Diamond Light Source for access to eBIC (funded by the Wellcome Trust, MRC and BBSRC) under proposal BI21643-4 with support from A. Klyszejko and Y. Song; the European Molecular Biology Laboratory for access to the cryo-EM facility under iNEXT proposal PID 4231 (funded by Horizon2020) with support from W. Hagen and F. Weis; SciLifeLab for access to the cryo-EM Swedish National Facility (funded by KAW, EPS and Kempe foundations); the Clinical Proteomics Mass Spectrometry facility of SciLifeLab; the Swedish Foundation for Strategic Research (FFL15:0325); the Ragnar Söderberg Foundation (M44/16); the European Research Council (ERC-2018-StG-805230); the Knut and Alice Wallenberg Foundation (2018.0080); the Max Planck Institute; and the Karolinska Institutet. Y.I. was supported by H2020-MSCA-IF-2017 (799399-Itohribo). J.R. is supported by the Wallenberg Fellowship Program (WAF 2017). A.A. is supported by the EMBO Young Investigator Program. P.S. is supported by Institute of Functional Genomics of the Lomonosov Moscow State University state funding.

Funding

Open access funding provided by Stockholm University.

Author information

Author notes

1. These authors contributed equally: Yuzuru Itoh, Anas Khawaja

Authors and Affiliations

1. Science for Life Laboratory, Department of Biochemistry and Biophysics, Stockholm University, Solna, Sweden

Yuzuru Itoh & Alexey Amunts

2. Department of Medical Biochemistry and Biophysics, Karolinska Institute, Stockholm, Sweden

Anas Khawaja, Miriam Cipullo & Joanna Rorbach

3. Max Planck Institute for Biology of Ageing-Karolinska Institutet Laboratory, Karolinska Institutet, Stockholm, Sweden

Anas Khawaja, Miriam Cipullo & Joanna Rorbach

4. Center of Life Sciences, Skolkovo Institute of Science and Technology, Moscow, Russia

Ivan Laptev & Petr Sergiev

5. Department of Chemistry, Lomonosov Moscow State University, Moscow, Russia

Ivan Laptev & Petr Sergiev

6. Belozersky Institute of Physico-Chemical Biology, Lomonosov Moscow State University, Moscow, Russia

Ivan Laptev & Petr Sergiev

7. Proteomics Core Facility, Max-Planck-Institute for Biology of Ageing, Cologne, Germany

Ilian Atanassov

8. Institute of Functional Genomics, Lomonosov Moscow State University, Moscow, Russia

Petr Sergiev

Contributions

Y.I., A.K. and I.L. prepared the samples for cryo-EM. Y.I. collected and processed the cryo-EM data. Y.I. and A.K. built the models. Y.I. and A.A. carried out the structural analysis. A.K., M.C. and J.R. performed the biochemical characterization. I.A and M.C. performed the proteomic analysis. All authors contributed to data interpretation and manuscript writing.

Corresponding authors

Correspondence to [Joanna Rorbach](#) or [Alexey Amunts](#).

Ethics declarations

Competing interests

The authors declare no competing interests.

Peer review

Peer review information

Nature thanks Yaser Hashem, Ricarda Richter-Dennerlein and the other, anonymous, reviewer(s) for their contribution to the peer review of this work. [Peer reviewer reports](#) are available.

Additional information

Publisher's note Springer Nature remains neutral with regard to jurisdictional claims in published maps and institutional affiliations.

Extended data figures and tables

[Extended Data Fig. 1 Cryo-EM maps of preSSU complexes with assembly factors.](#)

The combined map of local-masked refined maps for each state with colored factors. Overall resolution and those of the local-masked refinement for shoulder and platform are listed for each state. Unfolded rRNA is indicated by orange boxes.

[Extended Data Fig. 2 Resolution and model validation for preSSU-1 and preSSU-2 states.](#)

a, Overall-refined map and combined map of the local-masked refinements colored by local resolution for each state. The local masks are shown on the right. **b**, Fourier Shell Correlation curves of the half maps and local-masked refinements. The 0.143 criterion is shown as dashed lines. The class preSSU-3c consists of particles that have the same protein content and conformation as the respective class in MRM3 knockout study presented in the Extended Data Fig. [3a](#).

[Extended Data Fig. 3 Resolutions and model validation for preSSU-3, preSSU-4.](#)

a, Overall-refined map and combined map of the local-masked refinements colored by local resolution for states preSSU-3 and preSSU-4. The local masks are shown on the right. **b**, Fourier Shell Correlation curves of the half maps and local-masked refinements for states preSSU-3 and presSSU-4. The 0.143 criterion is shown as dashed lines.

[Extended Data Fig. 4 Resolutions and model validation for PIC-1, IC states, and LSU.](#)

a, Overall-refined map and combined map of the local-masked refinements colored by local resolution for SSU, PIC-1, IC, LSU. The local masks are shown on the right. **b**, Fourier Shell Correlation curves of the half maps and local-masked refinements for SSU, PIC-1, IC, LSU. The 0.143 criterion is shown as dashed lines.

Extended Data Fig. 5 Comparison between mammalian mitochondrial and bacterial RBFA.

a, RBFA in mammalian mitochondria has a mito-specific N-terminal and C-terminal extensions illustrated in the structure from this study. These mito-specific extensions are nearly twice the size of protein and contribute to multiple functions during the ribosome assembly. Inset shows the superposition of RBFA in human mitochondria and *E. coli* (PDB ID: 7BOG). **b**, Pairwise sequence alignment of human and mouse mitochondrial RBFAs with their bacterial orthologs. The conserved amino acids are highlighted in blue. The mito-specific N and C-terminal extensions are indicated by rectangular boxes on top, and their amino acid sequences are colored in purple.

Extended Data Fig. 6 Structure of preSSU1 state and accompanying RBFA.

a, Superposition of rRNA shows the head rotation towards the A-site that exposes the P-site region. As a result of RBFA binding, uS7m is displaced (zoom in panels). **b**, The arrangement of RBFA in preSSU1 is incompatible with mS37 in SSU. It engages the C-terminal extension of bS6m in the binding, which is dislocated by 24 Å. The formed turn is just after a mitochondria-specific iron-sulfur cluster that is coordinated by bS6m and bS18m. **c**, RBFA:rRNA contacts with SSU. Arg166, His167, and Asn177 of RBFA interact with the rRNA 3'-end, which interacts with mS37 in the mature SSU. Thr132, Ser136, and Arg139 at β1-β2 loop of RBFA interact with the rRNA h28.

Extended Data Fig. 7 Structures of preSSU1 and preSSU-2 states and accompanying structural changes.

a, TFB1M:rRNA interactions and comparison with the crystal structure of h45:TFB1M:SAM¹⁹. TFB1M interacts with the rRNA h23, h24, h27 and h45. The C-terminal α -helix, which is disordered in the crystal structure, further links TFB1M from h24 to the platform rRNA h23 through Arg323, Lys327, Lys330 and Gly333. **b**, The cryo-EM density maps with the models, comparing the N-terminal helix of mS38 between preSSU-1 and preSSU-2. The mS38 N-terminal helix is disordered in preSSU-1, whereas it is mostly mature in preSSU-2 where rRNA is more ordered.

Extended Data Fig. 8 Cryo-EM structure of the preLSU from MRM3 knockout cells.

Cryo-EM map of preLSU with the rRNA secondary structure diagram, where the unstructured regions are gray, A-loop red. The LSU assembly intermediate is consistent with a previous native preLSU study⁴⁴, where the interfacial rRNA is unstructured, and the associated protein module MALSU1:L0R8F8:ACP prevents a premature subunit joining. In the current study, the rRNA is even more unstructured, encompassing H65-71, H89-93 with the peptidyl transferase centre, suggesting an earlier state. A density near Ser112 of the ACP that could not be accounted for by a polypeptide. The 4'-phosphopantetheine with laurate as thioester fits the density well. Therefore, ACP is found on the preLSU with its substrate. Since ACP is also required for *de novo* synthesis of fatty acid in mitochondria, as well as assembly of complex I, and iron-sulfur cluster synthesis, our study further supports that it represents a coordinative signaling molecule for metabolic sensing with regard to mitochondrial biogenesis^{54,55}.

Extended Data Fig. 9 RBFA conformational change between preSSU-2 and preSSU-3, and structures of preSSU-3a,b,c states.

a, METTL15 from preSSU3 is superimposed with RBFA-*in* from preSSU-2 showing their clash. **b**, Comparison between RBFA-*in*, RBFA-*out*, *AlphaFold2* prediction shows that the predicted conformation is different from the known structure of RBFA-*in*. **c**, RBFA:METTL15 complex prediction with *AlphaFold2* shows the interaction through the RBFA CTE helix found in the structure. **d**, In preSSU-3a, METTL15 has tight interactions with the rRNA and the mito-specific insertion forms an α -helix.

The tip of h24 is shifted, which opens the space between h24 and h44, and shifts the entire SSU platform. In preSSU-3b, the mito-specific insertion is mostly disordered and METTL15 has a looser contact to h24, resulting in the mature conformation of h24, whereas h23 is extended and detached from the tip of h24. In preSSU-3c, the METTL15:rRNA interactions are the same in preSSU-2b and the rRNA is completely folded. **e**, Interactions between METTL15 and rRNA. The mito-specific insertion of METTL15 interacts with h23, h24, and h45, mainly through Asn343, Leu344 (mainchain), Val346 (mainchain) Arg347, and Asn349.

Extended Data Fig. 10 Biochemical characterization of MRM3 and GTPBP10 knockout cells.

a, CRISPR/Cas9 mediated targeted knockout of mS37, MRM3 and GTPBP10. The schematics illustrates the guide RNA design for targeted exon in each corresponding gene. Sequencing results and alignment with the wild type validates the knockouts indicated by bp deletions (gray dotted lines) and insertions. **b**, Metabolic labeling with [³⁵S]-methionine of mitochondrial translation products in wild type (WT) HEK293T, MRM3 and GTPBP10 knockouts and MRM3- and GTPBP10 rescue cells. Coomassie blue stained gel (bottom panel) is shown as a loading control. **c**, Mitoribosomal sedimentation on 10-30% sucrose gradient for WT HEK293T, MRM3 and GTPBP10 knockout cells. In panels b and c, representative gels from three independent biological experiments are shown. For source data, see Supplementary Fig. 6.

Extended Data Fig. 11 Steady-states levels of mitoribosomal subunits and assembly factors in GTPBP10 and MRM3 knockout cells.

a, Steady-states levels of mitoribosomal subunits and assembly factors in GTPBP10 and MRM3 knockout cells. Steady-state levels of mitoribosomal proteins (uS16m, mS35, mS37, mL37), assembly and initiation factors (MRM3, RBFA, METTL15, IF3) in the WT HEK293T, MRM3 knockout, MRM3- rescue, GTPBP10 knockout and GTPBP10-rescue cells were analyzed by immunoblotting with corresponding antibodies. SDHA was used as a loading control. Representative gels from three independent

biological experiments are shown. **b**, SILAC-based proteomic analysis of sucrose gradient fractions. Protein steady-state levels of SSU (yellow) and LSU (blue) components in MRM3^{KO} cells are presented relative to WT HEK293T (n = 3 biologically independent experiments). Limma t-test was performed; the adjusted P-value for mS37 is 0.000521. For source data, see Supplementary Fig. 4.

Extended Data Fig. 12 Structure of the Initiation Complex (IC).

a, The mRNA can be traced all the way from the mS39 docking platform, through the channel entry formed by uS5m-uS9m, A-site, P-site (pairing with tRNA^{Met}), and E-site (contacting uS7m). The mRNA residues at the E-site correspond to the 5' untranslated region (UTR) that fits with a purine in the position -1, and pyrimidines in the positions -2 and -3. Out of all the mitochondrial mRNAs, only two, namely those of COX1 and ND4, have the fitting residues, CUG and CCA, respectively. For the position -1, the density fits better with G than A, due to the differences in amino group locations 2 vs 6. In addition, in the start codon, the density supports AUG over AUA, and +4 fits pyrimidine, which is also present in COX1. Therefore, the cryo-EM map singles out COX1 as an enriched mRNA, associated with the resolved translation initiation complex. Structurally, the three 5' UTR residues in the E-site are stacked with their bases against each other and against Gly164 and Gly165 of uS7m, whereas a configuration of one or two UTR residues would not stack with uS7m in this region. The specific enrichment of the COX1 mRNA complex most likely represents the most stable variant of the pool of translation initiation complexes charged with mRNA that was trapped in our structure. **b**, Comparison with a reconstituted monosome complex. In addition to similar relative location of mtIF2 and mS37, a weak density that fits the C-terminal domain (CTD) of bL12m is observed next to the G-domain of mtIF2 (density shown as mesh). The bL12m CTD is also present in the complete initiation complex.

Supplementary information

Supplementary Information

This file contains Supplementary Figures 1–8; Supplementary Tables 1–4 and legends for Supplementary Videos 1–4

Reporting Summary

Peer Review File

Supplementary Video 1

Supplementary Video 2

Supplementary Video 3

Supplementary Video 4

Rights and permissions

Open Access This article is licensed under a Creative Commons Attribution 4.0 International License, which permits use, sharing, adaptation, distribution and reproduction in any medium or format, as long as you give appropriate credit to the original author(s) and the source, provide a link to the Creative Commons license, and indicate if changes were made. The images or other third party material in this article are included in the article's Creative Commons license, unless indicated otherwise in a credit line to the material. If material is not included in the article's Creative Commons license and your intended use is not permitted by statutory regulation or exceeds the permitted use, you will need to obtain permission directly from the copyright holder. To view a copy of this license, visit <http://creativecommons.org/licenses/by/4.0/>.

Reprints and Permissions

About this article

Cite this article

Itoh, Y., Khawaja, A., Laptev, I. *et al.* Mechanism of mitoribosomal small subunit biogenesis and preinitiation. *Nature* **606**, 603–608 (2022).
<https://doi.org/10.1038/s41586-022-04795-x>

- Received: 21 November 2021
- Accepted: 22 April 2022
- Published: 08 June 2022
- Issue Date: 16 June 2022
- DOI: <https://doi.org/10.1038/s41586-022-04795-x>

Share this article

Anyone you share the following link with will be able to read this content:

[Get shareable link](#)

Sorry, a shareable link is not currently available for this article.

[Copy to clipboard](#)

Provided by the Springer Nature SharedIt content-sharing initiative

This article was downloaded by **calibre** from <https://www.nature.com/articles/s41586-022-04795-x>

Amendments & Corrections

- [**Author Correction: Assembly of the basal mantle structure beneath Africa**](#) [27 May 2022]
-
- [**Author Correction: Fundamental immune–oncogenicity trade-offs define driver mutation fitness**](#) [31 May 2022]
-
- [**Publisher Correction: A stable hippocampal code in freely flying bats**](#) [30 May 2022]
-

- Author Correction
- [Published: 27 May 2022](#)

Author Correction: Assembly of the basal mantle structure beneath Africa

- [Nicolas Flament](#) ,
- [Ömer F. Bodur](#),
- [Simon E. Williams](#) &
- [Andrew S. Merdith](#)

Nature volume **606**, page E4 (2022)

- 390 Accesses
- 12 Altmetric
- [Metrics details](#)

The [Original Article](#) was published on 30 March 2022

Correction to: *Nature* <https://doi.org/10.1038/s41586-022-04538-y>
Published online 30 March 2022

In the version of this article initially published, there were labeling errors in the *x*-axis tick mark labels for Fig. 3b–d. The Fig. 3b labels now reading “0.70, 0.80, 0.90” appeared initially as “0.65, 0.70, 0.75,” the Fig. 3c labels now reading “−5, 0” originally read “−6, −4”, and the Fig. 3d labels now reading “0, 1.0” originally read “0, 0.5”. The *x*-axis labels have been corrected in the HTML and PDF versions of the article.

Author information

Author notes

1. Andrew S. Merdith

Present address: School of Earth and Environment, University of Leeds, Leeds, UK

Authors and Affiliations

1. GeoQuEST Research Centre, School of Earth, Atmospheric and Life Sciences, University of Wollongong, Wollongong, New South Wales, Australia

Nicolas Flament & Ömer F. Bodur

2. Department of Geology, Northwest University, Xi'an, China

Simon E. Williams

3. UnivLyon, Université Lyon 1, ENS de Lyon, CNRS, UMR 5276 LGL-TPE, Villeurbanne, France

Andrew S. Merdith

Corresponding author

Correspondence to [Nicolas Flament](#).

Rights and permissions

[Reprints and Permissions](#)

About this article

Cite this article

Flament, N., Bodur, Ö.F., Williams, S.E. *et al.* Author Correction: Assembly of the basal mantle structure beneath Africa. *Nature* **606**, E4 (2022). <https://doi.org/10.1038/s41586-022-04886-9>

- Published: 27 May 2022
- Issue Date: 16 June 2022
- DOI: <https://doi.org/10.1038/s41586-022-04886-9>

Share this article

Anyone you share the following link with will be able to read this content:

[Get shareable link](#)

Sorry, a shareable link is not currently available for this article.

[Copy to clipboard](#)

Provided by the Springer Nature SharedIt content-sharing initiative

This article was downloaded by **calibre** from <https://www.nature.com/articles/s41586-022-04886-9>

- Author Correction
- Open Access
- [Published: 31 May 2022](#)

Author Correction: Fundamental immune–oncogenicity trade-offs define driver mutation fitness

- [David Hoyos](#),
- [Roberta Zappasodi](#),
- [Isabell Schulze](#),
- [Zachary Sethna](#),
- [Kelvin César de Andrade](#),
- [Dean F. Bajorin](#),
- [Chaitanya Bandlamudi](#),
- [Margaret K. Callahan](#),
- [Samuel A. Funt](#),
- [Sine R. Hadrup](#),
- [Jeppe S. Holm](#),
- [Jonathan E. Rosenberg](#),
- [Sohrab P. Shah](#),
- [Ignacio Vázquez-García](#),
- [Britta Weigelt](#),
- [Michelle Wu](#),
- [Dmitriy Zamarin](#),
- [Laura F. Campitelli](#),
- [Edward J. Osborne](#),
- [Mark Klinger](#),
- [Harlan S. Robins](#),
- [Payal P. Khincha](#),
- [Sharon A. Savage](#),
- [Vinod P. Balachandran](#),

- [Jedd D. Wolchok](#),
- [Matthew D. Hellmann](#),
- [Taha Merghoub](#) ,
- [Arnold J. Levine](#),
- [Marta Łuksza](#) &
- [Benjamin D. Greenbaum](#)

Nature volume **606**, page E5 (2022)

- 378 Accesses
- 3 Altmetric
- [Metrics details](#)

The [Original Article](#) was published on 11 May 2022

Correction to: *Nature* <https://doi.org/10.1038/s41586-022-4696-z>, published online 11 May 2022.

In the version of this article initially published, the surname of author Chaitanya Bandlamudi was misspelt as Bandlamundi. The error has been corrected in the HTML and PDF versions of the article

Author information

Author notes

1. These authors contributed equally: David Hoyos, Roberta Zappasodi
2. These authors jointly supervised this work: Taha Merghoub, Arnold J. Levine, Marta Łuksza, Benjamin D. Greenbaum

Authors and Affiliations

1. Computational Oncology, Department of Epidemiology & Biostatistics, Memorial Sloan Kettering Cancer Center, New York, NY, USA

David Hoyos, Zachary Sethna, Sohrab P. Shah, Ignacio Vázquez-García & Benjamin D. Greenbaum

2. Swim Across America Laboratory and Ludwig Collaborative, Immunology Program, Parker Institute for Cancer Immunotherapy, Memorial Sloan Kettering Cancer Center, New York, NY, USA

Roberta Zappasodi, Isabell Schulze, Dmitriy Zamarin, Jedd D. Wolchok & Taha Merghoub

3. Department of Medicine, Weill Cornell Medical College, New York, NY, USA

Roberta Zappasodi, Dean F. Bajorin, Margaret K. Callahan, Samuel A. Funt, Jonathan E. Rosenberg, Dmitriy Zamarin, Vinod P. Balachandran, Jedd D. Wolchok, Matthew D. Hellmann & Taha Merghoub

4. Parker Institute for Cancer Immunotherapy, Memorial Sloan Kettering Cancer Center, New York, NY, USA

Roberta Zappasodi, Isabell Schulze, Vinod P. Balachandran, Jedd D. Wolchok, Matthew D. Hellmann & Taha Merghoub

5. Immunology and Microbial Pathogenesis Program, Weill Cornell Graduate School of Medical Sciences, New York, NY, USA

Roberta Zappasodi

6. Hepatopancreatobiliary Service, Department of Surgery, Memorial Sloan Kettering Cancer Center, New York, NY, USA

Zachary Sethna & Vinod P. Balachandran

7. Department of Medicine, Memorial Sloan Kettering Cancer Center, New York, NY, USA

Zachary Sethna, Dean F. Bajorin, Margaret K. Callahan, Samuel A. Funt, Jonathan E. Rosenberg, Dmitriy Zamarin & Vinod P. Balachandran

8. Division of Cancer Epidemiology and Genetics, Clinical Genetics Branch, National Cancer Institute, National Institutes of Health, Rockville, MD, USA

Kelvin César de Andrade, Payal P. Khincha & Sharon A. Savage

9. Department of Pathology and Laboratory Medicine, Memorial Sloan Kettering Cancer Center, New York, NY, USA

Chaitanya Bandlamudi & Britta Weigelt

10. Kravis Center for Molecular Oncology, Memorial Sloan Kettering Cancer Center, New York, NY, USA

Chaitanya Bandlamudi

11. Experimental and Translational Immunology, Health Technology, Technical University of Denmark, Lyngby, Denmark

Sine R. Hadrup & Jeppe S. Holm

12. Physiology, Biophysics & Systems Biology, Weill Cornell Medicine, Weill Cornell Medical College, New York, NY, USA

Sohrab P. Shah & Benjamin D. Greenbaum

13. Department of Surgery, Memorial Sloan Kettering Cancer Center, New York, NY, USA

Michelle Wu

14. Adaptive Biotechnologies, Seattle, WA, USA

Laura F. Campitelli, Edward J. Osborne, Mark Klinger & Harlan S. Robins

15. David M. Rubenstein Center for Pancreatic Cancer Research,
Memorial Sloan Kettering Cancer Center, New York, NY, USA

Vinod P. Balachandran

16. Human Oncology and Pathogenesis Program, Memorial Sloan
Kettering Cancer Center, New York, NY, USA

Jedd D. Wolchok & Taha Merghoub

17. Thoracic Oncology Service, Memorial Sloan Kettering Cancer Center,
New York, NY, USA

Matthew D. Hellmann

18. Simons Center for Systems Biology, Institute for Advanced Study,
Princeton, NJ, USA

Arnold J. Levine

19. Department of Oncological Sciences, Tisch Cancer Institute, Icahn
School of Medicine at Mount Sinai, New York, NY, USA

Marta Łuksza

Corresponding authors

Correspondence to [Roberta Zappasodi](#), [Taha Merghoub](#) or [Benjamin D. Greenbaum](#).

Rights and permissions

Open Access This article is licensed under a Creative Commons Attribution 4.0 International License, which permits use, sharing, adaptation, distribution and reproduction in any medium or format, as long

as you give appropriate credit to the original author(s) and the source, provide a link to the Creative Commons license, and indicate if changes were made. The images or other third party material in this article are included in the article's Creative Commons license, unless indicated otherwise in a credit line to the material. If material is not included in the article's Creative Commons license and your intended use is not permitted by statutory regulation or exceeds the permitted use, you will need to obtain permission directly from the copyright holder. To view a copy of this license, visit <http://creativecommons.org/licenses/by/4.0/>.

[Reprints and Permissions](#)

About this article

Cite this article

Hoyos, D., Zappasodi, R., Schulze, I. *et al.* Author Correction: Fundamental immune–oncogenicity trade-offs define driver mutation fitness. *Nature* **606**, E5 (2022). <https://doi.org/10.1038/s41586-022-04879-8>

- Published: 31 May 2022
- Issue Date: 16 June 2022
- DOI: <https://doi.org/10.1038/s41586-022-04879-8>

Share this article

Anyone you share the following link with will be able to read this content:

[Get shareable link](#)

Sorry, a shareable link is not currently available for this article.

[Copy to clipboard](#)

Provided by the Springer Nature SharedIt content-sharing initiative

This article was downloaded by **calibre** from <https://www.nature.com/articles/s41586-022-04879-8>

| [Section menu](#) | [Main menu](#) |

- Publisher Correction
- [Published: 30 May 2022](#)

Publisher Correction: A stable hippocampal code in freely flying bats

- [William A. Liberti III](#),
- [Tobias A. Schmid](#),
- [Angelo Forli](#),
- [Madeleine Snyder](#) &
- [Michael M. Yartsev](#)

Nature volume **606**, page E6 (2022)

- 347 Accesses
- 11 Altmetric
- [Metrics details](#)

The [Original Article](#) was published on 30 March 2022

Correction to: *Nature* <https://doi.org/10.1038/s41586-022-04560-0>
Published online 30 March 2022

In the version of this article initially published, there were labelling errors in the right-hand y-axis labels for the “Flight path 2” and “Flight path 3” in Fig. 2e, where the bottom lanes appeared as “Day 6” rather than “Day 5.” The labels have been corrected in the HTML and PDF versions of the article.

Author information

Author notes

1. These authors contributed equally: William A. Liberti III, Tobias A. Schmid

Authors and Affiliations

1. Department of Bioengineering, UC Berkeley, Berkeley, CA, USA

William A. Liberti III, Angelo Forli, Madeleine Snyder & Michael M. Yartsev

2. Helen Wills Neuroscience Institute, UC Berkeley, Berkeley, CA, USA

Tobias A. Schmid & Michael M. Yartsev

Corresponding author

Correspondence to [Michael M. Yartsev](#).

Rights and permissions

[Reprints and Permissions](#)

About this article

Cite this article

Liberti, W.A., Schmid, T.A., Forli, A. *et al.* Publisher Correction: A stable hippocampal code in freely flying bats. *Nature* **606**, E6 (2022).
<https://doi.org/10.1038/s41586-022-04885-w>

- Published: 30 May 2022

- Issue Date: 16 June 2022
- DOI: <https://doi.org/10.1038/s41586-022-04885-w>

Share this article

Anyone you share the following link with will be able to read this content:

[Get shareable link](#)

Sorry, a shareable link is not currently available for this article.

[Copy to clipboard](#)

Provided by the Springer Nature SharedIt content-sharing initiative

This article was downloaded by **calibre** from <https://www.nature.com/articles/s41586-022-04885-w>

| [Section menu](#) | [Main menu](#) |